Natural Resources Canada
Ressources naturelles Canada

GEOLOGICAL SURVEY OF CANADA
OPEN FILE 7838

Targeted Geoscience Initiative 4: Sediment-hosted Zn-Pb Deposits: Processes and Implications for Exploration

S. Paradis
Editor

2015

Canada

GEOLOGICAL SURVEY OF CANADA
OPEN FILE 7838

Targeted Geoscience Initiative 4: Sediment-hosted Zn-Pb Deposits: Processes and Implications for Exploration

S. Paradis (ed.)

Geological Survey of Canada, 9860 West Saanich Road, Sidney, British Columbia

Email: suzanne.paradis@nrcan-rncan.gc.ca

A Targeted Geoscience Initiatives 4 Contribution

2015

doi:10.4095/296328

Recommended citation
Paradis, S. (ed.), 2015. Targeted Geoscience Initiative 4: sediment-hosted Zn-Pb deposits: processes and implications for exploration; Geological Survey of Canada, Open File 7838, 297 p. doi:10.4095/296328

Table of Contents

Physico-geochemical characteristics of the hydrothermal system of sediment-hosted Zn-Pb deposits

Mineralogical, geochemical, and isotopic tools to vector to sediment-hosted Zn-Pb deposits

Processes controlling the surficial geochemical dispersion of metals around sediment-hosted Zn-Pb deposits

Regional-scale 3D geological modelling of the Purcell Basin, southern British Columbia

Preface

Sediment-hosted Zn-Pb deposits have been divided into two main subtypes, ‘clastic-dominated’ and ‘carbonate-dominated’ (Leach et al., 2005, 2010). The clastic-dominated deposits include SEDimentary EXhalative (SEDEX) mineralization hosted in shale, sandstone, siltstone, or mixed clastic rocks, and carbonate replacement mineralization in deep-water sedimentary rocks of basins. They typically formed in intracontinental or failed rift basins (e.g. Sullivan Pb-Zn-Ag deposit of the Purcell Basin) and rifted continental margins (e.g. Howard’s Pass and MacMillan Pass deposits of the Selwyn Basin). The term ‘carbonate-dominated’ refers to Mississippi Valley-type (MVT) deposits. These deposits occur mainly in platform carbonate sequences located in the foreland of orogenic belts or on the margin of active extensional basins (Leach et al., 2005, 2010; Wilkinson, 2014).

Sediment-hosted Zn-Pb deposits are primary sources for Zn and Pb, as well as significant sources of Ag, Au, Cu, Sb, Sn, barite, and fluorite. They account for more than 40% and 65% of the western world's Zn reserves and resources, respectively (Hunt, 2006). Although there are no sediment-hosted Zn-Pb deposits presently in production in Canada, there are several reasons, listed below, why a new look at these deposits is warranted.

1. Over the past 25 years, there has been a major decline in Canadian mineral reserves, and without sustained and effective exploration, the rate of Canadian Zn and Pb production will exceed the rate of additions to the reserves.
2. The current genetic model was formulated several decades ago, and many questions still remain unanswered. For example, controversy remains over the timing and genesis of the deposits of the Selwyn Basin: have they formed during, or soon after, deposition of their host sediments (i.e. syngenetic vs early diagenetic), or much later (epigenetic)?
3. Without the proper exploration tools, it is nearly impossible to identify sedimentary basins that can contain sediment-hosted Zn-Pb mineralization and at which stratigraphic level these deposits are most likely to occur.
4. New sediment-hosted Zn-Pb deposits may be buried far beneath the surface of the Earth. To find them, it is important to understand why certain sedimentary basins are enriched with Zn and Pb, while others are not. Knowing what controls the location, distribution and genesis of Zn-Pb districts is crucial to lowering the exploration risk inherent in searching for new deposits.
5. The mining industry is actively exploring for sediment-hosted Zn-Pb deposits (e.g. Howard’s Pass, Yukon, and Cirque and Akie, north-eastern British Columbia).

The papers in this open file are brief overviews of selected activities that were supported under the umbrella of the Targeted Geoscience Initiative 4 (TGI-4) program. TGI-4, a collaborative federal geoscience program, provided industry with the next generation of geoscience knowledge and innovative techniques to better understand, model, and detect buried mineral deposits, reducing some of the risks of exploration. The program focussed on seven ore systems, including SEDEX.

The papers presented in this open file will be superseded by publication of more detailed open files, theses, and refereed journal papers. Globally they represent a successful effort to better understand the genesis of Canadian sediment-hosted Zn-Pb deposits, and identify exploration tools and vectors towards mineralized domains within sedimentary basins.

The project was largely field- and laboratory-oriented and it brought together geology, mineralogy, geochemistry and three-dimensional basin reconstruction to improve our knowledge of these deposits in the Canadian Cordillera. The main objectives of the project were to:

- characterize the physico-geochemical processes of the hydrothermal system related to sediment-hosted Zn-Pb deposits,
- identify new mineralogical, geochemical, and isotopic tools to vector to sediment-hosted Zn-Pb deposits,
- understand the processes that control surficial geochemical dispersion of metals around sediment-hosted Zn-Pb deposits, and
- develop new methods for regional-scale 3D geological modelling in sedimentary basins.

This open file is divided into 4 parts following the above themes. The first part comprises papers focussing on processes related to the formation of sediment-hosted Zn-Pb deposits.

> **Paper 1** by Lydon (2015) *“The leachability of metals from sedimentary rocks”* provides quantitative information on one of the fundamental elements of the genetic model for SEDEX ore systems, i.e. can sediments in basins be the source for the ore metals and are there leaching windows during the course of burial metamorphism? To test this, the leachability of metals and other elements was measured on core samples of marine sedimentary rocks that represent burial depths ranging from 1 m to 20 km along a transect across western Canada. They range in age from modern Pacific Ocean sediments to Mesoproterozoic siliciclastic rocks of the Belt-Purcell Basin.
>
> **Paper 2** by Magnall et al. (2015) *“Widespread euxinic conditions are not a prerequisite for sediment-hosted base metal (Pb-Zn-Ba) mineralization at Macmillan Pass, Yukon”* challenges the current belief that the MacMillan Pass deposits involved synsedimentary precipitation of base metal sulphides from a euxinic water column following hydrothermal venting. The authors show that at Macmillan Pass the supporting evidences for this exhalative process are lacking. Detailed petrography followed by in-situ sulphur isotope microanalysis (secondary ion mass spectrometry - SIMS) of barite and pyrite shows that several generations of barite and two generations of pyrite formed during early diagenesis, pre-dating hydrothermal sulphides. All hydrothermal sulphides

(pyrite, sphalerite and galena) post-date and replace the diagenetic barite-pyrite assemblage. In situ sulphur isotope microanalyses support these observations.

Paper 3 by Gadd et al. (2015) *“In situ trace element and sulphur isotope analyses of pyrite constrain timing of mineralization and sources of sulphur in the Howard’s Pass SEDEX Zn-Pb District, Yukon”* carries the hydrothermal theme further by exploring the mineralizing processes within the Zn-Pb deposits of the Howard’s Pass district of the Selwyn Basin, and identifying minor and trace elements of hydrothermal origin that mimic the zonation within pyrite grains, and can be use as exploration tool. In situ sulphur isotope microanalyses done on galena and several generations of pyrite revealed the contribution of bacterially reduced and thermochemically reduced seawater sulphate.

The second part of the open file describes various mineralogical, geochemical, and isotopic tools that can be used to vector to sediment-hosted Zn-Pb deposits.

Paper 4 by Turner (2015) *“Base-metal enrichment in Stage-5 (mid-Cambrian) black shale of the Hess River Formation, Misty Creek Embayment, Selwyn Basin”* documents the lithostratigraphy and geochemistry (carbon isotopes and whole-rock geochemistry) of a succession containing deep-water turbiditic limestone and a >20 m-thick black shale interval with elevated base metal and barium content and geochemical evidence suggesting hydrothermal venting in the Misty Creek Embayment (Mackenzie Mountains, NT), a poorly known and economically underexplored part of the Selwyn Basin.

Paper 5 by Taylor et al. (2015) “*In situ sulphur isotope study of the Prairie Creek deposit, southern Mackenzie Mountains, Northwest Territories: Deciphering the conundrum of three deposit styles in one”* investigates the sulphur isotopes of three different styles of sulphide mineralization (Mississippi Valley-type (MVT), stratabound replacement, and quartz-carbonate-sulphide veins) within the Prairie Creek Embayment of the Selwyn Basin. This is done to uncover possible connections between the three styles of mineralization, including their likely temperatures of formation and any isotopic gradients that would indicate paleo-hydrothermal flow.

Paper 6 by Paradis (2015) *“Sulphides and nonsulphides of the Prairie Creek district; update on the isotope geochemistry”* continues on the theme of isotope geochemistry to improve our understanding of the genesis of these deposits. This paper reports results on stable and radiogenic isotopes (C, O, Sr) on carbonates from all three types of mineralization and associated oxidation zones at Prairie Creek. It presents a model that explains the transformation from sulphides to nonsulphides, and documents the fact that nonsulphides can form in cold and wet climatic conditions and be potentially economic.

Paper 7 by Peter et al. (2015) *"Application of visible-near infrared and short wave infrared spectroscopy to sediment-hosted Zn-Pb deposit exploration in the Selwyn Basin, Yukon"* explores the use of visible-near infrared and short wave infrared spectroscopy (VNIR-SWIR) in the exploration for sediment-hosted Zn-Pb deposits in Howard's Pass and Macmillan Pass districts of the Selwyn Basin.

The third part of the open file provides some insights into processes controlling the surficial geochemical dispersion of metals around the sediment-hosted Zn-Pb deposits of the Selwyn Basin.

Paper 8 by Stavinga et al. (2015) *"Geochemical and mineralogical controls on metal(loid) mobility in the oxide zone at Prairie Creek, Northwest Territories"* focuses on the characterization of the geochemical and mineralogical controls on metal(loid) mobility under mine waste disposal conditions, with particular attention to the metal-bearing nonsulphide minerals as a potential source of trace elements to the environment. The results have implications for assessing the economic value of the oxide zone and for predicting the geochemical controls on metal(loid) concentrations in drainage from future mine waste.

Paper 9 by Bryson et al. (2015) *"Geochemical signatures of the South MacMillan River in the MacMillan Pass, Yukon, including drainages from the Tom and Jason Pb-Zn deposits"* presents results from 17 sites along the South MacMillan River and some of its tributaries in the MacMillan Pass region of Yukon. It aims to characterize the geochemical signatures of stream waters of a system draining the sediment-hosted Zn-Pb Tom and Jason deposits and surrounding barren shales of the Devonian Earn Group.

The fourth part of this open file comprises several papers that outline the methods developed and the techniques used for the 3D structural-stratigraphic modelling of the Purcell Basin, hosts to the Sullivan SEDEX deposit.

Paper 10 by de Kemp et al. (2015) *"3D geological modelling of the Sullivan time horizon, Purcell Anticlinorium and Sullivan Mine, East Kootenay region, southeastern British Columbia"* provides an overview of the concepts behind the 3D geospatial model. It describes the management of geo-referenced surface and sub-surface data (stratigraphic, structural, and geophysical), 3D mathematical modelling, structural analysis and modelling, and detailed 3D modelling of the Sullivan Mine.

Paper 11 by Schetselaar et al. (2015) *"Drillhole database compilation from legacy archives in support of 3D geological modelling and mineral exploration in the Purcell Anticlinorium, British Columbia"* summarizes the compilation methodology used to build a 3D drillhole database of the Purcell Anticlinorium from the archives of industry drilling programs.

Paper 12 by Montsion et al. (2015) *"3D stratigraphic, structural and metal zonation modelling of the Sullivan Mine, Kimberley, British Columbia"* offers a three dimensional model of the Sullivan Mine with integrated metal zonation, stratigraphy and structural information in a 3D GIS (Geographic Information Systems) environment.

Paper 13 by Hillier et al. (2015) *"Implicit 3D modelling of geological surfaces with the generalized radial basis functions (GRBF) algorithm"* summarizes an interpolation algorithm that was developed to model 3D geological surfaces and its application to modelling regional stratigraphic horizons in the Purcell Basin.

Paper 14 by Thomas (2015) *"Magnetic modelling insights into the third dimension of the Purcell Anticlinorium"* offer other means of investigating the 3D structure of the Purcell anticlinorium by modelling magnetic anomalies that are distributed throughout the anticlinorium, especially in the areas of the Moyie anticline, Iron Range Fault and St. Mary Fault.

Paper 15 by Paradis (2015) *"TGI-4 sediment-hosted Zn-Pb deposits: research highlights"* summarizes the key activities and findings of the "TGI4-SEDEX" project, and highlights some important factors that may have application to the mineral exploration industry.

References

Hunt, B., 2006, Lead and zinc costs: Mines and projects, 2006 Edition: Surrey, England, Brook Hunt and Associates Ltd.

Leach, D.L., Sangster, D.L., Kelly, K.D., Large, R.R., Garven, G., Allen, C.R., Gutzmer, J., and Walter, S., 2005, Sediment-hosted lead-zinc deposits: A global perspective` *in* Hedenquist, J.W., Thompson, J.F.H., Goldfarb, R.J., and Richards, J.P., ed., Economic Geology, 100th anniversary volume, 1905-2005: Littleton, CO, Society of Economic Geologists, p. 561-607.

Leach, D.L., Bradley, D.C., Huston, D., Pisarevsky, S.A., Taylor, R.D., and Gardoll, S.J., 2010, Sediment-hosted lead-zinc deposits in Earth history: Economic Geology, v. 105, p. 593–625.

Wilkinson, J.J., 2014, Sediment-hosted zinc-lead mineralization: Processes and perspectives, *in* Scott, S.D., ed., Geochemistry of mineral deposits: Treatise on Geochemistry, v. 13 (second edition), p. 219–249.

Acknowledgements

The papers presented in this open file are based on research done under the Targeted Geoscience Initiative 4 (TGI-4) program. Michael Villeneuve, Cathryn Bjerkelund, Dan Richardson, Christine Hutton, and Angèle Miron are thanked for their mentorship, guidance, managerial, and financial oversights. Funding of some activities was through the Government of Canada - Research Affiliate Program (RAP) bursaries and research grants and contributions administered by the Geological Survey of Canada with the University of Alberta.

We thank British Columbia Geological Survey, British Columbia Oil and Gas Commission, Canadian Zinc Corporation, Eagle Plains Resources Ltd., Hudbay Mineral Resources, Mercer Contracting, Mira Geosciences Ltd., MMG Ltd., Northwest Territories Geoscience Office, Paradigm, Selwyn Resources Ltd., Selwyn Chihong Mining Ltd., Teck Resources, TerraLogic, Yukon Geological Survey, and Yukon Energy, Mines and Resources for their continued support, collaboration, and permission to publish the results.

Mentors and facilitators not included as co-authors in this volume include: Duncan Bains (Duncan Bains Consulting Ltd.), Gilles Bellefleur (GSC), Igor Bilot (GSC), Tiffany Chevrier (former student at Laurentian University), Fred Cook (Professor Emeritus, University of Calgary), Susan Co (Alberta Core Library), Kerry Cupit (Canadian Zinc Corporation), Jelle de Bruyckere (Selwyn Chihong Mining Ltd.), Chuck Downie (Eagle Plains Resources), Jason Dunning (Nyrstar), Beth Fisher (Northwest Territories Geoscience Office), Wayne Goodfellow (GSC), Dave Grieve (former geologist with British Columbia Geological Survey), Bob Hodder (Western University), Trygve Höy (consulting geologist), Pat Hunt (GSC), Jason Jacobs (East Kootenay Chamber of Mines), Fiona Katay (British Columbia Geological Survey), Craig Kennedy, Edith Martel (Northwest Territories Geoscience Office), Jim Logan (former geologist with British Columbia Geological Survey), Carmel Lowe (Fisheries and Oceans Canada), Margo McMechan (GSC), Don Murphy (Yukon Geological Survey), JoAnne Nelson (British Columbia Geological Survey), Mark Nowosad (Yukon Energy, Mines and Resources), Anna Oh (University of Alberta), Veronique Pascone (Carleton University), Ryan Olson (British Columbia Oil and Gas Commission), Jeanne Percival (GSC), Lee Pigage (Yukon Geological Survey), Dave Pighin (consulting geologist), Patrick Sack (Yukon Geological Survey), Ted Sanders (consulting geologist), Don Sangster (consulting geologist), Wolfgang Schleiss (Quartz Mountain Gold Corporation), George Simandl (British Columbia Geological Survey), John Slack (USGS), Quinn Smith (MMG), Alan Taylor (Canadian Zinc Corporation), Tim Termuende (Eagle Plains Resources Inc.), Melinda Yurkowski (Saskatchewan Subsurface Laboratory), Gabe Xue (Selwyn Chihong Mining Ltd.), Emily Mesesc and Yolanda Zhang (University of Waterloo), among others, for their continued assistance and collaboration.

Contributions to this volume were significantly improved by peer-reviews of George J. Simandl, Pearce Luck, Bruce Taylor, John Slack, Keith Dewing, Alexei Rukhlov, Hendrik Falck, Jeff Harris, Mike Thomas, Mike Parsons, James Zheng, Paul Ransom, John Lydon, Wayne Goodfellow, and Warner Miles. Technical editing was done by Jane Wynne, without whom this open file would not have been done.

Suzanne Paradis
Geological Survey of Canada
Sidney, BC,
Canada

The Leachability of Metals from Sedimentary Rocks

J.W. Lydon
Geological Survey of Canada, 601 Booth Street, Ottawa, ON, K1A 0E8
jlydon@nrcan.gc.ca

Abstract

Most models for SEDimentary EXhalative (SEDEX) and Mississippi Valley-type (MVT) ore systems envisage that metals were derived from the rocks of the sedimentary basins with which the deposits are spatially associated. To test whether sedimentary rocks could be the source for the ore metals and whether there are leaching windows during the course of burial, the leachability of metals and other elements has been measured on forty core samples of marine sedimentary rocks that represent burial depths ranging from 1 m to 20 km. The samples were taken along a transect across western Canada, and range in age from modern Pacific Ocean sediments to Mesoproterozoic siliciclastic rocks of the Belt-Purcell Basin. Four sequential leaches and an aqua regia leach of the samples were chemically analysed by ICP-MS and ICP-ES methods. Solid starting materials and leach residues were analysed for bulk chemistry by total dissolution and ICP-MS methods and for mineralogy by bulk XRD.

The contents of the metals that are commonly associated with SEDEX and MVT ore deposits (Zn, Pb, Cu, Ba, Mn) range over two orders of magnitude. A major cause for the variation of metal contents is the dilution of argillaceous and carbonaceous matter by quartz and carbonates. There is not an obvious correlation between metal content and depth of burial for these metals.

The first three sequential leaches by ammonium acetate, sodium pyrophosphate, and hydroxylamine, which purportedly extract only the labile metal content adsorbed on to clays, organic material and iron/manganese oxides, respectively, collectively leach on average 13% of the Zn, 33% of the Pb, 17% of the Cu, 10% of the Ba, 11% of the Fe and 22% of the Mn of the rocks. The fourth sequential leach by 1M HCl, dissolves most carbonates and monosulphides. The first three sequential leaches also solubilized on average about 50% of the Ca, 30% of the Mg, 20% of the Fe, and 5% of the K, which suggests that these leaches are not confined to eluting loosely bound cations but also dissolve or alter major rock forming minerals. The ratio between the proportion of a specific metal leached and the proportion of a specific major cation leached is reasonably constant from sample to sample for most leaches, which indicates that most metals in sedimentary rocks are contained within the structure of the rock-forming minerals. Furthermore, considering the low reactive capacity of natural fluids at low water:rock ratios, the results indicate that ore fluids containing >1 ppm base metal can only be produced by leaching during metamorphic mineralogical transformations driven by increasing temperature and pressure during burial.

Recommended citation
Lydon, J.W., 2015. The leachability of metals from sedimentary rocks, *in* Paradis, S., ed., Targeted Geoscience Initiative 4: sediment-hosted Zn-Pb deposits: processes and implications for exploration; Geological Survey of Canada, Open File 7838, p. 11-42. doi:10.4095/296328

Introduction

SEDimentary EXhalative (SEDEX) and Mississippi Valley-type (MVT) deposits (e.g. Leach et al., 2005) have been, and continue to be, the major source for the world's Zn and Pb supply (e.g. Goodfellow and Lydon, 2007). Compositions of fluid inclusions from ore and gangue minerals from SEDEX and MVT deposits (e.g. Roedder, 1984; Samson and Russell, 1987; Viets et al., 1996; Emsbo, 2009) indicate that ore-fluids for both types of ore deposits were evaporated sea water (Figure 1). In terms of major elements, the compositions of the fluid inclusions are very similar to the Na-Ca-Cl formational brines of oil-producing sedimentary basins, which also may contain up to tens or even hundreds ppm Pb and Zn (e.g. Hitchon, 1966; Rittenhouse et al., 1969; Hitchon et al., 1971; Carpenter et al., 1974; Sverjensky, 1984; Kharaka et al., 1987). Most genetic models for SEDEX and MVT ore deposits (e.g. Russell et al., 1981; Lydon, 1983) envisage that such metalliferous formational brines were the ore-forming fluid. The fundamental difference between the current genetic models for the two deposit types is the different flow paths of fluid expulsion from the basin (Figure 2). SEDEX deposits formed as the result of the upward cross-stratal flow of formational brines to the sea floor where the metals were deposited as stratiform sulphide bodies at or below the sediment-water interface (e.g. Lydon, 1983). In contrast, MVT deposits formed by lateral flow of formational brines from the basin to carbonate rocks on its adjacent shelf (e.g. Cathles and Smith, 1983) where the metals were deposited as sulphides within cavities in the carbonate rocks.

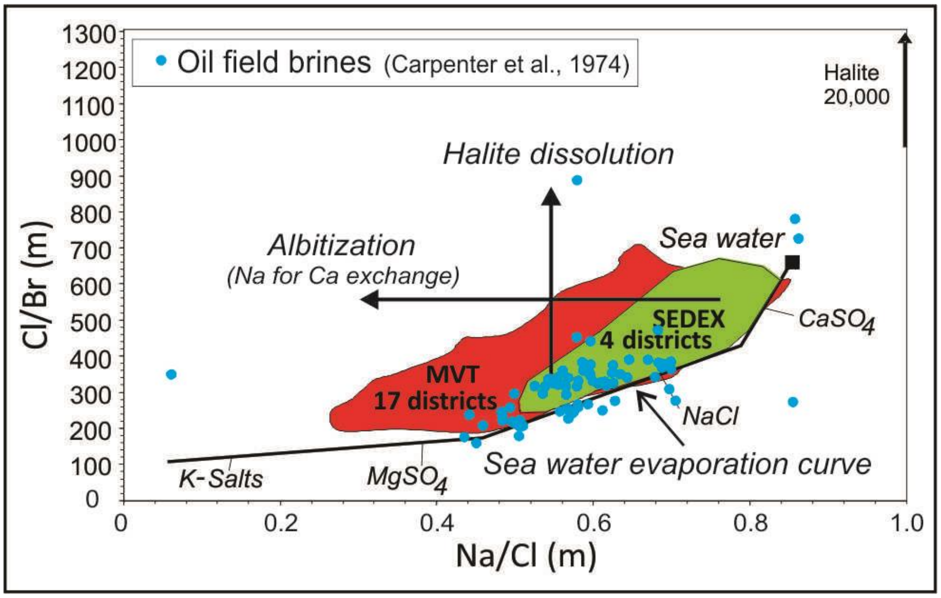

Figure 1. Fields for fluid inclusion compositions of ore minerals from SEDEX and MVT deposits (from Emsbo, 2009). Also plotted are data of Carpenter et al. (1974) for oil field brines in central Mississippi, US (blue dots). The similarity in compositions for all three populations suggests that the ore fluid for SEDEX/MVT ore systems are formational brines of sedimentary basins. Black square is modern sea water.

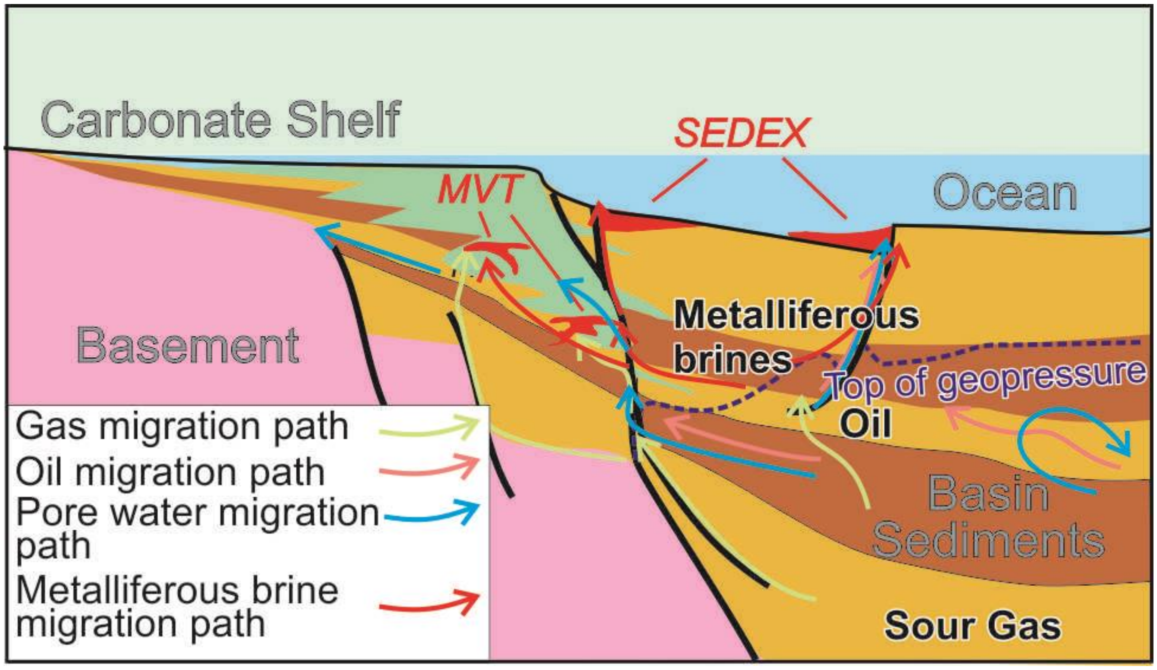

Figure 2. General model for SEDEX/MVT ore systems. Metalliferous brines are thought to exist in the deepest parts of sedimentary basins in the oil producing window but above the top of the geopressure boundary. At greater depths in the gas region, the second dehydration event of Burst (1969) is likely to dilute the brines, and the formation of sour gas likely precipitates metals as interstitial sulphides in the reservoir rocks. The main difference between genetic models for SEDEX and MVT deposits is that the brine expulsion is cross-stratal along synsedimentary faults to the contemporaneous seafloor for the former, but stratal and lateral into an adjacent carbonate shelf for the latter.

Irrespective of whether the mass flow of the formational fluids was caused by thermal convection (e.g. Russell, 1978; Yang et al., 2006), sediment compaction (e.g. Cathles and Smith, 1983), cross-stratal puncturing of geopressured reservoirs (e.g. Lydon, 1983), density-driven reflux of evaporitic brines (Emsbo, 2009), or topographically driven stratal flow (Garven and Freeze, 1985a and 1985b), the models assume that availability of metals is not an issue. Implicit in this assumption is that the brine will be able to elute or leach as much metal as is required to generate an ore-forming fluid before or during its migration to the site of ore deposition. This assumption seems to be supported by the empirical observation that most oil field brine samples containing >100,000 ppm Cl, also contain >1 ppm Zn (Figure 3) and >1ppm Pb (Hanor, 1996). The assumption also seems to be supported by experimental evidence. It has long been demonstrated that ore metals can be leached from sedimentary rock (e.g. Weiss and Amstutz, 1966; Ellis, 1968). More recently, Long and Angino (1982) used various chloride solutions to leach shales at temperatures of up to 90°C, their results indicating that up to 15% of the contained Zn and 100% of the contained Pb. could be leached. Zielenski et al. (1983) used a sequential series of weak selective leaches on Holocene-Pliocene red beds containing 31ppm to 110 ppm Zn and 12ppm to 37 ppm Pb. They found that about 20% of both metals were leached by the sequential extractions and that most of this leached metal was that adsorbed on to iron oxide coatings of quartz grains. They concluded that red beds which are well flushed by suitable pore fluids (oxidizing or reducing) may be sources of significant quantities of heavy metals. Lentini and Shanks (1983) used various artificial chloride brines at 200°C to leach an arkose and also found that several to tens ppm metal could be liberated from the rock. Bischoff et al. (1981) reacted a graywacke with an artificial Na-Ca-K-Mg-Cl brine, similar in composition to a 130°C central Mississippi oil field brine, at temperatures of 200°C and 300°C. They concluded that metal solubilization by the brine followed the order of abundance in the graywacke: Zn > Ni > Cu > Pb > Sb > Cd, suggesting a common matrix and no selective leaching effect. In other words, as a given increment of rock was altered, all of its component metals were released. Importantly, these researchers, unlike the other works cited, also measured the concentrations of major element cations in the leachate as well as the trace metals, and also determined the mineralogy of solid reactants and products. Their results allowed the interpretation that most of the metal leached was from illite and plagioclase during their alteration to chlorite-smectite and albite, respectively. Like other laboratory leaching experiments, Bischoff et al. (1981) used a high liquid to solid ratio (water/rock ratio) of 10:1 mass ratio. This is the reverse of a natural system, where, especially in sedimentary rocks undergoing burial, even at a high porosity of 20%, the water/rock is about 1:10. It has been calculated by Lydon (1986), that at these low water/rock ratios, if the leaching of metals require the metasomatic hydrothermal alteration of the source rock, then the leachate would lose its reactive capacity before any significant amount of metals could be leached. It is therefore uncertain whether the laboratory experimental results for the quantities of metal leached are directly applicable to natural systems.

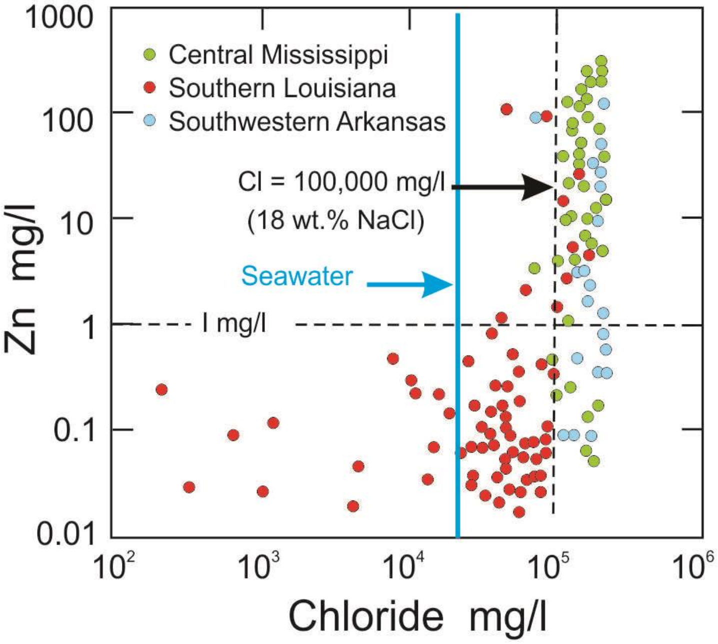

Figure 3. Relationship between concentrations of Zn and Cl in oil field brines of the USA. Modified after Hanor (1996).

A major knowledge gap in understanding SEDEX/MVT ore systems is how and when metalliferous brines of a sedimentary basin are generated. Can they be generated merely by brines being introduced as pore waters into a sedimentary basin and eluting loosely bound metals or are there specific metal leaching windows during basin evolution which allows metals to be leached during alteration of rock-forming minerals? Knowing how and when the metals are leached into a brine provides the knowledge needed to formulate the criteria by which a basin can be tested for its potential of having generated a SEDEX/MVT ore system. Fundamental to understanding the processes and timing that can leach metals is knowledge of the siting of metals in sedimentary rocks at successive stages of their burial history.

Argillaceous rocks usually form the bulk of the sedimentary basins (Garrels and Mackenzie, 1971) which are the sources of ore fluids for SEDEX and MVT deposits. The purpose of the study reported here was to determine the leachability and siting of base metals in argillaceous rocks of marine sedimentary basins in order to:

1. Determine whether argillaceous rocks are a viable source for ore metals in hydrothermal systems responsible for the formation of SEDEX and MVT deposits.
2. Determine whether argillaceous rocks have different degrees of susceptibility to metal leaching at different stages of burial metamorphism.
3. Use the results of the study to refine genetic models for SEDEX and MVT ore systems.

Methodology

Theoretical background

It has long been recognized (e.g. Turekian and Wedepohl, 1961) that metals may occur in rocks as:

i) diadochic substitutions for major elements in rock forming minerals;
ii) metallic mineral micro-inclusions in rock forming minerals;
iii) metallic minerals interstitial to rock forming minerals;
iv) adsorptions on to clays, iron and manganese oxides, organic matter.

Although the most direct determination of the form and siting of metals in rocks would be high precision micro-analysis of rock forming minerals and their intergranular regions, this method would be prohibitively time-consuming and expensive for a large number of samples of varied mineralogy. It was decided that a method of wet chemical sequential partial extractions would be more practicable and more closely simulate the natural leachability of metals. To facilitate interpretation of the leaching data, chemical and X-Ray diffraction (XRD) analysis of starting solid material and residues were also carried out, augmented by Scanning Electon Microscope (SEM) backscatter imagery, Energy Dispersive Spectrometry (EDS) and X-Ray mapping of grain mounts.

Interpretations of the results are based on the understanding that metals occurring within rock forming minerals (i and ii above) can only be leached to the extent of the reactive capacity of the solvent to alter/dissolve the host minerals and to the saturation limit of the metal in the leachate. Metals that are in metallic mineral interstitial to rock forming minerals or loosely bound to grain surfaces within the rock (iii and iv above) can be leached to the extent of saturation of the metal in the leachate.

Sample Collection

Forty core of marine argillaceous rocks were collected along a transect across western Canada (Figure 4), that range in age from modern ocean floor sediments to the Mesoproterozoic (Table 1) and represent burial depths that range from 1 m to 20 km. Modern ocean floor muds are from Middle Valley (Pacific Ocean) collected by piston coring in 1989. Samples collected along a transect across the Western Canada Sedimentary Basin, from eastern Saskatchewan to eastern British Columbia, are from oil well cores and range in age from Upper Cretaceous to Devonian. Other Paleozoic samples are from the White River Trough of eastern British Columbia, two of which are from outcrops. Mesoproterozoic samples are from the Purcell Basin, two of which are from outcrops.

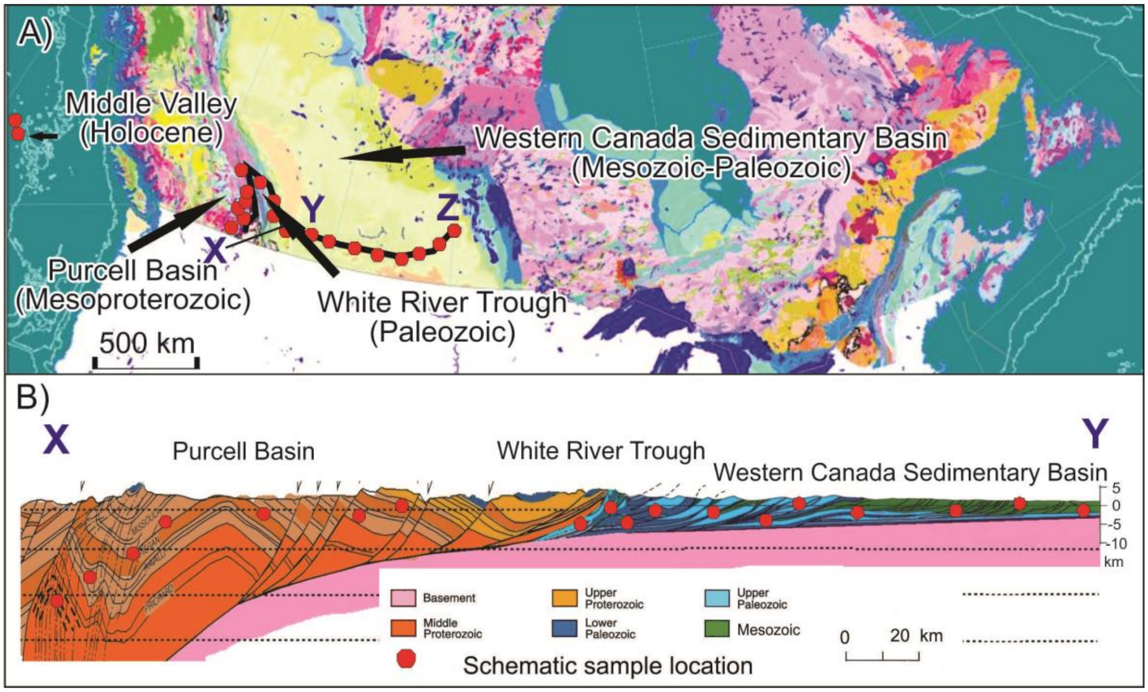

Figure 4. A) Geological map of the southern part of Canada showing schematic locations of samples used in this study. Accurate coordinates for the samples are given in Table 1. B) Geological cross section across western margin of the Western Canada Sedimentary Basin showing the schematic stratigraphic positions of samples used in this study.

Sample No	**Depth** (metres)	**Formation**	**Period**	**Latitude** (dd)	**Longitude** (dd)
LEA-89-TUL89D-28-0.5	0.5	Modern	Holocene	48.43330	-128.68080
LEA-89-TUL89D-28-5.3	5.3	Modern	Holocene	48.43330	-128.68080
LEA-12-Sask-8A	184.0	Lea Park	Cretaceous	52.10709	-102.44596
LEA-12-Sask-8B	223.0	Lea Park	Cretaceous	52.10709	-102.44596
LEA-12-ALB-1	201.5	Bearpaw Fm	Cretaceous	51.31125	-112.47107
LEA-12-ALB-3	576.0	Second W.S.	Cretaceous	50.35571	-110.55800
LEA-12-ALB-4	2,061.2	Second W.S.	Cretaceous	52.26396	-114.60415
LEA-12-ALB-8	1,783.8	Second W.S.	Cretaceous	52.91410	-116.10806
LEA-12-BC-1	1,066.1	Kaskapau	Cretaceous	54.93537	-120.09825
LEA-12-Sask-7A	2,072.0	Jolifu	Cretaceous	50.76796	-105.38921
LEA-12-Sask-2	667.3	Rierdon	Jurassic	50.26643	-101.91061
LEA-12-Sask-3	1,638.5	Rierdon	Jurassic	49.56910	-109.96514
LEA-12-ALB-7	2,185.3	Fernie Grp	Jurassic	53.53329	-115.09708
LEA-12-BC-2A	1,098.9	Fernie	Jurassic	56.41179	-120.06031
LEA-12-BC-3	2,320.8	Fernie	Jurassic	55.55308	-120.36790
LEA-12-FP3_578	578.0	Fernie	Jurassic	49.87623	-114.84406
LEA-12-Sask-5	0.0	Ashern	Devonian	52.69464	-104.98147
LEA-12-Sask-6A	1,037.3	Baakken	Devonian	49.71911	-101.56700
LEA-12-Sask-6B	1,038.7	Baakken	Devonian	49.71911	-101.56700
LEA-12-ALB-2	661.0	Ireton Fm	Devonian	52.81785	-110.52970
LEA-12-ALB-5	2,662.5	Ireton Fm	Devonian	55.03767	-117.45399
LEA-12-BC-6	1,959.0	Ireton	Devonian	58.07510	-121.89841
LEA-12-BC-5	1,863.0	Fort Simpson	Devonian	59.68137	-120.83037
LEA-12-BC-4	3,809.6	Fort Simpson	Devonian	56.94566	-122.07196
LEA-12-052	0.0	Eckshaw	Devonian	49.62598	-114.64814
LEA-12-CK-07-19-26	26.5	Harrogate	Devonian	49.96129	-115.46362
LEA-12-036	0.0	Jubilee	Cambrian	50.13163	-115.49644
LEA-12-FN10-01_20.1	20.2	Chancellor	Cambrian	50.51172	-115.57444
LEA-12-FN-10-01-282	282.6	Chancellor	Cambrian	50.51172	-115.57444
LEA-12-BD_002-36.8	36.8	Dutch Creek	Mesoprot.	50.36081	-116.39161
LEA-12-JI-97-04	129.5	Dutch Creek	Mesoprot.	49.59417	-116.66056
LEA-12-354-8	8.0	Creston	Mesoprot.	49.74133	-115.96385
LEA-12-354-879	879.0	Creston	Mesoprot.	49.74133	-115.96385
LEA-12-Z-03-07	676.0	Creston	Mesoprot.	49.43149	-116.15823
LEA-12-SG- 07-05-133.2	133.2	U. Aldridge	Mesoprot.	49.27432	-115.80716
LEA-08-239	239.0	M. Aldridge	Mesoprot.	49.72804	-115.58697
LEA--10-SD2-2461	2,461.0	L. Aldridge	Mesoprot.	49.75374	-116.03258
LEA-12-6406-192	192.0	M. Aldridge	Mesoprot.	49.71357	-115.89618
LEA-12-6423-1065	1,065.0	L. Aldridge	Mesoprot.	49.69374	-115.94598
LEA-12-ED2012-29	0.0	L. Aldridge	Mesoprot.	49.64189	-116.10593

Table 1. Stratigraphic position, geographic location and brief geological description of samples used in this study.

Sample No	Description
LEA-89-TUL89D-28-0.5	Thin bedded argillaceous to sandy marine turbidite
LEA-89-TUL89D-28-5.3	Thin bedded argillaceous to sandy marine turbidite
LEA-12-Sask-8A	Greenish grey mudstone
LEA-12-Sask-8B	Grey to black mudstone
LEA-12-ALB-1	Massive but fissile medium grey argillite
LEA-12-ALB-3	Laminated carbonaceous shale with layers of light grey ash(?)
LEA-12-ALB-4	Laminated black shale with thin beds and lenses of siltstone.
LEA-12-ALB-8	Carbonaceous shale
LEA-12-BC-1	Carbonaceous siltite with layers of current-bedded arenite.
LEA-12-Sask-7A	Black shale and intercalated siltite
LEA-12-Sask-2	Very soft greenish grey argillite.
LEA-12-Sask-3	Medium grey, weakly calcareous argillite with shell fragments.
LEA-12-ALB-7	Slightly micaceous black shale with silty laminae
LEA-12-BC-2A	Carbonaceous shale.
LEA-12-BC-3	Carbonaceous argillite with layers of dolomitic siltstone.
LEA-12-FP3_578	Glauconitic shale with large belemnites
LEA-12-Sask-5	Massive brownish grey marl with carbonaceous layers.
LEA-12-Sask-6A	Black shale at top of core.
LEA-12-Sask-6B	Laminated green and white argillite. Not calcareous.
LEA-12-ALB-2	Greenish grey dolomite marl with oil in vugs
LEA-12-ALB-5	Massive fissile shale with scattered pyrite nodules
LEA-12-BC-6	Weakly calcareous carbonaceous argillaceous siltite.
LEA-12-BC-5	Carbonaceous shale.
LEA-12-BC-4	Slightly calcareous carbonaceous and argillaceous siltite.
LEA-12-052	Black Shale.
LEA-12-CK-07-19-26	Light buff to khaki coloured, fine grained marl.
LEA-12-036	Shale layer from a nodular carbonaceous carbonate
LEA-12-FN10-01_20.1	Black Shale
LEA-12-FN-10-01-282	Black Shale
LEA-12-BD_002-36.8	Micaceous siltite
LEA-12-JI-97-04	Black Argillite
LEA-12-354-8	Weakly Carbonaceous argillite
LEA-12-354-879	Grey argillite
LEA-12-Z-03-07	Thin bedded light grey argillite
LEA-12-SG- 07-05-133.2	Thin bedded argillite
LEA-08-239	Laminated siltite
LEA--10-SD2-2461	CWL - Carrbonaceous Wacke Laminite
LEA-12-6406-192	Argillaceous biotitic turbidite
LEA-12-6423-1065	Thin bedded biotitic chloritic turbidite.
LEA-12-ED2012-29	Muscovite-silliminite schist.

Table 1 (continued).

Sample Processing

A sample of about 300 grams was cut with a water-cooled diamond saw to produce a slab for a polished thick section and the remainder crushed in a SEPOR mini steel jaw crusher to <3 mm fragment size. Approximately 20 grams of the crushed sample was pulverized to a <200 micron in a tungsten carbide shatter-box for two minutes and separated into subsamples of about 15 grams for whole rock chemical analysis and 5 grams for XRD analysis. The remaining crushed sample was pulverized in a SEPOR mini pulverizer disc mill with tungsten carbide plates and dry sieved until 70 grams of a 60-100 mesh sized fraction was obtained for sequential and partial wet chemical leaching analysis. The 60-100 mesh fraction was quickly stirred into distilled water and decanted after 10 seconds of settling, to remove the >100 mesh rock dust that may have collected on the 60 mesh fragments. This washing protocol was exercised to mitigate against the faster reaction rates of the very small grain size of the dust being a dominant factor in controlling the amount of different elements leached from the crushed rock by different reagents. This process of “cleaning” could not be applied to the Middle Valley and some Mesozoic samples, because they disaggregated in water.

Chemical analyses were carried out by Acme Laboratories of Vancouver. The 60-100 micron size fraction was analysed using the sequential extraction methods described below, followed by Inductively Coupled Plasma Emission Spectrometry (ICP-ES) or Inductively Coupled Plasma Emission Spectrometry (ICP-MS) detection. The solid starting material and the residue from both the sequential and aqua regia leach were analysed by a four acid “near total” extraction followed by ICP-ES or ICP-MS detection. The unsieved >200 mesh powder was also analysed by the four acid “near total” dissolution method to determine whether the sieving had caused significant preferential mineral loss or concentration.

Sections intended for petrography and SEM investigations were prepared by Vanpetro of Vancouver. However, because of the generally unconsolidated nature of argillaceous samples in the study suite and the limited benefits of transmitted light petrography for such fine grained rocks, it was elected to make thick polished section material that could be used for SEM work. Determination of the mineralogy of samples and residues by XRD analysis was carried out in the Geological Survey of Canada’s X-Ray laboratories at 601 Booth Street in Ottawa. SEM X-Ray mapping and EDS semi-quantitative analysis were carried out by the Geological Survey of Canada’s SEM laboratory at 601 Booth Street in Ottawa.

Chemical analyses

Subsamples of the whole rock (original material), the 60-100 mesh fraction, the residue from the sequential leach process on the 60-100 mesh fraction and the residue from an aqua regia leach of the 60-100 mesh fraction were analysed for total abundances of Si, Al, Fe, Mg, Ca, Na, K, Ti, P, Cr, LOI, Ba, Y, and Zr by

Acme Method 4A which involves ICP-ES following a lithium metaborate/tetraborate fusion and dilute nitric digestion of a 0.2 gram sample. Total carbon and total sulphur were determined by infrared spectroscopy after ignition in a LECO furnace at 1000°C. Carbonate carbon was determined by direct CO_2 evolution by digestion with HCl and LECO analysis. Organic carbon was calculated by the difference between total and carbonate carbon and thus includes graphite as well as kerogen and bitumen. Loss on ignition (LOI) was determined by weight difference between a sample dried at 105°C and after ignition at 1000°C. Mn, S, Ag, As, Au, Be, Bi, Cd, Co, Cr, Cs, Cu, Ga, Hf, In, Li, Mo, Nb, Ni, Pb, Rb, Re, Sb, Sc, Se, Sn, Sr, Ta, Te, Th, Tl, U, V, W, Zn, and the REE (Ce, La, Pr, Nd, Sm, Eu, Gd, Tb, Dy, Ho, Er, Tm, Yb, Lu) were analysed by ICP-mass spectrometry after total or near total dissolution by a four acid (HF-$HClO_4$-HNO_3-HCl) digestion. Statistics for selected elements for both the unsieved and sieved starting materials are given in Table 2. Note that the abundances of elements are reported as parts per million of the element, including the major elements, which conventionally are reported as parts per cent of the oxide.

The leachates of 30 grams subsample of the 60-100 mesh fraction were analysed by ICP-MS following each stage of the following sequential leaches, which are reputed to be selective for the indicated cation sites (e.g. Chao, 1984):

- 1.0 M ammonium acetate leach for exchangeable cations adsorbed by clay and elements co-precipitated with carbonates,
- 0.1 M sodium pyrophosphate leach for elements adsorbed by organic matter (humic and fulvic compounds),
- 0.25 M hydroxylamine leach for elements adsorbed by amorphous Fe hydroxide and Mn hydroxide,
- 1.0 M warm hydrochloric acid for dissolution of carbonates and monosulphides.

A 15 grams subsample of the 60-100 mesh fraction was analysed by an aqua regia partial digestion followed by an ICP-MS analysis.

Results for all chemical analyses are reported in a separate Geological Survey of Canada Open File (Lydon et al., in preparation) and partially graphically represented here in Figures 5, 6 and 7.

XRD analysis

The mineralogy of a whole rock powder and clay-sized separates was determined by XRD Bulk samples were further micronized using a McCrone mill in isopropyl alcohol until a grain size of around 5-10 µm was achieved. Samples were left to dry overnight and then back-pressed into an aluminium holder to produce a specimen with random orientation. For clay-sized separates, 40 mg of the sample were suspended in distilled water and pipetted onto glass slides and air-dried to produce oriented mounts. X-ray patterns of the pressed powders and

	Si	Al	Fe	Mg	Ca	Na	K
MDL	*50*	*50*	*300*	*60*	*70*	*75*	*80*
Whole Rock							
MAX	353,334	121,093	73,090	122,356	214,479	25,223	47,401
MIN	10,003	2,117	3,008	1,749	214	74	581
AVERAGE	259,560	73,358	33,249	19,709	39,138	7,252	26,199
60-100 Mesh fraction							
MAX	353,755	121,516	57,423	118,014	216,980	27,523	46,820
MIN	15,192	4,552	3,987	1,869	429	148	1,411
AVERAGE	258,674	72,318	32,618	19,662	40,603	7,124	25,830

	Ti	P	S	Carbonate as C	C-org as C	Calc H_2O
MDL	*60*	*60*	*200*	*55*	*55*	
Whole Rock						
MAX	6,892	6,016	36,600	111,942	187,362	117,435
MIN	120	61	400	49	227	19,910
AVERAGE	3,732	1,086	7,323	14,240	16,388	50,283
60-100 Mesh fraction						
MAX	7,072	12,457	36,300	120,681	166,601	125,343
MIN	300	122	200	55	645	1,000
AVERAGE	3,722	1,331	7,500	15,983	14,100	49,037

	Ba	Cu	Mn	Ni	Pb	Zn
MDL	*5*	*0.02*	*2*	*0.2*	*0.02*	0.2
Whole Rock						
MAX	3,039	99	2,144	218	121	1,398
MIN	80	1	39	4	4	5
AVERAGE	673	29	398	40	23	128
60-100 Mesh fraction						
MAX	3,380	204	3,280	231	101	1,955
MIN	77	3	33	5	4	7
AVERAGE	652	35	440	41	23	147

Table 2. Statistics for major elements and the trace metals important to SEDEX/MVT ore systems for the whole rock and the 60-100 mesh fraction of the 40 samples used in this study. Note that all values are in ppm. MDL - minimum detection limit.

air-dried samples were recorded on a Bruker D8 Advance Powder Diffractometer equipped with a Lynx-Eye Detector, Co Kα radiation set at 40 kV and 40 mA. The oriented samples were also X-rayed following saturation with ethylene glycol and heat treatment (550ºC).

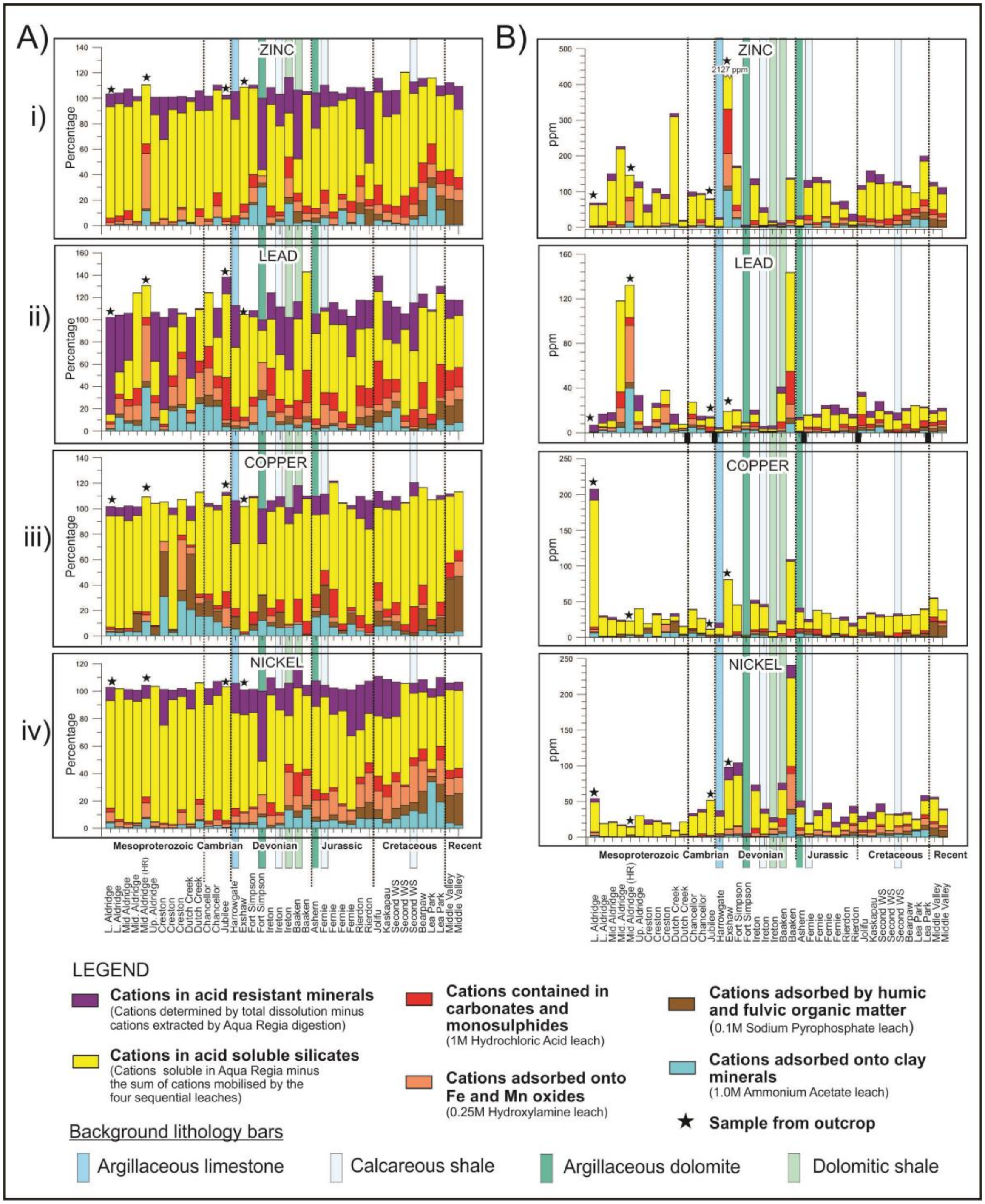

Figure 5. A) Relative proportions of selected metals in leachates and residues of argillaceous sedimentary rocks from Western Canada. The purported siting indicated by each leachate and residue is indicated in the legend. B) Contents of selected ore metals for the same argillaceous sedimentary rocks from Western Canada shown in A). Note that all contents are in ppm and that the samples are plotted from right to left in the same order as listed in Table 1. See text for discussion of results.

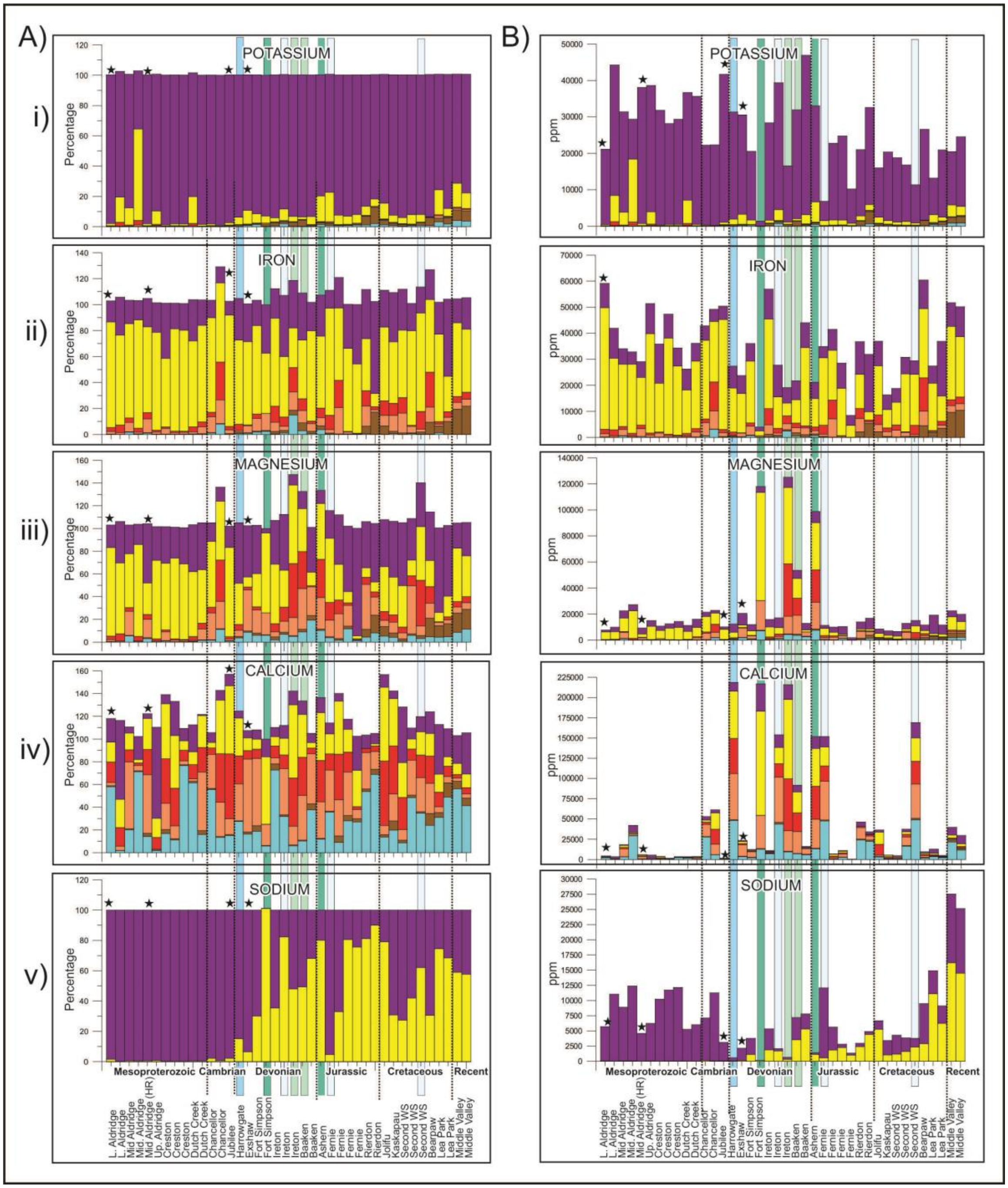

Figure 6. A) Relative proportions of selected major elements in leachates and residues of argillaceous sedimentary rocks from Western Canada. B) Contents of selected major elements for the same rocks shown in A). Note that all contents are in ppm. Legend is the same as in Figure 5. Sodium was analysed only in residues because of the use of sodium pyrophosphate in the sequential leach process. Silicon and aluminium were not analysed in leachates because of the low saturation levels of both these elements in the leachates. Note that all contents are in ppm and that the samples are plotted from right to left in the same order as listed in Table 1. See text for discussion of results.

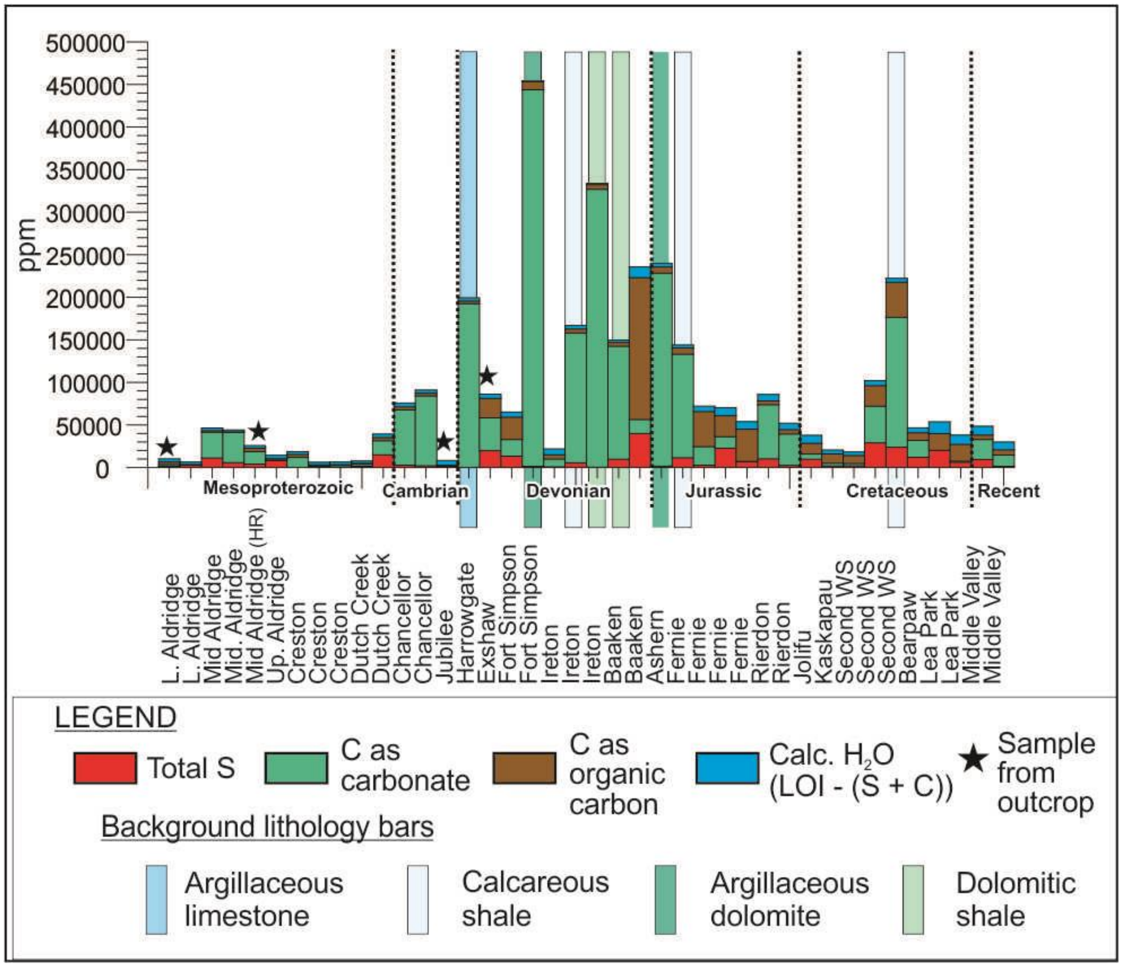

Figure 7. Contents of sulphur, carbonate carbon, organic carbon and calculated water in the 60-100 mesh fraction of argillaceous sedimentary rocks from western Canada. See text for discussion of results.

Initial identification of minerals was aided using EVA (Bruker AXS Inc.) software with comparison to reference mineral patterns using Powder Diffraction Files (PDF) of the International Centre for Diffraction Data (ICDD) and other available databases. Quantitative analysis is carried out using TOPAS (Bruker AXS Inc.), a PC-based program that performs Rietveld refinement (RR) of XRD spectra. This is based on a whole pattern fitting algorithm that relies on having particular mineralogical structure files (.cif) such that the reference minerals are as close a match to the unknown as possible.

SEM analysis

It was the intent to substantiate conclusions from the leaching experiment by examining polished grain mounts of the starting 60-100 mesh rock powders and leach residues by EDS and X-Ray mapping to identify the minerals that were leached and formed by the leaching reactions. However, it was found that the magnification required to identify corrosion and alteration of rock grains could not be achieved at the Geological Survey of Canada SEM laboratory, because of vibration effects on the 7th floor of a building. SEM investigations to date have been limited to back scatter imaging and EDS semi-quantitative analysis at a resolution scale of about 1 micron.

Results/Data Analysis

Metal and major element contents and proportions

The contents of metals that are commonly associated with SEDEX and MVT ore deposits (Zn, Pb, Cu, Ba, Mn) range over two orders of magnitude in the argillaceous rocks analysed in this study (Table 2; Figure 5). The statistics indicate that on average dry sieving of the samples did not result in any consistent significant preferential loss or concentration for most elements, with element contents of the 60-100 mesh fraction being between 98% and 102% of the values determined for the whole rock. The major exceptions are for P and Cu whose average values are 120% higher in the 60-100 mesh fraction. Maximum values for most elements in the 60-100 mesh fraction are also between 98% and 102% of the values determined for the whole rock. The main exceptions are depletions of Fe and Pb (78% and 84%, respectively) and enrichments of P, Cu, Mn and Zn (207%, 205%, 150% and 140%, respectively), compared to contents of the unsieved whole rock. The reasons for these apparent depletions and enrichments in the 60-100 mesh fraction for the affected samples have not been determined.

The relative proportions of metals extracted by the four sequential leaches (ammonium acetate, sodium pyrophosphate, hydroxylamine, and hydrochloric acid successively) are calculated with respect to the total metal content of the sample (as determined by the total dissolution analysis of the 60-100 mesh fraction). The amount of metal in acid soluble minerals is calculated as the metal content extracted by the aqua regia leach minus the metal content extracted by the four sequential leaches, and its relative proportion calculated with respect to the total metal content of the sample. The amounts of metals in acid insoluble minerals is calculated by subtracting the metals extracted by the aqua regia leach from the total metal content, and its relative proportion calculated with respect to the total metal content of the sample. The relative proportions of metals in the different sites commonly sum to >100% for several reasons. Concentrations of metals below detection limits were assigned the value of the detections limit, and therefore in these cases the summation of the different extractions exceeds the measured total metal content. There may also be discrepancies in the calibration of the different instruments used for the total dissolution (ICP-MS) and partial leaches (ICP-ES) with the latter giving higher results for some elements. For some samples, there may also be the nugget effect for some metals in some samples where the metals occur as intergranular grains of sulphides. These nuggets are more likely to occur in the 30 grams of samples used for the sequential leaches than the 1 gram sample used for complete dissolution.

Generally, the major cause for variation of metal contents is dilution of argillaceous and carbonaceous matter by carbonates, and to some extent quartz.

That samples with the highest carbonate contents generally have the lowest metal contents can be seen by comparing metal contents shown in Figure 5, with Ca and Mg contents on Figure 6, and the carbonate carbon content shown on Figure 7. This comparison is aided by the background bars colour coded for rocks with elevated carbonate contents, i.e. argillaceous limestone, calcareous shales, argillaceous dolomite and dolomitic shale. High contents of single metals are most commonly due to the presence of an interstitial diagenetic sulphide, e.g. Cu in the stratigraphically lowest Mesoproterozoic Lower Aldridge sample (LEA-12-ED2012-29), Pb, and to some extent Zn, in the two Mesoproterozoic Middle Aldridge samples (LEA-08-239 which is near the Kootenay King SEDEX deposit, and LEA-12-6406-192, which is just 5 km east of the Sullivan deposit). Other high metal spikes may be attributable to unusually high contents of metal-trapping components such as the high Pb, Cu and Ni associated with the high organic carbon content of the stratigraphically highest sample of the Devonian Baaken Formation (LEA-12-Sask-6A). Others, specifically the very high Zn content of the Devonian Exshaw Formation, represent a regional enrichment of unknown geological significance (P. Ransom, personal communication, 2012).

For the metals plotted in Figure 5, there is not an obvious correlation between metal content and depth of burial, except in the case of Ni, which generally decreases with depth (Figure 5iv). This Ni trend is broadly similar to the organic carbon trend (Figure 7), suggesting that Ni (along with V) migrates with oil. For major elements (Figure 6) there is a general increase in K, Fe and Mg contents with depth of burial, perhaps reflecting the normal diagenetic progression of smectite to illite transformation, the chloritization/illitization of feldspar, and the upwards migration of carbonate and silica due to pressure solution, dewatering and interstitial cement evolution (e.g. Milliken, 2004). There is a general decrease in organic carbon, water and sulphur contents with depth (Figure 7) reflecting devolatilization with increasing temperature with increasing burial depth. However, burial related compositional changes are difficult to distinguish from provenance-related and depositional-environment factors for this data set, which spans 1500 my in age and >1000 km in current distance. The amount of carbonate in the samples, and consequently Ca and/or Mg, appears to largely reflect the depositional environment. Half the samples of Paleozoic age are elevated in carbonate content (Figure 7) reflecting their deposition in or near a carbonate shelf environment.

The first three sequential leaches, which purportedly do not involve the destruction of host minerals but extract only the labile metal content, collectively leach on average 20 ppm Zn, 8 ppm Pb, 6 ppm Cu, 68 ppm Ba, 3480 ppm Fe and 180 ppm Mn (Table 3 and Figure 5B). These amounts represent 13% of the Zn, 33% of the Pb, 17% of the Cu, 10% of the Ba, 11% of the Fe, and 22% of the Mn originally present in the rocks, which is similar to the proportions reported in the literature for both low temperature partial leaching of sedimentary rocks by weak selective leaches (Zielenski et al., 1983) and chloride brines (Long and Angino, 1982) and high temperature (> 200^{o}C) brines (Bischoff et al., 1981;

Lentini and Shanks, 1983). The first three sequential leaches on average also solubilizes about 50% of the Ca, 30% of the Mg, 20% of the Fe, and 5% of the K (Figure 6). This suggests that these leaches, which supposedly leach only ions adsorbed on to minerals, in fact also significantly dissolves or alters the rock forming minerals. This means that at least a proportion of the metals extracted by the sequential leaches were likely contained in the structure of the rock forming minerals and not exclusively adsorbed on to the surfaces of clays, organic matter, and iron or manganese oxides. Thus this observation, and inferences that can be made from it, has very important consequences for both the interpretation of laboratory leaching experiments by partial extractions, but also on the assumptions of the selectivity of the leaches used in the work described here.

Siting of metals in marine argillaceous sediments

With the caveat of the inference, noted above, that the sequential selective leaches employed in this study may not be as specifically selective as they are purported to be, the data illustrated in the left hand columns of Figures 5 and 6 gives some insights into the siting of metals in marine argillaceous sediments. It is evident that in many cases, the relative proportions of elements frequently sum to >100%. The reasons for this have not been fully investigated, but there are several possibilities. A major reason could be that apportioning the elements to different sites relies on three different analytical procedures (sequential leach, aqua regia leach, and four acid “near total” dissolution), each with their own instrumentation and calibrations. Noting that the proportioning is relative to the four acid “near total” dissolution, an over estimation of the proportion of an element occurs if analysis of partial extraction leachates over-estimate the actual concentration. The discrepancies are most pronounced where the concentration of elements are close to the minimum detection limits of the method. The most pronounced discrepancies are for Pb among the metals and Ca among the major elements. Sodium was analysed only in residues, because of the use of sodium pyrophosphate in the sequential leach process. Silicon and aluminium were not analysed in leachates because of the low saturation levels of these elements in aqueous solutions.

Ammonium acetate leach – elements adsorbed by clay minerals

Considering that the samples were chosen for their argillaceous content, it was somewhat surprising that this leach generally extracted the smallest proportion of the sequential leaches. The leachable proportion is sporadic for Zn and Pb, but generally increases with increasing maximum burial depth for Cu until Aldridge Formation and generally decreases with maximum burial depth for Ni (Figure 5A). This leach generally does not extract more than 2% of major elements except for Ca (~20% and more) and Mg (up to 5%) (Figure 5A). These results suggest that the ammonium acetate leach attacks carbonates, particularly calcium carbonate.

Sodium pyrophosphate leach – elements adsorbed by organic matter

Although there are no strong correlations between any metal or major element and organic carbon, the proportion of metals (Figure 5A) and major elements (Figure 6A) extracted by this leach tends to decrease with increasing burial depth, mimicking the trend for whole rock organic carbon content (Figure 7). Of the major elements, Fe and Mg, and to a lesser extent K, are the most leachable, but only in rocks of Devonian age or younger. This may suggest that this leach also attacks smectite clays, chlorite and probably also calcite and dolomite.

Hydroxylamine leach – elements adsorbed by iron and manganese oxides

This leach fairly consistently extracts 5-10% of Zn, Pb and Cu, with the proportions tending to increase with the age of the rock. It also consistently extracts 10-20% of the Fe, 10-40% of the Mg, and 10-60% of the Ca but does not extract any significant amounts of K. Rocks with the lowest proportion of the major elements extracted by this leach are the youngest ones. The reason for this is unclear, but it may be that this leach, judging by the high proportions of Ca and Mg that it leaches in the older rocks, attacks mainly carbonates, particularly calcite. The low carbonate contents (as calcite) in the younger rocks (Figure 7) is largely removed by the ammonium acetate leach (Figure 6.i) leaving little in the residue to be leached by the subsequent hydroxylamine leach.

Hydrochloric acid leach – elements contained in carbonates and monosulphides

Surprisingly, this leach was not so selective for carbonates, particularly calcite, and metal monsulphides like sphalerite, galena and pyrrhotite, as expected. In calcareous rocks, more than half the Ca (as calcite?) was dissolved by prior leaches (Figure 6). The HCl leach extracts little Mg in dolomite-rich rocks, but up to 30% of the Mg of other carbonate-rich rocks, perhaps suggesting that it is magnesian calcite and not dolomite that is attacked in these cases. This leach does not extract K (Figure 6). The proportions of Zn, Pb, Cu and Fe that this leach extracts tend to decrease with increasing age of the rocks (Figure 5A). A possible explanation for this trend is that with increasing burial depth the trace metals are incorporated into minerals of higher metamorphic grade that are more stable and more resistant to chemical attack compared to minerals from shallower burial depths.

Aqua regia leach minus sum of sequential leaches – elements contained in acid-soluble minerals

For the great majority of samples, it is this category that contains the bulk of Zn, Pb, Cu, Ni and Fe contained in the rock. Most of the Fe extracted is probably contained in ferro-magnesian minerals, particularly smectite and chlorite (see next section). Judging from the co-extraction association of Ca with Mg, this leach also dissolves dolomite and ankerite. Noting the low metal contents in carbonate-rich rocks (Figure 5), it is therefore likely that most of the metal mobilized occurred in chlorite and/or smectite in the original rock. Very little K is extracted by this leach (Figure 6.i), attesting to the acid resistant properties of illite/muscovite* which likely contain the bulk of the K in these rocks. The small proportions that are mobilized are likely due to the attack of smectite in the younger rocks and biotite in the older, more metamorphosed rocks. In Devonian and younger rocks, 30-80% of the Na is leached by an aqua regia digestion, but very little is leached in the case in older rocks. The reason for this is that in the younger rocks, Na occurs in smectite, paragonite, plagioclase and, in the case of the Middle Valley samples, as sodium chloride of the original pore fluids, which are dissolved. In the older rocks, Na occurs almost exclusively in albite, which is resistant to an aqua regia digestion.

Residue from Aqua regia leach – elements contained in acid resistant minerals

This value was calculated as the difference between the whole rock "near total" content and the amount extracted by the aqua regia leach. It could have also be determined by the direct "near total" analysis of the aqua regia leach residue corrected for the weight loss of the solid reactant (rock powder) during aqua regia leaching. Both methods have their uncertainties because both use the results from two different methods of analysis. The results of both methods are very similar. The main minerals in the aqua regia residue are quartz, muscovite, albite, kaolinite, and minor minerals such as ilmenite, magnetite, rutile, etc. These acid resistant minerals general contain <10% of the Zn, Pb, Cu and Ni but on average contains 25% of the Fe and 90% of the Ba contained in the rock (Table 3).

Leach	**Site of metals**	**Zn**	**Pb**	**Cu**	**Ba**	**Fe**	**Mn**
1M Ammonium acetate	Clays	7.0	2.7	2.1	37.3	312.8	61.4
0.1M Sodium pyrophosphate	Organics	3.3	1.2	2.9	12.0	1,170.5	20.9
0.25M Hydroxylamine	Oxides	9.4	3.7	1.0	18.8	1,996.9	98.5
1M HCl	Carbonates and monosulphides	9.9	3.4	2.3	35.6	2,282.4	60.4
Aqua regia minus the sum of above sequential leaches	In minerals soluble in aqua regia	118.0	13.4	27.5	19.9	20,679.8	222.6
WR minus amount leached by aqua regia	In acid-resistant minerals	10.4	3.4	2.1	569.6	8,457.7	39.7
Average 60-100 mesh whole rock		147.0	23.0	35.0	652.0	32,618.0	440.0

Table 3. Average amounts of metals (in ppm) extracted by the different leaches and the sites in the rock where the metals are purported to occur.

* Because of the difficulty in distinguishing muscovite and illite by whole rock XRD in a rock that contains both (e.g. Verdel et al., 2011), muscovite and illite are referred to here as illite/muscovite in the text and as illite in diagrams.

Discussion

It is not surprising that there is much variation in the relative proportions of the siting and leachability of different metals and major elements of the samples used in this study, considering their different ages, provenances, depositional environments, and depths of burial which has controlled their present chemical and mineralogical compositions. Each sample is different, and responds differently to the different leaches. The generalizations made above are very broad and do not present general rules. In order to understand exactly what is happening during the different leaches, the data for each sample has to be analysed separately. At the time of writing, data analysis of individual samples is still being carried out. However, in order to give the reader insight into the methodologies of analysis, two examples are presented here and illustrated in Figures 8 and 9.

Sample LEA-12-ALB-2

Sample LEA-12-ALB-2 (Figure 8) is a dolomitic marl with oil-filled vugs from the Devonian Ireton Formation of western Alberta. The K-Mg-Ca ternary diagram shows the relative proportion of these elements in both the leachates and residues of the various experiments as indicated by the colour coding of the symbols. Other major elements listed in Figure 8D could also be used, but the plot shown gives the most spread of data across the diagram. As pointed out earlier, Si was not measured because of the low solubility of quartz in the leaches, and the use of sodium pyrophosphate as a leaching agent precludes the use of Na for analysing the leaching process. The solubility of Al in most leaches is usually limited by saturation with respect to kaolinite or dickite which collects in the insoluble residue, and therefore the amount of Al in the leachate is not a good measure of the amount of solubilisation of rock-forming minerals. Also shown on the diagram are the ranges of the relative proportions of K, Mg and Ca in the most common rock-forming minerals.

The SEM backscatter image (Figure 8B) and XRD analysis shows the sample to consist mainly of loosely packed dolomite grains with fine-grained quartz, illite/muscovite, and kaolinite in the interstices. The sample is oil-rich, and it is presumed that this also occupies the interstices. This dominance of dolomite in the sample is reflected in the high whole rock Ca and Mg contents (top row of Figure 8D) and the plotting of these whole rock contents close to the dolomite field in Figure 8A on a tie-line between dolomite and illite/muscovite. All leaches extract Ca and Mg in the same ratio that exists in dolomite which suggests that the main reaction occurring is the dissolution of dolomite, and not the selective leaching of adsorbed cations from different sites in the rock. If the leaching were from different adsorption sites then the ratios would not be constrained to those of mineral compositions. That the dissolution of dolomite is the main reaction for all leaches is substantiated by the compositions of the leach residues, which lie on a line from dolomite composition through the whole rock indicating the removal of dolomite. The residue of the aqua regia leach contains no dolomite (Figure 8A), consisting mainly of quartz, illite and kaolinite. The aqua regia

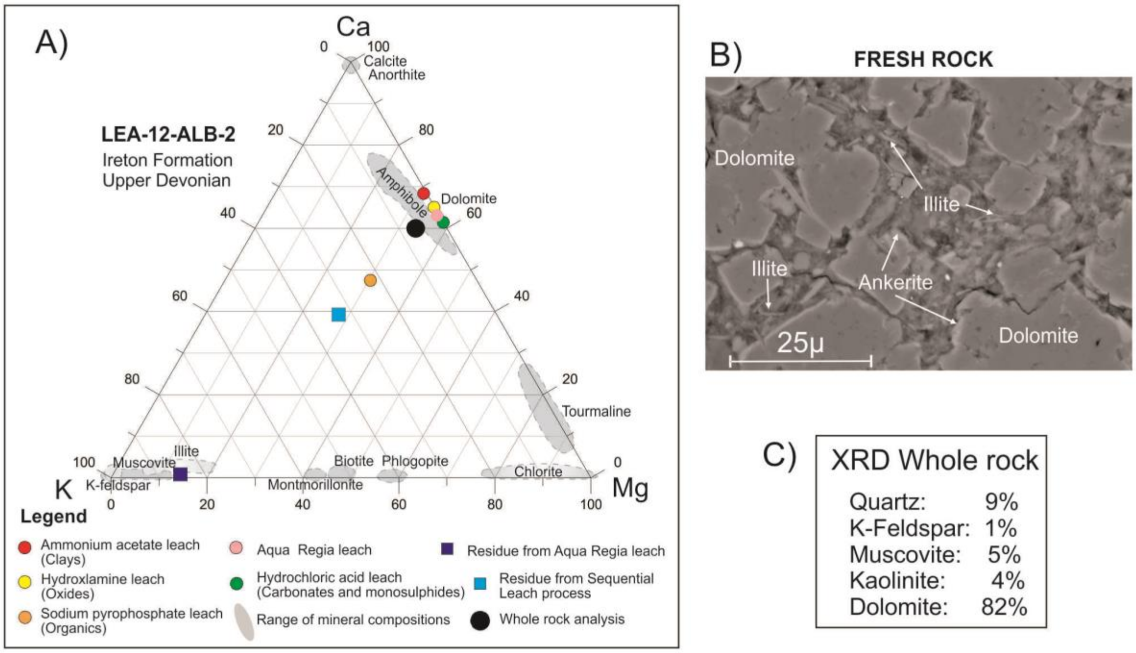

C)

XRD Whole rock

Quartz:	9%
K-Feldspar:	1%
Muscovite:	5%
Kaolinite:	4%
Dolomite:	82%

D)

Symbol	Al	Fe	Mg	Ca	K	Cu	Ni	Pb	Zn	unit
●	32,443.1	16,086.8	84,786.8	151,728.8	16,519.9	8.7	26.1	5.9	15.8	ppm
●	0.1	15.1	5.0	6.2	0.6	6.6	13.3	6.5	17.3	% of total
●	4.5	3.5	0.6	0.5	2.3	0.1	3.5	6.9	4.8	% of total
●	0.2	14.2	16.0	16.7	0.3	1.8	24.2	7.8	15.6	% of total
●	0.2	18.7	47.5	42.3	0.2	0.9	5.8	2.2	16.3	% of total
●	0.1	30.6	69.1	64.5	3.5	78.9	35.3	31.7	34.5	% of total
■	95.2	67.1	78.4	76.6	96.8	91.5	59.1	78.8	62.3	% of total
■	95.1	36.6	9.3	12.1	93.3	12.6	23.8	47.1	27.8	% of total

Figure 8. Summary of chemical and mineralogical analyses for sample LEA-12-ALB-2: A dolomite marl containing oil in vugs from the Upper Devonian Ireton Formation of western Alberta. A) Ternary K-Mg-Ca diagram showing relative proportion in leachates and residues of the 60-100 mesh fraction of a whole rock powder. Grey areas show the range of compositions of the indicated minerals from sedimentary basins (data from Lydon et al., 2000). B) SEM backscatter image of part of a rock grain prior to leaching. The rock is a porous dolomite with interstitial fine-grained dolomite, illite, and organics. C) Quantitative XRD analysis of whole rock powder. D) Summary of chemical compositions of the data points plotted in A). Top row is chemical composition of whole rock in ppm. Underlying five rows are the proportions of the indicated element extracted by the leach indicated by the symbol used in A), and the bottom row is the proportion of the elements that were not dissolved by aqua regia, calculated by subtracting the amount leached by aqua regia from the whole rock “near total” analysis. See text for discussion.

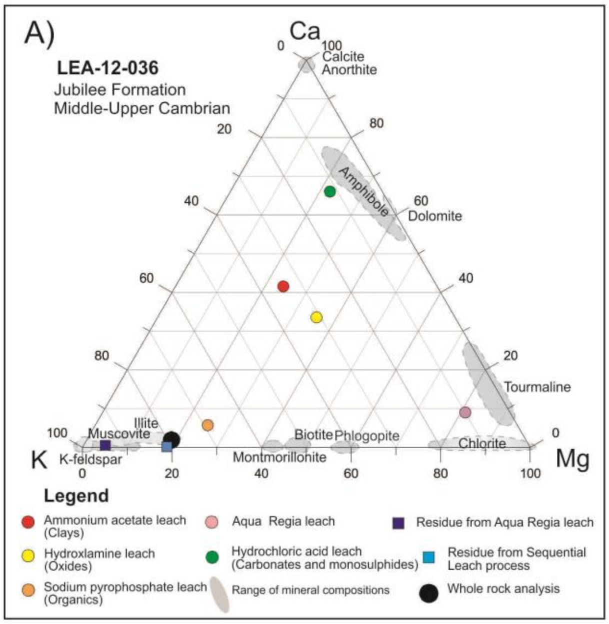

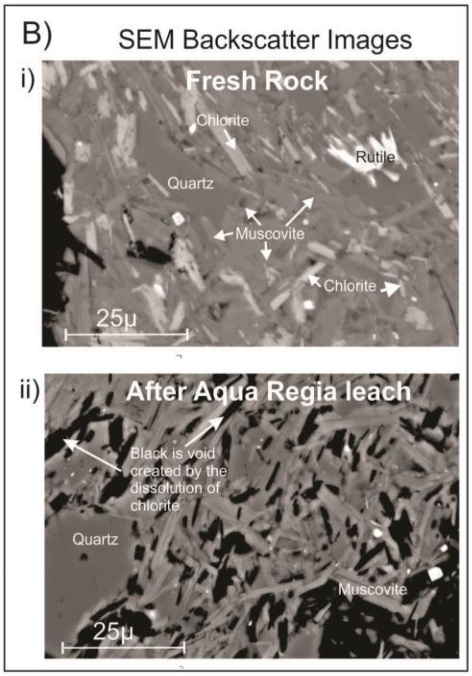

C) XRD Whole Rock

Quartz: 35%
Muscovite: 45%
Chlorite: 20%

D)

Symbol	Al	Fe	Mg	Ca	K	Cu	Ni	Pb	Zn	unit
●	121,516.0	49,169.6	9,950.1	1,000.6	41,590.4	10.2	50.3	10.6	78.4	ppm
🔴	0.1	0.1	0.9	15.0	0.3	6.8	0.5	4.0	0.2	% of total
🟠	0.6	0.6	0.4	1.0	0.3	0.1	0.4	2.9	0.7	% of total
🟡	0.5	2.9	1.5	13.9	0.3	15.1	2.6	2.9	2.4	% of total
🟢	0.7	2.6	1.9	57.0	0.2	12.9	2.3	38.2	2.4	% of total
○	17.1	85.9	78.6	60.1	1.5	75.5	97.3	75.1	93.9	% of total
🟦	98.8	96.4	97.2	70.1	99.1	78.0	96.5	90.2	96.8	% of total
🟪	81.6	10.5	18.6	10.1	97.6	2.5	0.0	15.1	2.9	% of total

Figure 9. Summary of chemical and mineralogical analyses for Sample LEA-12-036-2: A shale layer from a nodular carbonaceous limestone from the Cambrian Jubilee Formation of British Columbia. A) Ternary Ca-Mg-K diagram showing relative proportion in leachates and residues of the 60-100 mesh fraction of a whole rock powder. Grey areas show the range of compositions of the indicated minerals from sedimentary basins (data from Lydon et al., 2000). B) SEM backscatter images of part of a rock grain: i) Prior to leaching. The rock is a muscovite-chlorite-quartz argillite. ii) After leaching with aqua regia. Note that chlorite has been dissolved even within the grain interior but the muscovite has not been corroded. C) Quantitative XRD analysis of whole rock powder, confirming the muscovite-chlorite-quartz composition of the rock. D) Summary of chemical compositions of the data points plotted in A). Top row is chemical composition of whole rock in ppm. Underlying five rows are the proportions of the indicated element extracted by the leach indicated by the symbol used in A), and the bottom row is the proportion of the elements that were not dissolved by aqua regia, calculated by subtracting the amount leached by aqua regia from the whole rock “near total” analysis. See text for discussion.

residue contains 93% of the K present in the original rock and illustrates that muscovite/illite is very resistant to chemical attack and thus unlikely to be a source of metals for SEDEX/MVT ore systems. The major repository of Fe in the sample is in the iron-rich rim of dolomite grains, (Figure 8B), which is presumably a diagenetic ankerite alteration. The ammonium acetate leach, the first of the sequential leaches, extracts three times the proportion of Fe as it does Mg or Ca, and this ratio decreases with each subsequent leach, suggesting that the sequential leaches progressively corrode the dolomite grains, removing the ankerite rim and exposing the dolomite to chemical attack. The ratio of the proportion of Zn to the proportion of Fe extracted is approximately 1:1 for all leaches, suggesting that most Zn in the rock occurs as a substitution for Fe in ankerite. This systematic covariation of Zn with Fe, Ca and Mg, is strong evidence supporting the interpretation that most of the cations that are leached from the rock is a result of mineral dissolution, and not elution of loosely bound ions on the surface of mineral grains.

Space does not permit a full discussion of the other metals here, but it is interesting to note that the sodium pyrophosphate leach, which purportedly attacks organic matter, failed to leach significant amounts of Ni, despite the presence of oil in the sample and the propensity for Ni to concentrate in oil (e.g. Hitchon, 1966; Hitchon and Filby, 1983; Magaw et al., 2000). However, the sodium pyrophosphate extracted 2.5% of the K in the rock, but little Mg and Ca. What mineral the sodium pyrophosphate attacked is unknown, but is possibly the K-Feldspar identified by whole rock XRD.

Sample LEA-12-036

In contrast to the carbonate-rich rock described above, sample LEA-12-036 is a shale from the Cambrian Jubilee Formation of eastern British Columbia, consisting mainly of quartz, muscovite and chlorite (Figure 9C), with, judging from its chemical response to leaching; Figure 9A) small amounts of a calcic phase which is probably calcite. The sequential leaches collectively extract only very small proportions (<6%) of rock components, except for Ca, Pb and Cu. Nearly all the Ca can be attributed to calcite dissolution, most of which was extracted by the HCl leach. About 40% of the Pb but very little Zn is extracted with the Ca by the HCl leach. As in sample LEA-12-ALB-2, the sodium pyrophosphate leach preferentially extracted K compared to other components. The great bulk of the ore metals is extracted by the aqua regia leach, which element ratios of Figure 9A and 9D indicate, mainly involves the dissolution of chlorite and small amounts of muscovite and a calcic phase. The almost complete dissolution of chlorite but acid resistance of muscovite is shown by the SEM backscatter images in Figure 9B which compares a grain of the fresh rock with a grain from the aqua regia leach residue. The conclusion is that most of the zinc in this rock is contained in chlorite, and is only released if the chlorite is altered or dissolved. This figure also demonstrates the very rapid inter-granular mass transfer that is possible due to instability between a rock forming mineral and a fluid, noting that the dissolution of chlorite is complete even in the centre of the grain and is not confined to an alteration selvedge at the grain boundary. The response of this sample to the various leaches also illustrates the high resistance of a greenschist facies argillaceous rock to leaching, with 95% of the Zn and Ni, and 75% of the Cu and Pb, remaining in the rock after the sequential leaching process.

Proportion of Zn leached compared to proportions of other elements leached

The above examples both suggest that significant leaching of the metal content of a sedimentary rock involves the dissolution/alteration of rock forming minerals and therefore the metal reservoirs of the rocks are mainly within the structures of those rock-forming minerals. If this is universally the case then there should be a consistency in the ratios between a metal and the major elements of the rock forming minerals. Some variation can be expected because the same element can occur in more than one mineral.

The ratios of the proportion of Zn leached to the proportion of other elements leached are plotted in Figure 10. The column on the left has a major element as a denominator and the column on the right has a minor or trace element as a denominator. Points that plot above the line at the value of 1, signify that Zn is more leachable than the denominator element. Points that plot below the line at the value of 1, signify that Zn is less leachable than the denominator element. Samples that plot at the 10^4 value signify that the leachability of the denominator element is insignificant, whereas those that plot at the 10^{-4} value signifies that the leachability of Zn is insignificant, and usually due to very low Zn contents in the sample.

In general, there are certain consistencies to the ratio for the proportion of Zn extracted compared to the proportion of major element extracted (Figure 10A). For the great majority of samples and leaching method, the proportion of major element leached is in the order Ca>Mg>Fe>K>Al>Ti. This consistent order of the major elements suggests that their extractability of the major element is controlled by the relative solubilities of the mineral(s) containing the major element and not the more random quantity of the elutable amount of the element adsorbed on to substrate. This order of elements changes only for the aqua regia leach, where Ca is less leachable than Mg and Fe. The reason for this is likely because the HCl leach removes most of the calcite in the rock, leaving only the less soluble dolomite, plagioclase and perhaps amphibole for the aqua regia leaching.

The ratio of 1, which indicates that Zn and the major elements are leached in the same proportions by dissolution of a rock forming mineral containing the denominator element(s), is most consistent for Fe (Figure 10A.v) particularly for the aqua regia leach which extracts ~70% of Zn for most rocks. This indicates that most commonly Zn substitutes for Fe in minerals of sedimentary rocks. For aqua regia leaching of Paleozoic rocks, the Zn/Mg ratio is also close to 1,

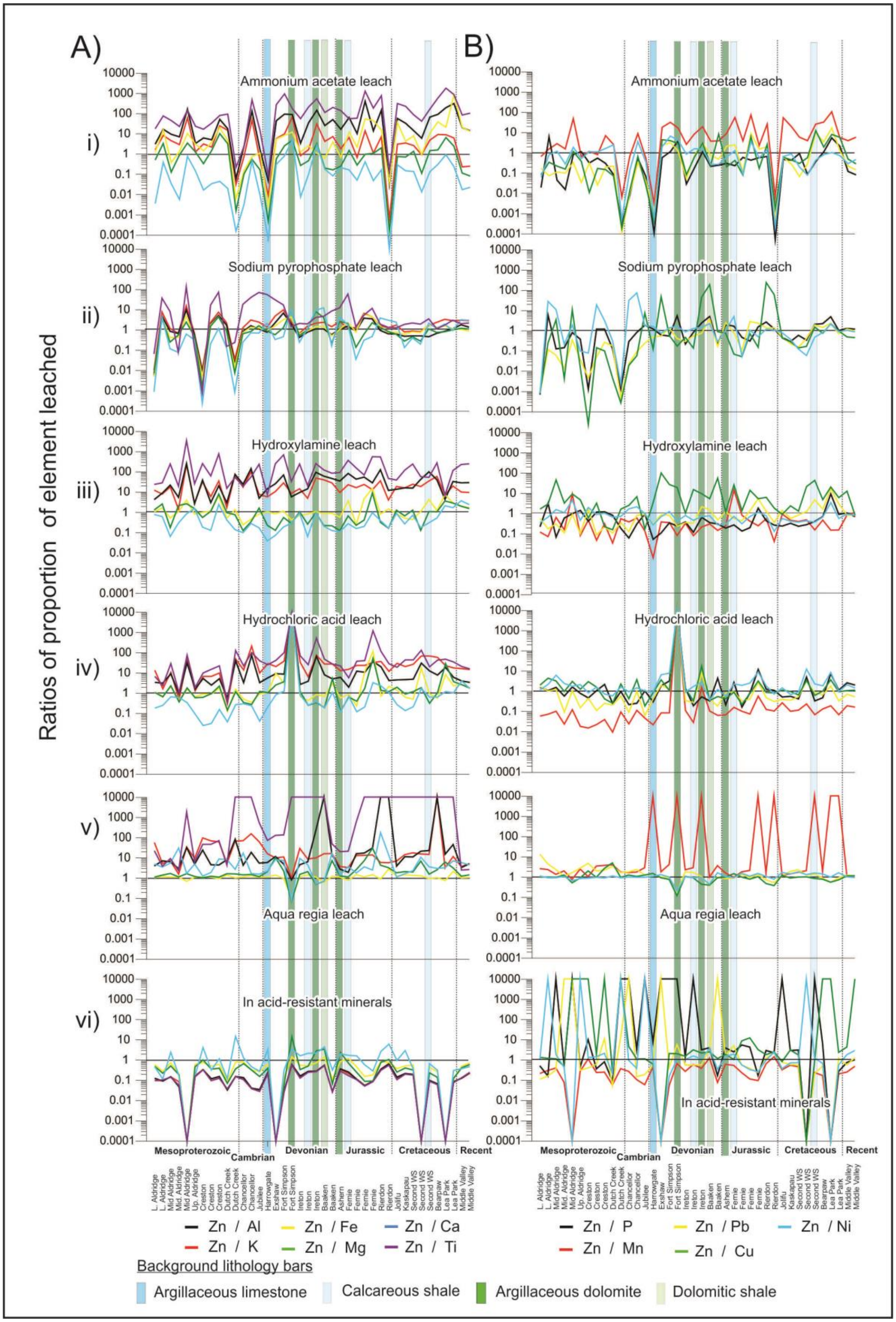

(Figure caption is on next page.)

Figure 10. The proportion of Zn extracted compared to the proportion of major elements extracted by different leaches in Column A and compared to the proportion of other trace elements in Column B. A value of 1 indicates that zinc and the denominator element are extracted in the same proportion, likely indicating that both are exclusively hosted by the same mineral. Values of >1 indicate that Zn is more leachable than the denominator element, and values <1 indicate that the denominator element is more leachable than Zn. See text for discussion.

indicating that Zn, Fe and Mg are proportionally extracted from the same mineral. As seen above for sample LEA-12-036, this is due to the dissolution of chlorite. The Zn/Mg ratio rocks is higher than the Zn/Fe of Mesozoic rocks by aqua regia leaching, probably because proportionally more Mg than Fe is leached by the first four sequential leaches (compare Figure 6A.ii and iii) and a higher proportion remains in the aqua regia residue as illite (judging from ternary K-Fe-Mg plots). The general gradual trend of decreasing proportions of Fe and Mg leached by the first four sequential leaches (Figure 6A.ii and A.iii) is consistent with the diagenetic change from illite-smectite to muscovite with increasing depth of burial. This suggests that because of the stability of muscovite, the proportion of Zn that can be extracted by weak leaches from argillaceous rocks, decreases with increasing depth of burial. This suggestion is corroborated by Figure 5A.i and 5B.i. This pattern is the opposite for Pb, which shows a trend of increasing tendency for extraction by weaker leaches with increasing depth of burial (Figure 5A.ii and 5B.ii). This difference in leaching response with increasing depth of burial of source rocks, may be the basis for the range of Zn:Pb ratios of SEDEX and MVT deposits.

The extractability of Zn compared to other metals (Figure 5B) depends upon the leach, and for the weaker leaches, upon the sample. For the ammonium acetate and sodium pyrophosphate leaches, generally the leachability follows the order Cu>Pb>P>Zn>Ni>Mn for Mesoproterozoic rocks and Cu>Ni>P>Zn>Pb>Mn for Mesozoic rocks, but with so much variability the validity of this generalization could be questioned. The relative extractability of metals is much more consistent for the hydroxylamine and hydrochloric acid leaches, with only Mn being consistently the most extractable for most samples. The metal ratios for the aqua regia leach are close to 1 for most samples, meaning that if Zn is contained mainly in smectite-chlorite at shallow burial depths and chlorite at greater burial depths, so are all the other metals. The zero values for P and Mn are artifacts of the method of calculation for the amounts of metal that would be removed by the aqua regia leach if it were in reality the last of the sequential leaches (see above) and not, as was the case, a separate leach of rock powder.

Conclusions

The data presented here emphasizes that trace metals in rocks are contained mainly within the structure of rock-forming minerals. The consistency between the amounts of metals leached and the amounts of major elements leached questions whether rocks contain significant quantities of metals that are loosely adsorbed on to a substrate. The data can also be used to question the assumption that the selective leaches used here are specific to the sites claimed for them when it comes to leaching rock powders. Although the sequential leach data for metals could be interpreted in accord with the conclusions of Zielenski et al. (1983) to indicate that metals supposedly adsorbed on to the surfaces of clays, organic matter, and/or iron and manganese oxides are readily leached to give concentrations sufficient to form ore deposits, the co-analysed major element data puts constraints on the applicability of the experimental leaching to natural systems. This major element data indicates that the major rock-forming elements are solubilized in about the same proportions as the metals, meaning that most of the metal content of sedimentary rocks is as diadochic substitutions or micro mineral inclusions in the rock forming minerals. In other words, to extract the 10-20% of metal content of the rock that weak selective leaches achieve (e.g. Zielenski et al., 1983), >10-20% of the rock would have to be dissolved or at least thoroughly altered by the same volume of fluid. As Lydon (1986) pointed out, this is impossible because the fluid would lose its reactive capacity even before <1% of the source rock was altered. This would imply that the availability of leachable metals in sedimentary basins is not a limiting control on the generation of SEDEX/MVT ore systems.

Bearing in mind the constraints of the major element data, the analyses presented here leads to conclusions similar to that of Bischoff et al. (1981):

1. The amount of metal that can be leached from a sedimentary rock is proportional to the amount of dissolution or alteration of the source rock and the concentration of metals in the rock-forming minerals.
2. The maximum amount of metal in the pore fluid depends on the concentration of metal-complexing ligands, particularly chloride, in the fluid, the temperature of the pore fluid, and the saturation limit with respect to a metallic mineral.

These conclusions point to further implications:

3. The need for chloride brines to leach metals to produce a SEDEX/MVT ore system, which, as the evidence noted above indicate are evaporated sea water, means that the sedimentary basin must have been at low latitudes adjacent to an extensive shallow continental shelf, at some time in its history.
4. Because the leaching of significant amounts of metal by pore fluids requires the alteration of the source rocks beyond the reactive capacity of a pore fluid to achieve, extraction of significant amounts of metals can only be accomplished during leaching windows afforded by metamorphic mineral-mineral reactions.
5. Considering that fluid inclusion filling temperatures for SEDEX/MVT deposits is generally <200°C (e.g. Wilkinson, 2001), the most likely metamorphic reaction zone is the 90-100°C of the smectite-illite transformation of the second dehydration event of Burst (1969).

Implications for Exploration

The implications of the results of this work for the generation of SEDEX/MVT ore systems are twofold:

1. Metal leaching in SEDEX/MVT systems is restricted to windows of mineral transformations during diagenesis. Because at normal water-rock ratios the reactive capacity of the pore fluids of a sediment are exhausted before any significant volume of rock is solubilized or altered, the only viable mechanism for leaching large quantities of metal is during the mineralogical transformations afforded by P-T driven metamorphic reactions (i.e. source rock alteration is driven by mineral-mineral disequilibrium and not by fluid-mineral disequilibrium).
2. SEDEX/MVT ore systems can develop only in those sedimentary basins with a prior history of evaporitic conditions. Because high concentrations of Zn and Pb in natural fluids are possible only in chloride brines, and large amounts of chloride brines can only be generated by solar evaporation of sea water, it follows that the sedimentary basin or adjacent platform must have experienced evaporitic conditions at some time during its history.

These two concepts severely restrain genetic models for SEDEX/MVT ore systems, and hence the exploration strategies based on these models. For example, basins that have not experienced low latitude climatic conditions at some time in its history, nor is adjacent to an extensive shallow water shelf on which evaporitic conditions can develop, are unlikely to be fertile for the development of a SEDEX/MVT ore system. The stratigraphic level at which evaporitic brines may have developed is the oldest stratigraphic level in the sedimentary basin at which SEDEX deposits can form. The restriction of metal leaching to windows of diagenetic mineral transformations, gives rise to the possibility of using the halide or base metal contents of minerals formed during these windows, such as apatite, ilmenite, etc., as a means for testing a basin for the former presence of metalliferous brines. In other words, this work brings a new perspective of how and when metalliferous brines are formed, and opens up new directions for both exploration strategies and exploration techniques.

Future Work

The large amount of data generated by this study has the capacity to yield further insights into the mobility of metals in sedimentary basins upon continued and further analysis. Important to future work in understanding SEDEX/MVT system, as alluded to several times above, is the relationship between the formation of metalliferous brines and the maturation of kerogens to form oil and gas, and the co-migrations of these fluids in the sedimentary basin. Collaboration between metallogenists with oil geologists would undoubtedly give more realistic insights into the hydrodynamic architecture and evolution of sedimentary basins. With this connection in mind, possible new insights might include using vanadium as a geochemical vector to SEDEX vent field, noting that any structure that allows the upward escape of metalliferous brines must also allow the upward escape of oil and gas and form a dispersion plume of metals contained in the oil. Since brine fields are density stratified and the halogen ratios of evaporated seawater are related to density (e.g. Worden, 1996), mapping of the halogen contents of, say, apatite might be a way to determine whether a basin contained brine during the leaching windows of diagentic mineral transformations.

This work also brings to attention other questions on SEDEX/MVT systems which need research. If metal leaching requires high density brines, then what is the mechanism to bring these brines to the sea floor? It cannot be convection, because fluid inclusions of SEDEX deposits suggest maximum temperatures of ~200ºC (e.g. Wilkinson, 2001), which is too low for >18 wt.% NaCl brines to become buoyant in sea water.

Acknowledgements

A large number of people contributed to this study. Paul Ransom, Dave Pighin and Chuck Downey helped collect or donated samples at the western end of the traverse line, some of which were from previous studies and stored in GSC archives. Veronique Pascone, Carleton University, compiled well log data from British Columbia, Alberta and Saskatchewan and carried out the crushing, grinding and sieving of the samples. Ryan Olson, Susan Co and Melinda Yurkowski facilitated the collection of cores at the British Columbia, Alberta and Saskatchewan core repositories respectively. Emily Mesesc, University of Waterloo, carried out SEM work and X-Ray mapping of Mesoproterozoic and Paleozoic samples. Yolanda Zhang, University of Waterloo, carried out much of the XRD analyses of the oil well cores and plotting of chemical data. Igor Bilot and Jeanne Percival of the Geological Survey of Canada's XRD lab supervised student use of the equipment and carried out the remaining XRD analyses. Pat Hunt operated the SEM for backscatter imaging, EDS analysis and X-Ray mapping.

References

Bischoff, J.L., Arthur S. Radtke, A.S., and Robert J. Rosenbauer, R.J., 1981, Hydrothermal alteration of graywacke by brine and seawater: roles of alteration and chloride complexing on metal solubilization at 200º and 350ºC: Economic Geology, v. 76, p. 659-676.

Burst, J.F., 1969, Diagnosis of Gulf Coast clayey sediments and its possible relation to petroleum migration: Bulletin of the American Association of Petroleum Geologists, v. 53, p. 73-93.

Carpenter, A.B., Trout, M.L., and Pickett, E.E., 1974, Preliminary report on the origin and chemical evolution of lead- and zinc-rich oil field brines in Central Mississippi: Economic Geology, v. 69, p. 191-206.

Cathles, L.M., and Smith, A.T., 1983, Thermal constraints on the formation of Mississippi Valley–Type lead-zinc deposits and their implications for episodic basin dewatering and deposit genesis: Economic Geology, v. 78, p. 983-1002.

Chao, T.T., 1984, Use of partial dissolution techniques in geochemical exploration: Journal of Geochemical Exploration, v. 20, no. 2, p. 101-135.

Ellis, A. J., 1968, Natural hydrothermal systems and experimental hot water/rock interaction: Reactions with NaCl solutions and trace metal extraction: Geochimica et Cosmochimica Acta, v. 32, p. 1356-1363.

Emsbo, P., 2009, Geologic criteria for the assessment of sedimentary exhalative (SEDEX) Zn-Pb-Ag deposits: United States Geological Survey, Open-File Report 2009-1209, 21 p.

Garrels, R.M., and F.T. Mackenzie, 1971, Evolution of sedimentary rocks: W.W. Norton & Co., New York. 397 p.

Garven, G., and Freeze, R.A., 1985a, Theoretical analysis of the role of groundwater flow in the genesis of stratabound ore deposits: 1. Mathematical and numerical model: American Journal of Science, v. 284, p. 1075-1124.

Garven, G., and Freeze, R.A., 1985b, Theoretical analysis of the role of groundwater flow in the genesis of stratabound ore deposits: 2. Quantitative results: American Journal of Science, v. 284, p. 1125-1174.

Goodfellow, W.D., and Lydon, J.W., 2007, Sedimentary exhalative (SEDEX) deposits, *in* Goodfellow, W.D., ed., Mineral deposits of Canada: A synthesis of major deposit-types, district metallogeny, the evolution of geological provinces, and exploration methods: Geological Association of Canada, Mineral Deposits Division, Special Publication no. 5, p. 163-184.

Hanor, J.S., 1996, Controls on the solubilization of lead and zinc in basinal brines, in Sangster, D.F., ed., Carbonate-hosted lead-zinc deposits: Society of Economic Geology, Special Publication no. 4, p. 483–500.

Hitchon, B., 1966, Formation fluids, Chap. 15 in Geological history of western Canada: Calgary, Alberta: Alberta Society of Petroleum Geologists, p. 201-217.

Hitchon, B., Billings, G.K., and Klovam, J.E., 1971, Geochemistry and origin of formation waters in the Western Canada basin-III. Factors controlling chemical composition: Geochimica et Cosmochimica Acta, v. 35, p. 567-598.

Hitchon, B., and Filby, R., 1983, Geochemical studies – trace elements in Alberta crude oils: Alberta Research Council for Alberta Energy and Utilities Board and Alberta Geological Survey, Open File report 1983-02, 150 p.

Kharaka, Y.K., Maest, A.S., Carothers, W.W., Law, L.M., Lamothe, P.J., and Fries, T.L., 1987, Chemistry of metal-rich brines from Central Mississippi salt dome basin, U.S.A.: Applied Geochemistry, v. 2, p. 543-561.

Leach, D.L., Sangster, D.F., Kelley, K.D., Large, R.R., Garven, G., Allen, C.R., Gutzmer, J., and Walters, S., 2005, Sediment-hosted lead-zinc deposits; a global perspective, *in* Hedenquist, J.W., Thompson, J.F.H., Goldfarb, R.J., and Richards, J.P., ed., Economic Geology, 100th anniversary volume, 1905-2005: Littleton, CO, Society of Economic Geologists, p. 561-607.

Lentini, M. R., and Shanks, W. C., III, 1983, Experimental study of brine-arkose interaction at 200 degrees C and 500 bars; origin of metalliferous oil field brines and Mississippi valley-type ore deposits, *in* Kisvarsanyi, G., Grant, S.K., Pratt, W. P., and Koenig, J. W., ed., International Conference on Mississippi Valley-type lead-zinc deposits: Proceedings volume, Rolla, MO, University of Missouri-Rolla, p. 195-205.

Long, D.T., and Angino, D.T., 1982, The mobilization of selected trace metals from shales by aqueous solutions: effects of temperature and ionic strength: Economic Geology, v. 77, p. 646-652.

Lydon, J.W., 1983, Chemical parameters controlling the origin and deposition of sediment-hosted stratiform lead-zinc deposits: Mineralogical Association of Canada Short Course Handbook, v. 8, p. 175-250.

Lydon, J.W., 1986, Models for the generation of metalliferous hydrothermal systems within sedimentary rocks and their applicability to the Irish Carboniferous Zn-Pb deposits, *in* Andrew, C.J., Crowe, R.W.A., Finlay, S., Pennell W.M., and Pyne, J.F., ed., The geology and genesis of mineral deposits in Ireland: Irish Association of Economic Geology and Geological Survey of Ireland, p. 555-577.

Lydon, J.W., Walker, R., and Anderson, E.H., 2000, Lithogeochemistry of the Aldridge Formation and the chemical effects of burial diagenesis, *in* Lydon, J.W., Höy, T. ,Slack, J.F., and Knapp, M.E., ed., The geological environment of the Sullivan deposit, British Columbia: Geological Association of Canada, Mineral Deposits Division, Special Publication no. 1, p. 136-179.

Magaw, R.I., McMillen, S.J., Gala, W.R., Trefry, J.H., and Trocine, R.P., 2000, Risk evaluation of metals in crude oils, *in* Sublette, K.L., ed., Proceedings of the 6th International Petroleum Environmental Conference, Houston, TX: SCG Inc., p. 460-473.

Milliken, K.L, 2004, Late diagenesis and mass transfer in sandstone and shale Sequences, *in* Holland, H.D., and Turekian, K.K., ed., Treatise on Geochemistry: Elsevier, Amsterdam, v. 7, p. 159-190.

Rittenhouse, G., Fulton, R.B., Grabowski, R.J., and Bernard, J.L., 1969, Minor elements in oil-field waters: Chemical Geology, v. 4, p. 189-209.

Roedder, E., 1984, Fluid inclusions: Mineralogical Society of America, Reviews in Mineralogy, v. 12, 644 p.

Russell, M.J., 1978, Downward-excavating hydrothermal cells in Irish type ore deposits: importance of an underlying thick Caledonian prism: Transactions Institute Mining and Metallurgy, v. 87, p. B168–171.

Russell, M.J., Solomon, M., and Walshe, J.L., 1981, The genesis of sediment-hosted, exhalative zinc + lead deposits: Mineralium Deposita, v. 16, p. 113-127.

Samson, I.M., Russell, M.J., 1987, Genesis of the Silvermines zinc–lead–barite deposit, Ireland: fluid inclusion and stable isotope evidence: Economic Geology, v. 82, p. 371–394.

Sverjensky, D.A., 1984, Oil field brines as ore-forming solutions: Economic Geology, v. 79, p. 23–37.

Turekian, K.K., and Wedepohl, K.H., 1961, Distribution of the Elements in some major units of the Earth's crust: Geological Society of America Bulletin, v. 72, p. 175-192.

Viets, J.G., Hofstra, A.H., and Emsbo, P., 1996, Solute compositions of fluid inclusions in sphalerite from North American and European Mississippi Valley-type ore deposits: ore fluids derived from evaporated seawater, *in* Sangster, D.F., ed., Carbonate-hosted lead–zinc deposits: Society of Economic Geology Special Publication no. 4, p. 465-482.

Verdel, C., Niemi, N., and van der Pluijm, B.A., 2011, Variations in the illite to muscovite transition related to metamorphic conditions and detrital muscovite content: insight from the Paleozoic passive margin of the southwestern United State: Journal of Geology, v. 119, p. 419–437.

Weiss, A., and Amstutz, G.C., 1966, Ion-exchange reactions on clay minerals and cation selective membrane properties as possible mechanisms of economic metal concentration: Mineralium Deposita, v. 1, p. 60-66.

Wilkinson, J.J., 2001, Fluid inclusions in hydrothermal ore deposits: Lithos, v. 55, p. 229–272.

Worden, R.H., 1996, Controls on halogen concentrations in sedimentary formation waters: Mineralogical Magazine, v. 60, p. 259-274.

Yang, J., Large, R.R., Bull, S., and Scott, D.L., 2006, Basin-scale numerical modeling to test the role of buoyancy-driven fluid flow and heat transfer in the formation of stratiform Zn-Pb-Ag deposits in the northern Mount Isa Basin: Economic Geology, v. 101, no. 6, p. 1275-1292.

Zielinski, R.A., Bloch, S., and Walker, T.R., 1983, The mobility and distribution of heavy metals during the formation of first cycle red bed: Economic Geology, v. 78, no. 8, p. 1574-1589.

Widespread Euxinic Conditions are not a Prerequisite for Sediment-Hosted Base Metal (Pb-Zn-Ba) Mineralization at MacMillan Pass, Yukon

J.M. Magnall, R.A. Stern, and S.A. Gleeson
Department of Earth and Atmospheric Sciences,
University of Alberta, Edmonton, AB, T6G 2E3
magnall@ualberta.ca

S. Paradis
Geological Survey of Canada, Box 6000, 9860 West Saanich Road,
Sidney, BC, V8L 4B2

Abstract

Late Devonian strata in the MacMillan Pass District, Selwyn Basin, Yukon, are host to two Pb-Zn-Ba deposits, Tom and Jason. Mineralization has previously been considered stratiform, and base metal sulphides (pyrite-sphalerite-galena) are thought to have precipitated from the water column, along with barite. A first order control on the precipitation of sulphides, therefore, is the presence of reduced sulphur in the water column (euxinic conditions). Over 400 samples of drill core intersecting the mineralization at Tom and Jason were obtained, in order to comprehensively evaluate the textural evidence for stratiform mineralization. The mineralogy and the paragenetic relationship between barite and base metal sulphides were determined using transmitted and reflected light, and backscatter electron imaging. The paragenetic framework provided a context within which to perform in situ sulphur isotope microanalysis (secondary ion mass spectrometry; SIMS) of barite and pyrite.

In the samples from both Tom and Jason, there is strong petrographic evidence that barite formed during early diagenesis, pre-dating hydrothermal input. In addition, there are at least two generations of diagenetic pyrite associated with the barite. All hydrothermal sulphides (pyrite, sphalerite and galena) clearly post-date and overprint the diagenetic barite-pyrite assemblage. This textural evidence raises the question as to whether mineralization is truly syn-sedimentary. Diagenetic pyrite comprises two end-member isotopic populations: framboidal pyrite (*py-I*; -23‰ to -28‰), and euhedral pyrite (*py-II*; 8‰ to 26‰). Barite intergrown with *py-II* has a median δ^{34}S composition of 28‰, and a range of 24‰ to 34‰. These $\delta^{34}S_{\text{-barite}}$ values overlap with the isotopic composition of Late Devonian seawater sulphate, which rules out near quantitative reduction of seawater sulphate in the water column as a mechanism for sulphide production. In the absence of euxinic conditions, an alternative source of reduced sulphur is

Recommended citation
Magnall, J.M., Stern, R.A., Gleeson, S.A., and Paradis, S., 2015. Widespread euxinic conditions are not a prerequisite for sediment-hosted base metal (Pb-Zn-Ba) mineralization at MacMillan Pass, Yukon, *in* Paradis, S., ed., Targeted Geoscience Initiative 4: sediment-hosted Zn-Pb deposits: processes and implications for exploration; Geological Survey of Canada, Open File 7838, p. 43-57. doi:10.4095/296328

required to account for base metal sulphide accumulation in the MacMillan Pass strata; barite replacement is one potential mechanism, and is supported by substantial textural and mineralogical evidence. Further work will be required to establish its importance from a mass balance perspective.

Introduction

MacMillan Pass, Yukon, is situated approximately 390 km NE of Whitehorse, adjacent to the Northwest Territories (NT) border (Figure 1a). It is the location of important sediment-hosted Zn-Pb-(Ba) mineralization, at the mineral occurrences of Tom and Jason (Figure 1b). Mineralization is hosted within Upper Devonian Selwyn Basin strata, comprised of organic-rich, siliceous mudstones that form part of the Earn Group (Figure 2) (Gordey et al., 1982). The MacMillan Pass deposits have traditionally been viewed as type-characteristic sedimentary exhalative (SEDEX) deposits (Goodfellow and Lydon, 2007); Tom and Jason both display a clearly defined zone of hydrothermal upflow (stockwork style veining), located stratigraphically above what is considered to be bedded to laminated, stratiform base metal sulphide mineralization in overlying mudstones (Figure 3). Models for this style of mineralization in the Selwyn Basin involve syn-sedimentary precipitation of base metal sulphides from the water column following hydrothermal venting (Goodfellow, 2007). A prerequisite for effective base-metal precipitation is therefore basinal euxinia, i.e. the buildup of H_2S in the water column, at the expense of bacterial sulphate reduction (BSR). At MacMillan Pass, the supporting evidence for this, aside from textural interpretations (e.g. stratiform sulphides), has been in the form of sulphur isotope data obtained from bulk rock analyses of pyrite and barite (Figure 2; replotted from Goodfellow and Jonasson, 1984). There is a sizeable fractionation of sulphur isotopes during BSR (Kaplan and Rittenburg, 1964), a result of the preferential reduction of $^{34}SO_4^{2-}$ over $^{34}SO_4^{2-}$. At MacMillan Pass, enrichments of ^{34}S in bedding paralle pyrite and barite are cited as evidence for basinal restriction and near quantitative reduction of seawater sulphate via BSR (Goodfellow and Jonasson, 1984). This model, it should be emphasized, is predicated on the assumption that reduced sulphur was generated almost exclusively by BSR in closed-system conditions, and that pyrite and barite formed coevally from a euxinic water column.

However, recent petrographic work has demonstrated that sulphide and barite mineralization is not strictly stratiform, rather stratabound, and thus could have originated below the sediment-water interface (SWI) (Magnall et al., 2014). It is possible that the diagenetic history of many of these samples was more complex, with multiple generations of barite and pyrite. Using bulk analytical techniques these details cannot be resolved, and there is the risk that the isotopic data, previously from bulk-sample analysis, represents a mixture of multiple generations of these minerals. This study presents comprehensive petrographic analysis, combined with sulphur isotope analysis of pyrite and barite, obtained using secondary ion mass spectrometry (SIMS), a micro-analytical technique that provides the necessary spatial resolution to analyse individual crystals (>15 μm). This approach offers the unique capability of being able to interpret isotopic

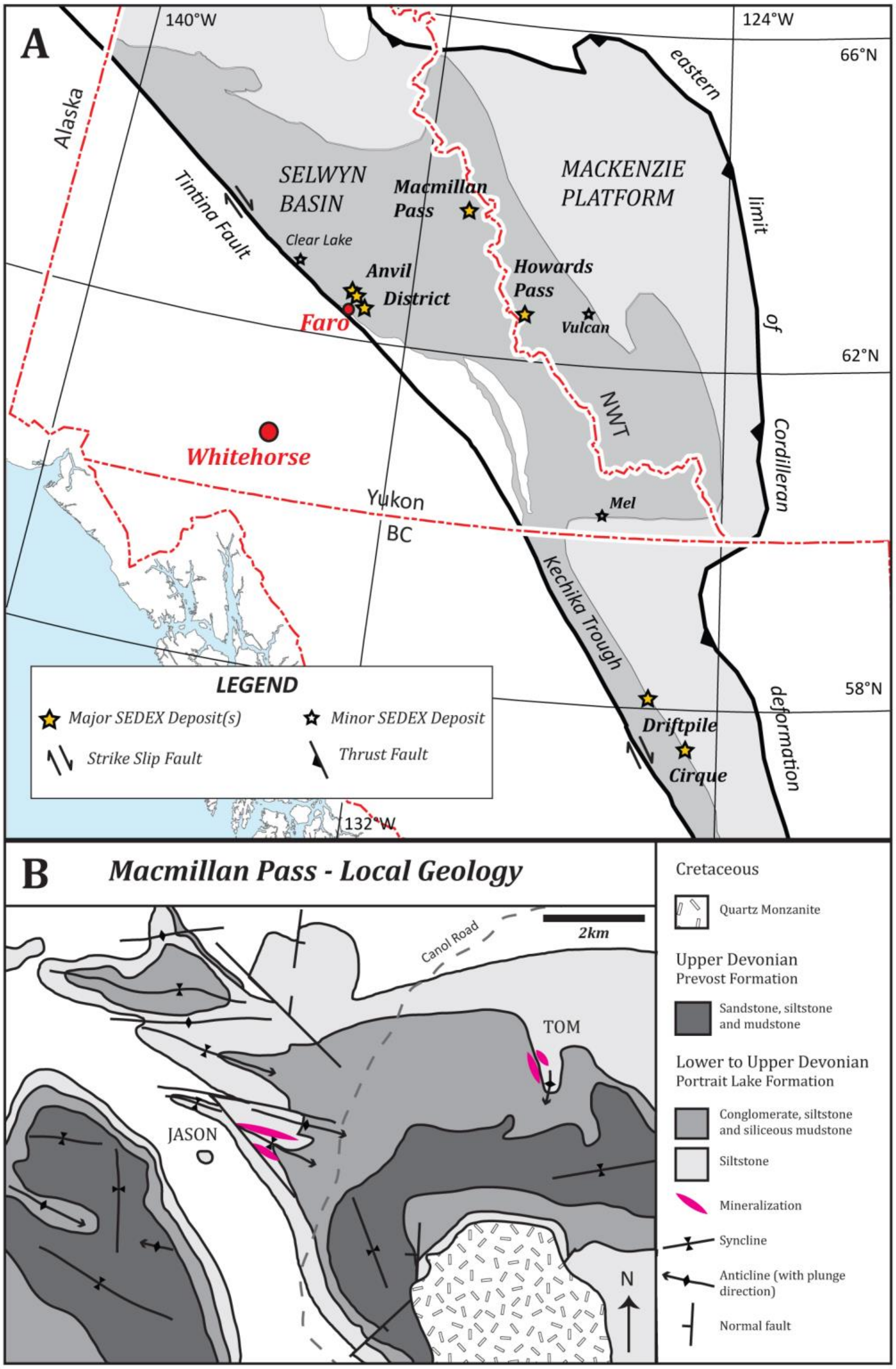

Figure 1. Regional map showing the geographical extent of the Selwyn Basin in western North America, with the location of major sediment-hosted base-metal districts highlighted (modified from Colpron and Nelson, 2011). The inset below shows the local geology of MacMillan Pass (modified from Abbott and Turner, 1990) and location of the Tom and Jason deposits.

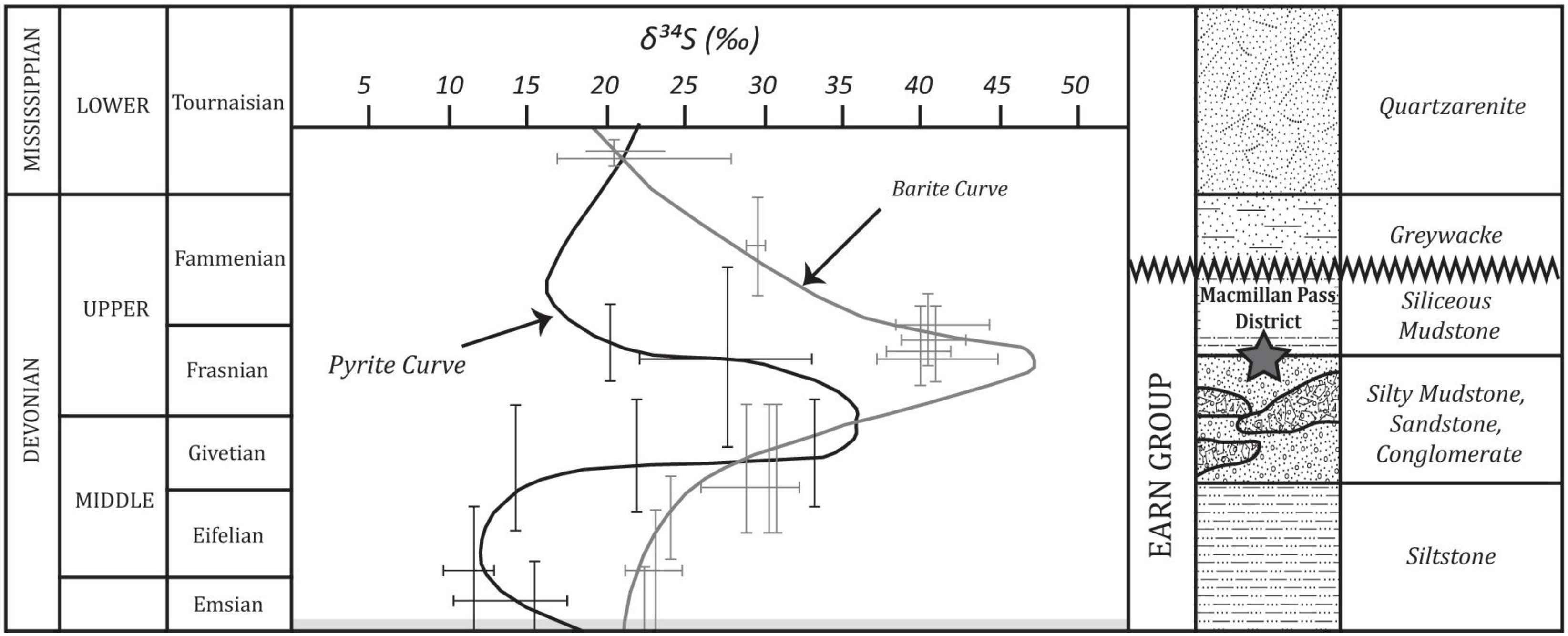

Figure 2. Late Devonian Selwyn Basin stratigraphy with the sulphur isotope curves for barite and pyrite of Goodfellow and Jonasson (1984). MacMillan Pass is denoted by the star in the Earn Group. The stratigraphy is compiled from Gordey and Anderson (1993) and Turner et al. (2011). Sulphur isotope data for barite (light grey) and pyrite (darker grey) are re-plotted from Goodfellow and Jonasson (1984).

composition in tandem with key mineralogical relationships, with the aim of evaluating the evidence for euxinia in the basin at MacMillan Pass during hydrothermal activity.

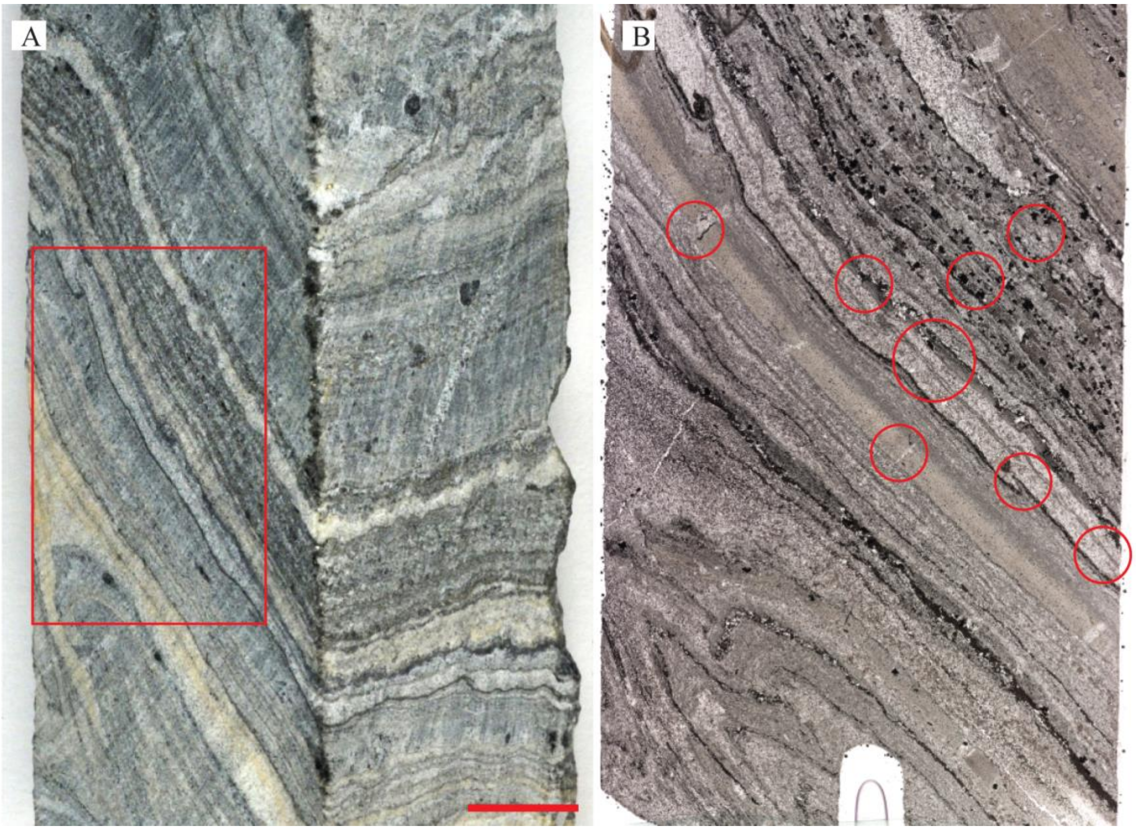

Figure 3. Photograph of a mineralized hand sample (TYK2-8) from the Tom deposit. Scale bar = 1cm. B - thin section of area in A marked by a red rectangle. Red circles indicate zones drilled out of thin section for SIMS microanalysis.

Results/Data Analysis

Methodology

Samples were collected during the summer field seasons of 2012 and 2013 from drill core stored at MacMillan Pass. Over 400 samples were collected from drill core from 10 drillholes from the Tom and Jason deposits. For the purposes of this study, care was taken to target the least deformed samples with the most representative mineralogical and textural relationships. These relationships were evaluated using a binocular microscope and transmitted and reflected light microscopy. A mineralogical paragenesis was developed on the basis of crosscutting relationships and evidence (or lack thereof) of textural equilibrium between key mineral phases.

Isotopic analysis of pyrite and barite, along with precursory sample preparation and imaging, were performed at the Canadian Centre for Isotopic Microanalysis (CCIM) at the University of Alberta, Edmonton, Canada, using a Cameca IMS-1280 ion microprobe. Samples were cored from either thin sections or rock chips using diamond core bits ranging between 2 and 3 mm diameter. The sample cores (n = 40) were cleaned, and cast in epoxy, along with pre-polished pieces of in-house barite and pyrite reference materials (RM's) to form two standard 25mm mounts (M1269 and M1270). The mounts were coated with 30nm Au, and imaged using a Zeiss EVO MA15 Scanning Electron Microscope (SEM). Greyscale cathodoluminescence (CL) images were also acquired using the SEM.

Sulphur isotope ratios ($^{34}S/^{32}S$) and oxygen isotope ratios ($^{18}O/^{16}O$) were determined using an IMS-1280 multi-collector ion microprobe. The isotopic composition of sulphur and oxygen are reported in terms of standard δ-notation, in reference to the composition of Vienna Canyon Diablo Troilite (VCDT) for sulphur (1), and Vienna Standard Mean Ocean Water (V-SMOW) for oxygen (2);

$$\delta^{34}S\ ‰ = 1000\ x\ [\ (^{34}S/^{32}S)_{\text{sample}} - (^{34}S/^{32}S)_{\text{VCDT}}\ ]\ /\ (^{34}S/^{32}S)_{\text{VCDT}} \qquad (1)$$

$$\delta^{18}O\ ‰ = 1000\ x\ [\ (^{16}O/^{18}O)_{\text{sample}} - (^{16}O/^{18}O)_{\text{VSMOW}}\ ]\ /\ (^{16}O/^{18}O)_{\text{VSMOW}} \qquad (2)$$

Key analytical parameters are summarized in Table 1. The primary beam used focused 20 keV$^{133}Cs^{+}$ ions to form a probe (diameter and beam current; Table 1). Rastering of the primary beam (area; Table 1), for 60 s prior to analysis, cleared the surface of contaminants and implanted Cs. The normal incidence electron gun was utilized for analysis of barite. Isotopes of interest ($^{32}S^{-}$, $^{34}S^{-}$, $^{16}O^{-}$, $^{18}O^{-}$) were analyzed simultaneously in Faraday cups (L'2 using 10^{10} Ω amplifier, and FC2 or H'2 with 10^{11} Ω, respectively); see Table 1 for mass resolutions and mean count rates. Analyses of unknowns were interspersed with the RM's in a 4:1 ratio. Instrumental mass fractionation (IMF) was determined for each analytical session from utilizing all the replicate analyses of the RM's. Final uncertainties are typically ±0.20 to 0.25 ‰ (Table 1) at 95% confidence interval (2σ), and propagate within-spot counting errors, between-spot errors (geometric effects) and between-session errors. Errors do not include the absolute uncertainty in the composition of the RMs (Table 1) of ±0.2 to 0. 5 ‰. No orientation-related biases have been found for SIMS analysis of pyrite or barite at CCIM (e.g. Kozdon et al., 2010). During the analytical sessions, a total of 176 $\delta^{34}S$ analyses of pyrite were performed, and 184 $\delta^{34}S$ and 121 $\delta^{18}O$ analyses of barite.

Petrography

Three pre-mineralization generations of barite are recognized; (1) *barite-I* occurs as small (<25μm) interstitial, anhedral crystals that form enrichments along and within individual mudstone laminae (Figure 4A), (2) *barite-II* forms a distinctive, commonly patchy replacement of mudstone (Figure 4B and C), but also occurs as equant, euhedral crystals in mono-minerallic stratiform laminations (Figure 4A), and discontinuous stratabound enrichments, (3) *barite-III* is present within irregular veinlets that cross-cut mudstone laminae and earlier generations of barite (Figure 4A). All three generations of barite formed before hydrothermal input and precipitation of sphalerite, galena and hydrothermal pyrite.

	δ^{34}S-pyrite	**δ^{34}S-barite**	**δ^{18}O-barite**
Cs probe diameter (µm)	10	15	12
Beam Current (nA)	0.85	2.5	2.5
Electron gun used	no	yes	yes
Implantation raster (µm)	18 x 18	20 x 20	20 x 20
Entrance & field apertures (µm, mm)	122, 5x5	122, 5x5	122, 5x5
Field magnification	100x	100x	100x
Energy slit	Full open	Full open	Full open
Detectors	L'2 (FC, $10^{10}\Omega$), FC2 (FC, $10^{11}\Omega$)	L'2 (FC, $10^{10}\Omega$), FC2 (FC, $10^{11}\Omega$)	L'2 (FC, $10^{10}\Omega$), H'2 (FC, $10^{11}\Omega$)
Mass Resolution	2000, 2100	2000, 2100	1950, 2275
Secondary ions detected and mean counts/s	$^{32}S^-$ = 1*10^9 $^{34}S^-$ = 4.5*10^7	$^{32}S^-$ = 7*10^8 $^{34}S^-$ = 3*10^7	$^{16}O^-$ = 3.5*10^9 $^{18}O^-$ = 7*10^6
RM identity	S0322A pyrite	S0327 barite	S0327 barite
RM composition	$\delta^{34}S_{VCDT}$ = -0.2 ± 0.2‰	$\delta^{34}S_{VCDT}$ = +22.3 ± 0.5‰	$\delta^{18}S_{VSMOW}$ = +11.0 ± 0.5‰
Peak counting time	75 s	75 s	75 s
Standard deviation of RM analyses	0.04‰	0.05‰	0.07‰ – 0.11‰
Typical ±2σ of unknowns	± 0.17‰	± 0.18‰	± 0.24‰

Table 1. Key analytical parameters

Two principal pre-mineralization generations of pyrite include: (1) *pyrite-I* is framboidal, mostly 10-20 µm in diameter (Figure 5A), (2) *pyrite-II* is euhedral, and forms either stratiform accumulations (Figure 5B) of euhedral pyrite (*pyrite-IIa*) or individual idiomorphic crystals (*pyrite-IIb*), which often occur within *barite-II* (Figure 5C). These two sub-generations of *pyrite-II* are associated with different δ^{34}S compositions (see below). Both *pyrite-I* and *pyrite-II* are present within samples from the stratabound mineralization, and also unmineralized mudstone samples.

Hydrothermal pyrite (*pyrite-III*) can be found in association with sphalerite and galena. It occurs as large, sub- to anhedral replacements and overgrowths of earlier-formed barite (Figure 5D), in a mineral assemblage with witherite and sphalerite. Galena is the last phase to form in the paragenesis, and occurs as anhedral, interstitial crystals that overprint earlier barite and pyrite along

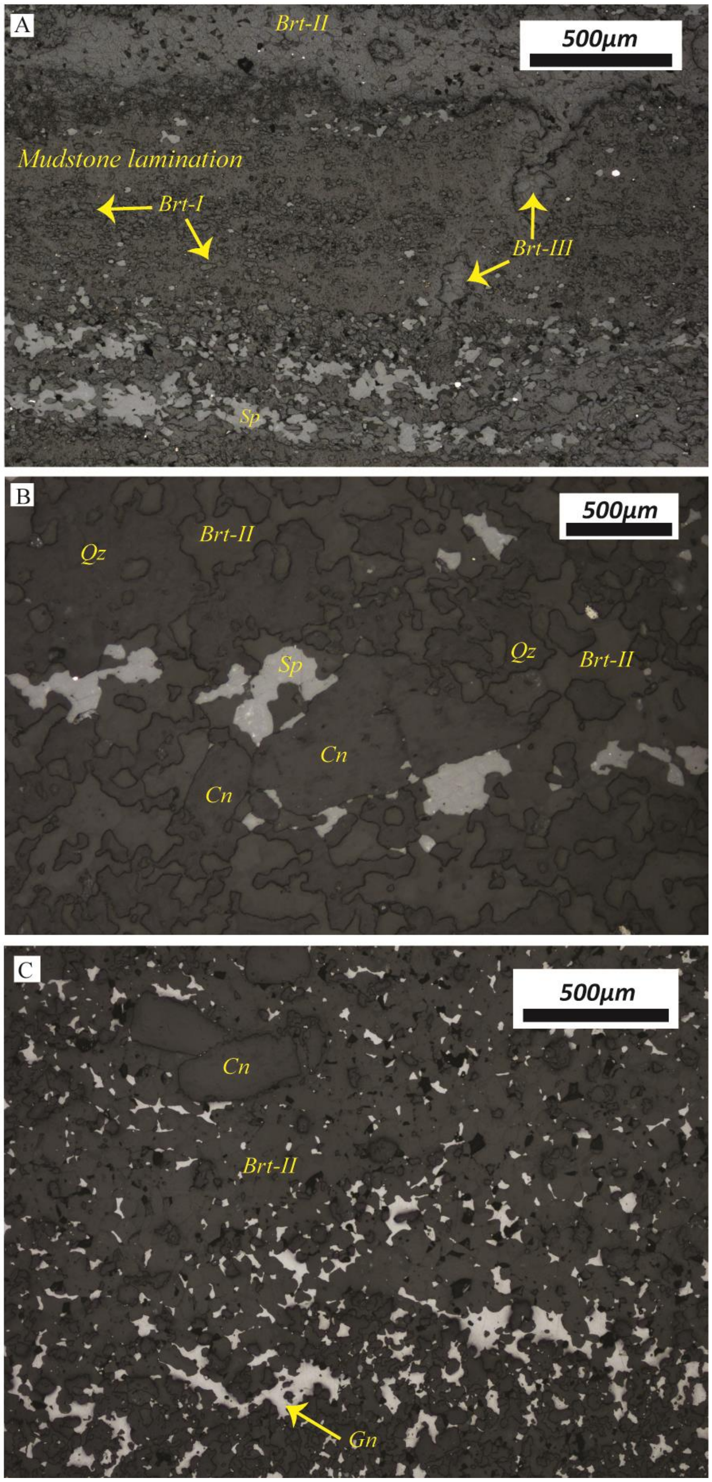

Figure 4. Photomicrographs in reflected light of: A - mudstone lamination with interstitial barite (Brt-I), interlaminated with Brt-II and cut by Brt-III. Sphalerite replaces barite towards bottom of the image. B - interstitial barite (Brt-II) in microcrystalline quartz (Qz). Barium feldspar (celsian; Cn) occurs in the centre of the image, partially replaced by barite. Sphalerite (Sp) occurs as interstital replacement of barite. C – interstitial replacement of *barite-II* by galena (Gn).

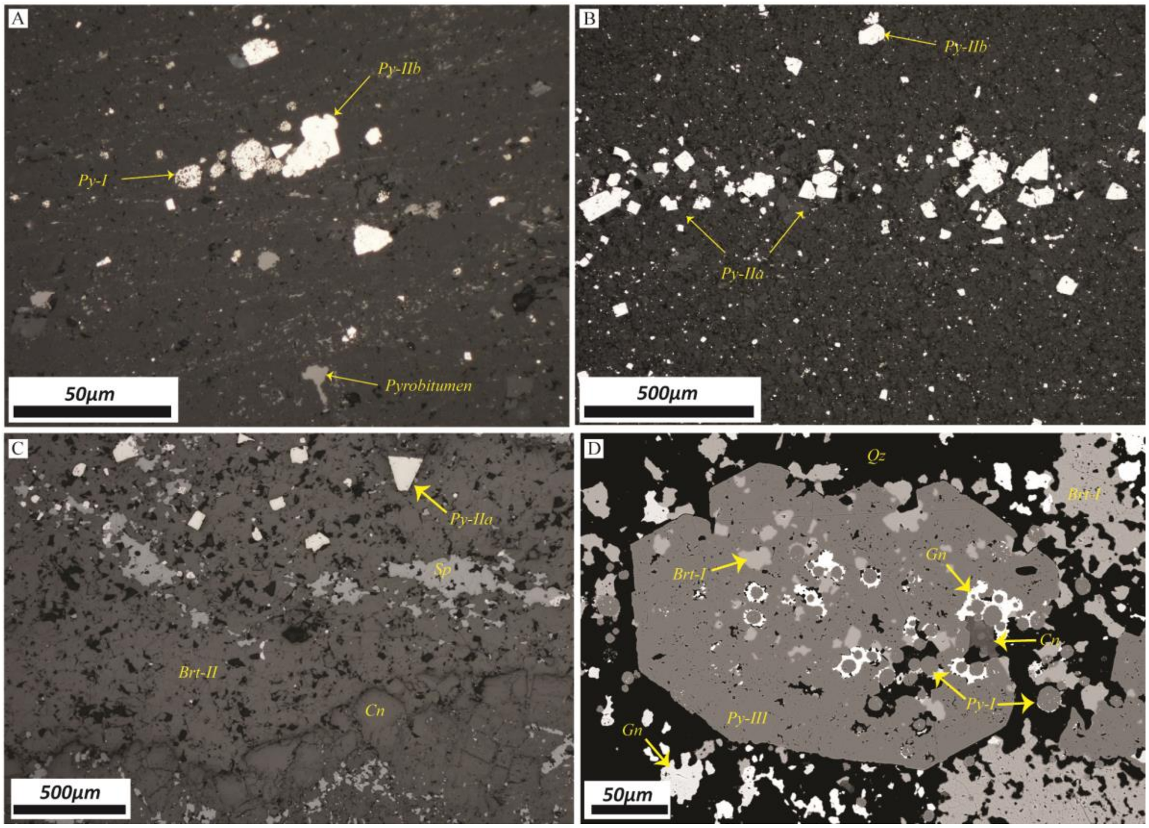

Figure 5. Photomicrographs in reflected light of: A - framboidal *Py-I* overgrown by euhedral *pyrite-IIb*, in a siliceous mudstone with interstitial pyrobitumen. B - *pyrite-IIa,* concentrated along a bedding parallel horizon. C - barium feldspar (celsian; Cn) precipitated along a stratal horizon, overlying and replaced by equant, euhedral barite (*Brt-II*). *Barite-II* is associated with euhedral pyrite crystals (Py-IIa), and both are replaced by subsequent sphalerite (Sp). D - backscatter electron image Of framboidal pyrite (*Py-I*) and barite (*Brt-I*) overprinted by later generation of pyrite (*Py-III*); framboidal pyrite seems to provide a porous framework for the mineralizing fluid to exploit, highlighted by the precipitation of galena.

stratiform layers (Figure 4C). Sphalerite and galena appear to precipitate and replace barite at triple-point junctions of crystals, leading to the development of anhedral, interstitial crystals within more euhedral barite.

Sulphur Isotopes

The sulphur isotope compositions of all generations of pyrite and barite are compiled in Figure 6. *Pyrite-I* has a distinctive isotopic composition, with $\delta^{34}S$ values between -28‰ and -15‰. Subsequent generations of pyrite (*pyrite-II* + *III*) overlap in isotopic composition, with a wide range of $\delta^{34}S$ values between 3‰ and 28‰. Barite, in contrast to pyrite, has a much narrower range of $\delta^{34}S$ composition, with values ranging between 24‰ and 34‰, and a median of 27‰. There are notable small-scale $\delta^{34}S$ variations, between barite crystals less than 50µm from each other, on the order of 3-4‰.

Discussion/Models

Textural Relationship of Barite and Pyrite

At the Tom and Jason deposits, there are some important mineralogical relationships that have not been documented in previous studies: (1) in all samples, barite pre-dates the ore forming sulphides (galena, sphalerite and *pyrite-III*); (2) there are multiple generations of barite, including vein barite (*barite-III*), which suggests that barium underwent remobilization within the host-rock; and (3) there are multiple generations of pyrite, including two that formed prior to Zn-Pb sulphide mineralization.

The mineralogy of these MacMillan Pass systems, although simple (pyrite – sphalerite – galena ± barite), is clearly complicated in terms of its temporal development. There are multiple generations of barite and pyrite that precede the main hydrothermal event, and only *barite-II* and *pyrite-IIb* formed coevally (Figure 5C). *Pyrite-III*, which was associated with hydrothermal input, shows clear disequilibrium textures with respect to earlier-formed barite and pyrite (Figure 5D). Therefore, in terms of bulk analyses, it is clear that previous sulphur isotope data (Goodfellow and Jonasson, 1984) represent a mixture of the isotopic compositions from multiple generations of barite and pyrite. Furthermore, at the micro-scale, there is minimal evidence of truly synsedimentary, laminated base metal sulphide precipitation (Magnall et al., 2014). It is therefore necessary to re-evaluate the isotopic evidence for basinal euxinia.

δ^{34}S Composition of Barite

The lowest $\delta^{34}S_{\text{-barite}}$ values (24‰) overlap with carbonate-associated sulphate (CAS) constraints on the δ^{34}S composition of Late Devonian seawater (John et al., 2010; Chen et al., 2013). This suggests that, with respect to sulphate at least, the Selwyn Basin was not restricted from circulation with the global oceans during hydrothermal activity. Furthermore, we have not found any extremely positive $\delta^{34}S_{\text{-barite}}$ values, which would support a model involving a Rayleigh sulphate reduction scenario in a closed system. Indeed, the narrow range in $\delta^{34}S_{\text{-barite}}$ is more typical of sulphate modified by BSR in open-system conditions, where sulphate resupply is greater than sulphate reduction.

Within the barite paragenesis, there is overlap in the δ^{34}S composition of different generations of barite, which likely means barite formed from fluids that had a similar source of sulphate. Using the criteria of Paytan et al. (2002), there is limited textural evidence for syn-sedimentary precipitation of barite; instead, the vast majority of barite is more consistent with formation below the sediment/water interface (SWI), in a diagenetic environment. The δ^{34}S composition of barite supports this conclusion, albeit in a diagenetic environment that is well connected with overlying seawater (perhaps 10 to 100 cm beneath the SWI), such that open-system conditions are maintained.

$\delta^{34}S$ Composition of Pre-mineralization Pyrite

The $\delta^{34}S$ isotopic composition of *pyrite-I* represents a large fractionation from Late Devonian seawater sulphate ($\Delta_{\text{-sulphate-sulphide}}$ = 49‰), and is consistent with slow rates of BSR (Goldhaber and Kaplan, 1975). As with $\delta^{34}S_{\text{-barite}}$, the range of $\delta^{34}S_{\text{-Py-I}}$ values we report are consistent with precipitation by BSR from the same diagenetic seawater pore fluid. The isotopic composition of barite and *pyrite-I* is not unique to formation from a system undergoing closed-system Rayleigh fractionation, and there is no evidence from the $\delta^{34}S$ analyses of barite that sulphate was reduced in near quantitative proportions. The relationship between barite and pyrite-I, whereby a large isotopic fractionation between $\delta^{34}S_{\text{-sulphate}}$ and $\delta^{34}S_{\text{-sulphide}}$ is preserved, is typical of BSR in normal marine mudstones (e.g. Canfield, 2004). The diameter of the framboidal pyrite analysed in this study (>7 µm) is also consistent with diagenetic pyrite formation, as opposed to precipitation from a euxinic water column (Wilkin et al., 1996).

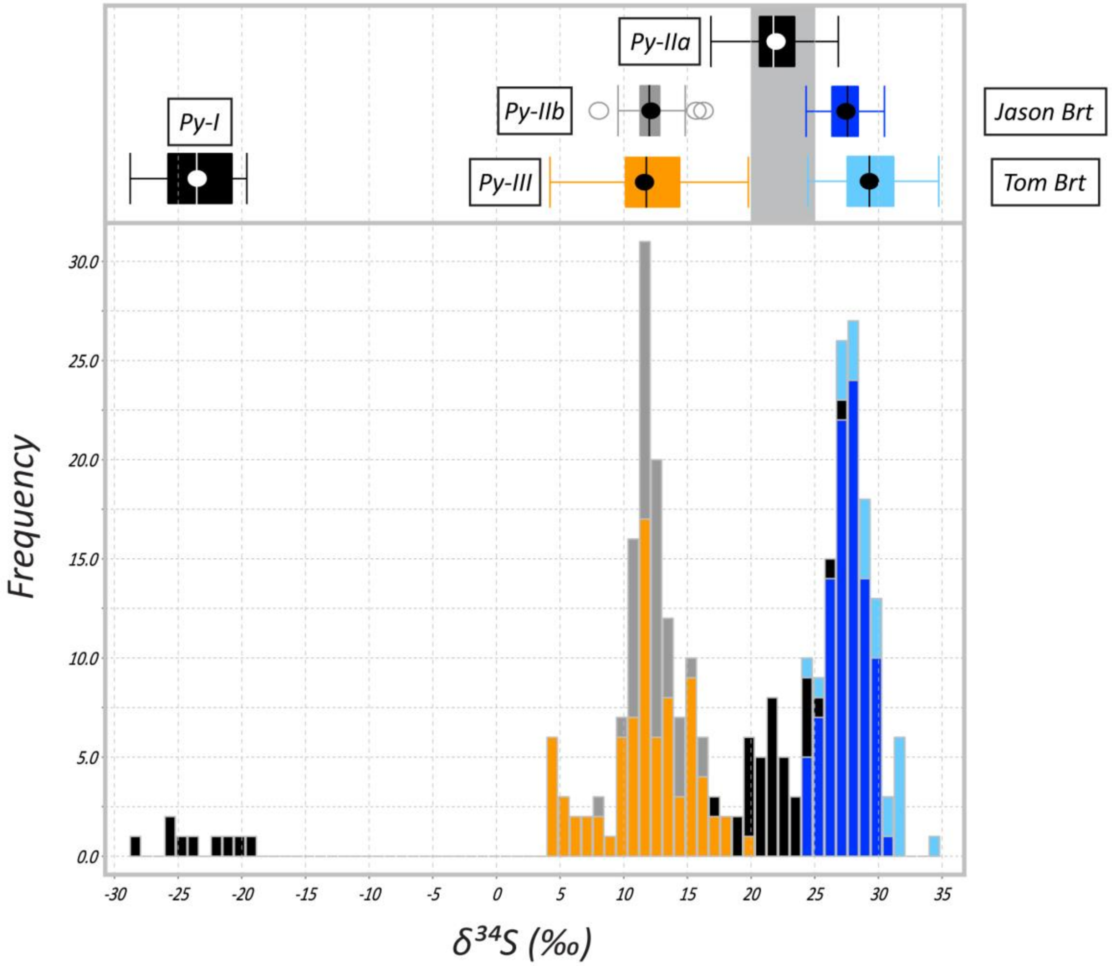

Figure 6. Histogram of compiled $\delta^{34}S$ results for entire study. Above the histogram are box and whisker representations summarizing the data in the histogram, along with labels. The grey box represents the $\delta^{34}S$ range of Frasnian seawater (John et al., 2010; Chen et al., 2013). Median values = vertical line; mean = circle; black box = interquartile (Q1 to Q3) range (IQR); lines extend to Q-n +(1.5*IQR) and circles outside lines are outliers.

Pyrite-II forms a distinct contrast to *pyrite-I*, both in morphology and $\delta^{34}S$ composition. In some cases, the $\delta^{34}S_{\text{-pyrite-II}}$ composition approaches coeval seawater sulphate ($\delta^{34}S \cong 24‰$; Figure 6) and the values reported by Goodfellow and Jonasson (1984). However, *pyrite-II* is also the only pyrite formed in direct association with barite, and in some cases (*pyrite-IIb*) textural equilibrium is observed (Figure 5C). The $\delta^{34}S$ composition of barite therefore forms an important constraint for interpreting the isotopic composition of pyrite. In particular, the $\delta^{34}S_{\text{-barite}}$ reflects the isotopic composition of unmodified Late Devonian seawater sulphate. Therefore, the positive $\delta^{34}S$ values recorded by *pyrite-II* cannot have been generated during the development of euxinic conditions. The end members that *pyrite-1* and *pyrite-II* form in terms of $\delta^{34}S$ composition, and their textural differences (crystal morphology, mineralogical relationship with barite), suggest a complex diagenetic history, and perhaps one in which reduced sulphur was produced by different processes. Importantly, these isotopic signatures were developed prior to hydrothermal input, in a diagenetic environment. Processes operating beneath the SWI, and not in the water column (i.e. euxinia), must have formed the metal trap in order to account for the accumulation of base metal sulphides in the strata at MacMillan Pass.

$\delta^{34}S$ Composition of Hydrothermal Pyrite

Pyrite-III displays a broad range in $\delta^{34}S$ composition (~4‰ to 20‰). The interquartile range (Q1 to Q3; *Pyrite-III*) overlaps with *Pyrite-IIb*, but also extends to lower and higher values of $\delta^{34}S$, and likely represents mixing of reduced sulphur from multiple sources. There is abundant textural evidence for barite dissolution and replacement by pyrite (Figure 7), and so one potential sulphur source would be the recycling of barite-sulphur by the hydrothermal fluid. In all samples, barite clearly pre-dates hydrothermal input. Figure 7 provides an example of a mineral assemblage that is commonplace in the mineralization at Tom and Jason, involving witherite-pyrite-sphalerite associated with barite dissolution. Witherite ($BaCO_3$) will only precipitate from high barium—low sulphate fluids (Hanor, 2000), and so is a likely by-product of barite dissolution coupled with sulphide precipitation. Barite replacement has been identified as a potential mechanism for sulphide precipitation at Red Dog, the world class Pb-Zn-Ba deposit (Kelley et al., 2004), however this is the first time it has been recognized at MacMillan Pass. However, it should be emphasized that the distribution of $\delta^{34}S$ values in *pyrite-III* is not consistent with quantitative recycling of barite-sulphur, and the broad range of values may reflect the mixing of the hydrothermal fluid with reduced sulphur in the diagenetic fluids, derived from other sources.

Implications for Exploration

The primary conclusion of this study is that euxinic conditions do not form a prerequisite for sediment-hosted base metal mineralization at MacMillan Pass. The $\delta^{34}S$ composition of barite provides no evidence that seawater sulphate underwent near quantitative reduction in the water column. This has important implications for the generation of base metal sulphide enrichments in Selwyn

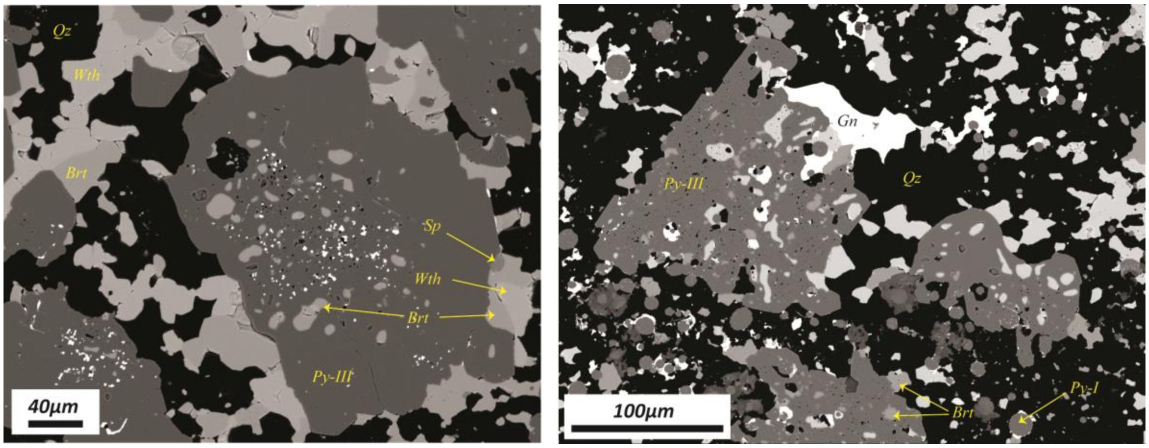

Figure 7. A – barite (Brt) dissolution association with sphalerite (Sp), witherite (Wth) and *Py-III* overgrowth. B – *Py-III* and galena (Gn) overprinting barite intergrown with quartz (Qz).

Basin strata. Although it does not rule out euxinia in other Selwyn Basin systems (Anvil District, Howards Pass), it does clearly show that positive excursions in the $\delta^{34}S_{\text{-pyrite}}$ record are not unique to the development of euxinic conditions, but can also be formed during diagenesis. At MacMillan Pass, this means that alternative sources of sulphur are required to account for base metal sulphide deposition; one such mechanism is barite replacement, and from an exploration perspective in Late Devonian strata, barite enrichments may represent fertile host-rocks for base metal sulphide enrichments. The relationship between barite enrichments and conduits for hydrothermal fluid flow (extensional fault systems) is likely to be an important control on the development of hydrothermal systems.

Future Work

There are two main components to the planned future work: (1) given the importance of pre-existing barite enrichments in the strata at MacMillan Pass what processes may be responsible for barite accumulation? Further analysis of barite, focusing on the oxygen isotope composition ($\delta^{18}O$) of barite-sulphate, will likely provide valuable information; and (2) the geochemical conditions under which sulphur is transformed from sulphate in barite to sulphide in galena, sphalerite and pyrite warrants further evaluation. Once the temperature and salinity of the hydrothermal fluid has been established (fluid inclusion studies), using geochemical modelling it will be possible to evaluate the conditions in which sulphide precipitation proceeds via barite replacement. In addition, the $\delta^{34}S$ composition of galena and sphalerite from mineralization at MacMillan Pass will be documented by in situ techniques (SIMS), which will provide important constraints on how sulphur isotopes are fractionated during barite replacement.

Acknowledgements

We would like to thank the Geological Survey of Canada, and specifically the TGI-4 initiative for funding this study, and Hudbay Mineral Resources for access to the drill core and camp at MacMillan Pass. Sample preparation for SIMS analysis was greatly assisted by Anna Oh.

References

Abbott, J.G., and Turner, R.J.W., 1990, Character and paleotectonic setting of Devonian stratiform sediment-hosted Zn-Pb-barite deposits, MacMillan Fold Belt, Yukon, *in* Abbott J.G., Turner R.J.W., ed., Mineral deposits of the northern Canadian Cordillera: Ottawa, International Association on the Genesis of Ore Deposits, Eighth Symposium, Field Trip 14 Guidebook, p. 99-136.

Canfield, D.E., 2004, The evolution of the earth surface sulfur reservoir: American Journal of Science, v. 304, p. 839-861.

Chen, D., Wang, J., Racki, G., Li, H., Wang, C., Ma, X., and Whalen, M.T., 2013, Large sulphur isotopic perturbations and oceanic changes during the Frasnian-Fammenian transition of the Late Devonian: Journal of the Geological Society, London, v. 170, p. 465-476.

Colpron, M., and Nelson, J.L., 2011, A digital atlas of terranes for the Northern Cordillera. geology.gov.yk.ca

Goldhaber, M.B., and Kaplan, I.R., 1975, Controls and consequences of sulfate reduction rates in recent marine sediments: Soil Science, v. 119, p. 42-55.

Gordey, S.P., Abbott, J.G., and Orchard, M.J., 1982, Devono-Mississippian Earn Group and younger in strata in east-central Yukon: Current Research, Part B; Geological Survey of Canada, Paper 82-1B, p. 93-100.

Gordey, S.P., and Anderson R.G., 1993, Evolution of the northern cordilleran miogeocline, Nahanni map area (105I), Yukon and Northwest Territories: Geological Survey of Canada, Memoir, v. 428, 214 p.

Goodfellow, W.D., and Jonasson, I.R., 1984, Ocean stagnation and ventilation defined by secular trends in pyrite and barite, Selwyn Basin, Yukon: Geology, v. 12, p. 583-586.

Goodfellow, W.D., and Lydon, J.W., 2007, Sedimentary exhalative (SEDEX) deposits, *in* Goodfellow, W.D., ed., Mineral deposits of Canada: A synthesis of major deposit types, district metallogeny, the evolution of geological provinces, and exploration methods: Geological Association of Canada, Mineral Deposits Division, Special Publication no. 5, p. 163-183.

Goodfellow, W.D., 2007, Base Metallogeny in the Selwyn Basin, Canada, *in* Goodfellow, W.D., ed., Mineral deposits of Canada: A synthesis of major deposit types, district metallogeny, the evolution of geological provinces, and exploration methods: Geological Association of Canada, Mineral Deposits Division, Special Publication no. 5, p. 553-579.

Goodfellow, W.D., and Rhodes, D., 1990, Geological setting, geochemistry and origin of the Tom stratiform Zn-Pb-Ag-barite deposits: *in* Abbott, J.G., and Turner, R.J.W., ed., Mineral deposits of the northern Canadian Cordillera: Ottawa, International Association on the Genesis of Ore Deposits, 8th symposium, field trip 14 guidebook, p. 177-244.

Hanor, J.S., 2000, Barite-Celestine Geochemistry and Environments of Formation: Reviews in Mineralogy and Geochemistry, v. 40, p. 193-275.

John, E.H., Wignall, P.B., Newton, R.J., and Bottrell, S.H., 2010, $\delta^{34}S_{CAS}$ and

$\delta^{18}O_{CAS}$ records during the Frasnian-Fammenian (Late Devonian) transition and their bearing on mass extinction models: Chemical Geology, v. 275, p. 221-234.

Kelley, K.D., Leach, D.L., Johnson, C.A., Clark, J.L., Fayek, M., Slack, J.F., Anderson, V.M., Ayuso, R.A., and Ridley, W.I., 2004, Textural, compositional, and sulfur isotope variations of sulphide minerals in the Red Dog Zn-Pb-Ag deposits, Brooks Range, Alaska: Implications for ore formation: Economic Geology, v. 99, p. 1509-1532.

Magnall, J.M., Gleeson, S.A., and Paradis, S., 2014, SEDEX mineralisation, MacMillan Pass (YT): Petrography, mineralogy and bulk geochemistry of the Tom and Nidd deposits: Geological Survey of Canada, Open File 7457, 19 p.

Paytan, A., Mearon, S., Cobb, K., and Kastner, M., 2002, Origin of marine barite deposits: Sr and S isotope characterization: Geology, v. 30, no. 8, p. 747-750.

Turner, E.C., Roots, C.F., MacNaughton, R.B., Long, D.G.F., Fischer, B.J., Gordey, S.P., Martel, E., and Pope, M.C., 2011, Stratigraphy, *in* Martel, E., Turner, E.C., and Fischer, B.J. ed., Geology of the central Mackenzie Mountains of the northern Canadian Cordillera, Sekwi Mountain (105P), Mount Eduni (106A), and northwestern Wrigley Lake (95M) map-areas, Northwest Territories: Special Volume 1, Northwest Territories Geoscience Office, p. 31-192.

Wilkin, R.T., Barnes, H.L., and Brantley, S.L., 1996, The size distribution of framboidal pyrite in modern sediments: an indicator of redox conditions: Geochimica et Cosmochimica Acta, v. 60, p. 3897-3912.

In situ Trace Element and Sulphur Isotope Analyses of Pyrite Constrain Timing of Mineralization and Sources of Sulphur in the Howard's Pass SEDEX Zn-Pb District, Yukon

M.G. Gadd and D. Layton-Matthews
Department of Geological Sciences and Geological Engineering,
Queen's University, 36 Union Street, Kingston, ON, K7L 3N6
mggadd3@gmail.com

J.M. Peter
Geological Survey of Canada, 601 Booth Street, Ottawa, ON, K1A 0E8

S. Paradis
Geological Survey of Canada, 9860 West Saanich Road, Sidney, BC,
V8L 4B2

Abstract

The Howard's Pass District, Yukon hosts twelve sedimentary exhalative (SEDEX) Zn-Pb deposits that contain approximately 393 Mt grading at 4.5% Zn and 1.5% Pb. Sulphide mineralization is hosted in carbonaceous and calcareous to siliceous mudstones. Pyrite is a minor but ubiquitous component. Detailed petrographic analysis reveals that pyrite has a complex and protracted growth history, with multiple generations of pyrite are preserved in single grains. Combined secondary ion mass spectrometry (SIMS) and laser ablation-inductively coupled plasma-mass spectrometry (LA-ICP-MS) analysis on paragenetically complex pyrite reveals that sulphur isotope and minor and trace element compositions mimic textural zonation. Sulphur isotope data imply that textural variability is genetically significant. In the SEDEX deposits, the earliest pyrite generation (i.e. framboids) have negative δ^{34}S values (mean -16.6‰), whereas later pyrite overgrowths and galena have positive δ^{34}S values (mean 29.1‰ and 22.4‰, respectively). The two sulphur isotope populations are interpreted to reflect contributions of bacterially reduced (negative) and thermochemically reduced (positive) seawater sulphate, and perhaps, of hydrothermally derived sulphate. LA-ICP-MS data provide information on the relative timing and cation content of depositional, hydrothermal and metamorphic fluids. These data also identify a suite of non-ore elements (Mn, As, Ag, Sb and Tl) associated with the Zn-Pb mineralizing fluids. These elements are spatially associated with both syngenetic to earliest diagenetic pyrite and with later diagenetic pyrite overgrowths. Together, these *in situ* analytical data suggest that SEDEX mineralization produced not only hydrothermal chemical sediments;

Recommended citation

Gadd, M.G., Layton-Matthews, D., Peter, J.M., and Paradis, S., 2015. In situ trace element and sulphur isotope analyses of pyrite constrain timing of mineralization and sources of sulphur in the Howard's Pass SEDEX Zn-Pb District, Yukon, *in* Paradis, S., ed., Targeted Geoscience Initiative 4: sediment-hosted Zn-Pb deposits: processes and implications for exploration; Geological Survey of Canada, Open File 7838, p. 58-74. doi:10.4095/296328

rather, dense metalliferous brine settled on, and percolated through, unconsolidated carbonaceous muds and precipitated metal sulphides in the subsurface.

Introduction

The Howard's Pass Zn-Pb District (HPD) of sedimentary exhalative (SEDEX) deposits comprises 12 Zn-Pb deposits that contain an estimated 393 Mt grading 4.5% Zn and 1.5% Pb (SCML, 2012). The HPD is located within the Selwyn Basin (Figure 1), a prolific metallogenic province that is primarily known for its world-class Zn-Pb (±Ag ±Ba) SEDEX deposits (Figure 1). SEDEX mineralization was discovered in the HPD in 1972 by following up regional stream-sediment geochemical anomalies. Exploration drilling during the 1970s and 2000s defined semi-continuous mineralization along a 38 km-long trend. The mineral deposits in the HPD remain undeveloped; however, an adit was driven in the XY deposit for test mining in 1981 (Goodfellow et al., 1983).

Mineralization in the HPD is composed mainly of massive and semi-massive sphalerite and galena hosted in carbonaceous mudstones; pyrite is a minor constituent (approximately 5.5 wt.%) of the mineralization. The trace element and stable isotope geochemistry of Howard's Pass pyrite has been the focus of previous studies (Morganti, 1979; Goodfellow et al., 1983; Goodfellow and Jonasson, 1984; Goodfellow, 1987) that used bulk analytical techniques on handpicked grains. Jonasson and Goodfellow (1986) identified several pyrite textures within the SEDEX deposits and their host rocks in the HPD, but separating very fine-grained intergrowths of sulphide minerals was not possible for bulk analysis.

Petrographic studies of pyrite with multi-generational growth textures have revealed changes in the morphology of pyrite in response to several stages of growth. In black shale successions, variations in pyrite textures have been interpreted to reflect spatial and temporal growth patterns (Berner, 1984; Raiswell and Berner, 1985; Large et al., 2014). During formation, pyrite is capable of sequestering numerous trace and minor elements (e.g. Ag, As, Au, Bi, Co, Cu, Mn, Mo, Ni, Pb, Sb, Se, Tl, Zn) and the contents of these reflect their availability during the various environments that existed during pyrite deposition (Large et al., 2009; Berner et al., 2013; Gregory et al., 2014). Texturally complex pyrite that experienced multiple generations of growth can record the ambient trace element budgets of the solutions from which it formed and can therefore be used as a proxy for the fluid history that may have involved one or more of hydrothermal, hydrogenous, diagenetic and metamorphic fluids. Pyrite that forms over a protracted period may also record variable sulphur isotope compositions (e.g. Eldridge et al., 1988; Eldridge et al., 1993; Ireland et al., 2004; Taylor, 2004). *In situ* sulphur isotope analyses (e.g. secondary ion mass spectrometry; SIMS) of different pyrite generations can therefore yield information about the mechanisms by which reduced sulphur was produced, as well as the sulphur budget of the ambient environment.

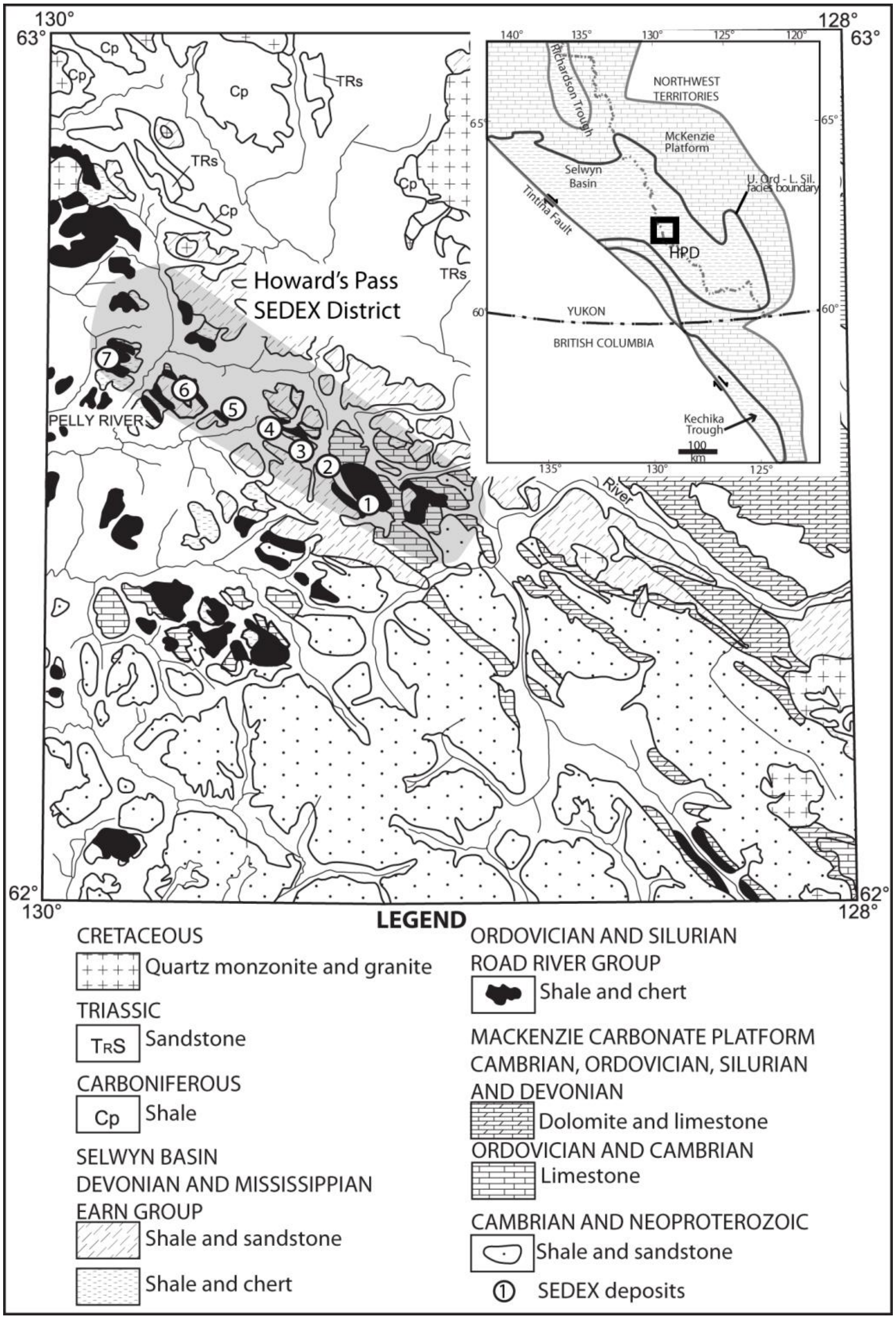

Figure 1: Generalized geologic map of the Howard's Pass district showing locations of SEDEX Zn-Pb deposits and mineralized zones with inset location of Selwyn Basin in the northern Cordillera. 1: XY zone (XY, XY Central and XY West deposits); 2: Brodel deposit; 3: HC zone (HC and HC West deposits); 4: Don zone (Don and Don East deposits); 5: Anniv Zone (Anniv and Anniv East deposits); 6: OP deposit; 7: Pelly North deposit.

We have used standard petrographic reflected light microscopy, together with field emission gun-environmental scanning electron microscopy (FEG-ESEM) and laser ablation-inductively coupled plasma-mass spectrometry (LA-ICP-MS) to determine the minor and trace element compositions of the different textural styles and generations of pyrite in host rocks and in Zn-Pb SEDEX deposits of the HPD. We have also used SIMS to determine the sulphur isotope compositions of these pyrites. The objectives of this study were to apply these *in situ* analytical techniques to differentiate between ore stage pyrite, diagenetic pyrite and metamorphic pyrite. Whereas bulk analysis is insensitive to textural complexity, our *in situ* data reveal that the trace element and sulphur isotope compositions of these various textural types and stages of pyrite reflect precipitation from hydrothermal, hydrogenous, diagenetic and metamorphic fluids.

Results/Data Analysis

Petrography and SIMS sulphur isotopes

The HPD is hosted in sedimentary strata of the Duo Lake Formation. These rocks are dominantly carbonaceous siliceous to calcareous mudstones. Locally, the Duo Lake Formation is subdivided into informal members that, from base to top, comprise the Calcareous Mudstone member (CCMS), Active member (ACTM) and Upper Siliceous Mudstone member (USMS) (Morganti, 1979). The Steel Formation conformably overlies the Duo Lake Formation and is locally named the Flaggy Mudstone member (FLMD) (Morganti, 1979). The ACTM hosts the major SEDEX Zn-Pb deposits in the HPD. Conodont age dating by Norford and Orchard (1985) reveals that the ACTM was deposited in the Early Silurian (~440 Ma). These authors also show that the ACTM is stratigraphically bracketed between two graptolite zones that restrict deposition to a maximum of 5 m.y. Pyrite is a minor but ubiquitous component of these sedimentary rocks and constitutes approximately 4.6 wt.% of the CCMS, 5.4 wt.% of the ACTM and 2.9 wt.% of the USMS (Gadd et al., unpublished data).

Reflected light microscopy reveals multiple generations of pyrite growth in the succession of sedimentary rocks of the HPD. Pyrite occurs as framboids, polyframboidal clusters (Figure 2A) and micro-euhedra, bedding parallel bands (Figure 2B), nodules (Figure 2C), and porphyroblasts and metamorphic overgrowths (Figure 2D). Pyrite framboids and minute euhedra (py1) consist of spherical aggregates of micro-crystalline pyrite and irregular aggregates of minute pyrite crystals, respectively. Individual framboids are generally <10 μm to 20 μm in diameter, and less commonly up to 50 μm in diameter. Framboidal py1 occurs locally as agglomerated masses of several hundred microns across, which form polyframboids. Minute (1-5 μm diameter) py1 euhedra occur as crystals in irregular masses. Although framboidal py1 occurs in the Duo Lake and Steel formations, it is most abundant in the upper portion of the ACTM, forming delicate laminae intercalated with carbonaceous sediments, sphalerite and galena. The sulphur isotope composition of py1 from the ACTM of the XY Central, Don, Don East and Anniv East deposits has negative $\delta^{34}S$ values that range from -26.1 to -7.5‰ (Figure 3). Framboids from the USMS also display negative $\delta^{34}S$ values (-21.0 to -15.7‰).

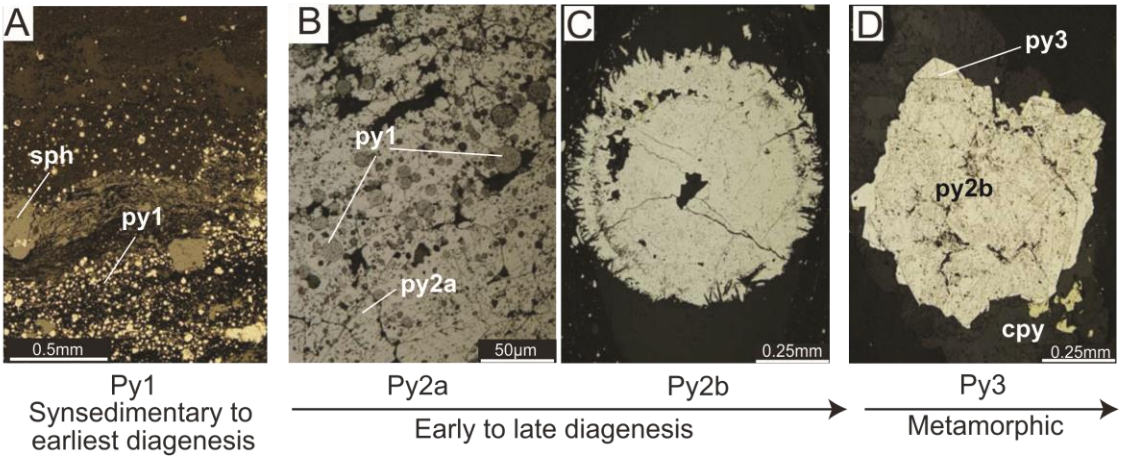

Figure 2: Pyrite paragenesis shown by representative photomicrographs of pyrite generations and textures. Abbreviations: py=pyrite; sph=sphalerite; cpy=chalcopyrite.

Bedding-parallel pyrite layers <1 mm to several mm thick (py2a) occur as wispy laminae of aggregated and intergrown subhedral to euhedral crystals (Figure 2B). Py2a forms wispy and discontinuous layers to well-formed continuous beds at the drill core scale. Py2a is common within the CCMS, ACTM and USMS, but is rare in the FLMD. Well-formed py2a layers overprint and preserve primary bedding of the host carbonaceous mudstones. Wispy py2a differs from laminated py1 in that the framboidal texture is either overprinted (Figure 2B) or obliterated due to post-depositional recrystallization. Pyrite nodules (py2b) comprise round to sub-round masses of intergrown and aggregated subhedral pyrite crystals that commonly show radial growth patterns and herringbone textures (Figure 2C). Nodules range in diameter from 0.5 to >1.5 cm and occur throughout the stratigraphic succession. Py2b nodules typically display complex growth textures that range from sooty (silicate inclusion-rich) to clear (inclusion-free). Etching of polished surfaces with concentrated HNO_3 enhanced textures and revealed growth relationships among pyrite generations, such as where py2b overprinted and recrystallized polyframboidal py1.

The diagenetic varieties of bedded (py2a) and nodular pyrite (py2b) are isotopically indistinguishable in a given stratigraphic unit and are, therefore, grouped together in the histograms of Figure 3. Diagenetic pyrites have exclusively positive sulphur isotope values. Within the CCMS ($\delta^{34}S$ +13.4 to 47.8‰), ACTM ($\delta^{34}S$ +21.9 to 47.7‰) and USMS ($\delta^{34}S$ +14.7 to 49.7‰), this type of pyrite contains broadly similar ranges of values. Within the FLMD, the $\delta^{34}S$ values have a slightly narrower range that is lower than for pyrite from the Duo Lake Formation ($\delta^{34}S$ +10.3 to 35.7‰). Samples that have diagenetic pyrite overgrowing framboidal pyrite, or diagenetic pyrite and framboidal pyrite coexisting, display more complex sulphur isotope systematics. In places, the heavy positive $\delta^{34}S$ values of diagenetic pyrite are juxtaposed by light negative values of framboids, resulting in $\Delta^{34}S_{py2-py1}$ of 40‰ over distances of <50 µm.

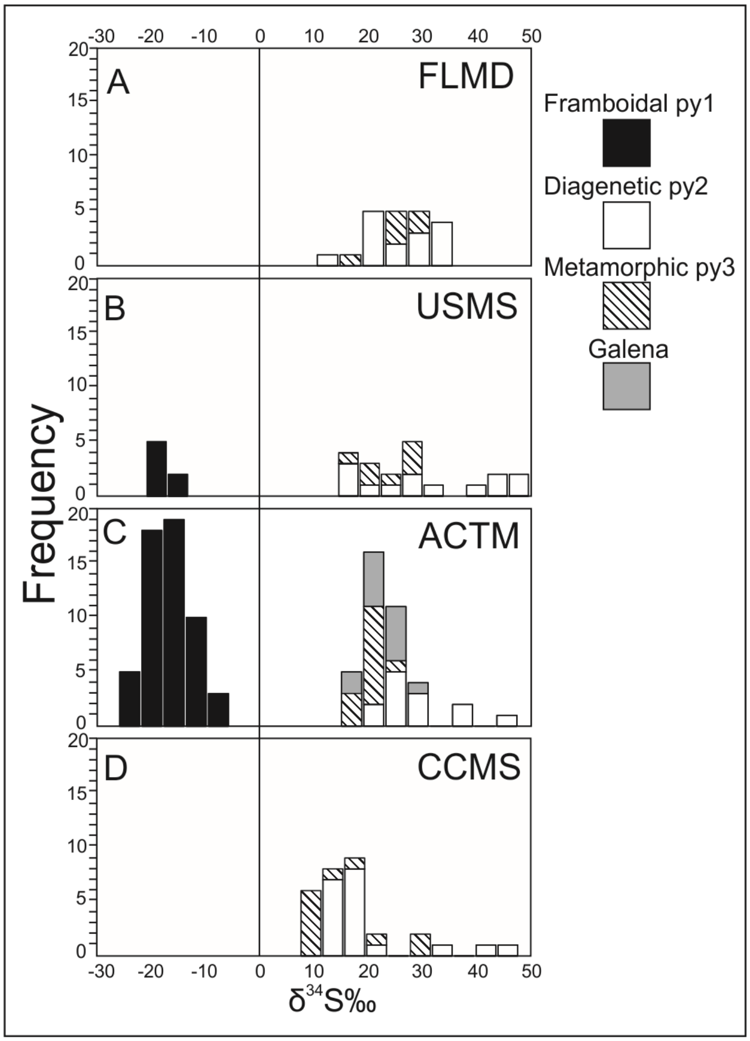

Figure 3: Histograms of SIMS sulphur isotope compositions of individual pyrite generations and galena from A) FLMD, B) USMS, C) ACTM and D) CCMS units.

Metamorphic pyrite (py3) occurs as both euhedral crystals and thin (<0.2 mm) overgrowths on pre-existing pyrites. Py3 is the latest stage of pyrite growth in the HPD and overgrows all preceding generations. Euhedral py3 crystals are between 0.1 and 50 mm in diameter and are crystallographically aligned with the regional cleavage. Metamorphic overgrowths of py3 form veneers on diagenetic pyrites (Figure 2D). The sulphur isotope values of py3 are also positive, but are generally lower than those of diagenetic pyrite. The $\delta^{34}S$ values of py3 range from moderately to highly positive (+7.5 to +30.4‰). Veneers of py3 on diagenetic pyrite are lighter than the diagenetic pyrite on which the veneers form, but the difference in $\delta^{34}S$ values (1 to 20‰) is not as pronounced as that between py1 and py2.

Sphalerite and galena occur together with pyrite throughout the Duo Lake Formation and are concentrated within the ACTM. Inclusions of sphalerite and galena in pyrite are generally small (<0.2 mm) and form fracture fillings within, and interstitial to, adjacent pyrite crystals. Sulphur isotope compositions of galena were determined for two samples (total of 13 spot analyses), for galena that shares grain boundaries with both framboidal and euhedral diagenetic-metamorphic pyrite. The $\delta^{34}S$ values of galena are highly positive (+17.0 to +27.3‰) and are, on average, 39.0‰ heavier than the framboids. Galena and adjacent diagenetic-metamorphic pyrite display nearly identical average sulphur isotope compositions; however, the average $\delta^{34}S$ value of diagenetic pyrite in the ACTM is 7‰ heavier than that of galena. Sphalerite was not analyzed using SIMS; however, the bulk $\delta^{34}S$ value of sphalerite in the HPD is moderately to highly positive (+12.6 to +23.3‰) (I.R. Jonasson, pers. comm., 2014).

LA-ICP-MS

The minor and trace element compositions of py1 (*n* = 114), py2a (*n* = 144), py2b (*n* = 229), and py3 (*n* = 112) were determined by LA-ICP-MS. A series of parallel and adjacent line rasters across pyrite crystals measured the distributions and contents of minor and trace elements. Pyrite within the HPD contains a broad suite of trace elements, the most abundant of which are Mn, Co, Ni, Cu, Zn, As, Se, Ag, Sb, Tl, and Pb. The contents of these elements vary among pyrite generations and the stratigraphic position of the host rocks in which they reside. Trace element variability in pyrite that displays multiple growth zones is coincident with textural and morphological variability (Figure 4).

All of these elements occur in variable quantities. However, pyrite is not the exclusive host of Zn, Pb, Cu, and Mn. Minute inclusions of sphalerite (Zn), galena (Pb), and chalcopyrite (Cu) are common within pyrite; LA-ICP-MS reveals that the highest contents of these elements are associated with such mineral inclusions. Calcite sequesters some Mn, but it also occurs in pyrite. The other trace elements present (Co, Ni, As, Se, Ag, Sb, and Tl) are predominantly hosted in pyrite. Within the ACTM, however, Se and Ag are mainly sequestered in galena.

Discussion/Models

Pyrite formation and timing of SEDEX mineralization

Goodfellow (2004) suggested that mineralizing fluids responsible for the HPD SEDEX deposits were dense, bottom-hugging brines that exhaled from a submarine vent distal to the deposits, in pulses related to the reactivation of early growth faults. In this model, the brine migrated to, and eventually settled into, a bathymetric low (i.e. the Howard's Pass sub-basin), and sphalerite, galena and framboidal pyrite are products of chemical sedimentation in a density- and redox-stratified water column.

The model of Goodfellow (2004) also stipulates that the water column is the primary reservoir of reduced sulphur, where bacterial sulphate reduction (BSR) consumed a diminishing quantity of sulphate. Goodfellow (1987) proposed that the effects of BSR and Rayleigh fractionation are recorded in the sulphur isotope

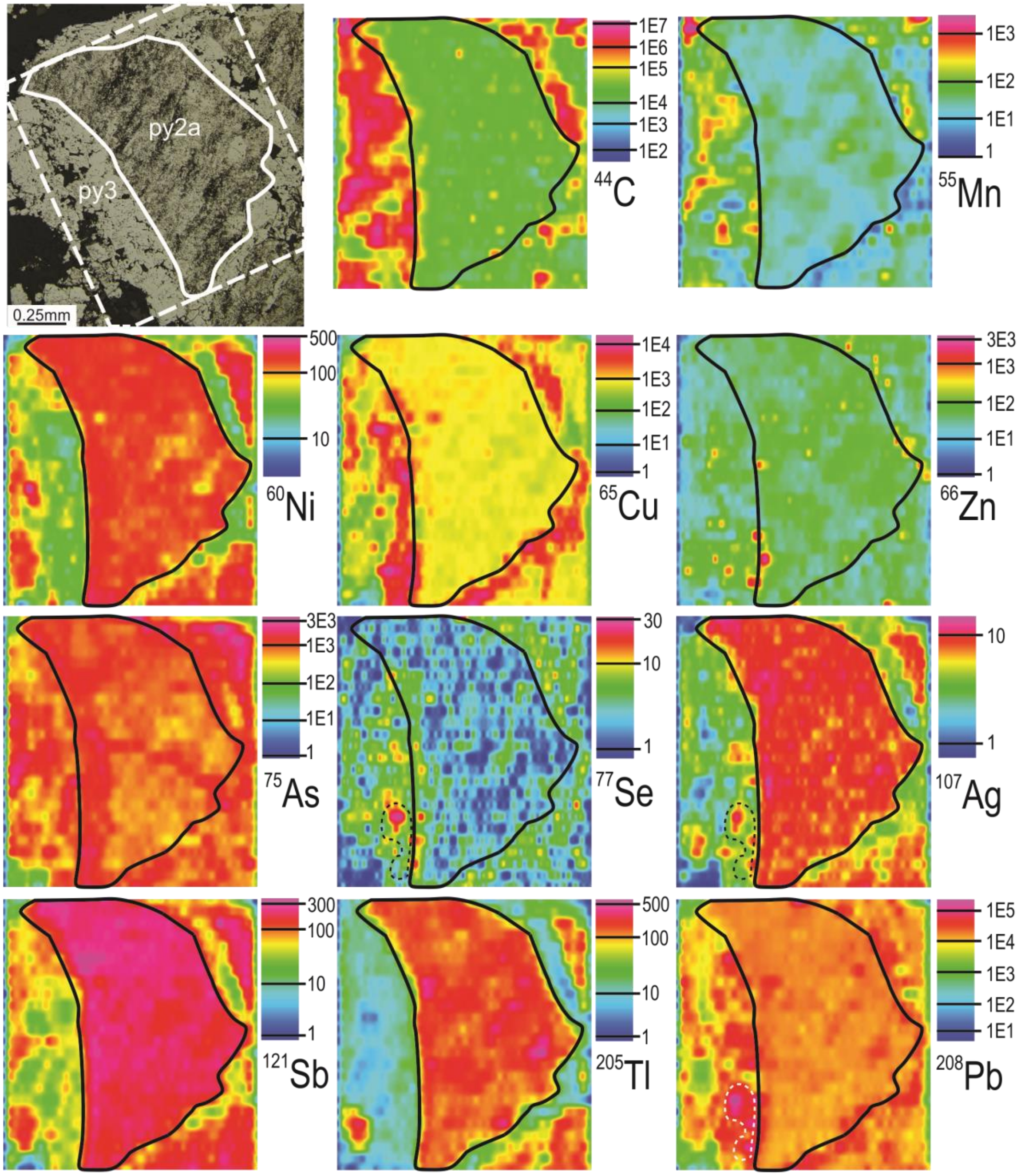

Figure 4: Photomicrograph (upper left) accompanying trace element distribution maps of py2a-py3 in ACTM sample Don-200-382.0. Framboidal py1, if present, has been pervasively recrystallized such that primary textures are obliterated. Colour ramps are shown in linear ppm except for Ca, which is in counts per second.

compositions of sedimentary pyrite, which become progressively heavier stratigraphically upward from the CCMS to the USMS (Figure 5). Whereas the SIMS data for diagenetic pyrite yield similar $\delta^{34}S$ values to those previously reported for pyrite in the HPD (Goodfellow, 1987), the sulphur isotope compositions of pyrite framboids are strikingly different (Figures 3C, 5). From a paragenetic standpoint, framboidal py1 is the earliest generation to form and it is likely that growth of this pyrite occurred either in an euxinic water near the sediment-water interface or in the uppermost sulphidic sediment porewaters of unconsolidated sediments. The $\delta^{34}S$ values of framboids, therefore, should provide the most reliable estimate of the sulphur isotope composition of ambient reduced sulphur (e.g. Lyons, 1997). If a kinetic fractionation of 45‰ is assumed between bacterially reduced parent sulphate and daughter sulphide (Sweeney and Kaplan, 1980; Strauss, 1999), then the $\delta^{34}S$ values of framboids in the SEDEX deposits of the HPD are consistent with derivation of sulphide from unfractionated coeval seawater sulphate (~28‰; Claypool et al., 1980; Kampschulte and Strauss, 2004). Significantly, $\delta^{34}S$ values of sphalerite (I.R. Jonasson, pers. comm., 2014) and galena (this study) are much heavier than those of framboidal pyrite. By inference, therefore, the base metal sulphides and framboids lack a common source of sulphur or are not coeval (see Ohmoto and Goldhaber, 1997).

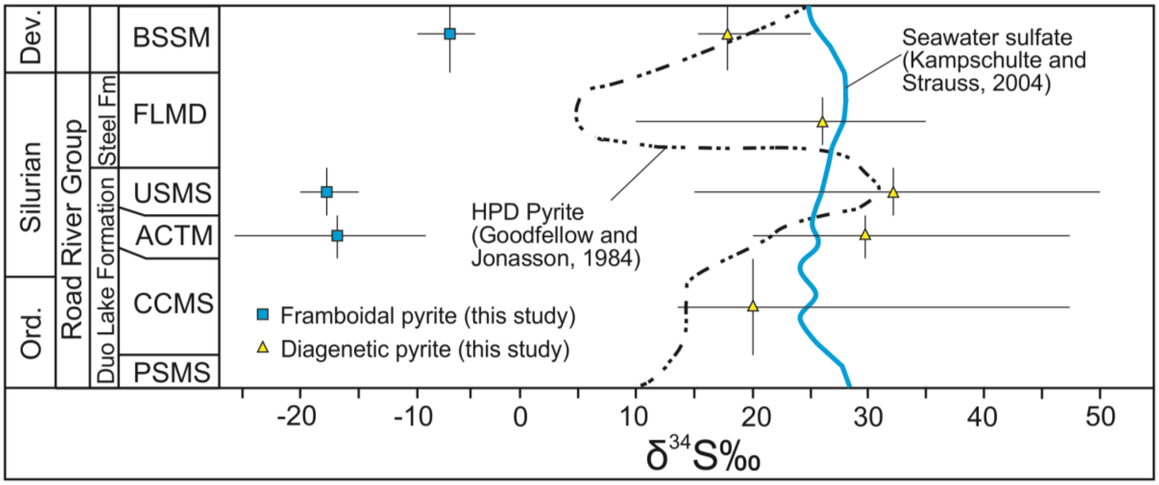

Figure 5: Secular distribution of $\delta^{34}S$ values for sedimentary pyrite (Goodfellow and Jonasson, 1984) and seawater sulphate (Kampschulte and Strauss, 2004) together with SIMS $\delta^{34}S$ values of framboidal and diagenetic pyrite. Note similarities between $\delta^{34}S$ values of diagenetic pyrite determined in this study and those of sedimentary pyrite reported by Goodfellow and Jonasson (1984). The $\delta^{34}S$ values of diagenetic pyrite is consistently heavier than those of framboidal pyrite (modified after Goodfellow and Jonasson, 1984).

Pyrite is a fairly refractory mineral and can retain its primary trace element and sulphur isotope compositions during low-grade metamorphism, but pervasive recrystallization in the presence of hydrothermal fluids can alter its primary composition (Williford et al., 2011; Large et al., 2014). Framboidal py1 contains relatively high contents of hydrothermal elements such as Tl, As, Mn and Sb. The highest contents of these elements in the ACTM, however, are generally within py2a and py2b that have nearly obliterated py1 (Figure 4). Preferential incorporation of such hydrothermal elements into py2a and py2b indicates that diagenetic pyrite in the ACTM formed during the Zn-Pb ore-stage. Py2a and py2b postdate py1, implying that the SEDEX mineralization postdates formation of the framboidal pyrite.

Hydrothermal fluid properties and transport

Sangster (2002) experimentally modelled the transport of dense brine into sedimentary basins and showed that the brines could travel relatively far from the source area. These experiments used sand as the sediment medium as opposed to fine-grained mud; lithified equivalents of the latter (mudstone, shale, slate) typically host SEDEX Zn-Pb (±Ba ±Ag) deposits. Mud is much less permeable than sand, but has high initial porosity that is retained for tens to hundreds of meters below the sediment-water interface (Einsele, 2000). Warm basinal brines are capable of carrying significant concentrations of dissolved metals (Hanor, 1979; Sangster, 2002; Yang et al., 2004). A consequence of the density contrast between the brines and sediment porewaters is the displacement of less dense sediment porewaters into the basin margins and into the overlying water column (Sangster, 2002). The products of this fluid exchange would be pyrite enriched in the trace elements of the dense brine, and depleted in those of the porewaters. Assuming that SEDEX fluid contained hydrothermal elements (Zn, Pb, Ag, Tl, As, Sb ± Mn) and was deficient in other elements (e.g. Co, Ni, Cu, Se, etc.), then this process could explain the different distributions of trace elements among pyrite types contained within the ACTM (Gadd et al., in review).

Unlike other SEDEX Zn-Pb districts (e.g. MacMillan Pass), a plumbing system has not been recognized within the HPD. Nevertheless, synsedimentary faults were likely the conduit for fluid delivery. Our data indicate that the mineralizing process was more complex than proposed by previous workers, and that framboidal pyrite was not a hydrothermal product; rather, framboids are solely of synsedimentary to early diagenetic origin. The model we propose involves the ponding of hydrothermal brine in a redox stratified water column, and percolation of this brine into sulphidic, unconsolidated carbonaceous muds (Figure 6A). Dense sinking brine forced sulphidic porewaters out of muddy sediments, resulting in hydrothermal chemical sedimentation in the lower brine pool where particulate galena, sphalerite and pyrite accumulated on the basin floor. As dense brine sank into muds, porewater sulphate was reduced by the oxidation of labile organic matter. *In situ* carbon dioxide generation and coeval base metal sulphide precipitation resulted in CO_2 build-up within partially cemented fine-grained muds. The loss of permeability by sulphide precipitation coupled with increased pCO_2 generated over-pressurized pore fluids and eventually resulted in upward migration of pore fluids. These features are preserved in the HPD as ‘dewatering pipes’ (e.g. Jonasson and Goodfellow, 1986) that cross-cut laminated sediments during diagenesis. Dewatering promoted further mixing at the brine-seafloor interface (Figure 6B).

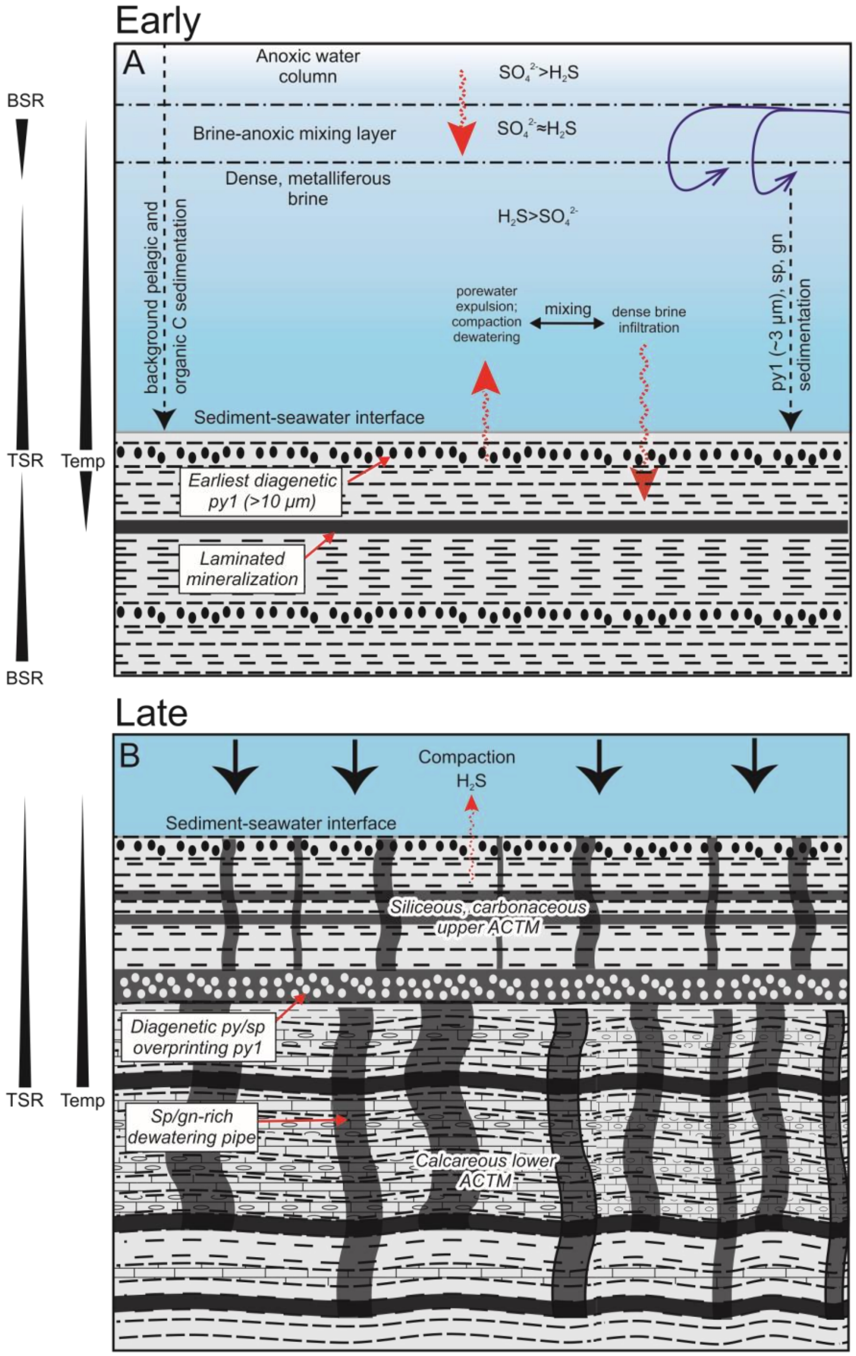

Figure 6: Schematic model for formation of SEDEX Zn-Pb deposits in HPD. The model accounts for SIMS sulphur isotope data and illustrates controls on sulphate-sulphide distribution and sulphate reducing processes. A) Synsedimentary sulphide deposition is accompanied by sinking of dense brine into permeable muds, where metals and sulphate are transported together. Dense brine sinking displaces less-dense sulphidic porewaters and promotes early TSR; B) sinking brines percolate into muds and precipitate diagenetic sulphides that form overgrowths on pre-existing sulphides and calcite intercalated with carbonaceous sediments. Loss of permeability is likely followed by compaction and dewatering, which promotes mixing at the sediment-water interface (no scale implied; adapted and modified from Ireland et al., 2004).

The SIMS sulphur isotope data support this model of SEDEX mineralization in the HPD. Limited permeability of fine-grained argillaceous sediments precludes deep (>100s m) brine percolation of brines (Einsele, 2000); however, in the HPD it is unlikely that mineral deposition occurred entirely in the water column because complex sulphur isotope systematics do not support a purely synsedimentary origin for the formation of SEDEX Zn-Pb deposits (cf., Goodfellow, 1987). Isotopically heavy $\delta^{34}S$ values for galena and diagenetic pyrite mantle framboids having very low values, suggesting that deposition of galena and py2 followed that of py1 in the ACTM. Goodfellow (1987) indicated that the reduced sulphur in the mineral deposits was entirely derived from an anoxic water column, but this model is difficult to reconcile with the discrepancy in the global secular curve for sulphur isotopic compositions of seawater sulphate and our data for sulphides (Figure 5). We propose that additional (oxidized) sulphur was delivered with base metals to an ambient euxinic water column and that both BSR and thermochemical sulphate reduction (TSR) generated reduced sulphur in the HPD SEDEX deposits (Figure 6). BSR was the most important process prior to the introduction of metalliferous hydrothermal fluids that provided a necessary catalyst for TSR. TSR superseded BSR following the introduction of metalliferous fluids because these fluids were too warm (>100°C) to support significant bacterial activity. In the early stage of hydrothermal activity, TSR was likely restricted to the lowermost water column, near the sediment-water interface (Figure 6A). Continued venting of dense brine resulted in its downward percolation into porous unconsolidated muds, where TSR reduced hydrothermally derived sulphate by the oxidation of labile organic carbon (Figure 6B).

Calcite, the most abundant carbonate mineral in the HPD, is a major component of the ACTM and is characterized by isotopically light $\delta^{13}C$ values (typically -3 to -6‰) (I.R. Jonasson, pers. comm., 2014). The calcite content of the ACTM is variable, and some of the highest calcite abundances occur immediately above sections of semi-massive to massive sphalerite and galena mineralization (Gadd et al., unpublished data). It should be noted that portions of the ACTM are predominantly calcareous without underlying sulphides. Importantly, the isotopically light $\delta^{13}C$ values for ACTM fall within a range consistent with those typically produced by TSR, whereas much lower $\delta^{13}C$ values would be expected for significant BSR or anaerobic methane oxidation calcite (Machel, 2001).

A similar model has been presented for the HYC Zn-Pb-Ag SEDEX deposit in northern Australia (Ireland et al., 2004). On the basis of mineral textures and sulphur isotope compositions, these authors proposed that synsedimentary and syndiagenetic mineralization are products of complex interactions among metalliferous brines, reduced porewaters and reduced bottom waters. These similarities suggest that the HPD (and perhaps other SEDEX deposits within the Selwyn Basin) and Australian SEDEX deposits have more in common than was recognized previously (Cooke et al., 2000). The dense, sinking brine pool model is not without shortcomings, however. Namely, the absence of empirical salinity and temperature data for the SEDEX mineralizing fluids imposes limitations on a brine pool model. Mound structures and footwall feeder zones also have not been identified in the HPD. Nonetheless, trace element and sulphur isotope variations between pyrite generations and the enrichment of SEDEX-associated elements in diagenetic pyrite reported here support this sinking brine pool model of Zn-Pb mineralization in the HPD.

Implications for Exploration

LA-ICP-MS analyses reveal strong textural control on the distribution of trace elements in pyrite from a variety of settings. This methodology is costly and time consuming, and it is unlikely that it will be widely adopted by industry; however, our data reveal that careful selection of pyrite for analysis can yield valuable information about the hydrothermal processes involved in SEDEX formation. Pyrite chosen for analysis should be sooty (i.e. inclusion-rich) and composed of fine-grained aggregates. Bedded (laminated) and nodular pyrite are both suitable, whereas coarse euhedral metamorphic pyrite is not. Large nodules (>2 cm) are suitable for trace element analysis. The interior, paragenetically earlier regions of nodular pyrite are more likely to contain higher contents of trace elements than the exterior, later regions. Etching flat pyrite surfaces with concentrated nitric acid can enhance textural variability and improve sample selection.

Pyrite sequesters several trace elements in the HPD, of which Tl, As, Sb and possibly Mn are considered hydrothermal in origin. Ore-stage diagenetic pyrite contains, on average, >50 ppm Tl, >800 ppm As, >70 ppm Sb and >500 ppm Mn. These abundances are not significantly higher than those of average Paleozoic diagenetic pyrite (Large et al., 2014), nor are they as high as the abundances that characterize other SEDEX deposits (e.g. Red Dog, Alaska; Graham et al., 2009); however, they are high in the HPD where associated with SEDEX Zn-Pb mineralization. The common occurrence of minute grains of sphalerite and galena within pyrite indicates that these elements should also be analyzed. For bulk analysis of pyrite separates, the recommended method of digestion is using aqua regia, because it dissolves sulphide minerals without also dissolving most silicates, thus effectively avoiding dilution by these less-soluble minerals.

Several Paleozoic SEDEX Zn-Pb districts in the Yukon and northeast British Columbia contain significant barite units that are genetically linked to SEDEX mineralization. Significantly, however, barite is absent within the SEDEX Zn-Pb deposits of the HPD. The Ba content of the ACTM, <1000 ppm, is much lower than that of the underlying and overlying sedimentary rocks of the Duo Lake Formation. Positive correlations between Ba, Al and K suggest that the Ba present in the ACTM occurs as hyalophane (Ba-feldspar) and not barite (see also Goodfellow and Jonasson, 1986). Barite is present in the FLMD, but this unit postdates mineralization by several million years, and hence it is unlikely that this barite is genetically related to the underlying SEDEX Zn-Pb mineralization. Therefore, exploration for SEDEX deposits similar those known in the HPD should not expect to find significant quantities of barite.

Future Work

The succession of rocks that host SEDEX deposits in the HPD is variably phosphatic, and the sedimentary rocks immediately above these deposits (USMS) contain up to 10 wt% P_2O_5. Previous studies in the 1980s interpreted this unit as being the product of metal-poor, phosphorus-rich hydrothermal venting. However, the body of research on sedimentary phosphorite deposition has grown considerably since these early studies. Preliminary studies by scientists from the U.S. Geological Survey have shown that phosphogenesis in the HPD is likely related to nutrient-rich upwelling, and is not the product of hydrothermal venting. This research will likely provide insights into the geochemically complex depositional and diagenetic environments of the HPD. Implications of this research could potentially redefine the depositional environment of the HPD, allowing the use of better-tailored exploration models for this genetically enigmatic seafloor-hydrothermal system.

The data we present here is exclusively on rocks that are proximal to the SEDEX mineralization (i.e, directly overlying and underlying the deposits). Sampling of unweathered, age-equivalent carbonaceous mudstone distal to mineralization should be undertaken to properly evaluate the presence and/or extent of widespread hydrothermal alteration of the host rocks in the region.

Acknowledgements

This research was jointly funded by TGI-4 of the Geological Survey of Canada, NSERC-DG and CAMIRO Project 08E04 “Geochemistry of Shales as Vectors to Ore Deposits”. We thank Jason Dunning, Gabe Xue, Wolfgang Schleiss and Jelle de Bruyckere of Selwyn Chihong Mining Ltd. for providing access to drill cores and technical information, without which this work could not have been done. We also thank the Society of Economic Geologists Canada Foundation for financial support.

References

Berner, R.A., 1984, Sedimentary pyrite formation: An update: Geochimica et Cosmochimica Acta, v. 48, p. 605-615.

Berner, Z., Puchelt, H., Nöltner, T., and Kramar, U., 2013, Pyrite geochemistry in the Toarcian Posidonia Shale of south-west Germany: Evidence for contrasting trace-element patterns of diagenetic and syngenetic pyrites: Sedimentology, v. 60, p. 548-573.

Claypool, G.E., Holser, W.T., Kaplan, I.R., Sakai, H., and Zak, I., 1980, The age curves of sulfur and oxygen isotopes in marine sulfate and their mutual interpretation: Chemical Geology, v. 28, p. 199-260.

Cooke, D.R., Bull, S.W., Large, R.R., and McGoldrick, P.J., 2000, The importance of oxidized brines for the formation of Australian Proterozoic stratiform sediment-hosted Pb-Zn (Sedex) deposits: Economic Geology, v. 95, p. 1-18.

Einsele, G., 2000, Sedimentary basins: Evolution, facies, and sediment budget:

Berlin Heidelberg, Springer, 792 p.

Eldridge, C.S., Compston, W., Williams, I.S., Both, R.A., Walshe, J.L., and Ohmoto, H., 1988, Sulfur isotope variability in sediment-hosted massive sulfide deposits as determined using the ion microprobe SHRIMP: I, An example from the Rammelsberg orebody: Economic Geology, v. 83, p. 443-449.

Eldridge, C.S., Williams, N., and Walshe, J.L., 1993, Sulfur isotope variability in sediment-hosted massive sulfide deposits as determined using the ion microprobe SHRIMP: II, A study of the H.Y.C. deposit at McArthur River, Northern Territory, Australia: Economic Geology, v. 88, p. 1-26.

Goodfellow, W.D., 1987, Anoxic stratified oceans as a source of sulphur in sediment-hosted stratiform Zn-Pb deposits (Selwyn Basin, Yukon, Canada): Chemical Geology: Isotope Geoscience Section, v. 65, p. 359-382.

Goodfellow, W.D., 2004, Geology, genesis, and exploration of SEDEX deposits, with emphasis on the Selwyn Basin, Canada, *in* Deb, M., and Goodfellow, W.D., ed., Sediment-hosted lead-zinc sulphide deposits: Attributes and models of some major deposits of India, Australia, and Canada: Delhi, India, Narosa Publishing House, p. 24–99.

Goodfellow, W.D., and Jonasson, I., 1986, Environment of formation of the Howards Pass (XY) Zn-Pb deposit, Selwyn Basin, Yukon, *in* Morin, J.A., ed., Mineral deposits of northern Cordillera: Canadian Institute of Mining and Metallurgy, special volume 37, p. 19-50.

Goodfellow, W.D., and Jonasson, I.R., 1984, Ocean stagnation and ventilation defined by $\delta^{34}S$ secular trends in pyrite and barite, Selwyn Basin, Yukon: Geology, v. 12, p. 583-586.

Goodfellow, W.D., Jonasson, I.R., and Morganti, J.M., 1983, Zonation of chalcophile elements about the Howard's Pass (XY) Zn-Pb deposit, Selwyn Basin, Yukon: Journal of Geochemical Exploration, v. 19, p. 503-542.

Graham, G.E., Kelley, K.D., Slack, J.F., and Koenig, A.E., 2009, Trace elements in Zn-Pb-Ag deposits and related stream sediments, Brooks Range Alaska, with implications for Tl as a pathfinder element: Geochemistry: Exploration, Environment, Analysis, v. 9, p. 19-37.

Gregory, D., Meffre, S., and Large, R., 2014, Comparison of metal enrichment in pyrite framboids from a metal-enriched and metal-poor estuary: American Mineralogist, v. 99, p. 633-644.

Hanor, J.S., 1979, Sedimentary genesis of hydrothermal fluids, *in* Barnes, H. L., ed., Geochemistry of hydrothermal ore deposits: New York, John Wiley and Sons, p. 137-168.

Ireland, T., Large, R.R., McGoldrick, P., and Blake, M., 2004, Spatial distribution patterns of sulfur isotopes, nodular carbonate, and ore textures in the McArthur River (HYC) Zn-Pb-Ag deposit, Northern Territory, Australia: Economic Geology, v. 99, p. 1687-1709.

Jonasson, I.R., and Goodfellow, W.D., 1986, Sedimentary and diagenetic textures, and deformation structures within the sulphide zone of the Howards Pass (XY) Zn-Pb deposit, Yukon and Northwest Territories, *in* Morin, J. A., ed., Mineral deposits of northern Cordillera: Canadian Institute of Mining and Metallurgy, special volume 37, p. 51-70.

Kampschulte, A., and Strauss, H., 2004, The sulfur isotopic evolution of Phanerozoic seawater based on the analysis of structurally substituted sulfate in carbonates: Chemical Geology, v. 204, p. 255-286.

Large, R.R., Danyushevsky, L., Hollit, C., Maslennikov, V., Meffre, S., Gilbert, S., Bull, S., Scott, R., Emsbo, P., Thomas, H., Singh, B., and Foster, J., 2009, Gold and trace element zonation in pyrite using a laser imaging technique: Implications for the timing of gold in orogenic and Carlin-style sediment-hosted deposits: Economic Geology, v. 104, p. 635-668.

Large, R.R., Halpin, J.A., Danyushevsky, L.V., Maslennikov, V.V., Bull, S.W., Long, J. A., Gregory, D.D., Lounejeva, E., Lyons, T.W., Sack, P.J., McGoldrick, P.J., and Calver, C.R., 2014, Trace element content of sedimentary pyrite as a new proxy for deep-time ocean–atmosphere evolution: Earth and Planetary Science Letters, v. 389, p. 209-220.

Lyons, T.W., 1997, Sulfur isotopic trends and pathways of iron sulfide formation in upper Holocene sediments of the anoxic Black Sea: Geochimica et Cosmochimica Acta, v. 61, p. 3367-3382.

Machel, H.G., 2001, Bacterial and thermochemical sulfate reduction in diagenetic settings—old and new insights: Sedimentary Geology, v. 140, p. 143-175.

Morganti, J.M., 1979, The geology and ore deposits of the Howards Pass Area, Yukon and Northwest Territories: the origin of basinal sedimentary stratiform sulphides deposits: unpublished PhD thesis, University of British Columbia, 351 p.

Norford, B.S., and Orchard, M.J., 1985, Early Silurian age of rocks hosting lead-zinc mineralization at Howards Pass, Yukon Territory and District of Mackenzie: Geological Survey of Canada Paper 83-18, 35 p.

Ohmoto, H., and Goldhaber, M.B., 1997, Sulfur and carbon isotopes, *in* Barnes, H.L., ed., Geochemistry of hydrothermal ore deposits: New York, John Wiley and Sons, p. 517-611.

Raiswell, R., and Berner, R.A., 1985, Pyrite formation in euxinic and semi-euxinic sediments: American Journal of Science, v. 285, p. 710-724.

Sangster, D., 2002, The role of dense brines in the formation of vent-distal sedimentary-exhalative (SEDEX) lead-zinc deposits: Field and laboratory evidence: Mineralium Deposita, v. 37, p. 149-157.

SCML, 2012, Selwyn announces updated mineral resource for XY West deposit: Vancouver, British Columbia, Canada, p. 1-5.

Strauss, H., 1999, Geological evolution from isotope proxy signals — sulfur: Chemical Geology, v. 161, p. 89-101.

Sweeney, R., and Kaplan, I., 1980, Stable isotope composition of dissolved sulfate and hydrogen sulfide in the Black Sea: Marine Chemistry, v. 9, p. 145-152.

Taylor, B.E., 2004, Biogenic and thermogenic sulfate reduction in the Sullivan Pb–Zn–Ag deposit, British Columbia (Canada): Evidence from micro-isotopic analysis of carbonate and sulfide in bedded ores: Chemical Geology, v. 204, p. 215-236.

Williford, K.H., Van Kranendonk, M.J., Ushikubo, T., Kozdon, R., and Valley, J. W., 2011, Constraining atmospheric oxygen and seawater sulfate concentrations during Paleoproterozoic glaciation: In situ sulfur three-isotope microanalysis of pyrite from the Turee Creek Group, Western Australia: Geochimica et Cosmochimica Acta, v. 75, p. 5686-5705.

Yang, J., Bull, S., and Large, R., 2004, Numerical investigation of salinity in controlling ore-forming fluid transport in sedimentary basins: Example of the HYC deposit, northern Australia: Mineralium Deposita, v. 39, p. 622-631.

Base-metal Enrichment in Stage-5 (mid-Cambrian) Black Shale of the Hess River Formation, Misty Creek Embayment, Selwyn Basin

E.C. Turner
Department of Earth Sciences / Mineral Exploration Research Centre
Laurentian University, ON
eturner@laurentian.ca

Abstract

Deep-water turbiditic limestone of the Cambrian Hess River Formation in the Misty Creek Embayment (Mackenzie Mountains, Northwest Territories), a poorly known and economically underexplored part of the sedimentary exhalative/ clastic-dominant (SEDEX/CD)-hosting Selwyn Basin, contains a >20 m-thick black shale interval with elevated base metal and barium content and geochemical evidence of hydrothermal venting. Carbon isotope stratigraphy of the formation in its type area shows that its deposition in the Cambrian spanned from at latest early Stage 5 to mid-Paibian, and that its upper, conformable contact with the Rabbitkettle Formation, as originally defined lithostratigraphically, is coincident with the Sauk II-III boundary in the chemostratigraphic reference curve. The black shale addressed by this study was deposited in latest Stage 5, and a further ~50 m may exist under scree above the studied interval, probably extending into the early Drumian. This depositional age may be identical to that of host strata of mineralisation in the Anvil District, Yukon, but the depositional age of host rocks and mineralisation in the latter are not well constrained. The newly established depositional age of the Hess River Formation in the Misty Creek Embayment identifies significant dating and correlation problems in the broader Selwyn Basin. Biostratigraphic data from base of the overlying Rabbitkettle Formation in its type area indicate a Drumian depositional age, yet the top of the Hess River Formation in its type area is Paibian (i.e. 9 m.y. of overlap with depositional span of Hess River Formation in its type area). This conflict highlights the difficulty of mapping, picking contacts in, and correlating monotonous deep-water successions with little biostratigraphically useful content, subtle differences among formations, and diachronous changes in sedimentation regimes in a basin that was tectonically active. Although it is not field-friendly, carbon isotope stratigraphy may be the only viable tool that can be applied to deciphering the Selwyn Basin's tectonic, stratigraphic, and metallogenic history.

Introduction

The Selwyn Basin, a Cambrian to Silurian deep-water region flanking the northwestern margin of Laurentia, contains SEDEX/CD past-producing deposits and showings at several stratigraphic levels (Goodfellow, 2007). The past-producing Anvil District was hosted by Cambrian deep-water strata (Pigage,

Recommended citation
Turner, E.C., 2015. Base-metal enrichment in Stage-5 (mid-Cambrian) black shale of the Hess River Formation, Misty Creek Embayment, Selwyn Basin, *in* Paradis, S., ed., Targeted Geoscience Initiative 4: sediment-hosted Zn-Pb deposits: processes and implications for exploration; Geological Survey of Canada, Open File 7838, p. 75-95. doi:10.4095/296328

2004; Goodfellow, 2007), but the exact age of the host rocks (Mount Mye and Vangorda formations) is not well constrained. Mid-Ordovician (or possibly Silurian-Devonian) deep-water strata contain the Vulcan showing (Mako and Shanks, 1984), which, although not a past-producing deposit, is significant because it records a temporally distinct episode of syndepositional base-metal mineralisation in a different part of the basin from the better known mining and exploration camps. Early Silurian deep-water strata host the Howards Pass deposits (Norford and Orchard, 1985). Younger SEDEX/CD deposits of the MacMillan Pass area are hosted by Devonian deep-water strata belonging to an unrelated, younger basin regime and, although in the same geographic region as the older deposits, are not considered here to be part of the Selwyn Basin.

The Selwyn Basin spans both the Yukon-Northwest Territories boundary and a geographic range in which Cordilleran deformation intensifies southwestward. This region encompasses the lower to middle Paleozoic northwestern margin of Laurentia, comprising several geographically complex embayments that are inferred to have resulted from anomalous extension during early to mid-Paleozoic passive-margin subsidence. The most northwestern of the embayments in the Selwyn Basin system is the Misty Creek Embayment (MCE; Figure 1), which is in the less-deformed, better-exposed eastern zone of the northern Canadian Cordillera. Owing to its remoteness, the MCE has not been extensively studied to unravel its geologic history, nor extensively explored to evaluate its economic potential.

The established understanding of the MCE is dominated by the regional stratigraphic synthesis of Cecile (1982), in which the thick and previously poorly known “Road River Group” was subdivided into formal stratigraphic units: the Hess River, Rabbitkettle, Duo Lake, and Cloudy formations, which together form the lower to middle Paleozoic deep-water succession in the MCE and other parts of the Selwyn Basin. The Hess River, Duo Lake, and Cloudy formations were defined in, and have type sections in, the MCE, whereas the Rabbitkettle Formation’s type section is farther south in the Mackenzie Mountains (Gabrielse et al., 1973), a geographic disparity that poses problems for defining the units’ contacts in the field.

The regional distribution of the MCE’s deep-water units relative to surrounding shallow-water carbonate-dominated environments was established (Figure 1), and the depositional evolution of the basin outlined by Cecile (1982). A number of representative sections were documented at reconnaissance scale, and biostratigraphic constraints were established as best as possible, given the dearth of fossil material. Depositional ages of the younger stratigraphic units were adequately constrained biostratigraphically (Cecile, 1982) but the depositional age of the Hess River Formation remained enigmatic owing to poor biostratigraphic control. This meant that the formation’s role in basin evolution could not be adequately characterised, and its relationship to metalliferous strata elsewhere in the Selwyn Basin has not been established.

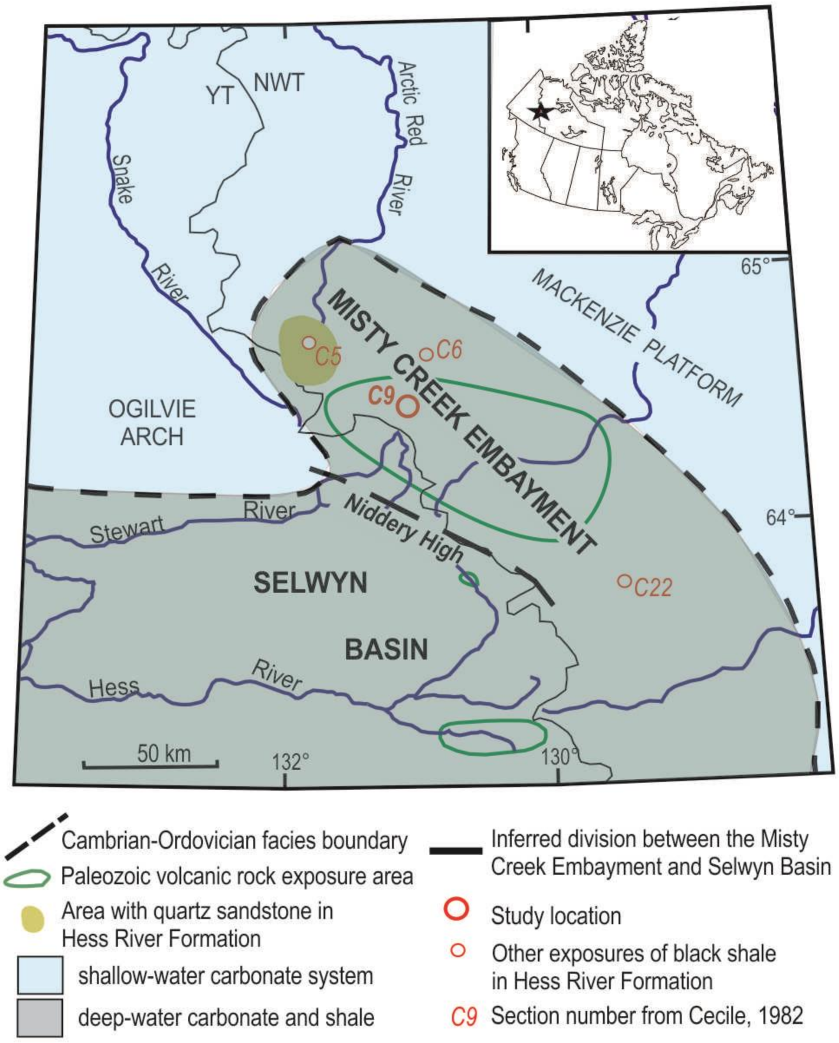

Figure 1. Location map of the deep-water Misty Creek Embayment and coeval, surrounding shallow-water environments, the study location (C9), and other stratigraphic sections mentioned in the text. Location C6 is the type section of the Hess River Formation.

The present work is part of a detailed sedimentological-stratigraphic study of one of the thickest and deepest-water sections originally documented by Cecile (1982), and is intended to follow up in greater detail on the depositional environments, processes, age, and base-metal prospectivity of the MCE. For this study, one very thick and continuous section through the deepest-water part of the embayment was measured and sampled in detail. The lowest part of the succession is not exposed at this location. Results of the field study (Chevrier and Turner, 2013a, b) showed that the Hess River and Rabbitkettle formations in the centre of the MCE are dominated by silt- and mud-grade material derived from contemporaneous shallow-water carbonate environments and deposited by very fine-grained turbidity currents on a gently sloping basin floor. Sedimentation was strongly carbonate-dominated during deposition of the Hess River and

Rabbitkettle formations, but became shale and chert-dominated when the Duo Lake Formation was deposited (Late Ordovician – Early Silurian), returning to carbonate-dominated deposition during accumulation of the Silurian Cloudy Formation.

Among the objectives of this study has been to identify, date, and evaluate any black shales in the succession. Four of the stratigraphic sections of Cecile (1982) depict black shale intervals in the lower part of the Hess River Formation in the Misty Creek Embayment. Fritz (1976, 1978, 1979) documented recessive intervals of “dark shale and platy limestone” that overlie the Lower Cambrian Sekwi Formation throughout a broader region of the western Mackenzie Mountains in NT. Although it is unclear whether any of these generalised intervals includes distinctly black shale like that addressed by the present study, they suggest the possibility of regionally distributed black shale in the lower Hess River Formation.

Analytical work for this project component has focussed on (a) establishing a carbon isotope curve for lower Paleozoic strata of the MCE, in order that its depositional history be better temporally constrained than has been possible using sparse biostratigraphic data, and so that the depositional age of any intervals of potential economic interest is known, and (b) analysing the geochemistry of a hitherto untested black shale interval in the lower Hess River Formation. This paper reports on the results of this analytical work.

Results/Data Analysis

Methods

A detailed stratigraphic section was documented at decimetric scale through approximately 3 km of lower to middle Paleozoic strata (Figure 2; Chevrier and Turner, 2013a, b) at the location of a previously measured reconnaissance section in the middle of the MCE (Cecile, 1982, section 9; Figure 1). Hand samples were collected approximately every 2-5 m for stable isotope analysis. Black shale was sampled where present by excavating pits (depth ~50-80 cm) through the shale scree to reach intact rock, which was then sampled using a pen knife.

The material sampled for stable isotope analysis consisted of well-preserved lime mudstone with little recrystallisation, no petrographic evidence of diagenetic alteration, and little to no tectonic veining. Samples were prepared from mud-grade parts of thin-section offcuts using a tungsten-carbide dental bur. The stable isotope analyses were performed at the GG Hatch isotope Laboratory at University of Ottawa following their standard protocol. Oxygen isotope results show little variation throughout the section, supporting the understanding of the succession as little altered and bearing near-depositional (original) stable isotope values.

Twelve samples from the black shale interval were subjected to whole-rock geochemical analysis at Acme Labs (Vancouver, British Columbia) using their standard aqua regia and lithium fusion inductively coupled plasma-mass

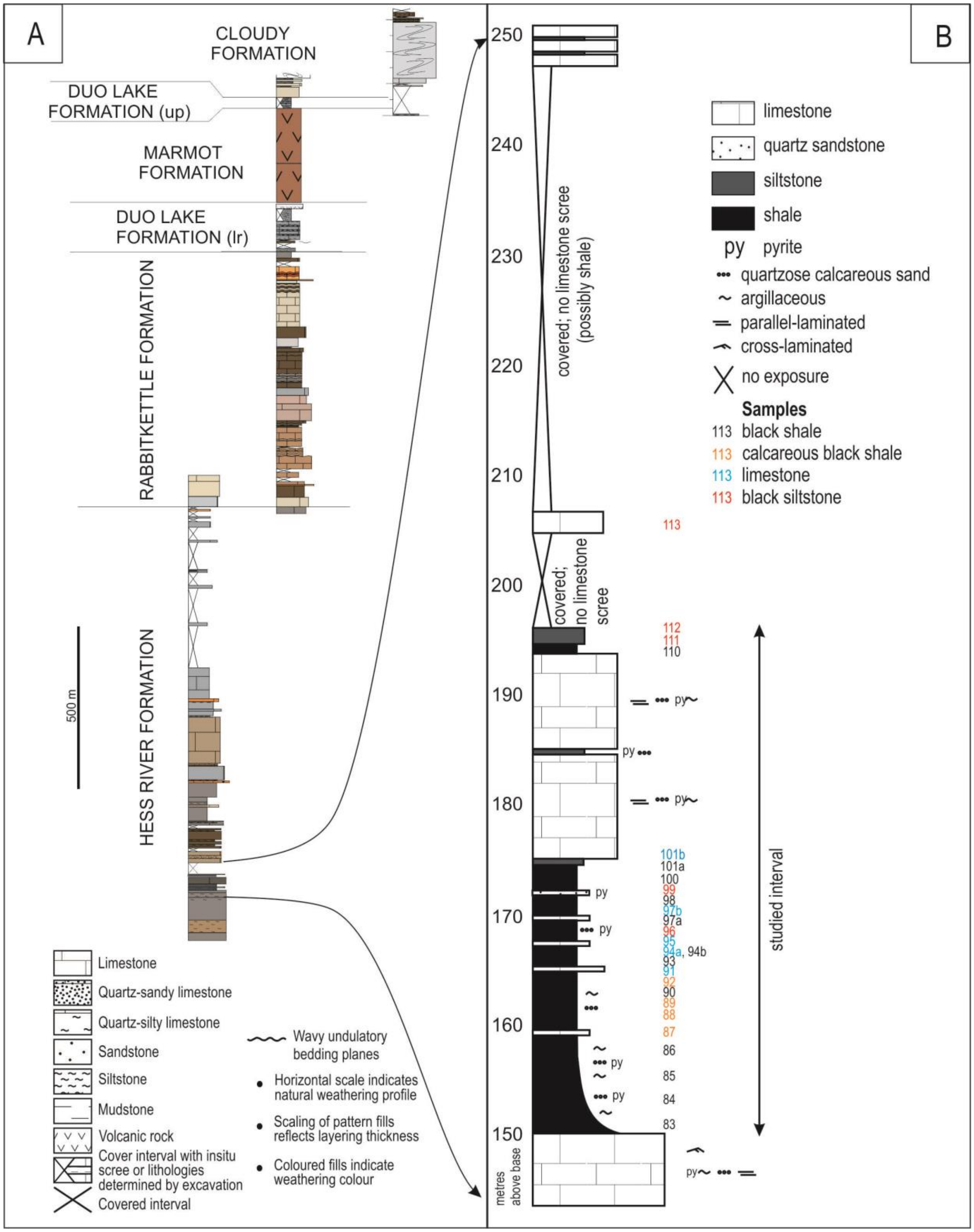

Figure 2. (A) Stratigraphic log for the entire lower to middle Paleozoic deep-water succession in the centre of the Misty Creek Embayment (after Chevrier and Turner, 2013a,b), measured in three increments. (B) Expanded log for the black shale interval in the lower Hess River Formation.

spectrometry (ICP-MS) protocols. Analytical results are normalised to the upper continental crust shale-equivalent standard “Mud of Queensland” (MUQ; Kamber et al., 2005). The possibility of BaO influencing Eu values was dismissed using inter-element correction.

Several samples were analysed for total organic carbon using Rock-eval pyrolysis at GSC-Calgary. One black shale sample was analysed for mineralogy using X-ray diffraction (XRD) at the Central Analytical Facility at Laurentian University.

Discussion/Models

Hess River Formation lithostratigraphy and sedimentation

The lithostratigraphy and sedimentology of the Cambrian part of the MCE succession (Figure 3; Hess River Formation and lower half of Rabbitkettle Formation; Chevrier and Turner, 2013a, b) record a predominantly deep-water environment dominated by carbonate mud to sand delivered to the deep basin-floor by turbidity currents from a coeval shallow-water carbonate environment in which the carbonate material had originally precipitated. The Hess River Formation, the subject of this study (~1370 m thick; basal contact not exposed), consists of lime mudstone with sparse laminae of peloidal calcarenite together with trace to (rarely) dominant fine-grained quartz sand (Figure 3F) to silt and abundant pyrite, and shale seams that separate limestone layers (Figure 3E). The coarser laminae (silt- to rarely fine-sand-sized) are graded and exhibit rare cross-lamination and micro load-casts. Quartz silt to sand, a minor but pervasive component of the Hess River Formation, co-occurs with carbonate material of the same grain-size (i.e. coarser than most of the carbonate material in the formation) in millimetric laminae, and so the coarser quartz (i.e. silt-sand, rather than clay-sized) is interpreted as having been delivered in carbonate-dominated turbidity currents. Interpreting the quartz sand/silt’s ultimate origin is beyond the scope of the present study.

The black shale interval is in the lower part of the exposed Hess River interval at the study site (Figure 3B-D), and is underlain and overlain by turbiditic lime mudstone to calcisiltite. The shale is very recessive, and contains sparse centimetre- to decimetre-thick argillaceous lime mudstone intervals. Minor rusty-weathering quartzose and calcareous silt laminae like those in the carbonate-dominated parts of the Hess River Formation are also present in the shale.

Depositional age using carbon isotope stratigraphy

A carbon isotope curve generated for the Hess River to lower Rabbitkettle formations (Figure 4) compares favourably to a global compilation curve for the Cambrian (Saltzman and Thomas, 2012) and especially well to details of the lower Paleozoic curve generated for southwestern Laurentia (Saltzman, 2005). This strong relationship to the well-constrained global and regional curves allows

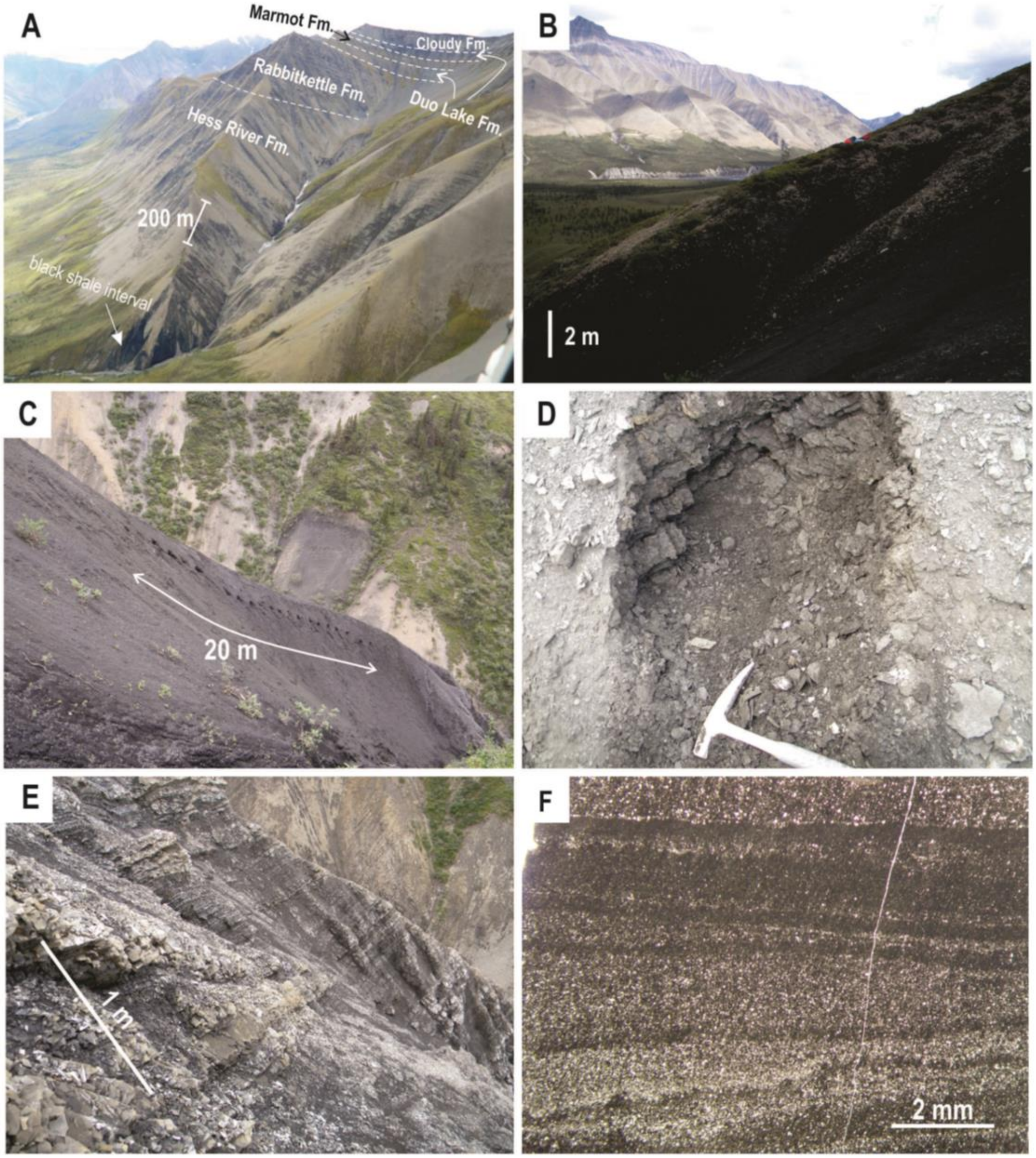

Figure 3. (A) Lower part of measured section, including Hess River Formation and its black shale interval. (B) Upper part of the black shale exposure. (C) Lower part of the black shale exposure, showing a series of shallow pits excavated for sampling of intact shale beneath a veneer of shale scree. Strata dip to the left. (D) A pit excavated for shale sampling. Upper centre shows intact shale layers that were sampled; sides show thin veneer of shale scree; lower centre is loose material produced by excavation. (E) Typical exposure of Hess River Formation limestone turbidites with minor argillaceous interbeds. (F) Thin section view in PPL of typical Hess River fine-grained graded beds with sharp contacts, silt-grade calcareous and quartzose material at layer bases, and evidence of pulsing tractional flow (repeated graded laminae).

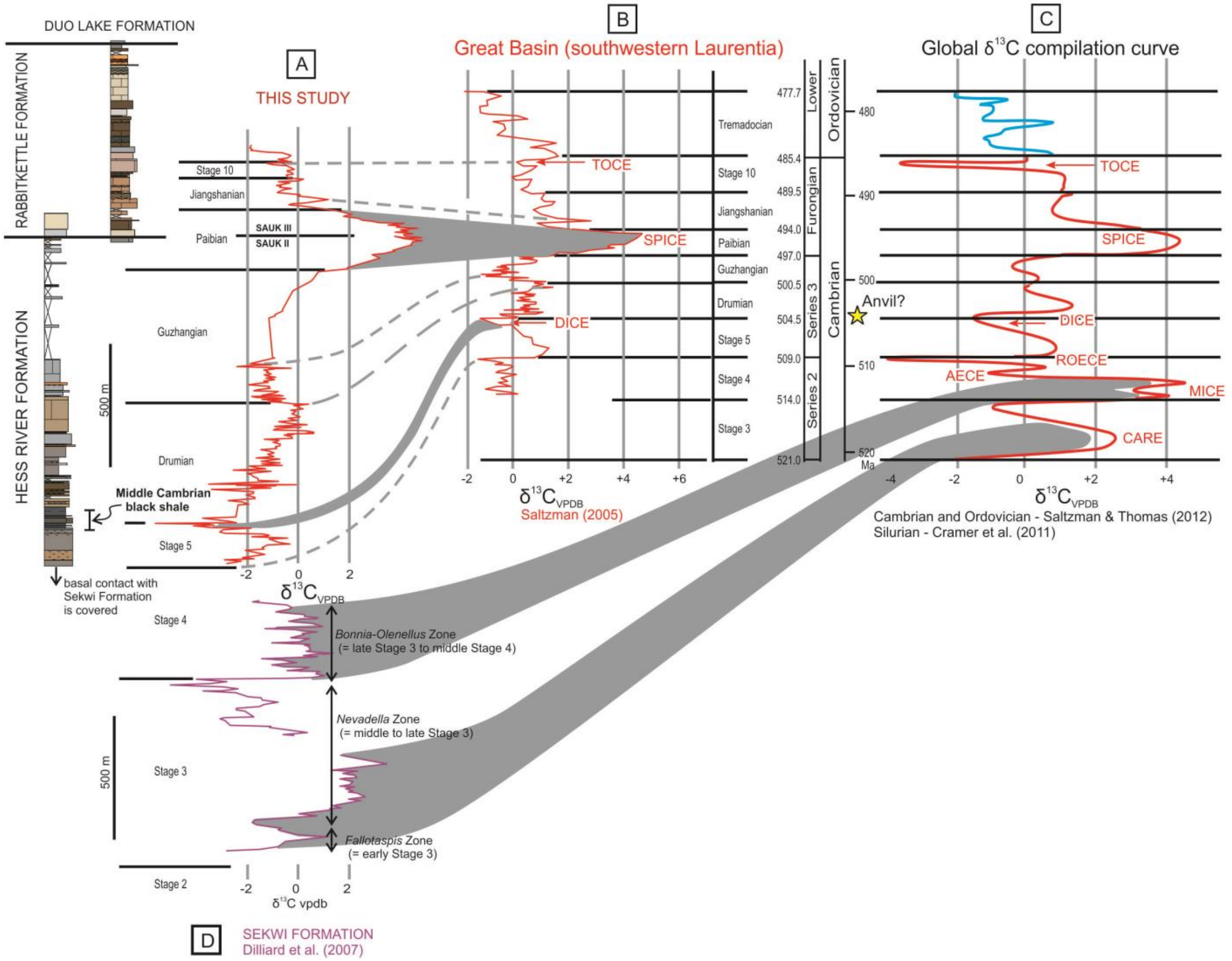

Figure 4. Carbon isotope curve for the Hess River and Rabbitkettle formations at the study site (A), compared to (B) detailed curve for southeastern Laurentia (Saltzmann, 2005), (C) global composite curve (Saltzman and Thomas, 2012), and (D) curve for the underlying Sekwi Formation (Dilliard et al., 2007). Hess River Formation black shale interval may be temporally equivalent to host rock of the Anvil district in the Selwyn Basin of Yukon (yellow star).

the Cambrian part of the MCE succession to be assigned confidently to global stages (Figure 4). The high accumulation rates in deep water attest to the robust capacity of Phanerozoic carbonate factories to produce carbonate particulates in shallow-marine environments and export them voluminously elsewhere. Given the sedimentology of the succession and the understanding of Phanerozoic carbonate dynamics, it is clear that the carbonate material preserved in the deep-water MCE initially formed under shallow-water conditions, where it could acquire the carbon isotopic signal of the uppermost water column, which was well mixed with global marine water, before being transported to and deposited in a deep-water environment that may not have been fully exchanged with the global water mass (Figure 5A).

Carbon isotope stratigraphy indicates that the black shale interval in the lower Hess River Formation was deposited in (Cambrian) late Stage 5, just prior to the negative $\delta^{13}C$ excursion known as the Drumian carbon isotope excursion (DICE), which marks the beginning of the Drumian (Figure 4; Saltzman and Thomas, 2012). Field evidence strongly suggests that black shale continues above the interval studied (possibly another ~50 m; Figure 2), which would indicate black shale depositional conditions that persisted into the early Drumian.

The time constraints placed on Hess River Formation deposition in the MCE using carbon isotope stratigraphy are generally compatible with the existing biostratigraphic data for the unit (Figure 6; Cecile, 1982), but with some serious caveats regarding the age and identification of the formation's lower and upper contacts. Fritz (1976) and Cecile (1982) suggested that the contact of the Hess River Formation with the underlying Sekwi Formation is diachronous. Chemostratigraphic data for the Sekwi Formation (Dilliard et al., 2007; Figure 4) do not contain two major Stage 4 (late Early Cambrian) carbon isotope excursions (Archeocyathan Extinction Carbon Isotope Excursion (AECE) and Redlichiid-Olenellid Extinction Carbon isotope excursion (ROECE)), and these anomalies are also absent from the lowermost exposed Hess River Formation in the present study, which could indicate a non-diachronous relationship involving a sedimentary hiatus. The basal contact of the Hess River Formation is not exposed at the study site, but at another section known to contain a black shale in the lower Hess River Formation (Cecile 1982, section 6) the lowest metre of Hess River Formation consist of quartz sandstone with sparse, 'floating' clasts of Sekwi Formation limestone, which suggests that base of the Hess River Formation may not be conformable. Furthermore, those sections of Cecile (1982) that contain a black shale interval depict variable thicknesses of Hess River Formation limestone below the black shale, which suggests that, if the black shale does indeed represent a temporally meaningful episode in basin history, the onset of accumulation of the underlying Hess River Formation turbiditic limestone varied temporally and geographically. Owing to the lack of any other reliable way to date these successions, the time relationship of the Sekwi – Hess River contact will probably only be solved with application of carbon isotope stratigraphy.

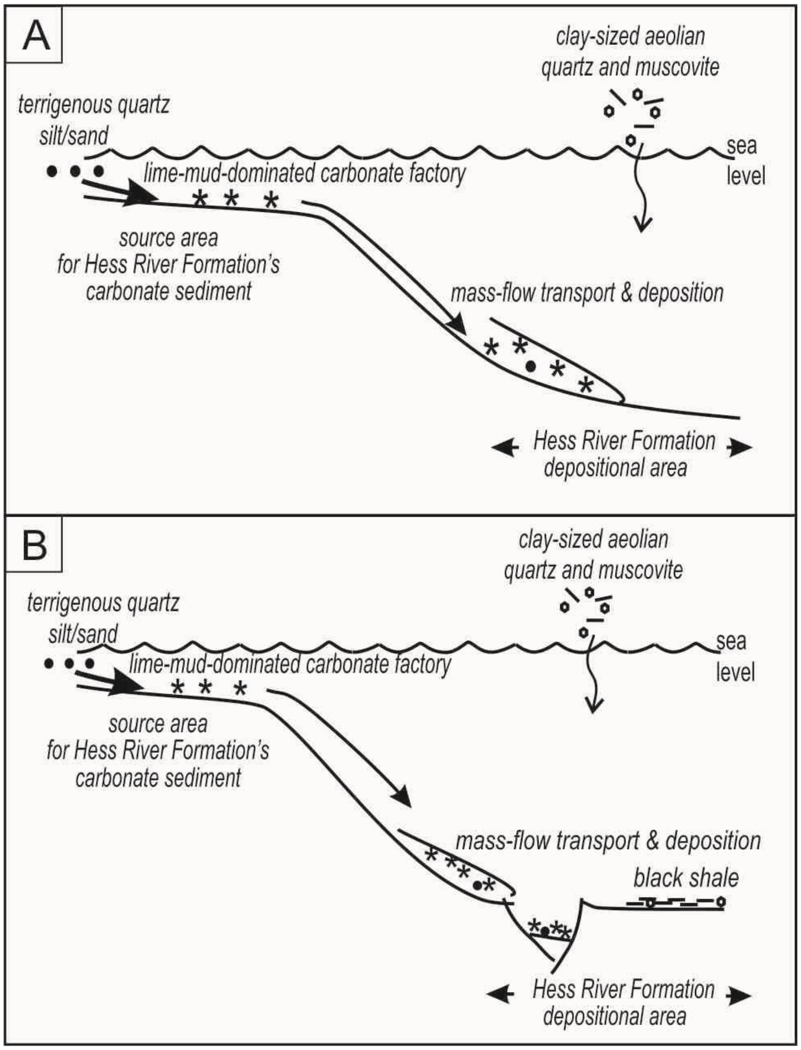

Figure 5. Depositional model for the Hess River Formation. (A) Background clay-sized aeolian sediment (hemipelagic quartz and muscovite) is fairly constantly supplied. Mud- to silt-sized carbonate material is supplied from a coeval, nearby, shallow-water carbonate factory that may be similar to the possibly contemporaneous Franklin Mountain Formation (Turner, 2011), and is delivered to the deep-water environment as fine-grained turbidity currents. Carbonate production and export to the deep-water basin was prolific, and almost always overwhelmed the background hemipelagic supply of clay-sized terrigenous silicate particles (shale seams). Silt-sized and coarser quartz was delivered to the basin floor along with carbonate mud to silt, but is not known to be present in possibly contemporaneous shallow-water formations. The (comparatively) coarser quartz may have been locally derived from uplifted blocks of older terrigenous strata (Windermere or Mackenzie Mountains supergroups). (B) Later, during black shale deposition, delivery of shallow-water-derived carbonate material to the study site ceased; given that there is no other evidence that the nearby carbonate factory may have been defunct at this time, a physical impediment that blocked or diverted sediment delivery is envisaged.

The contact between Hess River and overlying Rabbitkettle formations in Hess River Formation's type area in the MCE (Cecile, 1982) is placed at "the base of the first very thick succession (>10 m) of thin bedded limestone or silty limestone above which shale is a subordinate lithology within the Rabbitkettle Formation". The basal contact of the Rabbitkettle Formation in its type area, over 400 km south-southeast of the Hess River Formation's type area and well beyond the MCE, is an unconformity (Gabrielse et al., 1973). Trilobite biostratigraphic data for the Rabbitkettle Formation in its type area indicate that Rabbitkettle Formation deposition started in the Drumian (Figure 6; Pratt, 1988), yet in the MCE, where the Hess River Formation was established, the chemostratigraphic evidence shows that the Hess River-Rabbitkettle contact, as defined lithostratigraphically by Cecile (1982) is in the mid-Paibian, almost exactly equivalent to the Sauk II-III boundary (Figure 4). This substantial discrepancy in the position of the Hess River - Rabbitkettle contact (~9 m.y. difference) almost certainly results from the necessity of picking formation contacts in the field using lithostratigraphic evidence, in a biostratigraphically impoverished succession that is notoriously difficult to differentiate in the field and that probably had regionally variable timing in subtle sedimentation changes. The fact that changes in lithostratigraphic character seem to have been diachronous throughout the Selwyn Basin will continue to hamper stratigraphic correlation and comparison among the various parts of the basin system. Although it is not field-friendly, carbon isotope stratigraphy is probably the best way to define and correlate a succession that has subtle but important geographic variations in its sedimentological character, and which lacks biostratigraphic evidence that can be easily obtained and used in the field by non-specialists.

Using the new time-depositional constraints on Cambrian strata in the MCE to compare its stratigraphy to the stratigraphic record of base-metal mineralisation in the established mineral districts of the Selwyn Basin is complicated by the reality that the MCE succession is now better temporally constrained than the presumed coeval succession in the established exploration and mining camps (e.g. Pigage, 2004). The inferred depositional age of the oldest known base-metal depositional episode in the Selwyn Basin (middle Cambrian(?) Mount Mye Formation; Anvil district; Pigage, 2004), may correspond to the black shale interval at the study location in the MCE (Figure 4). Conversely, the >20-m-thick black shale interval in the MCE (Chevrier and Turner, 2013a,b) is now known to be early Stage 5 to Drumian (middle Middle Cambrian), an age for which no well-dated black shale episode or base-metal enrichment is known elsewhere in the peri-cratonic, deep-water, lower Paleozoic system in northwestern Canada. This depositional age is, however, identical to that of the Burgess shale Lagerstätte (British Columbia). The temporal coincidence of Burgess shale (Stephen Formation) deposition at the foot of a submarine escarpment and deposition of the lower Hess River Formation in an excessively subsiding basin 1750 km along strike to the north supports the well-established interpretation that the middle Cambrian was a time of exaggerated extension and subsidence throughout northwestern Laurentia.

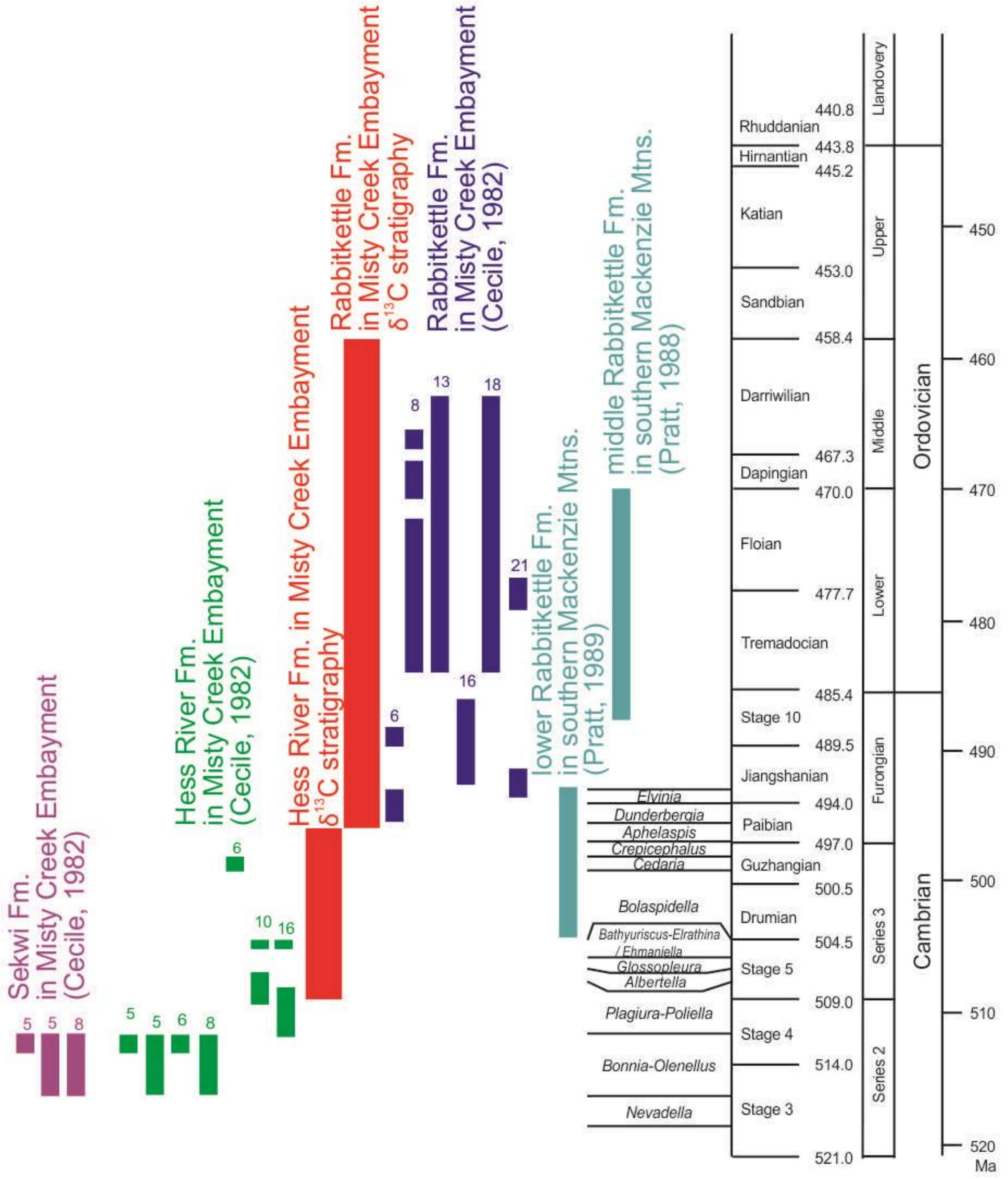

Figure 6. Comparison of temporal span of Hess River and Rabbitkettle formations in the MCE, based on biostratigraphic (Cecile, 1982) and chemostratigraphic (this study) data. The chemostratigraphic data (red) are compatible with biostratigraphic data (all other colours) for the MCE if the Sekwi and Hess River formations are interpreted to have a conformable contact in the *Bonnia-Olenellus* Zone (late Early Cambrian). The chemostratigraphic data, however, allow a more detailed temporal subdivision of the formations than do the sparse biostratigraphic data. Correlation into the southern Mackenzie Mountains (teal-coloured biostratigraphic data at right) is problematic, probably owing to unintentional placement of the Hess River-Rabbitkettle contact at different lithostratigraphic positions in the two respective type areas. Small numerals refer to section numbers in the cited material. Relevant Cambrian trilobite biozones are listed adjacent to the time scale.

Black shale petrography and mineralogical composition

No silicate, sulphide, or carbonate particles are discernible in Hess River Formation black shale thin sections under plane light. The mineralogical composition of one representative sample (ARR 90), determined by XRD, is quartz-dominated with significant muscovite and accessory jarosite and albite; the absence of clay minerals is to be expected, given the formation's pre-Devonian age (prior to the appearance of biologically active soil). The extremely recessive exposure in the black shale interval therefore reflects its very fine grain size rather than its mineralogical composition. The clay-grade quartz and muscovite that make the shale are interpreted as background sediment that was supplied steadily through time, probably by wind, upon which was superimposed, most of the time, the voluminous carbonate component transported by fine-grained mass-flow from a contemporaneous shallow-water carbonate factory such as that described by Turner (2011) for roughly contemporaneous shallow-water strata east of the MCE.

During Hess River Formation black shale deposition, carbonate delivery to the study location stopped almost completely. The carbon isotope curve shows that the shale's depositional interval was not protracted enough to eliminate, at the study site, any part of the carbon isotope record as established elsewhere in Laurentia (Figure 4; Saltzmann, 2005). The geographic and temporal extent of the black shale episode in the MCE remain unknown, although the presence of shale at possibly equivalent stratigraphic positions in several sections of Cecile (1982) suggests that the shale depositional area may have had a regional extent of at least 50 km along and strike (possibly as much as 150 km; Figure 1), and at least 25 km perpendicular to the embayment's long axis. The temporary, late Stage 5 to early Drumian suspension of carbonate delivery to the study site, and possibly more broadly, could represent either (a) an episode of no carbonate deposition in the nearby carbonate factory (source area), such that no material was available to be exported to the deep-water setting (e.g. subaerial exposure during sea-level lowstand; development of geochemically unfavourable conditions in shallow water), or (b) appearance of a temporary physical impediment to the continued delivery of carbonate material at this site. The continued, rare delivery of silt-grade material that is both quartzose and calcareous, to form millimetric laminae in the black shale, however, suggests that both carbonate production and minor delivery of non-aeolian (i.e. comparatively coarse) quartz were maintained in the nearby shallow-water environment. The suspension of carbonate delivery to deep water therefore probably indicates the presence of a physical impediment that developed between the shallow-water carbonate source and the study site during the black shale depositional interval. Given that the basin is understood to have been episodically tectonically active, it is probable that a tectonic impediment such as an uplifted fault block or intervening graben may have appeared somewhere between the sediment production area and the study site, and temporarily diverted the influx of shallow-water-derived material elsewhere (Figure 5B).

Shale Geochemistry

Whole-rock geochemical results for a subset of samples from the newly identified Stage 5 black shale interval yielded the following results.

Given the mineralogical composition provided by XRD, silicon - aluminium ratios between 0.45 and 0.66 (Figure 7) indicate quartz:muscovite ratio of approximately 3:1; a slight stratigraphic decrease in this value reflects a greater proportion of phyllosilicates to quartz up-section. The proportion of Al in this Cambrian shale is significantly lower than that of the MUQ (modern, oxic) shale-equivalent standard (Kamber et al., 2005) used for comparison in this study, presumably owing to the Hess River shale's pre-Devonian, and therefore pre-clay, age. Zr/Hf, Nb/Ta, and Nb/Th ratios are relatively constant stratigraphically, with one anomalously high Zr/Hf value (sample 94b) that may reflect a coarser grain size in the quartz component (a quartz silt lamina may have been included in the sample inadvertently); although its Si/Al ratio is unremarkable, the sample also has elevated CaO, and so the high Zr probably reflects a small influx of coarser quartz delivered with the carbonate from shallow-water, both superimposed on the background of extremely fine-grained, presumably aeolian quartz and muscovite.

A ternary plot of oxides (Figure 8) shows that the shales' Al_2O_3/MgO ratios resemble those of black shale standard USGS SDO-1 (http://crustal.usgs.gov/geochemical_reference_standards), but have variably higher CaO content, which reflects carbonate content (also noted in the field; Figure 2). The steady ratio of the non-calcareous oxides, however, indicates that the terrigenous material supplied to the basin had a consistent composition, and therefore that detrital silicate composition is not responsible for variable base and precious metal concentrations. Given the mid-Cambrian age of the material (prior to abundant radiolaria), SiO_2 content is assumed to be entirely terrigenous, and the total terrigenous content (sum of Al_2O_3, SiO_2, Na_2O, K_2O, and TiO_2; Figure 7) is comparatively steady at 65-78%; the lower total terrigenous values correspond to elevated CaO and presumed carbonate content, supplied, as deduced based on sedimentological constraints, as particulate carbonate from a nearby shallow-water carbonate factory. There is no correspondence between MgO and CaO, which reflects the calcitic, rather than dolomitic, composition of the carbonate component.

Rock-eval pyrolysis analysis of eleven shale samples (a different subset from that used for whole-rock analysis) yielded fairly constant total organic carbon (TOC) values between 1 and 2 wt% (Figure 7), which is considerably higher than background values in carbonate-dominated intervals of the MCE succession.

Total rare earth element (REE) content increases crudely up-section (Figure 7), but does not always covary with phyllosilicate (Si/Al) nor calcite (CaO), so it is unclear what drove the modestly increasing ΣREE trend. Black shale REE profiles (Figure 9) depict similar overall values and shapes. The light REE (LREE) are in general slightly enriched relative to middle REE (MREE) (La/Gd =

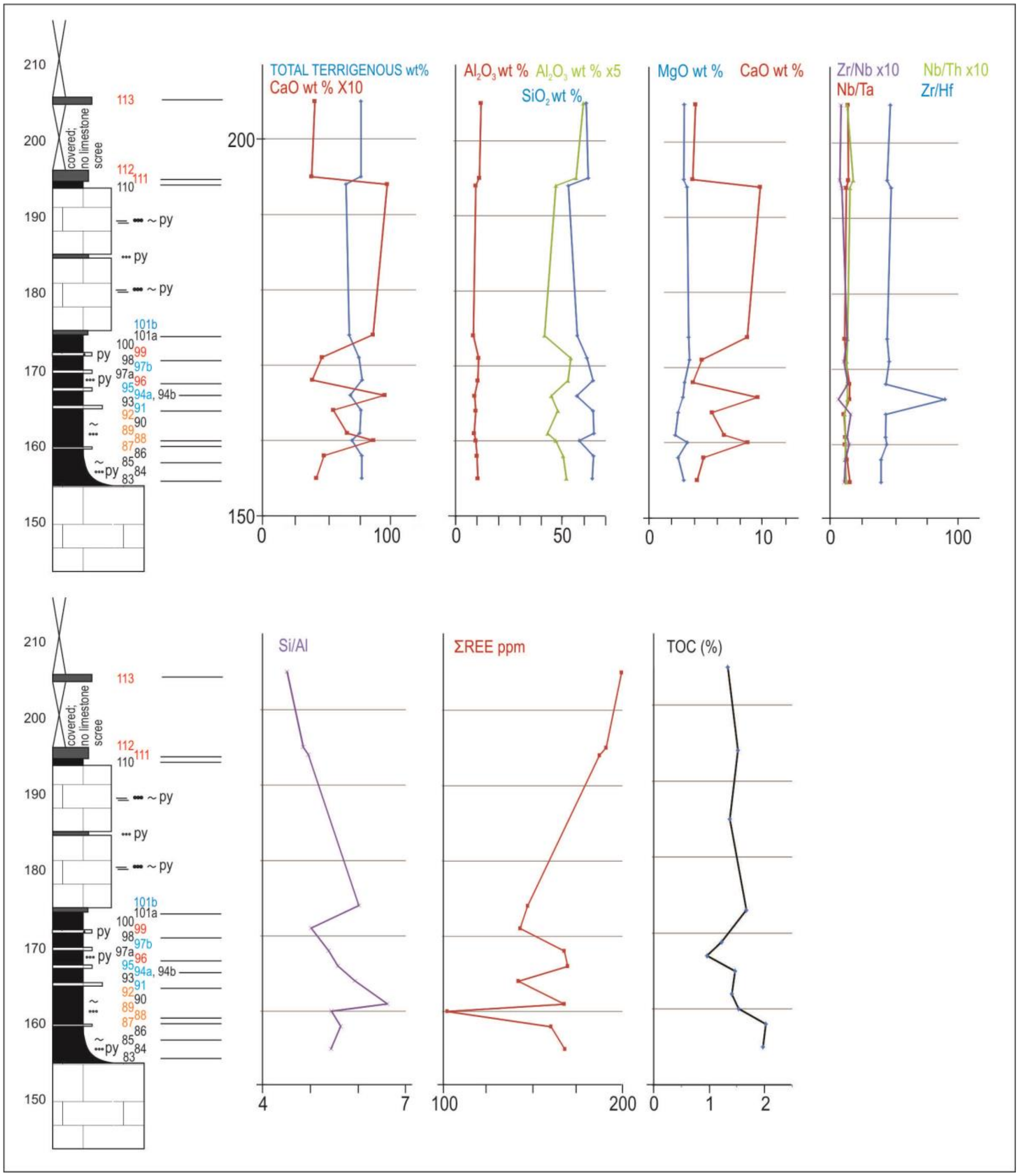

Figure 7. Stratigraphic patterns in major elements and terrigenous proxies. See text for interpretation.

1.1 to 1.3), but MREE are slightly depleted relative to heavy REE (HREE) (Gd/Lu <1), yielding profiles that are subtly dish-shaped and slightly negatively sloped. Such REE profiles indicate that the MCE's bottom water was not well exchanged with an open-marine water mass. La/La* and Gd/Gd* are near or above 1, and

Y/Ho is superchondritic (>26) indicating that although the MCE bottom water had evolved away from a ‘normal marine’ REE profile, its origin had originally been marine. Pr/Yb ratios are less than 1, except for the stratigraphically uppermost two values, indicating a restricted basin that may have become slightly better connected with the global ocean as time progressed.

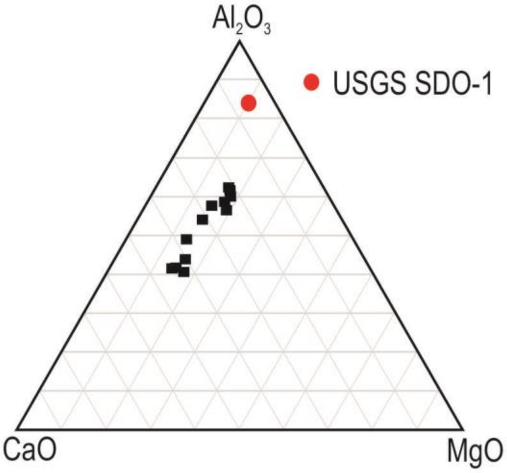

Figure 8. Ternary plot of major oxides. Hess River shale samples have a consistent ratio of Al_2O_3 to MgO, but variable CaO that is well above that of black shale standard USGS SDO-1. The steady ratio of Al to Mg indicates a compositionally consistent source of silicate material during black shale deposition. The difference in CaO concentration reflects the variable but ongoing contribution of shallow-water-derived carbonate to the basin floor even during the time of seeming sediment starvation recorded in the black shale.

All samples have pronounced negative Y anomalies and flat to subtly positive Ce/Ce*, suggesting mild anoxia (Figure 9). TOC values (Figure 7) are uniformly <2.5, putting them in the low-oxygen oxic region (Algeo and Maynard, 2004). Enrichment factors (EF) for the redox-sensitive elements As (7.2-10.5), U (3.5-6.4), and V (3.8-11.2) are moderately and variably elevated, but Ce/Ce* values are only barely anomalous (between 1 and 1.1), suggesting that anoxia was not pervasive (Figure 10). As_{EF} strongly covaries with Ce/Ce*, but U_{EF}, V_{EF}, and Cr_{EF} covary less strongly with Ce/Ce*, suggesting that these redox-sensitive elements had distinctive behaviours in the generally low-oxygen environment. The enrichment factor for Mo is generally high (40-113), but does not coincide with the Ce anomalies, suggesting that sulphidic conditions may have developed only below the sediment-water interface.

Zn (as enrichment factors normalised to MUQ; Kamber et al., 2005) is strongly elevated in several levels (Zn_{EF}=40 to 113; maximum concentration 520 ppm; Figure 10). Copper (EF=2-4), Pb (EF=1.5-2.8), and Ag (191-655 ppb) covary with Zn and are modestly elevated at the same stratigraphic levels. Stratigraphic levels with highest Mo_{EF} or with highest Ce/Ce*, however, do not correspond to

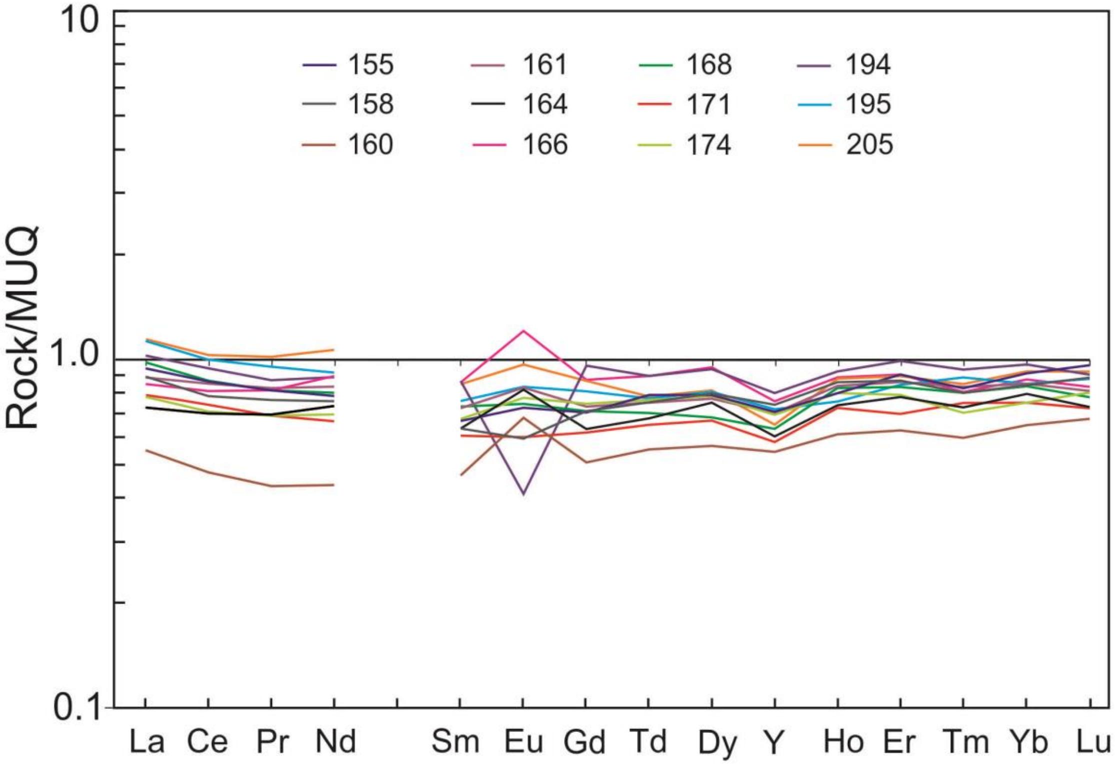

Figure 9. REE+Y in Hess River Formation black shale; samples are labelled by stratigraphic elevation. Slightly dish-shaped, slightly negatively sloped profiles indicate basin restriction and bottom-water evolution away from a 'normal-marine' signal. Cerium is very slightly positively anomalous in most samples, and Y is consistently negatively anomalous, suggesting mild anoxia. Positive Eu anomalies in most samples suggest the influence of hydrothermal sea-floor venting. Results are normalised to the upper continental crust shale-equivalent standard MUQ (Kamber et al., 2005).

elevated base-metal values, suggesting that base metal deposition did not strongly depend on euxinia or even anoxia. Base metal enrichment does not covary with CaO content (proxy for carbonate), and no relationship is evident with TOC.

The most notable of the black shale REE results are in Eu behaviour. Five of the 12 samples exhibit strongly positive Eu/Eu*, and another five are moderately positive, which may reflect hydrothermal venting (Figure 10). Stratigraphic levels with the most positive Eu/Eu* values, however, do not correspond to levels with highest EFs for base metals, and so the relationship between inferred venting and base metal concentration remains unclear. One negative Eu anomaly may reflect a transient episode of enhanced basin restriction.

Barium is enriched in the black shale, with particularly strong enrichment evident at 174 and 194 m; very little of the Ba is present in silicate phases, as shown by contrasting aqua regia and lithium fusion results. Although the Ba-rich samples are, predictably, not samples that exhibit elevated base metal content, and the Ba

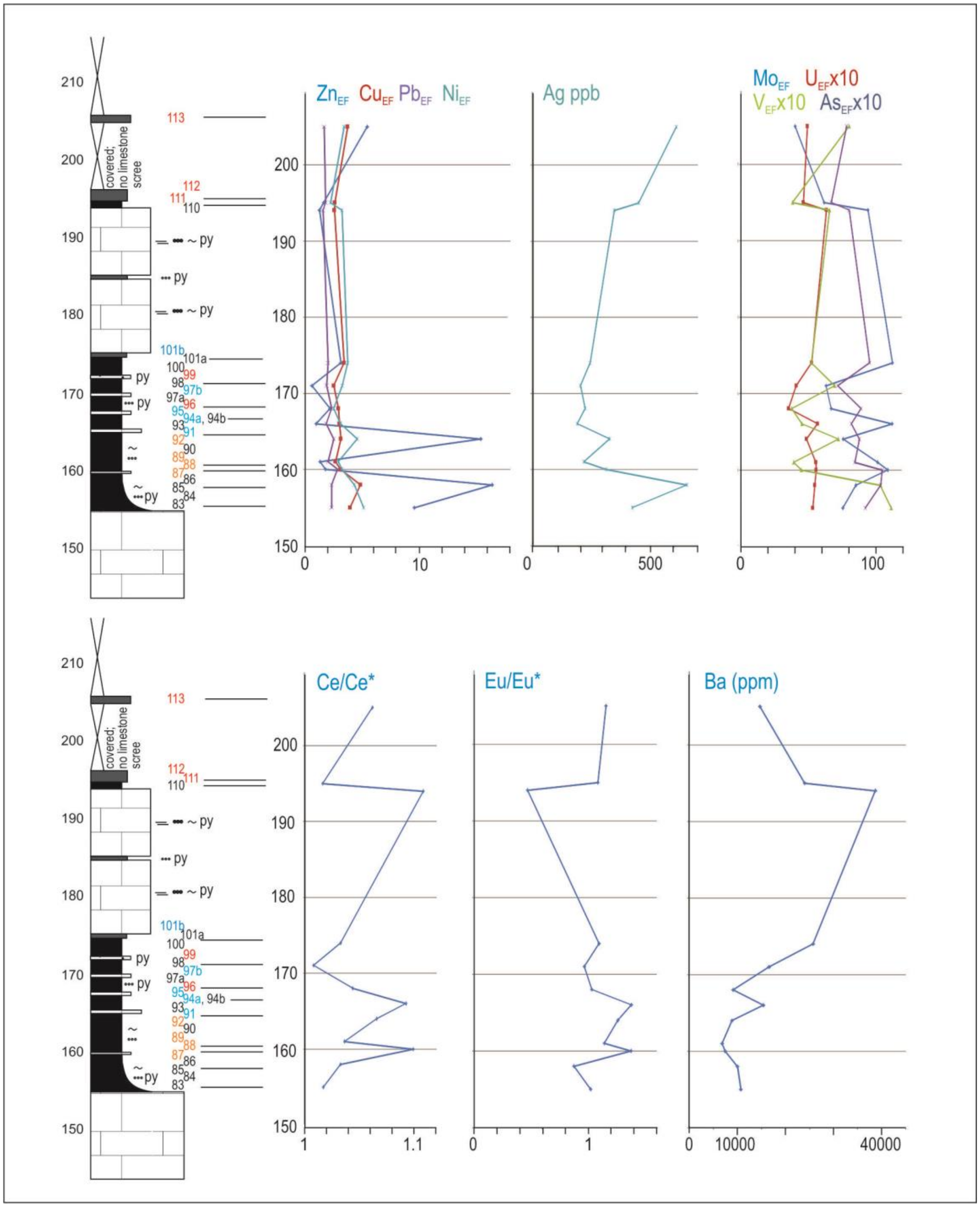

Figure 10. Stratigraphic patterns in base metal enrichment factors, [Ag], redox-sensitive elements, BaEF, paleoredox proxy Ce/Ce*, and hydrothermal proxy Eu/Eu*. Base metal enrichment factors generally covary, and Zn is conspicuously enriched. Base metal enrichment does not generally covary with RSEs or Ce/Ce*, suggesting that paleoredox conditions were not a strong control on base metal content. Seafloor venting of hydrothermal fluids is suggested by generally positive Eu/Eu*, but Eu anomalies do not coincide with levels of base-metal enrichment, suggesting that base-metal behaviour was not strongly linked to venting intensity. Enrichment factors for Ba are markedly elevated and antithetical to base-metal enrichment, but do not covary with proxies for paleoredox status of bottom waters or with Eu/Eu*.

content does not covary with Eu/Eu* (a proxy for venting), Ba concentration does appear to covary with the euxinia proxy Mo_{EF}, which is perplexing given that barite forms under oxic conditions. It is possible that the elevated Ba concentrations reflect barite that precipitated from vent-related fluid that had diffused both geographically away from its vent source and upward in the water column to a more oxidised level where barite could precipitate, and then settle as particulates to the sea-floor. Under such conditions, Ba_{EF} would not necessarily be expected to record the geochemical conditions that prevailed near the sea-floor, and might mix with unrelated sediment containing a more sea-floor, vent-related, and possibly less oxic geochemical signature.

Implications for Exploration

The middle Cambrian (Series 3) stratigraphic succession in the Misty Creek Embayment shows strong evidence of characteristics that are known to be associated with SEDEX/CD deposits: (1) synsedimentary tectonic instability; (2) sediment starvation leaving only black shale to accumulate through deposition of aeolian material; (3) restricted exchange of bottom water with the global marine reservoir; (4) proxy evidence of poorly oxygenated to anoxic conditions; (5) proxy evidence for synsedimentary sea-floor venting, and (6) elevated base and precious metal concentrations at some stratigraphic levels. Dating using carbon isotope stratigraphy shows that a shale interval in the lower Hess River Formation may have the same depositional age as the host rocks of the Anvil District, suggesting the possibility of a regional black shale and venting episode in late Stage 5 to early Drumian. The MCE is remote and has received very little exploration attention, but its litho- and chemostratigraphic characteristics are strongly encouraging with respect to its potential to contain SEDEX/CD mineralisation.

Future Work

The results reported here are from a focussed approach to a single stratigraphic transect in a stratigraphically and geochemically poorly known basin. The propitious geochemical results of the present, limited study suggest that the MCE may have SEDEX/CD potential. Further work to establish the regional dynamics of lower Paleozoic sediment deposition and the geology, chronology, and geochemical attributes of the Selwyn Basin’s carbonate and non-carbonate strata is warranted. Once the geologic history of the basin and its embayments is better understood, perhaps with the use of carbon isotope stratigraphy, comparing the regions and their economic potential will become possible, and intervals of potential economic interest can be more clearly identified and studied in better detail. The pursuit of these objectives has not been possible because a functional temporal framework for the basin’s evolution is lacking.

Acknowledgements

Field sections were measured by T. Chevrier and K. Hahn. B Fischer and E. Martel of Northwest Territories Geoscience Office are gratefully acknowledged for field support and lively discussion. A. Macdonald and W. Zhe are thanked for assistance and insight in XRD analysis. This is NTGO contribution 85.

References

Algeo, T.J., and Maynard, J.B., 2004, Trace-element behavior and redox facies in core shales of Upper Pennsylvanian Kansas-type cyclothems: Chemical Geology, v. 206, p. 289-318.

Cecile, M.P., 1982, The lower Paleozoic Misty Creek Embayment: Geological Survey of Canada Bulletin 335, 78 p.

Chevrier, T.S., and Turner, E.C., 2013a, Lithostratigraphy of deep-water lower Paleozoic strata in the central Misty Creek Embayment, Mackenzie Mountains, Northwest Territories: Geological Survey of Canada Current Research 2013-14, 25 p.

Chevrier, T.S., and Turner, E.C., 2013b, A lithostratigraphic section in the central Misty Creek Embayment, Northwest Territories: Northwest Territories, Open Report 2013-002, 1 sheet.

Dilliard, K.A., Pope, M.C., Coniglio, Hasiotis, S.T., and Lieberman, B.S., 2007, Stable isotope geochemistry of the lower Cambrian Sekwi Formation, Northwest Territories, Canada: Implications for ocean chemistry and secular curve generation: Palaeogeography, Palaeoclimatology, Palaeoecology, v. 256, p. 174–194.

Fritz, W.H., 1976, Ten stratigraphic sections from the lower Cambrian Sekwi Formation, Mackenzie Mountains, northwestern Canada: Geological Survey of Canada Paper 76-22, 42 p.

Fritz, W.H., 1978, Fifteen stratigraphic sections from the Lower Cambrian of the Mackenzie Mountains, northwestern Canada: Geological Survey of Canada Paper 77-33, 19 p.

Fritz, W.H., 1979, Eleven stratigraphic sections from the Lower Cambrian of the Mackenzie Mountains, northwestern Canada: Geological Survey of Canada Paper 78-23, 19 p.

Gabrielse, H., Blusson, S.L., and Roddick, J.A., 1973, Geology of the Flat River, Glacier Lake, and Wrigley map-areas, District of Mackenzie and the Yukon Territory (95E,L,M): Geological Survey of Canada Memoir 366, 153 p.

Goodfellow, W.D., 2007, Base metal metallogeny of the Selwyn Basin, Canada, *in* Goodfellow, W.D., ed., Mineral deposits of Canada: A synthesis of major deposit-types, district metallogeny, the evolution of geological provinces, and exploration methods: Geological Association of Canada, Mineral Deposits Division, Special Publication no. 5, p. 553-579.

Kamber, B.S., Greig, A., Collerson, K.D., 2005, A new estimate for the composition of weathered young upper continental crust from alluvial sediments, Queensland, Australia: Geochimica et Cosmochimica Acta, v. 69, p. 1041-1058.

Mako, D.A., and Shanks, W.C., 1984, Stratiform sulfide and barite-fluorite mineralization of the Vulcan prospect, Northwest Territories: exhalation of basinal brines along a faulted continental margin: Canadian Journal of Earth Sciences, v. 21, p. 78-91.

Norford, B.S., and Orchard, M.J., 1985, Early Silurian age of rocks hosting lead-zinc mineralization at Howards Pass, Yukon Territory and District of Mackenzie; local biostratigraphy of Road River Formation and Earn Group: Geological Survey of Canada, Paper 83-18, 35 p.

Pigage, L.C., 2004, Bedrock geology compilation of the Anvil District, central Yukon: Yukon Geological Survey Bulletin 15, 118 p.

Pratt, B.R., 1988, An Ibexian (Early Ordovician) trilobite faunule from the type section of the Rabbitkettle Formation (southern Mackenzie Mountains, Northwest Territories: Canadian Journal of Earth Sciences, v. 25, p. 1595 – 1607.

Saltzman, M.R., 2005, Phosphorus, nitrogen, and the redox evolution of the Paleozoic oceans: Geology, v. 33, p. 573-576.

Saltzman, M.R., and Thomas, E., 2012, Carbon isotope stratigraphy, Chap 11, *in* Gradstein, F.M., Ogg, J.G., Schmitz, M.D., and Ogg, M.D., ed., The geologic time scale 2012: Elsevier, p. 207-232.

Turner, E.C., 2011, A lithostratigraphic transect through the Cambro-Ordovician Franklin Mountain Formation in NTS 96D (Carcajou Canyon) and 96E (Norman Wells), Northwest Territories: Geological Survey of Canada Open File 6994, 28 p.

In situ Sulphur Isotope Study of the Prairie Creek Deposit, Southern Mackenzie Mountains, Northwest Territories: Deciphering the Conundrum of Three Deposit Styles in One

B.E. Taylor
Geological Survey of Canada, 601 Booth Street,
Ottawa, ON, K1A 0E8
Bruce.Taylor@NRCan-RNCan.gc.ca

S. Paradis
Geological Survey of Canada, 9860 West Saanich Road, Sidney, BC

H. Falck
Northwest Territories Geoscience Office, Yellowknife, NT

B. Wing
Department of Earth and Planetary Sciences,
McGill University, Montreal, QC

Abstract

The Prairie Creek district in the southern MacKenzie Mountains (Northwest Territories) includes base metal sulphide occurrences of three different styles: Mississippi Valley-type (MVT), stratabound replacement sulphide, and quartz-carbonate-sulphide veins. The Prairie Creek Zn-Pb-Ag deposit, itself, is comprised of two of these styles of mineralization, quartz-carbonate-sulphide veins and stratabound replacement base metal lenses. Discerning the relationship, if any, between these styles of mineralization may help develop exploration strategies. Sulphur isotope analyses are reported for 14 representative sulphide samples, including 12 of the stratabound replacement style, 1 vein sample, and 1 sample from an MVT occurrence, and compared to previously reported data, to characterize the isotopic compositions and states of equilibrium. We utilized a micro (in situ laser-assisted fluorination) high-spatial resolution analytical technique to document isotopic compositions of minerals within their textural context. The preliminary results of 214 individual analyses and the textural context of analyses in several selected samples are documented in this report. We hoped to uncover any connections between the three styles of mineralization, including their likely temperatures of formation and any isotopic gradients that would indicate paleo-hydrothermal flow.

Recommended citation

Taylor, B.E., Paradis, S., Falck, H., and Wing, B., 2015. In situ sulphur isotope study of the Prairie Creek deposit, southern Mackenzie Mountains, Northwest Territories: deciphering the conundrum of three deposit styles in one, *in* Paradis, S., ed., Targeted Geoscience Initiative 4: sediment-hosted Zn-Pb deposits: processes and implications for exploration; Geological Survey of Canada, Open File 7838, p. 96-133. doi:10.4095/296328

The overall range of $\delta^{34}S$ for stratabound replacement pyrite, sphalerite and galena was found to be large, ca. 16 ‰, but the distributions of $\delta^{34}S$ for pyrite and sphalerite are more restricted (1σ = 1.23 and 1.56 ‰, respectively), and less restricted for galena (1σ = 4.64 ‰). Analyses from an MVT sample from the Root River Formation, in which pyrite rims vugs in sparry dolomite, suggest that this style of mineralization may be unrelated to the stratabound replacement sulphides. The $\delta^{34}S$ of vein pyrite (from concentrate) corresponds rather well to pyrite from the stratabound replacement sulphides, and a similar relationship exists for galena. The similarity of sulphur isotope systematics for both veins and stratabound sulphides (including pyrite, sphalerite and galena) suggests a relationship between these two styles of mineralization, despite the fact that published Pb isotope investigations argue for separate origins (Paradis, 2007). The veins, or vein-related flow paths, may have acted as fluid conduits at various times, first as conduits for the fluids ($\delta^{34}S \approx 23$ ‰) that formed the stratabound lenses, and again at later time for the quartz-carbonate-sulphide veins. The presence of a principal vein, and its contained sulphide abundance, may constitute a guide for stratabound replacement sulphides at depth.

Isotopic variance on the millimetre-scale was such that average $\delta^{34}S$ values proved more practical for estimating temperatures of formation. However, isotopic disequilibrium was found to be common, and estimated isotopic temperatures are considered approximate at best. Our high-spatial resolution data suggest caution when interpreting sulphur isotope geothermometry in similar situations; whole-rock analysis may mask important variations. Estimates of formation temperatures for the stratabound bodies fell within the range of ca. 170-250°C. Veins appear to reflect similar, but perhaps a bit higher temperatures of formation. The principal stratabound sulphide lens (SD1) appears to record a variation in temperature, from higher values towards the centre and the main quartz-carbonate-sulphide vein, and cooler values towards the margins of the sulphide lens.

Introduction

The Prairie Creek deposit (61°33'11.6" N, 124°47'33.2" W; previously known as the Cadillac deposit), the largest carbonate-hosted Zn-Pb-Ag deposit in the southern Mackenzie Mountains, is situated in Silurian-Devonian carbonates on the edge of Mackenzie Platform, at the margin of the shale-dominated Selwyn Basin (Figure 1). Three styles of mineralization, classic Mississippi Valley-type (MVT), stratabound replacement sulphide (SRS), and quartz-carbonate-sulphide veins, characterize the Prairie Creek district. The latter two styles have been the focus of mineral exploration. The deposit currently contains 'measured plus indicated' resources of 3.7 Mt (vein-related) of 11.3% Zn, 12.4% Pb, 0.43% Cu and 202 g/t Ag and 1.281 Mt (stratabound) of 10.5% Zn, 6.1% Pb, and 65 g/t Ag (AMC Mining Consultants, Canada, 2012). Paradis (2007) provides a brief summary of exploration and mining history, from its first-mention in 1928 to 2007.

Paradis (2007) presented preliminary C, O, S, Sr, and Pb isotope data on samples from the contrasting mineralization styles in the Prairie Creek district, and suggested that SRS formed from bacterially-reduced seawater sulphate (BSR), as a replacement of carbonate units, along a basin margin, similar to interpretations of stratabound sulphide deposits in the Selwyn Basin, Yukon by Goodfellow and Lydon (2007). Vein sulphides were thought to be of a different origin, derived from basement fluids driven along deep faults (Paradis, 2007).

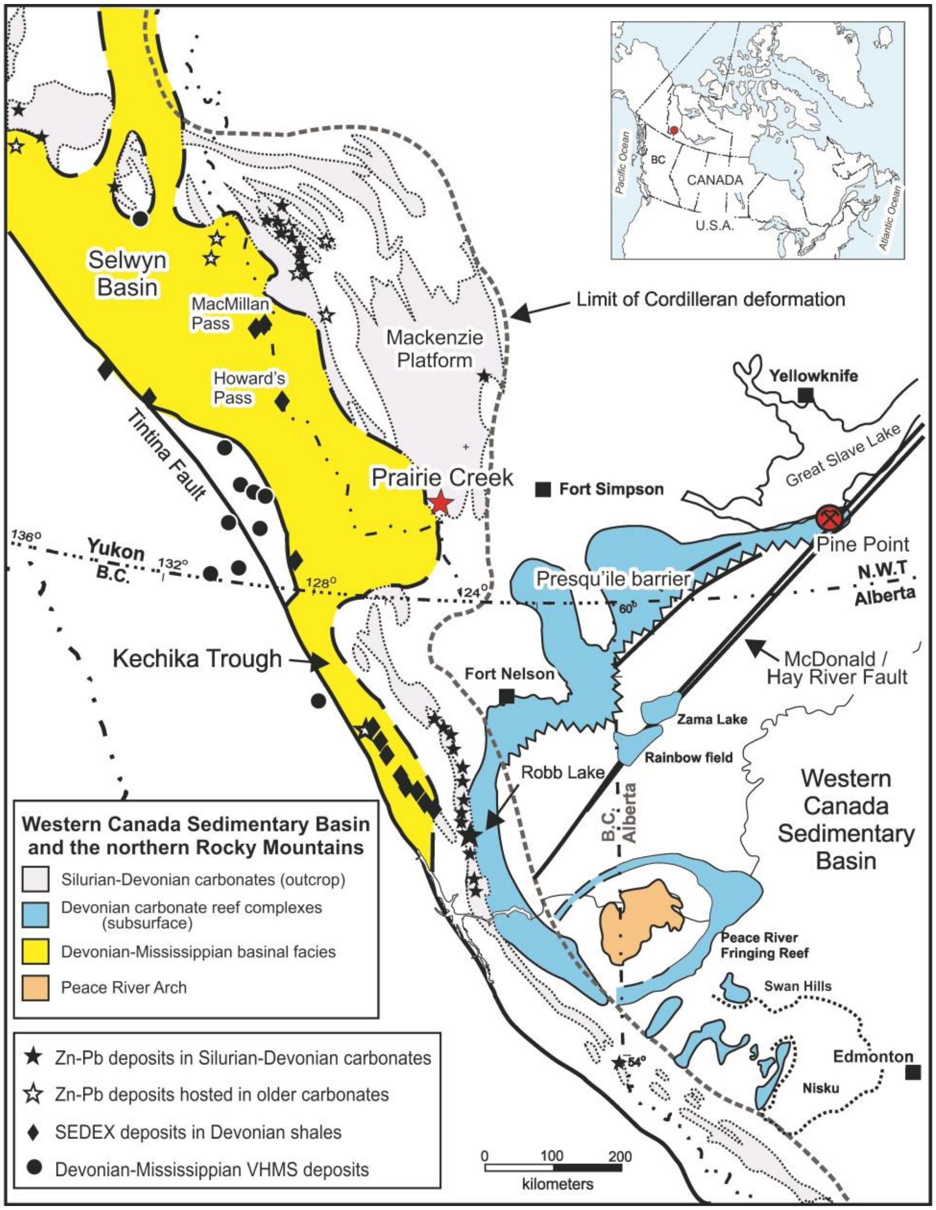

Figure 1. Regional map showing the location of the Prairie Creek deposit (red star), west of Fort Simpson, within the Mackenzie Mountains and carbonate rocks of the Mackenzie Platform (adapted from Paradis, 2007, and references therein). Note the association of deposit type with geologic terrane. Also shown is the location of the well-known Pine Point (MVT-style) deposit.

Geological Setting and Mineralization

Geological details of the Prairie Creek area are given by Morrow and Cook (1987), who sub-divided the Paleozoic strata into (bottom to top): 1) Sunblood Platform, 2) Mount Kindle-Root River Assemblage, 3) Prairie Creek Assemblage, and 4) Funeral-Headless Assemblage. The second subdivision, the Mount Kindle-Root River Assemblage is of principle relevance to the host strata of the Prairie Creek deposit. Paradis (2007, p.5) succinctly described the Assemblage as follows:

> "The Late Ordovician to Devonian Mount Kindle-Root River Assemblage consists of the Whittaker, Road River, and Root River formations. The Mount Kindle Formation, which is the shallow water reefal facies equivalent of the deeper water Whittaker Formation, is not present in the Prairie Creek area. Morrow and Cook (1987) divided the Whittaker Formation into three lithofacies: 1) a middle to upper Ordovician dark grey silty and sandy limestone (muOw1), 2) a middle to upper Ordovician fine-grained quartzite (muOw2), and 3) an upper Ordovician to Silurian laminated dark grey finely crystalline dolostone (OSw3), which hosts the stratabound sulphide mineralization at Prairie Creek. The lithofacies OSw3 has been subdivided into 7 subunits in the Prairie Creek deposit area by geologists of San Andreas Resources Corporation. The Silurian-Devonian Road River Formation comprises a sequence of graptolite-bearing shale and argillaceous bioclastic, shaly dolostone conformably overlying the Whittaker Formation. West of Prairie Creek, the Road River Formation thickens considerably in excess of 1000 m, and passes conformably upward into the Vera Formation. Eastward, in the Prairie Creek area, the Road River Formation thins to 170 m and is conformably overlain by the Cadillac and Root River formations. The Silurian Root River Formation is believed to be the shelf equivalent of the basinal facies of the Cadillac Formation. It consists of light grey, vuggy, micritic dolostone."

The history of structural deformation in the Prairie Creek district bears on the occurrence of both stratabound and vein style mineralization. In the area of the Prairie Creek deposit, north-south trending faults and fold axes have resulted in exposure of windows of Road River shale, cored by dolostones of the Upper Whittaker Formation, along the core of the Prairie Creek anticline. The anticline is doubly-plunging, with its axes plunging northward and southward from the mine site. The Prairie Creek anticline is structurally bounded to the east by the Prairie Creek Fault and to the west by the Gate Fault (Figure 2). These structures are presently north-south striking, west-dipping (65-90°) reverse faults that could have been originally normal faults (Earls, 1995; Fraser, 1996). The Prairie Creek Fault is a steeply dipping reverse fault with a thickness up to 40 m and a displacement of 1500 m (Morrow and Cook, 1987). Earls (1995) suggested that the Prairie Creek Fault might have initially been a west-side down, normal fault

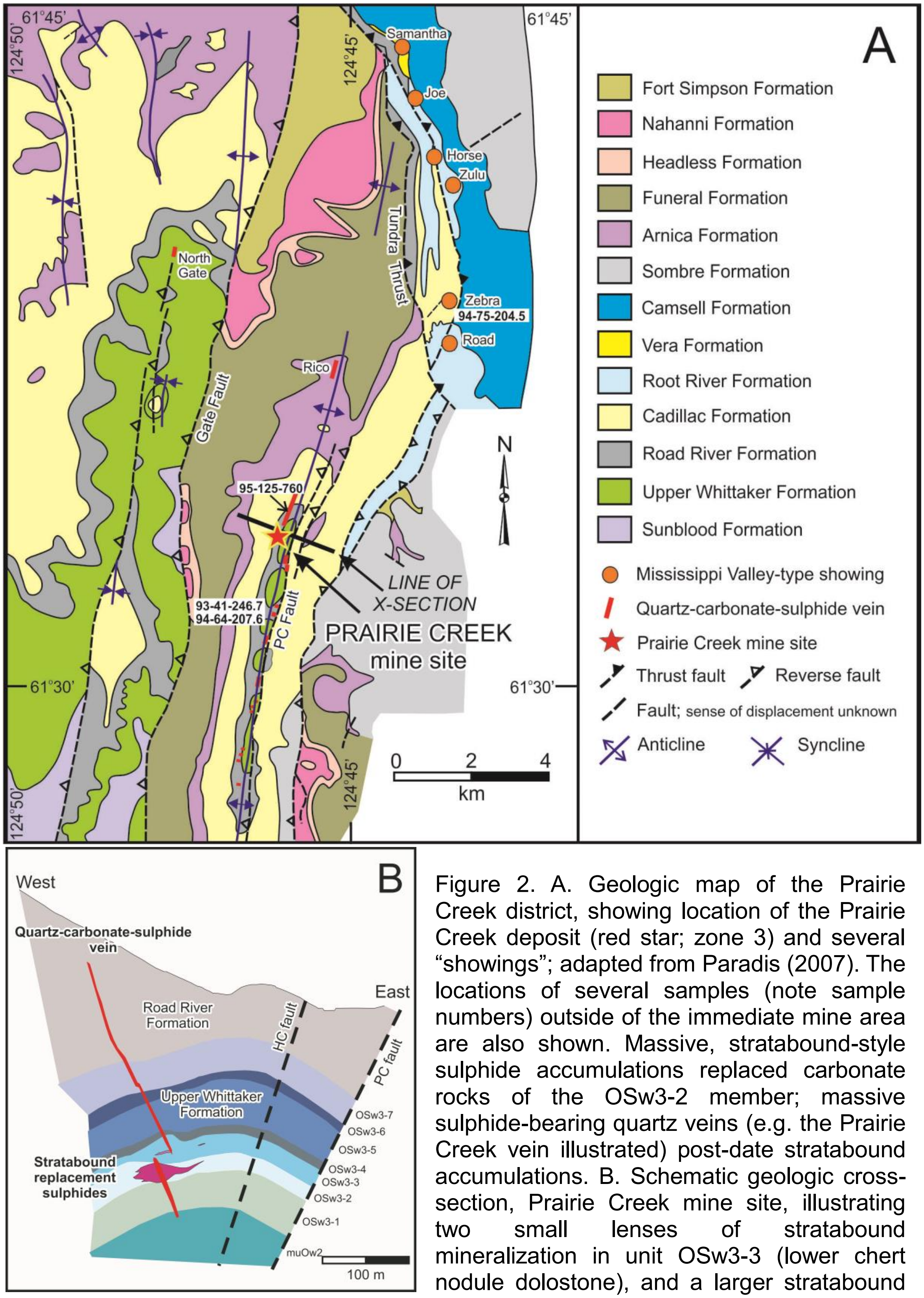

Figure 2. A. Geologic map of the Prairie Creek district, showing location of the Prairie Creek deposit (red star; zone 3) and several "showings"; adapted from Paradis (2007). The locations of several samples (note sample numbers) outside of the immediate mine area are also shown. Massive, stratabound-style sulphide accumulations replaced carbonate rocks of the OSw3-2 member; massive sulphide-bearing quartz veins (e.g. the Prairie Creek vein illustrated) post-date stratabound accumulations. B. Schematic geologic cross-section, Prairie Creek mine site, illustrating two small lenses of stratabound mineralization in unit OSw3-3 (lower chert nodule dolostone), and a larger stratabound lens in unit OSw3-2 (mottled dolostone) of the Upper Whittaker Formation; the section is located in A, above.

related to the formation of the Prairie Creek Embayment (see Morrow and Cook, 1987). Reactivation and reversal of movement would have occurred during the compressional event associated with the Laramide Orogeny.

Sulphide mineralization, as previously noted, occurs in the Prairie Creek district in three distinct styles: (1) SRS (likened to Irish type deposits: Earls, 1995; Findlay, 2000), which have replaced dolostone of the Upper Whittaker Formation; (2) quartz-carbonate-sulphide veins associated with the Prairie Creek fault, the fold axis of the Prairie Creek anticline, and other veins that cross-cut lower Paleozoic strata along 16 km of the exposed core of the Prairie Creek anticline; and (3) classic MVT sulphides that comprise open-space filling in vuggy shallow-water, shelf carbonates of the Silurian Root River Formation. Styles (1) and (2) have been the focus of mineral exploration.

Evidence of mineralization along some 16km of the north-south trending Prairie Creek fault, plus SRS up to 28m thick that occur discontinuously along a strike length of 3 km of the fault without surface expression, raise the need for exploration criteria. Understanding the origin(s) of the multi-faceted Prairie Creek deposit and various, broadly similar sulphide occurrences in the area, and their geologic controls, may provide essential knowledge for exploration. Are the three styles of sulphide occurrences related, i.e. are they textural/structural manifestations of the same mineralizing event, or do they have a distinct timing and origin? Initial sulphur isotope analyses reported by Paradis (2007) for samples of the vein, SRS, and MVT occurrences suggest that the MVT sulphides may be distinguished by having slightly lower δ^{34}S values (by ca. 8‰) relative to similar modes of analyses from the vein- and SRS. Strontium isotope ratios of calcite and dolomite from (14) samples of SRS, (3) samples of quartz-carbonate-sulphide veins, and (4) samples of MVT, in addition to (27) samples of host dolostone reported by Paradis (2007), exhibit a large range in values, and were noted to be markedly radiogenic. In particular, two samples of quartz-carbonate-sulphide veins plot at the upper end of the range, and have strontium isotope ratios as high as 0.7239 (Paradis, 2007).

The above observations suggest that mineralizing hydrothermal fluids were deeply sourced and had previously reacted with older crystalline rocks (Paradis, 2007). Lead isotope ratios, however, clearly distinguish sulphide minerals from vein and SRS mineralization on plots of ^{207}Pb/^{204}Pb or, ^{208}Pb/^{204}Pb vs. $^{206/204}$Pb. Stratabound replacement sulphides have ^{206}Pb/^{204}Pb and ^{207}Pb/^{204}Pb ratios that plot as an elongate group of data points primarily below the “shale curve” of Godwin and Sinclair (1982), but extending to intersect this growth curve at ca. 420 Ma. Paradis (2007) inferred a similar age for both the Prairie Creek SRS and the Devonian SEDEX deposits of the Selwyn basin. In contrast, the markedly different trend of Pb-isotope ratios for the quartz-carbonate-sulphide veins, which intersects the shale curve at ca. 250 Ma., i.e. about the Permian-Triassic transition, may indicate an age of formation different from that of the SRS

(Paradis, 2007). Without an absolute age determination, this possibility remains unproven, but if the quartz-carbonate-sulphide veins are younger than the SRS, then Pb-bearing fluids must have flowed through the vein-hosting structures at a later (post-replacement) time. In addition, the Prairie Creek fault, which is parallel in trend to the principal quartz-carbonate-sulphide vein (Figure 3), and perhaps other, vein-hosting faults, may have been re-activated during the Laramide Orogeny (Late Cretaceous; 70-80 Ma ago) as previously noted (see Morrow and Cook, 1987; Earls, 1995). In short, vein and SRS are not co-genetic. But, could they, nevertheless, be related?

Evidence necessary to better characterize the Prairie Creek deposit and determine its origin, state of sulphur isotope equilibrium and correct sulphide paragenesis, and possible paleo-thermal indicators of fluid flow, is locked within the sulphur isotope systematics of the sulphide minerals. We report on the sulphur isotope composition of sulphide minerals determined in their textural context by in situ methods. In situ, sulphur isotope analysis provides a unique means by which to address the unanswered question of whether multiple or single sources of sulphur (and/or fluids), or marked temperature contrasts were required to form the Prairie Creek deposit. Answers to these questions may provide a tool for regional exploration.

Sample Selection and Analytical Considerations

Fourteen samples were selected for the first phase of this study: 12 examples of SRS, and one example each of vein and MVT sulphides. Analytical work on an additional 28 samples is nearing completion. Sampled drillhole locations are shown in Figure 3. Samples are numbered with the drillhole number followed by drillhole depth (e.g. sample PC93-23-249.5 is from drillhole 93-23, and from a depth of 249.5 m. Sample descriptions, including sulphide mineral assemblages, for the 14 samples of phase I are presented in Appendix 1. Analytical work on an additional twenty eight samples is currently being completed that will extend the sample distribution throughout the Prairie Creek district.

In situ sulphur isotope analysis of mineral grains in polished, 1.0 mm-thick rock wafers, were carried out by laser-assisted fluorination, using MILES (Beaudoin and Taylor, 1994; Taylor and Beaudoin, 1993), as modified in Taylor (2004a; 2004b) at the Geological Survey of Canada, Ottawa. Sulphur isotope analyses were restricted to pyrite, sphalerite and galena, emphasizing high spatial resolution in order to permit analysis of adjacent grains, or intra-grain zoning. The sample chamber was often loaded with more than one sample, plus a chip of the laboratory internal standard (sphalerite from Broken Hill, Australia). Cooling the sample chamber and samples to ca. -100° to -60°C minimized the possibility of cross-contamination. The fluorinating agent employed was purified F_2 at low pressure, produced following the method of Asprey (1976; see Taylor, 2004b). The resultant micro-gas samples of SF_6 (typically ca. 0.1-0.3 μmoles; micromoles) were purified cryogenically (variable temperature trap: Taylor, 2004b) and sealed in 6 mm pyrex tubes for subsequent analysis for $\delta^{32}S$ and

δ^{34}S in a Thermo MAT 252 Isotope Ratio Mass Spectrometer (IRMS; Geological Survey of Canada, Ottawa), or for δ^{32}S, δ^{33}S, δ^{34}S and δ^{36}S in a Thermo-Electron MAT 253 IRMS, Department of Earth and Planetary Science, McGill University, Montreal. Further sample purification via gas chromatography was carried out on selected samples at McGill University prior to mass spectrometry.

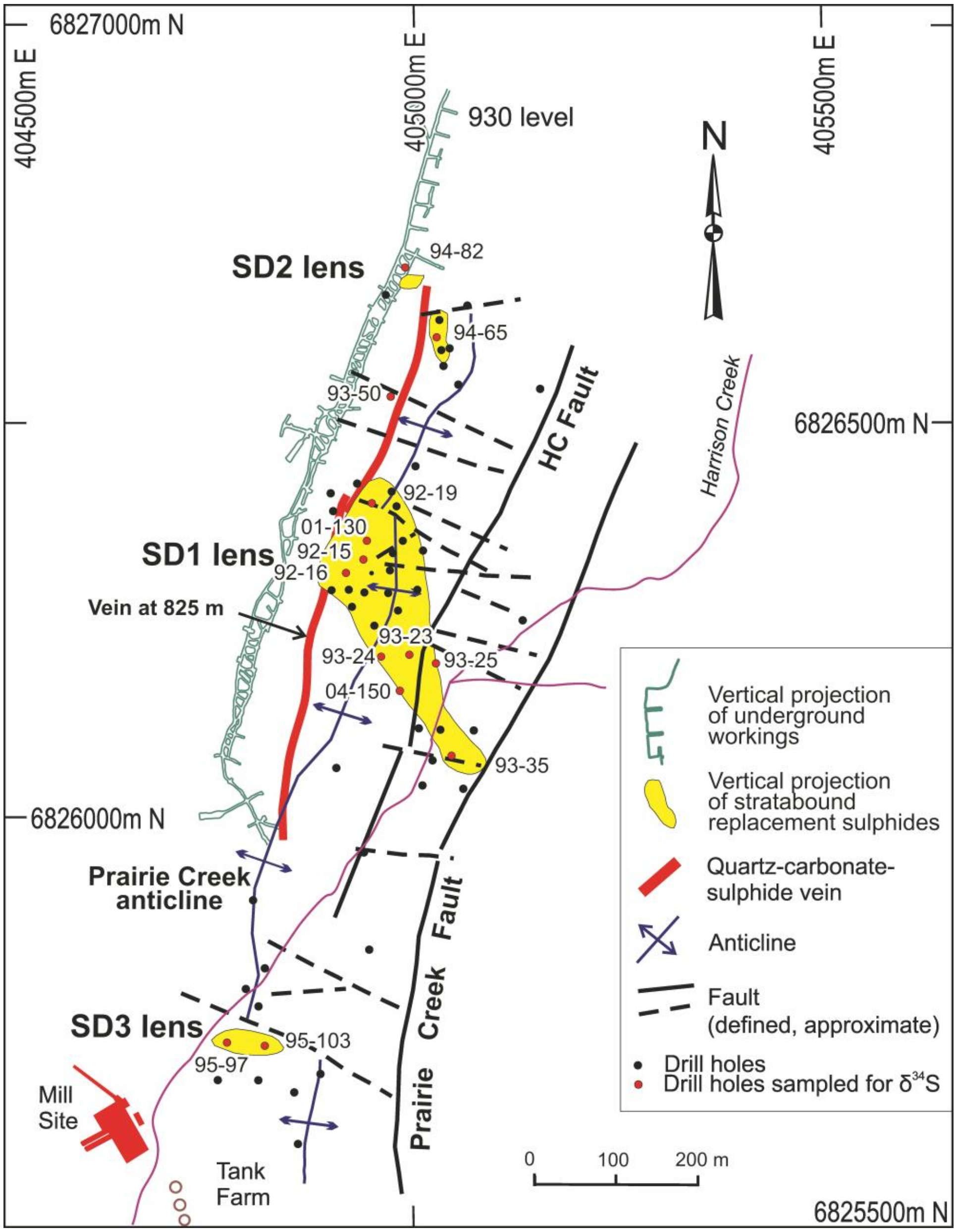

Figure 3. Map of the vicinity of the Prairie Creek minesite, showing vertical projections of stratabound sulphide occurrences, faults, fold axes, selected mine infrastructure, and the locations and identification numbers (e.g. 93-35) of sampled drillholes (see Appendices 1 and 2).

Gas chromatographic (GC) processing was found to be essential only for the accuracy of $\delta^{36}S$, since contamination of the ion beams by fluorocarbons is greatest at mass 131 SF_5^+; occasional exceptions do occur, however. The effect of beam contamination at mass 131 for samples not additionally purified via gas chromatography is very apparent from the variability and magnitude of results (in particular, $\delta^{36}S$). For in situ sampling, in particular (as opposed to grain samples of 1-3 mg), purification by gas chromatography should be routinely included as a 'best practice', for assurance.

Results/Data Analysis

The isotopic compositions of 214 in situ S-isotope analyses ($\delta^{34}S$, primarily, with some data for $\delta^{33}S$ and $\delta^{36}S$) of individual grains and/or analytical traverses within individual grains of pyrite, sphalerite, and galena are listed in Appendix 1. From 5 to 37 individual analyses were determined in each thin-section-sized polished wafer from examples of MVT, vein and SRS. Isotopic compositions are reported in the usual δ-notation ($\delta^{33}S$, $\delta^{34}S$, and $\delta^{36}S$), in per mil (‰) relative to V-CDT. Typical uncertainties are ≤0.2 per mil (2σ) for these in situ analyses, based on replicate in situ analyses of pure sphalerite from Broken Hill, Australia. Larger analytical uncertainties of in situ analyses of minerals can sometimes result using multi-mineral wafers due to reaction with other, unseen minerals beneath the sample surface, or reaction with adjacent minerals (although the reaction volume is minimized by use of a cold stage; Taylor, 2004a,b). The SF_6 gas samples produced in the process of in situ fluorination were on the order of 0.1 µmol, and were analyzed using a micro-volume inlet. Gas handling and potential variations in composition between aliquots of the reference gas during various analytical sessions at McGill University may have contributed additional uncertainty factors.

In Appendix 1, we report, in addition to $\delta^{33}S$, $\delta^{34}S$, and $\delta^{36}S$, values for $\delta^{33}S$ and $\delta^{36}S$, where, for example, $\delta^{33}S \equiv \delta^{33}S_{measured} - [(\delta^{34}S_{measured}/1000+1)^{0.515}-1] \times 1000$. The value of $\delta^{33}S$ provides a measure of deviation from the usual equilibrium mass-dependent fractionation, where $\delta^{33}S$ and $\delta^{34}S$ are related by a factor of 0.515. Marked deviations from this relationship, or '$\delta^{33}S$ anomalies', are typically ascribed to non-equilibrium, mass-independent fractionation (MIF) processes involving SO_2 in the Archean atmosphere, and primarily associated with Archean rocks older than ca. 2.2 Ga (e.g. Farquhar et al., 2010). Anomalous $\delta^{33}S$ values were not anticipated in this study, due to the age of the Prairie Creek deposit and host rocks; we focused on $\delta^{34}S$. However, all four sulphur isotopes were measured as a matter of course due to the arrangement of collectors in the Thermo-Electron MAT253 IRMS. We noted that several samples did deviate from the 0.515 linear relationship expected for mass-dependent sulphur isotope equilibrium, likely due to analytical issues rather than variance in S-source. Samples not GC-processed prior to mass spectrometry can be susceptible to errors in $\delta^{33}S$ and $\delta^{36}S$. The web-based stable isotope fractionation calculation tool of Beaudoin and Therrien (2004) facilitated ready calculation and comparison of the isotopic equilibration temperatures discussed in report.

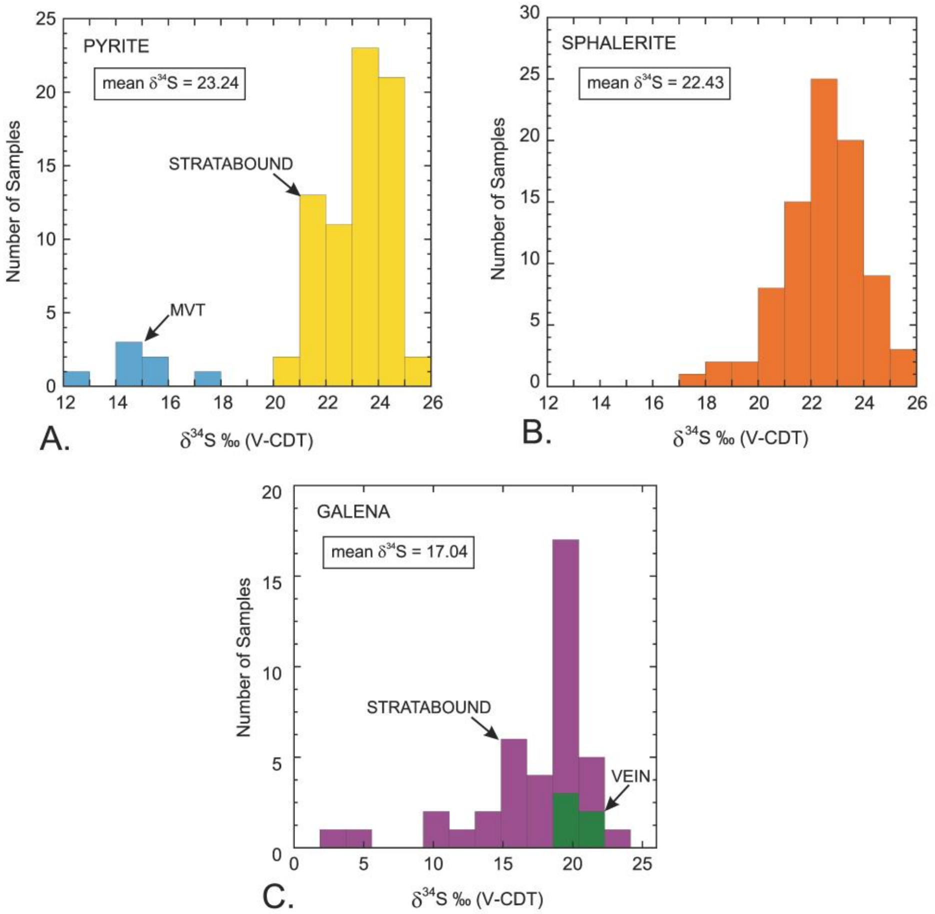

Figure 4. A. Histogram of in situ sulphur isotope analyses of pyrite illustrating a distinct population for the one sample of MVT sulphide occurrence analysed ($\delta^{34}S$ = ca. 14.7-17.1‰) from the Root River Formation. B. Histogram of results from in situ analysis of sulphur isotopes in sphalerite. A single population characterizes both stratabound and quartz-vein styles of sulphide occurrence; most analyses fall within a range of ca. 21-25‰. C. Histogram of in situ sulphur isotope analyses of galena. Two values for sample PC95-97-79.1 (stratabound sulphide in the OSw3-2 member) are strikingly anomalous. Similar to the data distributions for pyrite and sphalerite, a marked dominance occurs for one isotopic composition.

Histograms of $\delta^{34}S$ values for pyrite, sphalerite and galena from all in situ analyses are plotted and compared in Figure 4. The data for SRS dominate each of the histograms, whereas the ranges of $\delta^{34}S$ for each sulphide mineral are influenced by analyses from the MVT and vein samples. The ranges of $\delta^{34}S$ for SRS pyrite, sphalerite and galena were found to be large, up to ca. 16‰, whereas, the distributions of $\delta^{34}S$ for pyrite and sphalerite are rather restricted (σ =1.3 and 1.4‰, respectively), and less restricted for galena (σ = 4.5‰). Distributions for pyrite and galena (Figure 4) suggest two populations, although, in each case, the isotopically lighter results represent a single sample: pyrite ($\delta^{34}S$ = 14.7 – 17.1‰; PC94-75-204.5) in a sample from the Root River Formation, in which pyrite rims vugs in sparry dolomite and galena ($\delta^{34}S$ = 3.1

and 4.0‰; PC95-97-79.1) from the edge of massive sulphide in the Upper Whittaker Formation (Figure 3). Removal of data for these samples from the population in order to consider only stratabound occurrences, resulted only in a slight change in the mean value of $\delta^{34}S$ for sphalerite and galena of ca. 0.1 and 0.5‰, respectively.

The results of sulphur isotope analysis by oxidation to SO_2 of mineral concentrates from hand samples from the Prairie Creek district reported by Paradis (2007) differ in some respects from in situ analyses by fluorination reported here. The mean per mil fractionations (Δ) between pyrite and sphalerite and between sphalerite and galena for SRS ($\Delta_{\text{pyrite-sphalerite}}$: -2.08, and $\Delta_{\text{sphalerite-galena}}$: 1.64; Paradis, 2007) differ from those values reported here ($\Delta_{\text{pyrite-sphalerite}}$: 0.82, $\Delta_{\text{sphalerite-galena}}$: 5.09), and similarly for veins and MVT occurrences (although the data base of in situ analyses is small). Notably, the mean stratabound $\Delta_{\text{py-sp}}$; value reported by Paradis (2007) indicates a marked state of disequilibrium (i.e. it is a negative rather than a positive value). The reasons for this discrepancy require further investigation; isotopic variations on both local and district-wide scales may be involved. The nature of isotopic variation at the grain-to-grain scale is described below for several examples from the in situ analyses acquired in the present study.

The documentation of the textural environments of all in situ analyses carried out in this study requires more space than is practical for this report. All analyses are documented, however, in a separate Geological Survey of Canada Open File report (Taylor et al., in preparation); results and documentation of analyses in selected samples presented below provide examples of the textural-isotopic relationships encountered, as well as the apparent states of isotopic equilibrium (and implied paleo-temperature information) preserved. Traditional application of per mil isotopic fractionations between minerals for the estimation of temperatures of equilibration had often sought agreement for temperatures between three (or more) coexisting minerals. Multi-mineral isotopic equilibrium may not often be achieved in situations (e.g. as noted below) where hydrothermal replacement has occurred. Unfortunately, in the absence of agreement between three minerals constituting two co-existing pairs, the only guide to the accuracy of an isotopic temperature based on just one mineral pair is whether the result is ‘geologically reasonable’. Agreement with other examples from the same setting provides some assurance, if not confirmation. For the sake of consistency, we make use of the sulphur isotope fractionations determined by Kajiwara and Krouse (1971) to estimate the temperatures of formation of sulphide minerals in this study; comparison with several other fractionations determined by others for some of the mineral pairs suggest that those of Kajiwara and Krouse (1971) are sufficiently accurate for our purposes as we search for thermal gradients and compare the styles of mineralization in the Prairie Creek district.

The variation of values of $\delta^{34}S$ for individual, in situ analyses shown in Figures 5 to 11, suggests isotopic disequilibrium on a small scale, and raises several questions when calculating isotopic equilibration temperatures. Which point analyses should be used to construct an 'equilibrium mineral pair', or triplet (if possible)? Is it more prudent to calculate the average value in a sample for each mineral? The answers are not always straightforward. Here, we recognize the common state disequilibrium on the one hand, and attempt to make a 'best estimate' of equilibration temperature on the other hand, acknowledging that this estimate may have some uncertainty attached. The sample average and pair-wise per mil fractionations reported in Appendix 2 emphasize the difficulties at hand.

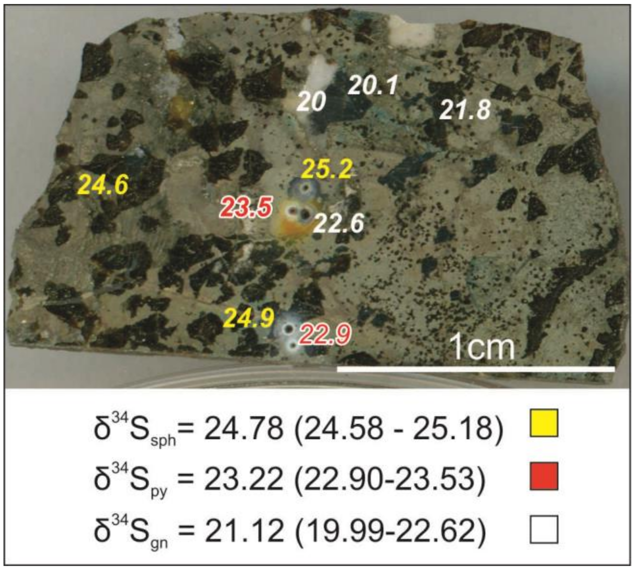

Figure 5. Photograph of sample PC93-23-249.7, an example of stratabound replacement sulphides from the Prairie Creek mine site, showing results of laser-assisted, in situ sulphur isotope analyses (colour coded as follows: yellow - sphalerite; red - pyrite; and white - galena), with sample averages and ranges for each mineral.

Stratabound Replacement Sulphides (SRS)

Sample **PC93-23-249.7** (Figure 5) of SRS shows idiomorphic sphalerite grains (ca. 20%) imbedded within fine-grained pyrite aggregate (ca. 50%). Several grains of galena (ca. 5%) and ca. 1% remnant dolostone (now coarse white spar calcite) and 3% chert are randomly distributed in this mottled dolostone member (OSw3-2) of the Whittaker Formation. Galena appears to have crystallized last, infilling remaining space. The relative isotopic compositions of pyrite and sphalerite are reversed from those expected for equilibrium, i.e. per mil fractionations between pyrite and sphalerite are negative (Appendix 2). This signifies isotopic disequilibrium, in contrast to the apparent textural equilibrium between the two minerals. Sphalerite evidently replaced pyrite without reaching isotopic equilibrium with its host. Similarly, the average pyrite-galena per mil fractionation (3.47‰) suggests an unreasonable average temperature of 317°C, likely due to the somewhat later crystallization of galena. Similarly, the per mil fractionation (0.91‰) between adjacent pyrite and galena grains (23.5 and

22.6‰, respectively) indicates a marked state of disequilibrium (T = 826°C, based on Kajiwara and Krouse, 1971). Yet, the similarity of compositions (20.1 and 20.0‰) measured in the same grain of galena (Figure 5) suggests that the other values of $\delta^{34}S$ noted elsewhere in the same sample (20.0 to 22.6‰) are likely valid. In situ measurements of separate grains of sphalerite and galena yield an average per mil fractionation of 3.66‰, consistent with a 'geologically reasonable' formation temperature of 220°C (Appendix 2).

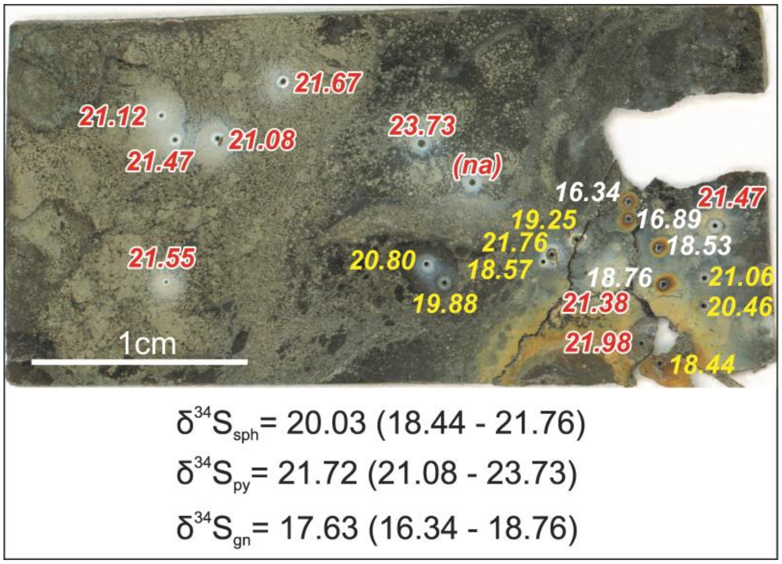

$$\delta^{34}S_{sph} = 20.03\ (18.44 - 21.76)$$

$$\delta^{34}S_{py} = 21.72\ (21.08 - 23.73)$$

$$\delta^{34}S_{gn} = 17.63\ (16.34 - 18.76)$$

Figure 6. Photograph of sample PC92-19-289.5, an example of stratabound replacement sulphides from the Prairie Creek mine site, showing results of laser-assisted, in situ sulphur isotope analyses (color coded as in Figure 5), with sample averages and ranges for each mineral. In contrast to the relatively homogeneous isotopic composition of pyrite across the sample, galena and sphalerite are more diverse (see text for discussion).

Sample **PC92-19-289.5** (Figure 6) of SRS in OSw3-3 (Whittaker Formation) illustrates the textural diversity of pyrite, dominated by very fine-grained pyrite that has seemingly amalgamated to ill-defined areas of coarser, recrystallized pyrite. For the most part, the pyrite is relatively homogeneous in grain to grain sulphur isotope composition (21.1-22.0‰, with one anomalous result of 23.7‰; Figure 6). In contrast, sphalerite is more variable in $\delta^{34}S$ (18.6 to 21.1) on the mm-scale. Galena sulphur isotope compositions comprise two distinct groups (16.3-16.9‰ and 18.5-18.8‰) suggesting 'steps' or rapid gradations in isotopic composition across the sample. The sphalerite-galena temperature of 210°C represents an average of a range of 138 to 416°C. Figure 6 illustrates the difficulty in selecting which data points to associate for purpose of geothermometry; an average is perhaps the prudent approach in this case. The pyrite-galena fractionation suggesting a temperature of 239°C (Appendix 2) may seem reasonable on the surface, but the fractionation of 1.72 and estimated temperature of 148°C for pyrite-sphalerite call into question the results for pyrite-galena, and suggest that the similarity of pyrite-galena and sphalerite-galena temperatures is a matter of coincidence rather than fact. From a textural perspective, sphalerite and galena appear in this sample (and others) to replace pyrite. In this case, attainment of isotopic equilibrium requires a multi-step process: dissolution, mixing, and precipitation. In addition, sphalerite replaced host dolostone, and sparry dolomite often occurs at the interface between dolostone and sphalerite during the mineralization process. We suggest that the sphalerite-galena temperature of 210°C is a reasonable estimate.

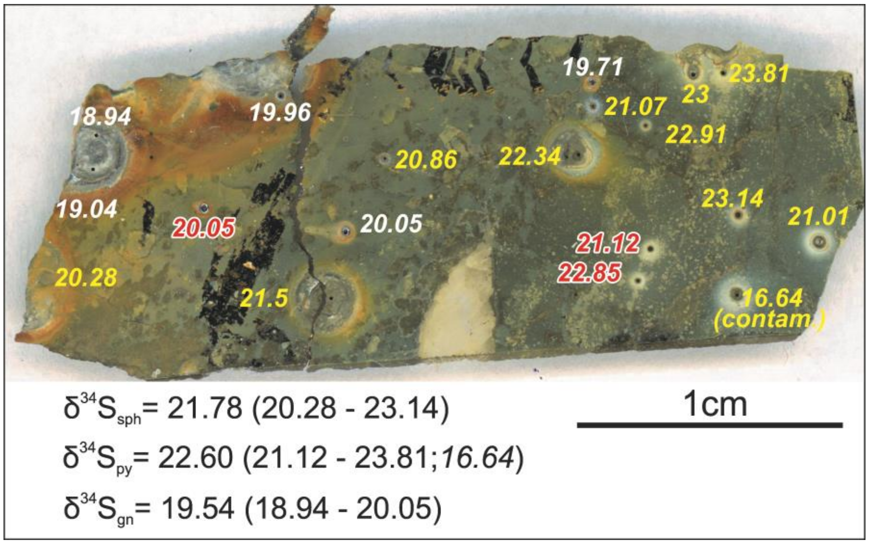

Figure 7. Photograph of sample PC94-64-207.6, an example of stratabound replacement sulphides from Zone 6, south of the Prairie Creek mine site (see Figure 2). Results for in situ analyses for sphalerite (yellow) and pyrite (red) suggest the presence of an isotopically enriched zone in the right hand half of the sample (see discussion in text).

Sample **PC94-64-207.6** (Figure 7) is representative of SRS in SD4 located in Zone 6, south of the Prairie Creek minesite (see Figure 2) in the upper spar unit, OSw3-6, of the Whittaker Formation. In situ analyses suggest compositional zoning on the millimetre-scale, with a band of higher $\delta^{34}S$ values found for sphalerite and pyrite in the right half of the sample, from the right of the carbonate filled vug. Per mil fractionations between bulk average compositions for pyrite, sphalerite and galena (Appendix 2) suggest broadly similar temperatures of 228°C (pyrite-sphalerite), 316°C (pyrite-galena) and 258°C (sphalerite-galena), excluding disequilibrium data. The individual pairing of data points does not always lead to a similar outcome in temperature, as the 'ne' (non-equilibrium) designation in Appendix 2 indicates. In the upper, central portion of the sample, however, nearest neighbour analyses of galena (19.7‰), and pyrite (22.3 and 22.9‰) yield temperatures of 281°C and 226°C; although pairing with the pyrite value of 21.1‰ (closest to the analyzed galena grain) yields an unrealistic temperature of 482°C. Thus, the fine-scale (µm to mm) inhomogeneity of sulphur isotope compositions in this sample, complicates the estimation of formation temperatures.

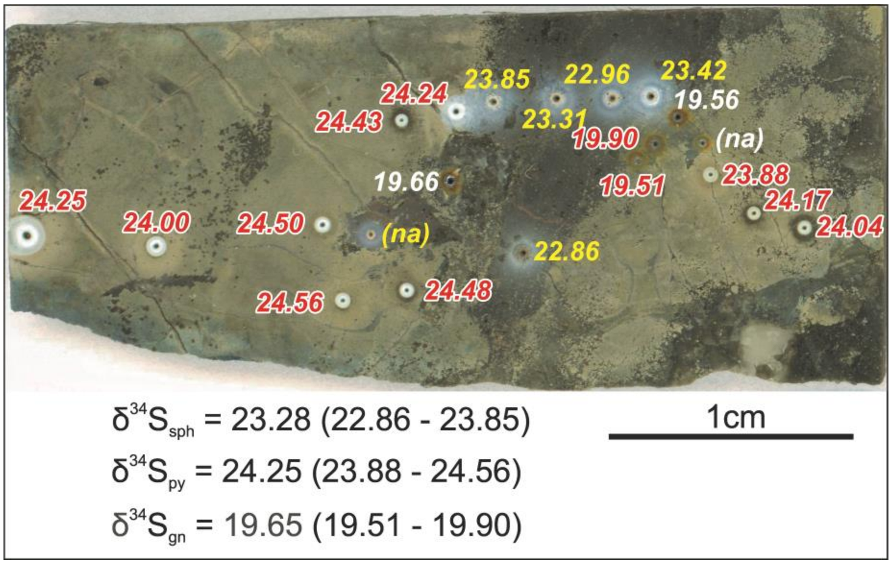

Figure 8. Photograph of sample PC93-25-251.9, an example of well-mineralized stratabound replacement sulphides in the OSw3-2 member of the Whittaker Formation (see Figure 2), from the outer margin of main sulphide body (see Figure 3). Results and locations of laser-assisted, in situ sulphur isotope analyses (colour code and abbreviations as in Figure 5) are shown, as well as sample averages and ranges for each mineral. Pyrite appears (ca. 60%) to form masses amalgamated from very-fine grained pyrite, consistent with its isotopic homogeneity across the sample. Sphalerite appears to increase in δ^{34}S as pyrite is approached, consistent with the replacement of pyrite by sphalerite (and, possibly later, galena). In addition to pyrite, the massive sulphide in this interval contains ca. 25% sph, 15% gal, 15% chert, 2% calcite, 2% quartz, and 2% white/gray dolomite.

Sample **PC93-25-251.9** (Figure 8) of SRS is from near the margin of the SD1 massive sulphide lens in OSw3-2 at the mine site (see Fig. 3). This sample represents a well-mineralized interval with 25% sphalerite and 15% galena, with accessory chert (15%), calcite (2%), quartz (2%), and white/gray dolomite (2%). Coarse sparry calcite (void fillings, or fragments?) is completely surrounded by galena. The homogeneous, nearly massive pyrite texture is matched by marked isotopic homogeneity (relative to some other samples), with a total apparent variation of ca. 1.0‰. Per mil fractionations between bulk average compositions for pyrite, sphalerite and galena (Appendix 2) suggest broadly similar temperatures of 282°C (pyrite-sphalerite), 216°C (pyrite-galena) and 164°C (sphalerite-galena). As with some other samples, the sphalerite-galena temperature can be the lowest of the three. In this case, its association with the outer limits of the sulphide body (see Figure 3) may have some significance.

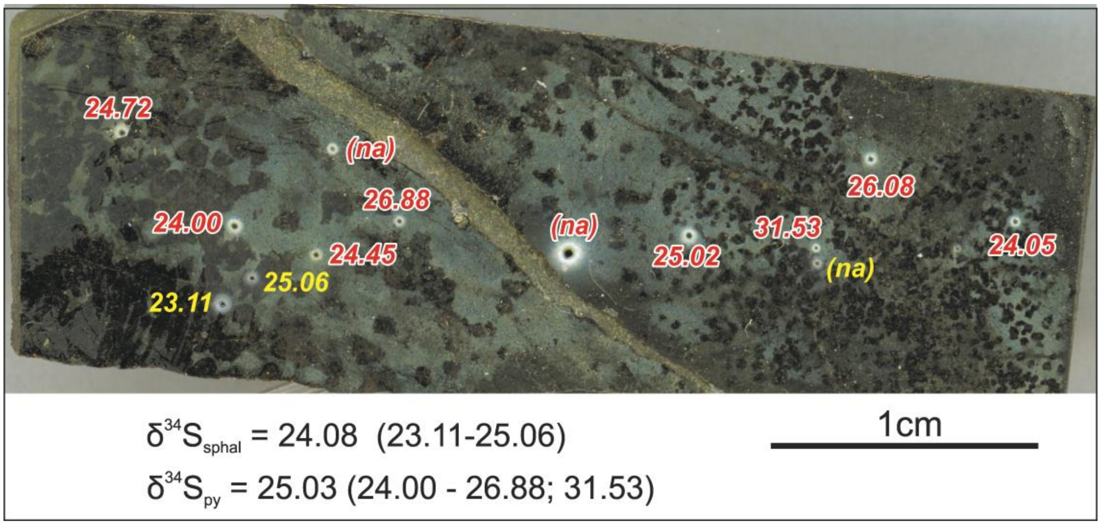

$\delta^{34}S_{sphal}$ = 24.08 (23.11-25.06)

$\delta^{34}S_{py}$ = 25.03 (24.00 - 26.88; 31.53)

Figure 9. Photograph of sample PC01-130-313.5, an example of stratabound replacement sulphides from near the central region of the main sulphide lens SD1, Prairie Creek mine site (see Figure 3). Results and locations of laser-assisted, in situ sulphur isotope analyses (colour code and abbreviations as in Figure 5) are shown, as well as sample averages and ranges for each mineral. A pyrite matrix supports idiomorphic sphalerite; $\delta^{34}S$ of pyrite appears to increase from left to right, in concert with a decrease in grain size in sphalerite. The pyrite is quite homogeneous in isotopic composition, whereas isotopic variation in sphalerite may reflect replacement of pyrite by sphalerite (see discussion in text; value of 31.5 is anomalous and not considered).

Sample **PC01-130-313.5** (Figure 9) is from the SRS replacing the mottled dolostone member of the upper Whittaker Formation (OSw3-2). The sample shows idiomorphic pinkish sphalerite of variable size (size decreases left to right) enclosed within matrix pyrite. Minor galena and calcite fill remaining space in parts of the sample (not shown, nor analyzed). Sulphur isotope data for pyrite imply a slight enrichment in ^{34}S in the right half of the specimen. Only two analyses of sphalerite are available; the two per mil difference is marked considering their close proximity. Per mil fractionations between bulk average compositions for pyrite and sphalerite (Appendix 2) suggest a temperature of 165°C. This is lower than in other samples.

Mississippi Valley-type (MVT) Sulphides

Sample **PC94-75-204.5** (Figure 10) is from the MVT “Zebra showing” in the Root River Formation. It consists of cavities that are filled by sparry dolomite and are rimmed by pyrite. Marked sulphur isotope variation characterizes the pyrite in this sample, grading from 14.7 to 17.1‰ as the vug-filling sparry dolomite is approached. Since an increase in $\delta^{34}S$, from 14.7‰ in the core to 15.9‰ at the rim can also be documented in one grain, we surmise that the 14.7 to 17.1‰ variation represents an increase in $\delta^{34}S$ in time, and may signify the ‘reservoir effect’ of a smaller ‘pool’ of sulphur (i.e. more nearly closed system) than evident for the formation of the SRS.

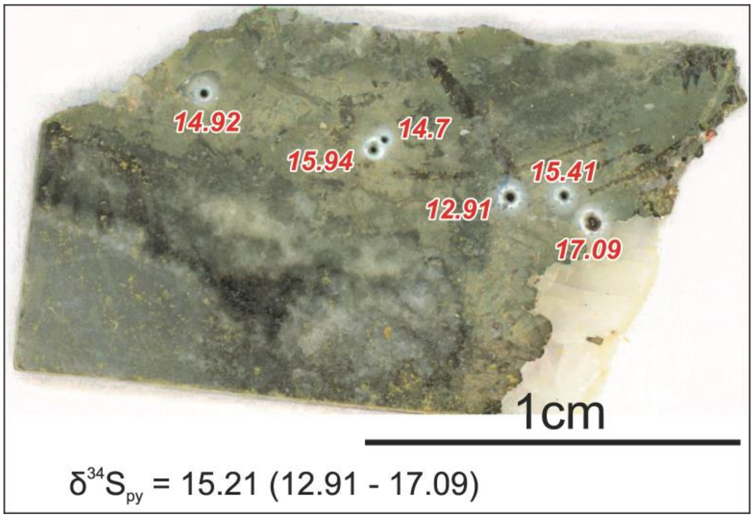

Figure 10. Photograph of sample PC94-75-204.5, an example of MVT-style sulphide mineralization from the Root River Formation. Marked sulphur isotope variation (see discussion in text) is consistent with a limited sulphur source (reservoir effect), or multiple sources of sulphur during formation (see text for discussion). The markedly lower sulphur isotope composition of pyrite in this sample relative to other, non-MVT style occurrences in the Prairie Creek district suggests a distinct origin.

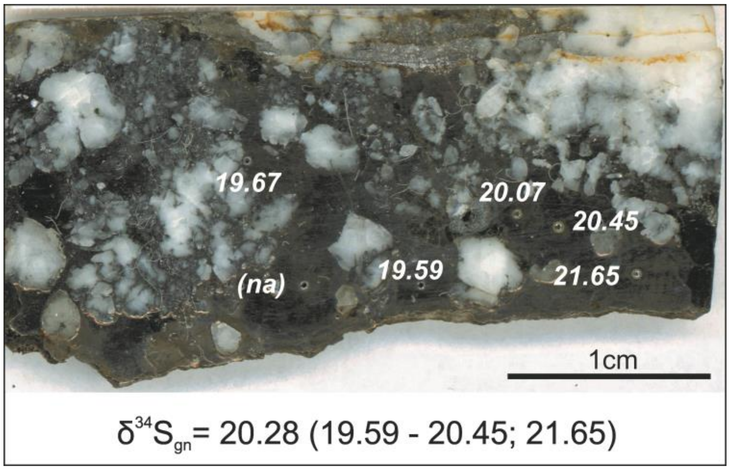

Figure 11. Photograph of sample PC95-125-760, an example of vein-style sulphide occurrence north of the Prairie Creek mine site (see Figure 2). The brecciated texture and stylolite-like contacts between some quartz grains suggests episodic vein filling and fault movement, followed by final annealing of groundmass galena. The sulphur isotope composition of galena suggests a gradient of increasing $\delta^{34}S$, left to right.

Quartz-carbonate-sulphide veins

Sample **PC95-125-760** (Figure 11) is from a quartz-carbonate-sulphide vein cross-cutting the Road River Formation north of the Prairie Creek mine site (see Figure 2A). It contains quartz, galena, occasional sphalerite, tetrahedrite-tennantite, and fragments (and/or void fillings) of calcite. The sample appears to have been brecciated, with quartz clasts ‘suspended’ in annealed galena matrix. Note the stylolite-like contacts between some quartz grains. In situ analyses of galena appear to document a sulphur isotope gradient in δ^{34}S, increasing from left to right. The orientation and global significance is not clear from this sample alone, but might be anticipated if vein-filling occurred over more than one episode, perhaps involving multiple fault movements and vein brecciation.

Discussion/Models

The juxtaposition of subsurface SRS lenses with the occasional outcropping of quartz-carbonate-sulphide veins and MVT occurrences in the Prairie Creek district, NT, prompted this study. The objective was to understand the origins and interrelationships, if any, of these three styles of base-metal sulphide occurrences with the hope of deriving useful criteria or guides for exploration. The fine-grained and texturally complex nature of the sulphide-bearing specimens called for the application of laser-assisted, micro-analysis to determine the sulphur isotope compositions of the essential minerals.

The principal questions addressed in this study included: 1) to what extent are the SRS, vein-, and MVT-style sulphide occurrences related? 2) What attributes of the mineralization processes (e.g. temperature) are related to sulphide occurrence and/or metal grade? 3) Are there any diagnostic, or helpful, isotopic characteristics that would be of use in mineral exploration (e.g. suggestive of sulphide deposition controls)? 4) Is it possible to discern the paleo-hydrology of the mineralizing fluids? As with any high-resolution investigation, some questions were answered, and new questions were generated.

Three Styles of Mineralization: Related or Not?

The occurrence of base metal sulphides as MVT, SRS, and quartz-carbonate-sulphide veins, in the same or similar host rocks of the Prairie Creek district begs the question as to their relationship. Are the products of these three ‘styles’ of mineralization genetically related, directly or indirectly, or not? Although addressed previously by Paradis (2007), who considered the vein and SRS unrelated, we re-examine the possible relationships in the light of this study.

The histogram plot of strontium isotope ratios (^{87}Sr/^{86}Sr) shown in Figure 12A illustrates the similarity between the compositions of the host dolostone and the quartz-carbonate-sulphide veins and SRS lenses. Carbonates analyzed from the sulphide occurrences represent unreplaced dolostone and/or recrystallized carbonate, now in the form of dolomite and calcite (sometimes referred to as ‘hydrothermal carbonate’). The latter have the highest ^{87}Sr/^{86}Sr ratios in the Prairie Creek district (see Appendix 1; Paradis, 2007). A caveat, however, in the Sr isotope data is the unknown extent to which radioactive decay in clastic sedimentary components in the carbonate rocks may have modified the apparent initial ^{87}Sr/^{86}Sr ratios. This caveat, notwithstanding, the correspondence in isotope ratios of host dolostone and carbonate gangue associated with sulphides suggests control by the host lithology of the strontium isotope ratio balance

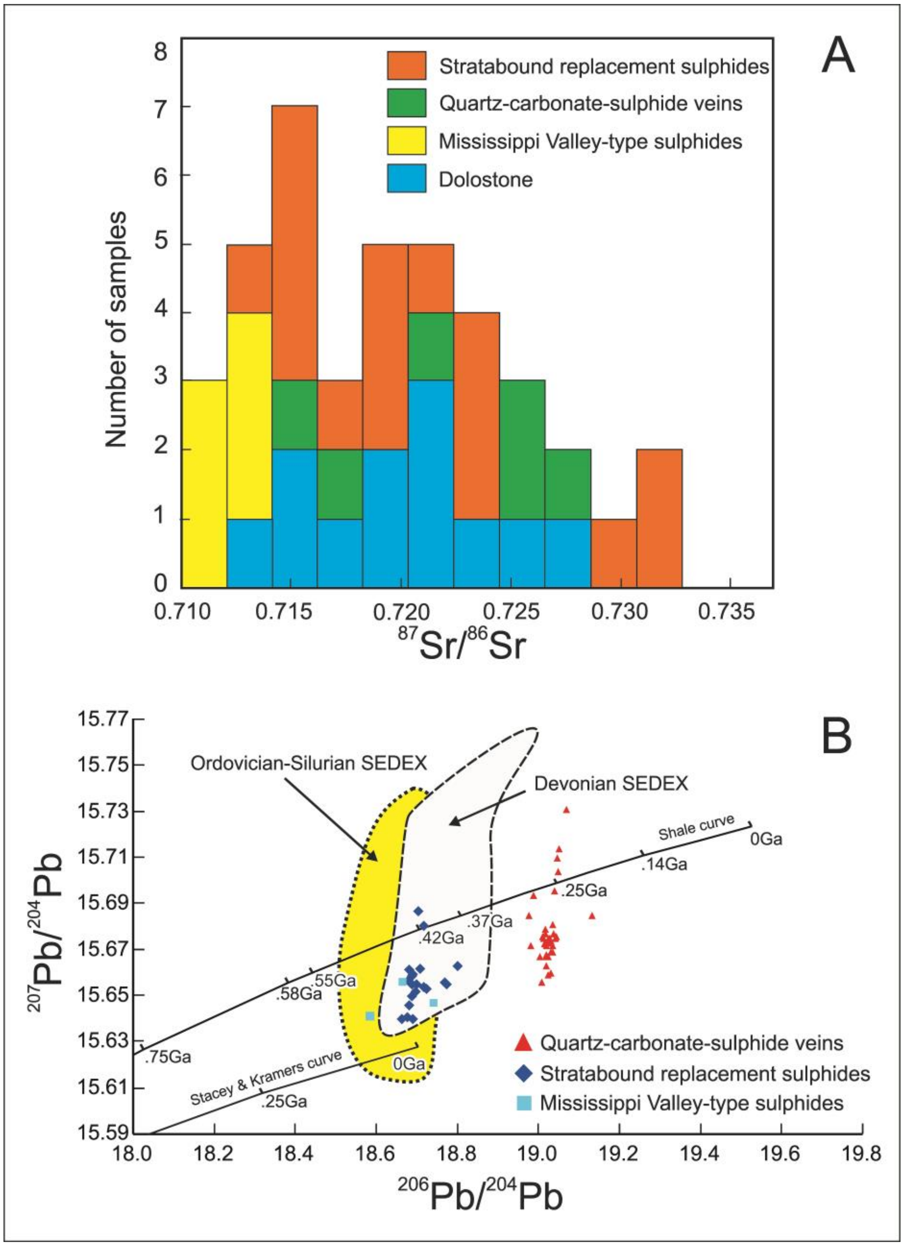

Figure 12A. Composite histogram of strontium isotope ratios measured on (primarily) carbonates from host dolostone and from stratabound, vein-type and MVT sulphide accumulations (data from Paradis, 2007, and references therein). The dolostone results represent those from the Upper Whittaker Formation, host to the vein and stratabound sulphides, whereas the MVT sulphides are hosted in the Root River Formation. The overlap in $^{78}Sr/^{86}Sr$ values indicates that the host-rocks control the strontium isotope abundances in the mineralized rocks. B. Plot of lead isotope ratios of Prairie Creek MVT, stratabound, and vein-style sulphide accumulations (Paradis, 2007). Whereas the stratabound and MVT types are of the same age, lead within the veins is consistent with a younger, perhaps Permian age, although the precise age is unknown. The "shale curve" is after Godwin and Sinclair (1982); the Stacey and Kramers terrestrial lead evolution curve is after Stacey and Kramers (1975).

during the mineralization process. Indeed, the MVT samples shown in Figure 12A are hosted within the Root River Formation, the latter of which yielded a low $^{87}Sr/^{86}Sr$ value of 0.7093 (see Figure 13C and p. 27 in Paradis, 2007), whereas vein- and stratabound sulphide samples hosted within the more radiogenic Upper Whittaker Formation yield higher values. Insofar as strontium isotopes are concerned as a tracer of fluid origins, the host rocks have, in each case, dominated the end result, masking any other possible source of strontium. In this respect, the veins and SRS may be said to share a common link. By virtue of different host rocks, the MVT sulphides do not share the same link.

In contrast to strontium isotopes, lead isotope ratios clearly distinguish the massive quartz-carbonate-sulphides from the SRS. In Figure 12B, the lead isotope ratios of sulphide minerals in vein occurrences plot on a trend suggesting a much later origin (e.g. Permian/Triassic transition) than the Silurian-Devonian origin implied for MVT and SRS. A distinct age is consistent with the observed relationship of the veins crosscutting the SRS lenses. The incorporation of 'younger' lead is a product, therefore, of later vein formation. In addition, the occurrence of tetrahedrite-tennantite as a few percent in the veins appears to be an additional, distinctive mineralogical characteristic. When found in SRS lenses, tetrahedrite-tennantite occurs only in trace amounts. Viewed in terms of lead isotope data only, the veins and SRS accumulations are not of the same age and not directly genetically related. In other words, the veins were not conduits for the hydrothermal fluids that formed the SRS lenses or the MVT sulphide occurrences. However, the tracer implications of the lead isotope data strictly apply to the lead (in galena) within the vein system. The possibility of similar sulphur and metal sources remains open.

Documentation of sulphur isotope compositions of the vein-, SRS- and MVT-style mineralization may contribute to understanding the genesis and possible relationships of the various sulphide occurrences. Previous sulphur isotope studies in the Prairie Creek district include those of Fraser (1996) and Paradis (2007), who analyzed samples of all three styles of mineralization. Comparison of the data acquired in this study and that acquired by Paradis (2007) and Fraser (1996) is necessary. However, the contrast in methods and analytical scales between the present study, using in situ laser-assisted fluorination producing single 130 μm reaction pits, and the averaging effects of mineral concentrates analyzed by oxidation to SO_2 (Fraser, 1996; Paradis, 2007) requires some interpretation/discussion when addressing isotopic characteristics and variations on larger scales.

Comparison of the sulphur isotope compositions of pyrite, sphalerite, and galena in the three styles of sulphide occurrences in the Prairie Creek district (Figure 13) indicates a variable degree of correspondence between the styles of sulphide occurrences, and between in situ measurements and bulk analyses of mineral concentrates. Although there are fewer measurements of 'bulk mineral concentrates' (Figure 13) compared to in situ measurements, there appears to be a general agreement of both sets of data for pyrite, sphalerite and galena. With regard to pyrite and sphalerite from veins, however, there appears to be little agreement in $\delta^{34}S$ with values for SRS mineralization, although the number of measurements of veins is few. For galena (Figure 13C), good agreement exists between results for veins and SRS mineralization, whether measured on mineral concentrates or by in situ analysis.

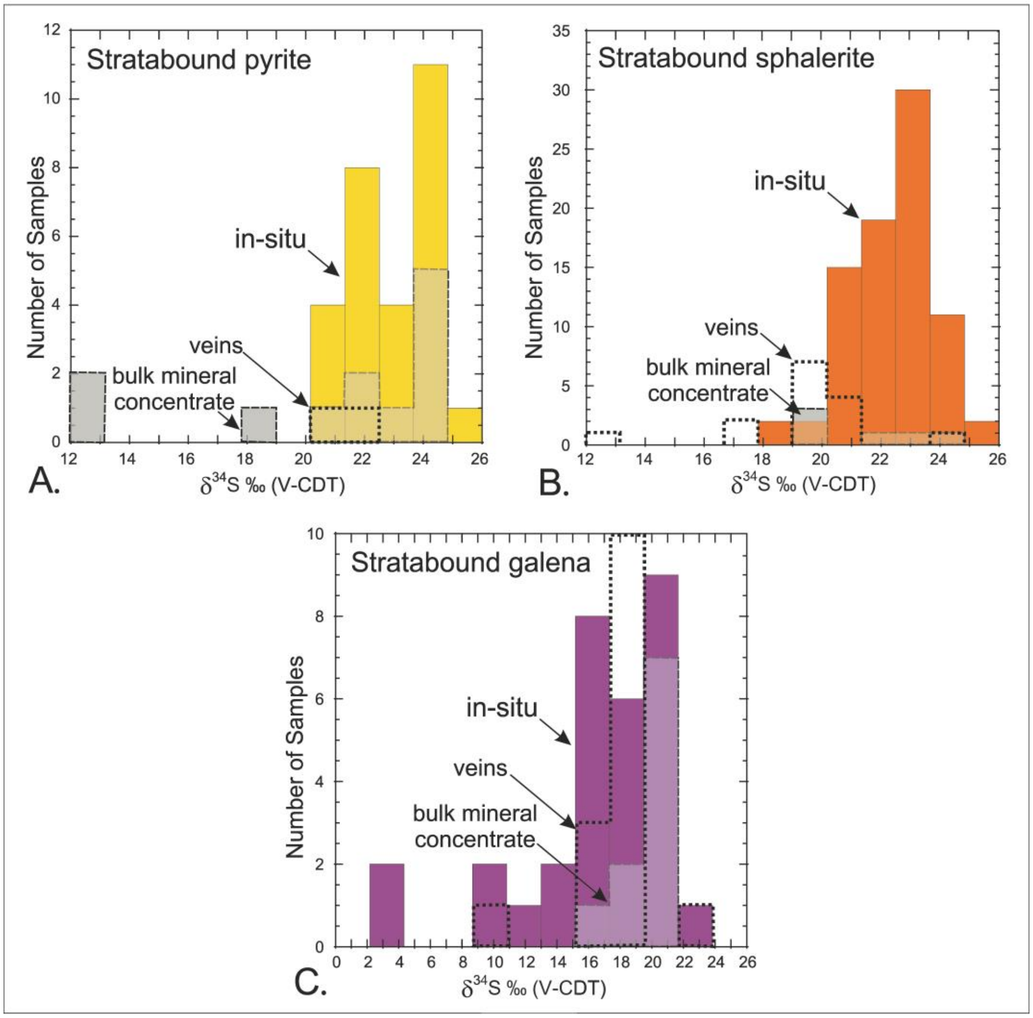

Figure 13. Composite histograms for sulphur isotope compositions of sulphide minerals from stratabound replacement sulphide lenses in the Prairie Creek district measured by in situ methods (this study), compared to results on mineral concentrates from vein and stratabound occurrences (Paradis, 2007).

Sphalerite is of particular interest inasmuch as the per mil fractionation between it and reduced hydrothermal sulphur is sufficiently small over the likely temperature range of formation of the SRS, MVT, and, perhaps, vein occurrences (e.g. Ohmoto and Rye, 1979), that sphalerite can form a proxy for the sulphur isotope composition of the mineralizing fluids (in this case, ca. 23‰). The correspondence between the $\delta^{34}S$ values of sphalerite from the SRS lenses and from the veins determined by in situ measurement and bulk mineral concentrates (Figure 13B) is close, but not exact. Modes of distributions of δ^{34}S values from the veins and SRS mineral concentrates (see Figure 13B) are ca. 3‰ lighter than the mode for the in situ measurements. This might raise the question of possible analytical issues as an explanation, considering the very small analytical area (ca. 130 µm) of the in situ samples (e.g. complications raised by the opaque surface of the sample, possibility of nearest-neighbour interactions, etc.), were it not for the similarity of ranges of δ^{34}S for the mineral concentrate data and in situ measurements (i.e. there is not a consistent 'off set' to consider). Moreover, the number of analyses of mineral concentrates from the veins and SRS is few in comparison to the in situ measurements.

Galena in samples of SRS is 'late' in the crystallization sequence. The histogram of sulphur isotope compositions shows the closest correspondence between the SRS (both bulk mineral concentrate and in situ analyses) and the veins. The contrast between the vein-SRS agreement on galena and disagreement involving pyrite and sphalerite is striking. Viewed solely from the perspective of galena, the veins and SRS lenses appear to be closely related in terms of their sulphur sources. It raises that question as to whether this agreement indicates some sort of communication between vein-forming fluids and the SRS lenses.

Despite the relative age differences of the SRS and vein sulphide occurrences, and ignoring the specific exceptions noted above, the general similarity of the sulphur isotope data illustrated in Figure 13A-C suggests a similar sulphur source. There are two possible scenarios by which this may be satisfied. Firstly, we may hypothesize that later, vein-forming fluids remobilized sulphides from SRS lenses in the sedimentary section. In support of this possibility, we note the spatial association of veins and stratabound lenses, the galena sulphur isotope systematics, perhaps the contrast in tetrahedrite-tennantite abundance noted previously, and the likelihood that sulphur isotope disequilibrium between earlier formed sulphides could have resulted from limited interaction with vein-forming fluids. Alternatively, the similarity in sulphur source may be explained by extraction of (S-bearing) pore fluids or dissolution of marine sulphate from similar aged rocks during vein and SRS formation.

Considering reduced sea water sulphate as a potential sulphur source for the SRS lenses (Paradis, 2007), we note that the mean sulphur isotope composition of marine sulphate changed markedly from the Silurian-Devonian (ca. 20-25‰) to the Permian (ca. 13‰), decreasing about 10‰ (Kampschulte and Strauss, 2004). Despite whatever transfer mechanism might be envisioned (e.g. expulsed pore fluids, dissolution evaporitic sulphate, etc), the vein-contained sulphur could not have been derived from reduced Permian sea water sulphate (ca. 13‰). The sulphur isotope similarity between pyrite from SRS and from veins is striking: Paradis (2007) reported mean values of 19.52‰ (σ = 6.14) and 21.39‰ (σ = 0.42), respectively. Again, this similarity suggests a similar source (or isotopic composition) of sulphur for both veins and SRS. Reduced (Silurian-Devonian) sea water sulphate (ca. 20-25‰; from pore fluid, or dissolution of sulphate minerals) is a permissible source for both. This scenario is perhaps broadly similar to that involving a "deeper, crustal source of sulphur" (see Paradis, 2007), but only if it satisfies the age constraint noted above.

The occurrence of nodular chert throughout the sedimentary host-rock section (see Appendix 2, Paradis, 2007) raises the question of "distance to source" with regard to sulphur, and bears on a topic not addressed in the current study: the causes of sulphide precipitation and whether more than one fluid was involved. The nodular texture of chert is commonly thought to derive from the replacement of sulphate minerals (directly) or by replacement of carbonates that are, themselves, replacements of earlier-formed sulphates (gypsum/anhydrite; e.g. Maliva and Siever, 1989; Henchiri and Slim-S'himi, 2006; Warren, 2006). The replacement process is thought to be early and may involve bacterial sulphate reduction. Transport of released sulphur into the basin, perhaps via saline fluids, would provide a source of appropriate age (and isotopic composition) sulphur (sulphide and/or sulphate). The very abundance of chert nodules might also suggest a source of sulphate for dissolution, subsequent to diagenesis.

The MVT occurrences in the Prairie Creek district (see Figure 2) have similar Pb isotope ratios for galena as found for the SRS mineralization (see Figure 12B) and are, therefore, of generally similar age (Paradis, 2007). The sulphur isotope compositions of the MVT sulphides, however, have markedly lower $\delta^{34}S$ values than either the SRS or the vein occurrences, and indicate a distinct sulphur source. Mean $\delta^{34}S$ values for MVT pyrite, galena and sphalerite reported by Paradis (2007) are 13.79‰, 13.06‰, and 13.61‰, respectively. These sulphides are clearly not in mutual isotopic equilibrium, but some 6‰ lower than in stratabound occurrences. This is likely due, in part, to sequential precipitation and/or recrystallization at different times and at different temperatures, probably from a more local source of sulphur than that which mineralized the Upper Whittaker Formation, forming SRS lenses. The isotopic gradients expressed by pyrite in PC94-75-204.5 (Figure 10), both from core (14.7‰) to rim (15.9‰) in one grain, and in the whole sample, from 12.9 to 17.1‰ indicate a changing sulphur isotope composition of the hydrothermal fluids during pyrite precipitation. This may have occurred by fluid (sulphur source) mixing, or, alternatively, and perhaps more likely in our view, a reservoir effect whereby the sulphur isotope composition of the hydrothermal fluid changed in response to sulphide precipitation. The latter scenario could be the consequence of a local sulphur source suggested above.

In reference to the SRS and quartz-carbonate-sulphide veins, the Pb and S isotope data indicate that the MVT occurrences appear to be genetically unrelated. The MVT occurrences formed about the same time as the SRS lenses, but from a different, local and limited source of sulphur. Local, host rock control of the Sr isotope compositions, in support of the above interpretation, was noted earlier.

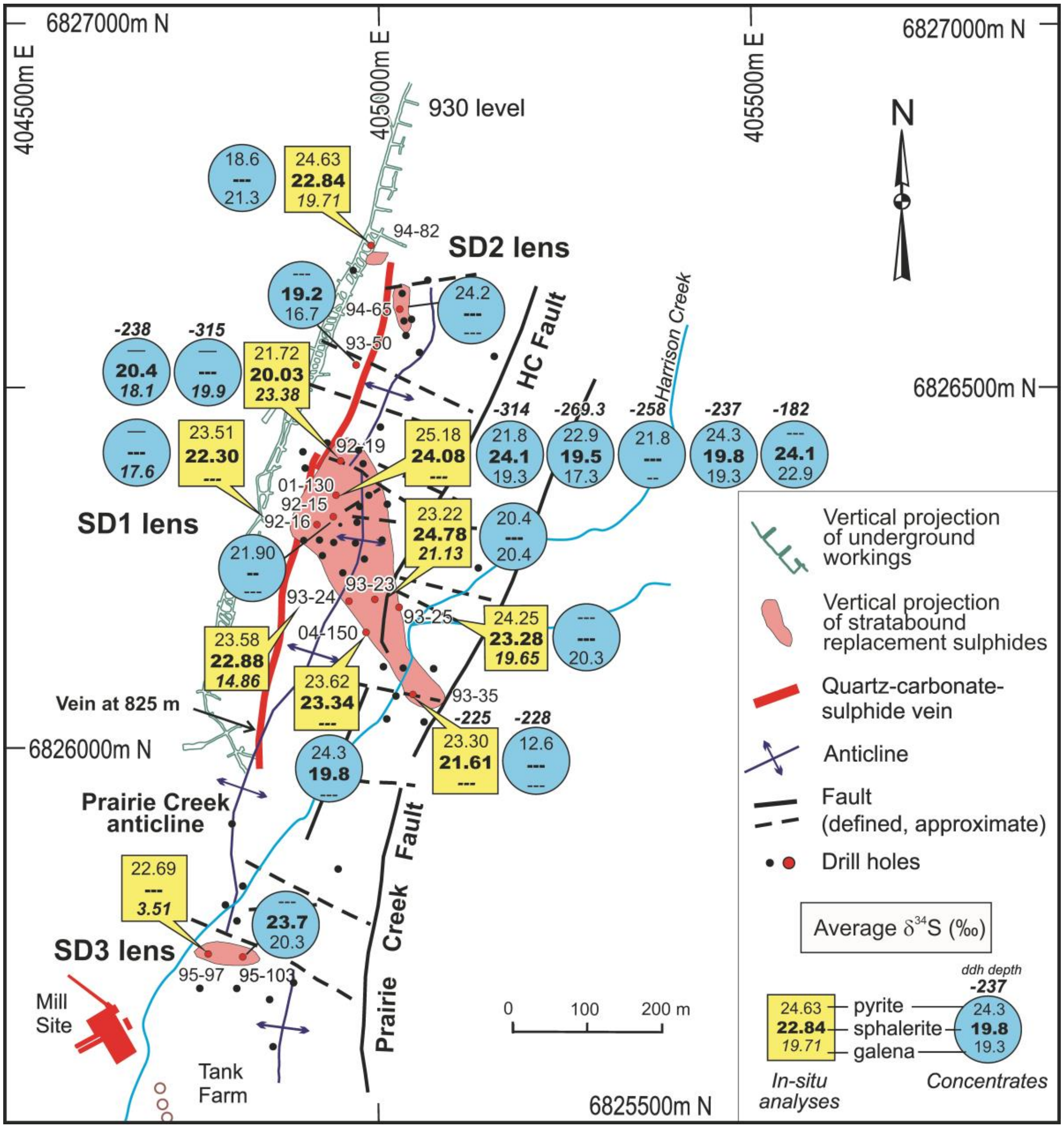

Figure 14. Map of the Prairie Creek mine area showing a projection of the stratabound replacement sulphide lenses, and the quartz-carbonate-sulphide veins, with $\delta^{34}S$ values for sphalerite, pyrite and galena from indicated sample sites. Data reported in yellow fields represents averages of in situ measurements in each samples (this study), whereas data plotted in blue fields are whole-rock analyses reported by Paradis (2007). For the latter, the depth intercepts of the core samples are noted (in meters). Little can be said regarding isotopic variation with depth, except for comparison of sphalerite from drill core 01-130 near the central axis of the projected ore body (Figure 14): the central portion of the stratabound massive sulphide body seems to be isotopically lighter than the upper and lower portions. In contrast, the margins of the stratabound sulphide lens SD1 seem to be isotopically heavier than the margins. Further investigation is needed to resolve these discrepancies.

Sulphur Isotope Variations within the Prairie Creek Mine Area

Average values of $\delta^{34}S$ for pyrite, sphalerite, and galena in samples of SRS were plotted in Figure 14, comparing data from whole-rock samples reported by Paradis (2007) and in situ measurements from this study, with the hope of elucidating general fluid pathways of the replacement process. A comparison using sample averages for in situ data provides a better basis when examining possible trends. Data from Paradis (2007) occasionally represent more than one sample per drillhole, permitting an assessment of vertical variation in $\delta^{34}S$ (the depth intercept of the sample in metres is shown with the isotopic compositions). In several cases, variations of several per mil occur within a few meters. More striking, however, is the occasional discordance in $\delta^{34}S$ between sample averages for in situ data and for whole-rock measurements. The discordance is most striking for pyrite (and galena in one anomalous sample; 95-97A, SD3 lens), and less so for sphalerite. The reason for these discrepancies is unclear at present. Therefore, we rely primarily on the in situ data set.

Sphalerite appears to be isotopically heaviest along the central axis of the projected outline of SD1 lens at the Prairie Creek mine site (Figure 14), between drillholes (DDH) 01-130 and 93-23. This could be used to infer that fluids flowed longest in this region, perhaps marking this as near an up-flow zone, since sphalerite, precipitating from a fluid of nearly constant sulphur isotope composition, increases in $\delta^{34}S$ with decreasing temperature (e.g. see Ohmoto and Rye, 1979). However, sulphur isotope gradients that might exist to map the flow paths of hydrothermal fluids are far from clear at this point, despite the present density of data. This suggests either a rather diffuse hydrothermal flow pattern, or that the replacement process occurred in such a way that simple flow paths were obscured by solution/redeposition occurring throughout a zone, guided by ever-changing, irregular porosity rather than by the progress of a simple replacement front. In this way, the small scale isotopic inhomogeneity documented in several samples may have resulted from the nature of fluid/rock interaction during replacement.

Thermal Variations and Possible Flow Directions in Stratabound Replacement Sulphides (SRS)

Paleotemperatures were estimated from the calibration equations of Kajiwara and Krouse (1971) based on per mil sulphur isotope fractionations between pyrite, sphalerite and galena. Although other calibrations are available in the literature, those of Kajiwara and Krouse provide a consistent basis for comparison. In addition, the calculated temperatures are reasonable, since the sphalerite-galena geothermometer was confirmed by close agreement with Rye (1974) who compared isotopic temperatures with fluid inclusion filling temperatures.

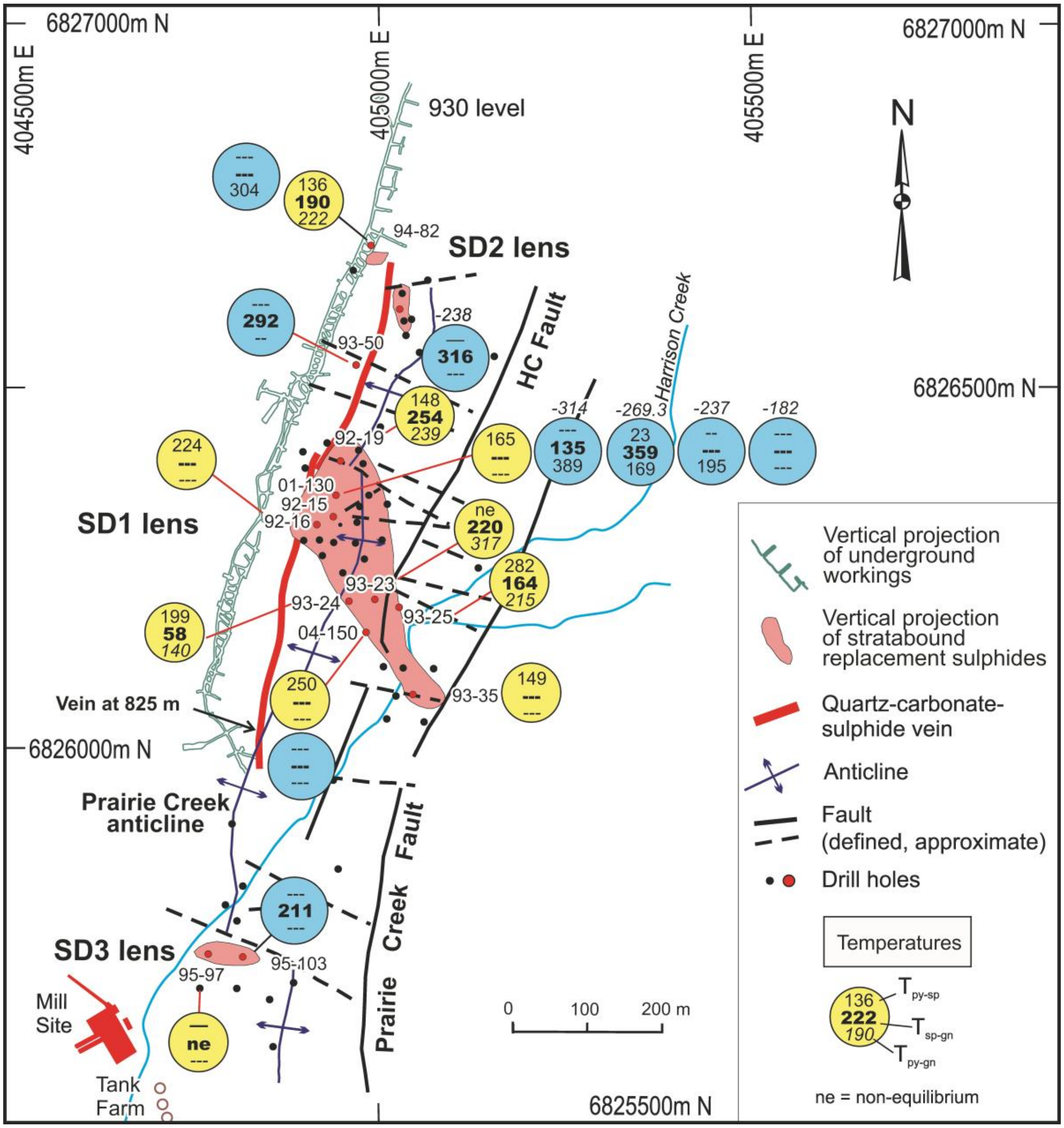

Figure 15. Map of the Prairie Creek mine area showing a projection of the stratabound sulphide lenses, and the quartz-carbonate-sulphide veins. Estimated temperatures (°C) based on average per mil S-isotope fractionations between sphalerite, pyrite and galena are shown based on in situ measurements (this study; yellow background) and whole-rock analyses (Paradis, 2007; blue background). In many cases, the calculated temperatures clearly indicate disequilibrium, which is denoted by dashed lines (also used where insufficient data, or a missing mineral, prevented an estimate of temperature). The intercept depths to each of several samples from the same drill core are shown as in Figure 14. The sphalerite-galena pair appears to provide the best temperature estimates, having formed together; these are ca. 165-255ºC. Additional temperature estimates will be available upon completion of this project, although disequilibrium is common (see text).

From inspection of the isotopic temperatures plotted in Figure 15, it appears that disequilibrium is the rule rather than the exception, most especially where pyrite is involved. Both the textural relationships and the relative degree of isotopic homogeneity compared to sphalerite present in, for example, PC92-19-289.5 (Figure 6) and PC93-25-251.9 (Figure 8), suggest that pyrite and sphalerite are not co-genetic. Rather, sphalerite appears to have partially replaced pyrite in some cases. In these situations, isotopic disequilibrium is not surprising, but characteristic of a protracted mineralizing process. Any remaining sulphate in the host rocks (i.e. unreplaced by chert) might have further promoted the disequilibrium. In other situations, such as those involving pyrite and galena, galena may have approached equilibrium with pyrite through the solution/redeposition processes of replacement. A number of pyrite-galena temperatures near 200°C (Figure 15) may have achieved their similarity in this way, even though pyrite and galena did not co-precipitate.

Based on sphalerite-galena temperatures, the central axial region of the projected outline of SD1, between DDH 92-19 and 93-23, seems to record higher temperatures than elsewhere. The data currently available suggest that sphalerite-galena pairs record a thermal gradient decreasing to the southeast, along the length of the projection of SD1 (Figure 15), away from the quartz-carbonate-sulphide vein. It may be that this massive vein follows, or is near to the ancestral position of a fault zone that had acted as a hydrothermal conduit for sulphide mineralization. Of course, the vein cross-cuts the folded sedimentary section (Figure 2) and cannot correspond, itself, to a paleo-hydrothermal channel. But, was the strike of the vein system influenced by an ancestral hydrothermal conduit? The locations of smaller sulphide bodies (e.g. SD2 and SD3) would be consistent with such a hypothesis.

Formation of the Stratabound Replacement Sulphide (SRS) Lenses

The precise age of formation of the SRS lenses is not known. The Pb isotope data provide a general answer consistent with a broadly similar age to the enclosing rocks, but permits an origin that could be somewhat later. The true age bears on the possible relationship of the mineralized Prairie Creek vein to the SRS lenses. The location of the main, SRS lens (SD1) near the high point of a doubly-plunging anticline in the Prairie Creek district, raises the possibility that replacement may have occurred early, during folding. Figure 2B illustrates the fact that the Prairie Creek vein is not axial planar with the present fold. But, was it initially? Was the Prairie Creek vein rotated somewhat during folding?

Sulphur isotope data discussed previously are compatible with a common source of sulphur, whereas Pb isotope data (see Figure 12) require a later phase of hydrothermal activity for the veins. The physical association of vein and SRS might suggest that the vein developed from what was originally a hydrothermal conduit. Textural evidence (Paradis, 2007) suggests multiple filling/deformation events in the Prairie Creek vein's history. Perhaps this is a record which developed during and subsequent to folding and early replacement of the mottled dolostone (Upper Whittaker Formation).

Implications for Exploration

We infer that up-welling, metalliferous hydrothermal fluids reacted with, and replaced, the stratigraphically lowest susceptible (carbonate-bearing) member of the Whittaker Formation. Any residual sulphate in the Whittaker Formation may have contributed a local source of sulphur. With this in mind, and the results of this study, the following implications are:

- An exploration focus on the same or similar (stratigraphically low) units to the OSw3-2 (mottled dolostone, Whittaker Formation) in the subsurface may prove useful.

- The location of replacement sulphide bodies (in plan view) may have been controlled by ancestral faults. The fact that such sulphide bodies seem to align with the principal anticlinal axis in the Prairie Creek district suggests that sulphide occurrences may have been at least partially responsible for, or otherwise involved with, fold axis localization. If so, similar structural settings may be provide for fruitful exploration.

- The quartz-carbonate-sulphide veins, which formed much later than the SRS lenses, seem to have filled post-ore faults that may have been either localized by ancestral, mineralization-related structural weaknesses, or related to folding of the sedimentary host rocks.

- The sulphur isotope compositions of the vein and are consistent with a similar sulphur source either by remobilization of earlier-formed, SRS, or by derivation of sulphur (pore fluid, or dissolution of marine sulphate) from the same or similar rocks, albeit at different times. Pb isotope ratios are consistent with latter scenario. Thus, the geographic occurrence and abundance of sulphides in veins may offer a clue to the subsurface mineral potential of the area.

- The limited data available on the “MVT-style” of sulphide occurrence indicates that they cannot be easily related to the SRS or vein sulphide occurrences, and may be of limited interest for exploration.

Future Work

Analyses from twenty-four samples currently in progress (extracted but requiring mass spectrometry) will geographically broaden the data base presently available, and facilitate a more comprehensive interpretation. Completion of the study as originally planned was made difficult by interruptions to analytical facilities and scheduling. The in situ and grain analyses in progress will allow a more comprehensive investigation of possible compositional variations in the Prairie Creek district, and address the difficult question of possible thermal gradients. Knowledge of thermal gradients in the SRS lenses, if they can be documented, may help to decipher fluid flow and vectors of use to exploration.

Acknowledgements

We are grateful to Canadian Zinc Corporation for granting access to the property and allowing us to sample drill core. All personnel of Canadian Zinc Corporation and, specifically, Alan Taylor and Kerry Cupit provided invaluable geological information that is much appreciated. André Pellerin and Thi Hao Bui (McGill University) were very helpful in providing an introduction to gas chromatographic (GC) purification of SF_6 gas samples prior to mass spectrometry. In addition, André Pellerin provided helpful suggestions during the addition, design and installation of a gas chromatograph and related vacuum plumbing on MILES (LSI lab, Ottawa), and during the design and installation (BET) of a micro-sample inlet on the mass spectrometer in the Department of Earth and Planetary Sciences, McGill University to measure the small samples from this study. The review comments of W.D. Goodfellow and A. Rukhlov are gratefully acknowledged.

References

AMC Mining Consultants (Canada), 2012, Prairie Creek Property, Northwest Territories, Canada. Technical Report for Canadian Zinc Corporation, unpublished report, rev. July 23, 2014, 209 p. [http://www.canadianzinc.com/projects/prairie-creek/resources].

Asprey, L. B., 1976, The preparation of very pure fluorine gas: Journal Fluorine Chemistry, v. 7, p. 359-361.

Beaudoin G, Taylor, B.E., 1994, High-precision and spatial-resolution sulfur isotope analysis using MILES laser microprobe. Geochimica et Cosmochimica Acta 58: 5055-5063.

Beaudoin, G., and Therrien, P., 2004, The web stable isotope fractionation calculator, *in* Handbook of stable isotope analytical techniques, Volume-I. De Groot, P.A., ed., Analytical Techniques 1: Elsevier, p. 1045-1047.

Earls, G., 1995, A review of the Prairie Creek deposit, NT, Canada: Internal Report, San Andreas Resources Corporation, 36 p.

Fraser, S.C.,1996, Geology and geochemistry of the Prairie Creek Zn, Pb, Ag deposits, Southern Mackenzie Mountains, Northwest Territories: Unpublished M.Sc. thesis, University of Alberta, Edmonton, Alberta, 146 p.

Godwin, C.I. and Sinclair, A.J.,1982, Average lead isotope growth curves for shale-hosted zinc lead deposits, Canadian Cordillera; Economic Geology, v. 77, p. 675-690.

Goodfellow, W.D., and Lydon, J.W., 2007, Sedimentary exhalative (SEDEX) deposits, *in* Goodfellow, W.D., ed., Mineral deposits of Canada: A synthesis of major deposit types, district metallogeny, the evolution of geological provinces, and exploration methods: Geological Association of Canada, Mineral Deposits Division, Special Publication no. 5, p. 163-183.

Henchiri, M., and Slim-S'himi, N., 2006, Silicification of sulphate evaporites and their carbonate replacements in Eocene marine sediments, Tunisia: two diagenetic trends: Sedimentology, v. 53, p. 1135-1159.

Kajiwara, Y., and Krouse, H.R., 1971, Sulphur isotope partitioning in metallic sulphide systems: Canadian Journal of Earth Science v. 8, p. 1397-1408.

Kampschulte, A., and Strauss, H., 2004, The sulphur isotopic evolution of Phanerozoic seawater based on the analysis of structurally substituted sulfate in carbonates: Chemical Geology, v. 302, p. 255-286.

Maliva, R. G., and Siever, R., 1989, Nodular chert formation in carbonate rocks: Journal of Geology, v. 97, p. 421-433.

Morrow, D.W., and Cook, D.G., 1987, The Prairie Creek Embayment and Lower Paleozoic strata of the southern Mackenzie Mountains: Geological Survey of Canada, Memoir 412, 195 p.

Ohmoto, H., and Rye, R. O., 1979, Isotopes of sulphur and carbon, *in* Barnes, H. L. ed., Geochemistry of Hydrothermal deposit: John Wiley & Sons, p. 509-567.

Paradis, S., 2007, Isotope geochemistry of the Prairie Creek carbonate-hosted zinc-lead-silver deposit, southern Mackenzie Mountains, Northwest Territories, *in* Wright, D. F., Lemkow, D., and Harris, J., ed., Mineral and energy potential of the proposed expansion to the Nahanni National Park Reserve, North Cordillera, Northwest Territories: Geological Survey of Canada, Open File 5344, p. 1-46.

Rye, R.O., 1974, A comparison of sphalerite-galena sulphur isotope temperatures with filling temperatures of fluid inclusions: Economic Geology, v. 69, pp. 26-32.

Stacey, J.S. and Kramers, J.D., 1975, Approximation of terrestrial lead isotope evolution by a two-stage model; Earth and Planetary Science Letters, v. 26, p. 207-221.

Taylor, B. E., 2004a, Biogenic and thermogenic sulfate reduction in the Sullivan Pb-Zn-Ag deposit, British Columbia (Canada): Evidence from micro-isotopic analysis of carbonate and sulphide in bedded ores: Chemical Geology, v. 204, p. 215–236.

Taylor, B. E., 2004b, Fluorination methods in stable isotope analysis, *in*, de Groot, P.A., ed., Handbook of Stable Isotope Analytical Techniques 1: Elsevier, p. 400 – 472.

Taylor, B.E., and Beaudoin, G., 1993, MILES laser microprobe, Part 1: System description: Geological Survey of Canada, Current Research, Part D, Paper 1993-ID, p. 191-198.

Taylor, B.E., Paradis, S., Falck, H., and Wing, B., in preparation, Sulphur isotope studies Pb-Zn mineralization, Prairie Creek, southern Mackenzie Mountains, Northwest Territories.

Warren, J.K., 2006, Evaporites: Sediments, resources and hydrocarbons: Springer-Verlag, Berlin. 1035 p.

Appendix 1. Sulphur isotope compositions of individual sulphide grains and/or analytical traverses within individual sulphide grains.

Extraction / Lab Number	General Sample Description	Field Spl No.	Mineral	$\delta^{33}S_{VCDT}$	$\delta^{34}S_{VCDT}$	$\delta^{36}S_{VCDT}$	$\Delta^{33}S_{VCDT}$	$\Delta^{36}S_{VCDT}$	$\delta^{34}Spy$	$\delta^{34}Ssphal$	$\delta^{34}Sgn$
MIV-104-2/LSI-05-09-1	SRS in mottled dolo unit of OSw3-2.	PC01-130-313.5	py	14.4	26.9	1551.42	0.65	1537.66	26.8**		
MIV-104-3/LSI-05-09-1	Bands of fg py in agg of fg pinkish sphal	PC01-130-313.5	py	12.9	24.5	793.89	0.37	781.37	24.5		
MIV-104-5/LSI-05-09-1	and fg py; gn and cc fill remaining	PC01-130-313.5	py	12.5	24.0	490.25	0.17	477.96	24.0		
MIV-104-6/LSI-05-09-1	spaces.	PC01-130-313.5	py	12.7	24.7	908.09	0.09	895.43	24.7		
MIV-103-10/LSI-05-09-1		PC01-130-313.5	py	13.6	26.1	6761.72	0.28	6748.37	26.1**		
MIV-103-11/LSI-05-09-1		PC01-130-313.5	py	19.0	31.5	14219.51	2.86	14203.39	31.5**		
MIV-103-9/LSI-05-09-1		PC01-130-313.5	py	14.3	24.0	1336.14	1.99	1323.83	24.0		
MIV-105-10/LSI-05-09-1		PC01-130-313.5	sphal	13.4	25.1	888.20	0.57	875.38		25.06	
MIV-105-9/LSI-05-09-1		PC01-130-313.5	sphal	11.9	23.1	246.30	0.04	234.46		23.11	
								AVG.	**24.3**	**24.08**	
MIV-107-10/LSI-05-09-2	SRS in OSw3-2.	PC04-150-238.6	py	13.8	24.3	170.65	1.36	158.22	24.3		
MIV-107-11/LSI-05-09-2	Sulphides comprise agg of fg py + sphal	PC04-150-238.6	py	12.9	23.8	213.12	0.66	200.93	23.8		
MIV-107-12/LSI-05-09-2	replacing the cherty dol.	PC04-150-238.6	py	12.0	23.4	215.36	-0.04	203.36	23.4		
MIV-107-2/LSI-05-09-2	Gn and cc fill remaining spaces.	PC04-150-238.6	py	13.6	22.8	347.27	1.99	335.61	22.8		
MIV-107-3/LSI-05-09-2		PC04-150-238.6	py	19.0	25.6	4261.45	5.93	4248.35	25.6**		
MIV-107-9/LSI-05-09-2		PC04-150-238.6	py	11.9	23.8	371.59	-0.31	359.40	23.8		
MIV-107-4/LSI-05-09-2		PC04-150-238.6	sphal	12.7	24.8	2421.36	-0.03	2408.66	24.8	24.79	
MIV-107-6/LSI-05-09-2		PC04-150-238.6	sphal	14.7	23.6	3050.80	2.63	3038.73		23.58	
MIV-107-7/LSI-05-09-2		PC04-150-238.6	sphal	12.3	24.1	2189.70	-0.04	2177.37		24.08	
MIV-107-8/LSI-05-09-2		PC04-150-238.6	sphal	12.3	23.5	211.09	0.27	199.08		23.46	
MIV-108-1/LSI-05-09-2		PC04-150-238.6	sphal	11.8	24.7	1880.82	-0.88	1868.16		24.73	
MIV-108-2/LSI-05-09-2		PC04-150-238.6	sphal	11.2	22.0	328.18	-0.08	316.89		22.04	
MIV-108-3/LSI-05-09-2		PC04-150-238.6	sphal	12.4	22.3	249.08	0.99	237.67		22.27	
MIV-108-4/LSI-05-09-2		PC04-150-238.6	sphal	11.6	22.9	352.14	-0.11	340.39		22.94	
MIV-108-5/LSI-05-09-2		PC04-150-238.6	sphal	11.8	24.5	743.58	-0.68	731.06		24.45	
MIV-108-6/LSI-05-09-2		PC04-150-238.6	sphal	11.9	23.5	539.69	-0.10	527.66		23.47	
								AVG.	**23.8**	**23.58**	
MIV-104-11/LSI-05-09-3	SRS in OSw3-2.	PC92-16-310.6	py	10.9	21.3	182.70	0.01	171.78	21.3		
MIV-104-7/LSI-05-09-3	Layered sulp mix with chert nodules.	PC92-16-310.6	py	11.9	22.1	248.82	0.61	237.53	22.1		
MIV-104-8/LSI-05-09-3	Sulph are fg mix of spha, py, gn.	PC92-16-310.6	py	11.4	22.3	265.82	-0.02	254.39	22.3		
MIV-105-2/LSI-05-09-3		PC92-16-310.6	py	12.3	22.9	514.37	0.58	502.62	22.9		
MIV-105-5/LSI-05-09-3		PC92-16-310.6	py	12.0	21.0	2916.70	1.26	2905.92	21.0		
MIV-105-6/LSI-05-09-3		PC92-16-310.6	py	11.6	22.5	1723.66	0.09	1712.13	22.5		
MIV-103-12/LSI-05-09-3		PC92-16-310.6	py	13.0	25.0	2637.08	0.17	2624.28	25.0		
MIV-104-9/LSI-05-09-3		PC92-16-310.6	sphal	13.4	25.8	896.49	0.16	883.29		25.79	
MIV-105-1/LSI-05-09-3		PC92-16-310.6	sphal	12.5	22.7	386.65	0.91	375.03		22.67	
MIV-105-3/LSI-05-09-3		PC92-16-310.6	sphal	11.7	22.5	262.37	0.16	250.84		22.50	
MIV-105-7/LSI-05-09-3		PC92-16-310.6	sphal	11.6	22.7	1007.55	-0.06	995.92		22.71	
MIV-105-8/LSI-05-09-3		PC92-16-310.6	sphal	11.4	22.3	310.93	-0.01	299.49		22.34	
								AVG.	**22.5**	**23.20**	
MIV-123-7/LSI-05-09-04	SRS in OSw3-3.	PC92-19-289.5	py	12.1	23.7	75.26	-0.01	63.11	23.7		
MIV-123-8/LSI-05-09-04	Fg agg of py adjacent to crystalline dol	PC92-19-289.5	py	11.1	21.7	78.51	0.00	67.40	21.7		
MIV-123-9/LSI-05-09-04	and cg gn.	PC92-19-289.5	py	10.8	21.1	85.16	0.05	74.36	21.1		
MIV-123-10/LSI-05-09-04		PC92-19-289.5	py	10.8	21.1	101.67	0.00	90.85	21.1		
MIV-123-11/LSI-05-09-04		PC92-19-289.5	py	11.0	21.5	71.55	-0.01	60.55	21.5		
MIV-123-12/LSI-05-09-04		PC92-19-289.5	py	11.0	21.6	105.11	-0.03	94.07	21.6		

Appendix 1 continued.

Extraction / Lab Number	General Sample Description	Field Spl No.	Mineral	$\delta^{33}S_{VCDT}$	$\delta^{34}S_{VCDT}$	$\delta^{36}S_{VCDT}$	$\Delta^{33}S_{VCDT}$	$\Delta^{36}S_{VCDT}$	$\delta^{34}Spy$	$\delta^{34}Ssphal$	$\delta^{34}Sgn$
MIV-122-4/LSI-05-09-04		PC92-19-289.5	py	11.3	22.0	186.27	0.05	175.02	22.0		
MIV-122-7/LSI-05-09-04		PC92-19-289.5	py	11.0	21.4	387.38	0.08	376.43	21.4		
MIV-122-8/LSI-05-09-04		PC92-19-289.5	py	11.4	21.5	401.00	0.42	390.00	21.5		
MIV-122-3/LSI-05-09-04		PC92-19-289.5	sphal	9.5	18.4	71.77	0.03	62.31		18.44	
MIV-122-5/LSI-05-09-04		PC92-19-289.5	sphal	9.9	19.2	287.89	0.05	382.69		19.25	
MIV-122-6/LSI-05-09-04		PC92-19-289.5	sphal	9.6	18.6	392.21	0.05	382.69		18.57	
MIV-122-9/LSI-05-09-04		PC92-19-289.5	sphal	10.9	21.1	289.03	0.10	278.24		21.06	
MIV-122-10/LSI-05-09-04		PC92-19-289.5	sphal	10.6	20.5	360.06	0.12	349.58		20.46	
MIV-123-3/LSI-05-09-04		PC92-19-289.5	sphal	11.1	21.8	67.82	-0.01	56.67		21.76	
MIV-123-4/LSI-05-09-04		PC92-19-289.5	sphal	10.8	20.8	108.48	0.19	97.82		20.80	
MIV-123-5/LSI-05-09-04		PC92-19-289.5	sphal	10.2	19.9	91.17	0.04	80.98		19.88	
MIV-122-11/LSI-05-09-04		PC92-19-289.5	gn	9.6	18.8	484.85	0.03	475.23			18.76
MIV-122-12/LSI-05-09-04		PC92-19-289.5	gn	9.5	18.5	255.39	0.00	245.89			18.53
MIV-123-1/LSI-05-09-04		PC92-19-289.5	gn	8.9	16.9	378.91	0.25	370.24			16.89
MIV-123-2/LSI-05-09-04		PC92-19-289.5	gn	8.6	16.3	201.22	0.17	192.84			16.34
								AVG.	**21.7**	**20.03**	**17.63**
MIV-120-4/LSI-05-09-05	SRS in OSw3-2.	PC93-25-251.9	py	12.4	24.0	724.67	0.07	712.36	24.0		
MIV-120-5/LSI-05-09-05	Fg agg of py with interstitial gn.	PC93-25-251.9	py	12.3	24.2	338.08	-0.07	325.71	24.2		
MIV-120-6/LSI-05-09-05	coarse sparry cc fills remaining spaces.	PC93-25-251.9	py	12.2	23.9	263.21	-0.06	250.99	23.9		
MIV-121-3/LSI-05-09-05	Composite content: 25% sphal, 15% gn,	PC93-25-251.9	py	12.4	24.2	643.71	0.01	631.30	24.2		
MIV-121-4/LSI-05-09-05	15% chert, 2% cc, 2% qz, and	PC93-25-251.9	py	12.6	24.4	1454.32	0.09	1441.82	24.4		
MIV-121-7/LSI-05-09-05	2% white/gray dol.	PC93-25-251.9	py	12.9	24.5	116.26	0.41	103.73	24.5		
MIV-121-8/LSI-05-09-05		PC93-25-251.9	py	12.7	24.6	104.32	0.12	91.75	24.6		
MIV-121-10/LSI-05-09-05		PC93-25-251.9	py	12.5	24.5	461.74	-0.05	449.19	24.5		
MIV-121-11/LSI-05-09-05		PC93-25-251.9	py	12.4	24.0	261.73	0.13	249.44	24.0		
MIV-121-12/LSI-05-09-05		PC93-25-251.9	py	12.4	24.3	128.12	-0.01	115.70	24.3		
MIV-120-11/LSI-05-09-05		PC93-25-251.9	sphal	12.0	23.4	123.37	0.01	111.38		23.42	
MIV-120-12/LSI-05-09-05		PC93-25-251.9	sphal	11.8	23.0	175.79	0.06	164.04		22.96	
MIV-121-1/LSI-05-09-05		PC93-25-251.9	sphal	12.1	23.3	1276.15	0.19	1264.21		23.31	
MIV-121--2/LSI-05-09-05		PC93-25-251.9	sphal	12.3	23.9	1715.26	0.07	1703.05		23.85	
MIV-121-6/LSI-05-09-05		PC93-25-251.9	sphal	12.2	22.9	5866.14	0.46	5854.43		22.86	
MIV-120-8/LSI-05-09-05		PC93-25-251.9	gn	10.0	19.5	372.79	0.02	362.79			19.51
MIV-120-9/LSI-05-09-05		PC93-25-251.9	gn	10.2	19.9	403.71	0.05	393.51			19.90
MIV-120-10/LSI-05-09-05		PC93-25-251.9	gn	10.1	19.6	224.45	0.04	214.42			19.56
MIV-121-5/LSI-05-09-05		PC93-25-251.9	gn	10.2	19.7	4247.37	0.09	4237.29			19.66
								AVG.	**24.3**	**23.28**	**19.65**
MIV-114-11/LSI-05-09-06	SRS in OSw3-2.	PC93-24-257.1	py	12.0	23.6	366.77	-0.07	354.65	23.6		
MIV-114-12/LSI-05-09-06	Diss fg py in cherty band, and sphal in	PC93-24-257.1	py	11.9	23.2	272.17	0.03	260.27	23.2		
MIV-115-6/LSI-05-09-06	siliceous dolo; veinlets of py criss-cut dolo.	PC93-24-257.1	py	11.8	23.3	109.21	-0.12	97.26	23.3		
MIV-116-1/LSI-05-09-06	Section resembles stringers.	PC93-24-257.1	py	11.9	23.5	207.88	-0.12	195.83	23.5		
MIV-116-10/LSI-05-09-06	Composite content: py (40%), sphal (10%),	PC93-24-257.1	py	12.2	23.7	657.86	0.09	645.75	23.7		
MIV-116-3/LSI-05-09-06	ga (3%), and 30% dark grey dol.	PC93-24-257.1	py	11.9	23.5	189.93	-0.12	177.89	23.5		
MIV-116-4/LSI-05-09-06		PC93-24-257.1	py	12.4	24.5	280.58	-0.16	268.03	24.5		
MIV-115-8/LSI-05-09-06		PC93-24-257.1	py	11.8	23.2	194.25	-0.06	182.36	23.2		
MIV-117-9/LSI-05-09-06		PC93-24-257.1	py	11.9	23.6	192.64	-0.14	180.56	23.6		
MIV-114-10/LSI-05-09-06		PC93-24-257.1	sphal	12.6	23.6	639.66	0.51	627.60		23.56	
MIV-114-8/LSI-05-09-06		PC93-24-257.1	sphal	17.2	22.6	840.50	5.64	828.93		22.57	

Appendix 1 continued.

Extraction / Lab Number	General Sample Description	Field Spl No.	Mineral	$\delta^{33}S_{VCDT}$	$\delta^{34}S_{VCDT}$	$\delta^{36}S_{VCDT}$	$\Delta^{33}S_{VCDT}$	$\Delta^{36}S_{VCDT}$	δ^{34}Spy	δ^{34}Ssphal	δ^{34}Sgn
MIV-114-9/LSI-05-09-06		PC93-24-257.1	sphal	12.3	23.3	557.32	0.32	545.37		23.33	
MIV-115-1/LSI-05-09-06		PC93-24-257.1	sphal	11.8	22.4	217.73	0.29	206.23		22.44	
MIV-115-10/LSI-05-09-06		PC93-24-257.1	sphal	12.6	24.8	104.18	-0.09	91.50		24.78	
MIV-115-2/LSI-05-09-0		PC93-24-257.1	sphal	12.1	22.5	206.15	0.62	194.63		22.49	
MIV-115-3/LSI-05-09-06		PC93-24-257.1	sphal	11.2	22.2	241.66	-0.11	230.30		22.16	
MIV-115-7/LSI-05-09-06		PC93-24-257.1	sphal	12.5	22.9	132.31	0.79	120.56		22.94	
MIV-115-9/LSI-05-09-06		PC93-24-257.1	sphal	12.3	24.0	153.56	-0.03	141.25		24.05	
MIV-116-11/LSI-05-09-06		PC93-24-257.1	sphal	11.1	22.5	471.62	-0.39	460.11		22.48	
MIV-116-12/LSI-05-09-06		PC93-24-257.1	sphal	12.1	23.9	221.05	-0.10	208.83		23.87	
MIV-116-2/LSI-05-09-06		PC93-24-257.1	sphal	11.6	23.0	224.34	-0.18	212.54		23.03	
MIV-116-5/LSI-05-09-06		PC93-24-257.1	sphal	12.0	23.5	161.41	-0.03	149.37		23.52	
MIV-116-6/LSI-05-09-06		PC93-24-257.1	sphal	10.7	20.8	276.45	0.08	265.79		20.80	
MIV-116-7/LSI-05-09-06		PC93-24-257.1	sphal	10.9	21.1	126.73	0.07	115.95		21.06	
MIV-117-2/LSI-05-09-06		PC93-24-257.1	sphal	13.3	23.9	230.47	1.06	218.24		23.89	
MIV-117-6/LSI-05-09-06		PC93-24-257.1	sphal	11.7	22.0	180.35	0.43	169.06		22.03	
MIV-117-7/LSI-05-09-06		PC93-24-257.1	sphal	12.3	22.6	109.54	0.72	97.94		22.65	
MIV-117-8/LSI-05-09-06		PC93-24-257.1	sphal	11.9	23.1	168.06	0.05	156.20		23.14	
MIV-115-11/LSI-05-09-06		PC93-24-257.1	gn	7.6	15.4	279.26	-0.29	271.38			15.36
MIV-115-12/LSI-05-09-06		PC93-24-257.1	gn	6.9	14.3	313.03	-0.38	305.71			14.26
MIV-115-4/LSI-05-09-06		PC93-24-257.1	gn	6.4	10.8	235.63	0.87	230.10			10.76
MIV-115-5/LSI-05-09-06		PC93-24-257.1	gn	8.3	12.6	357.20	1.89	350.74			12.57
MIV-116-8,-9/LSI-05-09-06		PC93-24-257.1	gn	8.7	18.0	588.49	-0.56	579.28			17.96
MIV-117-1/LSI-05-09-06		PC93-24-257.1	gn	7.7	15.6	312.40	-0.28	304.38			15.63
MIV-117-3/LSI-05-09-06		PC93-24-257.1	gn	30.5	20.4	13680.36	20.08	13669.92			20.38
MIV-117-4/LSI-05-09-06		PC93-24-257.1	gn	8.4	16.0	919.62	0.15	911.39			16.03
MIV-117-5/LSI-05-09-06		PC93-24-257.1	gn	6.0	10.8	341.55	0.46	336.00			10.80
								AVG.	**23.6**	**22.88**	**14.86**
MIV-110-2/LSI-05-09-7	SRS in OSw3-2.	PC93-35-224.8	py	19.0	36.3	5252.11	0.48	5233.60	*36.3***		
MIV-110-3/LSI-05-09-7	Section of fg mas py and pink to yellow	PC93-35-224.8	py	12.1	24.3	1055.28	-0.31	1042.84	*24.3***		
MIV-110-4/LSI-05-09-7	sphal cutting cherty dol. Pink sphal is mixed	PC93-35-224.8	py	11.6	23.0	713.44	-0.20	701.67	23.0		
MIV-110-5/LSI-05-09-7	with py; yellowish spha cut the agg of py.	PC93-35-224.8	py	11.5	23.3	735.72	-0.48	723.77	23.3		
MIV-110-8/LSI-05-09-7		PC93-35-224.8	py	11.7	23.5	672.12	-0.29	660.08	23.5		
MIV-110-9/LSI-05-09-7		PC93-35-224.8	py	11.4	22.4	627.79	0.00	616.34	22.4		
MIV-110-10/LSI-05-09-7		PC93-35-224.8	sphal	12.0	22.0	195.22	0.77	183.96		21.98	
MIV-110-11/LSI-05-09-7		PC93-35-224.8	sphal	11.9	23.0	865.14	0.14	853.37		22.99	
MIV-110-12/LSI-05-09-7		PC93-35-224.8	sphal	10.8	21.3	426.06	-0.16	415.12		21.34	
MIV-110-6/LSI-05-09-7		PC93-35-224.8	sphal	10.4	20.6	266.06	-0.14	255.51		20.60	
MIV-110-7/LSI-05-09-7		PC93-35-224.8	sphal	11.2	21.7	287.21	0.10	276.10		21.68	
MIV-111-1/LSI-05-09-7		PC93-35-224.8	sphal	10.9	21.2	440.84	0.08	429.97		21.20	
MIV-111-2/LSI-05-09-7		PC93-35-224.8	sphal	10.8	21.4	388.75	-0.14	377.81		21.36	
MIV-111-3/LSI-05-09-7		PC93-35-224.8	sphal	11.1	21.8	178.30	-0.06	167.15		21.76	
								AVG.	**23.0**	**21.61**	
MIV-126-1/LSI-05-09-08	SRS in OSw3-4.	PC93-41-246.7	py	11.2	21.8	132.12	0.00	120.96	21.8		
MIV-126-3/LSI-05-09-08	Sulphide zones connected by fine ca 1 mm	PC93-41-246.7	py	10.4	20.4	181.41	-0.06	170.97	20.4		
MIV-126-6/LSI-05-09-08	mineralized qz-sphal-py-gn stringers.	PC93-41-246.7	py	11.8	23.3	439.49	-0.08	427.57	23.3		
MIV-127-9/LSI-05-09-08		PC93-41-246.7	py	11.9	23.6	389.04	-0.16	376.98	23.6		
MIV-125-9/LSI-05-09-08		PC93-41-246.7	sphal	12.3	23.9	127.05	0.09	114.83		23.86	

Appendix 1 continued.

Extraction / Lab Number	General Sample Description	Field Spl No.	Mineral	$\delta^{33}S_{VCDT}$	$\delta^{34}S_{VCDT}$	$\delta^{36}S_{VCDT}$	$\Delta^{33}S_{VCDT}$	$\Delta^{36}S_{VCDT}$	$\delta^{34}Spy$	$\delta^{34}Ssphal$	$\delta^{34}Sgn$
MIV-125-10/LSI-05-09-08		PC93-41-246.7	sphal	11.4	22.4	120.65	-0.04	109.17		22.42	
MIV-126-12/LSI-05-09-08		PC93-41-246.7	sphal	9.0	17.6	123.17	0.01	114.17		*17.55***	
MIV-127-2/LSI-05-09-08		PC93-41-246.7	sphal	10.4	20.4	66.96	-0.08	56.52		20.37	
MIV-127-3/LSI-05-09-08		PC93-41-246.7	sphal	10.3	20.2	87.75	-0.01	77.40		20.18	
MIV-126-2/LSI-05-09-08		PC93-41-246.7	sphal	10.9	21.5	295.59	-0.08	284.59		21.47	
MIV-126-7/LSI-05-09-08		PC93-41-246.7	sphal	11.7	23.1	903.83	-0.17	892.00		23.11	
MIV-126-9/LSI-05-09-08		PC93-41-246.7	sphal	11.7	23.0	174.53	-0.06	162.75		23.01	
MIV-127-6/LSI-05-09-08		PC93-41-246.7	sphal	11.2	22.4	214.01	-0.21	202.55		22.36	
MIV-127-7/LSI-05-09-08		PC93-41-246.7	sphal	10.6	21.1	190.16	-0.15	179.36		21.07	
MIV-127-8/LSI-05-09-08		PC93-41-246.7	sphal	12.0	22.7	673.87	0.40	662.23		22.72	
MIV-127-10/LSI-05-09-08		PC93-41-246.7	sphal	12.3	24.2	283.29	-0.15	270.89		24.22	
MIV-127-11/LSI-05-09-08		PC93-41-246.7	sphal	11.5	22.5	125.33	0.01	113.79		22.53	
MIV-127-12/LSI-05-09-08		PC93-41-246.7	sphal	11.8	23.2	327.00	-0.07	315.14		23.16	
MIV-127-4/LSI-05-09-08		PC93-41-246.7	gn	7.9	15.8	149.66	-0.17	141.54			15.81
MIV-127-5/LSI-05-09-08		PC93-41-246.7	gn	7.6	15.2	225.71	-0.20	217.92			15.18
MIV-126-8/LSI-05-09-08		PC93-41-246.7	gn	7.3	14.6	332.23	-0.22	324.73			14.62
								AVG.	**22.2**	**22.34**	**15.21**
MIV-112-5/LSI-05-09-09	SRS in OSw3-6.	PC94-64-207.6	py	8.9	16.6	189.38	0.33	180.84	*16.6***		
MIV-112-6/LSI-05-09-09	Fg aggregates of py-sphal-gn.	PC94-64-207.6	py	11.6	22.9	191.62	-0.09	179.91	22.9		
MIV-112-7/LSI-05-09-09		PC94-64-207.6	py	10.8	21.1	210.63	-0.07	199.80	21.1		
MIV-112-8/LSI-05-09-09		PC94-64-207.6	py	12.4	23.8	210.80	0.16	198.60	23.8		
MIV-112-10/LSI-05-09-09		PC94-64-207.6	sphal	11.6	22.9	179.05	-0.12	167.31		22.91	
MIV-112-11/LSI-05-09-09		PC94-64-207.6	sphal	11.4	22.3	183.76	-0.03	172.32		22.34	
MIV-112-12/LSI-05-09-09		PC94-64-207.6	sphal	11.1	21.5	113.97	0.14	102.98		21.46	
MIV-112-3/LSI-05-09-09		PC94-64-207.6	sphal	11.0	21.0	223.98	0.22	213.22		21.01	
MIV-112-4/LSI-05-09-09		PC94-64-207.6	sphal	12.0	23.1	235.96	0.17	224.11		23.14	
MIV-112-9/LSI-05-09-09		PC94-64-207.6	sphal	11.9	23.0	146.79	0.16	135.01		23.00	
MIV-113-1/LSI-05-09-09		PC94-64-207.6	sphal	10.5	20.3	93.39	0.06	83.00		20.28	
MIV-113-4/LSI-05-09-09		PC94-64-207.6	sphal	10.6	20.9	116.61	-0.08	105.92		20.86	
MIV-113-8/LSI-05-09-09		PC94-64-207.6	sphal	10.6	21.1	144.25	-0.19	133.45		21.07	
MIV-113-2/LSI-05-09-09		PC94-64-207.6	gn	9.6	18.9	143.39	-0.10	133.67			18.94
MIV-113-3/LSI-05-09-09		PC94-64-207.6	gn	9.7	19.0	138.22	-0.10	128.46			19.04
MIV-113-5/LSI-05-09-09		PC94-64-207.6	gn	10.6	20.0	104.03	0.34	93.81			19.96
MIV-113-6/LSI-05-09-09		PC94-64-207.6	gn	10.2	20.1	130.86	-0.10	120.58			20.05
MIV-113-7/LSI-05-09-09		PC94-64-207.6	gn	10.0	19.7	135.64	-0.13	125.54			19.71
								AVG.	**22.6**	**21.78**	**19.54**
MIV-113-12/LSI-05-09-10	MVT sulph, Root River Fm.	PC94-75-204.5	py	7.6	14.9	114.47	-0.08	106.81	14.9		
MIV-114-1/LSI-05-09-10	Sample of sparry dol-filled vugs	PC94-75-204.5	py	7.4	14.7	143.38	-0.19	135.82	14.7		
MIV-114-1/LSI-05-09-10	rimmed by py.	PC94-75-204.5	py	7.4	14.7	143.38	-0.19	135.82	14.7		
MIV-114-2/LSI-05-09-10		PC94-75-204.5	py	8.0	15.9	156.82	-0.14	148.64	15.9		
MIV-114-3/LSI-05-09-10		PC94-75-204.5	py	6.6	12.9	140.46	-0.07	133.83	12.9		
MIV-114-4/LSI-05-09-10		PC94-75-204.5	py	7.7	15.4	261.57	-0.18	253.66	15.4		
MIV-114-5/LSI-05-09-10		PC94-75-204.5	py	8.7	17.1	325.15	-0.08	316.38	17.1		
								AVG.	**15.1**		
MIV-124-8/LSI-05-09-11	SRS in OSw3-4.	PC94-82-496.1	py	12.2	23.7	243.85	0.03	231.71	23.7		
MIV-124-10/LSI-05-09-11	Aggregate of fg py and sphal with	PC94-82-496.1	py	12.7	24.9	345.18	0.01	332.45	24.9		

Appendix 1 continued.

Extraction / Lab Number	General Sample Description	Field Spl No.	Mineral	$\delta^{33}S_{VCDT}$	$\delta^{34}S_{VCDT}$	$\delta^{36}S_{VCDT}$	$\Delta^{33}S_{VCDT}$	$\Delta^{36}S_{VCDT}$	$\delta^{34}Spy$	$\delta^{34}Ssphal$	$\delta^{34}Sgn$
MIV-124-11/LSI-05-09-11	interstitial gn.	PC94-82-496.1	py	12.9	24.6	6528.93	0.31	6516.35	24.6		
MIV-124-12/LSI-05-09-11		PC94-82-496.1	py	12.7	24.8	1295.28	0.02	1282.59	24.8		
MIV-125-2/LSI-05-09-11		PC94-82-496.1	py	12.8	24.4	152.87	0.33	140.37	24.4		
MIV-125-3/LSI-05-09-11		PC94-82-496.1	py	12.9	25.2	106.73	0.05	93.83	25.2		
MIV-125-4/LSI-05-09-11		PC94-82-496.1	py	12.9	24.9	139.94	0.16	127.21	24.9		
MIV-124-9/LSI-05-09-11		PC94-82-496.1	sphal	11.7	22.8	124.19	-0.03	112.49		22.84	
MIV-124-4/LSI-05-09-11		PC94-82-496.1	gn	11.3	21.8	504.49	0.14	493.33			21.78
MIV-124-6/LSI-05-09-11		PC94-82-496.1	gn	9.9	19.3	242.76	0.05	232.88			19.27
MIV-124-7/LSI-05-09-11		PC94-82-496.1	gn	9.0	17.3	764.79	0.16	755.91			17.32
MIV-125-5/LSI-05-09-11		PC94-82-496.1	gn	10.9	20.5	380.46	0.40	369.97			20.45
								AVG.	**24.6**	**22.84**	**19.71**
MIV-118-7/LSI-05-09-12	SRS in OSw3-2.	PC95-97-79.1	py	11.7	22.9	312.65	-0.01	300.93	22.9		
MIV-118-8/LSI-05-09-12	Mas to semi-mas sulph comprised of	PC95-97-79.1	py	11.6	22.8	314.98	-0.05	303.32	22.8		
MIV-118-12/LSI-05-09-12	fg py (50%), reddish-brown sphal (35%)	PC95-97-79.1	py	10.5	20.0	131.75	0.26	121.49	20.0		
MIV-119-1/LSI-05-09-12	and gn; sphal partially replaced black chert	PC95-97-79.1	py	12.7	23.7	144.65	0.60	132.52	23.7		
MIV-119-06/LSI-05-09-12	nodules.	PC95-97-79.1	py	11.1	21.6	141.08			21.6		
MIV-119-07/LSI-05-09-12		PC95-97-79.1	py	12.1	23.6	109.28			23.6		
MIV-119-08/LSI-05-09-12		PC95-97-79.1	py	12.0	23.6	129.90			23.6		
MIV-119-11/LSI-05-09-12		PC95-97-79.1	gn	1.7	3.1	1025.89	0.09	1024.32			3.06
MIV-119-12/LSI-05-09-12		PC95-97-79.1	gn	2.4	4.0	12157.80	0.39	12155.76			3.96
								AVG.	**22.6**		**3.51**
MIV-111-10/LSI-05-09-13	Qz-Carb-Sulph vein in Road River Fm.	PC95-125-760	gn	10.0	19.6	427.42	-0.08	417.37			19.59
MIV-111-12/LSI-05-09-13	Qz-gn +/- sphal, tetra-tenn vein with late	PC95-125-760	gn	9.8	19.7	530.68	-0.26	520.60			19.67
MIV-111-6/LSI-05-09-13	cc blobs.	PC95-125-760	gn	11.1	21.6	3363.89	-0.04	3352.79			21.65
MIV-111-7/LSI-05-09-13		PC95-125-760	gn	10.8	20.4	763.49	0.32	753.01			20.45
MIV-111-8/LSI-05-09-13		PC95-125-760	gn	10.0	20.1	668.72	-0.25	658.43			20.07
								AVG.			**20.28**
MIV-108-10/LSI-05-09-14	SRS in OSw3-2.	PC93-23-249.7	py	11.9	23.5	263.41	-0.18	251.36	23.5		
MIV-108-11/LSI-05-09-14	Agg of fg py and cg sphal, and ga grains.	PC93-23-249.7	py	11.4	22.9	333.48	-0.35		22.9		
MIV-108-7/LSI-05-09-14	Composite section: Sphal 20%, Gn 5%,	PC93-23-249.7	sphal	12.5	24.6	348.50	-0.08	335.91		24.58	
MIV-108-9/LSI-05-09-14	50% Py, 1% white spar, approx 3% chert.	PC93-23-249.7	sphal	12.5	25.2	399.81	-0.35	386.92		25.18	
MIV-109-6/LSI-05-09-14		PC93-23-249.7	sphal	12.6	24.6	533.54	0.00	520.95		24.60	
MIV-108-12/LSI-05-09-14		PC93-23-249.7	gn	12.8	20.0	19.99	2.53				19.99
MIV-108-8/LSI-05-09-14		PC93-23-249.7	gn	11.5	22.6	196.59	-0.09	185.00			22.62
MIV-109-1/LSI-05-09-14		PC93-23-249.7	gn	10.4	20.1	500.55	0.04	490.23			20.14
MIV-109-4/LSI-05-09-14		PC93-23-249.7	gn	10.7	21.7	3150.17	-0.48	3139.03			21.75
								AVG.	**23.2**	**24.78**	**21.12**

Abbreviations: py, pyrite; sphal, sphalerite; gn, galena; carb, carbonates; cc, calcite; dol, dolomite; jasp, jasper; qz, quartz; sulph, sulphides; tetra-tenn, tetrahedrite-tennantite; fg, fine-grained; cg, coarse-grained; dolo, dolostone; agg, aggregate; diss, disseminated; Fm, formation; spl, sample, MVT, Mississippi Valley-type; SRS, stratabound replacement sulphides.

** not included in average

Appendix 2. Sulphur isotope compositions and per mil mineral fractionations, Prairie Creek deposit, NT.

Sample / LSI number	$\delta^{34}S_{py}$	σ	$\delta^{34}S_{sphal}$	σ	$\delta^{34}S_{gn}$	σ	$\Delta^{34}S_{py\text{-}sphal}$	TºC**	$\Delta^{34}S_{py\text{-}gn}$	TºC	$\Delta^{34}S_{sph\text{-}gn}$	TºC
PC01-130-313.5 / LSI-S-05-09-01	26.88		25.06				1.82	132				
Stratabound replacement sulphides in OSw3-2	24.45		23.11				1.34	199				
	24.00						*-0.08*	*ne*				
	24.72						*0.64*	*400*				
	26.08						*2.00*	*111*				
	26.08						*2.00*	*111*				
	24.05						*-0.03*	*ne*				
Average (Δ and T°C: disequilibrium data excluded):	**25.18**	**1.15**	**24.08**	**1.38**			***1.56***	***165***				
PC04-150-238.6 / LSI-S-05-09-02	24.27		24.79				-0.52	*ne*				
Stratabound replacement sulphides in OSw3-2	23.81		23.58				0.22	894				
	23.42		24.08				-0.66	*ne*				
	22.77		23.46				-0.69	*ne*				
	23.81		24.73				-0.93	*ne*				
			22.04				*1.58*	*162*				
			22.27				*1.35*	*198*				
			22.94				*0.68*	*390*				
			24.45				*-0.83*	ne				
			23.47				*0.15*	*1140*				
Average (Δ and T°C: disequilibrium data excluded):	**23.62**	**0.56**	**23.34**	**1.02**			***0.22***	***250***				
PC92-16-310.6 / LSI-S-05-09-03	21.32		21.27				0.05	*ne*				
Stratabound replacement sulphides in OSw3-2	22.05		22.67				-0.62	*ne*				
	22.31		22.50				-0.19	*ne*				
	22.94		22.71				0.24	*ne*				
	21.03		22.34				-1.31	*ne*				
	22.51						*0.21*					
Average (Δ and T°C: disequilibrium data excluded):	**22.47**	**1.63**	**22.30**	**0.59**			**0.23**	***ne***				
PC92-19-289.7 / LSI-05-09-04	23.73		18.44		18.76		5.30	*ne*	4.97	197	-0.32	*ne*
Stratabound replacement sulphides in OSw3-2	21.67		19.25		18.53		2.42	*78*	3.14	318	0.72	*ne*
	21.08		18.57		16.89		2.51	*72*	4.19	239	1.68	416
	21.12		21.06		16.34		0.06	*ne*	4.78	206	4.72	138
	21.47		20.46				1.01	*271*	3.84	261	*2.83*	253
	21.55		21.76				-0.21	*ne*	*-1.83*	ne	*4.13*	166
	21.98		20.80				1.18	*230*	*-1.40*	ne	*3.17*	229
	21.38		19.88				1.50	*173*	*-2.00*	ne	*2.25*	323
	21.47						*1.44*	*183*		ne		*ne*
Average (Δ and T°C: disequilibrium data excluded):	**21.72**	**0.80**	**20.03**	**1.20**	**17.63**	**1.20**	**1.72**	***148***	**4.18**	**239**	**3.42**	**210**
PC93-25-251.9 / LSI-05-09-05	24.04		23.42		19.51		0.62	*422*	4.53	219	3.92	178
Stratabound replacement sulphides in OSw3-2	24.17		22.96		19.90		1.21	*224*	4.27	234	3.06	238
	23.88		23.31		19.56		0.57	*452*	4.32	231	3.75	188
	24.24		23.85		19.66		0.39	*603*	4.59	216	4.20	163
	24.43		22.86				1.57	*155*	4.78	206	*3.21*	226
	24.48						*1.20*	*226*	*4.83*	203	*4.83*	133
	24.56						*1.28*	*210*	*4.91*	199	*4.91*	130
	24.50						*1.22*	*222*	*4.85*	202	*4.85*	132
	24.00						*0.72*	*372*	*4.35*	229	*4.35*	155
	24.25						*0.97*	*282*	*4.60*	215	*4.60*	143
Average (Δ and T°C: disequilibrium data excluded):	**24.25**	**0.24**	**23.28**	**0.40**	**19.65**	**0.17**	**0.97**	***282***	**4.60**	**215**	**4.17**	**164**

Appendix 2. Continued.

Sample / LSI number	$\delta^{34}S_{py}$	σ	$\delta^{34}S_{sphal}$	σ	$\delta^{34}S_{gn}$	σ	$\Delta^{34}S_{py\text{-}sphal}$	T°C**	$\Delta^{34}S_{py\text{-}gn}$	T°C	$\Delta^{34}S_{sph\text{-}gn}$	T°C
PC93-24-257.1 / LSI-S-05-09-06	23.65		23.56		15.36		0.09	*ne*	8.29	90	8.20	*39*
Stratabound replacement sulphides in OSw3-2	23.23		22.57		14.26		0.66	400	8.97	76	8.31	37
	23.34		23.33		10.76		0.01	*ne*	12.57	*ne*	12.57	*ne*
	23.21		22.44		12.57		0.77	350	10.64	*ne*	9.87	*ne*
	23.53		24.78		17.96		-1.25	*ne*	5.57	170	6.82	*69*
	23.65		22.49		15.63		1.16	235	8.02	97	6.86	68
	23.51		22.16		20.38		1.35	198	3.13	319	1.78	397
	24.50		22.94		16.03		1.57	163	8.47	87	6.90	*ne*
	23.60		24.05		10.80		-0.45	*ne*	12.80	*ne*	13.25	*ne*
			22.48				*1.10*	*249*			*7.80*	*47*
			23.87				*-0.29*	*ne*			*9.19*	*ne*
			23.03				*0.55*	*465*			*8.35*	*ne*
			23.52				*0.06*	*ne*			*8.84*	*ne*
			20.80				*2.78*	*70*			*6.12*	*88*
			21.06				*2.53*	*70*			*6.38*	*ne*
			23.89				*-0.31*	*ne*			*9.21*	*ne*
			22.03				*1.55*	166			*7.35*	*ne*
			22.65				*0.93*	294			*7.97*	*ne*
			23.14				*0.44*	*552*			*8.46*	*ne*
Average (Δ and T°C: disequilibrium data excluded):	**23.58**	**0.39**	**22.88**	**1.20**	**14.86**	**3.19**	**1.28**	**210**	**7.08**	**120**	**6.56**	**75**
PC93-35-224.8 / LSI-S-05-09-07	24.30		21.98				*ne*	86				
Stratabound replacement sulphides in OSw3-2	22.99		22.99				*ne*	*ne*				
	23.34		21.34				2.00	114				
	23.51		20.60				2.91	*ne*				
	22.35		21.68				0.67	395				
			21.20				*2.10*	*104*				
			21.36				*1.94*	*119*				
			21.76				*1.55*	*166*				
Average (Δ and T°C: disequilibrium data excluded):	**23.30**	**0.71**	**21.61**	**0.70**			**1.90**	**124**				
PC93-41-246.7 / LSI-05-09-08	21.79		23.86		15.81		-2.07	*ne*	5.97	*ne*	8.05	*ne*
Stratabound replacement sulphides in OSw3-4	20.36		22.42		15.18		-2.06	*ne*	5.18	*ne*	7.24	*ne*
	23.28		17.55		14.62		5.73	*ne*	8.66	*ne*	2.93	*ne*
	23.56		20.37				3.20	*ne*	*8.35*	*ne*	*5.16*	120
			20.18				*2.07*	*107*			*4.97*	128
			21.47				*0.78*	*346*			*6.26*	84
			23.11				*-0.86*	*ne*			*7.90*	*ne*
			23.01				*-0.76*	*ne*			*7.80*	*ne*
			22.36				*-0.11*	*ne*			*7.15*	*ne*
			21.07				*1.18*	*230*			*5.86*	*ne*
			22.72				*-0.47*	*ne*			*7.51*	*ne*
			24.22				*-1.97*	*ne*			*9.01*	*ne*
			22.53				*-0.28*	*ne*			*7.32*	*ne*
			23.16				*-0.91*	*ne*			*7.95*	*ne*
Average (Δ and T°C: disequilibrium data excluded):	**22.25**	**1.48**	**22.00**	**1.75**	**15.21**	**0.60**	**1.34**	*199*	**7.04**	121	**5.06**	124
PC94-64-207.6 / LSI-S-05-09-09	16.64		22.91		18.94		-0.31	*ne*	-2.30	*ne*	3.96	176
Stratabound replacement sulphides in OSw3-6	22.85		22.34		19.04		0.26	493	3.81	264	3.30	219
	21.12		21.46		19.96		1.14	*ne*	1.17	117	1.51	454

Appendix 2. Continued.

Sample / LSI number	$\delta^{34}S_{py}$	σ	$\delta^{34}S_{sphal}$	σ	$\delta^{34}S_{gn}$	σ	$\Delta^{34}S_{py\text{-}sphal}$	T°C**	$\Delta^{34}S_{py\text{-}gn}$	T°C	$\Delta^{34}S_{sph\text{-}gn}$	T°C
	23.81		21.01		20.05		1.60	53	3.76	267	0.95	*ne*
			23.14		19.71		*-2.03*	*ne*	*3.60*	*279*	3.43	209
			23.00				*-1.89*	*ne*	*3.46*	*290*	*3.46*	207
			20.28				*0.84*	324	*0.73*	*ne*	*0.73*	*ne*
			20.86				*0.25*	*ne*	*1.32*	*ne*	*1.32*	505
			21.07				*0.04*	*ne*	*1.53*	*ne*	*1.53*	449
Average (Δ and T°C: disequilibrium data excluded):	**22.60**	**1.36**	**21.78**	**1.07**	**19.54**	**0.52**	**1.19**	**228**	**3.16**	**316**	**2.83**	**258**
PC94-75-204.5 / LSI-S-05-09-10	14.92											
Mississippi Valley-type (MVT) sulph	14.74											
in Root River Fm.	14.74											
	15.94											
	15.94											
	12.91											
	15.41											
	17.09											
Average (Δ and T°C: disequilibrium data excluded):	**15.21**	**1.22**										
PC94-82-496.1 / LSI-05-09-11	23.71		22.84		21.78		0.87	313	1.93	481	1.06	176
Stratabound replacement sulphides in OSw3-4	24.88				19.27		*2.04*	109	5.61	169	3.58	199
	24.56				17.32		*1.72*	144	7.24	*ne*	5.52	107
	24.79				20.45		*1.95*	119	4.33	230	2.39	405
	24.43						*1.59*	160	5.16	188		
	25.19						*2.35*	83	5.92	157		
	24.85						*2.01*	113	5.58	170		
Average (Δ and T°C: disequilibrium data excluded):	**24.63**	**0.47**	**22.84**		**19.71**	**1.89**	**1.79**	**136**	**5.32**	**181**	**3.14**	**231**
PC95-97-79.1 / LSI-05-09-12	22.88				3.06				19.82	*ne*		
Stratabound replacement sulph in OSw3-2	22.76				3.96				18.80	*ne*		
	20.03								*16.52*	*ne*		
	23.69								*20.18*	*ne*		
	21.59								*18.08*	*ne*		
	23.61								*20.10*	*ne*		
	23.55								*20.04*	*ne*		
Average (Δ and T°C: disequilibrium data excluded):	**22.59**	**1.34**			**3.51**	**0.64**			**19.31**	*ne*		
PC95-125-760 / LSI-S-05-09-13					19.59							
Quartz-carbonate-sulph vein in Road River Fm					19.67							
					21.65							
					20.45							
					20.07							
					20.28	**0.84**						
PC93-23-249.7 / LSI-S-05-09-14	23.53		24.60		22.62		-1.07	*ne*	0.91	*ne*	1.98	362
Stratabound replacement sulphides in OSw3-2	22.90		24.58		21.75		*-1.05*	*ne*	*1.47*	*ne*	2.83	258
			25.18		20.14		*-1.65*	*ne*	*3.08*	*324*	5.04	125
					19.99				*3.23*	*310*	4.79	135
Average (Δ and T°C: disequilibrium data excluded):	**23.22**		**24.78**	**0.34**	**21.13**	**1.27**			**3.47**	**317**	**3.66**	**220**

** Isotopic equilibration temperatures based on Kajiwara and Krouse (1971)

NOTE: "ne" indicates a clear instance of non-equilibrium

Sulphides and nonsulphides of the Prairie Creek district; update on the isotope geochemistry

S. Paradis
Geological Survey of Canada, 9860 West Saanich Road, Sidney, BC, V8L 4B2
suzanne.paradis@NRCan-RNCan.gc.ca

Abstract

The Prairie Creek Zn-Pb-Ag district comprises three distinct types of carbonate-hosted sulphide mineralization that includes quartz-carbonate-sulphide veins, stratabound replacement sulphides, and classic Mississippi Valley-type. The surface portion of the veins (down to a depth of 200m at the mine site) has undergone extensive oxidation, forming zones rich in smithsonite, cerussite, azurite, malachite, anglesite and hydrozincite. The pyrite and sphalerite within the Mississippi Valley-type showings are oxidized to hematite/goethite and smithsonite, respectively. The stratabound replacement sulphide lenses, which do not outcrop, are not pervasively oxidized.

Here we report results of a stable isotope study of carbonates from all three types of mineralization and associated oxidation zones. The results indicate that oxidation occurred under supergene conditions from local meteoric waters that interacted with the host carbonates at low temperatures. The oxidation of sulphides and formation of nonsulphide Pb, Zn, Cu minerals postdates the Laramide orogeny and is continuing at the present time.

Introduction

The Prairie Creek Zn-Pb-Ag district in Northwest Territories (NT), Canada, is located in shales and carbonates of the Prairie Creek Embayment, a north-south (N-S) paleo-depression of the Selwyn Basin filled by Ordovician to Devonian platformal and basinal sediments (Figure 1). It hosts three distinct types of carbonate-hosted Zn-Pb-Ag sulphide mineralization: a) quartz-carbonate-sulphide veins, b) stratabound replacement sulphides (SRS), and c) classic Mississippi Valley-type (MVT) deposits (Fraser, 1996; Findlay, 2000; Paradis, 2007; AMC Mining Consultants, 2014). The surface and near-surface exposures of the vein and MVT occurrences have been extensively oxidized.

Herein we present a brief overview of the regional and mine geology, and focus on the mineralogy and isotope geochemistry (C, O, Sr) of the metal carbonates (referred to as nonsulphides in this paper) and their carbonate host rocks. The objectives of this paper are to 1) introduce the deposits for the benefit of companion papers of Stavinga et al. (2015), and Taylor et al. (2015), 2) clarify the model that explains the transformation from sulphide to nonsulphide

Recommended citation
Paradis, S., 2015. Sulphides and nonsulphides of the Prairie Creek district; update on the isotope geochemistry, *in* Paradis, S., ed., Targeted Geoscience Initiative 4: sediment-hosted Zn-Pb deposits: processes and implications for exploration; Geological Survey of Canada, Open File 7838, p. 134-151. doi:10.4095/296328

mineralization, and 3) document the effects of the chemical weathering that results in the formation of the supergene nonsulphide mineralization in periglacial regions and supports textural evidence for the supergene origin of nonsulphide deposits using stable isotope data.

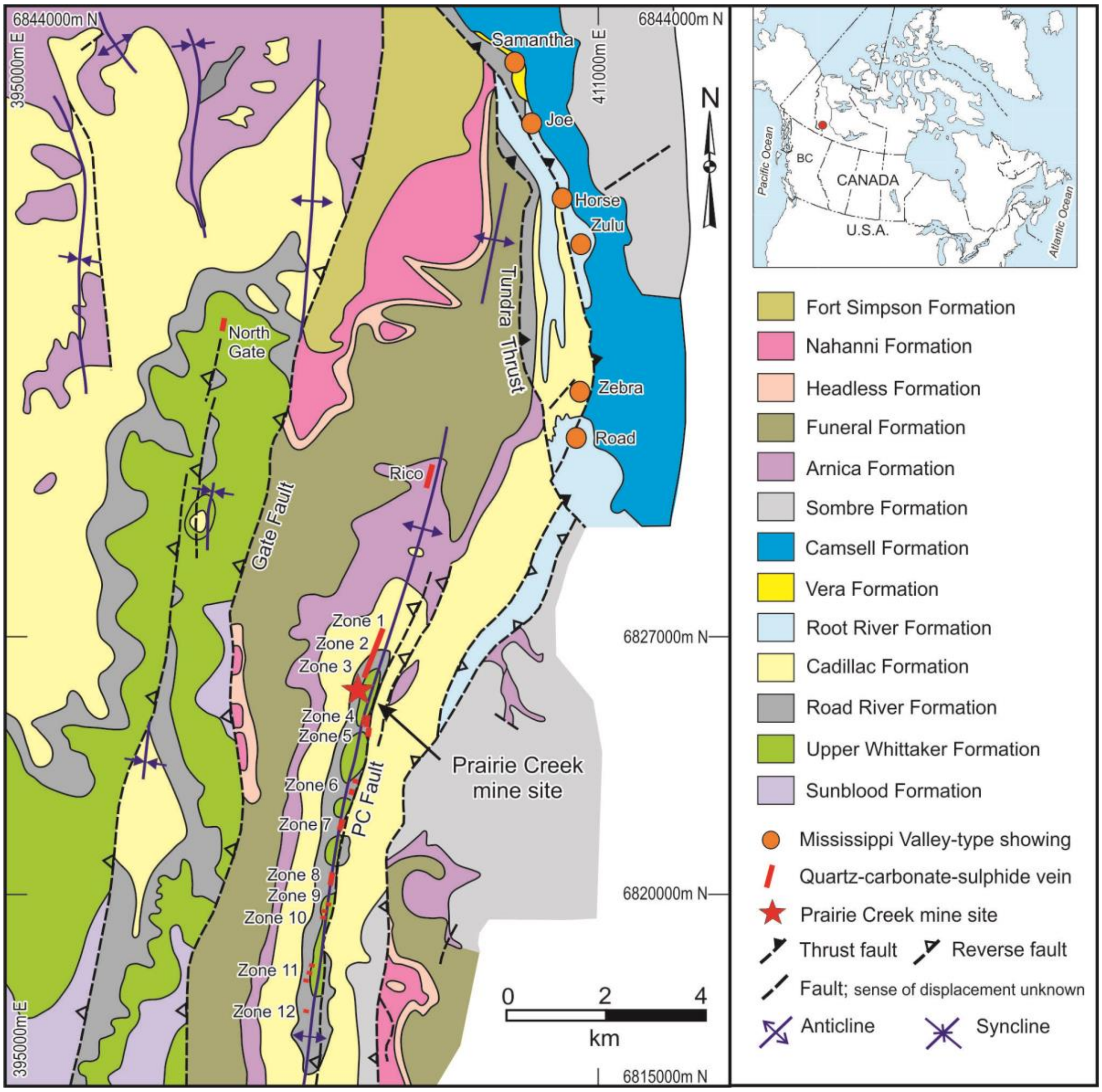

Figure 1. Geological map of the Prairie Creek deposit area showing the quartz-carbonate-sulphide vein system (zones 1 to 12), Rico, and North Gate, location of the mine site at zone 3, and location of the Mississippi Valley-type showings. According to Taylor (1995), the Zebra showing is hosted in a brecciated facies of the Cadillac Formation (i.e. Cadillac ET), which is a facies equivalent to the Root River Formation. The Samantha showing is associated with a 40°–trending and northwest-dipping normal fault, which brings the Vera Formation into contact with the Root River Formation. Note that the stratabound replacement mineralization, which does not outcrop, is not shown on this map (from Morrow and Cook, 1987; Canadian Zinc Corporation, http://www.canadianzinc.com).

Physiography, Vegetation and Climate

The Prairie Creek district is located in the Mackenzie Mountains that comprise low mountains (1200-1600m), with moderate to steep flanks and intervening narrow valleys. The Prairie Creek mine site is situated at an elevation of 850 m above mean sea level in an area characterized by an Alpine Forest-Tundra ecoregion of the Boreal Forest. Although located in Canada's north, the Prairie Creek district remained ice free and unaffected by Cordilleran Valley glaciers or the Laurentide Ice Sheet during the Late Pleistocene (Duk-Rodkin, et al., 2007), with the possible exception of meltwater flowing through the area (Duk-Rodkin, personal communication 2014). The Köppen-Geiger classification of the mine site's climate is sub-arctic (Peel et al., 2007). Mean summer and winter temperatures range between 10ºC to 14ºC and -15ºC to -26ºC, respectively. Most precipitation falls as rain during the summer months (approximately 300 mm, with total annual precipitation of 500 mm on average).

Geology

The district encompasses the lower to middle Paleozoic northwestern margin of Laurentia, comprising several geographically complex embayments that are inferred to have resulted from differential extension during early to mid-Paleozoic passive-margin subsidence. The Prairie Creek Embayment is located between the Mackenzie Platform and Selwyn Basin, at the transitional zone between basinal and platformal facies deposits. It is a north-south paleo-depression feature where thick accumulations of platformal carbonates and associated deep water basinal rocks occurred. It is bounded to the east by the east-dipping Tundra thrust fault, and 20 km to the west by the west-dipping Manetoe thrust fault (Morrow and Cook, 1987).

Morrow and Cook (1987) and Gordey and Anderson (1993) divided the lower to middle Paleozoic succession of Prairie Creek Embayment into four ascending subdivisions: 1) Sunblood Platform, 2) Mount Kindle-Root River Assemblage, 3) Prairie Creek Assemblage, and 4) Funeral-Headless Assemblage. The Sunblood Platform consists solely of the middle Ordovician shallow water argillaceous limestone and dolostone of the Sunblood Formation. The Late Ordovician to Devonian Mount Kindle-Root River Assemblage, which consists of the Whittaker, Road River, Cadillac, and Root River formations, hosts the sulphide and nonsulphide mineralization of the Prairie Creek district. The Whittaker Formation consists of three lithofacies: middle to upper Ordovician dark grey silty and sandy limestone, middle to upper Ordovician fine-grained quartzite, and upper Ordovician to Silurian laminated dark grey finely crystalline dolostone, which appears on Figure 1. The latter lithofacies is further subdivided into seven subunits (see Paradis, 2007). The Silurian-Devonian Road River Formation comprises a sequence of graptolite-bearing shale and argillaceous bioclastic shaly dolostone conformably overlying the Whittaker Formation. The Silurian-Devonian Cadillac Formation consists of carbonate-rich orange-weathering siltstone. The Silurian Root River Formation is a shelf equivalent of the basinal facies of the Cadillac Formation, and it consists of light grey vuggy micritic dolostone. The Silurian-Devonian Prairie Creek Assemblage is restricted to a local depression that was filled by the clastic Cadillac Formation and detrital components of the Sombre and Arnica formations. Gradual filling of the Prairie Creek Embayment was followed by deposition of the Funeral-Headless Assemblage marking the return to a simpler shelf to basin transition by the Middle Devonian (Morrow and Cook, 1987; Falck, 2007). For more information on these formations, and those shown on Figure 1 and not mentioned here (i.e. Vera, Camsell, Nahanni and Fort Simpson) see Morrow and Cook (1987).

The dominant structures in the Prairie Creek district are doubly plunging folds (Figure 1) with north-south trending fold axes which are cut by steeply dipping wrench faults that were subsequently rejuvenated as high angle reverse faults (Morrow and Cook, 1987). The reverse faults are post-dated by prominent north-trending nearly flat thrust faults, which occur primarily in the platform carbonates flanking the embayment (Morrow and Cook, 1987), and are related to regional compression during the Laramide Orogeny. Two major thrusts, the Tundra Thrust to the east (Figure 1) and the Manetoe Thrust 20 km to the west (not shown on Figure 1), define the present margins of the Prairie Creek Embayment (Morrow and Cook, 1987). In the immediate area of the Prairie Creek mine site (i.e. zone 3; Figure 1), faulting and folding axes trend north-south, resulting in windows of Road River shales and dolostones of the Whittaker Formation being exposed along the core of the Prairie Creek anticline. The anticline is structurally bounded to the east by the Prairie Creek (PC) Fault and to the west by the Gate Fault. These faults are presently north-south striking, reverse west-dipping (65° to 90°) structures that could have been originally normal faults (Earls, 1995; Fraser, 1996). The Prairie Creek Fault is a steeply dipping reverse fault that is up to 40 m in thickness and has a 1500 m displacement (Morrow and Cook, 1987).

All rocks in the study area have been compacted, lithified during burial, and subjected to increased heat and pressure during the Laramide Orogeny (latest Cretaceous to Eocene; Falck, 2007) and reached a maximum of prehnite-pumpellyite (sub-greenschist) facies). Foliation and cleavage are poorly developed, except in pelitic rocks that are characterized by a slaty cleavage.

Mineralization

The quartz-carbonate-sulphide vein mineralization was discovered in 1928 by Poole Field and was first described by Thorpe (1972). The SRS were discovered by Canadian Zinc Corporation (CZN) in 1992, while surface drilling was being carried out to extend the quartz-carbonate-sulphide vein resources at depth. In 1970, the Samantha showing, the first of the MVT showings was discovered, followed by the Joe showing in 1981 and the other ones in 1993 (Taylor, 1995). For the purpose of this paper, the various types of mineralization are presented and described here as they have been in previous studies (Fraser, 1996; Findlay, 2000; Paradis, 2007; AMC Mining Consultants, 2014).

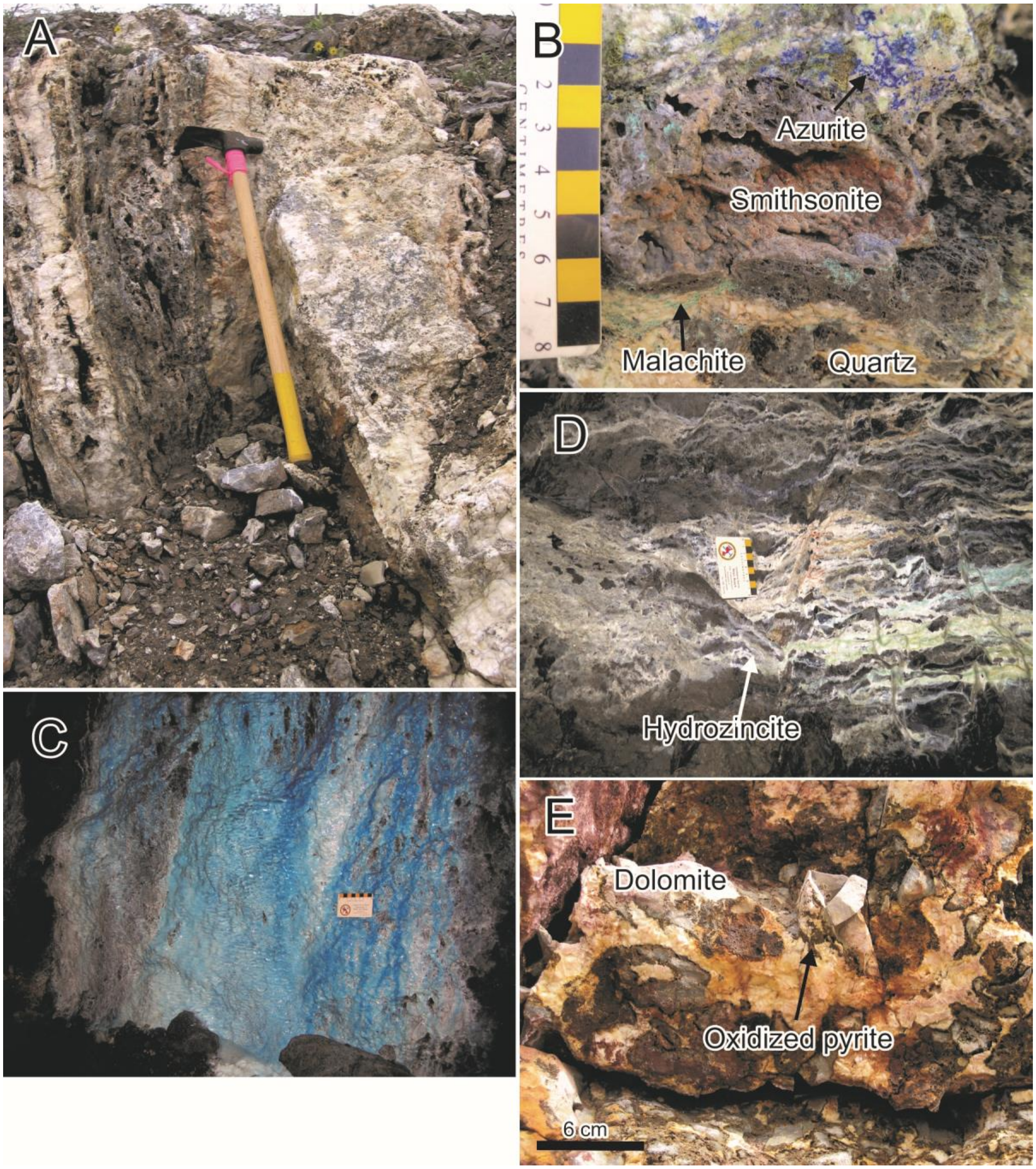

Figure 2. Field photos A) Photograph of the quartz-carbonate-sulphide vein exposure at zone 8 of the Prairie Creek deposit. B) Close-up view of the quartz-carbonate-sulphide vein exposure at zone 8. C) and D) Underground exposures of the quartz-carbonate-sulphide vein at the Mine site (zone 3) showing azurite (C) and hydrozincite (D) precipitating on the walls of the 930 level mine adit. E) Photograph of sparry dolomite filling cavities and oxidized pyrite rimming dolostone fragments at the Zebra showing (Mississippi Valley-type).

Quartz-carbonate-sulphide veins

The quartz-carbonate-sulphide veins are exposed in 12 showings (zones 1 to 12) along a N-S trending 16 km-long corridor (Figure 1). They strike approximately 320 to 360° and dip between 40° east to vertical (Canadian Zinc Corporation, 2010), and fill fractures parallel to regional-scale faults crosscutting the Lower Paleozoic strata (dolostones of the Upper Whittaker Formation, shales of the Road River Formation and dolostones of the Cadillac and Arnica formations) and the SRS. The veins are not folded but they are strongly sheared and brecciated.

The main sulphides within the veins are sphalerite and galena and they are accompanied by lesser concentrations of pyrite and tetrahedrite-tennantite. The sulphides form massive aggregates and disseminations in quartz, calcite, and locally dolomite gangue. In near-surface portions of the veins, sulphides were largely converted to smithsonite, cerussite, azurite, malachite, anglesite, and hydrozincite (Figure 2a, b). Stavinga (2014) and Stavinga et al. (2015) also detected a variety of arsenates [segnitite $PbFe_3^{3+}H(AsO_4)_2(OH)_6$, arsentsumebite $Pb_2Cu(AsO_4)(SO_4)(OH)$, beudantite $PbFe_3^{3+}(AsO_4)(SO_4)(OH)_6$, mimetite $Pb_5(AsO_4)_3Cl$, adamite $Zn_2(AsO_4)(OH)$, duftite $PbCu(AsO_4)(OH)$, bayldonite $Pb(Cu,Zn)_3(AsO_4)_2(OH)_2$], Pb-Sb-sulphide (bournonite $PbCuSbS_3$), Pb-Sb-oxide (bindheimite $Pb_2Sb_2O_6(O,OH)$), other sulphides (acanthite Ag_2S, cinnabar HgS, and covellite CuS), Fe-(oxy)hydroxide (goethite $Fe^{3+}O(OH)$), and sulphates (barite $BaSO_4$, christelite $Zn_3Cu_2(SO_4)_2(OH)_6{\cdot}4H_2O$) in minor amounts.

Nonsulphide zones are developed preferentially at the surface but they may extend to depths of 200 m below the surface. Figure 3 illustrates the distribution of PbO + ZnO (wt.%) within the quartz-sulphide vein system of zone 3 (Prairie Creek mine site), which reflects the oxidation of the primary sulphides (sphalerite, galena and tetrahedrite-tennantite). At the other zones, the depth of oxidation has not been determined. Within the underground exposures of zone 3, nonsulphides (mainly iron oxides, azurite, hydrozincite, and malachite) are developed along fractures and coat exposed walls (Figure 2c, d). In the underground workings, about 15-20% of the lead sulphides and 10% of the zinc sulphides have undergone oxidation (pHase Geochemistry, 2010) forming mixed ore (as defined by Simandl and Paradis, 2009). At the surface, all sulphides are variously oxidized. Sphalerite alters to smithsonite (Figure 4a, b), which forms spectacular botryoidal growths of many colours (medium to pale green, blue-green, brown, red, orange, yellow-off-white, and colourless) within the vein system. Galena alters to cerussite (Figure 4c, d) and/or anglesite, which form alteration rims. All of these secondary minerals also fill fractures and voids. Goethite replaces pyrite and forms rims around it, or completely pseudomorphoses it. Cerussite, smithsonite, arsenates, and Pb-Sb oxide commonly precipitate along the edges of altered pyrite (Stavinga, 2014). Tetrahedrite-tennantite oxidized mainly into Cu-carbonates (azurite, malachite), arsenates, bindheimite, and christelite (Stavinga, 2014). Several of the oxidation phases derived from tetrahedrite-tennantite coexist with cerussite, smithsonite, and anglesite as inclusions and precipitates along crystal boundaries, or they occur disseminated within the oxidized vein material. Covellite is locally present as a partial rim around galena, or it can be an intergrowth with anglesite, cerussite, and smithsonite (Figure 4e).

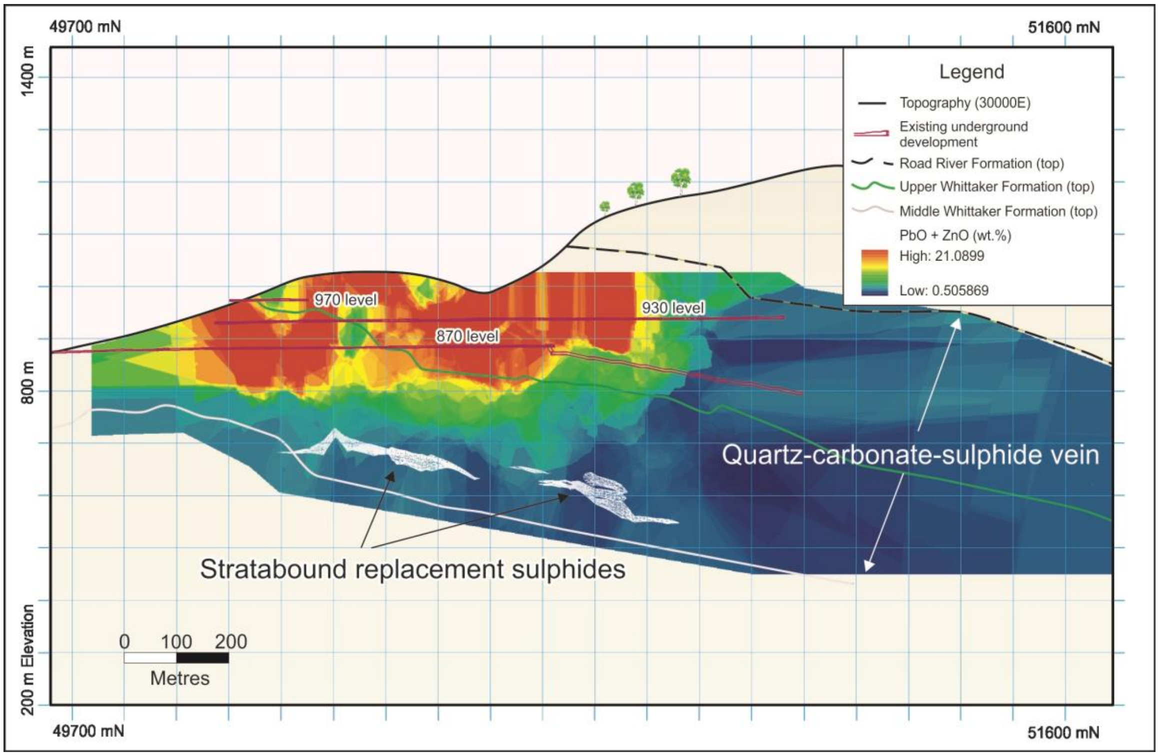

Figure 3. NNE-SSW longitudinal section (viewing along 30000E) illustrating the PbO + ZnO (wt.%) within the quartz-sulphide vein system at the Prairie Creek Mine site (zone 3). The coordinates are in NAD 1983 UTM Zone 10N. Figure was draw by K. Cupit from Canadian Zinc Corporation, and it is included here courtesy of Canadian Zinc Corporation.

Stratabound replacement sulphides (SRS)

The SRS, which do not outcrop, have been located by drilling in zones 3, 4, 5, and 6 along a strike length of more than 3 km. They form lenses replacing various dolostone facies of the Upper Whittaker Formation. The largest lens (SD1) has a minimum lateral dimension of 400 m by 100 m and a maximum thickness of 28 m (Earls, 1995; Findlay, 2000); it preferentially replaces the mottled dolostone unit (OSw3-2; see Paradis, 2007).

The SRS zones consist of pyrite, sphalerite, galena, and trace amount of tetrahedrite-tennantite in a gangue of quartz, dolomite, and calcite. The textures are complex ranging from complete to partial replacement of the dolostone by fine- to coarse-grained massive aggregates of pyrite, yellowish to pinkish sphalerite and galena to fine-grained laminated sulphides to rare open-space cavity-fill textures that resemble MVT style mineralization.

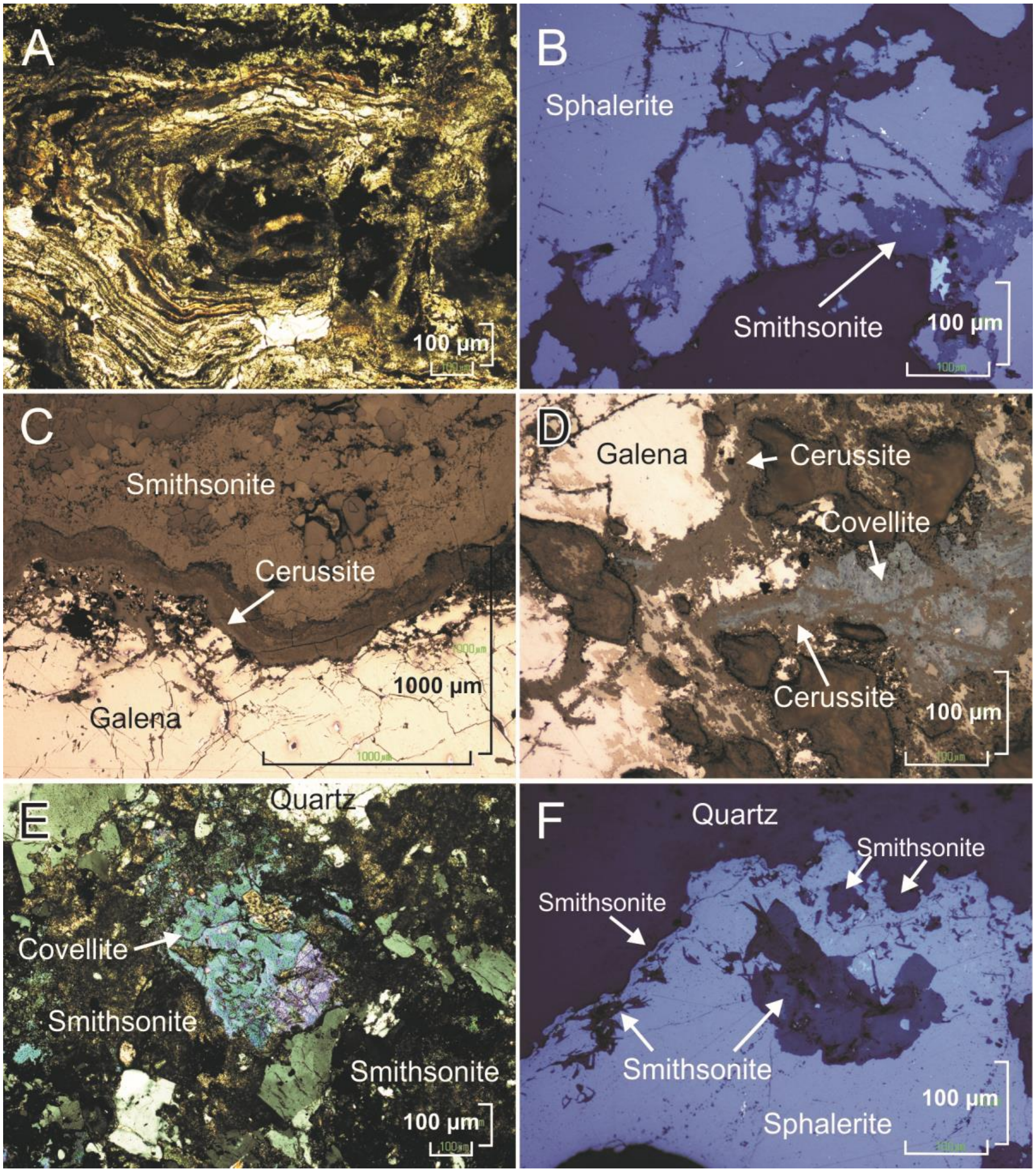

Figure 4. Photomicrographs of the oxide mineralization. A) Botryoidal growths of smithsonite in quartz-carbonate-sulphide vein, sample Z8-S7A, transmitted light. B) Smithsonite altering sphalerite in quartz-carbonate-sulphide vein, sample PCU07-21 at 98.7, reflected light. C) Cerussite forming a rim on galena in quartz-carbonate-sulphide vein, sample Z8-S7A, reflected light. D) Cerussite altering galena and intergrown with covellite in quartz-carbonate-sulphide vein, sample Z8-S7A, reflected light. E) Covellite in groundmass of smithsonite in quartz-carbonate-sulphide vein, sample S8, crossed polars. F) Smithsonite filling cavity in sphalerite and altering it along the edge and fractures of grain in stratabound replacement sulphide zone, sample PC11-209A at 209.67, reflected light.

SRS contain low concentrations of nonsulphide minerals relative to the quartz-carbonate-sulphide veins (Paradis, 2007; Canadian Zinc Corporation, 2010). However, when oxidation is present, it occurs as fracture- and void-fillings, and local replacement of sphalerite, galena, and pyrite. Sphalerite is locally altered to smithsonite along the edges and fractures of the grains (Figure 4f), and galena is partially altered to anglesite and/or cerussite. Pyrite is partially replaced by goethite.

Mississippi Valley-type sulphides

The MVT showings are discontinuously exposed over a distance of approximately 12 km in the coarse biohermal reefs and breccias of the Root River Formation (Figure 1). They are referred to, from north to south, as Samantha, Joe, Horse, Zulu, Zebra and Road showings. They consist of pyrite, sphalerite, and minor galena that form colloform textures rimming dolostone fragments in open-space breccias filled by sparry and saddle white dolomite, and crustiform pyrite-sphalerite veinlets crosscutting the dolostone (Figure 2e). Pyrite is commonly oxidized to hematite/goethite, and sphalerite is locally replaced by smithsonite. Malachite was observed in the trenches of some showings (e.g. Samantha).

Results/Data Analysis

Carbon, Oxygen, and Strontium Isotopes

Analytical Methods

Carbon and oxygen isotope analyses were done on pure carbonate phases at Delta-Lab of the Geological Survey of Canada in Québec City and at the G.G. Hatch Stable Isotope Laboratory of the University of Ottawa. Carbonate mineral species are reacted under vacuum at either 25.0°C or 50.0°C with anhydrous phosphoric acid to release CO_2 (McCrea, 1950). Isotopic ratios are converted by their respective fractionation factors. Results are reported in conventional per mil notation (‰) relative to Vienna Pee-Dee Belemnite (VPDB) and VSMOW standards. Precision, based on replication of international and internal standards, is ±0.1‰ for carbon and oxygen isotope analyses.

Strontium isotope analyses were done by Brian Cousens on dolomite and calcite at the Isotope Geochemistry and Geochronology Research Facility (IGGRF) of Carleton University, and by B. Davis at the geochronology laboratories of the Geological Survey of Canada. Splits of powder samples used for C and O isotope analyses were treated for Sr separation by standard ion exchange techniques. Mass spectrometry was performed on a ThermoFinnigan Triton thermal ionization (TI) mass spectrometer. Isotope ratios were normalized to $^{86}Sr/^{88}Sr = 0.11940$ to correct for fractionation and are presented relative to a value of 0.708043 for the NIST Standard Reference Material, Eimer and Amend (E&A) $SrCO_3$. Uncertainty in $^{87}Sr/^{86}Sr$ is expressed as ±2 sigma of the mean, equivalent to two standard errors (2σ).

Results

Averages of carbon, oxygen, and strontium isotope analyses are presented in Table 1, and the results are illustrated in Figure 5a and b. The complete data set will be published in a separate paper (Paradis et al., 2015b).

Dolostone of the Upper Whittaker Formation has $\delta^{18}O_{VPDB}$ and $\delta^{13}C_{VPDB}$ values ranging from -10.5 to -5.8‰ and -2.0 to 1.4‰, respectively. Argillaceous dolostone of the Road River Formation form a tight cluster on Figure 5a with $\delta^{18}O_{VPDB}$ and $\delta^{13}C_{VPDB}$ values ranging from -6.6 to -5.3‰ and -0.6 to 0.4‰, respectively. Dolostone of the Root River Formation have $\delta^{18}O_{VPDB}$ values of -7.2 to -5.3‰ and $\delta^{13}C_{VPDB}$ values of -1.4 to 1.7‰. The O and C values of these carbonates are similar to those of Ordovician and Silurian marine carbonates obtained by Veizer et al. (1999). Most samples from the Upper Whittaker Formation have $^{87}Sr/^{86}Sr$ values higher than 0.7120, which defines the "Maximum Sr Isotope Ratio of Basinal Shale" (MASIRBAS; Machel and Cavell, 1999) in the Cordillera (Figure 5b). They are also higher than Ordovician-Silurian marine carbonates (0.7078-0.7095; Veizer et al., 1999). The one sample from the Root River dolostone and one sample of the Upper Whittaker Formation taken west of the Gate Fault plot below MASIRBAS, similar to values published for the Western Canada Sedimentary Basin (WCSB), Presqu'ile barrier, and other dolostones of the northern Rocky Mountains (Paradis, 2007). $^{87}Sr/^{86}Sr$ values for the non-mineralized Upper Whittaker dolostone are variable; however they increase in proximity to the SRS mineralization (Fraser, 1996; Paradis, 2007).

Dolomite gangue associated with the SRS has $\delta^{18}O_{VPDB}$ values ranging from -6.9 to -14.9‰ and $\delta^{13}C_{VPDB}$ values ranging from -4.7 to -2.3‰. These values are lower in $\delta^{13}C_{VPDB}$ but similar in $\delta^{18}O_{VPDB}$ values (except for two samples with low $\delta^{18}O_{PDB}$ values of -12.2 and -14.9‰) to the host dolostone of the Upper Whittaker Formation. Their $^{87}Sr/^{86}Sr$ ratios (0.7138 to 0.7239**)** are similar to the host dolostone of the Upper Whittaker Formation that are in proximity to the stratabound replacement zones. All these values are more radiogenic than Ordovician-Silurian marine carbonates (0.7078-0.7095; Veizer et al., 1999).

Dolomite gangue associated with the quartz-carbonate-sulphide veins has variable $\delta^{18}O_{VPDB}$ values of -7.3 to -15.3‰, $\delta^{13}C_{VPDB}$ values of 0.3 to -6.3‰, and $^{87}Sr/^{86}Sr$ values of 0.7096 to 0.7285 (Table 1).

Sparry dolomites associated with MVT showings have $\delta^{18}O_{VPDB}$ values ranging from -17.6 to -10.7‰ and $\delta^{13}C_{VPDB}$ values ranging from -7.2 to -1.0‰ with a broad co-variance between the $\delta^{13}C$ and $\delta^{18}O$ values. Their $^{87}Sr/^{86}Sr$ values (0.7105 to 0.7127) plot in a small field on Figure 5; they are slightly more radiogenic than Silurian marine carbonates (0.7079-0.7088; Veizer et al., 1999), but they are similar to values of the coarse crystalline dolomite associated with the Manetoe facies in the Mackenzie Mountains, and the MVT Zn-Pb Robb Lake deposit in the northern Rocky Mountains (see Paradis, 2007).

Table 1. Oxygen, carbon, and strontium isotope values, Prairie Creek district, NT.

	$\delta^{13}C_{(VPDB)}$	$\delta^{18}O_{(VPDB)}$	$\delta^{18}O_{(VSMOW)}$	$^{87}Sr/^{86}Sr$
Dolostone of the Whittaker Formation				
Number of samples	36	36	36	9
Range	-2.0 to 1.4	-10.5 to -5.8	20.1 to 24.9	0.7096 to 0.7267
Average	-0.1	-8.2	22.5	0.7191
Standard deviation	0.7	1.3	1.3	0.0057
Argillaceous dolostone of the Road River Formation				
Number of samples	5	5	5	
Range	-0.6 to 0.4	-6.6 to -5.3	24.0 to 25.4	-
Average	0.2	-6.2	24.5	-
Standard Deviation	0.4	0.5	0.6	-
Dolostone of the Root River Formation				
Number of samples	8	8	8	1
Range	-1.4 to 1.7	-7.2 to -5.4	23.4 to 25.3	0.7093
Average	0.8	-6.1	24.5	0.7093
Standard Deviation	1.0	0.7	0.7	-
Dolomite gangue associated with stratabound replacement sulphides				
Number of samples	15	15	15	11
Range	-4.7 to -2.3	-14.9 to -6.9	15.5 to 23.8	0.7138 to 0.7239
Average	-3.0	-8.9	21.7	0.7184
Standard Deviation	0.6	2.1	2.2	0.0035
Dolomite gangue associated with quartz-carbonate-sulphide veins				
Number of samples	4	4	4	3
Range	-6.3 to 0.3	-15.3 to -7.3	15.2 to 23.4	0.7096 to 0.7252
Average	-3.1	-12.3	18.2	0.7211
Standard Deviation	2.7	3.6	3.7	0.0101
Dolomite gangue associated with Mississippi Valley-type deposits				
Number of samples	10	10	10	6
Range	-7.2 to -1.0	-17.6 to -10.7	12.7 to19.8	0.7105 to 0.7127
Average	-3.3	-14.6	15.9	0.7117
Standard Deviation	1.9	2.1	2.1	0.0009
Smithsonite associated with quartz-carbonate-sulphide veins				
Number of samples	14	14	14	1
Range	-5.8 to -3.5	-16.7 to -15.1	13.6 to 15.3	0.7254
Average	-4.5	-16.0	14.3	-
Standard Deviation	1.0	0.9	0.9	-
Cerussite				
Number of samples	1	1	1	
Range	-8.6	-16.8	13.5	-

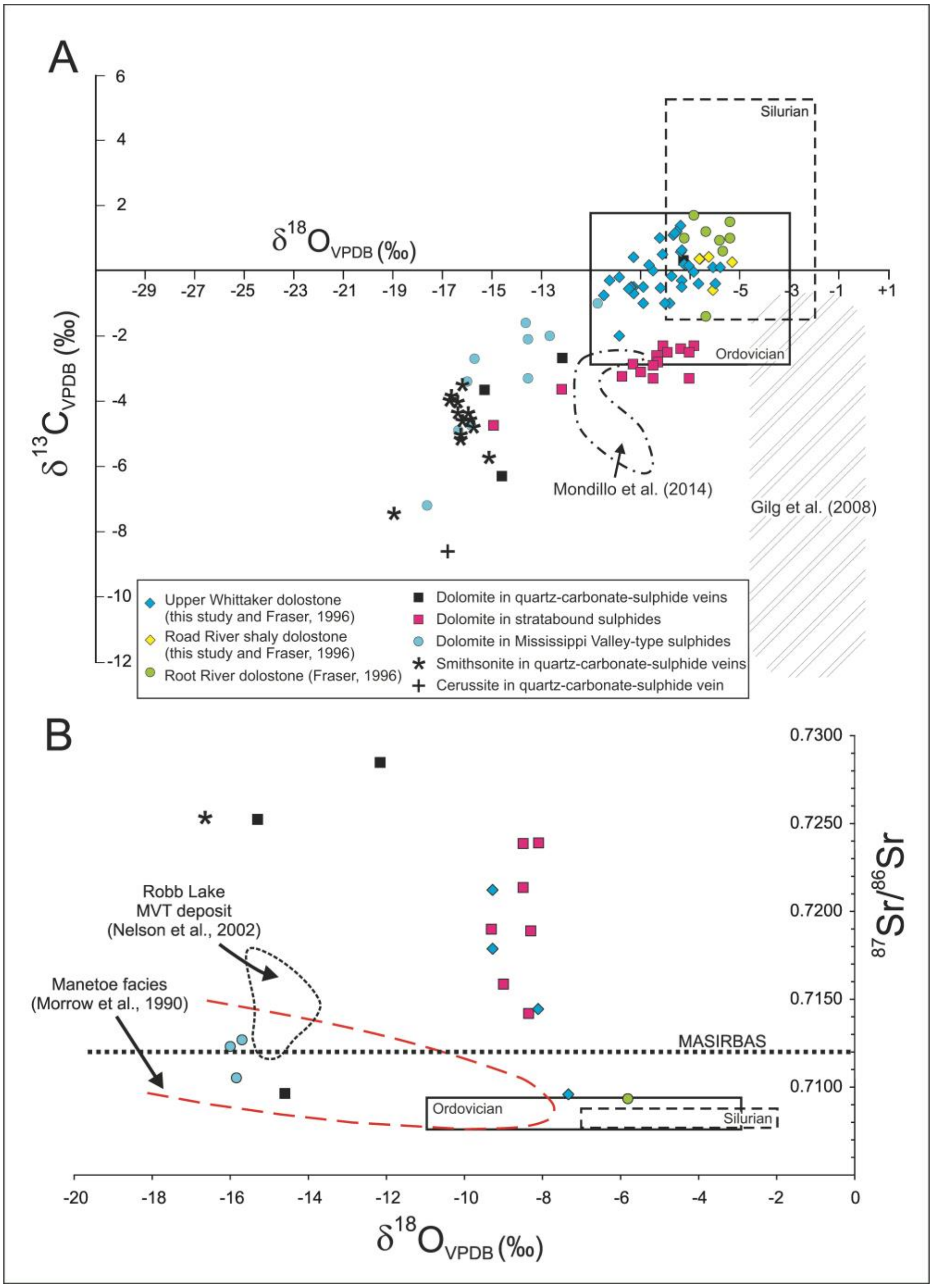

Figure 5. A) Plot of $\delta^{18}O_{VPDB}$ and $\delta^{13}C_{VPDB}$ values of the host dolostones, and dolomite, smithsonite, cerussite associated with SRS, quartz-carbonate-sulphide veins, and MVT mineralization. The fields for supergene smithsonite from the Jabali deposit (Yemen; Mondillo et al., 2014) and from the compilation of Gilg et al. (2008) are shown for comparison. B) $^{87}Sr/^{86}Sr$ versus $\delta^{18}O_{VPDB}$. Fields of Ordovician and Silurian marine carbonate values are from Veizer et al. (1999). The fields for coarsely crystalline dolomite associated with the Robb Lake Zn-Pb MVT deposit in the northern Rocky Mountains and the Manetoe hydrothermal facies in the Mackenzie Mountains are shown for comparison. Maximum Sr isotope ratio of basinal shale (MASIRBAS) is from Machel and Cavell (1999).

Smithsonite samples from the quartz-carbonate-sulphide veins have a narrow range of $\delta^{18}O_{VPDB}$ values (-16.7 to -15.1‰) and $\delta^{13}C_{VPDB}$ values of -5.8 to -3.5‰. One sample that consists of a mixture of smithsonite and cerussite has $\delta^{18}O_{VPDB}$ value of -18.9‰ and $\delta^{13}C_{VPDB}$ values of -7.5‰. The $\delta^{18}O_{VPDB}$ and $\delta^{13}C_{VPDB}$ ratios of a single cerussite sample (courtesy of Drew Stavinga) are -16.9‰ and -8.6‰, respectively. One smithsonite sample has a $^{87}Sr/^{86}Sr$ value of 0.7254.

Models/Discussion

Prairie Creek district is unusual because it hosts 3 types of carbonate-hosted Zn-Pb-Ag deposits (veins, SRS and MVT). Outcropping and near-surface portions of the vein and MVT sulphides have undergone extensive oxidation with the precipitation of smithsonite, cerussite, azurite, malachite, and anglesite as the main nonsulphide minerals. Other secondary metal carbonates, arsenates, and sulphides are present as accessories (Stavinga, 2014). Oxidation is not as well developed in the SRS compared to the veins and MVT deposits because the SRS lenses occur at depth (on average more than 200 m below the surface).

The age of the oxidation process is uncertain, but indirect geological evidences suggest that it may have started forming after the Laramide Orogeny (latest Cretaceous to Eocene) and is still ongoing. Nonsulphides worldwide typically formed between 11ºC to 35ºC (Boni et al., 2003; Gilg et al., 2008), in warm to temperate climatic conditions. Several warmer climatic periods (warmer than today) occurred during the Cenozoic (Lower Oligocene and Lower to Middle Miocene, Pliocene, and Holocene) providing conditions that were favourable for supergene oxidation of sulphides. It has been suggested that nonsulphide deposits in southern and central British Columbia (BC) started forming before or slightly after the last glacial maximum (~14,500 ^{14}C yr BP), with the best climatic conditions occurring around 10,000–7,000 ^{14}C yr BP (Paradis et al., 2011; Paradis et al., 2015a). Similar ages have been postulated for supergene nonsulphide deposits in the northern Canadian Cordillera with ^{14}C dating of the supergene Zn deposit at Howards Pass, Yukon, established to be younger than 9610 ± 100 ^{14}C yr BP, i.e. Holocene in age (Jonasson et al., 1983). This can also be the case for the nonsulphide minerals at Prairie Creek. Additionally, the Prairie Creek district seems to have escaped the last glaciation events during the Late Pleistocene (Duk-Rodkin, personal communication, 2014), and this would explain the excellent preservation of the nonsulphide zones.

The C and O isotopic composition of unaltered dolostones of the Upper Whittaker dolostone, Root River shaly dolostone and Road River dolostone form overlapping clusters within the field of Ordovician carbonates (Figure 5a) in agreement with a sedimentary origin. Dolomite gangue from Mississippi Valley-type deposits form a trend originating in the field of Ordovician carbonates and showing progressively lower $\delta^{18}O_{VPDB}$ and $\delta^{13}C_{VPDB}$ ratios. Dolomites from the quartz-carbonate-sulphide veins also plot along this trend, and those from the stratabound replacement sulphide zones follow a similar trend. These trends suggest that dolomite gangue formed from fluids that equilibrated with the host rocks. With the exception of two samples, gangue dolomite from SRS has the same $\delta^{18}O_{VSMOW}$ values as the Upper Whittaker dolostone, but lower $\delta^{13}C_{VPDB}$ values, which indicate a mixed contribution of inorganic carbon from the Whittaker dolostone and another source. Smithosonite and cerussite from the quartz-carbonate-sulphide veins have negative $\delta^{18}O_{VSMOW}$ and $\delta^{13}C_{VPDB}$ values (Figure 5a), coinciding with the most negative $\delta^{18}O_{VPDB}$ and $\delta^{13}C_{VPDB}$ of the dolomites from the mineralized veins confirming that the supergene fluids gradually equilibrated with the carbonate-hosted mineralized veins. Smithsonite from quartz-carbonate-sulphide veins at Prairie Creek has lower $\delta^{18}O_{VSMOW}$ values than those of supergene smithsonite worldwide (compilation of Gilg et al., 2008; and data of Mondillo et al., 2014) but their $^{13}C_{VPDB}$ values overlap (Figure 5a). The narrow range in $\delta^{18}O_{VSMOW}$ values of smithsonite from Prairie Creek is characteristic of supergene smithsonite worldwide and indicates equilibration with meteoric waters (Gilg et al., 2008). It also suggests a constant formation temperature and a single meteoric fluid source. The wide range of $\delta^{13}C_{VPDB}$ values are explained by a different provenance of the carbon within the supergene fluids. In the Prairie Creek case, $\delta^{13}C$ values indicate a contribution of inorganic carbon from the host rock carbonates.

Using the oxygen isotope fractionation equation for water and smithsonite of Gilg et al. (2008):

$$\ln \alpha_{\text{smithsonite-water}} = 3.10\ (10^6/T^2) - 3.50$$

the calculated formation temperature of smithsonite can be approximated. Precipitated water in northern Canada is strongly depleted in ^{18}O because water vapor in high latitudes contains less ^{18}O as a result of preferential rainout of the heavy isotope during the transfer of air masses from low to high latitudes (Rozanski et al., 1993; Bowen and Wilkinson, 2002; Delavau et al., 2011). In Yellowknife, for example, present day's annual $\delta^{18}O_{VSMOW}$ value is ~ -21.2‰ with average values around -16.4‰ in summer and -24‰ in winter [Canadian Network for Isotopes in Precipitation (CNIP) database]. This high variability in $\delta^{18}O_{VSMOW}$ values is strongly dependent on temperature, as the sub-arctic region is subjected to strong temperature contrasts between summer (10ºC to 14ºC and winter months (-15ºC to -26ºC). If we use the average $\delta^{18}O_{VSMOW}$ value of -21.2‰ for the meteoric water, calculated precipitation temperature for the smithsonite would be around 9ºC, which is low compare to typical precipitation temperatures of nonsulphides worldwide (11ºC to 23ºC, Gilg et al., 2008; 20ºC to 35ºC; Boni et al., 2003), but comparable to temperatures obtained for the precipitation of supergene smithsonite at the Reef Creek deposit in Alaska (Santoro et al., 2014). If we assume that smithsonite (and the other nonsulphides) precipitated during the summer months, the calculated precipitation temperatures are around 29ºC, which is also realistic for supergene minerals precipitating in the vadose zone. If the nonsulphides started forming immediately after the Laramide orogeny at around 55 Ma, the average $\delta^{18}O_{VSMOW}$ values of the meteoric waters would be less negative due to warmer climate than today, and the resulting temperature of formation could be higher than 29ºC. This supports the hypothesis that nonsulphides can form and be preserved in the sub-arctic regions of Canada. Overall, the absence of glaciation favours preservation of the nonsulphide mineralization; but nonsulphide deposits with favourable morphology and orientation would survive the glaciation regardless (Simandl and Paradis, 2009). Other glaciated areas in the world previously regarded as unfavourable may be prospective for nonsulphide deposits.

Implications for Exploration

The characterization of the carbonate-hosted nonsulphide Zn-Pb deposits is essential for the formulation of integrated exploration programs targeting these deposits across Canada, and for understanding and facilitating eventual mineral processing. Zinc or lead oxides, silicates and carbonates are direct indicators for nonsulphide base metal deposits and indirect indicator minerals in exploration for MVT, SEDEX, Irish-type, and vein-type Zn-Pb deposits.

Most of the supergene nonsulphide deposits in the world formed in warm to temperate climate conditions (Boni et al., 2003; Hitzman et al., 2003), and only a few formed in arid environments (Namibia and Iran, Reichert and Borg, 2008). Until recently, it was believed that nonsulphide minerals could not form in cold and wet climatic conditions. Examples in BC (Salmo and Quesnel districts; Paradis et al., 2011, 2015a), Yukon (Howards Pass; Jonasson et al., 1983), Alaska (Reef Creek; Santoro et al., 2014 and now the Northwest Territories (Prairie Creek), disprove this hypothesis.

Future Work

This research gives some insight into the genesis of nonsulphides at Prairie Creek. It complements the geochemical work of Stavinga et al. (2015) and the sulphur isotopic work of Taylor et al. (2015). However, the lack of radiometric ages on the sulphide and nonsulphide deposits limits our ability to refine the genetic models for the deposit-types of the Prairie Creek district. Nonsulphide minerals can be used as indicators in exploration for base metal deposits. Their resistance to transportation and their dispersion trains should be characterized.

Acknowledgements

I am extremely grateful to all personnel of Canadian Zinc Corporation and more specifically to Alan Taylor and Kerry Cupit who provided invaluable geological information on the Prairie Creek deposit and its district. Canadian Zinc Corporation is also thanked for giving us access to the property, allowing us to sample the drill cores and providing pertinent geological information.

References

AMC Mining Consultants (Canada) Ltd., 2014, Prairie Creek property, Northwest Territories, Canada: Technical Report for Canadian Zinc Corporation. [Online] Available at: http://www.canadianzinc.com/projects/prairie-creek [Accessed 01-12-2014].

Boni, M., Gilg, H., Aversa, G., and Balassone, G., 2003, The “Calamine” of SW Sardinia (Italy): geology, mineralogy and stable isotope geochemistry of a supergene Zn-mineralization: Economic Geology, v. 98, p. 731–748.

Bowen, G.J., and Wilkinson, B., 2002, Spatial distribution of δ^{18}O in meteoric precipitation: Geology, v. 30, p. 315– 318.

Canadian Zinc Corporation, 2010, http://www.canadianzinc.com/

Canadian Network for Isotopes in Precipitation (CNIP) http://www.science.uwaterloo.ca/~twdedwar/cnip/cniphome.html

Delavau, D., Stadnyk, T., and Birks, J., 2011, Model based spatial distribution of Oxygen-18 isotopes in precipitation across Canada: Canadian Water Resources Journal, v. 36 (4), p. 313-330.

Duk-Rodkin, A., Huntley, D., and Smith, R., 2007, Quaternary geology and glacial limits of the Nahanni National Park Reserve and adjacent areas, Northwest Territories, Canada, *in* Wright, D.F., Lemkow, D., Harris, J.R., ed., Mineral and energy resource assessment of the Greater Nahanni Ecosystem under consideration for the expansion of the Nahanni National Park Reserve, Northwest Territories: Geological Survey of Canada, Open File 5344, p. 125-129.

Earls, G., 1995, A review of the Prairie Creek deposit, Northwest Territories, Canada: Internal Report, San Andreas Resources Corporation, 36 p.

Falck, H., 2007, A review of the bedrock geology of the Nahanni River region and its context in the Northern Cordillera, *in* Wright, D.F., Lemkow, D., Harris, J.R., ed., Mineral and Energy Resource Assessment of the Greater Nahanni Ecosystem Under Consideration for the Expansion of the Nahanni National Park Reserve, Northwest Territories: Geological Survey of Canada, Open File 5344, p. 327-365.

Findlay, A., 2000, Geology and exploration potential of the stratabound replacement massive sulphides, Prairie Creek Mine, Northwest Territories: Internal Report,Canadian Zinc Corporation, 17 p.

Fraser, S.C., 1996, Geology and Geochemistry of the Prairie Creek Zn, Pb, Ag deposits, Southern Mackenzie Mountains, Northwest Territories: Unpublished M.Sc. thesis, University of Alberta, Edmonton, Alberta, Canada, 146 p.

Gilg, H. A., Boni, M., Hochleitner, R., and Struck, U., 2008, Stable isotope geochemistry of carbonate minerals in supergene oxidation zones of Zn–Pb deposits: Ore Geology Reviews, v. 33, p. 117–133.

Gordey, S.P. and Anderson, R.G., 1993, Evolution of the Northern Cordilleran Miogeocline, Nahanni map area (105I), Yukon and Northwest Territories: Geological Survey of Canada, Memoir 428, 214 p.

Hitzman, M.W., Reynolds, N.A., Sangster, D.F., Cameron, R.A., and Carman, C.E., 2003, Classification, genesis, and exploration guides for nonsulfide zinc deposits: Economic Geology, v. 98, p. 685–714.

Jonasson, I.R., Jackson, L.E., and Sangster, D.F., 1983, A Holocene zinc orebody formed by supergene replacement of mosses: Journal of Geochemical Exploration, v. 18, p. 189–194.

Machel, H.G. and Cavell, P.A., 1999, Low-flux, tectonically-induced squeegee fluid flow ("hot flash") into the Rocky Mountain foreland basin: Canadian Petroleum Geology, Bulletin v. 47, p. 510-533.

McCrea, J. M., 1950, On the isotopic chemistry of carbonates and a paleotemperature scale: Journal of Chemical Physics, v. 18, p. 849-857.

Mondillo, N., Boni, M., Balassone, G., Joachimski, M., and Mormone, A., 2014, The Jabali nonsulfide Zn–Pb–Ag deposit, western Yemen: Ore Geology Reviews, v. 61, p. 248–267.

Morrow, D.W. and Cook, D.G., 1987, The Prairie Creek Embayment and Lower Paleozoic strata of the southern Mackenzie Mountains: Geological Survey of Canada, Memoir 412, 195 p.

Paradis, S., 2007, Isotope geochemistry of the Prairie Creek carbonate-hosted zinc-lead-silver deposit, southern Mackenzie Mountains, Northwest Territories, *in* Wright, D.F., Lemkow, D., Harris, J.R., ed., Mineral and energy resource assessment of the Greater Nahanni Ecosystem under consideration for the expansion of the Nahanni National Park Reserve, Northwest Territories: Geological Survey of Canada, Open File 5344, p. 131-176.

Paradis, S., Keevil, H., Simandl, G.J. and Raudsepp, M., 2011, Geology and mineralogy of carbonate-hosted nonsulphide Zn-Pb mineralization in southern (NTS 082F/03) and central (NTS 093A/14E, 15W) British Columbia, *in* Geoscience BC Summary of Activities 2010: Geoscience BC, Report 2011-1, p. 143–168.

Paradis, S., Keevil, H., Simandl, G.J., and Raudsepp, M., 2015a, Carbonate-hosted nonsulphide Zn-Pb mineralization of southern British Columbia, Canada: Mineralium Deposita, in press.

Paradis, S., Taylor, B., Stavinga, D.B., and Falck, H., 2015b, Carbonate-hosted Zn-Pb deposits of the Prairie Creek district, Northwest Territories, Canada; unusual sulphide and nonsulphide mineralization in an embayment of the Selwyn Basin, in preparation.

Peel, M. C., Finlayson, B. L., McMahon, T. A., 2007, Updated world map of the Koppen- Geiger climate classification: Hydrology and Earth system sciences, v. 11, p. 1634-1644.

pHase Geochemistry, 2010, Geochemical characterization of paste and paste components, Prairie Creek project, Northwest Territories, Canada: Appendix 4 of Developer’s Assessment Report, Canadian Zinc Corporation submission to Mackenzie Valley Review Board Environmental Assessment of Prairie Creek Mine EA 0809-002.

Reichert, J., and Borg, G., 2008, Numerical simulation and geochemical model of supergene carbonate-hosted non-sulphide zinc deposits: Ore Geology Reviews, v. 33, p. 134–151.

Rozanski, K., Araguas-Araguas, L., and Gonfiantini, R., 1993, Isotopic patterns in modern global precipitation, *in* Swart, P.K., et al., ed., Climate change in continental isotopic records: American Geophysical Union Geophysical Monograph 78, p. 1–36.

Santoro, L., Boni, M., Woodman, J., 2014, The Reef Ridge supergene nonsulfide zinc mineralization, Alaska [abs.]: 21st General Meeting of the International Mineralogical Association, Johannesburg, South Africa.

Simandl, G.J., and Paradis, S., 2009, Carbonate-hosted, nonsulphide, zinc-lead deposits in the southern Kootenay arc, British Columbia (NTS 082F/03), *in* Geological Fieldwork 2008, British Columbia Ministry of Energy and Mines, Paper 2009-1, p. 205–218.

Stavinga, D.B., 2014, Trace element geochemistry and metal mobility of oxide mineralization at the Prairie Creek Zn-Pb-Ag deposit, Northwest Territories: unpublished M.Sc. thesis, Queen's University, Kingston, Ontario, Canada, 153 p.

Stavinga, D.B, Jamieson, H., Paradis, S., and Falck, H., 2015, Geochemical and mineralogical controls on metal(loid) mobility in the Oxide Zone at Prairie Creek, Northwest Territories, *in* Paradis, S., ed., Targeted Geoscience Initiative 4: Sediment-hosted Zn-Pb deposits: processes and implications for exploration: Geological Survey of Canada, Open File 7838, p. 173-187.

Taylor, A.B., 1995, Geological Summary of the Northern Sector Pb-Zn Trend on the Prairie Creek property, Northwest Territories; Internal report, San Andreas Resources Corporation, 31 p.

Taylor, B.E., Paradis, S., Falck, H., and Wing, B., 2015, In situ sulphur isotope study of the Prairie Creek deposit, southern Mackenzie Mountains, Northwest Territories: Deciphering the conundrum of three deposit styles in one, *in* Paradis, S., ed., Targeted Geoscience Initiative 4: Sediment-hosted Zn-Pb deposits: processes and implications for exploration: Geological Survey of Canada, Open File 7838, p. 96-133.

Thorpe, R.I., 1972, Mineral exploration and mining activities, mainland Northwest Territories, 1966 to 1968; Geological Survey of Canada, Paper 70-70, 139 p.

Veizer, J., Ala, D., Azmy, K., Bruckschen, P., Buhl, D., Bruhn, F., Carden, G.A.F., Diener, A., Ebneth, S., Godderis, Y., Jasper, T., Korte, C., Pawellek, F., Podlaha, O.G., and Strauss, H., 1999, $^{87}Sr/^{86}Sr$, $\delta^{13}C$ and $\delta^{18}O$ evolution of Phanerozoic seawater: Chemical Geology, v. 161, p. 59-88.

Application of Visible-Near Infrared and Short Wave Infrared Spectroscopy to Sediment-hosted Zn-Pb Deposit Exploration in the Selwyn Basin, Yukon

J.M. Peter
Central Canada Division, Geological Survey of Canada, 601 Booth Street,
Ottawa, ON, K1A 0E8

D. Layton-Matthews, M.G. Gadd, S. Gill, S. Baker, S. Plett
Department of Geological Sciences and Geological Engineering,
Queen's University, Kingston, ON, K7L 3N6

S. Paradis
Pacific Division, Geological Survey of Canada, 9860 West Saanich Road,
Sidney, BC, V8L 4B2

Abstract

The use of visible-near infrared and short wave infrared spectroscopy (VNIR-SWIR) in the exploration for sediment-hosted Zn-Pb [a.k.a. SEDimentary EXhalative (SEDEX)] deposits was tested in basinal shale environments of the Howard's Pass and MacMillan Pass districts, Selwyn Basin. The Howard's Pass District hosts twelve SEDEX Zn-Pb deposits. Mineralization is hosted in Early Silurian carbonaceous and calcareous to siliceous mudstones. Mineralization is bedded, and no vent complex or strong hydrothermal alteration has been documented. The two main deposits in the MacMillan Pass District are Tom and Jason. Host rocks to the Tom deposit are interbedded chert-pebble conglomerate, diamictite, and black laminated shale and chert of the Late Devonian Lower Earn Group. Mineralization at Tom is comprised of a well-preserved vent complex and overlying bedded sulphides, and an underlying stringer zone that is comprised of veins and replacements of silica, siderite, mica, sulphides and barite. Spectra were collected from drill cores in the field using an ASD Fieldspec® Pro 3 with a contact probe. Given the high carbon and pyrite contents of the host rocks of the Howard's Pass and MacMillan Pass districts, spectra typically exhibit low reflectance and weak absorption features.

In the Howard's Pass District, footwall and hanging wall rocks are for the most part spectrally unresponsive over a 40 km-long strike length of discontinuous sulphide mineralization. One unit in the hanging wall (Flaggy Mudstone) is

Recommended citation
Peter, J.M., Layton-Matthews, D., Gadd, M.G., Gill, S., Baker, S., Plett, S., and Paradis, S., 2015. Application of visible-near infrared and short wave infrared spectroscopy to sediment-hosted zinc-lead deposit exploration in the Selwyn Basin, Yukon, *in* Paradis, S., ed., Targeted Geoscience Initiative 4: sediment-hosted Zn-Pb deposits: processes and implications for exploration; Geological Survey of Canada, Open File 7838, p. 152-172. doi:10.4095/296328

weakly spectrally responsive with scattered, weak to moderately abundant muscovite, phengite, siderite, montmorillonite, and kaolinite. The unit hosting the mineralization (Active Member) is spectrally weak to unresponsive, except in and adjacent to significant mineralization where spectral zones are comprised of siderite, montmorillonite, and phengite; these zones are also characterized by high mean spectral reflectances. Based on the Al-OH absorption feature, muscovite (2209 nanometers [nm] and below) prevails everywhere except within and immediately below the Active Member, where phengite predominates (2214 nm and higher wavelengths).

In the MacMillan Pass District, siderite, muscovite, phengite and montmorillonite are spectrally identified within the feeder zone of the Tom West deposit. At the base of the bedded sulphide-barite mineralization situated above the feeder zone, there is a 5 m-wide interval of siderite-montmorillonite that has high reflectance values. However, the immediate hanging wall and footwall rocks to mineralization (cherty carbonaceous mudstone) do not have a spectral expression.

Many of the key minerals spatially associated with the sediment-hosted Zn-Pb mineralization in the Selwyn Basin (apatite, pyrite, sphalerite, barite, K-Ba feldspar) do not have a spectral signature. However, we find that siderite, muscovite, phengite, and montmorillonite spatially associated with mineralization do have spectral signatures, but they are quite subtle. Further work is currently focused on integration of the spectral signatures with field and laboratory whole rock geochemical analyses.

Introduction

Optical spectroscopy is a non-destructive tool that can be used to analyze rocks and minerals and provide valuable information about their chemical and physical properties, including mineralogy and, in some cases mineral chemistry. Optical spectroscopic data can be collected using satellite-based, airborne, field portable ground, and laboratory spectrometers. Optical remote sensing data record the interaction of electromagnetic radiation with different elements. The electromagnetic spectrum ranges from gamma radiation at short wavelengths to long radio wavelengths. Several wavelength regions are useful for geological studies, and one of the most commonly used is the short wavelength infrared region (SWIR, 1000-2500 nm).

Hyperspectral (narrow spectral bands over a continuous spectral range) data in the visible-near infrared and short wave infrared (VNIR-SWIR) are becoming increasingly used in mineral exploration, and are particularly useful in the exploration for hydrothermal mineral deposits such as volcanogenic massive sulphide (VMS; e.g. Laakso et al., 2015; Laakso et al., in press) and orogenic

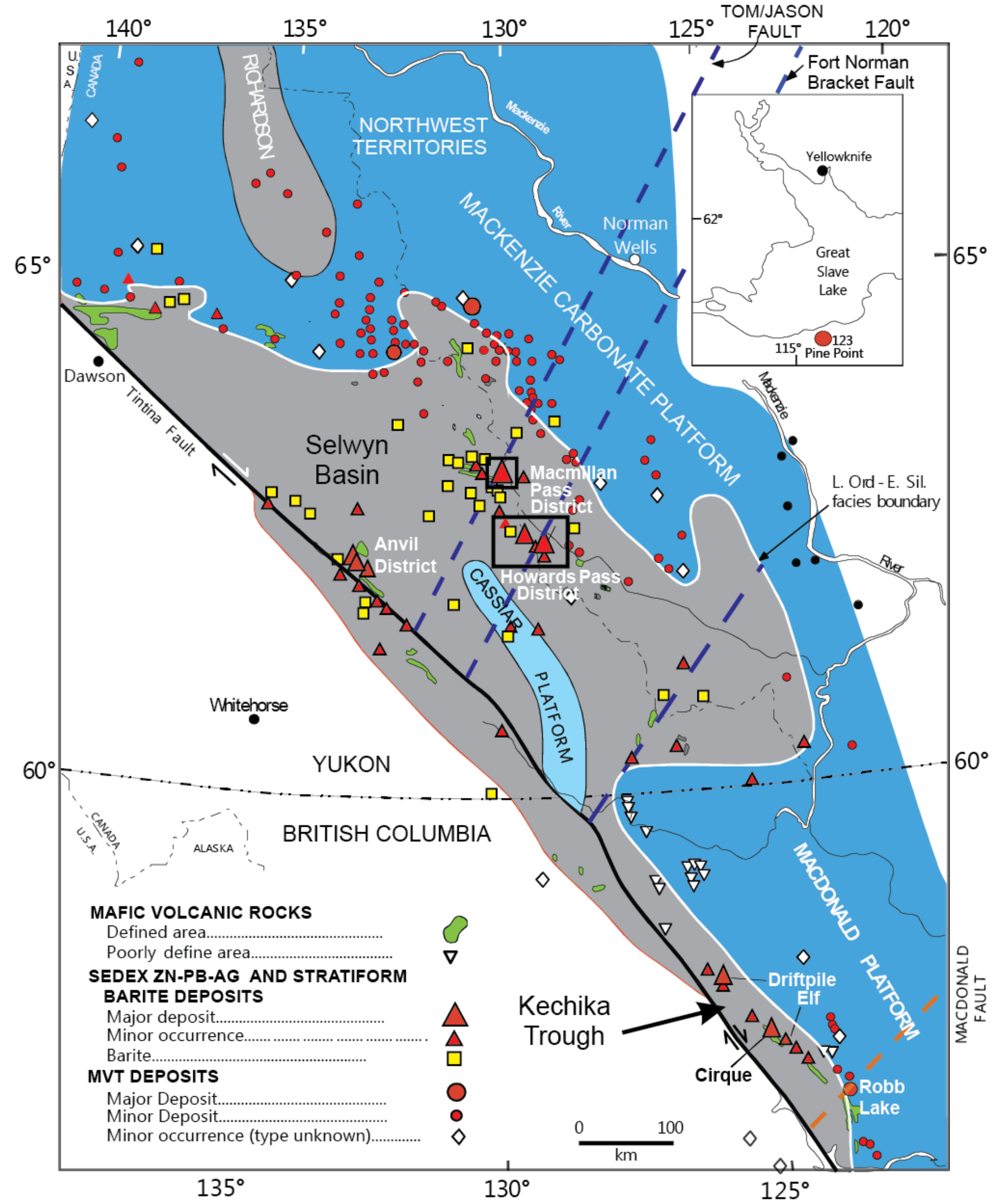

Figure 1. Map of Selwyn Basin showing the MacMillan Pass (northern box) and Howard's Pass (southern box) study areas, two of the major Zn-Pb districts within the basin (modified from Goodfellow, 2007).

and epithermal gold deposits (e.g. Bierwirth et al., 2002; Yarra et al., 2014) because the hydrothermal alteration minerals associated with these deposits (e.g. chlorite, white mica, carbonate) have characteristic spectral signatures in the SWIR (e.g. Clark et al., 2007). The application of this technology in the exploration for sediment-hosted Zn-Pb deposits in Canada, however, remained untested to now, aside from a few measurements conducted on non-georeferenced, representative samples from the Sullivan deposit, B.C., and the Faro deposit, Anvil district, Yukon (AusSpec International Ltd., 2008). The objective of the present study was to perform such a test in basinal shale environments of the Howard's Pass District (HPD) and MacMillan Pass District (MPD), Selwyn Basin (Figure 1). This study is ancillary to that of Gadd et al. (2015), which aims to develop exploration vectors using microanalytical methods.

Geology

Howard's Pass District

There are twelve Zn-Pb SEDEX deposits in the HPD that collectively contain an estimated 393 Mt grading 4.5% Zn and 1.5% Pb (Selwyn Chihong Mining Limited, 2012). The HPD is located within the Selwyn Basin (Figure 1), a prolific metallogenic province that is primarily known for its world-class sediment-hosted Zn-Pb [a.k.a. SEDimentary EXhalative (SEDEX)] deposits. Mineralization occurs along four discrete time-stratigraphic horizons (oldest to youngest: Anvil District—Cambrian; Vulcan—Middle Ordovician; Howard's Pass District—Silurian; MacMillan Pass and Gataga districts—Devonian; Goodfellow, 2007).

Mineralization in the HPD is hosted by a sequence of carbonaceous pelagic and hemipelagic mudstone, shale and chert of the Early Silurian "Active Member" (ACTM) of the Howard's Pass (Duo Lake) Formation (Figures 3, 4, 5). Immediately overlying the ACTM (Figure 5A) is the Upper Siliceous Mudstone (USMS; Figure 5B), and above that the Upper Silurian Flaggy Mudstone Member (FLMD; Figure 5C) of the Steel Formation. Immediately below the ACTM are the Lower Cherty Mudstone (LCMS; Figure 5D) and the Calcareous Mudstone (CCMS; Figure 5E). Mineralization is bedded/laminated (where not deformed; Figure 5D), and no vent complex and/or strong hydrothermal alteration has been observed in the district. For more detail on the geology and stratigraphy of the HPD, the reader is referred to Goodfellow and Jonasson (1986).

Tom Deposit Area, MacMillan Pass District

Host rocks to the Tom deposit in the MPD (Figures 6 and 7) are interbedded chert-pebble conglomerate and chert clast grits (MCG; Figure 8A), diamictite consisting of chert pebble conglomerate, sand-striped mudstone, and mudstone clasts in a mudstone matrix (MD), black carbonaceous mudstone with light grey sand and silt interbeds (MMA; Figure 8B) and black carbonaceous siliceous mudstone and chert with pyrite and barite laminae (TCh) of the Late Devonian Lower Earn Group. Mineralization is comprised of a well-preserved vent facies complex (veins, breccias, replacements of sulphides, Fe-carbonates, and quartz) (TS; Figure 8C) and overlying interbedded barite, chert, sphalerite, galena and pyrite (TB; Figure 8D), and an underlying stringer zone that is comprised of veins and replacements of silica, siderite, mica, sulphides and barite. MMA, MCG, MD, and TCh form the stratigraphic footwall to mineralization (TB, TS), and TCh and various carbonaceous and siliceous mudstones (some radiolarian-bearing) form the stratigraphic hanging wall. For a detailed description of the geology of the MPD, the reader is referred to Goodfellow and Rhodes (1990).

Our sampling and spectral measurement strategy was to obtain data for most proximal (feeder zone and vent complex) mineralization of the Tom West deposit (represented by drillholes TS91-014 and TYK-001) and move systematically away along-strike from the proximal to distal mineralization in drillholes TYK-004, TYK-005, TS-009, TS91-19, JS76-017, and JS76-008 (see Figure 6).

Results/Data Analysis

Methodology

The objective was to determine if there are variations in the spectral parameters that may serve as an indicator of mineralization, or a vector toward it. Spectra were systematically collected in the field from drill cores of the mineralized sequence, or favourable stratigraphy, if unmineralized, and stratigraphic hanging wall and footwall in both the HPD "Zinc Corridor" and the Tom West deposit in the MPD. Measurements were made using an ASD FieldSpec® Pro 3 (Figure 2) that records in the 350-2500 nm wavelength region with a spectral resolution of 10 nm and a sampling interval of 2 nm in the short-wave infrared wavelength region. The spectrometer was equipped with a fore optic contact probe (1 cm diameter circular field of view) to ensure consistent illumination conditions during data acquisition. Radiance values were converted to reflectance values by means of a panel of pressed polytetrafluoroethylene, commercially known as Spectralon™ (Labsphere, New Hampshire, US; Bruegge et al., 1993). Dark current and white reference measurements were repeated periodically throughout the day during data acquisition in order to ensure consistency in the spectral measurements.

Figure 2. Collecting optical reflectance spectra from drill core samples with a field portable spectrometer in the Selwyn Chihong Mining Limited Don Camp core logging and sampling facility, Howard's Pass District, Selwyn Basin, Yukon.

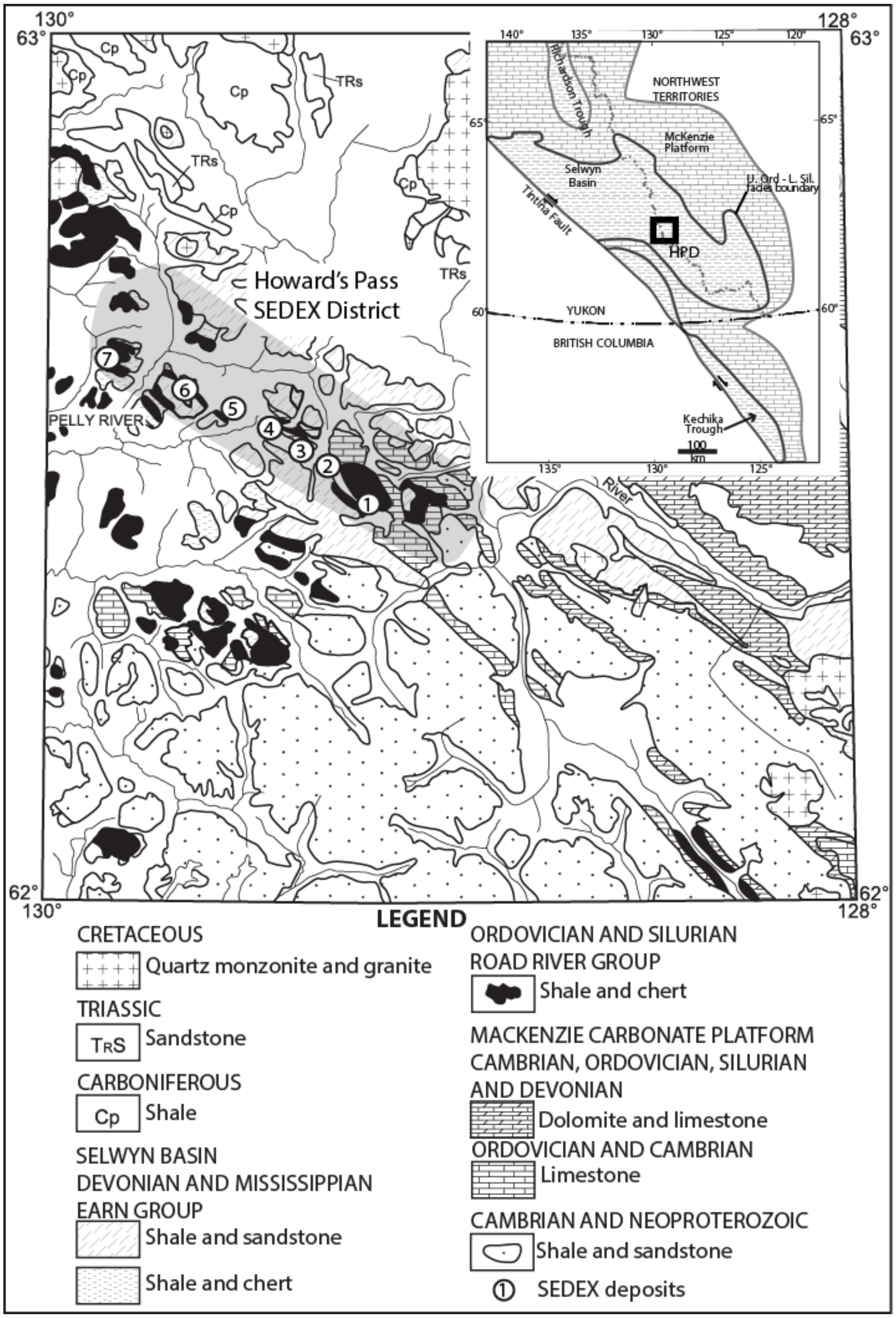

Figure 3. Regional geologic map of the Howard's Pass District (from Gadd et al., 2015). Also shown are the sediment-hosted Zn-Pb deposits and mineralized zones that define the >40 km-long "Zinc Corridor": 1: XY zone (XY, XY Central and XY West deposits); 2: Brodel deposit; 3: HC zone (HC and HC West deposits); 4: Don zone (Don and Don East deposits); 5: Anniv Zone (Anniv and Anniv East deposits); 6: OP deposit; 7: Pelly North deposit. Inset shows location of Selwyn Basin in the northern Cordillera.

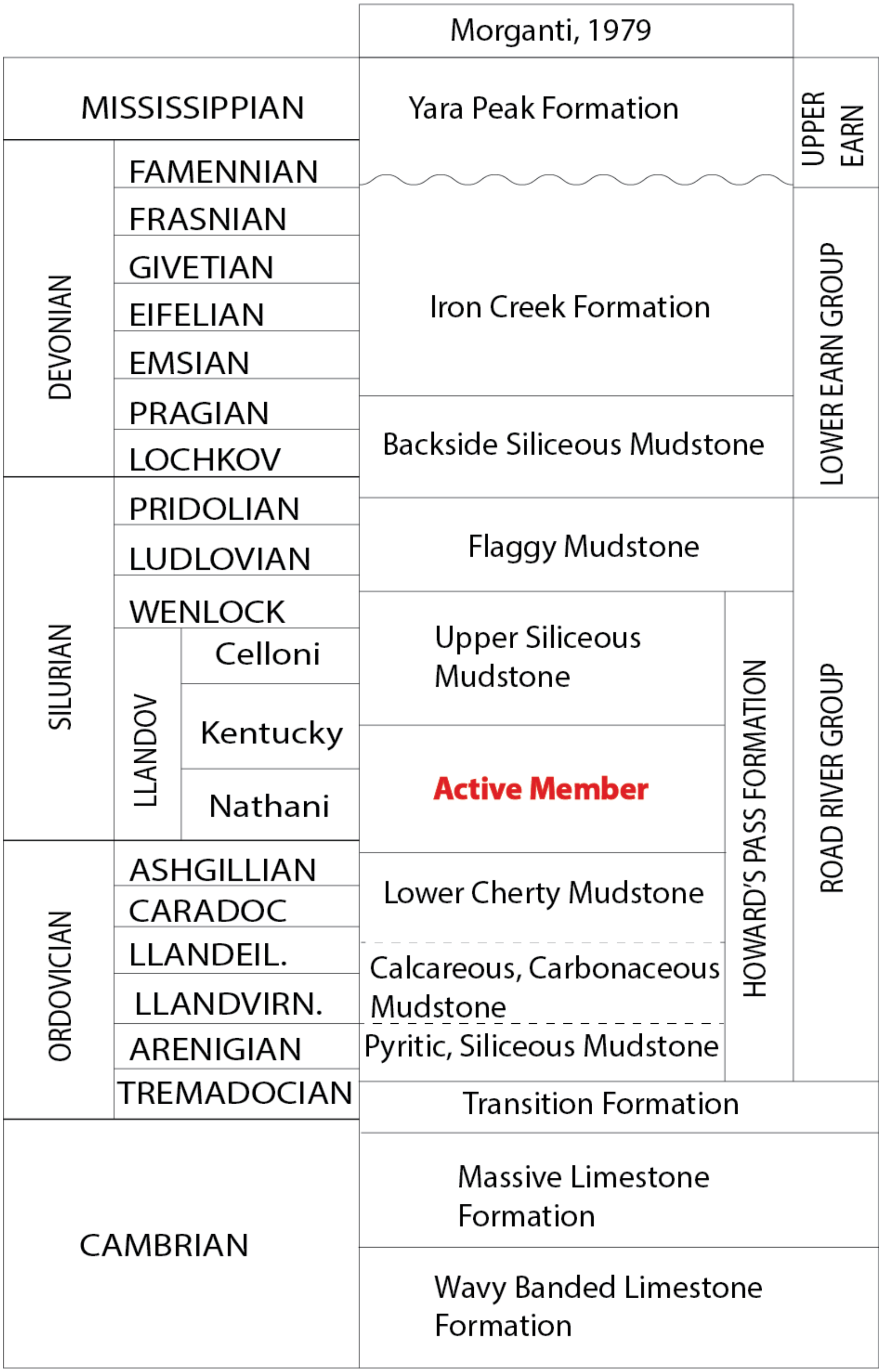

Figure 4. Stratigraphic section of the Howard's Pass District (modified from Goodfellow and Jonasson, 1986). The Active Member is the unit that hosts the mineralization.

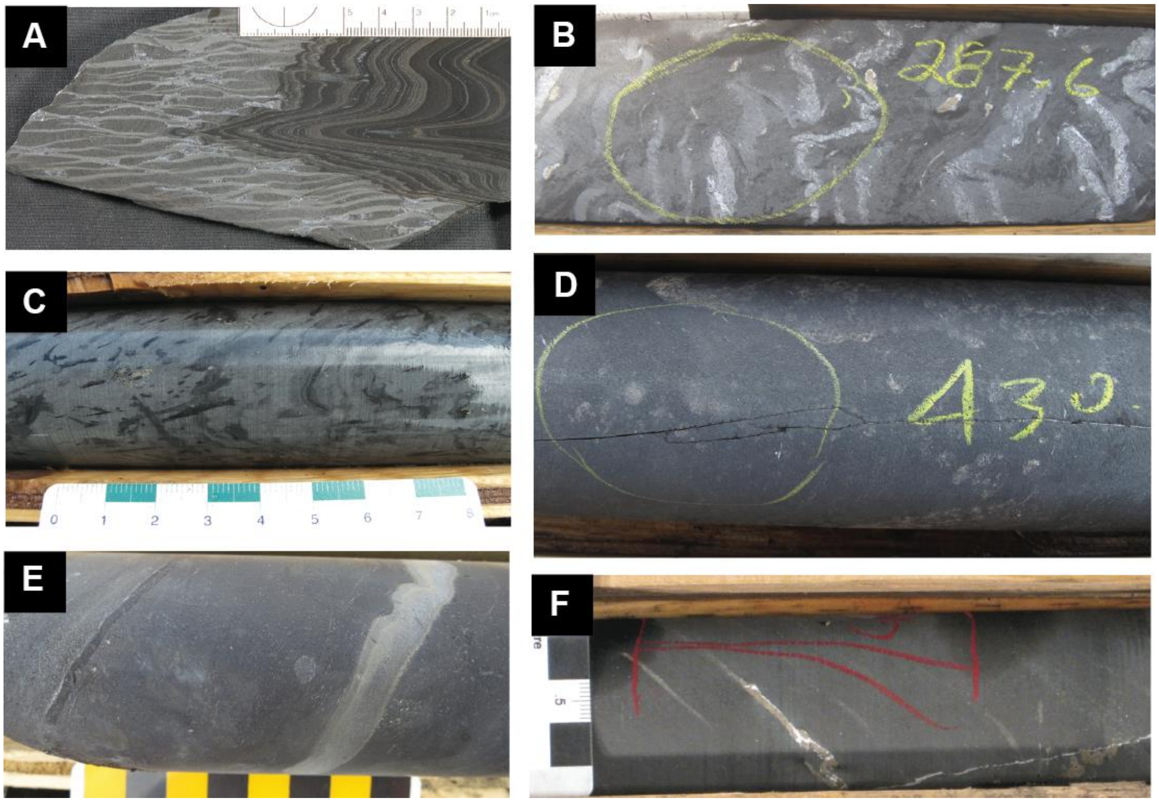

Figure 5. Drillcore photographs of representative samples from the stratigraphic succession in the Howard's Pass District. Terminology is from Morganti (1979). A) Backside Siliceous Mudstone (BSMS); B) Flaggy Mudstone (FLMD); C) Upper Siliceous Mudstone (USMS). Drillcore diameter is 4.8 cm; D) Active Member (ACTM); E) Lower Cherty Mudstone (LCMS). Drillcore diameter is 4.8 cm; F) Calcareous Carbonaceous Mudstone (CCMS).

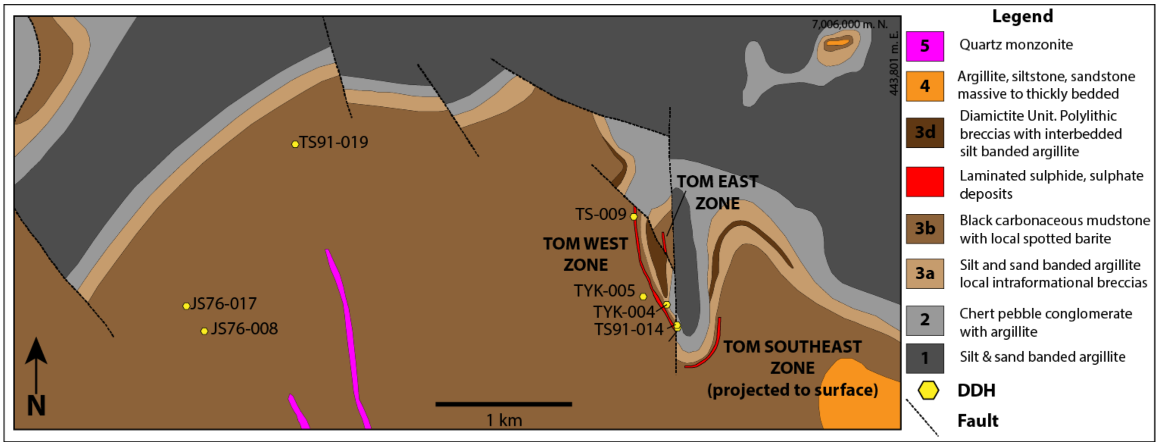

Figure 6. Geological map of the Tom deposit area, MacMillan Pass District, Selwyn Basin, Yukon (modified from Cameron, 1992). Shown are the locations of diamond-drill holes (DDH) from which systematic spectral data were collected from the mineralization (or favourable horizon) and stratigraphic footwall and hanging wall. Legend colours correspond to those in the stratigraphic section of Figure 7.

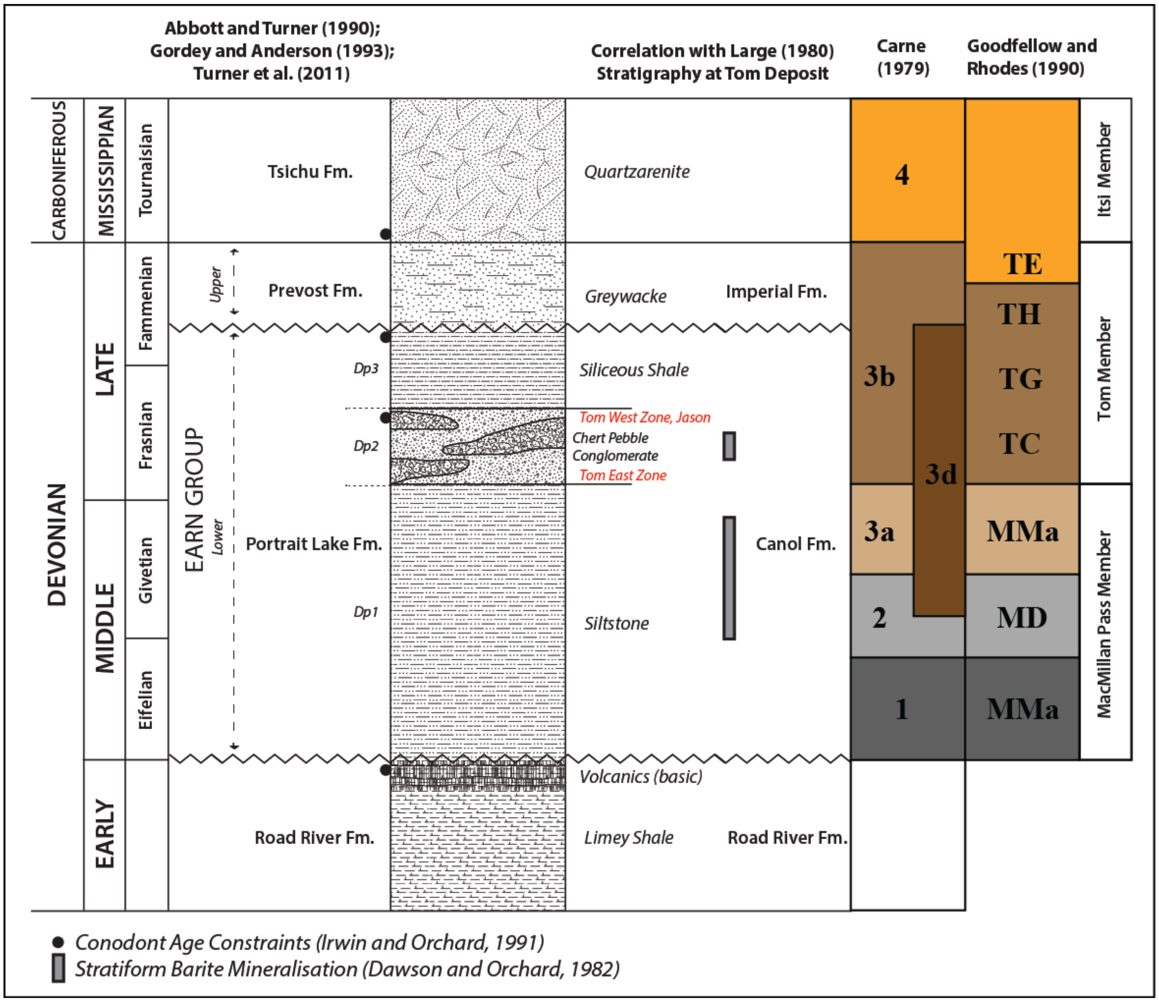

Figure 7. Stratigraphic section of the MacMillan Pass District, Yukon (modified from Magnall et al., 2014). Colours correspond to those in the geological map of Figure 6.

Given the high carbon and pyrite contents of the host rocks in both the HPD and MPD, collected spectra typically exhibit low reflectance and weak absorption features, such that absolute reflectance was used, together with a calibration file supplied by the instrument manufacturer. Additionally, a spectrum averaging value of 200 was used rather than the commonly used value of 60 for typical (i.e. more spectrally responsive) rocks. Spectral readings with low signal-to-noise ratios or failed readings were discarded. The spectra were analyzed using the "The Spectral Geologist-Core" software (TSG. version 7; AusSpec International Ltd., 2012). Spectral were hull quotient-corrected to reduce the effects of the background spectral slope when the absorption feature wavelength is to be accurately recorded (Clark and Roush, 1984). The hull quotient correction (continuum removal) is conducted by fitting straight-line segments (convex hull points) over the shoulders (maxima) of an absorption feature, and dividing the reflectance values of the absorption feature by these convex hull points. The resulting hull quotient values are normalized to a 0-1 scale hence removing the effects of albedo variance in the spectrum.

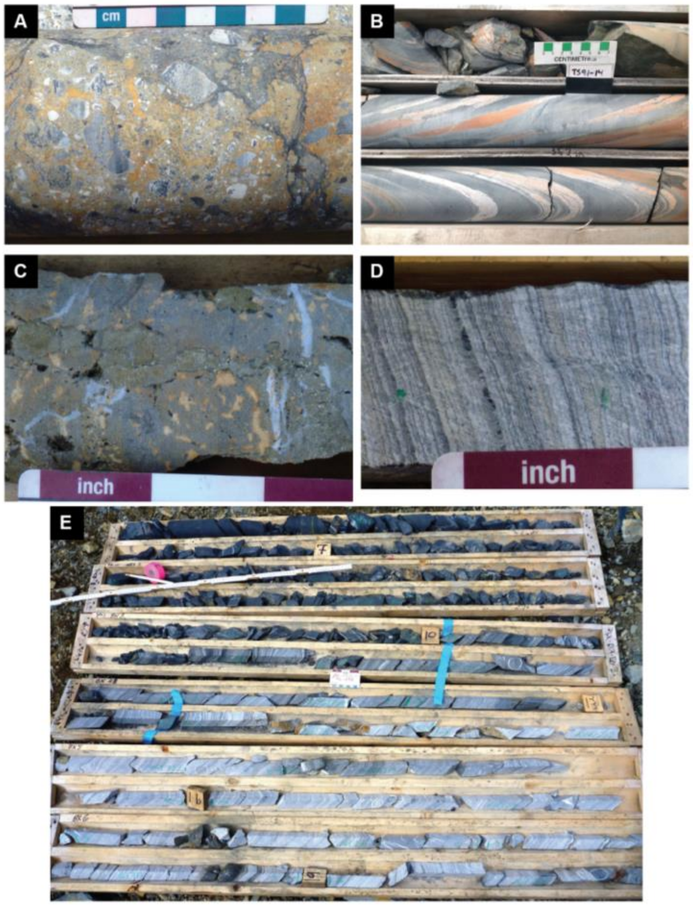

Figure 8. Drill core photographs of representative samples from the stratigraphic succession in the MacMillan Pass District. Terminology is from Goodfellow and Rhodes (1990). A) Chert pebble conglomerate (MCG) with orange weathering Fe carbonate-rich matrix (hydrothermal breccia), DDH TYK001, 078.6 m; B) Interbedded silt/sand and mudstone (MMA; footwall to mineralization) with orange weathering Fe carbonate, DDH TS91-14, 350-354 m; C) Vent complex massive sulphide (TS) with orange weathering Fe carbonate, DDH TYK001, 39.0 m; D) Bedded massive sulphide (TB), DDH TYK001, 021.5 m; E) Transition from hanging wall black carbonaceous mudstone (TCh; top 2 ½ core boxes) to bedded massive sulphides (TB; lower 3 ½ core boxes), DDH TYK001, 0-20 m.

Reflectrance Spectroscopy of the "Zinc Corridor", Howard's Pass District

In the HPD, we collected 1499 spectra from 16 drill cores along a 40 km-long strike length of discontinuous mineralization that comprises the "Zinc Corridor", extending from the XY zone (i.e. XY, XY Central and XY West deposits) in the southeast to the Pelly North deposit in the northwest (see Figure 3). Deposits and drill cores measured are as follows: XY (Central): diamond-drill holes XYC-190, XYC-208, XYC-224, XYC-243; Don: DON-076, DON-083, DON-200, DON-239; Anniv (Central): ANC-109; Anniv (East): ANE-108; Pelly North: PLN-003, PLN-005, PLN-007; OP: OPX-011, OPX-017; Brodel: BRO-010. The spectral features of the samples from these drillholes are typified by the representative spectra shown in Figure 9A and B. Prominent absorption features occur at or around 1060, 1290, 1425, 1800, 1920, 2200, and 2330 nm, indicative of the presence of Fe-carbonates, montmorillonite, and white mica (see below).

The chemical composition of the phyllosilicate minerals may change through several substitutions such as simple Mg-Fe substitution or Tschermak substitution, in which octahedral Mg and Fe substitute for Al concurrently with tetrahedral Si for Al (Miyashiro and Shido, 1985; Guidotti and Sassi, 1998). These substitutions can be observed as spectral shifts within the Al-OH and Fe-OH absorption features near 2200 nm and 2250 nm, respectively (Clark et al., 2007). The wavelength position of the Al-OH absorption feature, present in dioctahedral muscovite, shifts systematically toward shorter wavelengths as the Al content of the octahedral sites increases, and the opposite effect, or a systematic shift toward longer wavelengths, takes place when the relative proportion of octahedral Mg and Fe increases (Post and Noble, 1993; Duke, 1994). These dioctahedral minerals form a solid solution series between paragonite, muscovite and phengite (Velde, 1965; Li et al., 1994) and are commonly termed white micas.

The chemical composition of carbonates affects their spectral response, with the prominent absorption occurring at ≈2300 nm in Mg carbonates, 2320 nm in Mg-Fe carbonates, ≈2330 nm in Fe carbonates, ≈2340 nm in Ca carbonates, 2360 nm in Mn carbonates, and ≈2400 in Zn carbonates. Ferrous iron absorptions (between ≈900 and ≈1300 nm) are common to all Fe carbonates (ankerite, siderite, Fe-calcite), and their intensity varies with Fe content. In practice, determination of siderite is difficult due to the variable Mg and Fe content possible in carbonates. The presence of siderite in the HPD was confirmed based on the presence of absorption features at 2330, 1060 and 1290 nm.

Montmorillonite (Al-smectite) has absorptions at ≈1400, 1800, ≈1900, and ≈2200 nm, and is distinguished from illite in that the former does not have the secondary Al-OH absorption features at 2360 and 2450 nm typically present in illite. Montmorillonite is distinguished from kaolinite in that the former does not have a 2160 nm absorption feature. On this basis, montmorillonite is identified in the spectra of the HPD.

The ACTM which hosts Zn-Pb mineralization at HPD is generally spectrally weak to unresponsive, except in and adjacent to significant sulphide mineralization where spectral zones are comprised of siderite (evidenced by prominent absorption features around 1060 nm, 1290 nm and a less pronounced absorption around 2330 nm), montmorillonite (evidenced by a prominent absorption features around 1800 nm, but without the characteristic secondary Al-OH absorption features at 2360 and 2450 nm), and white mica (phengite, as evidenced by the wavelength of the prominent Al-OH absorption feature around 2200 nm) (Figure 9A). These zones are also characterized by high mean spectral reflectances. The

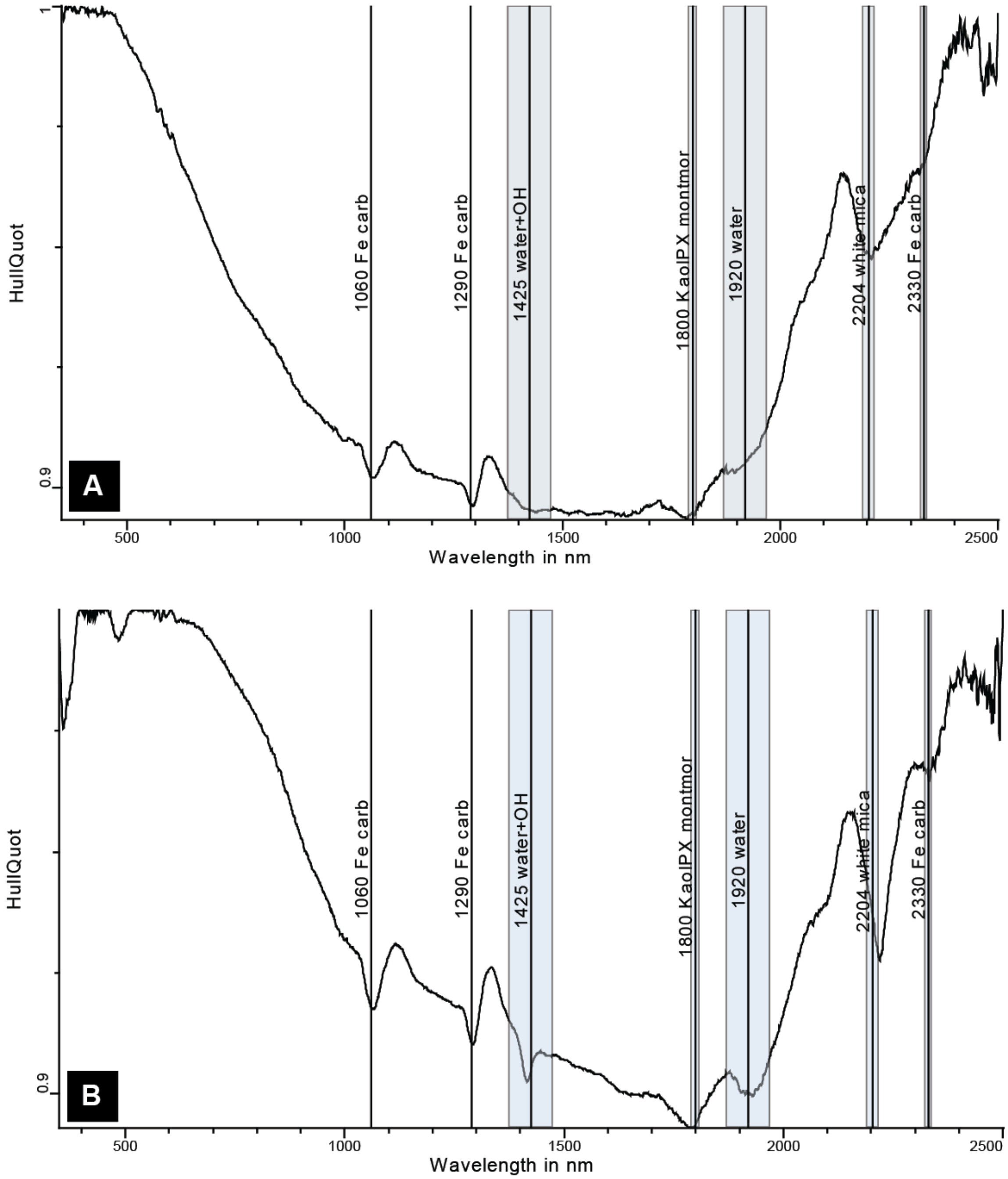

Figure 9. A) Representative hull quotient reflectance spectral plot from lower part of the mineralized Active Member (ACTM), Howard's Pass District, DDH XYC-224 (XY Central deposit), 186.2m. Absorption features indicate the presence of white mica, Fe carbonate, and montmorillonite. In many samples, Fe carbonate is not identified in the spectra; B) Representative hull quotient reflectance spectral plot from Flaggy Mudstone (FLMD), Howard's Pass District, DDH DON-76 (Don East deposit), 108.2m. Absorption features indicate the presence of white mica, Fe carbonate, and montmorillonite. Abbreviations: Fe carb = Fe carbonate; KaolP X montmor = kaolinite/montmorillonite.

USMS (unit immediately above the ACTM), LCMS (unit immediately below the ACTM) and CCMS (unit immediately below the LCMS) are, for the most part, spectrally unresponsive. The FLMD generally is weakly spectrally responsive with scattered, little to moderately abundant muscovite, phengite, siderite, montmorillonite, and kaolinite (all evidenced by the absorption features outlined above) (Figure 9B).

The composition of white mica can be determined by using the wavelengths of the Al-OH absorption feature that varies depending on the octahedral Al content. Variation occurs in the following manner: paragonite (Na-sericite; high Al) 2180-2190 nm; muscovite (“normal” potassic) 2200-2210 nm; phengite (Mg-Fe substituted; low Al) 2216-2228 nm. Using these criteria, phengite (higher wavelengths) predominates within and immediately below the ACTM, and muscovite (2209 nm and below) prevails elsewhere (Figure 10A).

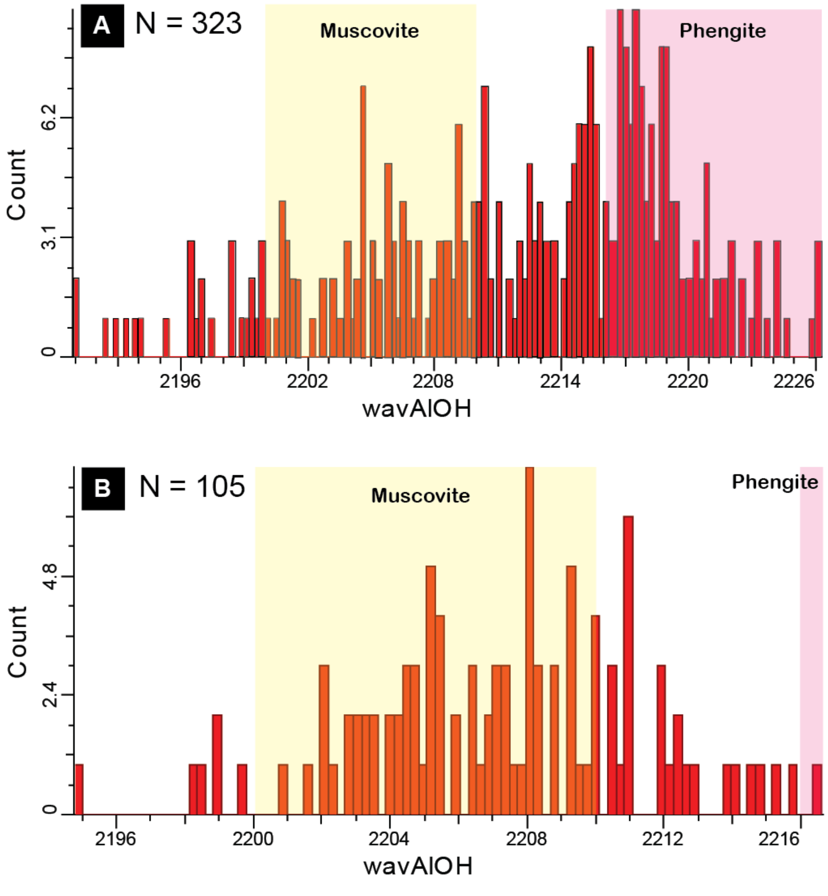

Figure 10. A) Histogram of Al-OH absorption wavelengths in DDH XYC-190 (XY Central deposit). There are two compositional ranges in white micas from muscovite (2200-2210 nm; shown in yellow) to phengite (2216-2228 nm; shown in pink), with the latter associated with the Active Member (ACTM); B) histogram of Al-OH absorption wavelengths in DDH TS91-14, MacMillan Pass District. A single population shows compositional variation in white micas that ranges from muscovitic to phengitic, with most being muscovitic (2200-2210 nm).

Reflectrance Spectroscopy of the Tom West Deposit, MacMillan Pass District

We collected 313 spectra from 4 drill cores extending from the core of the Tom West deposit (TYK-001 and TS91-14) up to 400 m away along strike (TYK-004 and TYK-005). We also collected additional data from drill cores that are even more distal from mineralization (TS-91-019, JS76-017, JS76-008, TS-009; Figure 6), but these have not yet been analyzed. At the base of (and within) the sulphide-barite bedded mineralization, situated immediately above the feeder zone, there is a 5 m-wide interval of siderite-montmorillonite that has high reflectance values. Siderite is evidenced by prominent absorption features around 1060 nm and1290 nm (and the characteristically shaped trough formed by them) and a less pronounced absorption around 2330 nm. Montmorillonite is characterized by a subtle absorption feature around 1800 nm, but without the secondary Al-OH absorption features at 2360 and 2450 nm (Figure 11A). Siderite, muscovite (Al-OH absorption feature at 2209 nm and below), phengite (Al-OH absorption feature range from 2216 to 2228 nm) and montmorillonite (absorptions at 1800 and 1920 nm, but not at 2160, 2360 and 2450 nm) are spectrally identified within the feeder zone (MCG, MD, MMA) (Figure 11B).

However, the immediate hanging wall and footwall rocks to Pb-Zn-Ba mineralization (cherty carbonaceous mudstone; TC) do not have a spectral expression. Al-OH absorption wavelengths, which are a robust indicator of white mica composition, show a single population, with a compositional range from muscovitic to phengitic, with muscovitic compositions predominating (Figure 10B).

Discussion/Models

Reflectance parameters vary between the various host lithologies of deposits of the HPD and the Tom West deposit in the MPD, but there are no systematic discernable variations that can be used to unambiguously indicate proximity to mineralization or vector toward it. In the HPD, calculations of the white mica crystallinity index ([depth of Al-OH absorption feature at 2200 nm] / [depth of water absorption feature at 1900 nm]) for almost all drill cores shows no systematic variation within and between the stratigraphic units. Calculations of the depth of the Al-OH absorption feature for almost all drill cores in the HPD shows no systematic variations that can be used to indicate proximity to mineralization or vector toward it. However, in several drill cores (AN-108 from the Anniv deposit, DON-76 from the Don deposit, and OP-17 from the OP deposit) values are at their maxima in the immediate footwall to sulphide mineralization. At the Tom West deposit, the values for the depth of the Al-OH absorption feature are highest in the carbonaceous mudstone that is the immediate footwall (drill cores TYK-001 and TYK-005) and hanging wall to sulphide-barite mineralization (drill core TYK-004).

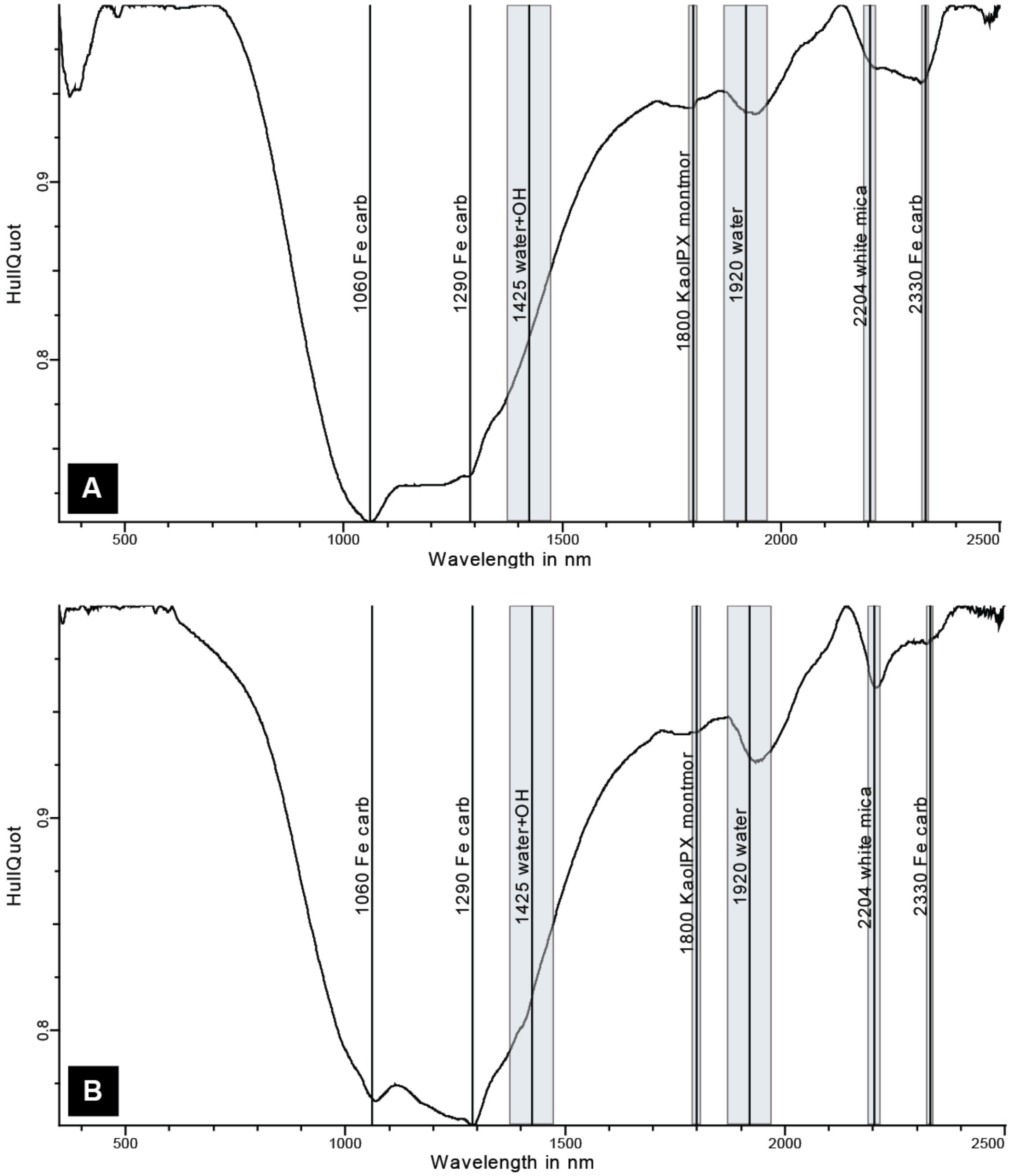

Figure 11. A) Representative hull quotient reflectance spectra from bedded massive sulphide (TB) with minor carbonaceous mudstone laminae (TC), MacMillan Pass District DDH TYK-001, 034.2m. Absorption features indicate the presence of white mica (muscovitic), Fe carbonate (siderite), and very minor montmorillonite; B) Representative hull quotient reflectance spectra from feeder zone (quartz-siderite veins and replacements) in chert pebble conglomerate (MCG), MacMillan Pass District, DDH TYK-001, 078.6m. Absorption features indicate the presence of white mica (muscovitic), Fe carbonate (siderite), and very minor montmorillonite. Abbreviations: Fe carb = Fe carbonate; KaolP X montmor = kaolinite/montmorillonite.

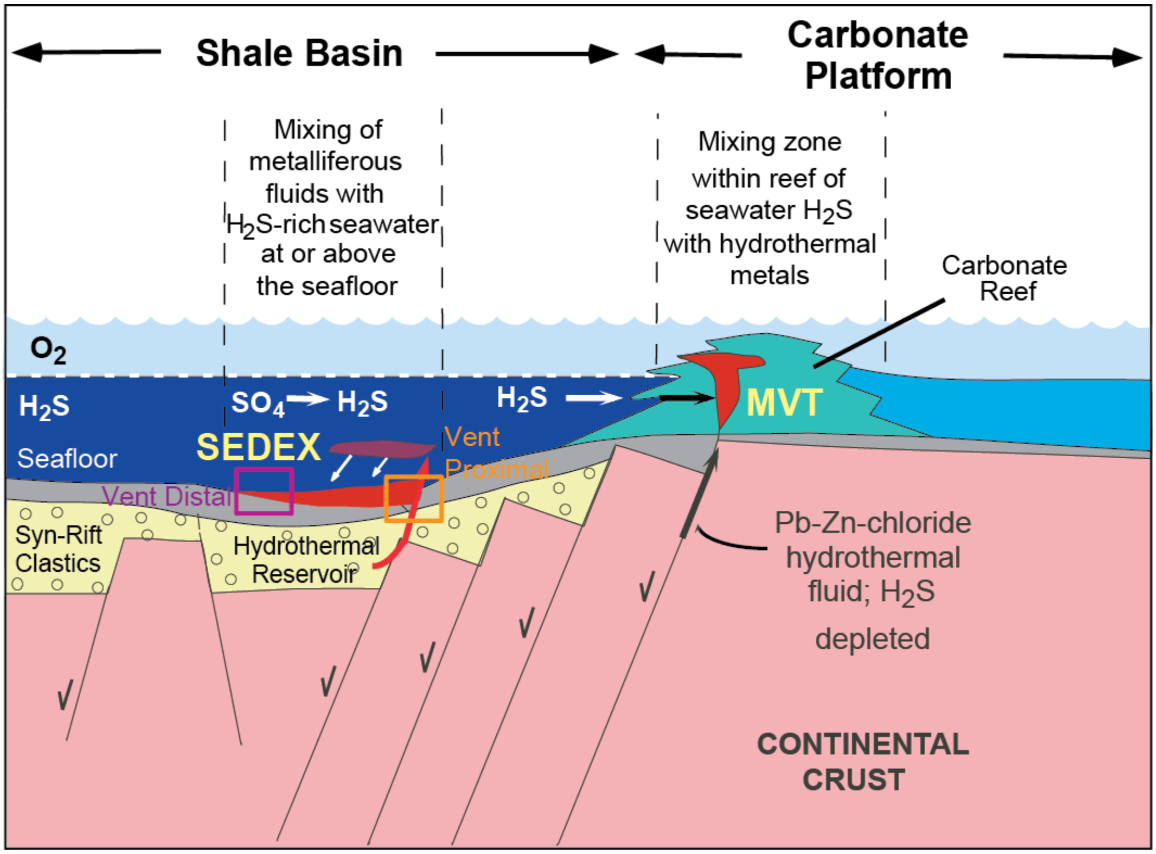

Figure 12. Genetic model for formation of sediment-hosted Zn-Pb and coeval Mississippi Valley-type (MVT) deposits in Selwyn Basin (from Goodfellow, 2007). Note the relative positions (no scale implied) of vent-proximal sediment-hosted Zn-Pb deposits such as Tom West in the MacMillan Pass District (orange box) and vent-distal sediment-hosted Zn-Pb deposits such as those (XY, Brodel, Don, HC, Anniv, OP, Pelly North) of the “Zinc Corridor” in the Howard’s Pass District (purple box). Vent-proximal deposits are situated over a vent complex, whereas vent-distal deposits are situated far from the site of the venting fluids.

The Zn-Pb-Ba mineralization in the MPD (Tom and Jason deposits) were interpreted by Goodfellow and Rhodes (1990) and Goodfellow (2007) as vent-proximal deposits (see orange coloured box in Figure 12), whereas the Zn-Pb deposits along the HPD “Zinc Corridor” were interpreted as vent-distal (no feeder systems have been identified) deposits (Goodfellow, 2007; see purple coloured box in Figure 12). Note that Figure 12 is a schematic representation of one mineralizing event (horizon), whereas there are four known such horizons, and the deposits of the MPD and HPD actually occur at different horizons. Nevertheless, in the MPD, spectrally responsive vent-related hydrothermal alteration minerals may potentially be recognized, together with spectrally responsive minerals within the mineralization (that formed in the water column or diagenetically from pore waters in the sediments). However, in the HPD only the latter are expected. Our data show that in the MPD, siderite is a spectrally responsive vent-related mineral, but it is ubiquitous in the sediments up to at least 400 m from the vent site. Further, siderite is also present in vent-distal mineralization within the HPD. On this basis, the spectral recognition of siderite cannot be used to vector toward mineralization.

In order to determine whether (dark grey to black) carbonaceous matter within the host units and mineralization suppresses reflectance, the following calculation (S. Pontual (Principal Geologist, AusSpec International), pers. comm., 2013) was made: [2100 nm mean reflectance value] / [600 nm mean reflectance value]. The basis for this is that in the samples measured, white mica is the dominant highly reflective mineral, and the ratio of the dominant Al-OH absorption at 2100 nm to reflectance at a wavelength where none of the diagnostic features of white mica occur (600 nm) provides a good measure of the brightness or reflectance. In some drill cores, such as DON-200 from the Don deposit, AN-108 from the Anniv deposit, XYC-190 and XYC-224 from the XY (Central) deposit, maximum values occur within the ACTM. At the Tom West deposit, maxima occur within the massive sulphide mineralized intervals (TB, TS) in drill cores TYK-001, TYK-004, and TYK-005. However, the spectral proxy for the carbonaceous matter content does not vary systematically in a manner that can be used to vector toward mineralization.

Based on the Al-OH absorption feature wavelengths, along the “Zinc Corridor” of the HPD, phengite (2216 to 2228 nm) predominates within and immediately below the ACTM, and muscovite (2209 nm and below) prevails elsewhere. Phengitic mica can form from high temperature (250-350°C) from hydrothermal fluids (Hulen and Nielson, 1986), but this temperature range is deemed too high for the mineralizing fluids in the HPD, based on metal solubility considerations (Lydon, 1983). Another influence on the chemical composition of white micas is the chemical composition of the hydrothermal fluids (Cathelineau, 1988). Elevated Mg^{2+} and Fe^{2+} (relative to Al^{3+}) contents of the hydrothermal fluid favor the formation of phengite (Yang et al., 2011). Therefore, the presence of phengitic mica immediately beneath the ACTM could reflect the greater availability of Fe than elsewhere in the host rocks of the HPD.

In the Tom West deposit area, the Al-OH absorption feature wavelengths show a single population, with a compositional range from muscovitic to phengitic, with muscovitic compositions predominating. As mentioned above, the formation of phengitic over muscovitic mica can be controlled by fluid temperature and/or fluid chemistry. However, muscovitic through phengitic white mica compositions are identified in the feeder zone at Tom West and there appears to be no systematic spatial variation/zonation that can be used for vectoring. Fluid inclusion homogenization temperatures in the hydrothermal vents at Tom and Jason (≈250°C; Gardner and Hutcheon, 1985; Ansdell et al., 1989) fall within the temperature range for phengite formation, as discussed above, but the chemical composition of the fluids may also have governed the formation of phengite over muscovite.

Conclusions

Many of the key minerals spatially associated with sediment-hosted Zn-Pb mineralization in the Selwyn Basin (apatite, pyrite, sphalerite, barite, K-Ba feldspar) do not have spectral signatures in the VNIR-SWIR portion of the electromagnetic spectrum. However, our data indicate that other minerals that are spatially associated with mineralization (siderite, muscovite, phengite, and montmorillonite) do have spectral signatures, although they are quite muted. Our data broadened a very minimal publicly available dataset, and will be useful to compare with similar datasets that may be collected elsewhere in the Selwyn Basin, or may be made available in the future.

Implications for Exploration

The sediment-hosted Zn-Pb deposits of the HPD and MPD clearly have less pronounced hydrothermal alteration signatures than Australian Proterozoic examples hosted by calcareous sediments (Large et al., 2005), and which have more pronounced spectral signatures (AusSpec International Ltd., 2008). Our work to date show that hyperspectral optical reflectance spectroscopy will be of limited use in delineating favourable horizons and vectoring toward mineralization along them in both the HPD and MPD of the Selwyn Basin.

Future Work

Further work is currently focused on analysis of additional spectral measurements made distal (further than 400 m away) from the Tom West deposit and incorporating these data into the dataset presented here. These spectral analyses will be integrated with field portable x-ray fluorescence and laboratory whole rock geochemical data to develop geochemical exploration vectors focused on “ore” and pathfinder metals, and redox sensitive elements indicative of ambient conditions.

Acknowledgements

We gratefully acknowledge the logistical and in-kind support provided by Selwyn Resources Ltd., Selwyn-Chihong Mining Ltd., HudBay Minerals Inc., and Mercer Contracting. Discussions with Wayne Goodfellow (Geological Survey of Canada; GSC) regarding the geology and geochemistry of the SEDEX deposits in both the HPD and MPD were very helpful. We also thank Sasha Pontual, AusSpec International Ltd. for input on SWIR data analysis of our data and Jeff Harris (GSC) for reviewing this contribution.

References

Abbott, J.G., and Turner, R.J.W., 1990, Character and paleotectonic setting of Devonian stratiform sediment-hosted Zn, Pb, Ba deposits, MacMillan Fold Belt, Yukon, *in* Abbott, J. G., and Turner, R. J. W., ed., Mineral deposits of the northern Canadian Cordillera (Eighth Symposium Field Trip 14 Guidebook): Ottawa, International Association on the Genesis of Ore Deposits, p. 99-136.

Ansdell, K.M., Nesbitt, B.E., and Longstaffe, F.J., 1989, A fluid inclusion and stable-isotope study of the Tom Ba-Pb-Zn deposit, Yukon Territory, Canada: Economic Geology, v. 84, p. 841-856.

AusSpec International Ltd., 2012, The Spectral Geologist Pro, v. 7.1; URL: http://www.thespectralgeologist.com/tsg_pro.htm

AusSpec International Ltd., 2008, GMEX Spectral analysis guides for mineral exploration, sedimentary exhalative deposits, v. 9, 3rd edition, 39 p.

Bierwirth, P., Huston, D., and Blewett, R., 2002, Hyperspectral mapping of mineral assemblages associated with gold mineralization in the Central Pilbara, Western Australia: Economic Geology, v. 97, p. 819-826.

Bruegge, C.J., Stiegman, A.E., Rainen, R.A., and Springsteen, A.W., 1993, Use of Spectralon as a diffuse reflectance standard for in-flight calibration of earth-orbiting sensors: Optical Engineering v. 32, p. 805-814.

Cameron, R.S., 1992, Assessment report on the 1991 diamond drill program, Jason Property, MacMillan Pass, Yukon, Canada, Mayo Mining Division: Vancouver, B.C., unpublished report for Phelps Dodge Corporation of Canada, Ltd., 122 p.

Carne, R.C., 1979, Upper Devonian stratiform barite-lead-zinc-silver mineralization at Tom claims, MacMillan Pass, Yukon Territory: Unpublished M.Sc. thesis, University of British Columbia, 149 p.

Cathelineau, M., 1988, Cation site occupancy in chlorites and illites as a function of temperature: Clay Minerals, v. 23, p. 471–485.

Clark, R., and Roush, T., 1984, Reflectance spectroscopy: quantitative analysis techniques for remote sensing applications: Journal of Geophysical Research, v. 89, p. 6329–6340.

Clark, R., Swayze, G., Wise, R., Livo, E., Hoefen, T., Kokaly, R., and Sutley, S., 2007, USGS digital spectral library splib06a: United States Geological Survey, Digital Data Series 231 (http://speclab.cr.usgs.gov/spectral.lib06).

Dawson, K.M., and Orchard, M.J., 1982, Regional metallogeny of the northern Cordillera: biostratigraphy, correlation and metallogenic significance of bedded barite occurrences in eastern Yukon and western District of Mackenzie: Geological Survey of Canada Paper 82-1C, p. 31-38.

Duke, E., 1994, Near infrared spectra of muscovite, Tschermak substitution, and metamorphic reaction progress: Implications for remote sensing: Geology, v. 22, p. 621–624.

Gadd, M.G., Layton-Matthews, D., Peter, J.M., and Paradis, S., 2015, In situ trace element and sulphur isotope analyses of pyrite constrain timing of mineralization and sources of sulphur in the Howard’s Pass SEDEX Zn-Pb District, Yukon, *in* Paradis, S., ed., Targeted Geoscience Initiative 4: sediment-hosted Zn-Pb deposits: processes and implications for exploration: Geological Survey of Canada Open File, 7838, p. 58-74.

Gardner H.D., and Hutcheon, I., 1985, Geochemistry, mineralogy, and geology of the Jason Pb-Zn deposits, MacMillan Pass, Yukon, Canada: Economic Geology, v. 80, p. 1257–1276.

Goodfellow, W.D., 2007, Base metal metallogeny of the Selwyn Basin, Canada, *in* Goodfellow, W.D., ed., Mineral deposits of Canada: A synthesis of major deposit-types, district metallogeny, the evolution of geological provinces, and exploration methods: Geological Association of Canada, Mineral Deposits Division, Special Publication No. 5, p. 553-579.

Goodfellow, W.D., and Jonasson, I.R., 1986, Environment of formation of the Howards Pass (XY) Zn-Pb deposit, Selwyn Basin, Yukon, *in* Morin, J. A., ed., Mineral deposits of northern Cordillera: Canadian Institute of Mining and Metallurgy, Special Volume 37, p. 19-50.

Goodfellow, W.D., and Rhodes, D., 1990, Geology, geochemistry and origin of the Tom stratiform Zn-Pb-Ag-barite deposits, *in* Abbott, J. G., and Turner, R. J. W., ed., Mineral deposits of the northern Canadian Cordillera, Yukon and Northeastern British Columbia (Field Trip Guidebook 14): Ottawa, 8th International Association on the Genesis of Ore Deposits Symposium, p. 177-242.

Gordey, S.P., and Anderson, R.G., 1993, Evolution of the northern Cordillera miogeocline, Nahanni map area (105I), Yukon and Northwest Territories: Geological Survey of Canada Memoir, v. 428, 214 p.

Guidotti, C., and Sassi, F., 1998, Petrogenetic significance of Na-K white mica mineralogy: Recent advances for metamorphic rocks: European Journal of Mineralogy, v. 10, p. 815–854.

Hulen, J., and Nielson, D., 1986, Hydrothermal alteration in the Baca geothermal system, Redondo Dome, Valles Caldera, New Mexico: Journal of Geophysical Research, v. 91, p. 1867– 1886.

Irwin, S.E.B., and Orchard, M.J., 1991, Upper Devonian-Lower Carboniferous conodont stratigraphy of the Earn Group and overlying units, northern Canadian Cordillera: Geological Survey of Canada Bulletin 417, p. 185-213.

Laakso, K., Rivard, B., and Peter, J.M., 2015, Hyperspectral eflectance spectrometry in the exploration for VMS deposits using the Izok lake Zn-Cu-Pb-Ag deposit, Nunavut as a test site, *in* Peter, J. M., and Mercier-Langevin, P., ed., Targeted Geoscience Initiative 4: Contributions to the understanding of volcanogenic massive sulphide deposit genesis and exploration methods development: Geological Survey of Canada, Open File 7853.

Laakso, K., Rivard, B., Peter, J., White, H., Maloley, M., Harris, J., and Rogge, D., in press, Application of airborne, laboratory and field hyperspectral methods to mineral exploration in the Canadian Arctic: recognition and characterization of volcanogenic massive sulphide-associated hydrothermal alteration in the Izok Lake deposit area, Nunavut, Canada: Economic Geology.

Large, D.E., 1980, Geological parameters associated with sediment-hosted, submarine exhalative Pb-Zn deposits: an empirical model for mineral exploration: Geologisches Jahrbuch, v. D40, p. 59-129.

Large, R.R., Bull S.W., McGoldrick, P.J., Walters S., Derrick G.M., and Carr G.R., 2005, Stratiform and stratabound Zn-Pb-Ag deposits in Proterozoic sedimentary basins, northern Australia, *in* Hedenquist J.W., Thompson J.F.H., Goldfarb R.J., and. Richards, J.P., ed., Economic Geology, 100th anniversary volume, 1905-2005: Littleton, CO, Society of Economic Geologists, p. 931-963.

Li, G., Peacor, D.R., Merriman, R.J., and Roberts, B., 1994, The diagenetic to low-grade metamorphic evolution of matrix white micas in the system muscovite-paragonite in a mudrock from Central Wales: Clays and Clay Minerals v. 42, p. 369-381.

Lydon, J.W., 1983, Chemical parameters controlling the origin and deposition of sediment-hosted stratiform lead-zinc deposits, *in* Sangster, D.F., ed., Short course in sediment-hosted stratiform lead-zinc deposits: Mineralogical Association of Canada, Short Course Handbook, v. 8, p. 175-250.

Magnall, J.M., Gleeson, S.A., and Paradis, S, 2014, SEDEX mineralisation, MacMillan Pass (YT): Petrography, mineralogy and bulk geochemistry of the Tom and Nidd deposits: Geological Survey of Canada, Open File 7457, 37 p.

Miyashiro, A., and Shido, F., 1985, Tschermak substitution in low- and middle-grade pelitic schists: Journal of Petrology, v. 26, p. 449–487.

Morganti, J.M., 1979, The geology and ore deposits of the Howards Pass area, Yukon and Northwest Territories: the origin of basal sedimentary stratiform sulphide deposits: Unpub. Ph.D. thesis, University of British Columbia, 351 p.

Post, J., and Noble, P., 1993, The near-infrared combination band frequencies of dioctahedral smectites, micas, and illites: Clays and Clay Minerals, v. 41, p. 639–644.

Selwyn Chihong Mining Limited, 2012, Selwyn announces updated mineral resource for XY West deposit: Vancouver, British Columbia, Canada, Press Release, 5 p.

Turner, E.C., 2011, Stratigraphy of the Mackenzie Mountains supergroup in the Wernecke Mountains, Yukon, *in* MacFarlane, K.E., Weston, L.H., and Relf, C., ed., Yukon Exploration and Geology 2010: Whitehorse, YT, Yukon Geological Survey, p. 207-231.

Velde, B., 1965, Phengite micas: Synthesis, stability, and natural occurrence: American Journal of Science, v. 263, p. 886-913.

Yang, K., Huntington, J., Gemmell, J., and Scott, K., 2011, Variations in composition and abundance of white mica in the hydrothermal alteration system at Hellyer, Tasmania, as revealed by infrared reflectance spectroscopy: Journal of Geochemical Exploration, v. 108, p. 143–156.

Yarra, D.R., Peter, J.M., Harris, J., and Fueten, F., 2014, Recognition of hydrothermal alteration using airborne hyperspectral imagery and gold favourability mapping in the Hope Bay volcanic belt, Nunavut: Geological Survey of Canada, Open File 7470, 1 sheet, doi:10.4095/293727

Geochemical and Mineralogical Controls on Metal(loid) Mobility in the Oxide Zone at Prairie Creek, Northwest Territories

D.B. Stavinga*
Geological Sciences and Geological Engineering, Queen's University, Kingston, ON
Drew.Stavinga@gmail.com

H. Jamieson
Geological Sciences and Geological Engineering, Queen's University, Kingston, ON

S. Paradis
Geological Survey of Canada, Pacific Geoscience Centre, Sidney, BC

H. Falck
Northwest Territories Geoscience Office, Yellowknife, NT

**Now at Arktis Solutions, Harrowsmith, ON*

Abstract

Prairie Creek is an unmined high grade Zn-Pb-Ag deposit in the southern Mackenzie Mountains of the Northwest Territories. The upper portion of the primary quartz-carbonate-sulphide vein mineralization has undergone extensive oxidation, forming high grade zones rich in smithsonite ($ZnCO_3$) and cerussite ($PbCO_3$). This weathered zone represents a significant resource and a potential component of mine waste material. This study is focused on the characterization of the geochemical and mineralogical controls on metal(loid) mobility under mine waste conditions, with particular attention to the metal carbonates as a potential source of trace elements to the environment. Analyses were conducted using a combination of microanalytical techniques and the elements of interest included Zn, Pb, Ag, As, Cd, Cu, Hg, Sb and Se.

Results include the identification of minor phases previously unknown at Prairie Creek, including cinnabar (HgS), acanthite (Ag_2S), metal arsenates, and Pb-Sb-oxide. Anglesite ($PbSO_4$) may also be present in greater proportions than suggested by previous work. Smithsonite is the major host for Zn but this mineral also contains elevated concentrations of Pb, Cd, Cu, Fe, and Mn, while cerussite (which may be removed as Pb concentrate) also hosts Zn, Cu and Cd. Variable concentrations of Fe, As, Sb, Hg, Ag, and Se are also present in smithsonite and cerussite (listed in approximately decreasing order). A significant proportion of

Recommended citation
Stavinga, D.B., Jamieson, H., Paradis, S., and Falck, H., 2015. Geochemical and mineralogical controls on metal(loid) mobility in the oxide zone at Prairie Creek, Northwest Territories, *in* Paradis, S., ed., Targeted Geoscience Initiative 4: sediment-hosted Zn-Pb deposits: processes and implications for exploration; Geological Survey of Canada, Open File 7838, p. 173-187. doi:10.4095/296328

the trace metal(loid)s may also be hosted by other secondary minerals associated with mineralization. Processing will remove significant sources for these elements, but the original mine plan calls for leaving the smithsonite fraction as tailings. Significant Hg and Ag could remain in tailings from cinnabar and acanthite that is trapped within smithsonite grains.

In a mine waste setting, near-neutral pH will encourage retention of trace metal(loid)s in solids. Regardless, oxidation, dissolution and mobilization is expected to continue in the long term, which may be slowed by saturated conditions, or accelerated by localized flow paths and acidification of isolated, sulphide-rich pore spaces.

Introduction

The Prairie Creek Zn-Pb-Ag deposit is located 500 km west of Yellowknife in the southern Mackenzie Mountains and is surrounded by the recently-expanded Nahanni National Park Reserve. The district contains several types of carbonate-hosted mineralization, including stratabound replacement massive sulphides, quartz-carbonate sulphide veins, and classic Mississippi Valley-type (Paradis, 2007; Paradis, this open file). The quartz-carbonate-sulphide veins and the stratabound replacement sulphides have undergone extensive oxidation and alteration, forming zones rich in smithsonite and cerussite, which is referred to as the “oxide zone”. There is a wide range of trace elements associated with the oxide zone of the deposit, including Ag, Cu, As, Sb, Cd, Se, and Hg, some of which are of potential economic or environmental significance.

The objective of this research project was to understand how these trace elements are mineralogically hosted in the oxide zone of the Prairie Creek deposit. The results have implications for assessing the economic value of the oxide zone and for predicting the geochemical controls on metal(loid) concentrations in drainage from future mine waste.

The site was developed in the 1980s but was never mined. The current owner, Canadian Zinc Corporation, intends to bring the property into production (Canadian Zinc Corporation, 2010, 2014). Although acid rock drainage is not anticipated due to the substantial amount of carbonate associated with the mineralization, metal(loid) leaching occurs from the portal and is predicted from geochemical tests (MESH Environmental, 2008). Post-production plans include underground deposition of all tailings as paste backfill. Results from this research have been used to predict the leaching behaviour of paste backfill made with the oxide zone tailings.

This research formed part of the MSc thesis of Drew Stavinga in the Department of Geological Sciences and Geological Engineering at Queen’s University and detailed results are available therein (Stavinga, 2014).

Results/Data Analysis

Field Sampling

Fieldwork in August 2013 resulted in 29 samples of surface exposures of vein mineralization, 19 samples of the main quartz-carbonate-sulphide vein from the 930 level of the underground workings, 83 samples from on-site core, and 3 samples from the ore stockpile representing the 870 underground level. Samples were chosen based on the presence of "oxide zone" mineralization and, where available, elevated concentrations of the elements of interest. Seven additional samples of surface exposures were supplied by the Northwest Territories Geoscience Office (NTGO) and 10 thin sections from the Geological Survey of Canada (GSC) collection were analysed. Sample locations are shown in Stavinga (2014).

Analysis

Lithogeochemistry

A subset of 53 samples, chosen to represent various degrees and styles of oxidation, were digested via *aqua regia* and analysed for 45 elements by inductively coupled plasma - optical emission spectrometry (ICP-OES) at AGAT laboratories in Vancouver. A non-sulphide leach using ammonium acetate (for Pb) and ammonium chloride/ammonium acetate (for Zn) was used to obtain Pb and Zn concentrations that were considered to represent cerussite and smithsonite, although this was not explicitly tested. Samples with Ag concentrations greater than 500 ppm were subjected to Fire Assay Fusion with Gravimetric finish. Complete results, including results on blanks, replicates and reference materials are available in Stavinga (2014).

Detailed Mineralogical and Trace Element Analysis

Polished thin sections were made from 38 samples selected on the basis of elevated concentrations of elements of interest, presence of Pb or Zn carbonates and location within the deposit. These were examined by petrographic microscopy, and analysed by scanning electron microscopy (SEM), electron microprobe analysis (EMP), Laser Ablation - Inductively Coupled Plasma - Mass Spectrometry (LA-ICP-MS), X-ray diffraction (XRD), synchrotron based trace element mapping, synchrotron-based grain-scale micro-X-ray Diffraction (µXRD), micro-X-ray Fluorescence (µXRF), and SEM-based quantitative mineralogy using Mineral Liberation Analysis (MLA). The results of µXRD analysis provided the general mineral classifications that were applied to the results of MLA. Further details on analytical methods can be found in Stavinga (2014).

Results

Lithogeochemistry

The complete analytical results and correlation matrices for the lithogeochemical analyses can be found in Stavinga (2014). In general, most samples of the oxidized main quartz-carbonate-sulphide vein material showed higher average concentrations of Ag (422 ppm), As (1587 ppm), Cu (8786 ppm), Cd (1374 ppm), Hg (491 ppm), Pb (16.4%), and Sb (3563 ppm) when compared to the adjacent host rock. Except for two samples, Se was mostly below detection limit (<50 ppm). Total Zn concentrations are relatively consistent between the vein (15.8%) and the immediately adjacent host rock of the hanging wall (15.2% for a sample within 10 cm), but are lower in the footwall. Non-sulphide Zn follows a similar pattern, with an average concentration of 9.9% and 8.2% in the vein and hanging wall, respectively. Iron concentrations were found to be similar among the footwall (0.4%), hanging wall (0.4%), and vein material (0.6%). Although Cd and Hg have higher average concentrations in the vein than the host rocks, their values generally fall within the range of concentrations occurring within the hanging wall, with the exception of a few outliers. Digestion by non-sulphide leach found non-sulphide Pb concentrations are generally higher (average 8.1%) in the mineralized vein, are slightly lower in the hanging wall (average 3.6%), and much lower in the footwall (average 0.3%).

Mineralogy

Table 1 lists all minerals identified through a combination of analytical techniques, including SEM, EMP, XRD and synchrotron-based µXRF and µXRD. The most common and abundant minerals identified consist of the primary sulphides (galena, sphalerite, pyrite) and sulfosalts (tetrahedrite-tennantite), the host rock and gangue minerals (calcite, dolomite, quartz), and the secondary metal carbonates (smithsonite, cerussite, malachite, azurite). The list of positively identified minerals provides at least one host for almost every element of concern. Elements without an obvious host, notably Cd and Se, likely occur as minor or trace substitutions and possibly as a tentatively identified phase (i.e. greenockite, tiemannite). Tentatively identified phases, 26 in all, were distinguished by SEM but did not diffract well enough to be firmly identified by µXRD.

Figure 1 is a box plot showing elemental concentrations on a logarithmic scale. Analyses of the metal carbonates and anglesite (a Pb-sulphate oxidation product of galena) by EMP and LA-ICP-MS indicate that they host many of the elements of concern. Some elements are preferentially hosted by certain minerals over others; for instance Ag and Se are higher in the Pb-carbonate and Pb-sulphate than in the Zn-carbonate, while the opposite is true for Cd. Anglesite also contains higher concentrations of Ag, As, Cu, Sb and Se than the Pb and Zn carbonates. Other secondary oxidation products include goethite, which replaces pyrite and is also a common inclusion in smithsonite. Detectable concentrations of metal(loid)s, primarily Pb, Sb, Zn, As, and Cu, are concentrated along the edges of goethite grains or evenly dispersed throughout them. Lead is the predominant metal of interest hosted by goethite, in both pyrite replacement rims and smithsonite inclusions.

In many cases, elements of interest are hosted by secondary minerals present as small inclusions within smithsonite and cerussite, as illustrated in Figure 2. Previous work (MESH Environmental, 2008; pHase Geochemistry, 2010)

Table 1. Minerals identified by one or more microanlaytical technique within the quartz-carbonate-sulphide vein and stratabound massive sulphide-type mineralization. An additional 26 minerals were tentatively identified by SEM but not confirmed by μXRD (Stavinga, 2014).

Mineral	Formula
Positively Identified Phases	
Major Minerals	
Galena	PbS
Pyrite	FeS_2
Sphalerite	$(Zn,Fe)S$
Tennantite-Tetrahedrite	$(Cu,Ag,Fe,Zn)_{12}As_4S_{13}$ - $(Cu,Fe,Ag,Zn)_{12}Sb_4S_{13}$
Anglesite	$PbSO_4$
Azurite	$Cu_3(CO_3)_2(OH)_2$
Calcite	$CaCO_3$
Cerussite	$PbCO_3$
Dolomite	$(Ca,Mg)(CO_3)_2$
Malachite	$Cu_2CO_3(OH)_2$
Smithsonite	$ZnCO_3$
Quartz	SiO_2
Minor minerals	
Acanthite	Ag_2S
Bournonite	$PbCuSbS_3$
Cinnabar	HgS
Covellite	CuS
Goethite	$FeO(OH)$
Bindheimite	$Pb_2Sb_2O_6(O,OH)$
Hydrozincite	$Zn_5(CO_3)_2(OH)_6$
Barite	$BaSO_4$
Christelite	$Zn_3Cu_2(SO_4)_2(OH)_6{\cdot}4H_2O$
Adamite	$Zn_2(AsO_4)(OH)$
Arsentsumebite	$Pb_2Cu(AsO_4)(SO_4)(OH)$
Bayldonite	$Pb(Cu,Zn)_3(AsO_4)_2(OH)_2$
Beaudantite	$PbFe_3^{3+}(AsO_4)(SO_4)(OH)_6$
Duftite	$PbCu(AsO_4)(OH)$
Mimetite - Clinomimetite	$Pb_5(AsO_4)_3Cl$
Segnitite	$PbFe_3^{3+}H(AsO_4)_2(OH)_6$

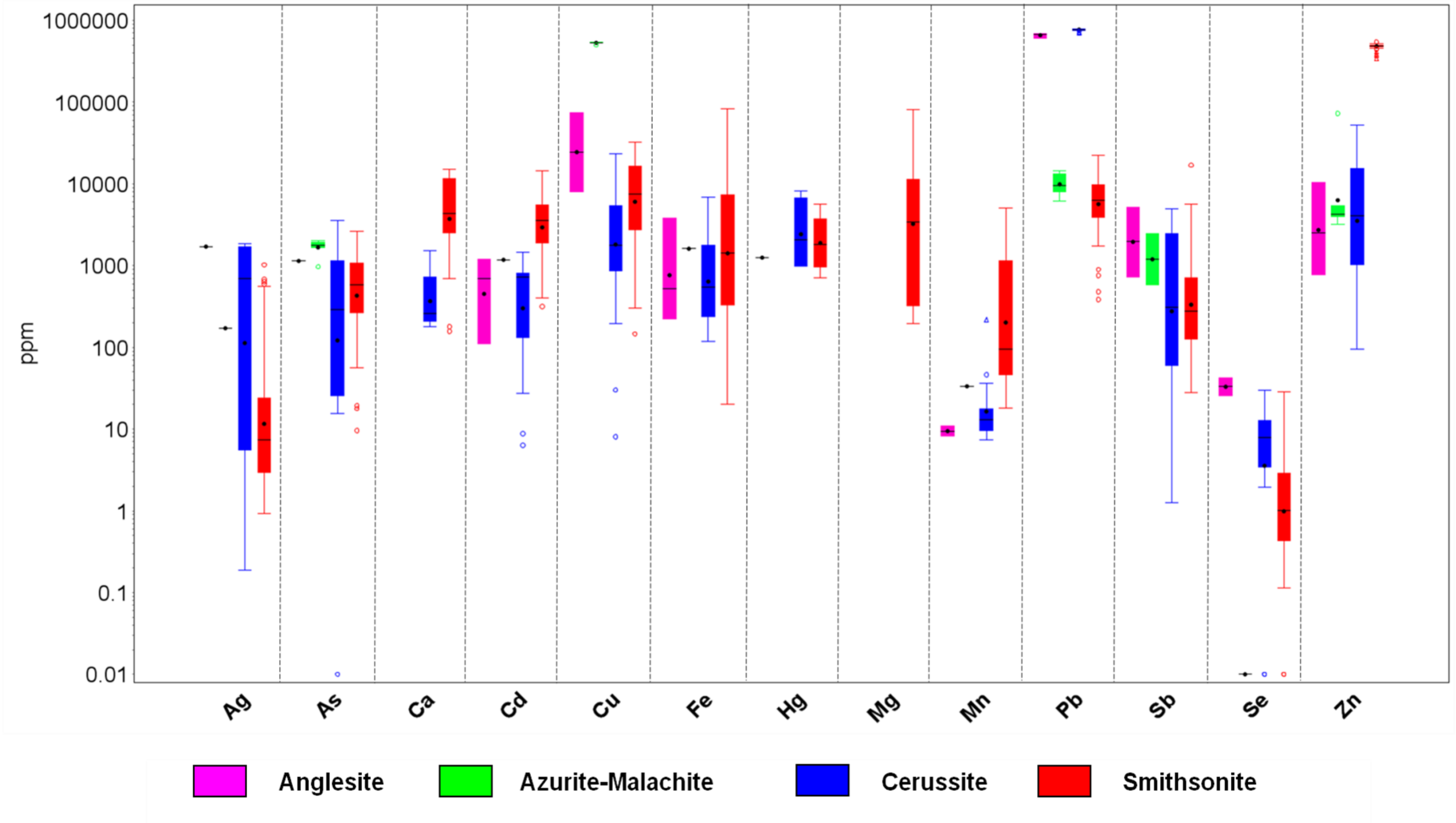

Figure 1. EMP and LA-ICP-MS results for selected elements of interest in secondary oxide minerals. EMP concentrations below detection limit and LA-ICP-MS concentrations greater than one order of magnitude above the calibration curve limit are omitted.

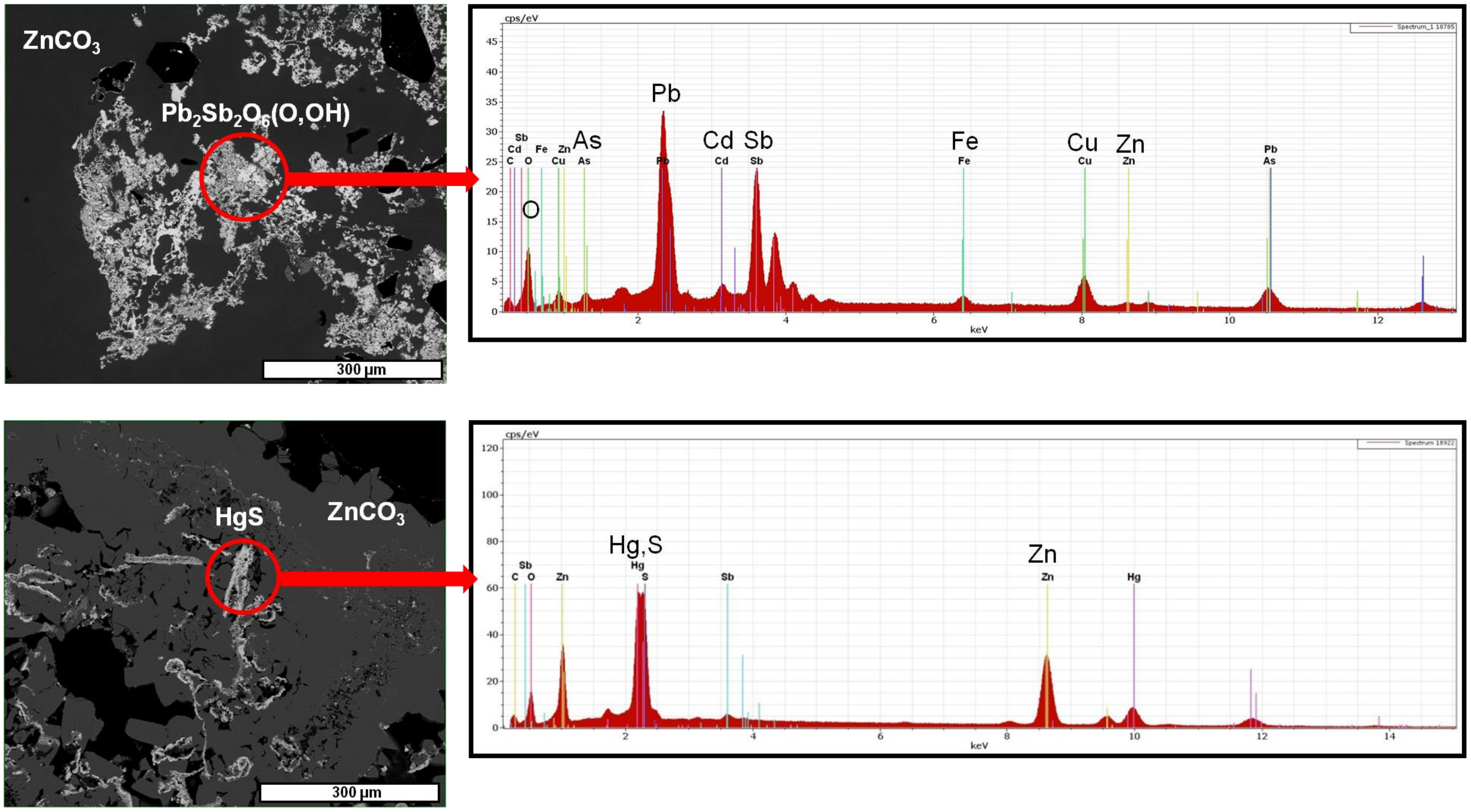

Figure 2. Backscattered-electron images and energy-dispersive spectra showing elements of interest hosted in mineral inclusions included in smithsonite (A) Pb-Sb-O phase, (B) Hg-S phase. Mineral composition based on µXRD.

attributes dissolution of the metal carbonates as the primary source of mobilized metal(loid)s from simulated tailings material. However, our results indicate that some of the metal(loid)s are actually hosted in minerals other than smithsonite and cerussite.

Trace element mapping employing synchrotron-based µXRF illustrates the textural relationship of minerals hosting the elements of interest. For example, Figure 3A and 3B shows arsenate minerals forming rims along the edges of other minerals. Both Cd (Figure 3C) and Cu (not shown) are concentrated within discrete bands in smithsonite.

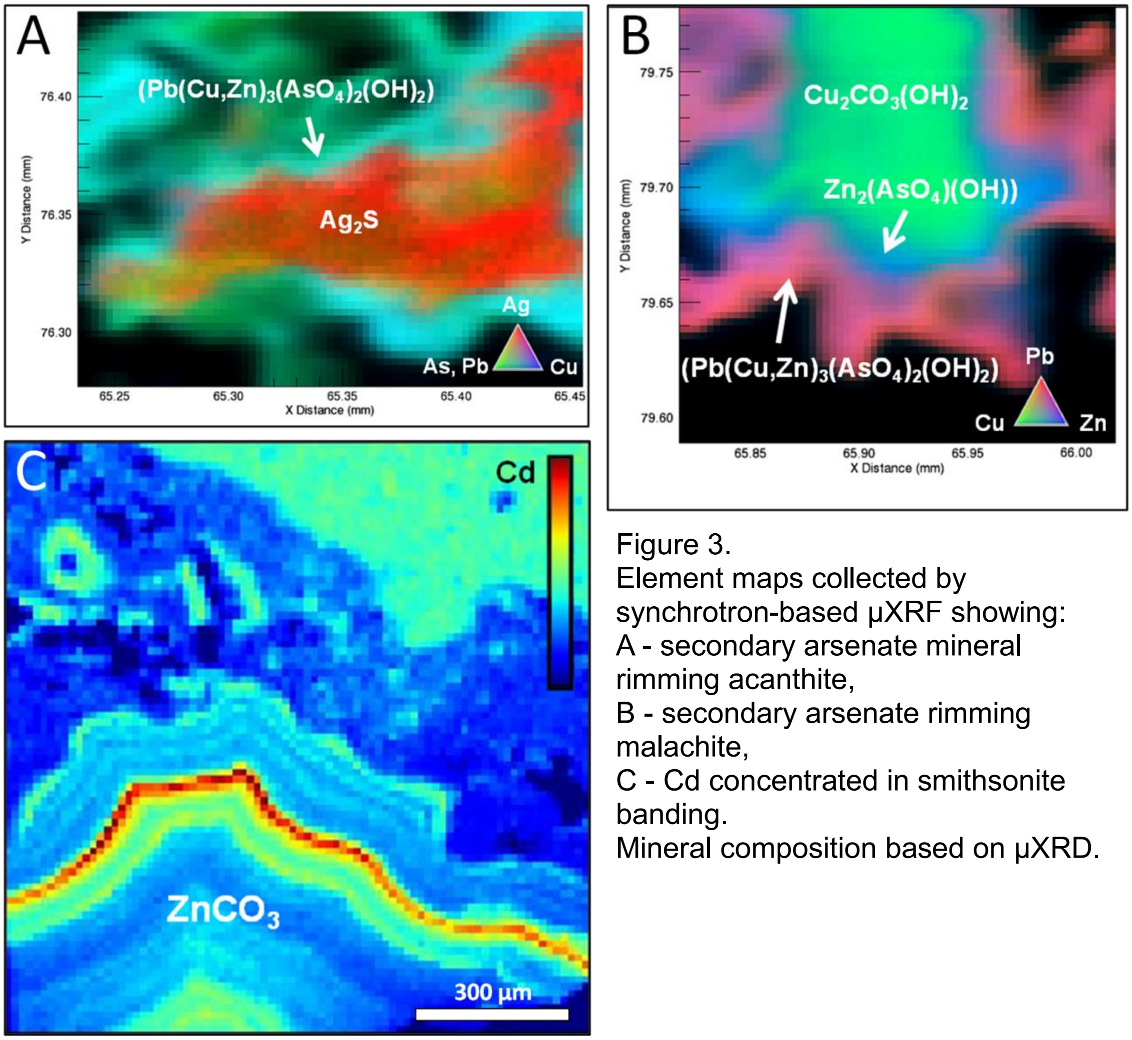

Figure 3.
Element maps collected by synchrotron-based µXRF showing:
A - secondary arsenate mineral rimming acanthite,
B - secondary arsenate rimming malachite,
C - Cd concentrated in smithsonite banding.
Mineral composition based on µXRD.

Mineral mapping of thin sections by SEM-MLA provides information on mineral proportions, grain sizes and mineral associations (Figure 4). These results reveal that anglesite is present in greater proportions than previously thought (Stavinga, 2014). The other secondary phases identified may also exist in high enough proportions to influence metal(loid) mobility. The grain sizes of some, namely cinnabar and acanthite, were found to be relatively fine and hosted primarily by smithsonite (Figure 4C). Textural evidence of dissolution of the metal carbonates and other secondary phases is also seen in strongly weathered material.

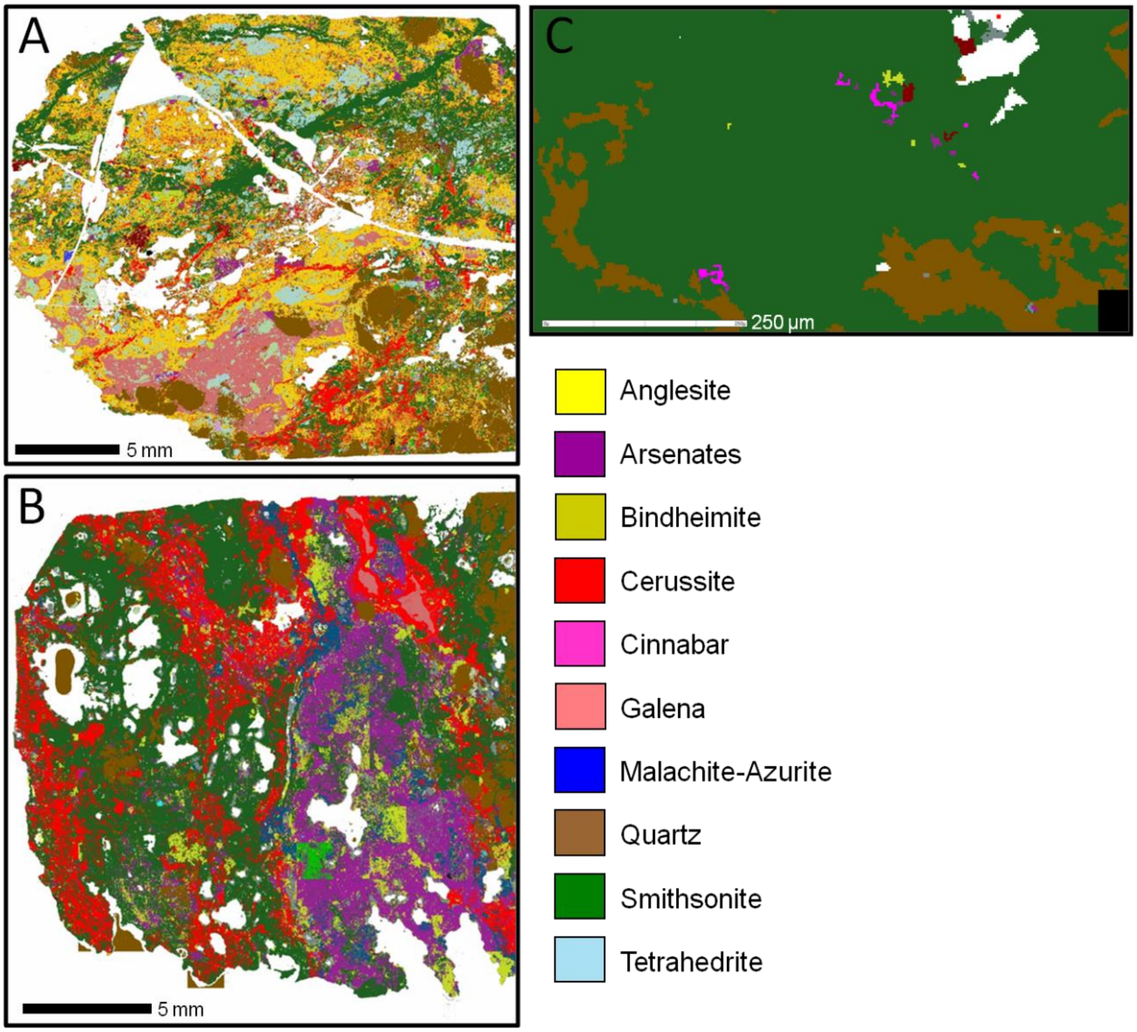

Figure 4. Examples of mineral maps generated by SEM-MLA used for calculating mineral proportions and observing grain size and textures. A - Strongly oxidized sample of quartz-carbonate-sulphide vein from the underground mine containing abundant anglesite (yellow), sample A930-11, B - Strongly oxidized sample of quartz-carbonate-sulphide vein from surface, containing abundant arsenate (purple) and bindheimite (yellow-green), sample Z6-S7, C - Cinnabar and associated arsenate and bindheimite inclusions in smithsonite, sample Z7-S6a.

Discussion

Comparison of Analytical Techniques

Overall, in the context of this research project, analysis by EMP proved to be most useful for determining the elemental composition of specific minerals. However, LA-ICP-MS did prove essential in quantifying trace element concentrations, which were subsequently used to estimate the average concentration of elements within a particular mineral, and the distribution of elements. Characterization of texture and mineral associations was best accomplished using the SEM, while MLA contributed to its understanding and proved to be the best tool for estimating relative proportions and specific element speciation. Synchrotron-based analysis proved instrumental in identifying unknown phases, while giving important insight into the distribution of elements of concern and their valence states that would not otherwise have been known (i.e. Hg and Se associations, and Sb valence; see Stavinga (2014) for details regarding Sb oxidation state measured by synchrotron-based X-ray absorption). Each analytical technique complemented the others, and their combined use greatly increased the quality of the results achieved.

Trace Element Geochemistry and Speciation of the Oxide Zone

The distribution of elements amongst minerals in each thin section analyzed by MLA is estimated by combining the estimated average concentrations for each mineral (Table 2) with the modal mineralogy calculated by the MLA software (details in Stavinga, 2014). Thus, the major sources of elements of interest are revealed for each sample (Figure 5). Reconciliation assays that compare the total concentration of each element calculated by MLA for a thin section agree fairly well with the overall whole rock geochemical results, usually falling within the range of measured total element concentrations. The heterogeneous nature of the mineralization, however, means a direct comparison of concentrations between the same samples is less reliable, resulting in small to large differences as the material used for each analysis could vary in mineral proportions. Nevertheless, this suggests that speciation analysis of a large suite of thin sections could give concentrations that are relatively representative of the overall geochemistry of the deposit.

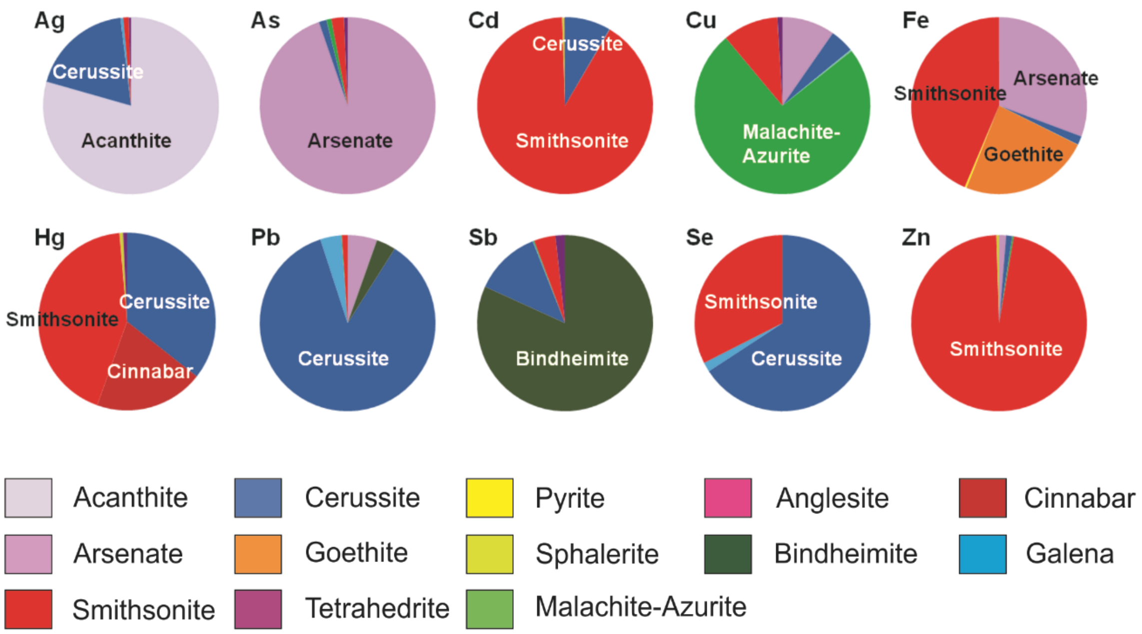

Figure 5. Distribution of elements between different minerals for a single thin section of mineralized material, based on SEM-MLA mineral maps and measured average element concentrations from EMP and LA-ICP-MS analyses.

Table 2. Concentration ranges from EMP and LA-ICP-MS analysis of primary sulphides and sulfosalts and secondary oxide minerals. Values below detection limit are listed as '< [Detection Limit]'. Values one order of magnitude above or below the ICP-MS calibration curve limit are listed as '>[Limit]' and '<[Limit]', respectively. No Hg standard was available for LA-ICP-MS.

Mineral	Method	Ag ppm	As ppm	Ca ppm	Cd ppm	Cu ppm	Fe ppm	Hg ppm	Mg ppm	Mn ppm	Pb ppm	Sb ppm	Se ppm	Zn ppm
Galena	EMP	-	<290	-	<550 - 555	<564 - 1500	<363 - 981	<491	-	-	84.9% - 87.3%	<889	-	<433 - 8312
	LA-ICP-MS	25 - >2000	4 - 384	-	3-140	21 - >4000	55 - 2.7%	-	-	2 - 30	>4000	12 - 3956	1- 18	20 - >5000
Sphalerite	EMP	<324	<659	-	936 - 5516	<485 - 3968	<262 - 1.5%	<497 - 3869	-	-	<1294 - 2668	<647	-	64.4% - 70.1%
Tennantite-Tetrahedrite	EMP	<323 - 3.3%	1.5% - 17.7%	-	1295 - 9615	32.6% - 42.7%	<286 - 2360	1972 - 6892	-	-	<1289 - 6%	3.8% - 25%	-	7.1% - 10.3%
Pyrite	EMP	<323	<445	-	<361	<507	46.8% - 47.2%	<491	-	-	1481- 2699	<705	-	<384
Bournonite	EMP	<323	2.4% - 2.7%	-	<361 - 520	13.1% - 13.6%	<286	<491 - 506	-	-	43.3% - 43.5%	20.6% - 20.9%	-	<384 - 1363
Smithsonite	EMP	<385 - 1021	<356 - 2650	157 - 1.5%	<301 - 1.4%	<452 - 3.3%	<277 - 8.3%	<593 - 5679	<182 - 8.1%	<275 - 5026	761 - 2.2%	<235 - 1.7%	<603	34.5% - 54.9%
	LA-ICP-MS	1 - 593	10 - >2600	-	1497- >1600	146 - >4000	20 - 8.3%	-	-	18 - 3117	384 - >4000	28 - >5000	<0.02 - 29	>5000
Cerussite	EMP	<578 - 915	<407- 3558	<160 - 1530	<453 - 1475	<605 - 2.4%	<420- 3025	<675- 8139	<157	<408	70.7% - 79.5%	<327 - 1709	<560	<597 - 5.3%
	LA-ICP-MS	0.2 - >2000	<0.3 - >2600	-	6 - >1600	8 - >4000	119 - 6954	-	-	7 - 219	>4000	1 - >5000	<0.02 - 30	96 - >5000
Anglesite	EMP	<578	<578- 3944	<160	692 - 1191	<605 - 7.5%	<420 - 521	<675 - 1254	<157	<408	60.1% - 68.6%	<327 - 5187	<560	782 - 1%
	LA-ICP-MS	1709 - >2000	1140 - >2600	-	112- >1600	>4000	225 - 3815	-	-	8 - 11	>4000	719 - >5000	26 - 43	2505 - >5000
Malachite	EMP	<385	973 - 2047	-	<425	50.3% - 54.5%	<319	<593	-	-	<1349 - 1.5%	<557 - 582	<603	3177 - 7.3%
Azurite	LA-ICP-MS	172	>2600	-	1180	>4000	1611	-	-	33	>4000	2453	<0.02	>5000

Sulphide Oxidation Under Alkaline Conditions

Oxidation of the sulphides is occurring at Prairie Creek despite the alkalinity and effective buffering capacity offered by the carbonate host rocks. Although sphalerite oxidation decreases with increasing pH, it begins to increase again above pH 7, primarily due to the influence of the oxidant O_2 (Ziping et al., 2012). Oxidation may also be aided in part by armouring of the host rock by gypsum and hydrous ferric oxide, inhibiting fast neutralization of the acidic solution produced by oxidation of the sulphides and allowing the establishment and stability of an acidic pH within the oxidation zone (Reichert and Borg, 2008). At Prairie Creek, dissolution and alteration is more apparent with sphalerite as opposed to galena, likely due to anglesite and cerussite rims protecting the galena from further oxidation (Stavinga, 2014). This may explain why in highly oxidized samples the only trace of original sulphides is usually galena.

Prediction of Metal(loid) Mobility from Mine Waste

Samples analyzed in this study were collected from quartz-carbonate-sulphide veins and stratabound replacement massive sulphides *in situ*, except samples collected from drill core, which have been stored at surface for up to 22 years, and the 870 level samples, which have been undergoing weathering in the ore stockpile for approximately 30 years. Little mineralogical difference is observed between the samples collected directly from the orebody and surface showings and those from stored drill core and the stockpile. When mining commences, the final tailings will be ground to a fine grain size (~80% at < 80 µm), increasing their potential reactivity, and for paste backfill, tailings will be mixed with binders and cement. Most of the Pb and Zn sulphides will be removed, and Pb and Zn oxides (cerussite and smithsonite) may be removed as well. The mine plan calls for underground storage of all tailings as paste backfill. This may or may not include the smithsonite fraction, depending on the final mine plan. It has been suggested in previous studies (MESH Environmental Inc., 2008) that the metal carbonates will likely dissolve and contribute to the alkalinity and dissolved metal(loid) content of the mine water, with smithsonite supposedly more likely to dissolve than cerussite. This is due to the tendency of cerussite to alter to anglesite rather than dissolve and release Pb ions (Sato, 1992); the release of Zn ions from smithsonite should therefore occur at a greater rate. Except in strongly weathered surface showings, samples usually show only minor dissolution of the metal carbonates under the current *in situ* conditions. However, should dissolution of the metal carbonates occur, Zn, Pb and other trace elements of concern would be released into the pore waters, increasing concentrations significantly if conditions do not favour their attenuation. The dissolution of metal carbonates, in addition to the oxidation of sulphides, is therefore likely to be a major factor controlling the mobility of the trace elements.

Infiltration of the tailings by mine water may generate similar reactions to that experienced by the ore stockpile from rainwater infiltration. The mineralogical characterization by Skeries (2013) of the sediments present in the stockpile, which has been exposed for 30 years, may indicate which minerals are likely to dissolve. The sulphides, metal carbonates (smithsonite, cerussite) and anglesite may also dissolve, as indicated by observed dissolution textures. However, the formation of secondary rims on sulphides, such as cerussite and anglesite on galena and goethite on pyrite, should slow their oxidation and release of metal(loid)s. Goethite is the most common Fe-(oxy)hydroxide formed under alkaline conditions (Bigham, 1994) and is a predominant precipitate in the ore stockpile and, along with Mn-oxide coatings, in the waste rock pile (Skeries, 2013). It is therefore likely to remain stable in the tailings, possibly increasing in content along with Mn-oxides, and, through attenuation, act as an efficient immobilizer of the metal(loid)s of concern. Significant amounts of precipitated azurite, christelite, hydrozincite and possibly aurichalcite also coat the mine adit walls, signifying these phases act as major controls on Zn and Cu mobility once they migrate out of the vein.

Potential flooding of the mine workings after production ends at Prairie Creek would result in the saturation of the backfilled tailings. Exposure to oxygen would be limited, and further oxidation of remaining sulphides would be slowed. However, the oxide tailings will include non-sulphide metal-hosting minerals and their geochemical behaviour under water-saturated conditions is uncertain (Stavinga, 2014).

Implications for Exploration

The focus of this research was to understand how trace elements of economic value and environmental concern are mineralogically hosted in the oxide zone of the quartz-carbonate-sulphide veins and stratabound replacement sulphides at Prairie Creek. Our results show that detailed mineralogical analyses using multiple techniques revealed the presence of Ag (a valuable commodity) hosted in acanthite and Hg (an environmental concern) hosted in cinnabar. Overall, however, the metal carbonates smithsonite and cerussite are the major sources for the elements of concern, and a small, even local decrease in pH may result in metal(loid) release (Stavinga, 2014). There is also the possibility that saturation of tailings used for paste backfill could release metal(loid)s through reductive dissolution of waste from the smithsonite-cerussite “oxide” zone. Mine planning (Canadian Zinc Corporation, 2010) includes consideration of a three-concentrate scheme where most of the smithsonite would go to the tailings. The SEM-MLA calculations suggest that this fraction would carry a significant concentration of Ag, Hg, Cd and other trace elements. Canadian Zinc Corporation is currently considering revising their mine plan to ship Zn carbonate (i.e. smithsonite) concentrate for this and other reasons (Alan Taylor, VP Exploration, personal communication, 2014).

Future Work

This project is complete except for publication of journal articles, and conference presentations (see Stavinga et al., 2014a, 2014b). The MSc thesis is available at http://library.queensu.ca/research/format/finding-theses.

The results were presented at the annual meeting of the Geological Society of America in October 2014, and at the Geoscience Forum in November 2014. We expect to publish the results in Geochemistry: Exploration, Environment and Analysis.

Acknowledgements

The authors would like to thank the Geological Survey of Canada, particularly the TGI-4 program for supporting this research. Canadian Zinc Corporation provided access, in-kind support and advice. Funding was also provided by the Northern Studies Training Program, the Society of Economic Geologists, and an NSERC Discovery Grant to H.E. Jamieson. Synchrotron analysis was done at beamline X26A, National Synchrotron Light Source, Upton, New York.

References

Bigham, J. M., 1994, Mineralogy of ochre deposits, *in* Jambor, J.L., and Blowes, D.W., ed., Short Course Handbook on Environmental Geochemistry of Sulphide Mine-Wastes. Waterloo, Ontario: Mineralogical Association of Canada, p. 103-132.

Canadian Zinc Corporation, 2010, Main report for Developer's Assessment Report, Canadian Zinc Corporation submission to Mackenzie Valley Review Board in support of environmental assessment of Prairie Creek Mine EA 0809-002, 339 p.

Canadian Zinc Corporation, 2014, Prairie Creek. [Online] Available at: http://www.canadianzinc.com/projects/prairie-creek [Accessed 09 06 2014].

MESH Environmental Inc., 2008, Geochemical characterization report for the Prairie Creek project, Northwest Territories: Project No. M004-001, 246 p.

Paradis, S., 2007, Isotope geochemistry of the Prairie Creek carbonate-hosted zinc-lead-silver deposit, southern Mackenzie Mountains, Northwest Territories, *in* Wright, D.F, Lemkow, D., and Harris, J., ed., Mineral and Energy Resource Assessment of the Greater Nahanni Ecosystem Under Consideration for the Expansion of the Nahanni National Park Reserve, Northwest Territories: Geological Survey of Canada, Open File 5344, p. 131-176.

pHase Geochemistry, 2010, Geochemical characterization of paste and paste components, Prairie Creek project, Northwest Territories, Canada, Appendix 4 of Developer's Assessment Report: Canadian Zinc Corporation submission to Mackenzie Valley Review Board Environmental Assessment of Prairie Creek Mine EA 0809-002, 163 p.

Reichert, B., and Borg, G., 2008, Numerical simulation and a geochemical model of supergene carbonate-hosted non-sulphide zinc deposits: Ore Geology Reviews, 2008, v. 33, p. 134-151.

Sato, M., 1992, Persistency-field Eh-pH diagrams for sulphides and their application to supergene oxidation and enrichment of sulphide ore bodies: Geochimica et Cosmochimica Acta, v. 56, p. 3133-3156.

Skeries, K.A., 2013, Characterization of geochemical and mineralogical controls on metal mobility in the Prairie Creek Mine area, Northwest Territories: MSc thesis, Department of Geological Sciences and Geological Engineering, Queen's University, 305 p.

Stavinga, D.B., 2014, Trace element geochemistry and metal mobility of the oxide mineralization at the Prairie Creek zinc-lead-silver deposit, Northwest Territories: MSc thesis, Department of Geological Sciences and Geological Engineering, Queen’s University, 355 p.

Stavinga, D.B., Jamieson, H.E., Falck, H., and Paradis, S., 2014a, Trace element geochemistry and metal mobility of oxide mineralization at the Prairie Creek Zn-Pb-Ag deposit, Northwest Territories: Geological Society of America Annual Meeting, Vancouver, British Columbia, v. 46, No. 6, p. 679.

Stavinga, D.B., Jamieson, H.E., Falck, H., and Paradis, S., 2014b, Trace element geochemistry and metal mobility of oxide mineralization at the Prairie Creek Zn-Pb-Ag deposit, Northwest Territories: Yellowknife Geoscience Forum, November 2014.

Ziping, P., Lin, Y., Tiegeng, L., Zengtao, C., Wei, G., and Yulong, Y., 2012, A simulation experimental study on oxidative kinetics of sphalerite under hypergene condition: Chinese Journal of Geochemistry, v. 31, p. 457-464.

Geochemical Signatures of the South MacMillan River in the MacMillan Pass, Yukon, Including Drainages from the Tom and Jason Pb-Zn Deposits

S.E. Bryson
Department of Earth Sciences, University of Ottawa, Ottawa, ON, K1N 6N5
ed_bryson@hotmail.com

D. Fortin
Department of Earth Sciences, University of Ottawa, Ottawa, ON, K1N 6N5

M.W. McCurdy
Geological Survey of Canada, Ottawa, ON, K1A 0E8

A. Nyheim-Rivet
Department of Earth Sciences, University of Ottawa, Ottawa, ON, K1N 6N5

Abstract

During the summer of 2013, streams in the MacMillan Pass, Yukon, were sampled to characterize the stream waters of a system draining the sediment-hosted Zn-Pb (±Ag, ±Ba) Tom and Jason Pb-Zn deposits and surrounding barren shales. Streams sampled have wide ranging pH values of 2.9 to 8.2. Tributaries to the main channel are either acidic (pH <3.5), or neutral to alkaline (pH >7). Intermediate waters are found along the main channel of the South MacMillan River. Dissolved metal concentrations vary widely with water source and pH. This site is particularly interesting as streams draining the Tom and Jason deposits are acidic and neutral, respectively. The Tom deposit drainage is extremely high in dissolved and fine sediment fraction lead, as well as dissolved zinc. Neutral streams draining the Jason deposit have less dramatic metal concentrations, but do show elevated dissolved zinc and fine sediment fraction lead concentrations. This paper provides an orientation survey with signatures that an exploration geologist might expect to find downstream from a sulphide ore deposit, and indicates certain signatures which deserve further analysis before discounting a watershed as barren of ore deposits.

Recommended citation

Bryson, S.E., Fortin, D., McCurdy, M.W., and Nyheim-Rivet, A., 2015. Geochemical signatures of the South MacMillan River in the MacMillan Pass, Yukon, including drainages from the Tom and Jason Pb-Zn deposits, *in* Paradis, S., ed., Targeted Geoscience Initiative 4: sediment-hosted Zn-Pb deposits: processes and implications for exploration; Geological Survey of Canada, Open File 7838, p. 188-203. doi:10.4095/296328

Introduction

Surficial geochemical exploration methods, such as surveys performed by the Geological Survey of Canada, have a history of recorded success. Much of this success has been attributable to mechanically transported glacial drift and stream sediments (Boyle, 1979; Levson, 2001). Mechanical dispersion is limited to ore bodies exposed to surface erosion during recent geological history. In contrast, groundwater can penetrate deeply in the earth's crust and transport constituents back to the surface through dissolution, dispersion, and possible re-precipitation (Miller, 1979; Johnson, 2009). Thus, dispersion haloes created by aqueous transport have the potential to carry the geochemical signatures of ore bodies not visible in detrital sediments. While chemical weathering and mineral precipitation in stream sediments are well documented, the effect of varying environmental conditions on exploration samples are not always well understood or accounted for. Additionally, documented geochemical signatures from undisturbed ore bodies, known as orientation surveys, are limited.

Mountainous areas are particularly promising for geochemical exploration since water can interact with buried geology and resurface along a generally downward flowpath. Metal mobility, however, is extremely dependant on the properties of the water (Hermann, 1985). This becomes important for exploration since the oxidation of pyrite can generate extremely acidic, metal rich conditions known as acid rock drainage (ARD), which may or may not be related to the presence of an economic ore deposit (Kelley and Taylor, 1997; Kwong et al., 2009). Conversely, if sufficient carbonates are present within the ore body, waters may remain pH neutral with low overall metal concentrations despite the presence of economic levels of sulphide mineralization (Kwong et al., 2009). As water surfaces and enters stream flow, pH, temperature and bulk chemistry can rapidly change, limiting or enhancing the ability of elements to be carried in aqueous solution. The literature reveals few, if any, documented successes of ore bodies being located based on water chemistry alone. This limited success has not gone unnoticed and a need for method development has been a recurring theme. Refinements of existing methods have been proposed such as thermodynamic modelling of waters (Miller, 1979; Leybourne and Cameron, 2010), analysis of oxide precipitates (Carpenter et al., 1975; Huelin et al., 2006) and analysis of the suspended sediment fraction (Telmer et al., 2002). These methods attempt to measure previously dissolved metals, which have either precipitated into mineral form or adsorbed onto charged particulate material.

Clays, oxides and organics are particularly adept at adsorbing metal ions (Moore et al., 1991; Hua et al., 2012). This effect can rapidly decrease dissolved metal concentrations in stream water minimizing the size of a geochemical anomaly. Secondary metal-oxide minerals complicate inter-stream comparisons due to their susceptibility to thermodynamic conditions. As such, stream water chemistries can only meaningfully be compared to streams with similar conditions, particularly pH. Targeting highly adsorptive particles by analysing suspended sediments has the potential to both enhance the contrast of an anomaly, and increase the lateral extent of its dispersal (Telmer et al., 2002). By targeting only stream deposited fine sediments, this effect may already be visible.

The aqua regia extraction commonly used in sediment sampling programs, is a partial digestion which dissolves most base metals, sulphides, oxides, and altered silicates (Chen, 2001). Unfortunately aqua regia extractions alone do not allow for the separation of those metals contained in mechanically transported primary ore minerals (such as metal-sulphides), from those precipitated with and absorbed to oxides, clays and organics. Partial dissolution of structural silicates can also be expected to dilute the geochemical signal of an ore body with distance. Instrumental neutron activation analysis (INAA) of sediments is commonly performed by the laboratories of the Geological Survey of Canada and this is believed to represent total metal concentration including structural silicates.

In August 2013, streams in the MacMillan Pass area were sampled extensively to further the development of geochemical sampling techniques. The MacMillan Pass area provides an interesting opportunity as the Tom and Jason sediment-hosted Zn-Pb (±Ag, ±Ba) deposits are drained by acidic and neutral streams, respectively. Neighbouring streams have a wide pH range while draining no known ore deposits. In 2006, Gartner Lee performed a regional water quality, sediment and benthic invertebrate assessment of this area as a baseline study to establish water quality objectives prior to potential mining (Gartner Lee, 2007). Kwong et al. (2009) also studied selected streams in the MacMillan Pass area due to their naturally acidic properties, but no connections to mineral exploration were made. However, this site is similar to the nearby Howard's Pass, whose water were characterized for mineral exploration purposes in a Geological Survey of Canada open file (Goodfellow, 1983). Study of the acidic streams draining sediment-hosted Zn-Pb (±Ag, ±Ba) deposits of the Howard's Pass has shown Zn to be highly mobile in these environments. Conversely, Pb rapidly accumulates in sediments causing dissolved concentrations to fall significantly with distance from the metal source. In light of the three decades that have passed, it seems an opportune time to revisit this area and apply recent analytical and modelling techniques with a new orientation survey.

Site

The MacMillan Pass area is located along the south central portion of the Yukon-Northwest Territories border. It is on the eastern margin of the Selwyn Basin, an epicratonic marine basin developed during Protorozoic rifting of the North American western continental margin (Goodfellow, 2004). This rifting and associated hydrothermal activity created the Tom and Jason sediment-hosted Zn-Pb (±Ag, ±Ba) deposits Tom Zn-Pb-Ag-barite and Jason Zn-Pb-barite, are hosted in interbedded carbonaceous mudstone, diamictite, siltstone and siliceous shales of Devonian lower Earn Group rocks known as the Portrait Lake Formation (Goodfellow, 1991; Goodfellow and Rhodes, 1991). Figure 1 illustrates the regional geology relative to the sampling locations.

The site is accessed by the Canol Road, a summer access road following the valley sides. Peat-rich wetlands are common in the valley bottom, while slopes are scree covered. The South MacMillan River follows the steeply sided valley from the water divide in the MacMillan Pass for roughly 20 kilometres before entering a larger open drainage basin. Smaller tributary streams drain the surrounding mountains to the South MacMillan River at regular intervals (Figure 2).

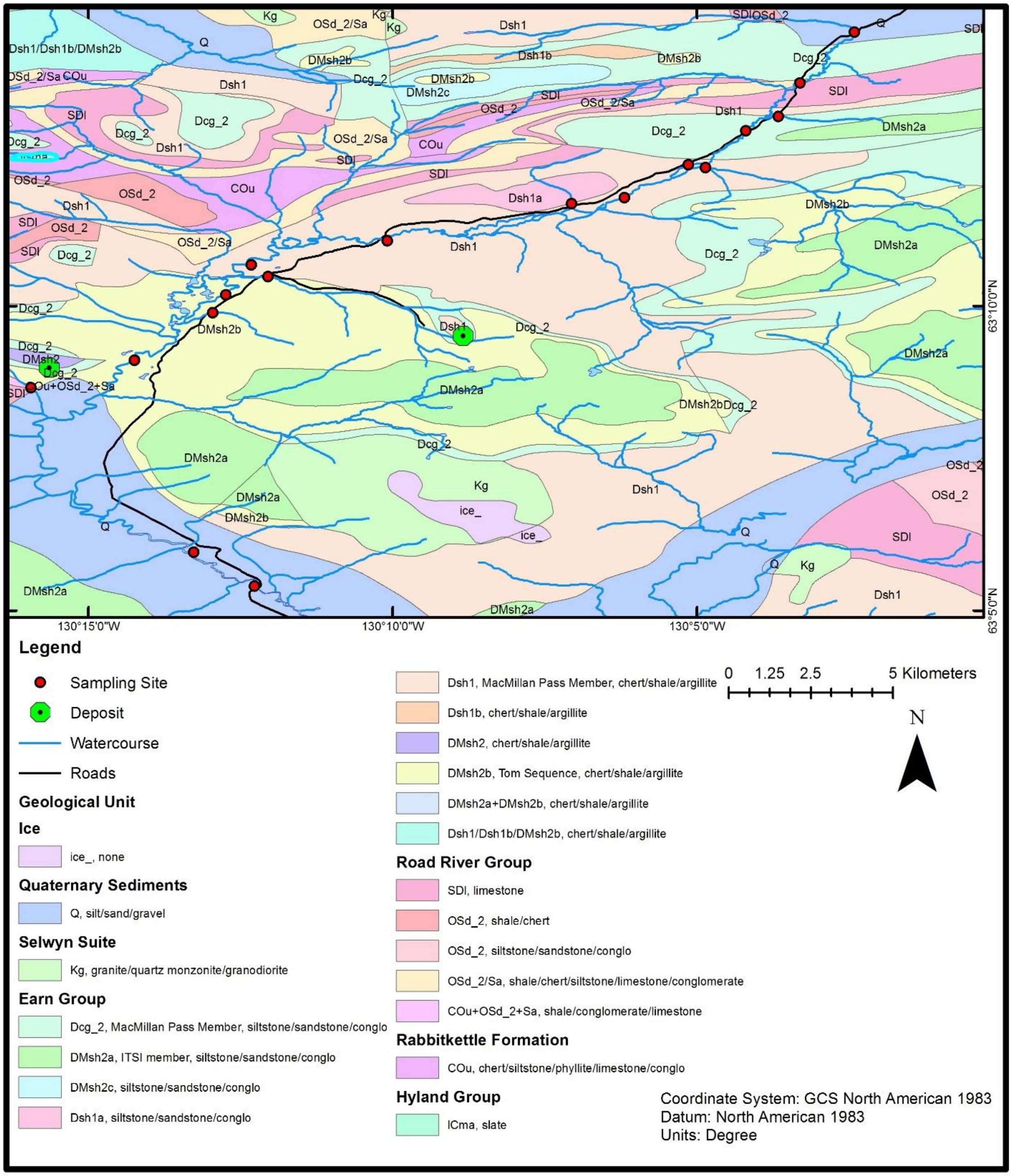

Figure 1. Geological map of the MacMillan Pass area showing stream network and sampling locations. (Modified from Gordey and Makepeace, 1999, same geological unit abbreviations used); National Topographic Data Base 105-O/1, 1990; Goodfellow and Rhodes, 1991).

Detrital stream sediments are composed of silt to boulder lag deposits. These are overlain by ferricretes in the most acidic waters (pH <3.2) (Figure 3), red Fe-oxide rich precipitates in moderately acidic waters (pH 4-5) and white Al-oxides in slightly acidic waters (pH 5-6). Neutral to basic waters without acidic tributaries have no visible precipitates.

Tributaries to the main channel are either acidic (pH <3.5), or neutral to alkaline (pH >7). The bottom of the South MacMillan River was often covered in up to a centimetre of Fe-oxide and Al-oxide precipitates under clear, calmly flowing regions. River reaches with faster flows suspended this finer material, clearing the river bed of all but the largest boulders and giving the waters a decidedly rusty appearance. At the Tom deposit, exploration tunnelling has been performed and untreated waters from the adit feed Seckie Creek 2. No processing is known to have occurred on site.

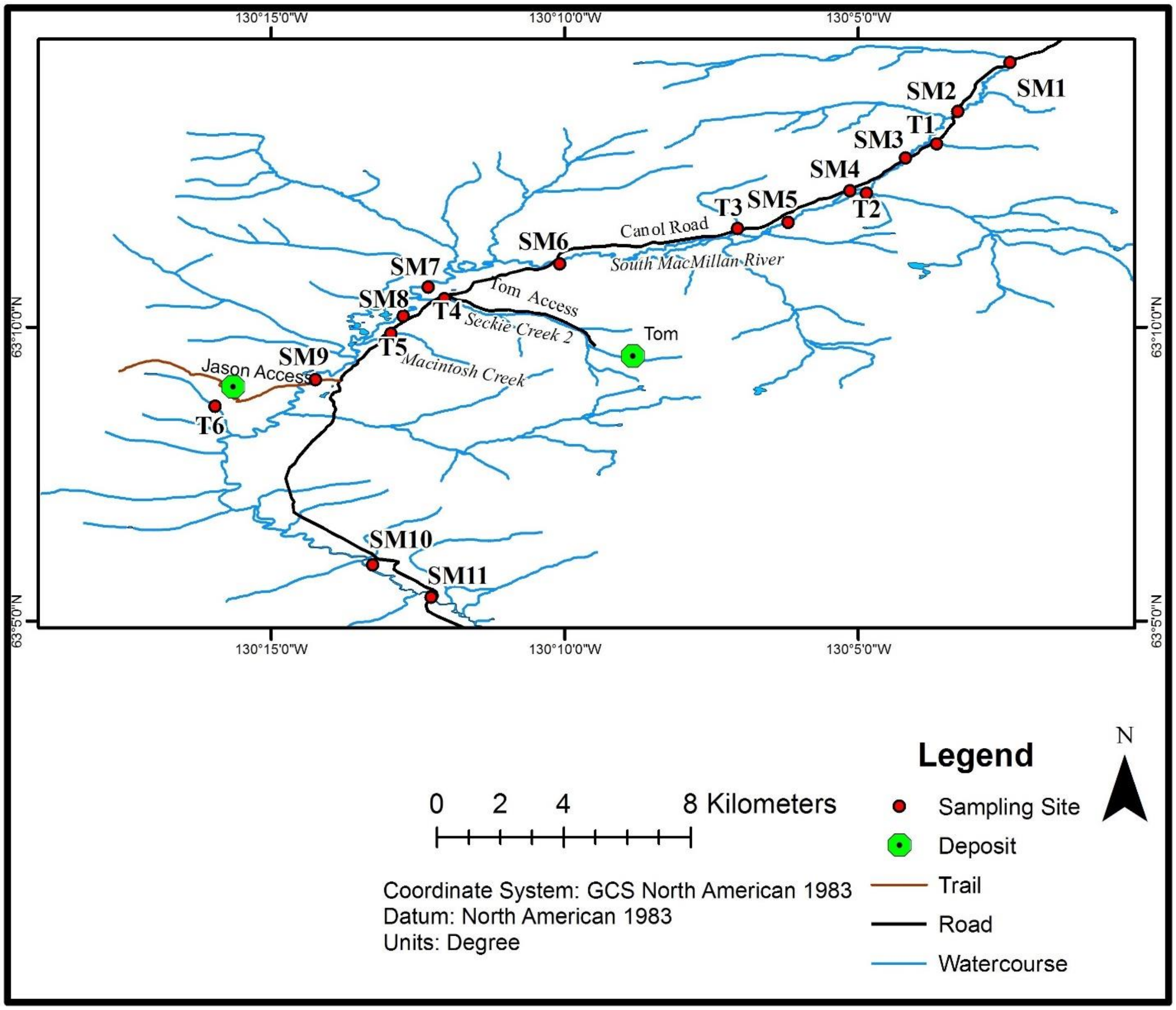

Figure 2. Site map showing sampling locations on the South MacMillan River (SM) and tributaries (T) as well as the Canol Road and Tom and Jason access roads. The South MacMillan River flows towards the bottom of the map (southwest). (Modified from the National Topographic Data Base 105-O/1, 1990).

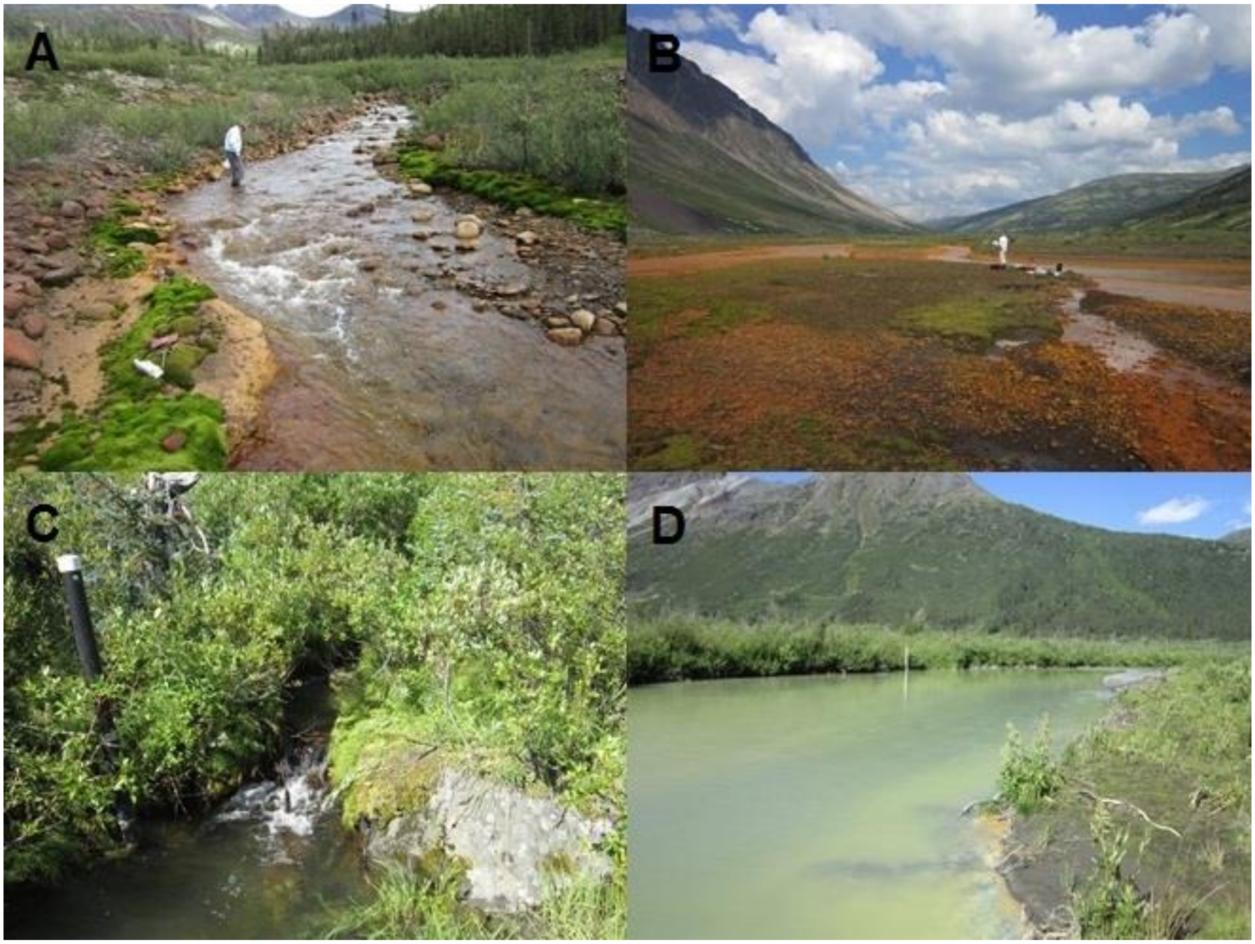

Figure 3. A) Acidic stream (pH 3.4) at site T1 showing ferricrete stream bottom and clear waters. B) Moderately acidic stream (pH 4) at site SM5 showing heavy Fe-oxide precipitation. C) Neutral tributary at site T6 downstream of the Jason deposit showing clear waters. D) Site SM7 on the South MacMillan River with mildly acidic waters (pH 5.3) showing Al-oxide precipitation with minor Fe-oxides.

Results/Data Analysis

Methods

Sampling was performed during August, 2013 at 17 sites along the South MacMillan River and its tributary streams. Sampling and analysis followed standard Geological Survey of Canada field and laboratory procedures for stream geochemical surveys unless otherwise specified. For further information see McCurdy et al. (2012), which provides detailed field and laboratory procedures.

Where roads were in proximity to the stream or a bridge crossing is present, samples were taken immediately upstream of these locations. Water samples for dissolved cation analysis were collected mid-stream. Filtration was performed with new, 60 ml syringes rinsed with sample water through disposable 0.45 µm PAL brand filters. The initial filter discharge was used as a rinse and was not collected. Fe and Al-oxides in water courses regularly caused filter blockages and all attempts were made to change filters before excessive pressure was required to force water through the filter. Sample water was collected in new, Environment Canada issue, 250ml, HDPE bottles, which were rinsed three times with filtered sample water. For the purposes of this analysis, 'dissolved' includes all materials passing through filtration. Samples were acidified with pre-measured nitric acid (HNO_3) provided by ALS laboratories, Whitehorse, on the day of sample collection and placed into coolers. Water parameters including pH, conductivity (µS/cm), ORP (mV) and temperature (°C) were recorded on site immediately after sampling using a YSI multi-parameter meter which was calibrated daily. Samples were kept cool with ice packs and air shipped to Ottawa in these same coolers. Analysis was done by inductively coupled plasma emission spectroscopy (ICP-ES) and inductively coupled plasma mass spectrometry (ICP-MS) at the laboratories of the Geological Survey of Canada, Ottawa. Quality assurance was provided by three blind duplicates collected in the field, one lab duplicate, and two known standards, acid blanks and filter blanks, analysed by the laboratory. No blind standards were used. Additional sampling and field measurements were performed at these locations and analysed at the University of Ottawa for characterization of metal transport in the waters and thermodynamic modelling. These results were not finalized at the time of writing.

Stream sediment samples were collected by hand after water sampling was completed. Samples were collected at various locations over 5 to 20 m along the active stream channel in sediment sampling bags and allowed to drain and air dry on clean tarps. After being wrapped in individual plastic bags and taped shut, samples were shipped by truck to the laboratories of the Geological Survey of Canada in steel pails. Next they were dry sieved to collect the -80 mesh (<177 microns) fraction. Three splits of the fine fraction were taken with one set being stored for later use. Three blind duplicates and two known reference standards were then inserted into the other two sample splits. One sample split was sent to Becquerel Laboratories, Mississauga, Ontario, for INAA analysis providing total concentrations of 35 elements. A second sample split was sent to ACME Analytical Laboratories, Vancouver, British Columbia, for analysis by aqua regia digestion followed by inductively coupled plasma mass spectrometry (ICP-MS), providing concentrations of 65 elements. Only a subset of these elements are reported here due to space constraints. Stream precipitates were collected at some sites for analysis at the University of Ottawa with the additional water samples and the analyses were not finalized at the time of writing.

Results

Water Samples

Streams sampled had pH values ranging from 2.9 to 8.3 (Table 1) and moderate water temperatures of 8 to 14°C. The primary driver of variability was pH, with acidic (pH<4) streams having high metal loads, and neutral to basic (pH>6.9) streams having relatively low metal loads.

Many tributaries were not sampled due to time and accessibility; in at least one location the South MacMillan River appears to be significantly impacted by those tributaries that were missed. Due to mixing of tributaries, pH of the main river channel fluctuates between 3.5 and 7.1 (Figure 4). The South MacMillan River is initially acidic at site SM1 and SM2, but inputs between sites SM2 and SM3 neutralize the stream. Tributary site T2 returns

	pH	Mg	Al	Ca	Cr	Mn	Fe	Co	Ni	Cu	Zn	As	Cd	Pb
Site		ppm	ppm	ppm	ppb	ppb	ppm	ppb	ppb	ppb	ppb	ppb	ppb	ppb
LOD		0.005	0.002	0.02	0.1	0.1	0.005	0.05	0.2	0.1	0.5	0.1	0.02	0.01
SM1	3.4	4.15	10.85	18.1	0.9	444	1.2	35.3	242	69.1	914	< 0.1	10.8	0.19
SM2	4.4	4.22	7.69	18.5	0.5	334	0.5	25.7	180	50.1	679	< 0.1	7.9	0.11
T1	7.0	1.44	0.01	5.1	< 0.1	0	< 0.01	0.1	14	0.8	25	< 0.1	0.2	< 0.01
SM3	7.1	10.48	0.03	35.8	< 0.1	179	0.1	14.4	109	2.6	266	0.2	4.8	0.01
SM4	6.9	10.14	0.02	33.7	< 0.1	198	1.0	16.5	120	3.8	329	0.2	4.9	< 0.01
T2	3.3	7.95	22.14	16.9	16.9	648	24.0	68.3	435	231.0	2136	2.5	70.8	0.20
SM5	4.0	10.14	10.60	28.8	3.3	598	2.7	43.7	276	102.8	1110	< 0.1	31.4	0.08
T3	8.3	14.34	0.06	69.6	0.2	0	< 0.01	0.1	31	0.8	21	0.4	0.7	< 0.01
SM6	4.4	13.74	8.72	28.3	1.0	678	0.4	37.1	265	80.3	1078	< 0.1	30.6	0.09
SM7	5.3	16.21	1.08	37.0	0.4	493	0.2	26.9	224	48.6	931	0.1	21.5	0.02
T4	3.0	19.69	122.16	30.5	122.5	2703	193.8	238.2	1913	507.0	14575	25.6	701.8	33.61
SM8	3.9	17.49	8.71	38.7	4.1	583	7.6	39.3	337	75.6	1759	0.4	61.5	1.55
T5	2.9	33.42	202.53	25.0	322.5	1655	334.1	295.3	2674	305.6	7931	78.2	265.2	0.08
SM9	5.4	16.62	10.87	36.5	1.4	573	5.9	37.7	324	67.2	1634	0.2	54.0	0.63
T6	7.7	4.38	0.03	20.7	< 0.1	74	0.3	0.3	6	0.6	58	0.8	0.2	0.03
SM10	4.5	14.00	8.51	32.7	0.8	458	2.9	30.5	268	51.6	1335	0.2	42.3	0.34
SM11	4.5	12.83	6.52	30.8	0.7	432	2.4	26.6	236	45.7	1187	0.2	35.7	0.38

Table 1. Dissolved metal concentrations and pH measurements from the MacMillan Pass. Analysis performed by inductively coupled plasma emission spectroscopy (ICP-ES) for Mg, Ca and Fe; and inductively coupled plasma mass spectrometry (ICP-MS) for Al, Cr, Mn, Co, Ni, Cu, Zn, As, Cd and Pb. LOD is limit of detection.

the river to a pH of 4 by SM5. The two most acidic tributary streams, midway down the valley proximal to the Tom deposit, have a pronounced effect on the river, significantly lowering the pH. Downstream of these inputs, the main channel remains acidic and, despite reaching over 6 m wide, has a low pH of 4.5 at the most downstream sampling site. The mixing of these diverse waters causes the South MacMillan River to be extremely precipitate-rich, with red and white Fe and Al-oxide minerals visible throughout.

Metal concentrations along the South MacMillan River oscillate with the various measured and unmeasured inputs. Fe, Al, Cd, Cr, Cu, Mn, Co, Ni, Pb and Zn all show initial peaks after known acidic inputs followed by diminishing concentrations. The concentrations of Fe, Cd, and Pb in particular have large fluctuations. Ca and Mg show matching patterns; an initial increase in concentrations after the stream inputs between SM2 and SM3 followed by a generally stable trend.

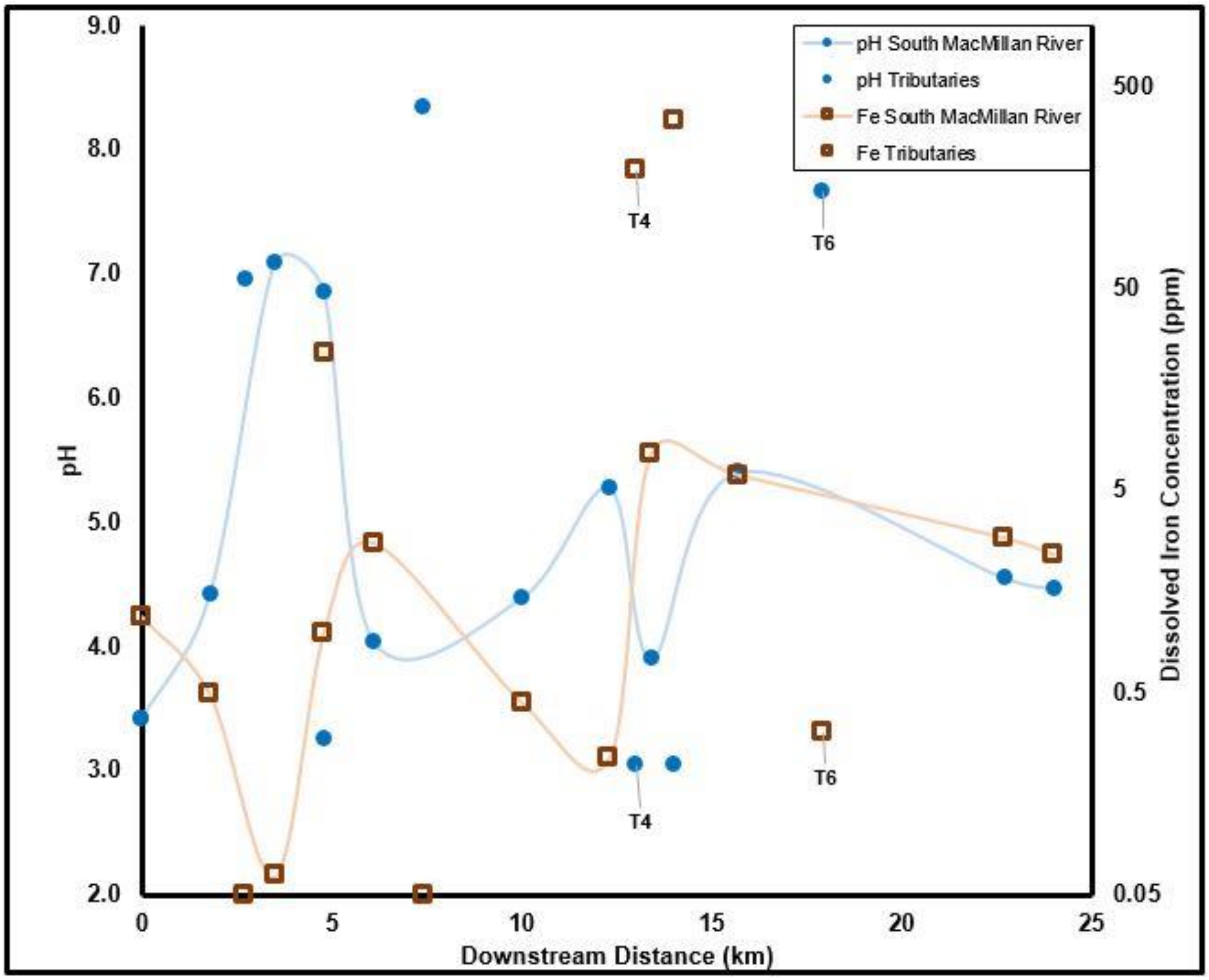

Figure 4. Highlighting the extreme variability of the study sites, this graph shows pH (left axis) and dissolved iron (right axis) with regards to distance from the most upstream site on the South MacMillan River (SM1). Sites along the South MacMillan River proper are connected while tributaries are individual point. Sites T4, draining the Tom and T6, draining the Jason deposit, are highlighted. Note that dissolved iron is plotted on a logarithmic scale.

High acidity in Macintosh Creek's waters (T5) corresponds with the highest concentrations of Al, Cr, Co, Ni, Fe, and Mg. Seckie Creek 2 (T4), draining the Tom deposit, has significantly higher concentrations of Mn, Cu, Zn, Cd and Pb. Dissolved Pb at this site is an extremely high 33.6 ppb. The only other sampling location to exceed a Pb concentration of 1 ppb was immediately downstream of the confluence of Seckie Creek 2 and the South MacMillan River.

Acidic site T2 provides an interesting contrast to Seckie Creek 2 and Macintosh Creek where, except for Cu, dissolved metal concentrations are closer to that found along the South MacMillan River. Site SM1 represents the main channel of the South MacMillan River at its headwaters. It is the only acidic tributary with no ferricrete hardpan and metal concentrations are not notably high.

Neutral to basic streams T1, T3 and T6 have by far the lowest concentrations of dissolved Mn, Co, Ni, Cd and Zn. T3 is the most basic stream sampled with a pH of 8.3. It is characterized by high Ca concentrations approaching 70 ppm. Site T1, also with neutral waters, has the lowest Ca concentration measured at just over 5 ppm.

Fine Fraction Sediment Samples

With the exception of Cr, results by aqua regia/ICP-MS analysis show similar trends to those of total sediment concentration analysis conducted by INAA. Superior detection limits, precision, and greater data set size make aqua regia/ICP-MS the preferred analytical method, which will be discussed here.

Fe concentrations are highest at T2, T4, and T5, which are underlain by Fe-oxide ferricretes (Table 2). Mn concentrations are highest at neutral drainage sites and lowest at acidic sites. Cu and Co have similar patterns to Mn, but are notably absent at site T6 and have an extreme spike at site T1. The highest Ni concentrations are found at neutral tributaries T1 and T3. The highest Al values are found at site SM7, which had extensive white Al-oxide precipitates while the lowest concentrations were acidic tributaries SM1, T2, T4, and T5. Ca and Mg are highest at the neutral upstream sites T3, SM3 and SM4.

Pb and Zn are the most notable elements in the data set. Pb’s profile is characterized by an extreme spike at sampling location T4 on Seckie Creek 2, immediately downstream of the Tom deposit. While no other sediment samples exceeded 60 ppm, the concentration measured at T4 is an elevated 483 ppm. Meanwhile Zn has an extreme peak at T2, where no known ore deposit exists.

Discussion/Models

Acidic tributaries are closely associated with the Earn Group, and its geological subsets containing shales. These include the Itsi Member, Tom Sequence and Lower Earn Group. The Tom Sequence appears particularly adept at producing acidic drainages. The neutral to basic waters measured at sites SM3 and T6 have significant portions of their drainage areas underlain by the same shale bearing formations; however, both also drain areas underlain by the Road River Group, which is composed of limestone and shale (the Lower Earn Group also contains significant quantities of limestone). In the upper reaches, an un-sampled, inaccessible stream joining the South MacMillan River between sites SM2 and SM3 drains the Rabbittkettle Formation which is dominantly composed of limestone. It is notable that the stream sampled at location T1 does not appear to drain either shales or limestones, with its watershed located almost entirely within a chert pebble conglomerate known as the MacMillan Pass Member.

Characteristics of the South MacMillan River itself appear to be dominated more by mixing dynamics of the various tributary streams than interactions with the underlying geology. Downstream of major confluences, Fe-oxides rapidly precipitate, as can be seen by the dissolved Fe concentrations in Table 1 which show sharp increases at confluences followed by more gradual declines. Co, Cu, Zn, Cd, Mn and Cr show similar but more subdued patterns, likely due to their absorption to Fe and Al-oxides. The formation of Fe and Al-oxides is also acid generating, which will serve to maintain the relatively low pH values observed in the South MacMillan River along the study area.

Site	Mg %	Al %	Ca %	Cr ppm	Mn ppm	Fe %	Co ppm	Ni ppm	Cu ppm	Zn ppm	As ppm	Cd ppm	Pb ppm
	Aqua regia/ICP-MS												
LOD	0.01	0.01	0.01	0.5	1	0.01	0.1	0.1	0.01	0.1	0.1	0.01	0.01
SM1	0.07	0.49	0.03	19.5	61	12.85	2.5	14.3	90.9	78	41.6	0.22	22.1
SM2	0.09	0.76	0.10	16.0	226	6.26	10.0	36.4	90.0	168	40.0	0.64	20.1
T1	0.13	1.46	0.17	12.7	1008	2.74	83.8	247.4	140.6	637	22.7	3.21	15.5
SM3	0.26	1.10	0.68	10.7	457	4.85	28.2	120.9	171.4	530	75.3	6.23	28.6
SM4	0.24	1.80	0.55	10.9	546	4.98	36.0	125.4	226.2	635	68.7	7.16	26.5
T2	0.10	0.35	< 0.01	55.7	36	24.83	1.0	6.0	43.9	44	67.3	0.15	13.5
SM5	0.10	1.28	0.17	32.9	263	11.19	19.0	67.9	118.0	252	64.1	1.42	19.8
T3	0.31	1.32	1.38	17.3	834	3.70	34.7	507.6	327.6	2354	41.0	22.01	22.0
SM6	0.09	1.29	0.15	26.2	230	7.42	12.9	59.2	118.2	250	56.7	1.36	25.6
SM7	0.09	2.86	0.32	22.1	375	5.66	19.9	97.6	219.6	486	57.4	4.36	24.4
T4	0.01	0.17	0.02	53.4	19	18.74	0.9	6.0	25.8	549	120.5	2.65	483.1
SM8	0.07	1.54	0.23	24.0	307	6.92	17.6	88.6	136.2	398	63.2	3.34	55.8
T5	0.02	0.17	< 0.01	219.9	7	29.91	0.4	4.0	6.5	17	318.1	0.35	21.4
SM9	0.06	2.06	0.24	39.4	164	11.40	9.4	69.3	120.4	342	62.5	3.07	52.3
T6	0.14	0.46	0.32	8.3	804	2.49	8.8	52.7	41.9	470	36.1	2.31	53.1
SM10	0.09	1.44	0.29	21.6	138	6.37	9.2	66.7	92.5	321	56.3	1.91	40.8
SM11	0.10	1.55	0.31	23.1	420	6.12	23.9	88.6	98.6	447	69.5	3.30	46.9
	INAA												
LOD	-	-	-	20	-	0.2	5	20	-	100	0.5	5	-
SM1	-	-	-	72	-	15.0	< 5	26	-	<100	50	< 5	-
SM2	-	-	-	61	-	7.8	10	40	-	170	48	< 5	-
T1	-	-	-	73	-	3.0	79	230	-	600	24	< 5	-
T2	-	-	-	71	-	32.8	< 5	< 20	-	<100	83	< 5	-
SM5	-	-	-	87	-	12.0	18	67	-	280	73	< 5	-
T3	-	-	-	100	-	4.8	36	540	-	2400	49	21	-
SM6	-	-	-	83	-	9.2	12	68	-	270	64	< 5	-
SM7	-	-	-	79	-	6.1	20	100	-	420	61	< 5	-
T4	-	-	-	69	-	24.2	< 5	< 20	-	550	140	< 5	-
SM8	-	-	-	100	-	8.4	18	97	-	450	77	< 5	-
T5	-	-	-	250	-	34.1	< 5	< 20	-	<100	333	< 5	-
SM9	-	-	-	80	-	12.0	10	70	-	310	65	< 5	-
T6	-	-	-	65	-	3.1	10	54	-	440	40	< 5	-
SM10	-	-	-	79	-	7.2	7	67	-	310	61	< 5	-
SM11	-	-	-	36	-	6.4	23	70	-	360	68	< 5	-

Table 2. Metal concentrations in fine sediment fraction (-80 mesh, <177 microns) by inductively coupled plasma mass spectrometry (ICP-MS) and instrumental neutron activation analysis (INAA). Aqua regia is a partial digestion while INAA is considered to provide a complete measurement.

With regards to the Tom and Jason deposits, the waters draining each site are significantly different. The Tom deposit is drained by the acidic Seckie Creek 2, which was sampled at site T4. While this stream is highly acidic and metal rich, it is less so than the neighbouring Macintosh Creek sampled at site T5. Macintosh Creek may be geographically close to Seckie Creek 2, but it is draining a distinctly separate area from the Tom deposit itself. The extremely elevated levels of Pb in both water and sediment samples, with marginally higher Zn concentrations in the water make Seckie Creek 2 distinct from the other acidic streams (Figure 5). While the exploration disturbance to the Seckie Creek 2 drainage area may seem minimal, it is unknown whether this distinction would exist in an undisturbed watershed.

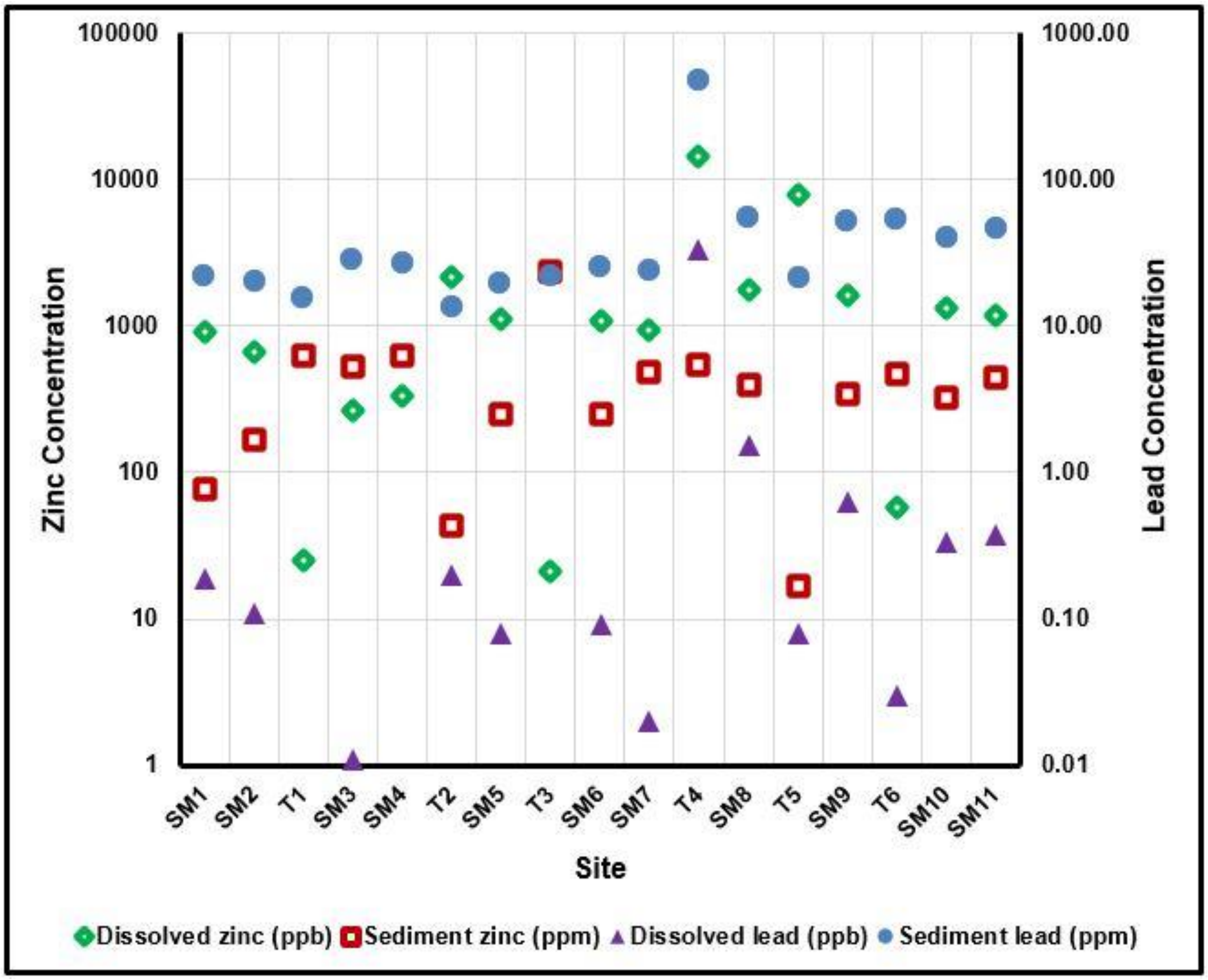

Figure 5. Zinc (left) and lead (right) concentrations in waters and sediments at various sampling sites. Sediment concentrations are those obtained by aqua regia digestion and ICP-MS analysis. Note the elevated levels of dissolved lead, dissolved zinc and sediment bound lead at site T4 downstream of the Tom deposit. The lack of sediment bound zinc at both T2 and T6 (the Jason deposit) is also notable.

The stream draining the Jason deposit sampled at site T6 also drains significant portions of the acid generating Tom Sequence; however, the carbonates occurring within the Jason deposit and the nearby Road River Group appear to neutralize any acidity initially generated. This acid neutralization also appears to have removed metals released through weathering of the Jason deposit. While the waters of this stream are somewhat distinct from waters sampled at sites T1 and T3, there is little to indicate that it is downstream of a significant ore body. In particular, Zn concentrations in the sediments are significantly lower than at the other two neutral tributaries. Pb concentrations are higher in the sediments, but it seems these alone would be inadequate to justify further exploration in this area, or even attract an individual's attention. Additionally dissolved Pb values are roughly equal to the other neutral tributary streams. Dissolved Zn concentrations are higher at T6 then at the other neutral tributary sites T1 and T3, but lower than the Zn concentrations at the two neutral sites along the South MacMillan River (SM3 and SM4). It would therefore seem unlikely that the dissolved Zn and sediment Pb values at site T6 would be enough to attract further attention.

These results are consistent with previous studies showing that Pb is quickly scavenged from the dissolved phase onto charged surfaces, and as such, is not normally found in the dissolved phase downstream of a base metal sulphide deposit. Instead, high Pb values have been commonly associated with the sediment fraction (Goodfellow, 1983). In this situation Seckie Creek 2 is close enough to the metal source for Pb to be anomalous in the dissolved fraction. Any Pb release from the Jason deposit, however, has already been scavenged and is primarily found in elevated sediment concentrations. Zinc was slightly elevated at sites downstream of ore deposits. This is again supported by studies in the Howard's Pass, where elevated dissolved and sedimentary zinc dispersal occur up to four kilometres from the ore body (Goodfellow, 1983). This is attributed to the formation of stable dissolved zinc complexes which are not readily adsorbed by surface charges on suspended materials. Unfortunately, due to its elevated mobility, Zn levels can also remain high if acidic waters draining barren shales are neutralized. The MacMillan Pass data is significant since it shows that Goodfellow's work extends beyond streams which are initially acidic to ore bodies which have acidity attenuated *in situ* or before the ground surface.

Implications for Exploration

It is clear that total metal concentrations alone are not enough to indicate an anomaly, as total metal loads are closely associated with acidity. However the results of this study strongly support the findings of Goodfellow in the Howards Pass district. They also partially extend his findings beyond the acidic surface waters to those neutralized before reaching the surface or *in situ*. In this situation, while the traditional analysis described readily locates the Tom deposit based on elevated Pb concentrations, it seems unlikely to have located the Jason deposit. One metal concentrations are viewed in context with pH however, the sedimentary Pb – dissolved Zn signature was significant enough to support further investigation in the region of the Jason deposit. Residual Zn from the neutralization of acidic waters also threatens to lead an exploration project astray, highlighting the importance of finding several indicators before drawing conclusions.

Perhaps most important, is the recognition that a lack of extreme metal concentrations does not necessarily indicate the absence of a base metal sulphide deposit. Subtle signatures appear more important, and may provide valuable support for findings from other techniques (such as geophysics) into a larger exploration program.

Future Work

Research is currently underway to evaluate some of the proposed refinements highlighted in the introduction. In particular, three distinct steps are underway to better characterize the waters of the South MacMillan River and its tributaries. These are: 1) analysing unfiltered water samples to determine the metal content of suspended sediment, 2) X-ray diffraction analysis of the sediments to identify the secondary mineral phases, and 3) thermodynamic modelling of the waters to determine the stable mineral phases and their relative saturation indexes. These three steps should provide more baseline data for the proposed refinements highlighted in the introduction. They may also help locate unknown sulphide deposits with subdued signatures, such as that generated by the Jason deposit.

Acknowledgements

This project would not have been possible without the timely intervention of Suzanne Paradis and Jan Peter. I would also like to thank Mark Nowosad of Yukon Energy, Mines and Resources for his incredible efforts to provide us with supplies during a period of logistical challenges. This paper is also rightfully, partially the work of Dr. James Zheng for his incredibly thorough and well researched comments during revision. This paper is greatly improved by it.

References

Boyle, R.W., 1979, Geochemistry overview, *in* Hood, P.J., ed., Geophysics and geochemistry in the search for metallic ores: Geological Survey of Canada Economic Geology Report 31, p. 25-31.

Carpenter, R.H., Pope, T.A., and Smith, R.L., 1975, Fe-Mn oxide coatings in stream sediment geochemical surveys: Journal of Geochemical Exploration, v. 4, p. 349-363.

Chen, M., and Ma, L.Q., 2001, Comparison of three aqua regia digestion methods for twenty Florida soils: Soil Science Society of America Journal, v. 65, p. 491-499.

Goodfellow, W.D., 1983, Stream sediment and water geochemistry of the Howard's Pass (XY) Zn–Pb deposit and Nor Zn–Pb–Ba occurrence, Selwyn Basin, Yukon and Northwest Territories: Geological Survey of Canada Open File 845, 27 p.

Goodfellow, W.D., 1991, Jason stratiform Zn - Pb - barite deposit, Selwyn Basin, Canada [NTS 105 - O - 1]: Geological setting, hydrothermal facies and genesis, *in* Abbott, J.G., and Turner, R.J.W., ed., Mineral deposits of the northern Canadian Cordillera, Yukon – northeastern British Columbia (field trip 14): Geological Survey of Canada Open File 2169, p. 177-191

Goodfellow, W.D., 2004, Geology, genesis and exploration of SEDEX deposits, with emphasis on the Selwyn Basin, Canada, *in* Deb, M., and Goodfellow, W.D. ed., Sediment-hosted lead-zinc sulphide deposits: attributes and models of some major deposits of India, Australia and Canada: Narosa Publishing House, Delhi, p. 24-99

Goodfellow, W.D., and Rhodes, D., 1991, Geological setting, geochemistry and origin of the Tom stratiform Zn - Pb - Ag - barite deposits, *in* Abbott, J.G., and Turner, R.J.W., ed., Mineral Deposits of the northern Canadian Cordillera, Yukon – northeastern British Columbia (field trip 14): Geological Survey of Canada Open File 2169, p. 137-175.

Gordey, S.P., and Makepeace, A.J., compilers, 1999, Yukon bedrock geology: Geological Survey of Canada Open File 1999-1(D).

Johnson. R.H., 2009, The influence of shallow and deep ground-water discharge on stream-water quality in a watershed with historical mining, Prospect Gulch, Colorado, USA, *in* Proceedings, International Conference on Acid Rock Drainage: 8th, Skellefteå, Sweden, 9 p.

Hermann, R., and Neumann-Mahlkau, P., 1985, The mobility of zinc, cadmium, copper, iron, and arsenic in ground water as a function of redox potential and pH: The Science of the Total Environment, v. 43, p. 1-12.

Hua, X., Dong, D., Liu, L., Gao, M., and Liang, D., 2012, Comparison of trace metal adsorption onto different solid materials and their chemical components in a natural aquatic environment: Applied Geochemistry, v. 27, p. 1005-1012.

Huelin, S.R., Longerich, H.P., Wilton, D.H.C., and Fryer, B.J., 2006, The determination of trace elements in the Fe-Mn oxide coatings on pebbles using LA-ICP-MS: Journal of Geochemical Exploration, v. 91, p. 110-124.

Kelley, K.D., and Taylor, C.D., 1997, Environmental geochemistry of shale-hosted Ag-Pb-Zn massive sulfide deposits in northwestern Alaska: natural background concentrations of metals in water from mineralized zones: Applied Geochemistry, v. 12, p. 397-409.

Kwong, Y.T.J., Whittley, G., and Roach, P., 2009, Natural acid rock drainage associated with black shale in the Yukon Territory, Canada: Applied Geochemistry, v. 24, p. 221-231.

Levson, V.M., 2001, Regional till geochemical surveys in the Canadian Cordillera: sample media, methods and anomaly evaluation, *in* McClenaghan, M.B., Bobrowsky, P.T., Hall, G.E.M., and Cook, S.J., ed., Drift exploration in glaciated terrain: Geological Society, London, Special Publications 185, p. 45-68.

Leybourne, M.I., and Cameron, E.M., 2010, Groundwater in geochemical exploration: Geochemistry: Exploration, Environment, Analysis, v. 10, p. 99-118.

McCurdy, M.W., McNeil, R.J., and Day, S.J.A., 2012, Geochemical, mineralogical and kimberlite indicator mineral data for silts, heavy mineral concentrates and waters from two geochemical surveys (2010 and 2011) on Victoria Island, Northwest Territories (NTS 87G, 87H, 88A and 88B): Geological Survey of Canada Open File 7198, 16 p.

Miller, W.R., 1979, Application of hydrogeochemistry to the search for base metals, *in* Hood, P.J., ed., Geophysics and geochemistry in the search for metallic ores: Geological Survey of Canada Economic Geology Report 31, p. 479-487.

Moore, J.N., Luoma, S.N., and Peters, D., 1991, Downstream effects of mine effluent on an intermontane riparian system: Canadian Journal of Fish and Aquatic Sciences, v. 48, p. 222-232.

National Topographic Data Base 105-O/1, 1990, Department of Natural Resources, Canada Centre for Topographic Information.

Telmer, K., Pass., H.E., and Cook, S., 2002, Combing dissolved, suspended and bed load stream geochemistry to explore for volcanic massive sulfide deposits: Big Salmon Complex, northern British Columbia: Journal of Geochemical Exploration, v. 75, p. 107-121.

3D Geological Modelling of the Sullivan Time Horizon, Purcell Anticlinorium and Sullivan Mine, East Kootenay Region, Southeastern British Columbia

E.A. de Kemp
Geological Survey of Canada 615 Booth Street, Ottawa, ON, K1A 0E9
edekemp@nrcan.gc.ca

E.M. Schetselaar, M.J. Hillier
Geological Survey of Canada, 615 Booth Street, Ottawa, ON, K1A 0E9

J.W. Lydon
Geological Survey of Canada, 601 Booth Street, Ottawa, ON, K1A 0E8

P.W. Ransom
9452 Clearview Road, Cranbrook, BC, V1C 7E2

R. Montsion
University of Ottawa, Ottawa, ON, K1N 6N5

J. Joseph
Geological Survey of Canada, 1500 - 605 Robson Street, Vancouver, BC, V6B 5J3

Abstract

Regional and mine scale 3D geological models, highlighting the Mesoproterozoic Sullivan time horizon (~ 1470 Ma) have been developed throughout the Purcell Anticlinorium in the East Kootenay region. The 3D geospatial model of the region has been constrained with an extensive surface and sub-surface database of stratigraphic, structural and geophysical observations distributed throughout the study area. The Purcell 3D activity, entitled Purcell-3D, was developed as a contribution to the “SEDEX” project of the Targeted Geoscience Initiative 4 (TGI-4) program over a 4 year period (2011 to 2015). The model includes what is locally referred to as the 'LMC' or Lower - Middle Aldridge stratigraphic contact, a map unit at the very top of the lower Aldridge Formation where the Sullivan Pb-Zn-Ag deposit is located. Local detailed and unique stratigraphy of the various ore and waste bands and closely associated beds inter-finger with the LMC boundary unit to form the Sullivan Sub-basin. The detailed Sullivan Mine model placed in the context of the regional LMC model, provides a much needed geospatial reference used to characterize and understand SEDEX ore systems. It also provides mineral exploration stakeholders with a key target horizon and spatial information from which to conduct further investigations.

Recommended citation

de Kemp, E.A., Schetselaar, E.M., Hillier, M.J., Lydon. J.W., Ransom, P.W., Montsion, R., and Joseph, J., 2015. 3D Geological modelling of the Sullivan time horizon, Purcell Anticlinorium and Sullivan Mine, East Kootenay Region, southeastern British Columbia, *in* Paradis, S., ed., Targeted Geoscience Initiative 4: sediment-hosted Zn-Pb deposits: processes and implications for exploration; Geological Survey of Canada, Open File 7838, p. 204-225. doi:10.4095/296328

Introduction

The Mesoproterozoic Aldridge Formation within the Purcell Anticlinorium in the East Kootenay region of Southeastern British Columbia, Canada, has been extensively mapped on surface, prospected and drilled and subject to numerous geological, geochemical, seismic, electromagnetic and potential field surveys. The Purcell-3D activity has been driven largely by the mineral potential of a region that is host to one of the world's largest Pb-Zn-Ag SEDEX deposits, the Sullivan Mine in Kimberley, British Columbia. This deposit has contributed close to $50 billion in current US dollars throughout its life. The abundant data collected over one century of mining and exploration activities, has been compiled, analyzed and interpreted in a 3D geospatial environment. Herein are the results of a 4 year GSC-led project focused on developing a 3D regional-scale structural and stratigraphic model.

Historically the tendency to examining basin architecture for indications of SEDEX deposits (e.g. presence of synsedimentary faults, sub-basins, geophysical responses, geochemical dispersal patterns) resulted in 'conceptual' models often influenced by corporate or individual bias which were difficult to test, to communicate and to reconcile among multiple disciplines. This is mitigated to a certain extent, as 3D geological modelling is increasingly being employed in mineral exploration. In historical, well-explored mining camps like Sullivan, we can take advantage of 3D modelling technology and expertise that exists. It is now possible to make a constrained 3D regional-scale model of a stratiform ore horizon, because laterally-persistent stratigraphic markers extracted from a digital geologic map series can be integrated with the same stratigraphic markers recognized in local clusters of drillholes. This regional-scale 3D geologic model can then be converted to a curvilinear grid, with the geometry defined by the contacts of the lithostratigraphic units. This geologic grid model can then in turn be used for future exploration targeting, taking advantage of a variety of quantitative analytical and 3D GIS query tools (de Kemp et al., 2010). This more regional scale 3D modelling is becoming important in enhancing geological understanding of the subsurface and exploring for mineral deposits at greater depths.

Objective and Scope

The main objective of developing the regional scale Purcell 3D model was to give a wider spatial perspective of the structural and stratigraphic geology of the subsurface. Building on a previous 2D GIS geoscience data compilation (9 Open File 1:50,000 scale geology maps covering NTS 82F01, 02, 07, 08, 09, 10, 15, 16, 82G04, 05, 12, 13), (Brown et al., 2011; Joseph et al., 2011a, b), a re-processed seismic compilation (Cook and Van der Velden, 1995) and using British Columbia TRIM Digital Elevation Model for vertical control, an initial 3D data set was developed for the Purcell Anticlinorium. This was supplemented with inclusion of identified markers and 3D path calculation from information contained in regional legacy drillhole logs (see Schetselaar et al., 2015 for details). From the integration of this extensive data set and some follow up field work in 2011 and 2012, a 3D structural and stratigraphic regional model of the southern Purcell Anticlinorium and a more detailed Sullivan Mine model were developed (see Figures 1, 2 and 3).

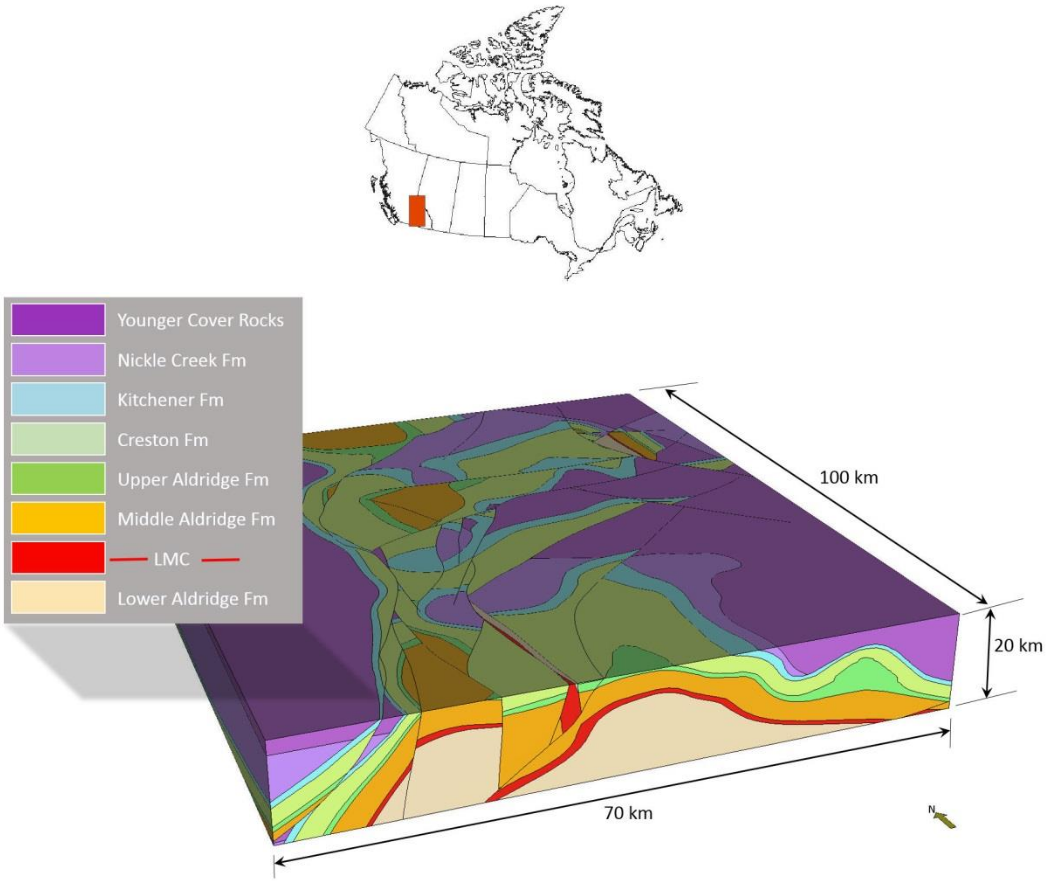

Figure 1. Location and regional extent of the Purcell-3D model. Thickness of Lower – Middle Aldridge (LMC) is approximate.

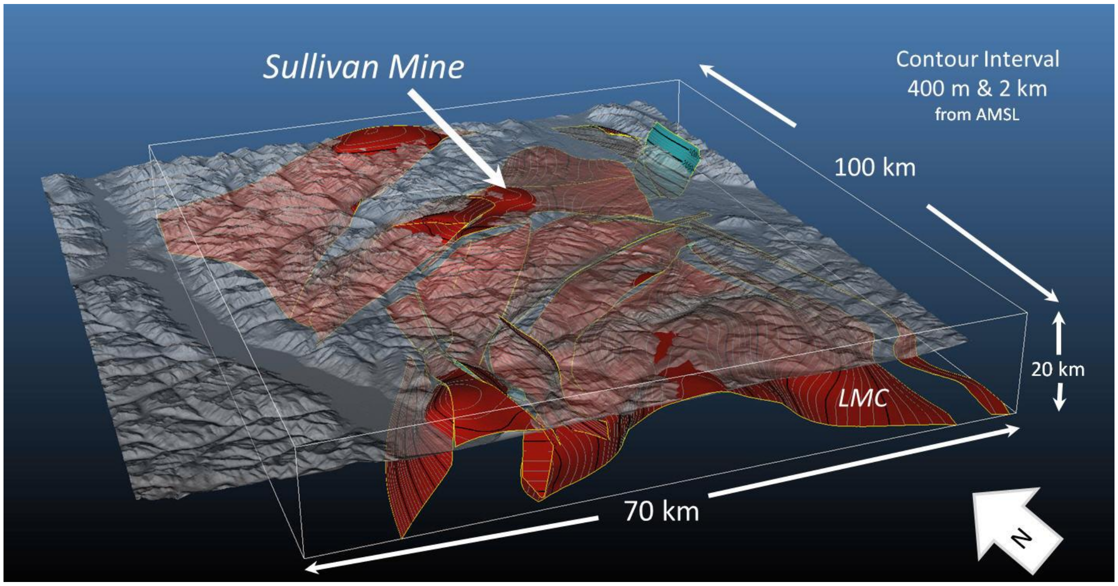

Figure 2. Red contoured surface represents the Sullivan time horizon or 'LMC' (Lower – Middle Aldridge contact) where the Pb-Zn-Ag Sullivan deposit is located. Contour interval is 500 m. AMSL = Above mean sea level.

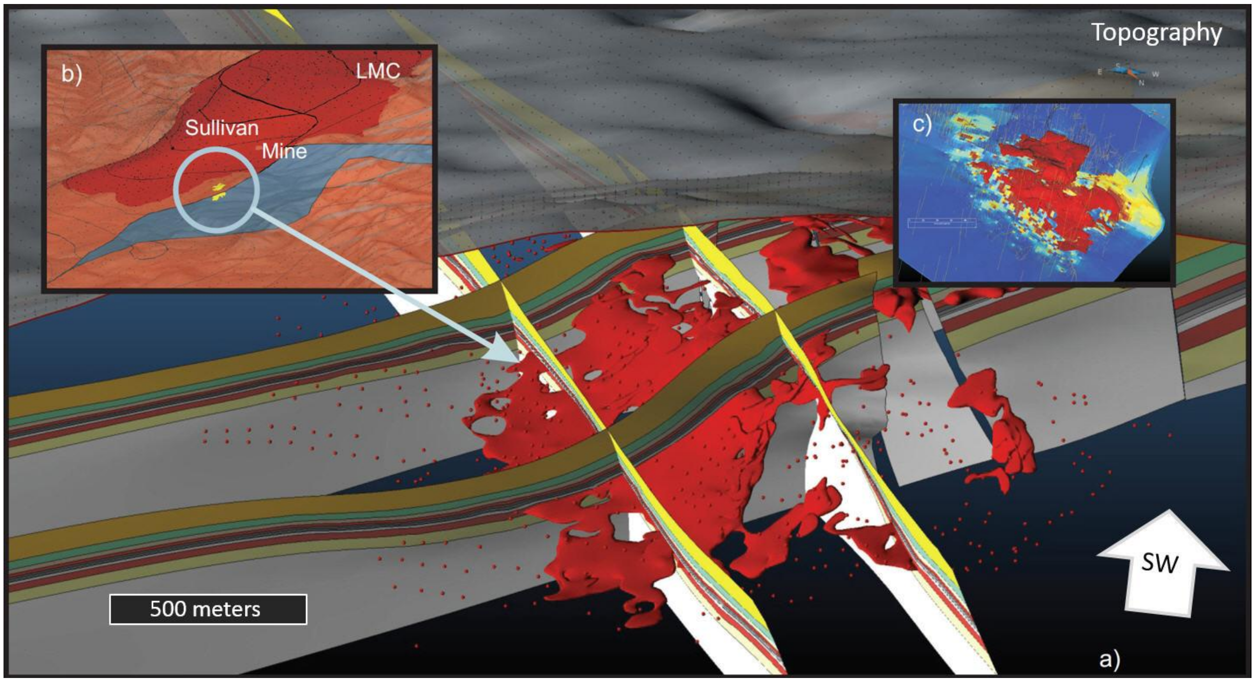

Figure 3. Sullivan Mine model looking towards the southwest. a) Orebody in red and mine stratigraphy cross-sections with top Main Band markers as red points; b) location of Sullivan Mine (yellow) along the regional LMC (Lower – Middle Aldridge contact) modelled surface (red); c) Kriged Pb zonation map at top of Main Band. See Montsion et al. (2015) for details of Sullivan Mine model.

Beyond the new drillhole database and Sullivan 3D model (Schetselaar et al., 2015; Montsion et al., 2015) a 3D interpretation was made for the mine site. The development of useful 3D geological models at various scales (mine, camp or *brown-field*, regional or *green-field*) is critical for coherent geologic data integration, prediction and ultimately targeting. 3D geologic modelling and integration has been successfully applied in mineral exploration and in mine camps worldwide over the last two decades (Pflug and Harbaugh, 1992; Dubois and Benn, 2003; Feltrin et al., 2009; Schetselaar et al., 2010). However, to go to broader scales (i.e. regional), new 3D modelling methods are needed where the distribution of subsurface constraints is generally sparse. Interpretive support is needed for constructing regional-scale 3D geological models, such as interpolation tools, that estimate spatial continuity or 'trends' of subsurface geological contacts beyond drillhole and outcrop constraints. In a conformable series of strata, this can be achieved by incorporating, in addition to drillhole markers, strike and dip measurements of the strata. These bedding orientation data are either acquired at surface by geological mapping or in the subsurface by drillhole measurements or analysis of bedding-drill core angles. This is an underdeveloped area of research in which sample distribution and anisotropy of the structures being modelled play an important role. For this reason we included a significant research component in the Purcell 3D activity for the development of new interpolation methods in sparse data environments. Results of this work are presented in Hillier et al. (2014, 2015). If key exploration features, such as a prospective target horizon, can be better interpreted and spatially integrated with other 3D data (electromagnetic, potential fields, seismic, drillhole data), then reproducible subsurface models of mineral systems can be generated and used in *green-field* mineral exploration.

The regional and Sullivan 3D model and supporting geoscience data presented herein are currently in GoCad / SKUA 2014 software from Paradigm®. The LMC (Lower-Middle Contact) horizon, markers points, structural observations, faults, younger Purcell stratigraphy above the Aldridge Formation and the DEM, will be released also as exported DXF, GoCad ASCII, ArcScene and Leapfrog scenes and as a 3D GIS geodatabase release in ArcGIS in the near future.

Geologic Context

The Purcell Anticlinorium in the East Kootenay region of southern British Columbia (Figure 4) is a 100 km scale shallowly northward plunging upright fold system (Price and Sears, 2000; Sears, 2007) with a shallowing upward sequence from deeper water basin turbidites to basin edge facies carbonates (Höy, 2000; Lydon et al., 2000). The succession of the Belt-Purcell Supergroup represents a major pericratonic rift-fill succession (Chandler, 2000) formed at the leading western edge of North America in Mesoproterozic times (1.47 – 1.40 Ga) and extends from the East Kootenays in Canada through northern Washington, Idaho, Montana to Wyoming in the US (for more information see: Price and Sears, 2000; Sears, 2007; Lydon et al., 2000; Lydon, 2007).

Commonly referred to as the Belt-Purcell, in Canada it has over 25 km in stratigraphic thickness (Figure 5) with the Lower Aldridge (15 km) being extensively thickened by Moyie gabbro-dioritic sills, at least one of which was most likely a significant heat engine for the evolving Sullivan SEDEX system (Lydon, 2007). The Sullivan (Pb, Zn, Ag) SEDEX deposit and its hosting Sub-basin sits within and is enveloped by the distinctive and regionally extensive uppermost unit (20 metres thick in the Kimberley region) of the Lower Aldridge Formation (Ransom and Lydon, 2000). This interval, termed the LMC (Lower-Middle Contact), consists predominantly of massive carbonaceous wacke laminate (CWL) (Ransom and Lydon, 2000). The Middle Aldridge Formation, is about 2.5 km thick and is dominated by turbidites and contains numerous diagnostic laminated siltstone markers (Huebschman, 1973) recognized by Cominco geologists in the mid-1960s. The sets of unique micro laminae of these markers have been correlated over distances as great as 300 km (Figure 6). The stratigraphic position of these markers is exploited by exploration geologists to target the LMC.

There are two early pulses of deformation and metamorphism in the region. The first event referred to as the East Kootenay Orogeny (1350-1300 Ma, McMechan and Price, 1982) terminates rift related sedimentation, involves folding, regional metamorphism and granitic intrusion (i.e. Hellroaring Creek stock). The second event, the Goat River orogeny (900-800 Ma) is a Windermere equivalent uplift event, involving block faulting and low-grade metamorphism. These events produce at least one high-grade sillimanite-bearing metamorphic zone along the St. Mary River within the Lower Aldridge and higher grade looking rocks in the core of the anticlinorium north of the Hall Lake Fault (McFarlane and Pattison, 2000) and south of the Moyie Fault. Generally rocks in the region are metamorphosed in the sub-greenschist facies and display well preserved primary structures common in turbiditic sediments, such as graded bedding

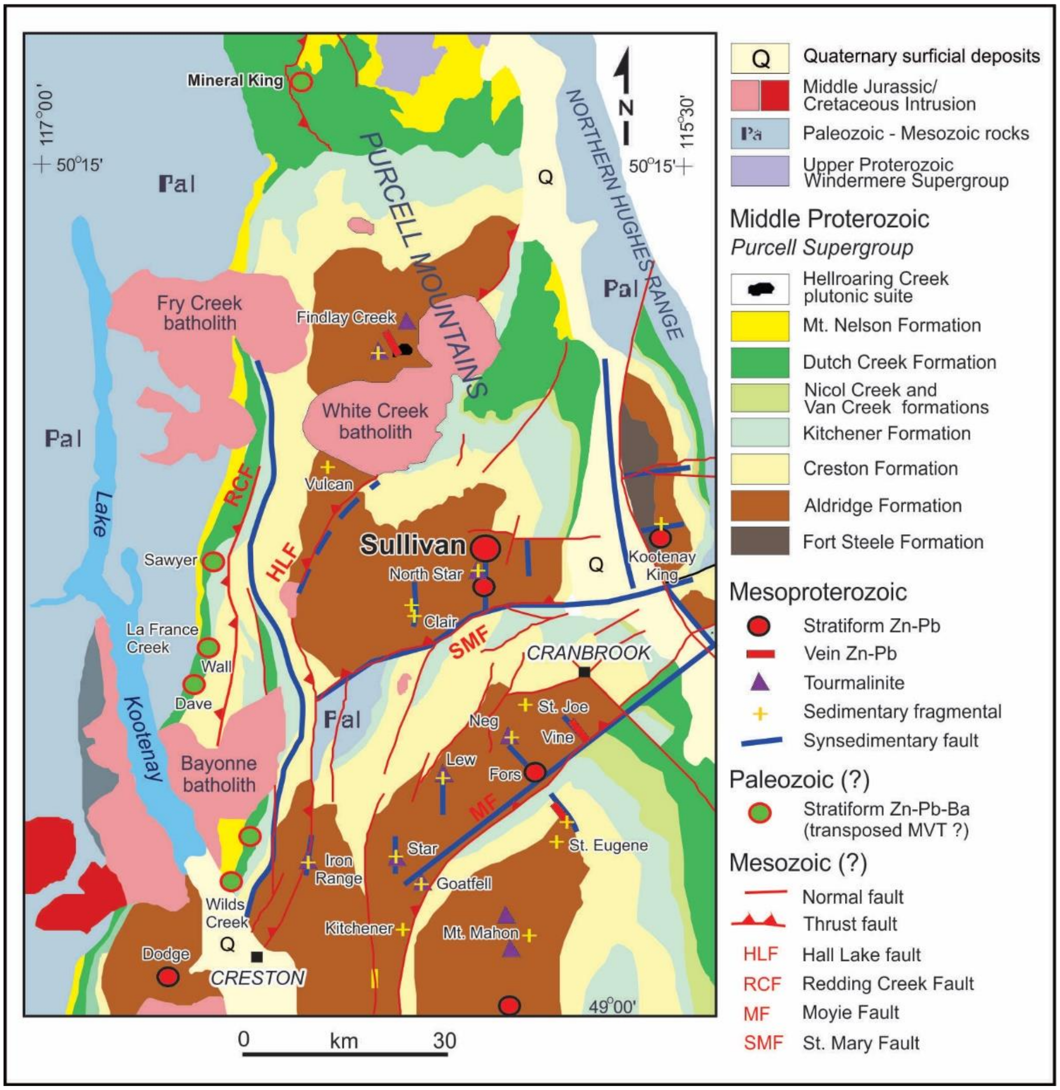

Figure 4. Generalized geological map of the Purcell Anticlinorium with overlay of SEDEX ore system elements (Sullivan and satellite massive sulphide deposits, tourmalinite alteration, sedimentary fragmental rocks and inferred synsedimentary faults; from Lydon et al. (2000).

load casts and flame structures, which constrain younging direction in modelling. The main phase of deformation occurred in the Phanerozoic, with the western Cretaceous-Tertiary Laramide orogeny, which produces the common folding and thrusting patterns observed in rocks of the region (Price and Sears, 2000; Sears, 2007). These are characterized by upright, east vergent, shallow, north-plunging folds separated by wider spaced more regional east-north-east trending, northwest-dipping, generally dextral, top to the east thrust systems that affect the entire stratigraphy of the Belt-Purcell (Figures 7 and 10). The last significant movement occurred from extensional fault systems in the

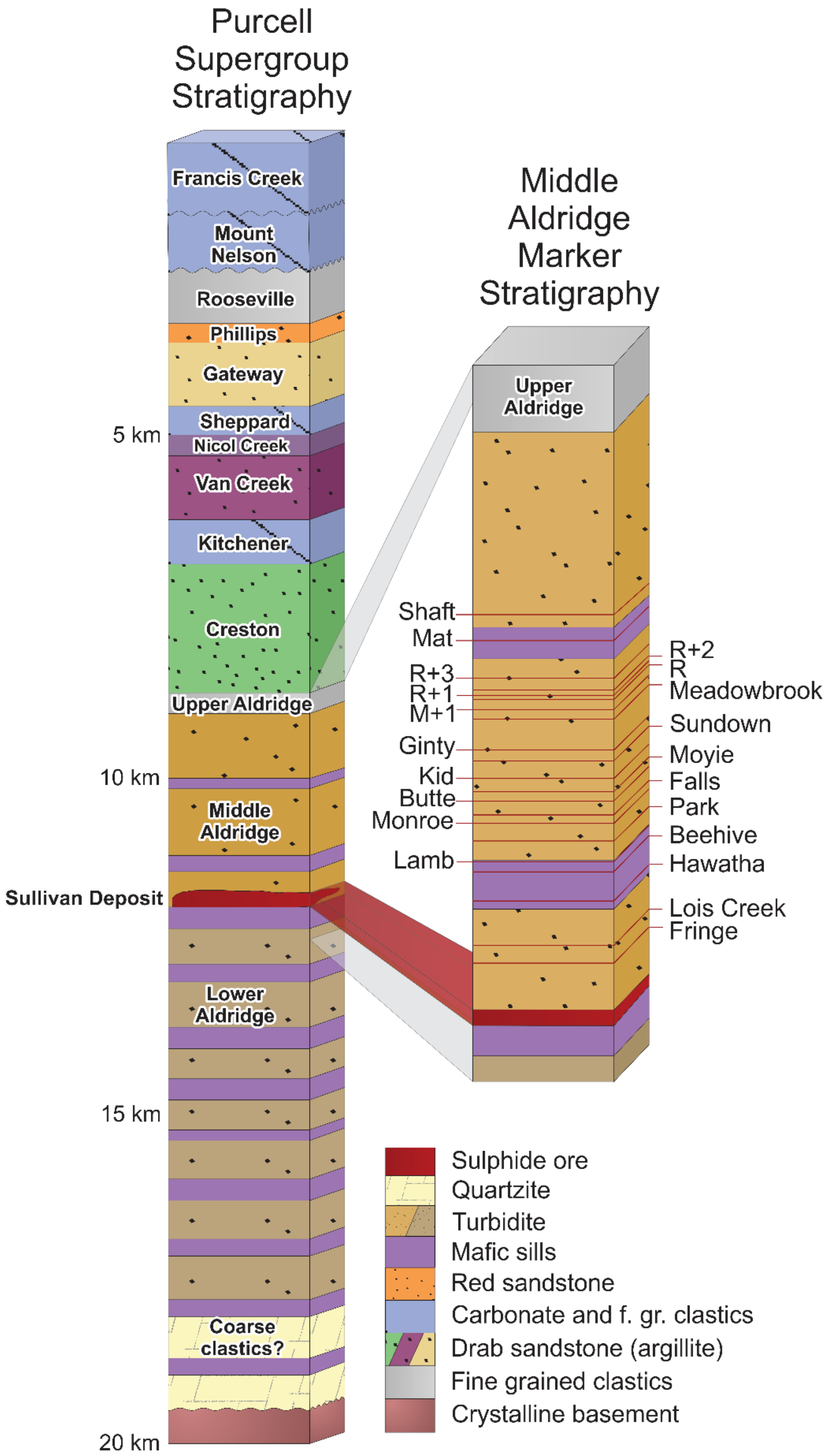

Figure 5. General lithostragraphic column of the Purcell Supergroup after Höy et al. (2000). Marker stratigraphy after Hagen (1983).

Eocene (50-33 Ma), such as the Rocky Mountain Trench (RMT) with up to 10 km of throw and which cuts the eastern portion of the Purcell Anticlinorium. It is important to appreciate that the deformation history that has affected the region has completely re-oriented and dissected the original Purcell Basin geometry, obscuring the effects of features responsible for controlling ore formation. We believe that in order to better understand the ore system, we need to treat the deformation as part of that system with 3D reconstruction, and ultimately 4D structural restoration. This will all contribute to developing a more precise understanding of ore forming processes.

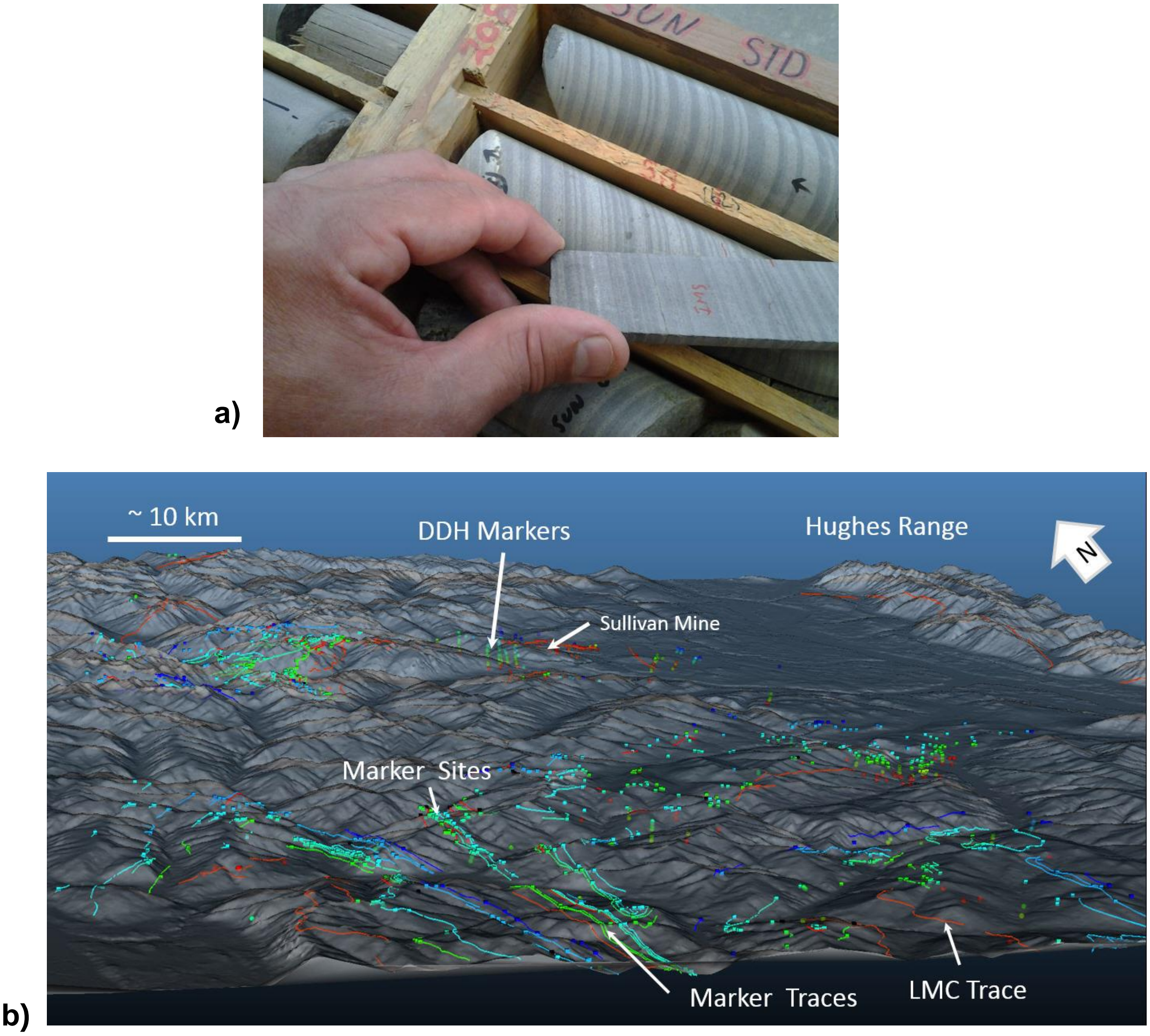

Figure 6. Individual 'marker beds' of the Middle Aldridge Formation are used to correlate stratigraphic position throughout the Purcell Anticlinorium. a) Photo demonstrating marker matching exercise, in this case part of the SUNDOWN marker section from standard set several km away. b) Distribution of makers from sites and drillholes (dots) and traces on topographic surface. Each colour indicates the trace of a different marker. Red starts at the LMC and progress to green and blue indicating the highest marker in the middle Aldridge stratigraphy.

Results / Data Analysis

Geospatial Database Management

Much effort was applied to organize all spatial data used for this project including the sub-surface constraints from drillhole and seismic data used for modelling the Sullivan time horizon. All the relevant geoscience data, including those from legacy archives, were stored in a 3D GIS environment in which the various source datasets were inspected, standardized, corrected and reconciled. Development of this 3D geospatial data store has been critical to the success of this project and represented over 80% of the total effort. The 3D data integration activity included compilation of a drillhole database from the legacy archives of exploration programs consisting of 675 drillholes with over 1000 lithostratigraphic markers (Schetselaar et al., 2015), subsurface data from the Sullivan Mine (over 4000 drillhole logs) and surface mapped contacts as well as more than 11,000 surface structural measurements, including bedding and foliation. In addition, all 2D seismic profiles acquired from previous projects (Cook and Van der Velden, 1995), as well as 2D potential field forward models (Thomas et al., 2013) were imported into the 3D GIS database.

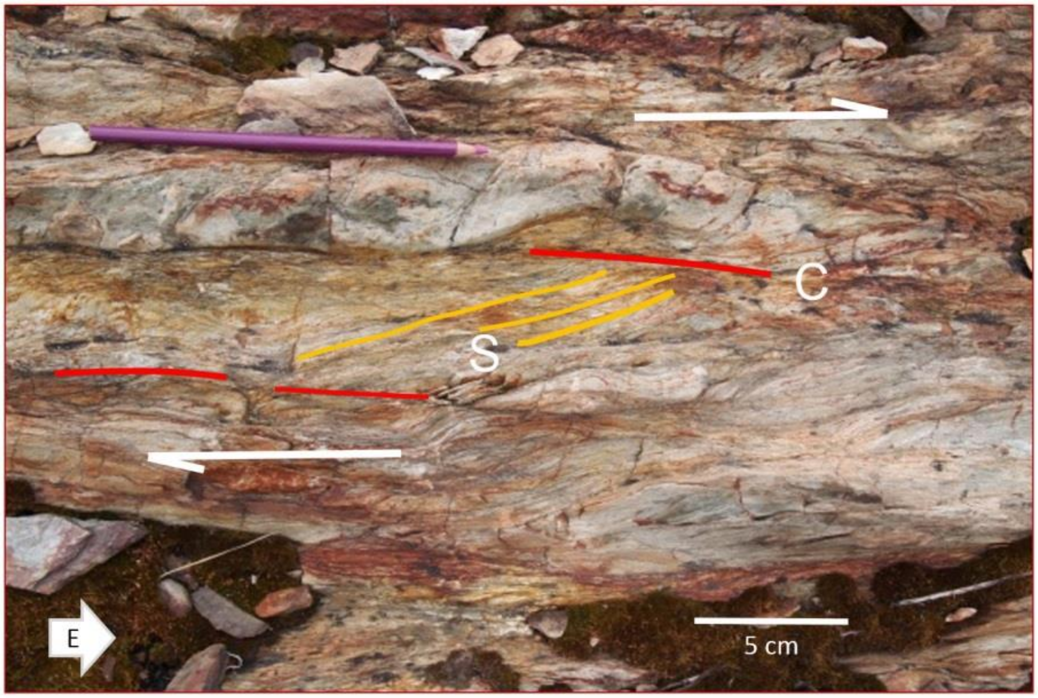

Figure 7. C-S fabric developed in Lower Aldridge turbidites, hanging wall of Moyie Thrust, indicating apparent dextral sense of movement. View towards north.

3D Modelling of Lithostratigraphic Surfaces and Faults

An innovative calculation engine was developed during the course of the Purcell 3D project, based on an implicit modelling approach. The approach is widely used in 3D geological modelling (i.e. Geomodeller, GoCad/SKUA, Leapfrog), but we extend and enhance the approach with an algorithm entitled GRBF (General Radial Basis Function, see Hillier et al. 2014, 2015) (Figure 8). This new algorithm employs markers of lithostratigraphic contacts (from drillholes and outcrop data) as well as structural orientation data (bedding, fold axis) to compensate for the sparse and clustered distribution of drillholes on a regional scale. This allowed us to model faults and horizons without use of oil and gas seismic interpretation workflows dependent on 3D seismic surveys, which do not exist for this area.

The GRBF method is useful in upscaling and integrating mine and regional data by making it easier to develop consistent models that use both dense and sparse data. For example, regional distributed outcrop-scale contacts and dense drillhole contacts can be combined with strike and dip data to model the contact surface.

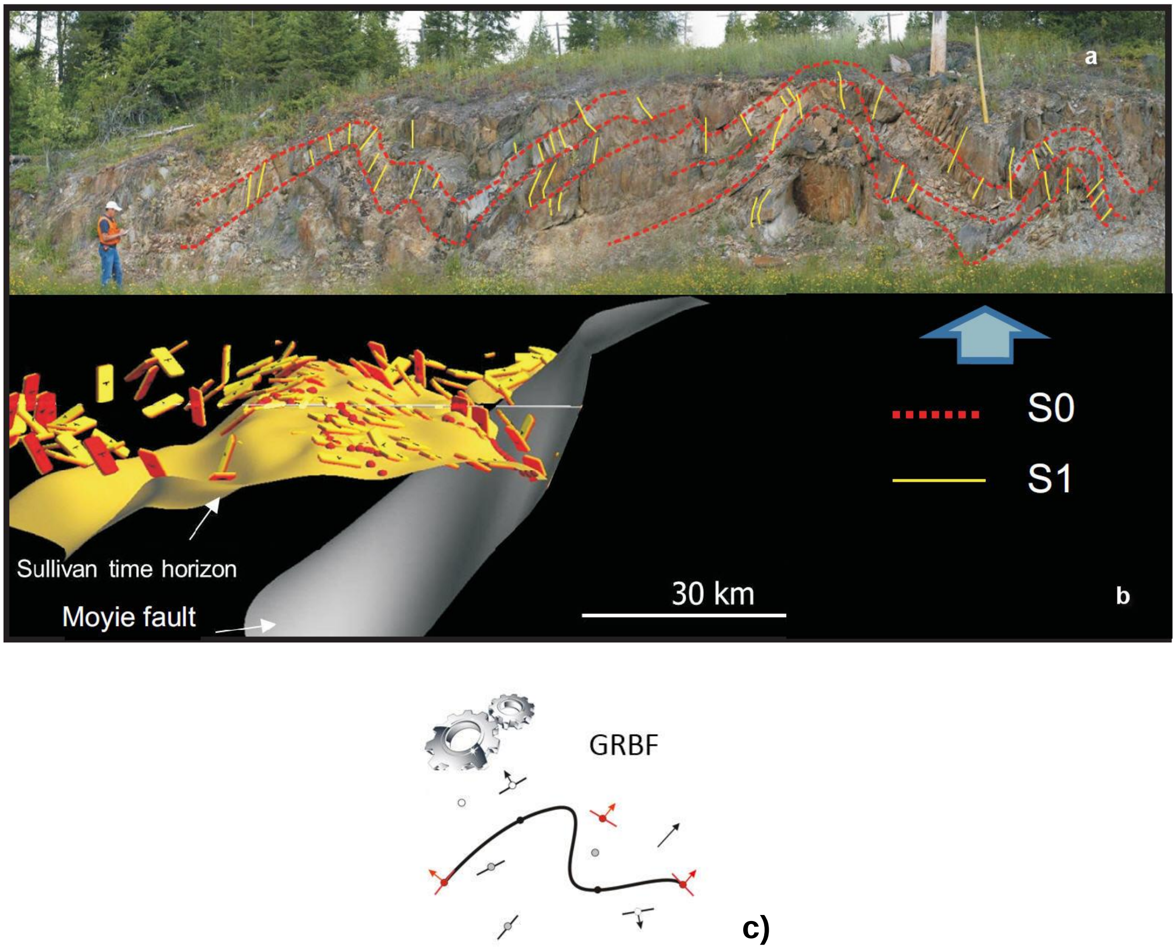

Figure 8. a) Geologic measurements of S0 (bedding) and S1 (axial plane cleavage) at outcrop scale can constrain larger features, such as the LMC regional surface viewed in b). c) LMC is interpolated with a new implicit algorithm called GRBF (General Radial Basis Function), which enables the input of bedding orientation and contact locations.

Discussion/Models

Structural Analysis and Modelling

Bedding-cleavage relationships, fold vergence and the plunge geometry of fold axis of outcrop-scale folds in Aldridge Formation and younger rocks generally fit with the regional scale picture of an east to south-east vergent shallowly north-plunging upright fold and thrust system produced during Laramide convergence (Figure 9a, b).In order to better model the Purcell Anticlinorium, the region was divided into structural domains (Figure 10a), which are areas bounded by significant faults. The domains are also divided at a finer scale into local sub-domains (Figure 10b), which display more common structural styles, and are at least partially bounded by faults. Individual domains can display strong internal contrasts in structural style, which become more accentuated within sub-domains. For example, the Goat sub-domain where rocks of the Creston and Kitchener formations are exposed through a series of steep thrust faults bounding steeply dipping units (Figure 10b) contrasts with the apparently flatter less faulted St. Mary's domain (Figure 10a).

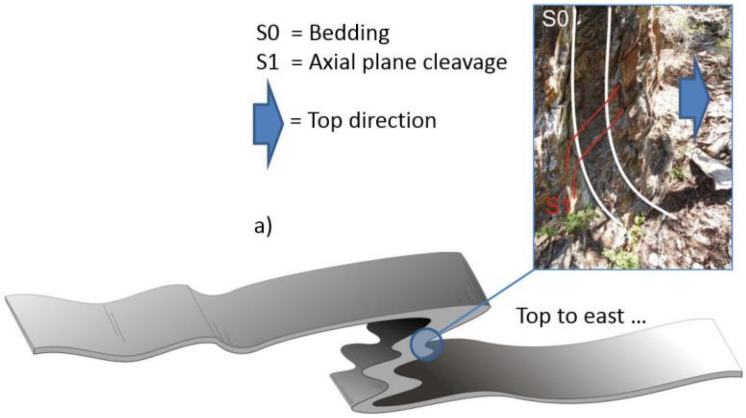

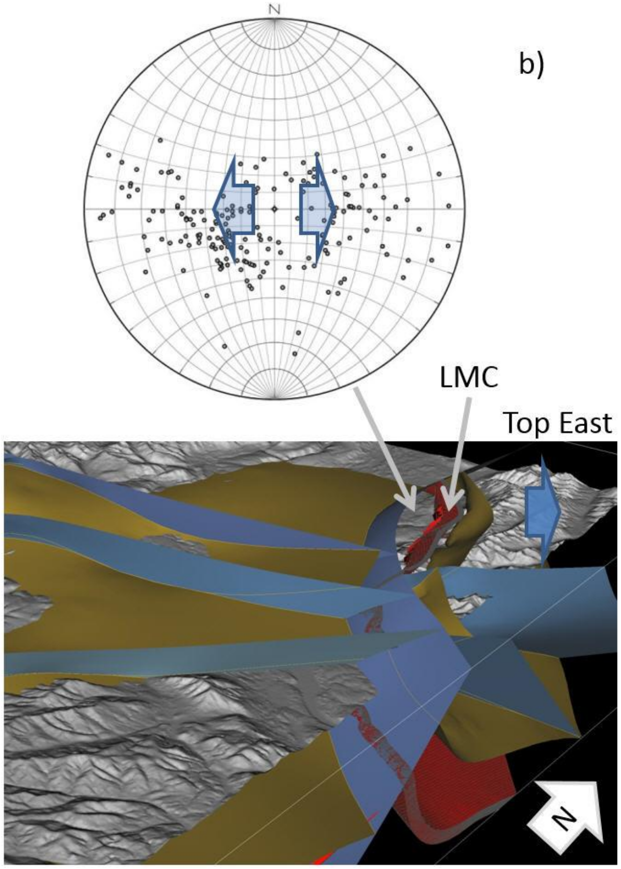

Figure 9. Fold geometries throughout the Purcell Anticlinorium are generally characterized by upright, shallow (5º-25º) north plunging, east verging and occasional short eastward overturning of fold limbs. These folds patterns show up at outcrop-, mine- and regional-scales. a) Measurement of bedding and cleavage orientations and intersection angles along with top indicators support development of the 3D model. b) In the Rocky Mountain domain, outcrop-scale overturned structures are reflective of the regional steep to overturned character of the region; for example this is well illustrated by the LMC (red plane). The blue surfaces are regional faults, and the olive green surface is the top of the Middle Aldridge formation. The stereonet shows poles to bedding in the Rocky Mountain domain. The blue arrows show the directions of rotation of these poles, thus indicating fold axis of rotation.

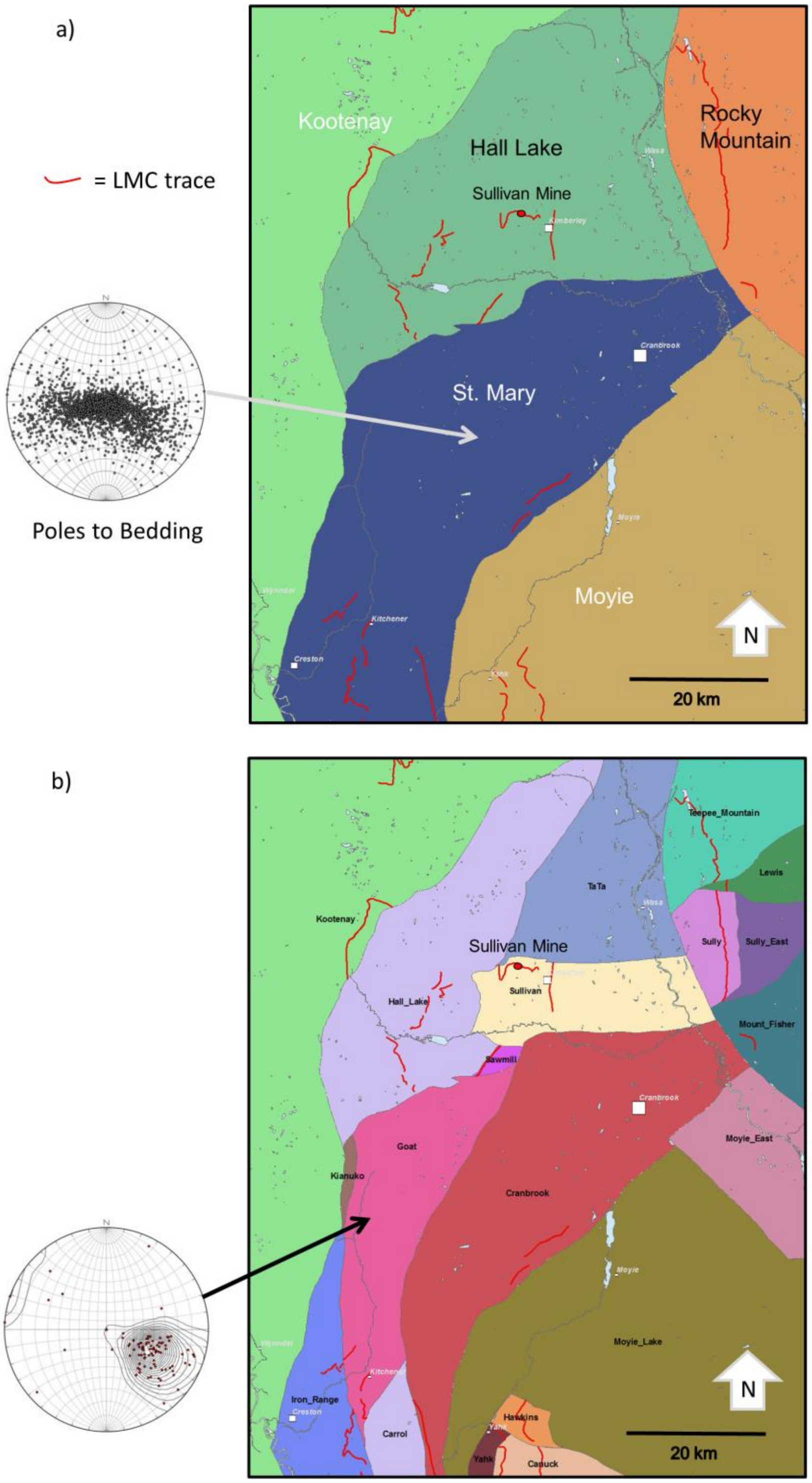

Figure 10. Reconstruction of the regional structural architecture involves characterization of structural domains, which corresponds to fault blocks. Domains are separated into a) coarse regional domains, and b) finer structural sub-domains. Significant contrasts can exist between domains at all scales. Regional domains can mask internal steep structures; for example a) St. Mary's domain (poles to bedding shown on the stereonet) masks the predominately steep features of the Goat sub-domain show in b).

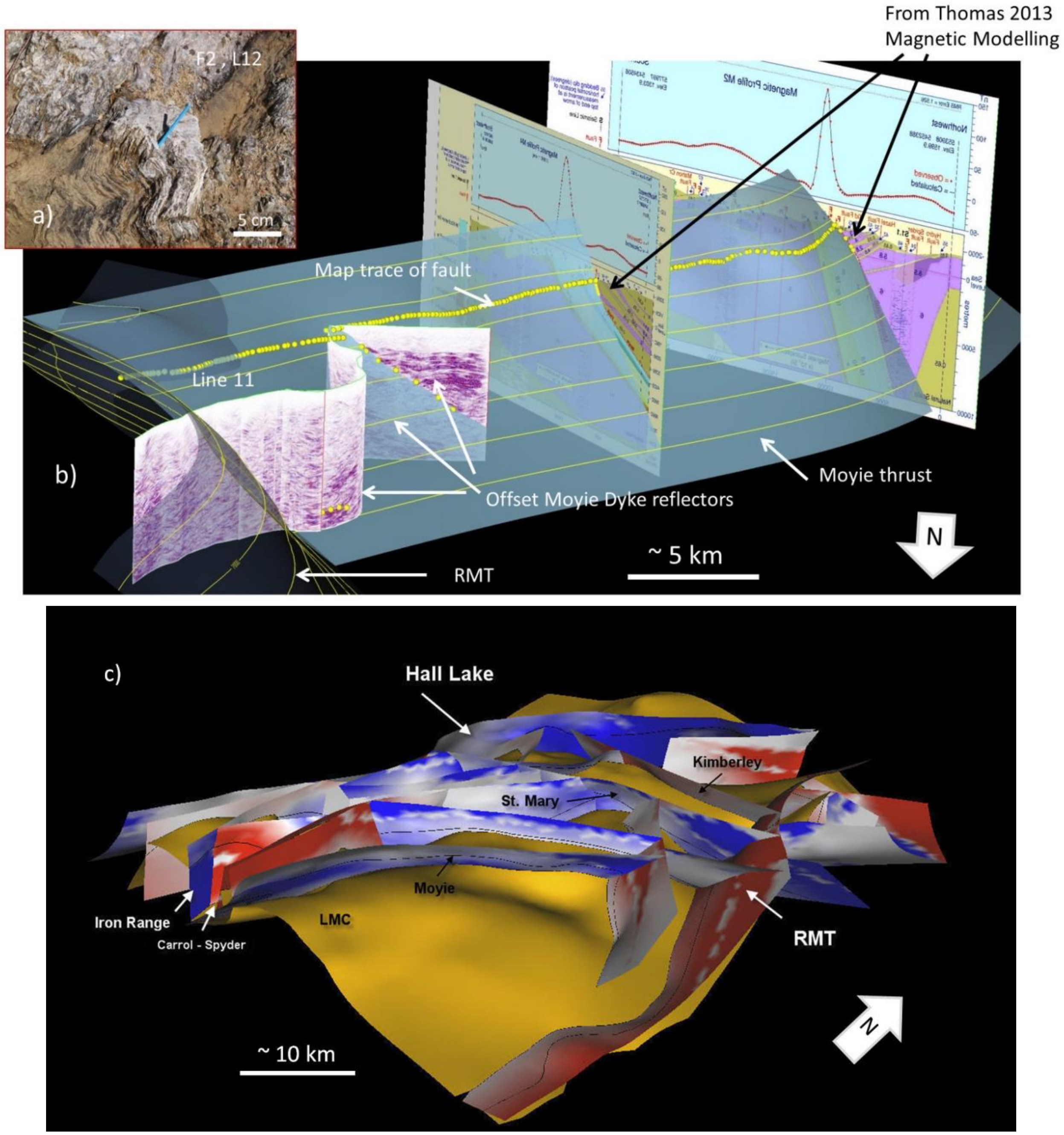

Figure 11. Data integration and 3D interpretation of the regional fault network. Major fault traces from 2D maps were corroborated with field observations of high strain zones represented by C-S fabrics, steep F2-L12 mega-crenulation L12 intersection lineation (photo in a), as well as contrasting stratigraphic levels. b) Integration of seismic data from 2D (3 sec depth corrected) profiles (Cook and Van der Velden, 1995), dip estimations from cross sections and magnetic modelling (Thomas et al., 2013) illustrated for the Rocky Mountain Trench (RMT). c) The interpreted 3D fault traces and dip estimates are input into the GRBF calculation which outputs a 3D fault surface. Once the stratigraphic and fault surfaces are developed the local throw of faults can be calculated to produce on-fault displacement values for the major thrust faults (blue) and normal faults (red). This displacement field could in turn be used to constrain future fault restoration models.

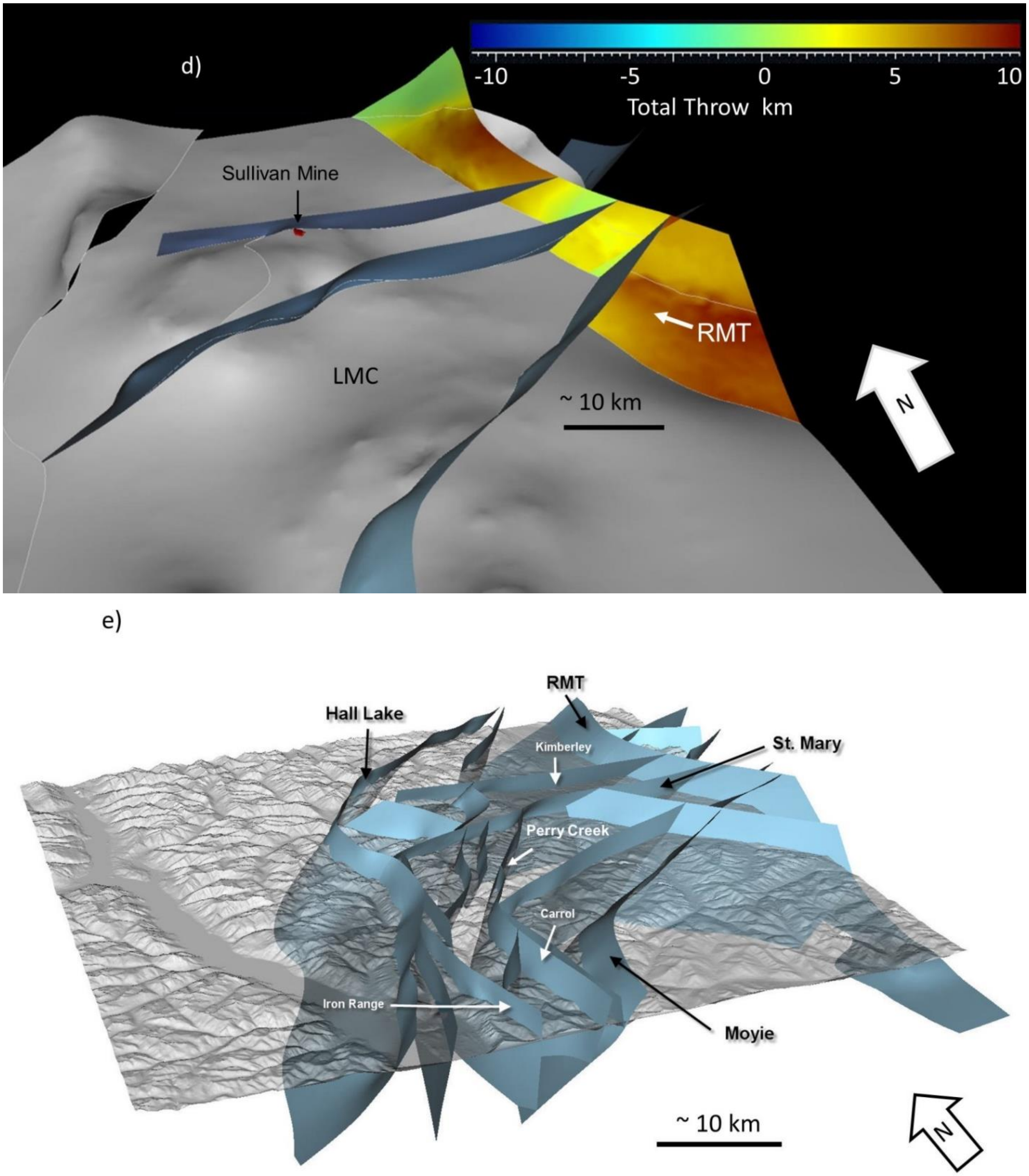

Figure 11 (continued). d) Differential displacement on the Rocky Mountain Trench (RMT) showing normal offset of 2 to 10 km. e) Final fault network model.

Units overlying the Aldridge Formation are exposed in the Goat domain, which sits in the footwall of the St. Mary Fault. Throw on the St. Mary Fault creates this contrast in stratigraphic level. Additionally, reverse and normal throws of steep local faults in the Goat domain show a more complex earlier movement history than in the St. Mary domain. The central St. Mary domain poses a modelling challenge north of the Perry Creek Fault (Figure 11d) where the Middle Aldridge markers are not exposed and drilling on the northern edge of the domain has not penetrated deep enough to intersect the Middle Aldridge strata. In contrast, the Moyie Lake domain south of Moyie Lake has broad open folds with relatively shallowly dipping beds that are laterally continuous for kilometres. Perhaps one explanation is the structural strengthening from the greater than 50% volume of Moyie sills within the Lower Aldridge Formation underlying much of the Moyie Lake domain. The structural characteristics of a given domain between these two end-member styles determines how these areas can be modelled in 3D, and in turn, the degree of predictability for mineral exploration strategies.

Other areas in the 3D model also show local steepening of the LMC; for example between the Carrol and Spyder normal faults in the south of the study area (Figure 11c), as well as overturned LMC in the Hughes Range east of the RMT. It is interesting that the model indicates some local overturned horizons only on the east footwall side of these normal structures. One possible explanation is that these steep zones may be localized by early, more regional, Laramide upright and eastward verging fold hinges which could provide axial zones of weakness for later extensional breaks.

The 3D modelling indicates along-strike differential displacement along many of the major faults (Figure 11). This can be observed along the Hall Lake Fault, St. Mary Fault, and RMT. There is a high degree of uncertainty in displacement estimates of these faults, which perhaps are over or under estimated where data is most sparse. However, the uncertainty is worth noting as this could help either improve the model (assuming specific fault segments must show less partitioned displacement fields) or the patterns may indicate the complex partitioning history of movement along these networks. For the RMT, late differential normal movement may explain any lateral differential displacement along perpendicular faults truncated by the RMT such as the Moyie and St. Mary thrust faults, which also abut along the RMT. Significant internal deformation of Laramide compressional fabrics is expected in areas of extreme block faulting with rotations up to 56° indicated by reconnaissance paleomagnetic study of late Cretaceous plutons east of the RMT (Ransom et al., 2015). Importantly, partitioned extensional movement along the RMT could account for throw discrepancies along adjacent St. Mary and Moyie thrust-related transverse faults. Such complicated fault histories are likely to occur on several other faults as well. Previous studies have suggested several stages of movement history along the Kimberley Fault, acting on an early graben system transfer feature, overprinted by local Laramide folding and reverse dextral motion and later dominant sinistral transcurrent (Eocene ?) motion (Turner et al., 2000). Identification of the Sullivan Mine stratigraphy north of the Kimberley Fault makes this early graben-related link for the Kimberley Fault impossible. Eocene extension in piano key like partitions along the RMT, superimposed on a fold and thrust system, which in turn may have earlier syndepositional history, would be difficult to restore since original throws on the earliest fault systems are not easily recovered.

The regional fault model presents one interpretation of the present day fault topology, largely interpreted from surface geological map patterns. More work needs to be done to determine the importance and relative timing of the faults if proper kinematic restoration studies are to be undertaken.

Metal Zonation and Mine Stratigraphic Modelling

Detailed mine-scale data integration and modelling from historical drillhole data was under-taken for the Sullivan Mine (Montsion, 2014; Montsion et al., 2015). This exercise resulted in a 3D digital stratigraphic, structural and metal zonation (Pb, Zn, Ag, Fe) model (Figures 3, 11 and 12). Over 4,000 drillholes with stratigraphic picks (i.e. determination or estimation of the depth of a specific horizon in the subsurface) and metal abundances within the Sullivan Mine were used from historical litho-stratigraphy-assay logs. Coordinate conversion from Sullivan Mine grid to UTM NAD 83 Zone 11 and geometric recalculation of the drillhole paths was done to position all the extracted information more accurately. The data were developed into a geodatabase in ArcGIS and then exported to GoCad / SKUA for modelling. For details on the conversion, integration methodology and the linear geo-referencing used in ArcGIS, see Montsion et al. (2015).

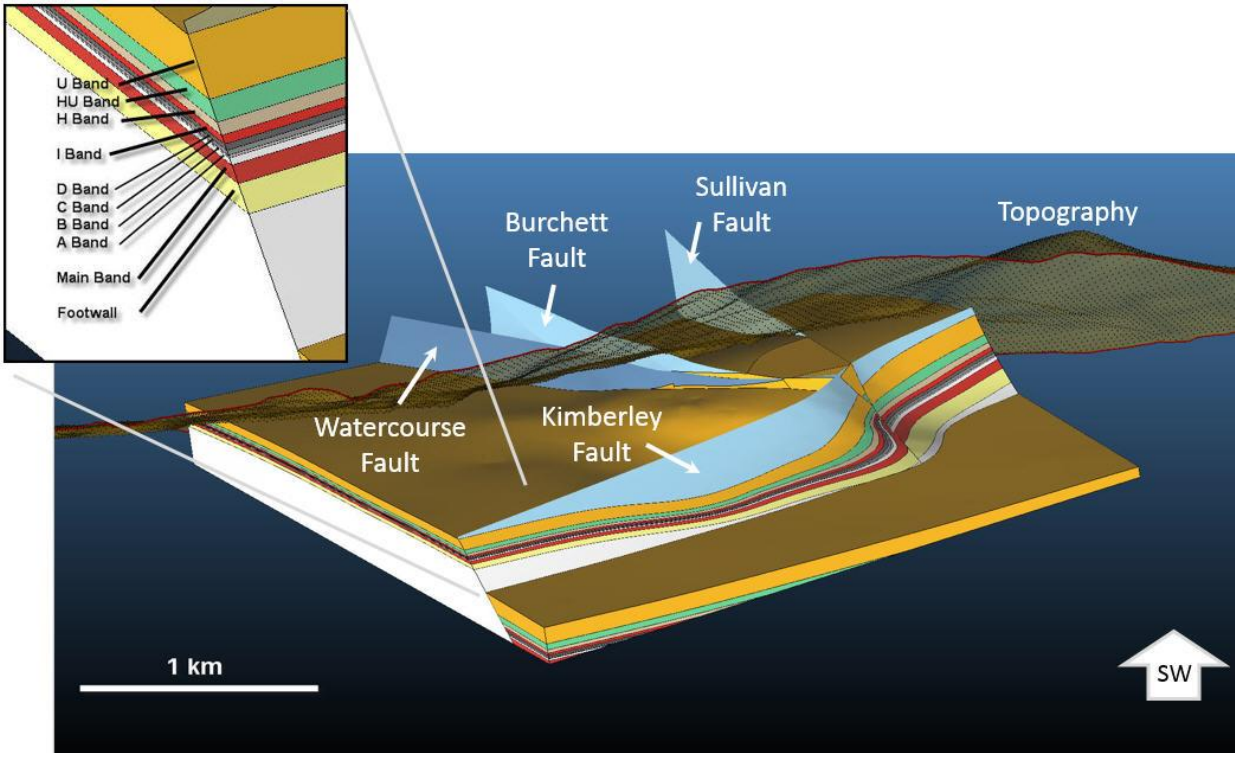

Figure 12. Sullivan Mine volumetric model representing the mine Band stratigraphy and major faults. Inset showing detailed Ore Band stratigraphy. The mine structural stratigraphic model is a curvilinear gridded volume referred to as a GEOGRID in GoCad/SKUA software, which acts as a container for metal and lithostratigraphic property modelling. View from the northeast to the southwest.

From the Sullivan Mine modelling exercise, the metal zonation patterns clearly corroborate previous studies that delineate the 3 main ore facies: Vent Complex, Transition, and Bedded Ores (Lydon et al., 2000; Montsion, 2014). Locally the metal-rich zones have abundance contours (Pb and Zn), which cross-cut the mine Band stratigraphy giving support for an in situ replacement process (as opposed to an exhalative only process), however the major concentration of ore is constrained to the Main Ore Band (Figure 3). The variogram trends show local as well as more regional trends which are strongest for Pb and to a lesser extent for Zn and Ag. There is a short ~ 75 m trend and a much longer regional Pb trend up to ~ 650 m at 160º (Figure 13b). This trend matches well with the orientation defining the boundary of the bedded ore on the east side of the Sullivan deposit. The variogram analysis also matches reasonably well with several proposed synsedimentary graben systems from previous studies (Hagen, 1983; Turner et al., 2000) such as the Sullivan-Stemwinder-North Star trend, Sullivan west graben, the Clair trend, and the Star and Lew trends of the Moyie Lake domain. The analysis supports the development of horizon controlled estimations using existing Pb and Zn assay data to other prospective Middle Aldridge sediments at the 0.5 to 1 km scale, and vertical ranges of less than 100 m. Tourmaline occurrences at the Sullivan Mine essentially delineate the extent of the vent facies, so the presence of tourmaline can be considered a proximal indicator within 100-200 m of the active ore system.

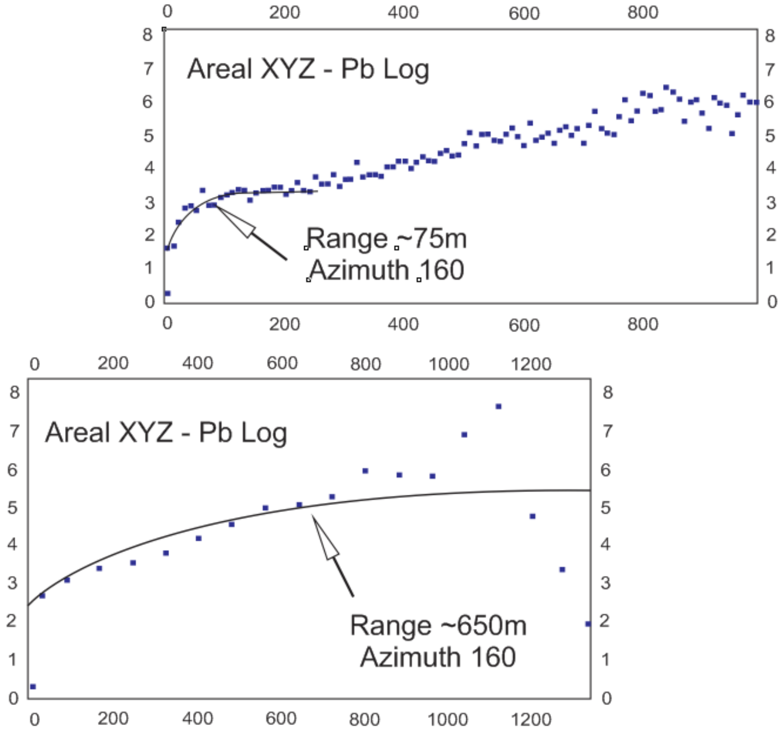

Figure 13. a) Semi-variogram has horizontal axis as distance in metres, vertical axis is semi-variance. Direction for both diagrams is 160º. Variogram analysis indicates strong bedding controlled metal anisotropy for Pb, Zn and Ag within the Bedded Ores; short lag and long lag semi-variograms of Pb indicate two ranges, a 75 metres and a farther 650 metres range both in the 160º direction.

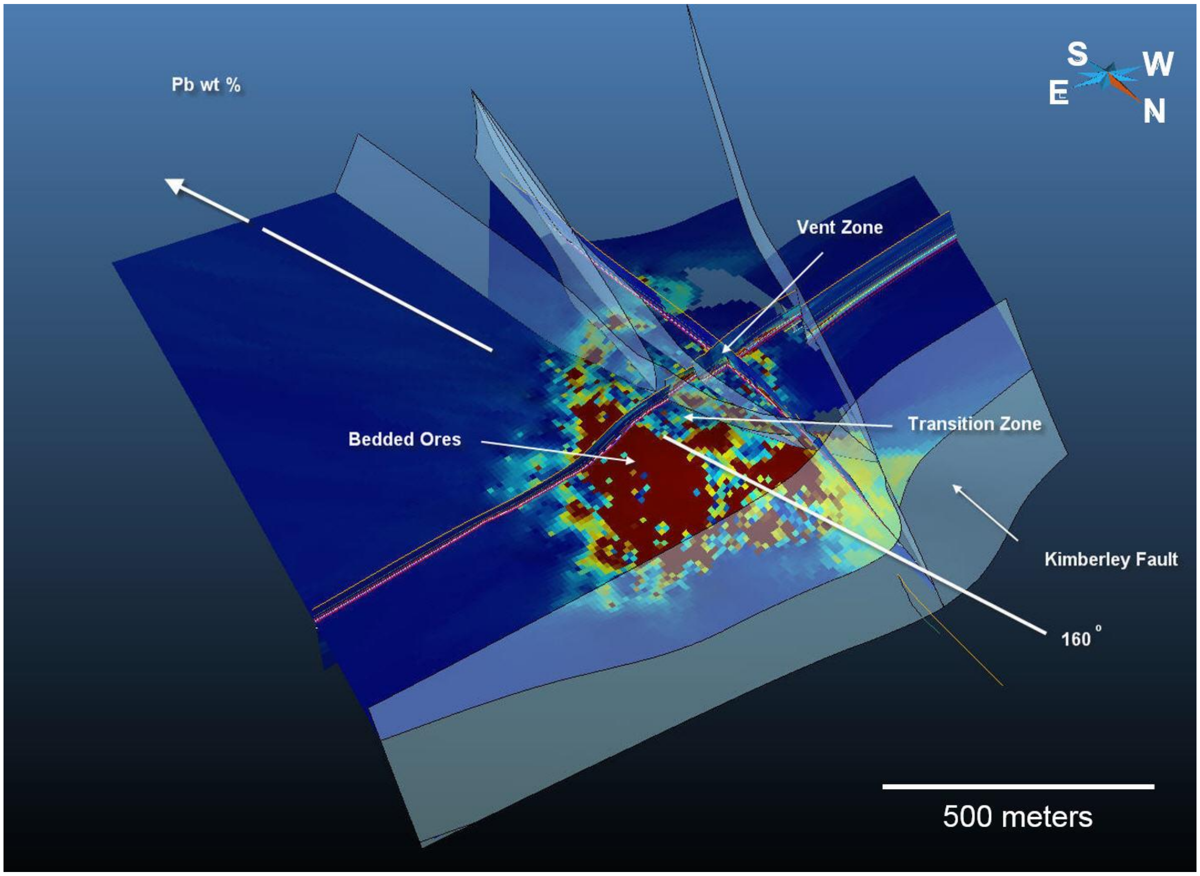

Figure 13b) Kriged Pb assay values at the top of the Main Band of the Sullivan deposit showing plan view and highlighting the 160º trend.

Implications for Exploration

There are several opportunities for enhancing exploration for SEDEX deposits in the East Kootenay region through the development of the Purcell 3D models. First, there is now a 3D framework to more accurately set up specific targeting activities. All surface and sub-surface data and modelled objects are 3D, and in a common UTM coordinate system. All of this information is stored in one repository, which saves mineral exploration companies time and money. Practically and because of this, there is now a block by block mapping of depth and dip estimation for the LMC throughout the region. The model provides a depth estimate and structure (dip estimate) of the SEDEX-hosting Sullivan time horizon, as well as a reference datum for drill targeting in the region. Of interest are areas containing steeper, and occasionally, overturned LMC, such as the Hughes Range, east of the RMT, and the Spyder-Carrol fault block. There are also many areas, which have relatively shallow LMC, that are in the north-south to 160-180º trend line with known deposits (i.e. St. Eugene and Star). It would be advantageous to develop more detailed 3D models in prospective areas such as Findlay Creek, Vulcan, Vines, and Kootenay King (Figure 4).

Second, the value of new data can be immediately enhanced by integration with the existing 3D database. Many exploration companies face the challenge to upscale information available in densely drilled mine sites to regional 3D models in sparsely drilled environments. Our case study demonstrates how integration of geological map, drillhole and geophysical data is leveraged in a 3D environment to support interpretation of the entire ore system, thereby increasing the potential for deep discovery.

Third, data management best practices supporting 3D geological modelling can only benefit the mineral exploration industry. The development of the Purcell Anticlinorium and Sullivan Mine models demonstrates how important it is for exploration and ore system studies to use modern data management practices. The efficacy gains when everyone is looking at the same data sets in a realistic 3D interpretive environment are multifold. Initiating this cultural shift toward rigorous spatial data management and 3D modelling allows for full use of 3D GIS as a decision support tool, quantitative targeting (Figure 14), training, and supporting regional scientific analysis.

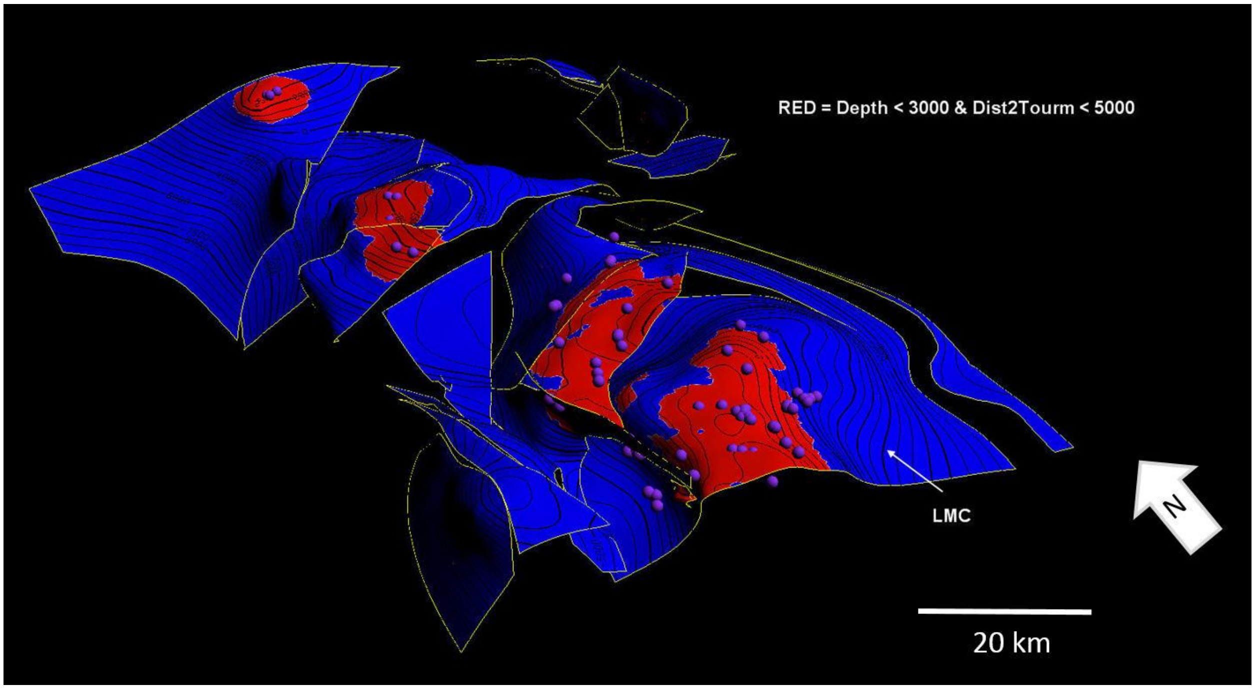

Figure 14. Example of simple exploration query using the LMC surface (blue), digital elevation model and occurrences of tourmaline (purple spheres). Favorable zones shown in red are defined by depth from topographic surface (not shown) to LMC < 3 km and distance to an occurrence of tourmaline less than 5 km.

Future Work

New drilling or field observations will be more accurately plotted within the 3D model, potentially giving more meaningful representation to the data while explorationists try to reconcile and interpret these in a consistent spatial framework. Significantly for the Sullivan region, the Mine stratigraphy and geological information (lithofacies, structures, assays, and alteration) can be compared to information from regional exploration holes, since they now have a common 3D spatial framework. This could prove useful for future work in delimiting the extent of the depocentre or sub-basin hosting the Sullivan deposit, and providing leads for exploration throughout the Purcell Basin.

Studies of the association between early tectonic and/or synsedimentary structures through regional inter-marker thickness and lateral lithofacies variation estimates, can now be better addressed. Ultimately doing a full structural kinematic restoration would improve our understanding of the paleo-geographic setting of the Aldridge Formation and the discovery of SEDEX deposits. Undertaking a palinspastic restoration was beyond the scope of the current study but the development of the regional 3D Purcell model makes this a possibility for future work.

Acknowledgements

We gratefully acknowledge and appreciate the collaboration of local expertise and data provision by individuals and corporate entities which made this project a success, including: Dave Grieve and Fiona Katay (BCGS, Ministry of Energy and Mines, British Columbia), Jason Jacobs (East Kootenay Chamber of Mines), Teck Resources Limited, Tim Termuende and Chuck Downie (Eagle Plains Resources Inc.), TerraLogic, Dave Pighin, Craig Kennedy and Ted Sanders, Quinn Smith (MMG). We enjoyed the wealth of knowledge and field trip guidance provided by Paul Ransom and Trygve Höy, as well as from Margo McMechan (GSC). We thank Fred Cook for kindly providing the Seismic data along with Gilles Bellefleur (GSC) who helped with the data conversion. The GRBF software development applied in this project was undertaken in collaboration with Mira Geosciences Ltd. through a collaborative industry-government research agreement, their support in continuing to advance 3D modelling methods for mineral exploration is gratefully acknowledged. Academic software was generously provided through the GoCad Research Consortia by Paradigm® and Mira Geoscience Ltd.

References

Brown, D.A., MacLeod, R.F., Wagner, C.L., and Chow, W., (compilers), 2011, Geology Skoocumchuk, Cranbrook, Moyie Lake, Boswell, Dewar Creek, Yahk River, Kaslo, Crawford Bay, St. Mary Lake, Grassy Mountain, British Columbia: Geological Survey of Canada, Open Files 6301-6310, 2011; 10 sheets, doi:10.4095/288543-288546, doi: 10.4095/288563-288568

Chandler, F.W., 2000, The Belt-Purcell Basin as a low-latitude passive rift: implications for the geological environment of Sullivan type deposits, *in* Lydon, J.W., Höy, T., Slack, J.F., and Knapp, M.E., ed., The geological environment of the Sullivan deposit, British Columbia: Geological Association of Canada, Mineral Deposits Division, Special Publication no. 1, p. 82-112.

Cook, F.A., and Van der Velden, A.J., 1995, Three-dimensional crustal structure of the Purcell Anticlinorium in the Cordillera of southwestern Canada: Geological Society of America Bulletin, v. 107 (6), p. 642-664.

de Kemp, E.A., Monecke, T., Sheshpari, M., Girard, E., Lauzière, K., Grunsky, E., Schetselaar, E.M., Goutier, J., Perron, G., and Bellefleur, G., 2010, 3D GIS as a support for mineral discovery: Geochemistry - Exploration, Environment, Analysis, v. 11, p. 117-128.

Dubois, A.J., and Benn, K., 2003, Structural analysis and three-dimensional modelling of the southwestern Sudbury Basin: implications and recommendations for mineral exploration: Ontario Geological Survey, Open File Report 6121, 38 p.

Feltrin L., McLellan, J.G., and Oliver N.H.S., 2009, Modelling the giant, Zn–Pb–Ag Century deposit, Queensland, Australia: Computers & Geosciences, v. 35, p. 108–133.

Hagen, A. S., 1983, Sullivan-North Star graben system: unpublished report, Cominco Ltd., 11 p.

Hillier, M.J., d e Kemp, E.A., and Schetselaar, E.M, 2015, Implicit 3D modelling of geological surfaces with the generalized radial basis functions (GRBF) algorithm, *in* Paradis, S., ed., Targeted Geoscience Initiative 4: Sediment-hosted Zn-Pb deposits: processes and implications for exploration: Geological Survey of Canada, Open File 7838, p. 253-266.

Hillier, M.J., Schetselaar, E.M. de Kemp E.A., and Perron, G., 2014, 3D modelling of geological surfaces using generalized interpolation with radial basis functions: Mathematical Geology, v. 46, p. 931-953.

Höy, T., Anderson, D., Turner, R.J.W., and Leitch, C.H.B., 2000, Tectonic, magmatic and metallogenic history of the early synrift phase of the Purcell Basin, southeastern British Columbia, *in* Lydon, J.W., Höy, T., Slack, J.F., and Knapp, M.E., ed., The geological environment of the Sullivan deposit, British Columbia: Geological Association of Canada, Mineral Deposits Division, Special Publication no. 1, p. 32-60.

Huebschman, R.P., 1973, Correlation of fine carbonaceous bands across a Precambrian stagnant basin: Journal of Sedimentary Petrology, v. 43, p. 688-699.

Joseph, J.M.R., Brown, D., MacLeod, R., Wagner, C., Chow, W., and Thomas, M., 2011a, Purcell Basin interactive maps, British Columbia: Geological Survey of Canada, Open File 6478; 1 CD-ROM, doi:10.4095/289069

Joseph, J.M.R., Brown, D., and Walker, R., 2011b, Diamond drill-hole database of the Purcell Basin: Geological Survey of Canada, Open File 6549; 1CD-ROM, doi: 10.4095/288015

Lydon, J.W., 2007, Geology and metallogeny of the Belt-Purcell Basin, *in* Goodfellow, W.D., ed., Mineral Deposits of Canada: A synthesis of major deposit-types, district metallogeny, the evolution of geological provinces, and exploration methods: Geological Association of Canada, Mineral Deposits Division, Special Publication no. 5, p. 1-27.

Lydon, J.W., Paakki, J.J., Anderson, H.E., and Reardon, N.C., 2000, An overview of the geology and geochemistry of the Sullivan Deposit, *in* Lydon, J.W., Höy, T., Slack, J.F., and Knapp, M.E., ed., The geological environment of the Sullivan deposit, British Columbia: Geological Association of Canada, Mineral Deposits Division, Special Publication no. 1, p. 505-522.

McFarlane, C.R.M., and Pattison, D.R.M., 2000, Geology of the Matthew Creek metamorphic zone, southeast British Columbia: a window into Middle Proterozoic metamorphism in the Purcell Basin: Canadian Journal of Earth Sciences, v. 37, p. 1073-1092.

McMechan, M.E, and Price, R.A., 1982, Transverse folding and superposed deformation, Mount Fisher area, southern Canadian Rocky Mountain thrust and fold belt: Canadian Journal of Earth Sciences, v. 19, p. 1011-1024.

Montsion, R., 2014, Zonation of Pb, Zn, Ag and Fe along the Sullivan Horizon, Kimberley, British Columbia, Unpublished B.Sc. thesis, Carleton University, Ottawa, April 2014, p. 72.

Montsion, R., de Kemp, E.A., Lydon, J., and Joseph, J., 2015, 3D stratigraphic, structural and metal zonation modelling of the Sullivan Mine, Kimberley, British Columbia, *in* Paradis, S., ed., Targeted Geoscience Initiative 4: sediment-hosted Zn-Pb deposits: processes and implications for exploration; Geological Survey of Canada, Open File 7838. p. 236-252.

Pflug, R., and Harbaugh, J.W., 1992, Computer graphics in geology: three-dimensional computer graphics in modeling geologic structures and simulating geologic processes: Springer-Verlag, Berlin; New York, 298 p.

Price, R., and Sears, J., 2000, A preliminary palinspastic map of the Mesoproterozoic Belt-Purcell Supergroup, Canada and USA: Implications for the tectonic setting and structural evolution of the Purcell anticlinorium and the Sullivan deposit, *in* Lydon, J.W., Höy, T., Slack, J.F., and Knapp, M.E., ed., The geological environment of the Sullivan deposit, British Columbia: Geological Association of Canada, Mineral Deposits Division, Special Publication no. 1, p. 61-81.

Ransom, P.W., and Lydon, J.W., 2000, Geology, sedimentology and evolution of the Sullivan Sub-basin, *in* Lydon, J.W., Höy, T., Slack, J.F., and Knapp, M.E., ed., The geological environment of the Sullivan deposit, British Columbia: Geological Association of Canada, Mineral Deposits Division, Special Publication no.1, p. 440-469.

Ransom, P.W., Day, T., and Enkin, R., in press, Block faulting of the northern Hughes Range east of the Rocky Mountain Trench near Kimberley, British Columbia.

Schetselaar, E., de Kemp, E., Ransom, P., Buenviaje, R., Nguyen, K., Montsion, R., and Joseph, J., 2015, 3D Drill-hole database of the Purcell Anticlinorium: Geological Survey of Canada, Open File 7817, 14 p.

Schetselaar, E., Pehrsson, S., Devine, C., Currie, M., White, D., and Malinowski, M., 2010, The Flin Flon 3D knowledge cube: Geological Survey of Canada, Open File 6313, 2010; 35 p., doi:10.4095/285614

Sears, J., 2007, Belt-Purcell Basin: Keystone of the Rocky Mountain fold-and-thrust belt, United States and Canada: Geological Society of America Special Papers, 433, p. 147-166.

Thomas, M.D., Schetselaar, E.M., and de Kemp, E.A., 2013, Magnetic contribution to 3D crustal modelling in the Purcell Anticlinorium, southeastern Cordillera (Poster): Geological Survey of Canada, Open File 7321, doi: 10.4095/292187

Turner, R.J.W., Leitch, C.H.B., Höy, T., Ransom, P.W., Hagen, A., and Delaney, G.D., 2000, Sullivan graben system: District-scale setting of the Sullivan deposit, *in* Lydon, J.W., Höy, T., Slack, J.F., and Knapp, M.E., ed., The geological environment of the Sullivan deposit, British Columbia: Geological Association of Canada, Mineral Deposits Division, Special Publication no. 1, p. 295-332.

Drillhole Database Compilation from Legacy Archives in Support of 3D Geological Modelling and Mineral Exploration in the Purcell Anticlinorium, British Columbia

E.M. Schetselaar
Geological Survey of Canada 615 Booth Street, Ottawa, ON, K1A 0E9
Ernst.Schetselaar@NRCan.gc.ca

E.A. de Kemp
Geological Survey of Canada, 615 Booth Street, Ottawa, ON, K1A 0E9

P.W. Ransom
9452 Clearview Road Cranbrook, BC, V1C 7E2

R. Buenviaje
Geological Survey of Canada, 615 Booth Street, Ottawa, ON, K1A 0E9

K. Nguyen
Geological Survey of Canada, 615 Booth Street, Ottawa, ON, K1A 0E9

R. Montsion
University of Ottawa, ON, K1A0E9

J. Joseph
Geological Survey of Canada, 1500 - 605 Robson Street, Vancouver, BC,
V6B 5J3

Abstract

This paper summarizes the compilation methodology used to build a 3D drillhole database of the Purcell Anticlinorium from archives of industry drilling programs from 1912 to recent. This drillhole database was used to extract key lithostratigraphic markers to support regional-scale 3D geological modelling of regional faults and key lithostratigraphic contacts, including the SEDEX-hosting Sullivan horizon. The drillhole database stores collar information and deviation log surveys systematically linked to thematic logs, encoding lithostratigraphy, lithology, alteration, mineralization, structure and facies of the Sullivan Sub-basin. The multi-thematic drillhole data can be visualized with geological map data in 3D and can be queried to support exploration planning and drill targeting projects in the region.

Recommended citation

Schetselaar, E.M., de Kemp, E.A., Ransom, P.W., Buenviaje, R., Nguyen, K., Montsion, R., and Joseph, J., 2015. Drillhole database compilation from legacy archives in support of 3D geological modelling and mineral exploration in the Purcell Anticlinorium, British Columbia, *in* Paradis, S., ed., Targeted Geoscience Initiative 4: sediment-hosted Zn-Pb deposits: processes and implications for exploration; Geological Survey of Canada, Open File 7838, p. 226-235. doi:10.4095/296328

Introduction

A central objective of the Geological Survey of Canada fourth Targeted Geoscience Initiative Program (TGI4) is to develop knowledge and techniques to enhance the effectiveness of deep mineral exploration. Towards this objective a regional-scale 3D modelling initiative was undertaken to enhance insight into the subsurface geology of the Purcell Anticlinorium (southeast British Columbia) to support exploration for SEDEX deposits. This paper presents the methodology that was used to compile a Microsoft-ACCESS© relational database populated with drillhole data acquired over several decades by industry exploring for SEDEX, carbonate-hosted Zn-Pb and gold deposits in this region. Because drillhole data provide important subsurface constraints for generating 3D geological models (e.g. XYZ-referenced subsurface markers of formation contacts, alteration zones, mineralization occurrences and structural controls) this is an essential resource that can support planning exploration projects and 3D modelling endeavours in the Purcell Anticlinorium. For detailed descriptions and discussions of Sullivan deposit geology, the Sullivan Sub-basin and regional geology, reference to the Geological Association of Canada publication on the geological environment of the Sullivan deposit (Lydon et al., 2000) is recommended.

Results/Data Analysis

The drillhole database of the Purcell Anticlinorium archives 726 drillholes from exploration drilling programs conducted from 1912 to recent by operational firms exploring the 150 MT Sullivan SEDEX deposit and surrounding area, its satellites and other base metal and gold deposits. It contains lithologic and lithostratigraphic drill log descriptive data organized in eight thematic tables that are relationally linked to tables containing deviation log surveys and drill collar locations georeferenced in mine and UTM NAD83 coordinates. Figure 1 shows the location of the drillholes against a backdrop of a generalized geological map of the Purcell Anticlinorium compiled from TGI3 digital geology archives (Brown and MacLeod, 2011a, b, c, d; Brown et al., 2011a, b, c, d, e, f; Glombick et al., 2011a, b). The MS Access© database also contains genetic lithofacies interpretations of the Sullivan horizon, assay data and structural observations, digitized mainly from legacy Cominco Ltd. archives. Many drillhole collar identifiers, their coordinates and metadata were obtained from a previous TGI3 publication of legacy drillhole archives (Joseph et al., 2011a). All the tables of the MS Access© database are also provided in .CSV ASCII format stored in a separate folder, for users who want to inspect the drillhole data in spreadsheet format and/or import the data into 2D/3D GIS software. The Collar table is also stored in MS Excel© format to retain hyperlinks to the mineral exploration assessment reports on the British Columbia government website.

3D visualization of the drillhole data is provided through the free downloadable Leapfrog© 3D viewer to accommodate users who do not have access to dedicated 3D GIS or modelling software packages. Regional 3D views of the database show annotated drillhole lithology, lithostratigraphy, alteration and mineralization themes together with a seamless 3D compilation of the TGI3

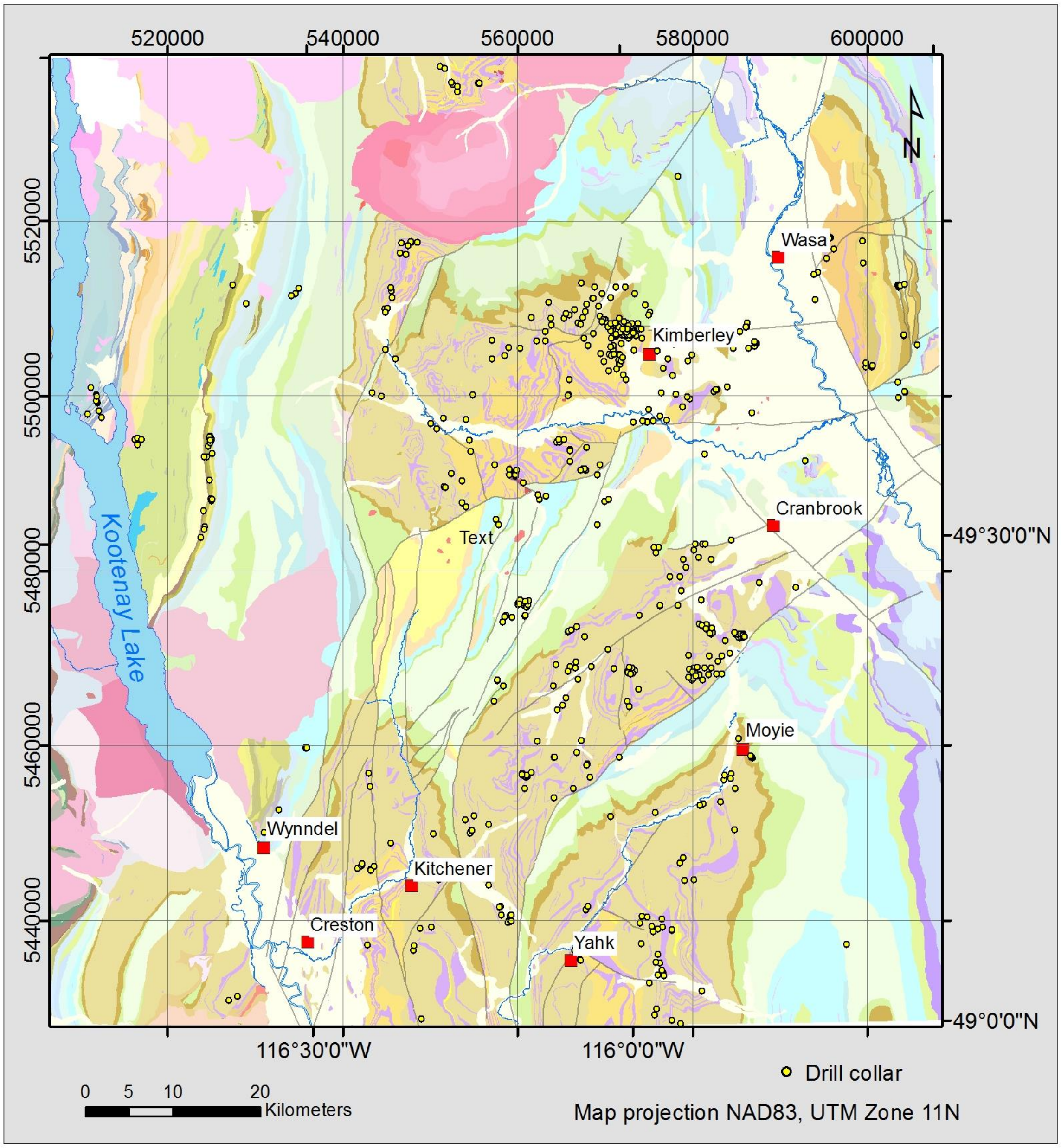

Figure 1. Map showing collar locations of drillholes contained in the drillhole database. Generalized geology (after Brown and MacLeod, 2011a, b, c, d; Brown et al., 2011a, b, c, d, e, f; Glombick et al., 2011a, b) is shown on the background.

geological map (Brown and MacLeod, 2011a, b, c, d; Brown et al., 2011a, b, c, d, e, f; Glombick et al., 2011a, b; Figure 2). A more detailed 3D view of the Sullivan Sub-basin is also provided that includes, in addition to the themes of the regional view, specific lithofacies drillhole intervals of the Sullivan horizon.

The drillhole database, 3D scenes and detailed descriptions of the tables and database fields can be downloaded from an accompanying Open File publication (Schetselaar et al., 2015).

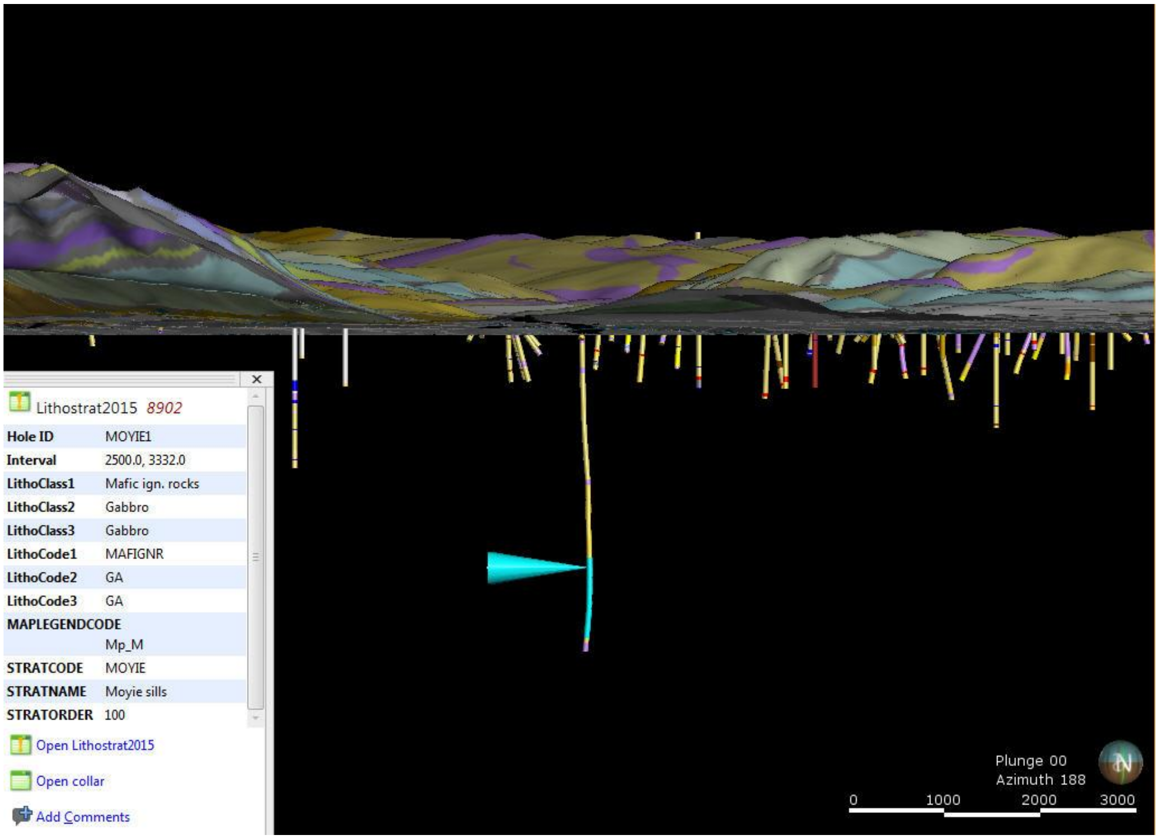

Lithostrat2015 8902

Hole ID	MOYIE1
Interval	2500.0, 3332.0
LithoClass1	Mafic ign. rocks
LithoClass2	Gabbro
LithoClass3	Gabbro
LithoCode1	MAFIGNR
LithoCode2	GA
LithoCode3	GA
MAPLEGENDCODE	Mp_M
STRATCODE	MOYIE
STRATNAME	Moyie sills
STRATORDER	100

Figure 2. 3D image of the Purcell drillhole database showing example of interactive query of lithostratigraphic information of a FROM-TO interval.

Geometric Registration of Drillhole Collars

The drillhole database is georeferenced to UTM, Zone 11N, North American Datum (NAD83) coordinates. The drillhole collar locations, either precisely surveyed or originally registered on a variety of hard copy topographic maps and mine grids, were digitized in UTM coordinates using surveyor provided conversion factors or affine transformations that were estimated from control points digitized from these legacy map archives, including mine grids and topographic landmarks such as intersections and bends in rivers and roads. Some of the drillhole collar locations, however, were more recently surveyed using single handheld GPS units. As a result, the planimetric (xy) root mean square error of drill collar locations significantly varies, with an estimated range of 5 to 250 metres (1 sigma). It should be noted that these error estimates refer to the collar locations and not to the accuracy of the drillhole logs themselves, which are also cumulatively dependent on errors in deviation log readings down the drillhole. Many of the drillhole paths were surveyed using older instruments with relatively low standards in accuracy and precision as compared to modern deviation log surveys. Moreover a significant portion of the older drillholes do not have deviation log surveys and are therefore assumed to be straight line projections from the recorded collar orientation. Although the value of these particular holes for exploration planning on detailed map scales may be limited, they may still be useful at more regional map scales, considering that they provide the only available subsurface geologic data around their collar positions.

Drillhole Database Compilation

Drillhole descriptive attributes, including lithology, lithostratigraphy, structure, alteration and mineralization were obtained from approved mineral exploration assessment reports maintained by the B.C. government (British Columbia Ministry of Energy and Mines, undated) and unpublished industry reports (mainly from Cominco Ltd.). Where available hyperlinks to the B.C. Ministry of Energy and Mines ARIS (assessment report indexing system) are provided in the database (‘Collar’ table) so that the digitized information can be easily compared with the source archives maintained on the B.C. Ministry of Energy and Mines website. Records for drillholes that were deepened at a later stage were combined in a single ‘HoleID’ record in the ‘Collar’ table. For these drillholes the ARIS report code and associated hyperlink field refer to the latest drilling activity in the hole.

Six thematic tables, including lithology, lithostratigraphy, alteration, mineralization, structure and Sub-basin facies (described in more detail below) were compiled from legacy drill log descriptions (Figure 3). The drillhole lithology logs were originally coded by industry and consulting geologists using locally established lithological and lithostratigraphic terminology. The lithology table also contains a field ‘StratCode’ to encode the lithostratigraphic formations of the Purcell Supergroup and Mesoproterozoic and Mesozoic intrusive suites (Höy et al., 2000). The lithostratigraphic classification includes ‘barcode’ siltstone markers consisting of millimetric to centimetric alternating dark grey and light grey laminated siltstone within the turbiditic sequence of the Middle Aldridge Formation (Huebschman, 1973). These unique ‘barcode’ patterns that characterize basin-wide fine-grained sediments formed when they settle from suspension during time intervals between turbidite flows, facilitate lithostratigraphic correlation over distances up to 300 km (Chandler, 2000). The position along the drillhole and thickness of the laminated siltstone markers were recovered from drill core stored at the Vine property and from Cominco’s legacy archives to facilitate 3D lithostratigraphic modelling.

Drillhole Database Structure

The MS Access© database ‘PurcellDrillholeDatabase.mdb’ consists of ten tables including five thematic drill log tables (Figure 4), describing: (1) lithology and lithostratigraphy (2) presence/absence of hydrothermal alteration and associated mineral species, (3) sulphide mineralization type (e.g.’massive’, ‘disseminated’) occurrence (e.g. ‘vein’, ‘bleb’) and mineral species (4) structures with their core-angle to the drill path and (5) descriptions of sedimentary facies found in the Sub-basin that hosted the now mined-out 150 Mt Sullivan massive sulphide deposit. The database normalization into five themes was essential to support hole-to-hole correlation of lithostratigraphic markers over large distances

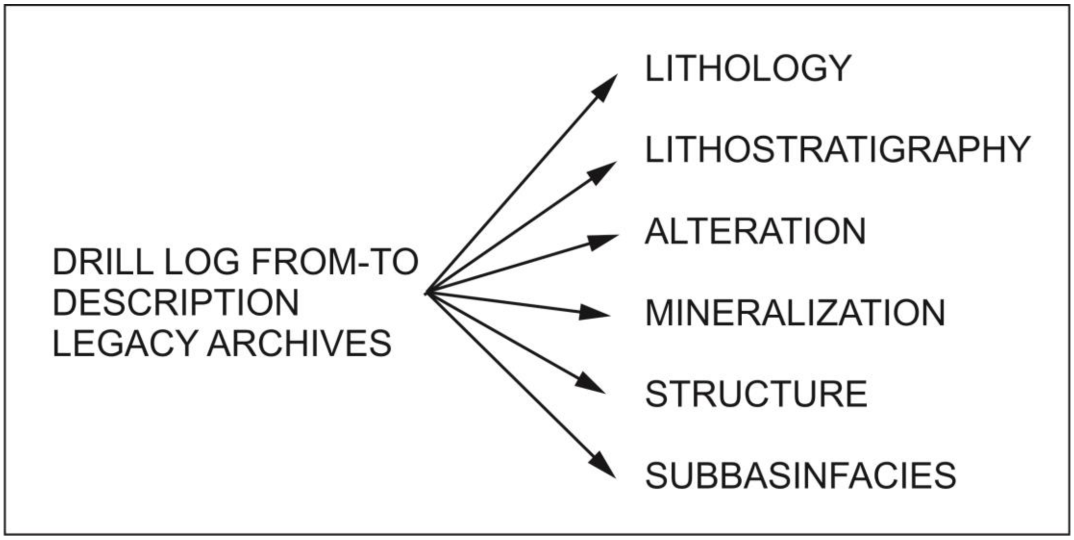

Figure 3. Attribute themes (right) parsed out from industry drill log archives (left) for normalizing the drillhole database into six themes. The lithology and lithostratigraphy themes were integrated in a single table because their ‘FROM’ – ‘TO’ descriptions refer to the same interval.

underpinning, in combination with mapped geological contacts, 3D regional-scale modelling of the contacts between the Mesoproterozoic formations of the Purcell Supergroup, including the Sullivan horizon.

As shown in Figure 4, the records in the five thematic drill log tables are linked by their drillhole identifier ‘HoleID’ to the ‘Collar’ table and to the ‘DeviationLog’ table in many-to-one relationships. The ‘Litholog’ and ‘SubbasinFacies’ tables are also linked to classification tables, which facilitate translating database fields with abbreviated codes to full text descriptions. The lithology classification table is hierarchically-structured, which permits recoding the most detailed drill log classification at multiple levels of generalization (Figure 5). The hierarchical structure is also used to encode mixtures of different lithofacies within a particular FROM-TO interval. The ‘LithoCode2’ field encodes either the dominant lithology or a mixture of lithology components when they are approximately equally abundant. The ‘LithoCode3’ field, regardless of the abundance of the components, always presents the abbreviation for the coarsest-grained lithology (if applicable) as the first character(s) of the code in cases where more than one lithology is present. So when the interval consists of more than one lithology, the 'Lithocode3' field encodes all the lithologies that occur in the interval, while 'Lithocode2' field encodes the most abundant. The Litholog table has in addition to this hierarchically-structured lithological information, a field that encodes the lithostratigraphy of the Mesoproterozoic formations of the Purcell Supergroup, including the names of the siltstone markers of the Middle Aldridge formation. Full descriptions of the database tables and the fields contained within them are provided in Schetselaar et al. (2015).

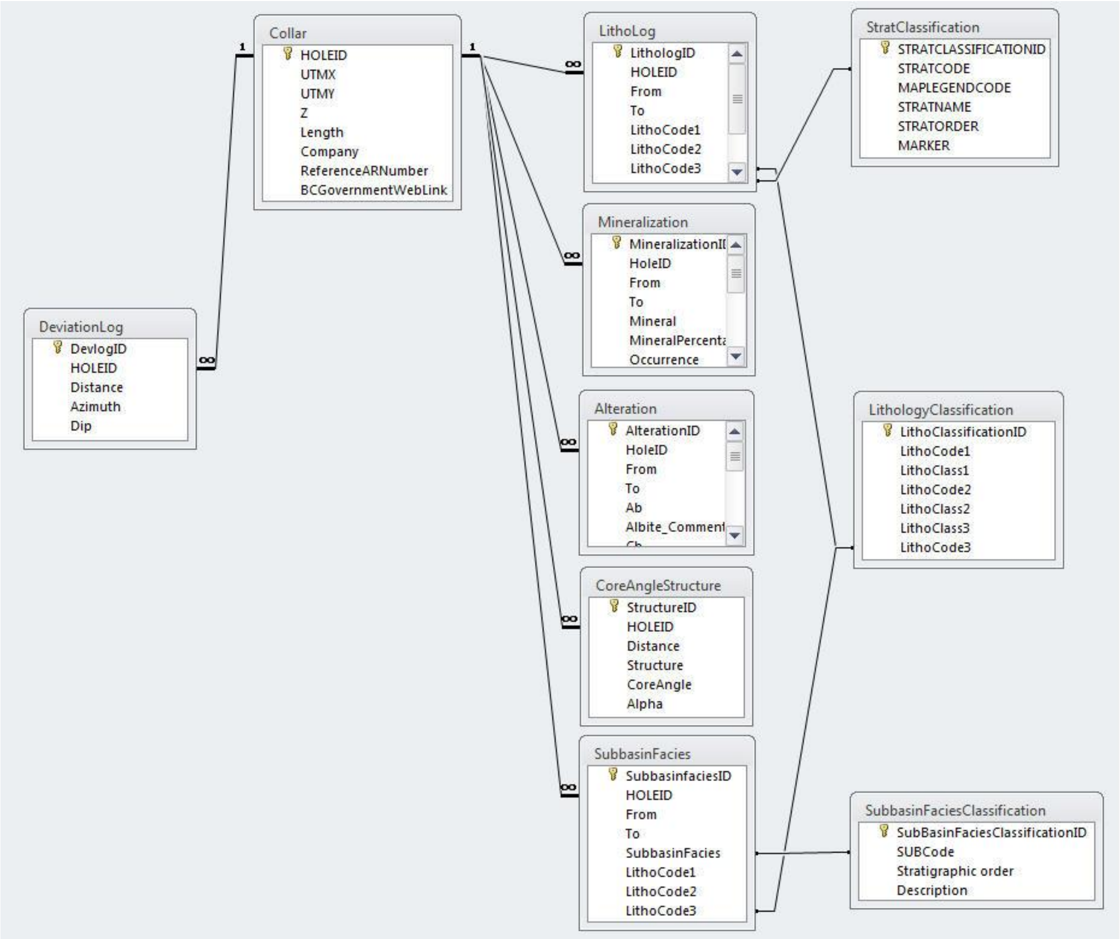

Figure 4. Database structure of the MS Access© relational drillhole database of the Purcell Anticlinorium.

Lithology encoding for single lithologies

LithoCode1: SEDCL = clastic (meta)sedimentary rocks
LithoCode2: W = wackestone
LithoCode3: Wl = laminated wackestone

Lithology encoding for mixed lithologies

LithoCode1: SEDCL = clastic (meta)sedimentary rocks
LithoCode2: W = wackestone
LithoCode3: QWl = laminated wackestone dominant / minor quartzite

LithoCode1: SEDCL = clastic (meta)sedimentary rocks
LithoCode2: Q = quartzite
LithoCode3: QWl = quartzite dominant / minor laminated wackestone

LithoCode1: SEDCL = clastic (meta)sedimentary rocks
LithoCode2: QW = quartzite and wackstone in approximately equal abundance
LithoCode3: QWl = quartzite / laminated wackestone

Figure 5. Examples of hierarchical lithology encoding of single and mixed FROM-TO intervals.

Discussion/Models

Limitations of the database

The drillhole data were compiled from a variety of sources some of which date back to the early 1900s. Starting in the 1960s exploration drilling became guided by structural and stratigraphic constraints in the search for SEDEX deposits. This compilation involved reconciling industry coding and lithological descriptions of a large number of geologists from a variety of exploration firms that logged drill core in the Purcell Anticlinorium. Although the drill log records were checked against their original interval descriptions in the legacy archives, it is possible that data transcription errors, inconsistencies in rock classification and coding errors were propagated. Inconsistencies in lithological and lithostratigraphic drill log coding may also be due to ambiguities in interpreting drill log interval descriptions, particularly for the most detailed interval descriptions that often contain lithofacies mixtures, such as alternating intervals of mudstone, siltstone, wacke and subwacke.

It should be noted that a significant proportion of the alteration and mineralization tables have overlapping FROM-TO intervals, as a result of parsing mineral species from text descriptions linked to different but overlapping intervals. Therefore it is recommended that separate queries be made for each mineral. Another significant limitation of this database is related to positioning of some of the drillhole collars that were carried out before the GPS era using topographic maps and/or air photographs. As a result, a few coordinates of, and shown drillhole collar locations may be tens to a maximum of a few hundreds of metres from their actual location.

Implications for Exploration

The relational database structure and standardized descriptive information of the drillhole data, including alteration and sulphide mineralization logs and a lithostratigraphic classification that matches the legend codes of the previously published TGI3 digital geologic map database (Brown and MacLeod, 2011a, b, c, d; Brown et al., 2011a, b, c, d, e, f; Glombick et al., 2011a, b) enables defining a wide range of spatial and attribute queries in support of exploration in the Purcell Anticlinorium with applicability to geological feasibility studies, mineral potential mapping, drill targeting and 3D modelling projects. This 3D database also provides the first comprehensive digital archive of the siltstone ’barcode’ markers of the Middle Aldridge Formation that can be correlated over hundreds of kilometres and play an unique role in the subsurface prediction of favourable horizons hosting SEDEX mineralization, including the Sullivan horizon.

Acknowledgements

We thank Dave Pighin, Trygve Höy, John Lydon, Craig Kennedy and staff of Eagle Plains Ltd. for sharing their expertise on the economic geology and lithostratigraphy of the Purcell Anticlinorium. We also thank Dave Pighin for providing access to drill core storage facilities at the Vine, Cranbrook. Staff of Eagles Plain Ltd. is gratefully acknowledged for providing additional drill core archives.

References

British Columbia Geological Survey, undated, ARIS assessment report indexing system: British Columbia Ministry of Energy and Mines, http://www.empr.gov.bc.ca/mining/geoscience/aris/pages/default.aspx

Brown, D.A., and MacLeod, R.F. (Compilers), 2011a, Geology, Boswell, British Columbia: Geological Survey of Canada, Open File 6310, Map at scale of 1: 50,000, doi: 10.4095/288546

Brown, D.A., and MacLeod, R.F. (Compilers), 2011b, Geology, Cranbrook, British Columbia: Geological Survey of Canada, Open File 6302, Map at scale of 1: 50,000, doi: 10.4095/288544

Brown, D.A., and MacLeod, R.F. (Compilers), 2011c, Geology, Skookumchuck, British Columbia: Geological Survey of Canada, Open File 6301, Map at scale of 1: 50,000, doi: 10.4095/288543

Brown, D.A., and MacLeod, R.F. (Compilers), 2011d, Geology, Yahk River, British Columbia: Geological Survey of Canada, Open File 6304, Map at scale of 1: 50,000, doi: 10.4095/288564

Brown, D.A., MacLeod, R.F., and Wagner, C.L. (Compilers), 2011a, Geology, Dewar Creek, British Columbia: Geological Survey of Canada, Open File 6305, Map at scale of 1: 50,000, doi: 10.4095/288563

Brown, D.A., MacLeod, R.F., and Wagner, C.L. (Compilers), 2011b, Geology, Kaslo, British Columbia: Geological Survey of Canada, Open File 6306, Map at scale of 1: 50,000, doi: 10.4095/288565

Brown, D.A., MacLeod, R.F., and Wagner, C.L. (Compilers), 2011c, Geology, St. Mary Lake, British Columbia: Geological Survey of Canada, Open File 6308, Map at scale of 1: 50,000, doi: 10.4095/288567

Brown, D.A., MacLeod, R.F., Wagner, C.L., and Chow, W. (Compilers), 2011d, Geology, Crawford Bay, British Columbia: Geological Survey of Canada, Open File 6307, Map at scale of 1: 50,000, doi: 10.4095/288566

Brown, D.A., MacLeod, R.F., Wagner, C.L., and Chow, W. (Compilers), 2011e, Geology, Grassy Mountain, British Columbia: Geological Survey of Canada, Open File 6309, Map at scale of 1: 50,000, doi: 10.4095/288568

Brown, D.A., MacLeod, R.F., Wagner, C.L., and Chow, W. (Compilers), 2011f, Geology, Moyie Lake, British Columbia: Geological Survey of Canada, Open File 6303, Map at scale of 1: 50,000, doi: 10.4095/288545

Chandler, F.W., 2000, The Belt-Purcell basin as a low-latitude passive rift: implications for the geological environment of Sullivan type deposits, *in* Lydon, J.W., Höy, T., Slack, J.F., and Knapp, M.E., ed., The geological environment of the Sullivan deposit, British Columbia: Geological Association of Canada, Mineral Deposits Division, Special Publication no. 1, p. 82-112.

Höy, T., Anderson, D., Turner, R.J.W., and Leitch, C.H.B., 2000, Tectonic, magmatic and metallogenic history of the early synrift phase of the Purcell basin, south-eastern British Columbia, *in* Lydon, J.W., Höy, T., Slack, J.F., and Knapp, M.E., ed., The geological environment of the Sullivan deposit, British Columbia: Geological Association of Canada, Mineral Deposits Division, Special Publication no. 1, p. 32-60.

Huebschman, R.P., 1973, Correlation of fine carbonaceous bands across a Precambrian stagnant basin: Journal of Sedimentary Petrology v. 43, p. 688-699.

Glombick, P., Brown, D.A., and MacLeod, R.F. (Compilers), 2011a, Geology, Creston, British Columbia: Geological Survey of Canada, Open File 6152 (revised), Map at scale of 1: 50,000, doi: 10.4095/288925

Glombick, P., Brown, D.A., and MacLeod, R.F. (Compilers), 2011b, Geology, Yahk, British Columbia: Geological Survey of Canada, Open File 6153 (revised), Map at scale of 1: 50,000, doi: 10.4095/288927

Joseph, J.M.R., Brown, D., and Walker, R., 2011a, Diamond drillhole database of the Purcell Basin: Geological Survey of Canada, Open File 6549; 1CD-ROM, doi: 10.4095/288015

Joseph, J.M.R., Brown, D., MacLeod, R., Wagner, C., Chow, W., and Thomas, M., 2011b, Purcell Basin interactive maps, British Columbia: Geological Survey of Canada, Open File 6478, 2011; 1 CD-ROM, doi:10.4095/289069

Lydon, J.W., Höy, T., Slack, J.F., and Knapp, M.E. (editors), 2000, The geological environment of the Sullivan deposit, British Columbia, Geological Association of Canada, Mineral Deposits Division, Special Publication no. 1, 834p.

Schetselaar, E., de Kemp, E.A., Ransom, P., Buenviaje, R., Nguyen, K., Montsion, R., and Joseph, J., 2015, 3D drillhole database of the Purcell Anticlinorium: Geological Survey of Canada, Open File 7817, 14 p.

3D Stratigraphic, Structural and Metal Zonation Modelling of the Sullivan Mine, Kimberley, British Columbia

R. Montsion
University of Ottawa, ON, K1N 6N5
rebecca.montsion@gmail.com

E.A. de Kemp
Geological Survey of Canada 615 Booth Street, Ottawa, ON, K1A 0E9

J.W. Lydon
Geological Survey of Canada, 601 Booth Street, Ottawa, ON, K1A 0E9

P.W. Ransom
9452 Clearview Road, Cranbrook, BC, V1C 7E2

J. Joseph
Geological Survey of Canada, 1500 - 605 Robson Street, Vancouver, BC, V6B 5J3

Abstract

Detailed mine scale data integration and modelling from historical drillhole data was undertaken for the giant SEDEX Sullivan orebody in Kimberley, British Columbia. This exercise resulted in 3D digital stratigraphic, structural and metal zonation (Pb, Zn, Ag, Fe) models. Over 4,000 drillholes with stratigraphic points and metal abundances were used from historical litho-stratigraphy-assay logs. Coordinate conversion from the Sullivan Mine grid to UTM coordinates and the geometric recalculation of the drill paths was undertaken to position the data to a more universally useable 3D data set. The data were developed into a geodatabase in ArcGIS and then exported to GoCad / SKUA for modelling. Metal zonation patterns corroborate previous studies that delineate the 3 main ore facies: Vent Complex, Transition and Bedded Ore zones. Locally, metal rich zones have abundance contours, which cut across the bedded mine stratigraphy giving support for an in situ replacement process. However, the major proportion of ore in the Bedded Ore zone is contained within the sulphide-rich Ore Bands predominantly the Main Ore Band. Variogram analysis was used on standard and transformed stratigraphic grids to help characterize metal and lithofacies distribution patterns in 3D. The 3D database and models give a detailed snap shot of a significant SEDEX deposit. This will contribute to a better characterization of the global SEDEX systems, as well as supporting local correlations within the Sullivan Sub-basin.

Introduction

With improving technology, geologists are able to model and interpret complex geological structures at depth. Previously, the mining industry interpreted geological

Recommended citation
Montsion, R., de Kemp, E.A., Lydon, J.W., Ransom, P.W., and Joseph, J., 2015. 3D Stratigraphic, structural and metal zonation modelling of the Sullivan Mine, Kimberley, British Columbia, *in* Paradis, S., ed., Targeted Geoscience Initiative 4: sediment-hosted Zn-Pb deposits: processes and implications for exploration; Geological Survey of Canada, Open File 7838, p. 236-252. doi:10.4095/296328

bodies using close-spaced two dimensional sections to visualize trends in the third dimension. With the emergence of three dimensional imaging and modelling systems, the majority of modern mine records have been updated to include multi-dimensional digital models. These models improve visualization of the geological setting and allow for complex statistical analysis of three dimensional data with the aim of revealing ore system relationships.

The extent of the Sullivan orebody, a SEDEX deposit near Kimberley, British Columbia, was almost fully mined before the digital age. The deposit originally contained about 160 million tonnes of ore with a grade of 6.1% Pb, 5.9% Zn, 68 g/t Ag (Hamilton et al.,1982); however, when the deposit closed in 2001 due to depletion of its reserves, the mine had produced 149,173,608 tonnes of ore grading 5.65% Pb, 5.33% Zn, 62.1 g/t Ag (BC Minfile 082FNE052, 1985).

Until now, 3D modeling has been limited to small areas of active mining in the southeastern part of the deposit. Developing a larger scale model requires a large database of stratigraphic, structural, assay and drillhole data. Drillhole data was provided by Joseph and Ransom (2008). Other mine data was gathered from archived drill logs by several sources including Lydon et al. (2000) and Montsion (2014). To date no digital model encompasses the entire deposit or integrates metal zonation, stratigraphy and structural information in a 3D GIS (Geographic Information Systems) environment. This study is the first phase of developing a fully integrated three dimensional model of the Sullivan orebody.

This study seeks to model metal concentrations of lead (Pb), zinc (Zn), silver (Ag), and iron (Fe) of the Sullivan mine, utilizing horizon gridding with three dimensional kriging estimation techniques. The estimated metal zonation patterns can potentially be compared with a stratigraphic and structural three dimensional model in a more rigorous quantitative manner.

Geological setting

The Sullivan orebody is hosted by the Aldridge Formation of the Mesoproterozoic Belt-Purcell Basin which outcrops over an area of about 200,000 km^2 in Montana, Idaho and Washington of the U.S. and southeastern British Columbia in Canada (Lydon, 2007). The Belt-Purcell is an intracratonic rift basin and it consists of an early rift-fill sequence of deep water marine turbidites and intercalated tholeiitic sills, and a later rift-sag sequence consisting of shallow marine to lagoonal and fluviatile environments. The rift-fill sequence (turbidites and sills) is termed the Aldridge Formation in Canada and the Prichard Formation in the U.S. and is up to 12 km thick (Höy et al., 2000). The Sullivan orebody is located on the east side of the Purcell Mountains, British Columbia (Figure 1).

The Sullivan deposit and its host rocks have been affected by at least two phases of tectonic and metamorphic activity which caused deformation, faulting and metamorphism. There are two zones of sulphide ore (east and west), which are separated by a structurally complex Transition zone. The western zone has been

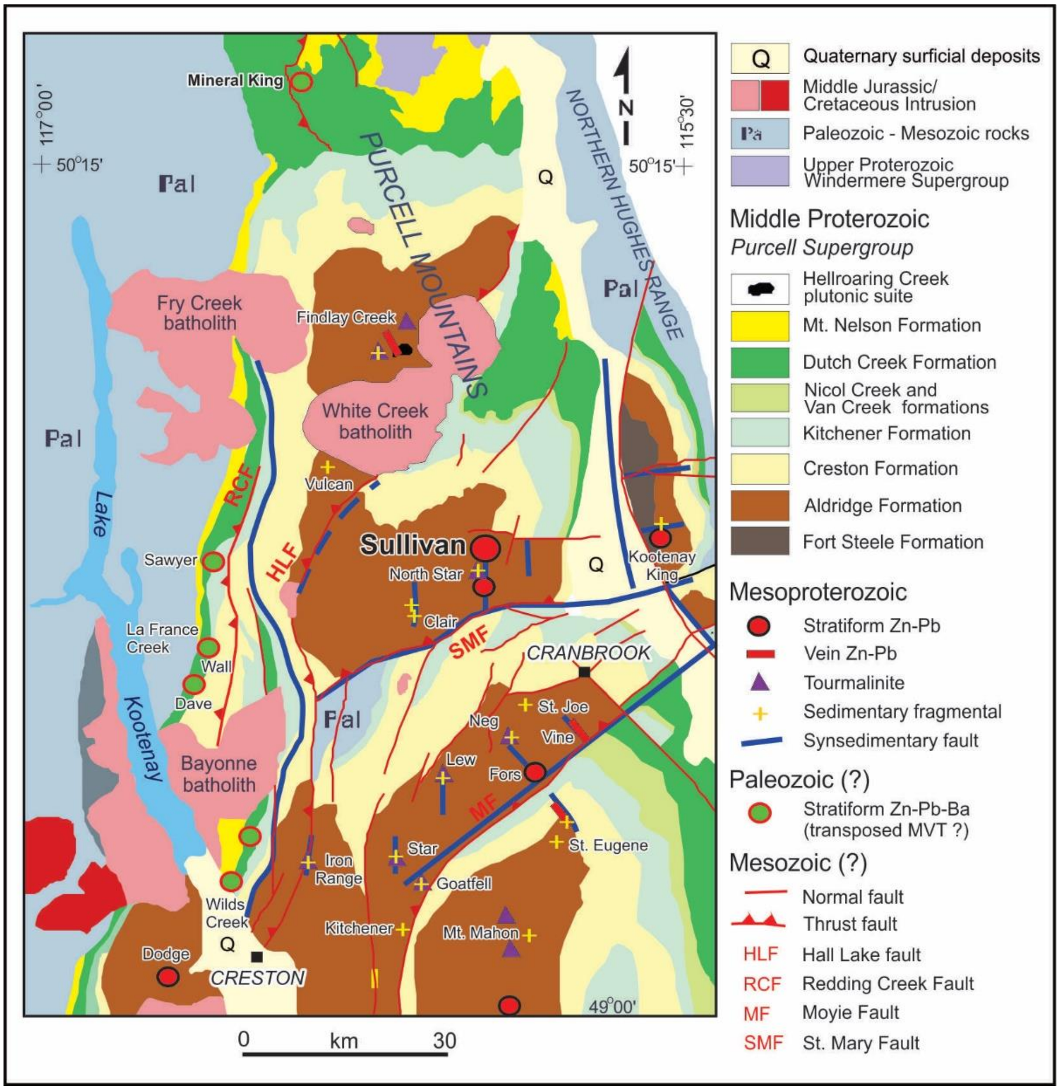

Figure 1. Location of the Sullivan mine in south-eastern British Columbia with geological map of the Purcell Anticlinorium. Overlay of SEDEX ore system elements (i.e. Sullivan and satellite massive sulphide deposits, tourmalinite alteration, sedimentary fragmental rocks and inferred synsedimentary faults). From Lydon et al. (2000).

termed the Vent Complex where metal enriched hydrothermal fluids emerged from the subsurface at the time of formation. Roughly 70% of the ore is contained within this zone (Lydon, 2007). The eastern zone contains the Bedded Ores, the separate ore layers being termed from the stratigraphic base to the stratigraphic top as the ‘Main Band’, ‘A Band’, ‘B Band’, ‘C Band’ and ‘D Band’ (Hamilton et al., 1982) (Figure 2). The major geologic features of the Sullivan deposit are illustrated in Figures 2 and 3.

Geological Formation

Sullivan is a SEDimentary EXhalative (SEDEX) deposit. SEDEX deposits form by the discharge of metalliferous hydrothermal fluids at and immediately below the seafloor of a sedimentary basin (Carne and Cathro, 1982). There has been some recent debate about how the Sullivan and other SEDEX deposits formed. Typically, at least part of a

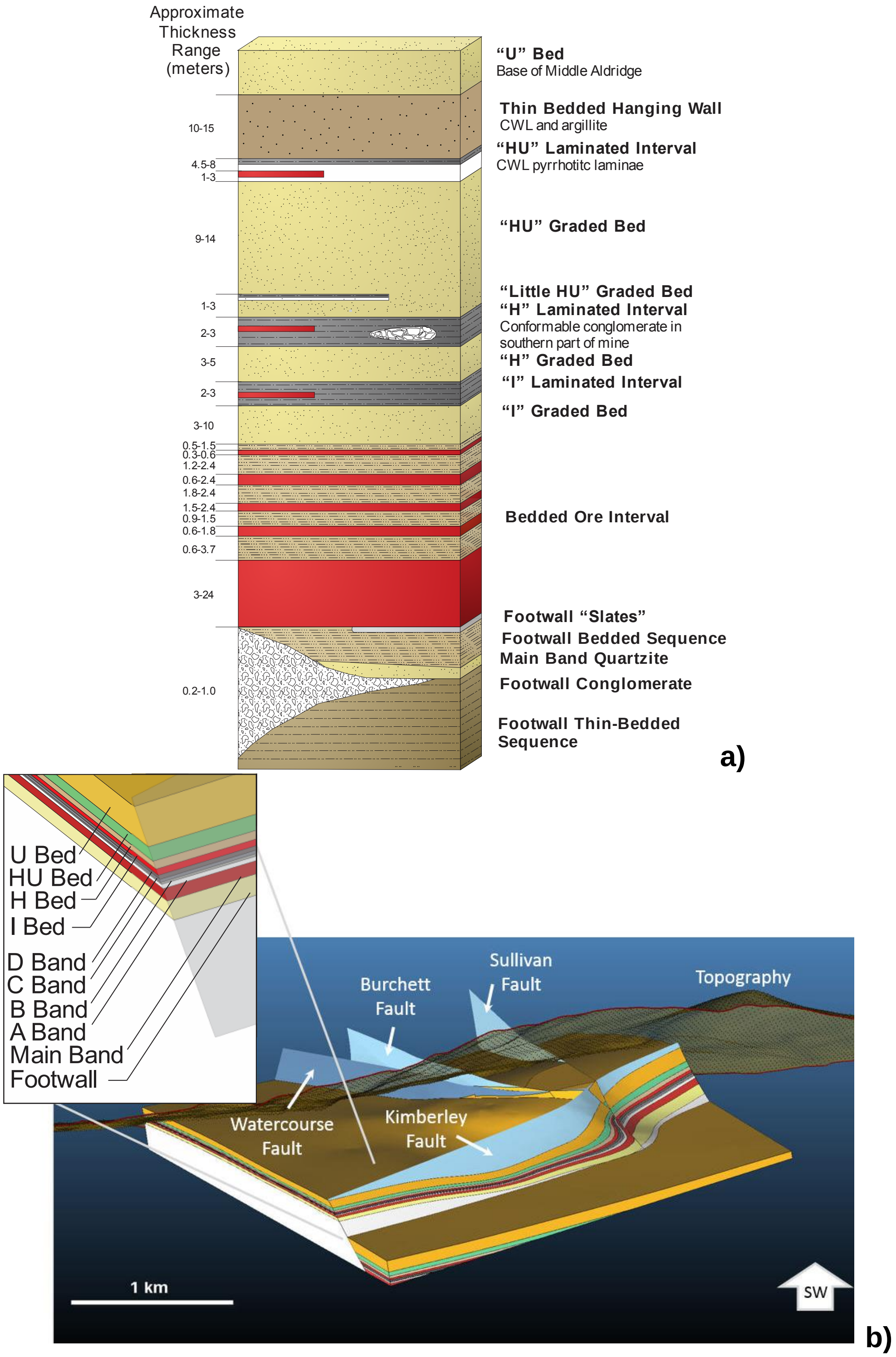

Figure 2. Bedded Ores stratigraphy from the eastern ore zone at Sullivan. a) Stratigraphic column of Bedded Ores (after Hamilton et al., 1982). b) Ore beds dipping to the northeast below surface topography.

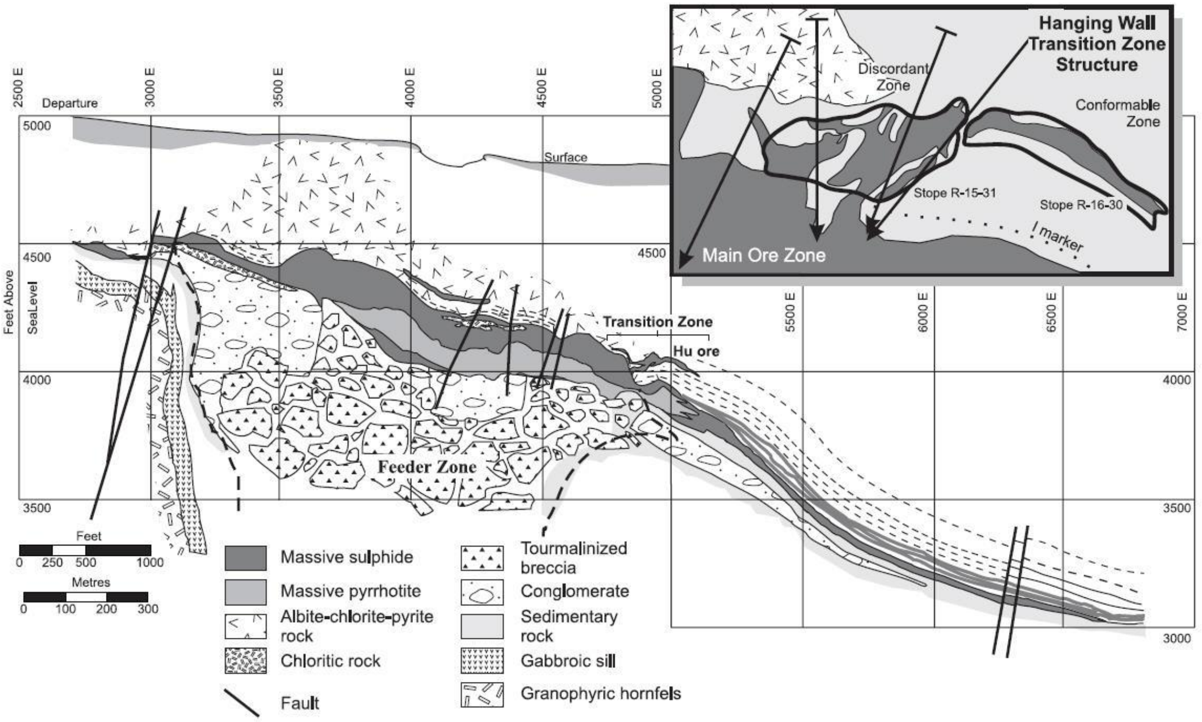

Figure 3. Generalized west-east geological cross-section at 11600N showing the distribution of the hanging wall sulphide zones (after Hamilton et al., 1982). The inset illustrates the complex nature of the "HU" sulphide zone along the Transition Ore zone (from Conly et al., 2000) and reflects a mechanical mobilization of sulphides along a major piercement structure (Paakki et al., 1995).

SEDEX deposit consists of concordant laminated ore beds, similar to those seen in the eastern Bedded Ores at Sullivan. The geometry, mineral assemblages and textures of these apparently stratiform sulphide deposits have given rise to two models of ore deposition. The first is nucleation of sulphides in the water column followed by precipitation as laminated metalliferous sediments parallel to bedding. The second is subsurface replacement of pre-existing laminated sediments with metal-rich sulphides along bedding planes of weakness (Goodfellow and Lydon, 2007).

Both models envisage hydrothermal fluids containing dissolved metals ascending through faults to vents on the seafloor, where the metals were precipitated by a reaction with hydrogen sulphide. This reaction can be represented by an equation that depicts a metal chloride complex ($MeCl_n$) reacting with dissolved hydrogen sulphide (H_2S) to form a metal sulphide (MeS), two hydrogen ions ($2H^+$) and *n* chlorine ions (nCl^-).

$$MeCl_n \quad + \quad H_2S \quad \overset{H_2O}{\longleftrightarrow} \quad MeS \quad + \quad 2H^+ \quad + \quad nCl^-$$

The result of the reaction is the formation of a metal sulphide precipitate. Through this reaction, metal precipitate is formed and hydrogen ion is released, which in turn alters the host rocks.

The first ore deposition model postulates that once vented to the seafloor, hydrothermal fluids reacts with anoxic bottom water containing bacteriogenic H_2S (formed by the reduction of seawater sulphate) to form a metalliferous precipitate, thereby chemically trapping the metals. The precipitate settled out of suspension and was deposited as laminated sediments on the seafloor proximal to the vent, giving a stratiform appearance to the mineralization (Goodfellow and Lydon, 2007). The second ore deposition model postulates that there was interaction between the hydrothermal fluid and sulphide in the shallow subsurface, with the sulphide source being bacteriogenic H_2S, hydrothermal H_2S, and/or pre-existing sulphide minerals. Sulphides were precipitated in pore spaces of the shallow sediments, thereby mimicking the porosity architecture of the sediments, or by replacement of pre-existing sedimentary or early diagenetic sulphides. In both cases, the resultant sulphidic rock shows sedimentary textures. Both models of ore deposition may contribute to a single deposit (Ridley, 2013). Both mechanisms of ore deposition probably contributed to development of the rich Sullivan orebody (Lydon et al., 2000); however one may have dominated during deposition. The most recent genetic model for the Sullivan deposit (Lydon, 2004) invokes heating of saline pore fluids by gabbro sill intrusion into unconsolidated sediments to form a large hydrothermal diaper, and the consequent leaching of metals from the sediments into a high salinity phase and boron of the sediments into a low salinity phase. The less-dense boron-rich fluids arrived at the surface first, forming the prominent footwall tourmalinite alteration zone beneath the Vent Complex, and the saline fluids arrived at the surface later, forming the Bedded Ores.

Deformation of the sulphide layers during the Cordilleran Laramide (150-110 Ma) orogeny is expressed as localized contorted folding (Figure 4), as tight north-south shallow plunging upright folds with slightly overturned to the east short limbs, and as irregular ore piercement structures (Figure 5). Additionally low angle thrusting can repeat the mine stratigraphy (Ransom and Merber, 2000). Overall these effects are most prominent in the Transition zone, between the main vent facies, on the west side of the Sullivan deposit, and the Bedded Ores zone on the east side of the deposit. The high ductility and strength contrast between various metal sulphides and host turbidite beds at the layer scale (1cm to 10 m) produced much of these deformation effects and the bigger scale strength gradient in the footwall between a mechanically rigid tourmalinized rock volume beneath the vent facies and weaker altered turbidites beneath the Bedded Ores facies producing the spatial distribution of the different styles of deformation (McClay, 1983; Lydon, 2004).

Results / Data Analysis

Through data integration and analysis, it was found that the Ordinary Kriging method (Isaaks and Srivastava, 1990), using an exponential semi-variogram model, best suited interpolation of the datasets. A structural and stratigraphic curvilinear grid or ‘GEOGRID’ was developed in GoCad/SKUA 3D modelling software from Paradigm® using drill core stratigraphic points (Lydon et al., 2000; Joseph et al., 2011b; Montsion, 2014), cross section points (Joseph et al., 2011a), and Ore Band tops and faults defined from previous work (Leitch and Turner, 2007). The Sullivan Mine GEOGRID follows the stratigraphic layering and proved useful for calculating the final metal models in the

Figure 4. Folded bedded sulphides from the Sullivan deposit. Sample courtesy of Paul Ransom.

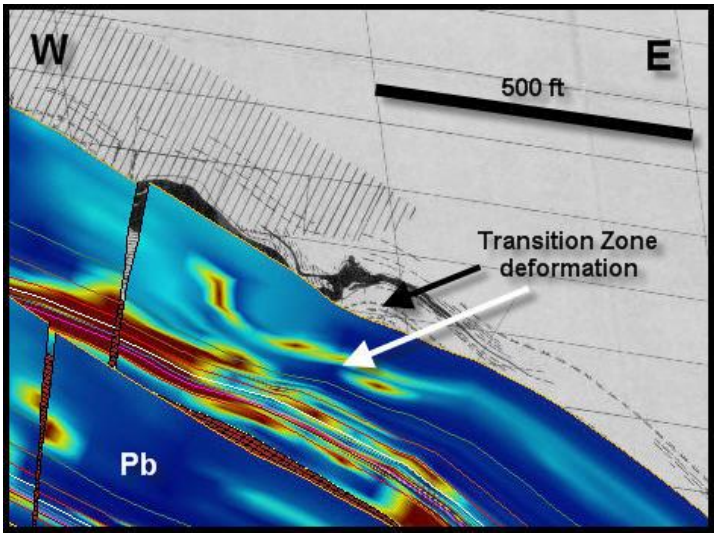

Figure 5. Transition zone deformation, hanging wall piercement cusp structure (Paakki et al., 1995) shown on historical Cominco general mine section (black and white section) and on interpolated Pb (Ordinary Kriging) sections in foreground. View looking to the north.

Bedded and Transition Ores, but a simple Cartesian grid, based on UTM coordinates, was used to calculate the Vent Complex zone. The Vent Complex metal modelled results were then sampled back into the GEOGRID for representation and comparison. All four metals (i.e. Zn, Pb, Ag, Fe) showed similar concentration in the Vent Zone where there is one large volume of high metal content (Figure 6), consistent with the maximum fixation of metals in and around a submarine hydrothermal vent. The laterally continuous metal-rich bands in the eastern ore zone (Figure 7), supports the concept of a sedimentary origin or control to the geometry of the deposit. These zones are separated by a structurally complex transition region where the Bedded Ores have been tectonically contorted and mechanically remobilized during thrusting of the Laramide orogeny (McClay, 1983; Paakki et al., 1995).

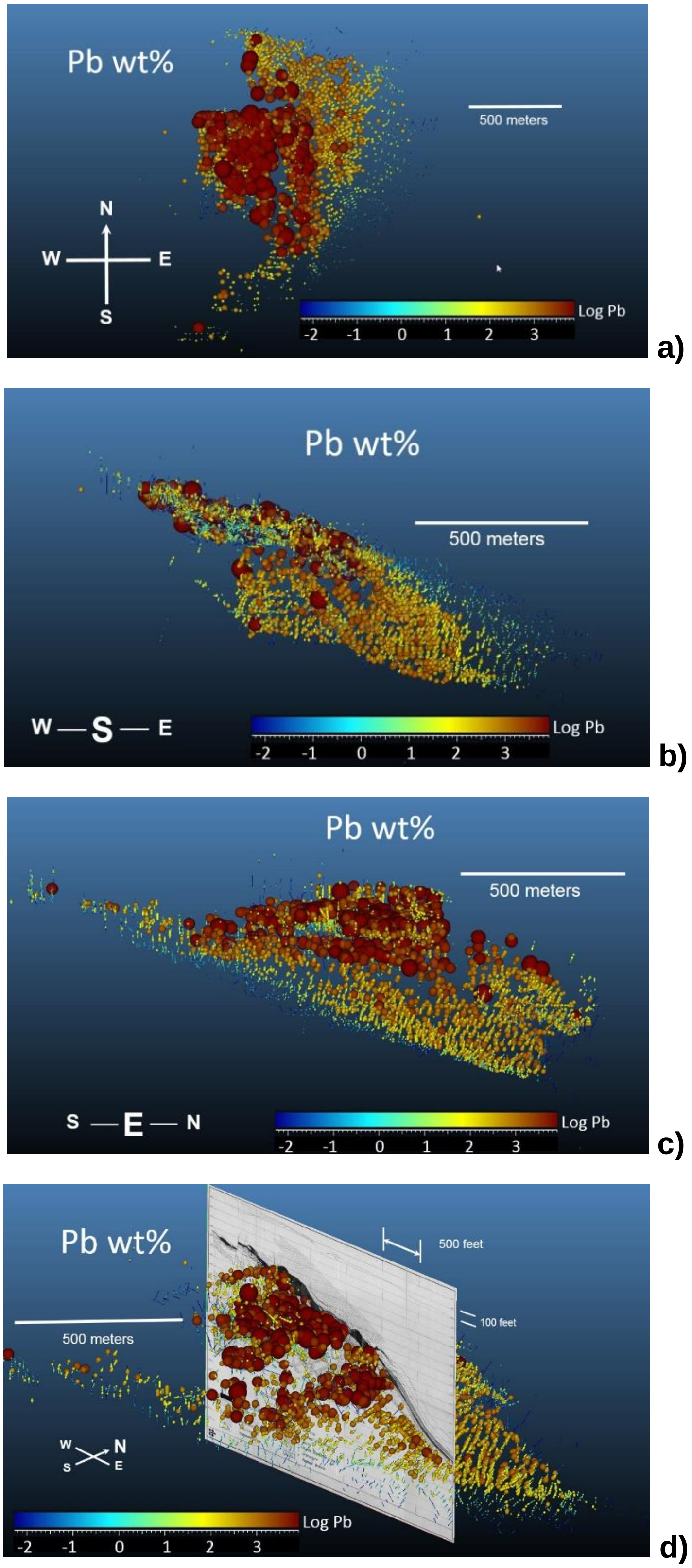

Figure 6. Pb assay value distribution in Sullivan mine. a) Top view; b) southern view; c) eastern view; d) northwest view superimposed on 11600 N cross section. From Freeze (1966).

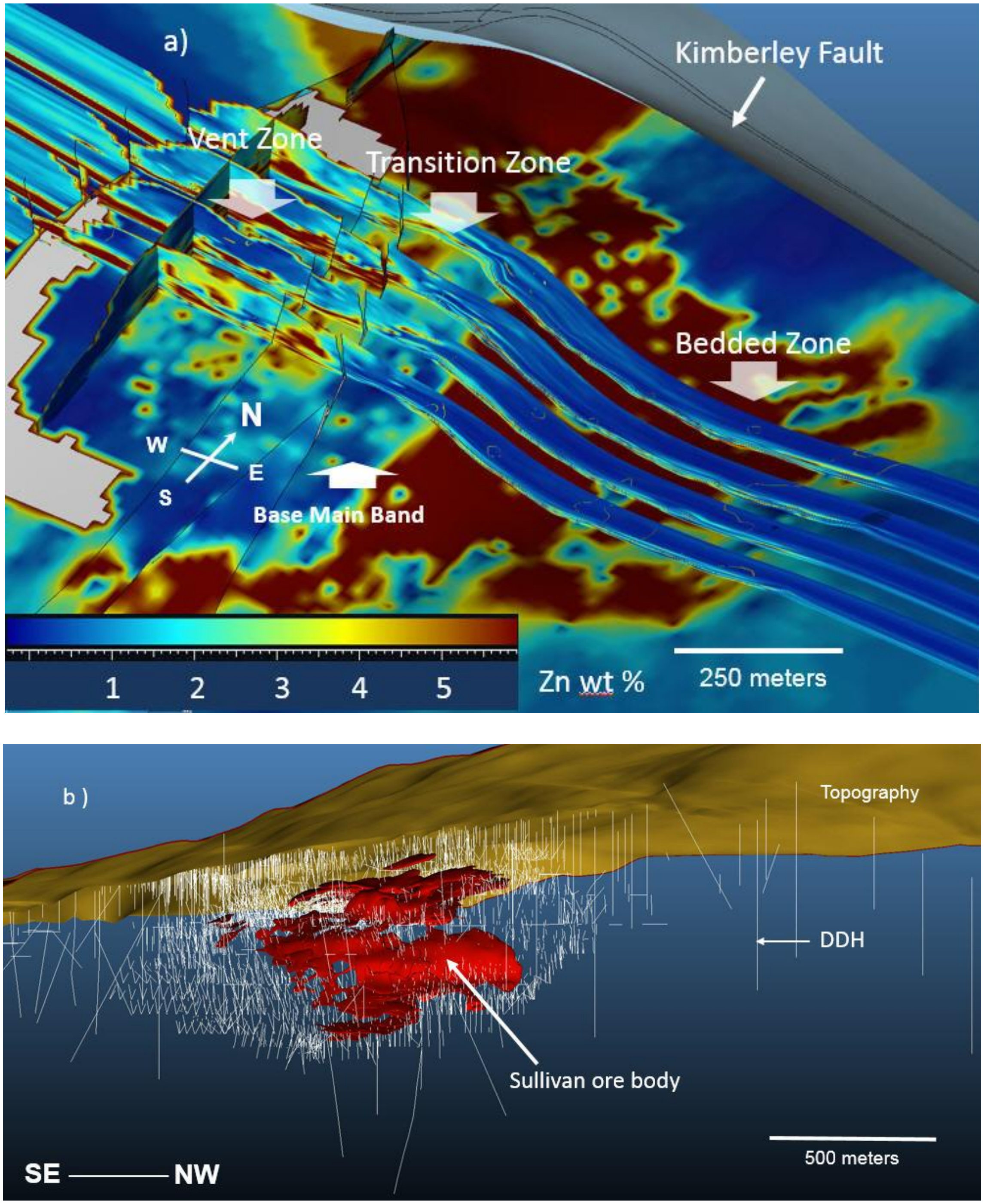

Figure 7. Bedded Ore geometry. a) Inverse distance weighting interpolated Zn values; b) distribution of drillholes and red zone of >10% Zn below brown surface topography (view from the northeast).

Statistical Analyses

Histograms

The metals Pb, Zn, and Ag show a naturally skewed univariate pattern (Figure 8). To emphasize the ore process, we stretched these skewed data values with a log-transform before doing Inverse Distance Weighted (IDW) or Ordinary Kriging interpolation. After a metal property model was calculated, a back log transform was done to represent the natural ranges of our modelled results. Fe showed a non-skewed range of values, so we interpolated the values directly.

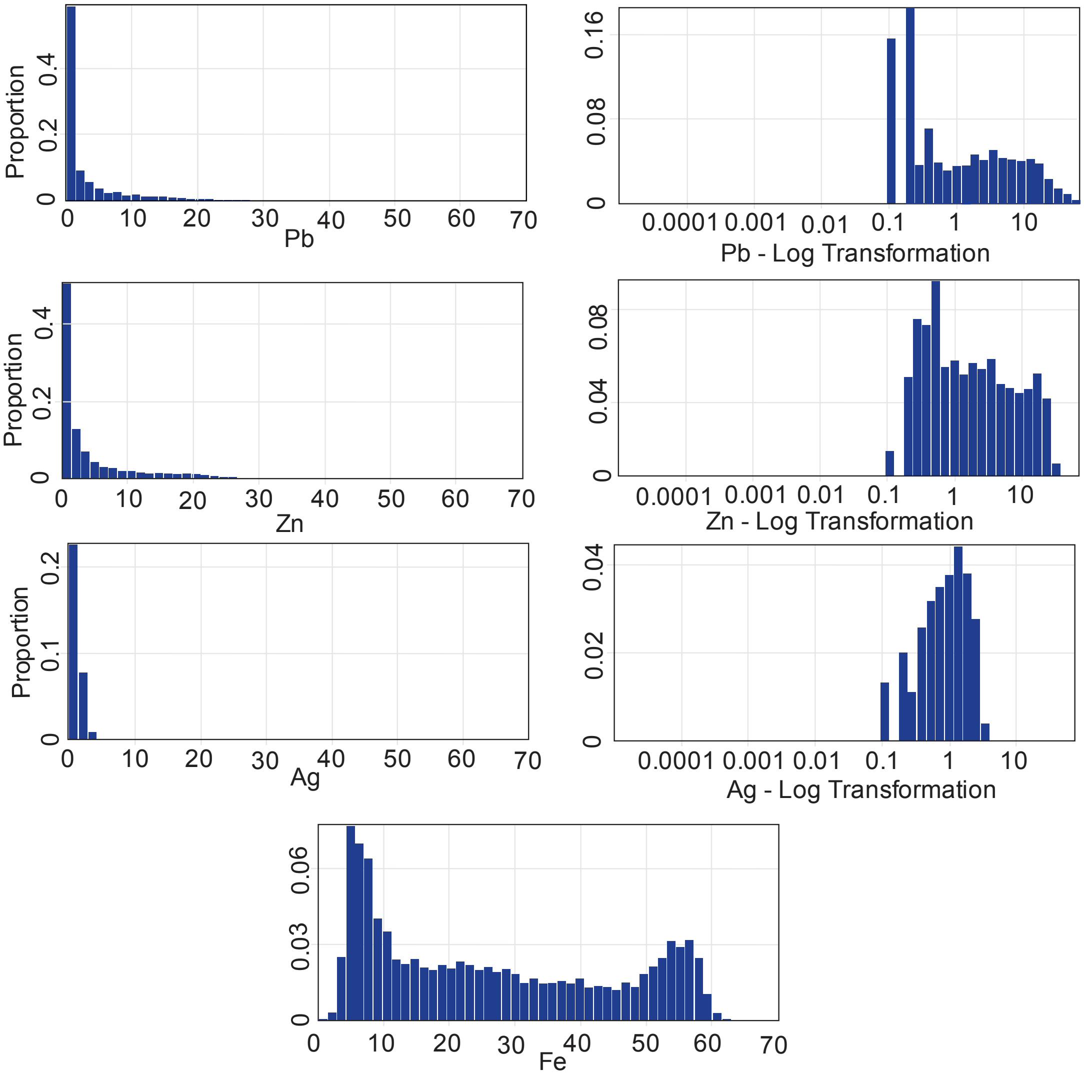

Figure 8. Histogram summaries of all Sullivan mine data. NPb = 109,626, NZn = 109,757, NAg = 101,364, NFe = 109,777.

Spatial Statistics

Geological impacts on semi-variogram patterns are prominent in the raw XYZ semi-variograms which can be difficult to interpret, especially with oscillations and/or drop-offs of point pair variability along the sills (Figure 9a). These could be controlled by the

Ore Bands, which repeat metal concentrations and display internal layering between ore and waste portions vertically. Alternatively, oscillations and discontinuities could be due to local folding and faulting. These patterns were smoothed out when geostatistical analysis was done with respect to the GEOGRID (UVW) instead of raw (XYZ) Cartesian space (Figure 9b). The GEOGRID was modeled after the geometry of mine stratigraphy (Figure 9c).

Within the GEOGRID coordinate system, the gross geological influences were minimized because the grid was already reflecting the spatial continuity of the data. This was especially true where there was good stratigraphic control, such as in the Bedded Ores. It was possible to evaluate the accuracy of the grid using point pair oscillations along the semi-variogram sill. If oscillations were present, the container grid didn’t accurately represent the gross geology within the study area. Despite the deficiencies inherent in the container grid model, the amplitude of waves within the GEOGRID semi-variogram plots were reduced compared to plots in XYZ space, thus indicating that the Sullivan GEOGRID was reasonable to use for this exercise.

Implications for Exploration

From the Sullivan Mine modelling exercise, metal zonation patterns clearly corroborate previous studies that delineated the 3 main ore zones (Vent, Transition and Bedded) as shown in Figure 10 (Freeze, 1966; Hamilton, 1982; Lydon et al., 2000). Locally in the Bedded Ores, the metal rich zones have abundance contours which cut across ore stratigraphy (Figure 11), but the major concentration of metals in the Bedded Ores is in the Main Band (Figure 12). Through data integration and analysis, it was found that the Ordinary Kriging method using an exponential semi-variogram model best suited the metal datasets of the stratigraphically concordant ore layers. The use of a curvi-linear stratigraphically and structurally constrained container grid, dramatically increased auto-correlation and, therefore, estimation results. Making similar geological grids for other SEDEX deposits should prove useful. The spatial trends of the interpolated concentrations of Pb, Zn and Ag, are similar to a strong north-south to 160º-340º trend reflecting structural attitudes and thicknesses in the Bedded Ores. This trend is visible in Figure 10.

The variograms show both local and regional trends, which are strongest for Pb and to a lesser extent for Zn and Ag. There is ~ 75 metres with a 160º trend and a much longer regional trend for at least 650 metres in the same direction. These trends match with the orientation defining the start of the Bedded Ores on the east side of the Sullivan deposit. The elongate 160º trend indicated by variogram analysis also matches reasonably well with the directions of several proposed synsedimentary graben systems delineated by previous studies (Hagen, 1983; Höy et al., 2000; Turner et al., 2000), such as the Sullivan-Stemwinder-North Star trend, Sullivan west graben, Clair trend, Star trend, and Lew trend (see Figure 1). The analysis supports the interpolation of data within a horizontal distance range of 0.5 to 1 km (i.e. parallel to bedding) and vertical range of < 100 m in the Middle Aldridge Formation.

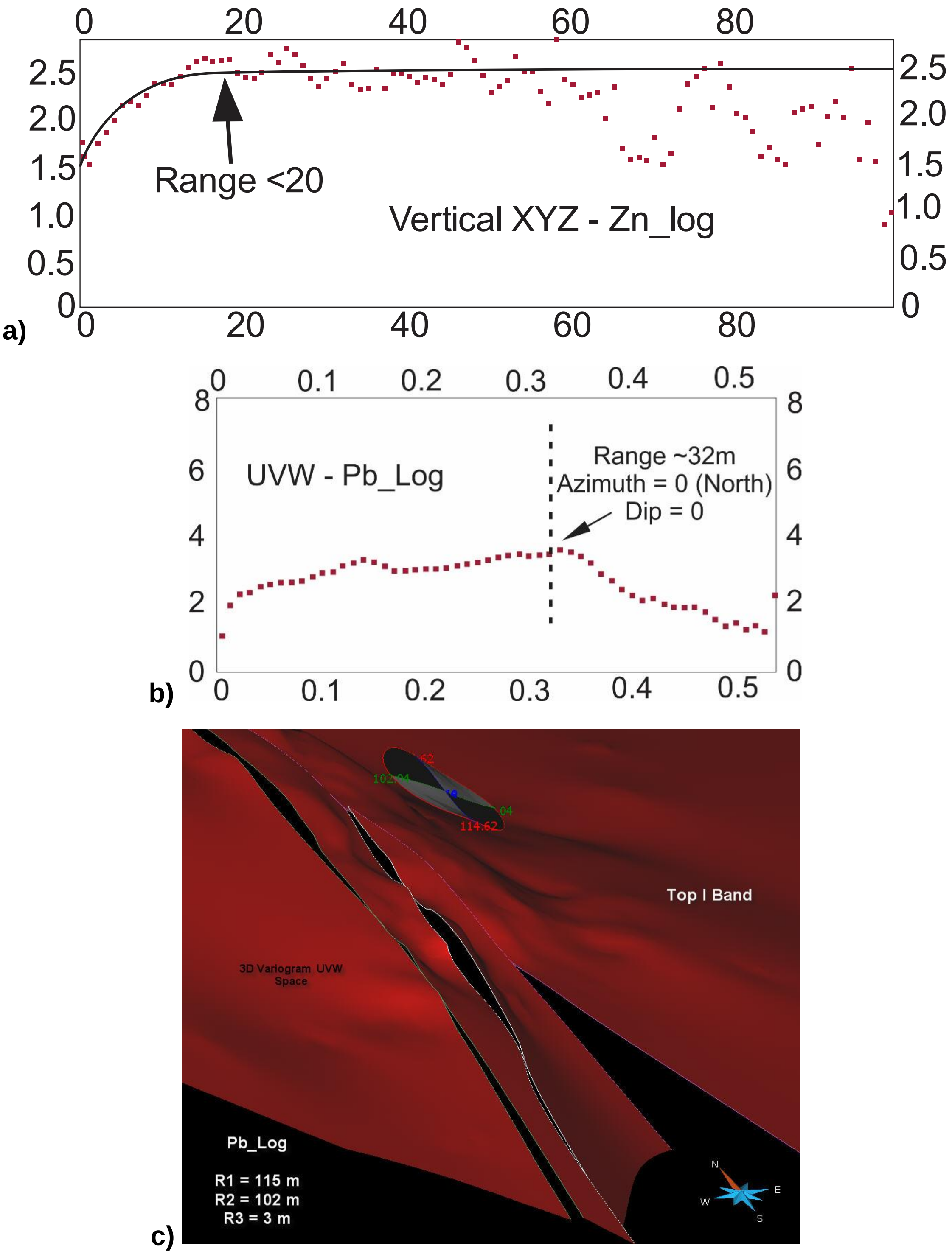

Figure 9. Variogram analysis. a) Vertical semi-variograms for Log transformed Pb and Zn from the entire Sullivan data; b) GEOGRID (UVW) based semi-variogram for log transformed Pb indicating smoother short (0.05) and long (0.3) ranges. Short range used for Kriging metal zonation models. c) Perspective close up view of top of I Bed showing distance converted semi-variogram ranges and 3D black and white ellipsoid. Notice relatively short distance in R3 which is roughly vertical or cross strata direction, which reflects our desire to optimize interpolation for stratiform mineralization at least in the Bedded Ores.

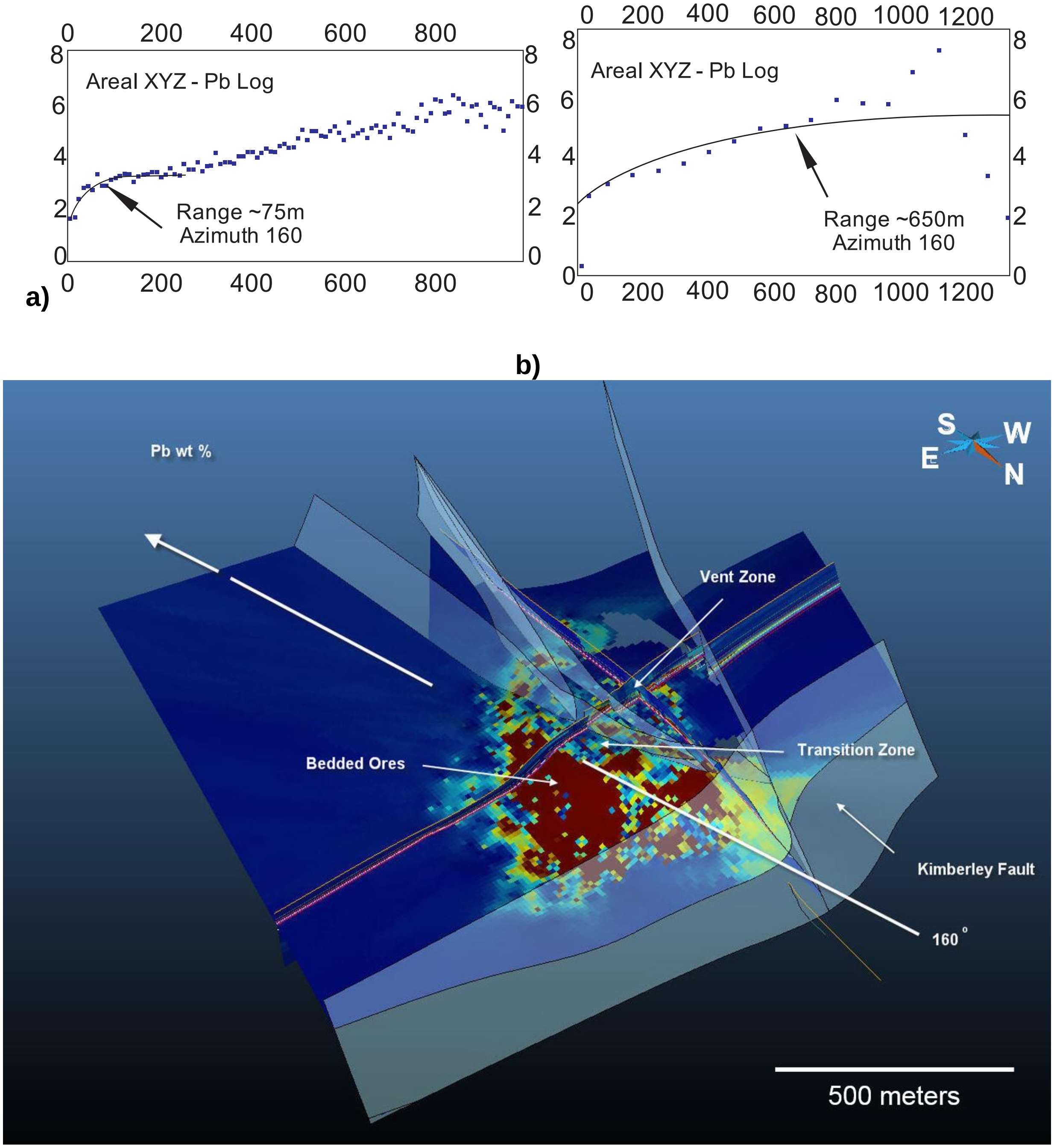

Figure 10. a) Variogram analysis indicates strong bedding controlled metal anisotropy for Pb, Zn and Ag within the Bedded Ores, as well as a subtle 160o trend in metal content; b) plan view of Sullivan orebody with delineation of Bedded Ores, Transition Zone and Vent Zone. Kriged Pb Assay values at the top of the Main Band show 160°/340° trend.

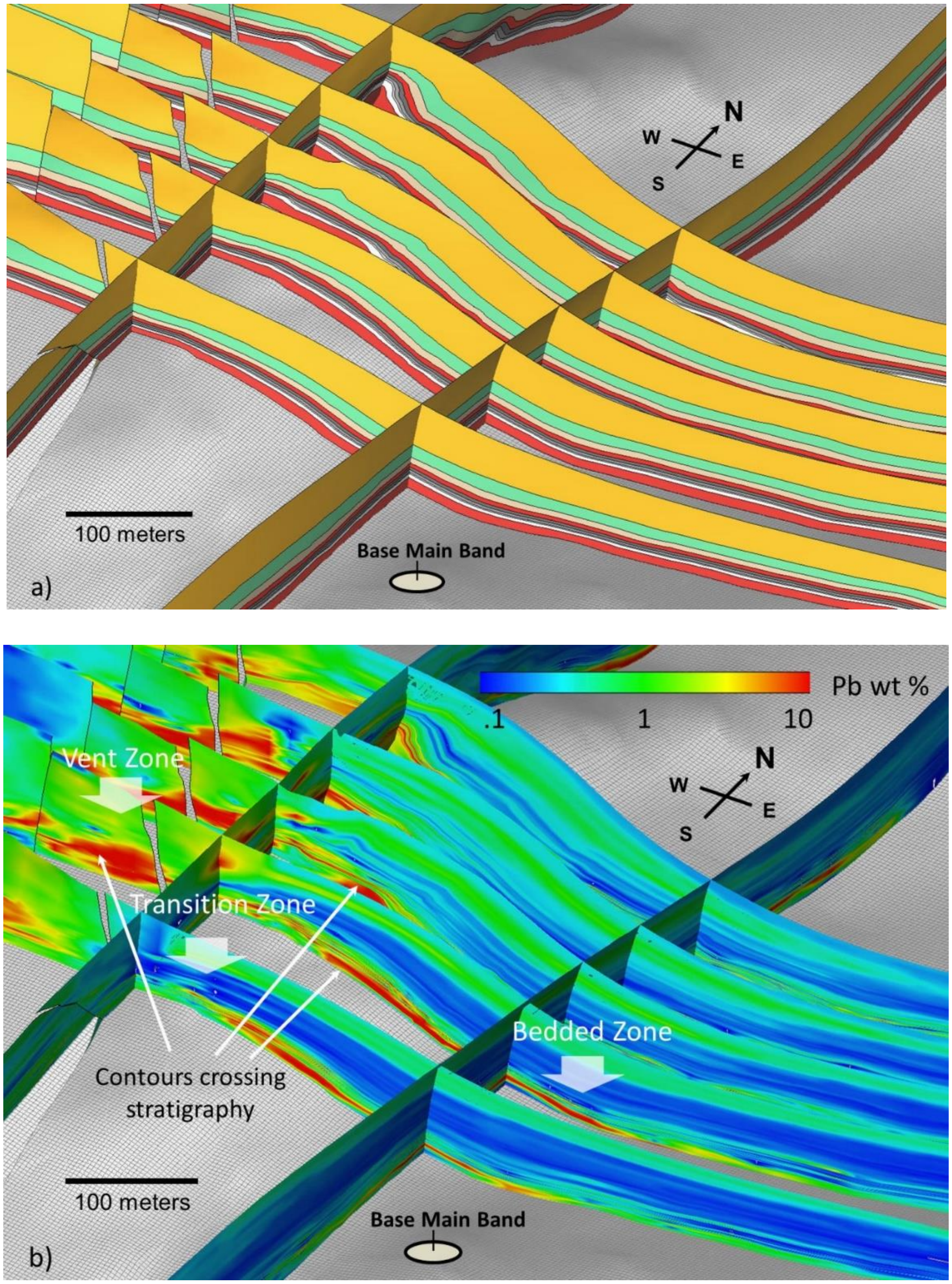

Figure 11. a) Close up of east-west vertical cross-sectional views of Sullivan stratigraphy (refer to Figure 2 for coloured legend scheme); b) same sections with Kriged Pb-Zn ratio indicating strong continuity with Main Band stratigraphy but also disconformity of Main Band crossing contours in the Bedded Ores. Linear concentration zones to the east are unsupported anomalies from the interpolation.

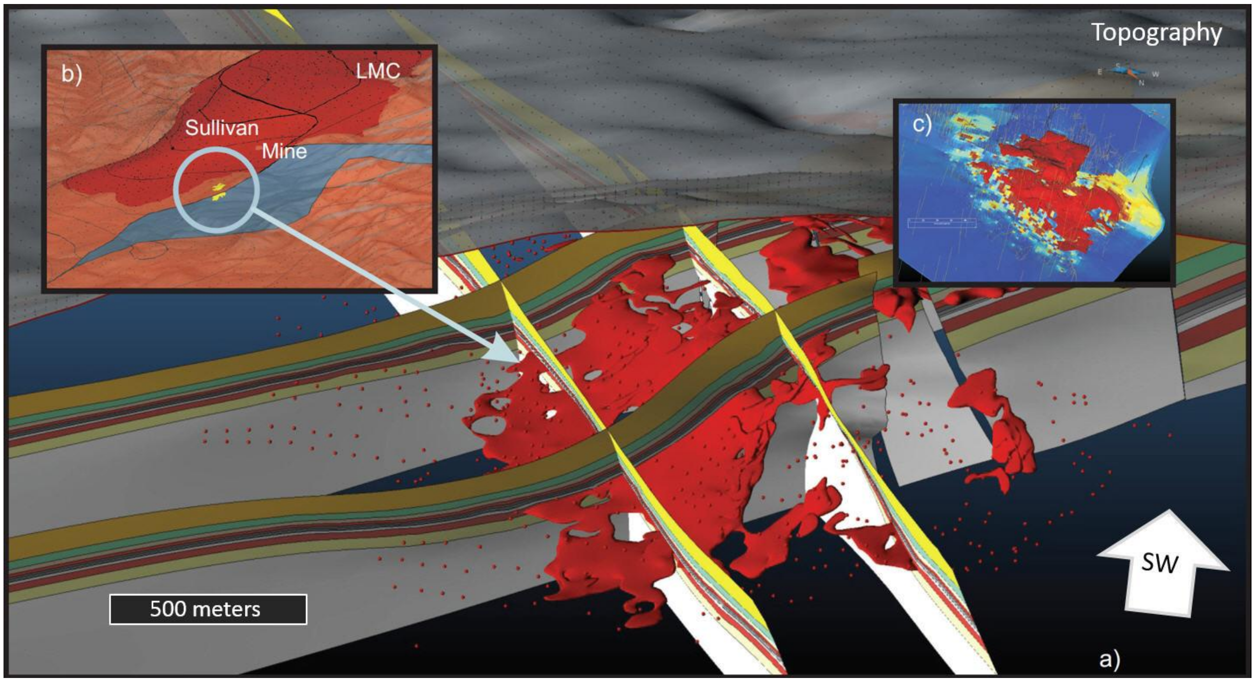

Figure 12. Sullivan Mine model looking towards the southwest. a) Orebody in red and mine stratigraphy cross-sections with top Main Band markers as red points); b) location Sullivan mine (yellow) at regional Lower – Middle Aldridge Contact (LMC) modelled surface (red), also looking to the southwest; c) Kriged Pb zonation map at top of Main Band.

Acknowledgements

Many thanks to Ernst Schetselaar (Geological Survey of Canada) for helping with lithostratigraphic data integration, drill core conversion and geostatistical analysis. On site access to the Sullivan Mine property and use of historical data was much appreciated from Teck (Cominco). Thanks to Richard Laframboise (Geological Survey of Canada) who collaborated in the development of the ArcGIS Drill Core Loader software. GoCad/SKUA software support was generously provided through the GoCad Research Consortia through Paradigm® and Mira Geoscience Ltd.

References

Carne, R.C., and Cathro, R.J., 1982, Sedimentary exhalative (sedex) zinc-lead-silver deposits, northern Canadian Cordillera: CIM Bulletin (1974), v. 75, no. 840, p. 66–78.

Conly, A.G., Goodfellow, W.D., Taylor, R.P., and Lydon, J.W., 2000, Geology, geochemistry and sulphur isotope geochemistry of the hanging wall sulphide zones and their related hydrothermal alteration, Sullivan Zn-Pb-Ag deposit, *in* Lydon, J. W., Höy, T., Slack, J.F., and Knapp, M.E., ed., The geological environment of the Sullivan deposit, British Columbia: Geological Association of Canada, Mineral Deposits Division, Special Publication no. 1, p. 541-573.

Freeze, A.C., 1966, On the origin of the Sullivan orebody, Kimberley, British Columbia, A symposium on the tectonic history and mineral deposits of the Western Cordillera: Canadian Institute of Mining and Metallurgy, Special Volume 8, p. 263-294.

Goodfellow, W.D., and Lydon, J.W., 2007, Sedimentary exhalative (SEDEX) deposits, *in* Goodfellow, W.D., ed., Mineral deposits of Canada: A synthesis of major deposit-types, district metallogeny, the evolution of geological provinces, and exploration methods: Geological Association of Canada, Mineral Deposits Division, Special Publication no. 5, p. 163–184.

Hagen, A.S., 1983, Sullivan-North Star graben system; unpublished report, Cominco Ltd., p. 11.

Hamilton, J.M., Bishop, D.T., Morris, H.C., and Owens, O.E., 1982, Geology of the Sullivan Orebody, Kimberley, B.C., Canada, *in* Hutchinson, R.W., Spence, C.D., and Franklin, J.M., ed., Precambrian sulphide deposits: Geological Association of Canada, Special Paper 25, H.S. Robinson Memorial Volume, p. 597-665.

Höy, T., Andreson, D., Turner, R.J.W., and Leitch, C.H.B., 2000, Tectonic, magmatic and metallogenic history of the early synrift phase of the Purcell Basin, southeastern British Columbia, *in* Lydon, J.W., Höy, T., Slack, J.F., and Knapp, M.E., ed., The geological environment of the Sullivan deposit, British Columbia: Geological Association of Canada, Mineral Deposits Division, Special Publication no. 1, p. 32-60.

Isaaks, E., and R. Mohan Srivastava, 1990, An introduction to applied geostatistics: Oxford University Press, Oxford University Press, p. 592.

Joseph, J.M.R, Brown, D., MacLeod, R., Wagner, C., Chow, W., and Thomas, M., 2011a, Purcell basin interactive maps, British Columbia: Geological Survey of Canada, Open File 6478; 1 CD-ROM, doi:10.4095/289069.

Joseph, J.M.R., Brown, D., and Walker, R., 2011b, Diamond drillhole database of the Purcell Basin: Geological Survey of Canada, Open File 6549, 1CD-ROM, doi: 10.4095/288015.

Joseph, J.M.R., and Ransom, P.W., 2008, Geoscience data archive from the Sullivan Mine, southeastern British Columbia: Geological Survey of Canada, Open File 5913, 1 DVD, doi:10.4095/226168.

Leitch, C.H.B., and Turner, R.J.W. (with contributions by Sullivan Mine Staff), 2007, Composite lithology and alteration sections, Sullivan Mine, British Columbia: Geological Survey of Canada, Open File 5701, 2 sheets, scale 1:4620.

Lydon, J. W., 2004, Genetic Models for Sullivan and other SEDEX deposits, *in* Deb, M., and Goodfellow, W.D., ed., Sediment-hosted lead-zinc sulphide deposits: Narosa Publishing House, New Delhi, p. 149-190.

Lydon, J.W., 2007, Geology and metallogeny of the Belt-Purcell Basin, *in* Goodfellow, W.D., ed., Mineral Deposits of Canada: A synthesis of major deposit types, district metallogeny, the evolution of geological provinces, and exploration methods: Geological Association of Canada, Mineral Deposits Division, Special Publication no. 5, p. 581-608.

Lydon, J.W., Paakki, J.J., Anderson, H.E., and Reardon, N.C., 2000, An overview of the geology and geochemistry of the Sullivan deposit, *in* Lydon, J. W., Höy, T., Slack, J.F., and Knapp, M.E., ed., The geological environment of the Sullivan deposit, British Columbia: Geological Association of Canada, Mineral Deposits Division, Special Publication no. 1, p. 505-522.

McClay, K.R., 1983, Structural evolution of the Sullivan Fe-Pb-Zn-Ag orebody, Kimberley, British Columbia, Canada: Economic Geology, v. 78, p. 1396-1424.

Montsion, R., 2014, Zonation of Pb, Zn, Ag and Fe along the Sullivan Horizon, Kimberley, British Columbia: Unpublished B.Sc. Thesis, Carleton University, Ottawa, p. 72.

Paakki, J.J., Lydon, J.W., and Del Bel Belluz, N., 1995, Durchbewegt sulphides, piercement structures, and gabbro dyke displacement in the vent complex of the Sullivan Pb-Zn deposit, British Columbia, *in* Current Research 1995-A: Geological Survey of Canada, p. 81-90.

Ransom, P.W., and Merber, D., 2000, Low-angle thrusts in the southeast fringe of the Sullivan mine, *in* Lydon, J.W., Höy, T., Slack, J.F., and Knapp, M.E., ed., The geological environment of the Sullivan deposit, British Columbia: Geological Association of Canada, Mineral Deposits Division, Special Publication no. 1, p. 534-540.

Ridley, J., 2013, Reservoir modeling, September 2013, ore deposit geology, Cambridge University Press, New York, ISBN-9781107022225.

Turner, R.J.W., Leitch, C.H.B, Höy, T., Ransom, P.W., Hagen, A., and Delaney, G.D., 2000, Sullivan graben system: district-scale setting of the Sullivan deposit, *in* Lydon, J.W., Höy, T., Slack, J.F., and Knapp, M.E., ed., The geological environment of the Sullivan deposit, British Columbia: Geological Association of Canada, Mineral Deposits Division, Special Publication no. 1, p. 370-407.

Implicit 3D Modelling of Geological Surfaces with the Generalized Radial Basis Functions (GRBF) Algorithm

M.J. Hillier
Geological Survey of Canada, 615 Booth Street, Ottawa, ON, K1A 0E9
Michael.Hillier@NRCan.gc.ca

E.A. de Kemp
Geological Survey of Canada, 615 Booth Street, Ottawa, ON, K1A 0E9

E.M. Schetselaar
Geological Survey of Canada, 615 Booth Street, Ottawa, ON, K1A 0E9

Abstract

We summarize an interpolation algorithm, which was developed to model 3D geological surfaces, and its application to modelling regional stratigraphic horizons in the Purcell Basin, a study area in the SEDEX project under the Targeted Geoscience Initiative 4 program. We developed a generalized interpolation framework using radial basis functions (RBF) that implicitly models 3D continuous geological surfaces from scattered multivariate structural data. The general form of the mathematical framework permits additional geologic information to be included in the interpolation in comparison to traditional interpolation methods using RBF's such as: (1) stratigraphic data from above and below targeted horizons (2) modelled anisotropy and (3) orientation constraints (e.g. planar and linear).

Introduction

Models of 3D geological surfaces provide valuable information of the subsurface commonly used in earth resource exploration. Currently, explicit and implicit surface modelling approaches are used to model 3D geological surfaces (Caumon et al., 2007). Important differences between the approaches are: (1) the explicit approach is only concerned with the particular surfaces being modelled whereas the implicit approach models entire volumes; and (2) the explicit approach is more interpretative and driven by user-based modelling decisions and models are not reproducible whereas the implicit approach is more data driven and models are reproducible. The latter approach is used in this paper.

In the past, high computational costs were normally associated with implicit approaches due to the fact that a single mathematical function, a linear sum consisting of as many terms as there are data points, is fitted by solving a system of equations. Furthermore, to visualize the modelled result the function has to be

Recommended citation

Hillier, M.J., de Kemp, E.A., and Schetselaar, E.M., 2015. Implicit 3D modelling of geological surfaces with the generalized radial basis functions (GRBF) algorithm, *in* Paradis, S., ed., Targeted Geoscience Initiative 4: sediment-hosted Zn-Pb deposits: processes and implications for exploration; Geological Survey of Canada, Open File 7838, p. 253-266. doi:10.4095/296328

evaluated at every point in a 3D grid. Therefore, as the number of data points increases, the corresponding set of computational resources required to fit and evaluate the function in reasonable times significantly increases. However, as a result of Moore's Law (Moore, 1965), computational resources have expanded exponentially. In addition, significant progress made in numerical methods (e.g. matrix solvers, fast evaluators, domain decomposition methods) permit the use of implicit approaches to be applied on data sets containing up to millions of points (Beatson et al., 2000; Cuomo et al., 2013).

In implicit modelling, the fitted mathematical function describes a scalar field typically representing a signed distance from a surface defined by a scalar function $f(\boldsymbol{x}) = 0$ where $\boldsymbol{x}$ is a 3D position vector. Following the evaluation of the function in a 3D grid, a surface is triangulated by tracing everywhere the scalar field is zero by using a marching cube (Lorensen and Cline, 1987) or marching tetrahedral (Treece et al., 1999) algorithm. The major advantage of implicit modelling is that very complex surfaces can be accurately modelled from scattered data sampling. However, current implicit radial basis function (RBF) approaches (Turk and O'Brien, 1999; Carr et al., 2001), when applied to modelling geological surfaces from sparse data suffer from the following four limitations: (1) Artificial offset points are required to specify local geometry. Using local normal measurements, offset points are projected above and below surface points and their corresponding scalar field are respectively defined as $f(\boldsymbol{x}) = 1$ (above) and $f(\boldsymbol{x}) = -1$ (below). The magnitude by which they are projected is a user-specified parameter. This characteristic can create significant issues in largely varying structures such as isoclinal folding since an offset point may be projected on the incorrect side of a fold causing topological problems. (2) Common lithological constraints, such as markers that are stratigraphically above or below particular geological contacts are not included. (3) Strike/dip observations with polarity are not included. (4) Data mined structural anisotropy are not incorporated. Our developed generalized radial basis function algorithm (GRBF) overcomes all aforementioned limitations.

Results/Data Analysis

GRBF algorithm

The GRBF algorithm, written in the C++ programming language, was incorporated into GoCad/SKUA, a sophisticated geological modelling application, as a plugin. GRBF plugins for GoCad/SKUA versions 2011.2p2 and 2013.2 have been developed. The 2013.2 plugin has a user-interface illustrated in Figure 1.

This section of the paper is organized as follows. First, a detailed description of the input data used by the algorithm is given. Second, the sequence of steps performed by the algorithm is described. Third, advanced modelling parameters are explained. Finally, applications of the GRBF algorithm in various geological settings with varying degrees of structural complexity are shown.

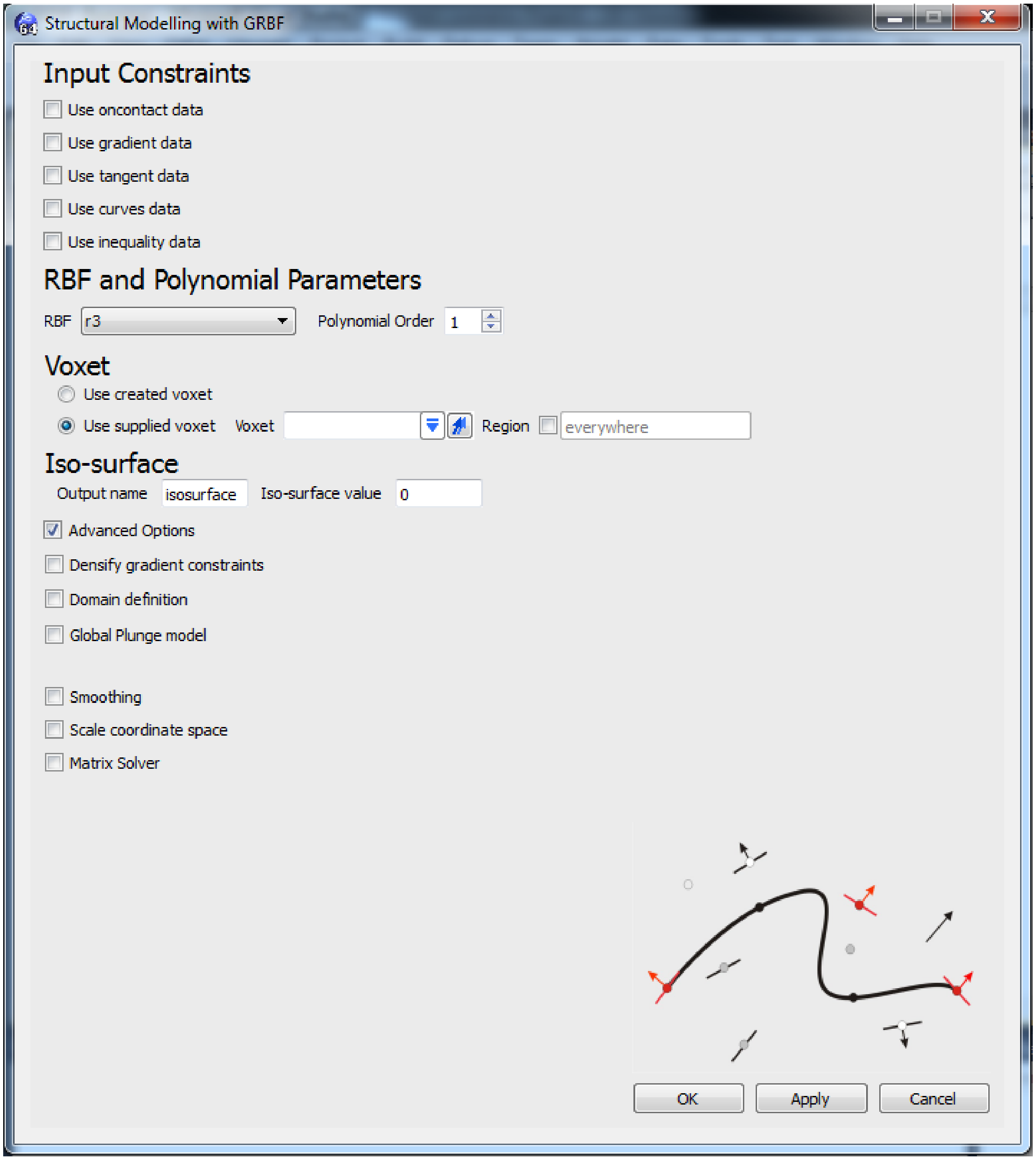

Structural Modelling with GRBF

Input Constraints

☐ Use oncontact data
☐ Use gradient data
☐ Use tangent data
☐ Use curves data
☐ Use inequality data

RBF and Polynomial Parameters

RBF r3 Polynomial Order 1

Voxet

○ Use created voxet
● Use supplied voxet Voxet Region ☐ everywhere

Iso-surface

Output name isosurface Iso-surface value 0

☑ Advanced Options
☐ Densify gradient constraints
☐ Domain definition
☐ Global Plunge model
☐ Smoothing
☐ Scale coordinate space
☐ Matrix Solver

Figure 1. User interface for the generalized radial basis function GRBF algorithm plugin in GoCad/SKUA.

Input data

The types of geological observations used by the algorithm are shown in Figure 2. On-contact constraints are sampled 3D point locations of the geological surface and can come from outcrop or drill core information. Gradient constraints encapsulate strike/dip with polarity (younging direction) observations sampling planar orientations of contact surfaces or off-contact horizons. Tangent constraints are linear orientation constraints of lines tangent to stratigraphic horizons (e.g. apparent dip and fold axes constraints). Inequality constraints are sampled 3D point locations above or below a particular geological surface.

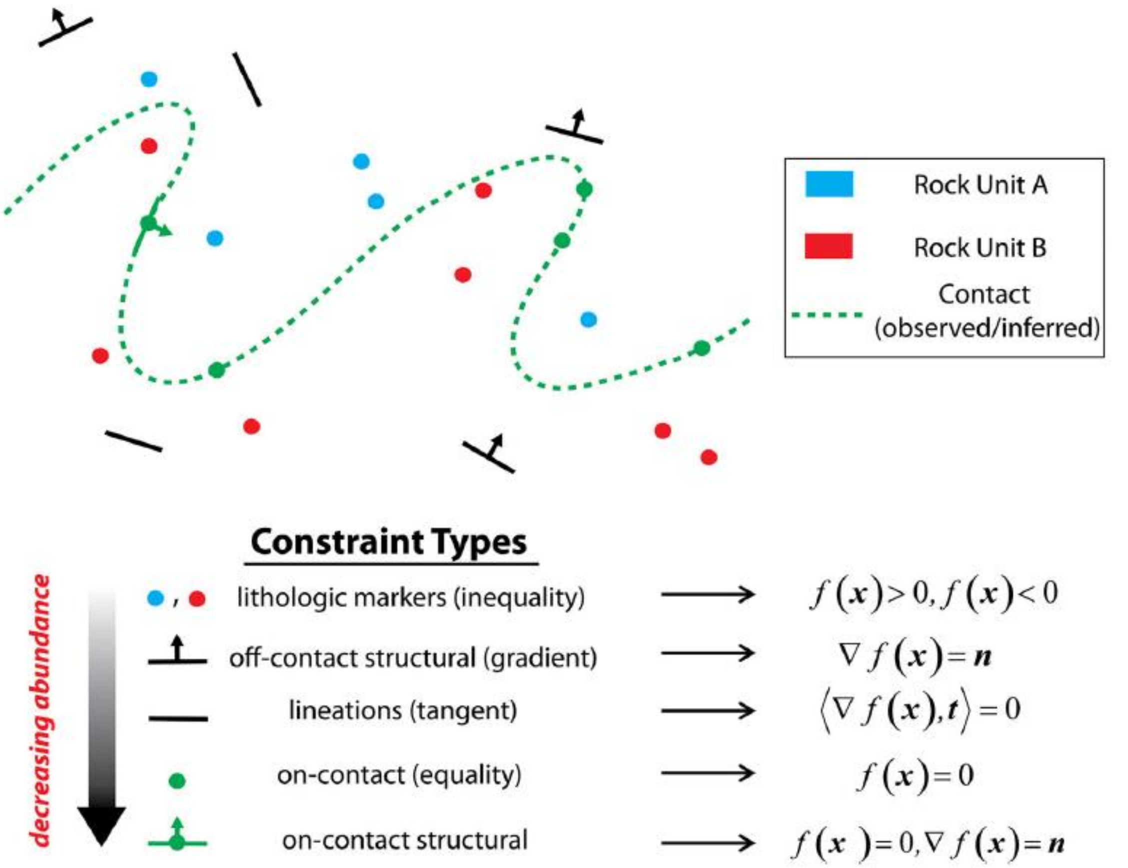

Figure 2. Structural constraint types used for implicit modelling in sparse environments. (Taken from Hillier et al., 2014)

Algorithm steps

The algorithm first constructs a system of equations using the inputted set of geological observations and solves the system for weight coefficients, w_j, from the following mathematical function called the interpolant:

$$s(\boldsymbol{x}) = \sum_{j}^{N} w_j \, \lambda_j^{\boldsymbol{x}'} \varphi(\boldsymbol{x}, \boldsymbol{x}') + p(\boldsymbol{x})$$

where $\lambda_j^{\boldsymbol{x}'}$ are linear functionals acting on a radial basis function $\varphi(\boldsymbol{x}, \boldsymbol{x}')$ with respect to $\boldsymbol{x}' = (x', y', z')$ (a 3D position vector) and $p(\boldsymbol{x})$ is a low degree polynomial. Note that all of mathematical and implementation details of the algorithm can be found in Hillier et al. (2014). For the second step, determined weight coefficients are used to evaluate the interpolant everywhere in a 3D grid to compute the scalar field. As an example, the scalar field for a synthetic anticlinal structure with sampled on-contact point locations and off-contact gradient constraints is illustrated in Figure 3. The third and final step of the algorithm uses a marching cube technique to triangulate the surface everywhere the computed scalar field is zero.

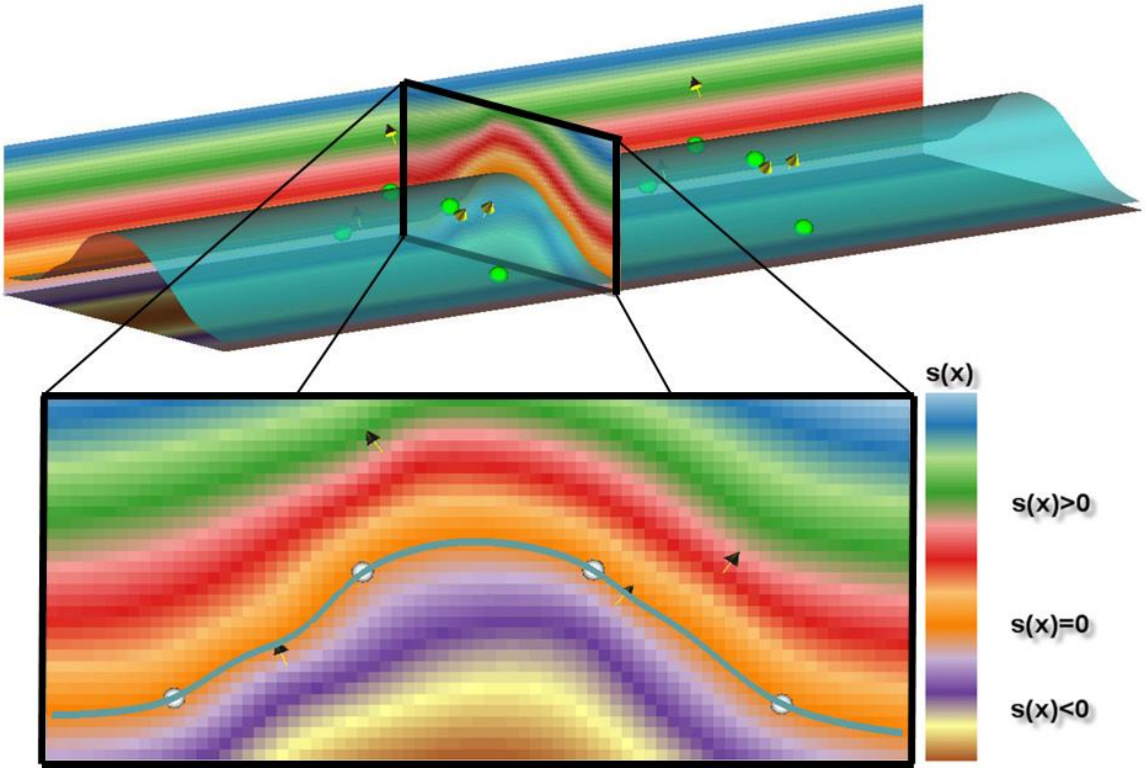

Figure 3. Scalar field for a synthetic anticlinal structure. (Top) 3D perspective with corresponding modelled surface extracted from 3D grid. (Bottom) Cross section view with scalar field colour map.

Advanced options

The advanced options section of the user interface (Figure 1) contains options that can largely affect the modelled results and improve the computation speed. Each advanced option is described in this section.

Densify gradient constraints

The "densify gradient constraints" option will attempt to remove any topological errors, such as holes, in modelled surfaces. These types of errors can occur in localized dense sampling of on-contact points possessing large structural variability. Figure 4 illustrates topological errors that can be produced in modelled surfaces and the effect of using the "densify gradient constraints" to rectify such errors. When this option is selected the set of strike/dip with polarity observations are used to estimate the normal vector (gradient) at on-surface observations where there are no structural measurements. The estimated normal vector attempts to correctly assign the polarity and its direction of the scalar field at on-surface points to force modelled surfaces to be topologically consistent across the entire model space.

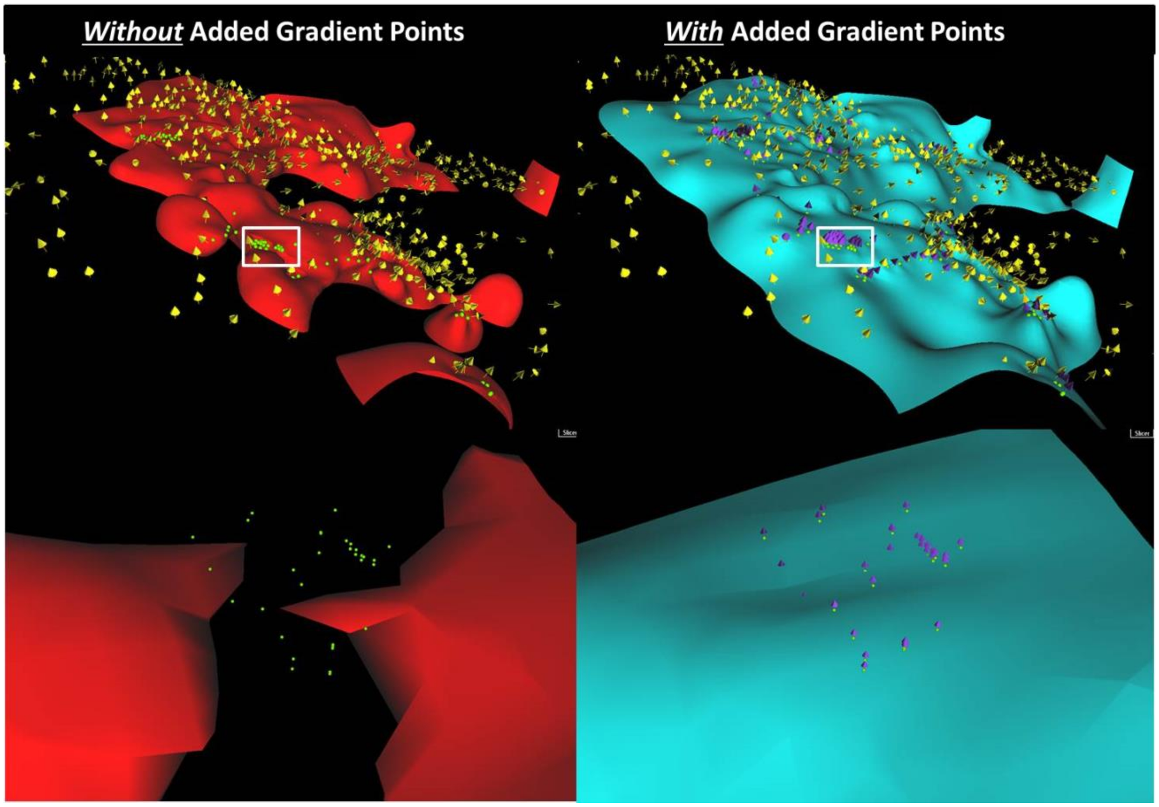

Figure 4. The effect of using the "densify gradient constraints" option on modelling results of the LMC (Lower-Middle Aldridge contact) horizon in the Purcell Basin. (Left) Not using the option and (Right) with using the option.

Domain decomposition

The "domain decomposition" option can significantly improve computations times. As an example, for a data set including 149 on-contact, 53 inequality, and 164 gradient points and using a 1.6 million cell 3D grid, the total algorithm computation time was improved by 360 times (5 hours to 50 seconds) when using this option. The partition of unity method (Babuska and Melenk, 1997) was used for the domain decomposition method because it was flexible enough to be used within the mathematical framework developed in this project. The basis of the method involves breaking the problem into many smaller problems. This is accomplished by using a kd-tree data structure (Bentley, 1975) to subdivide the 3D space into smaller rectangular sub-domains as illustrated in Figure 5a. Local data sets are assigned to each sub-domain which overlaps neighbouring sub-domains. These data sets are determined by finding all data points that are contained within a sphere positioned at the center of the subdomain. Sphere radii are chosen such that at a minimum the sphere will enclose the rectangular subdomain, illustrated in Figure 5b. Separate interpolants are then determined for each sub-domain using local data sets. To compute the scalar field at a particular point in space (green star in Figure 5b) all interpolants whose sub-domain's sphere overlaps the evaluation point gets used to smoothly blended multiple interpolant results together.

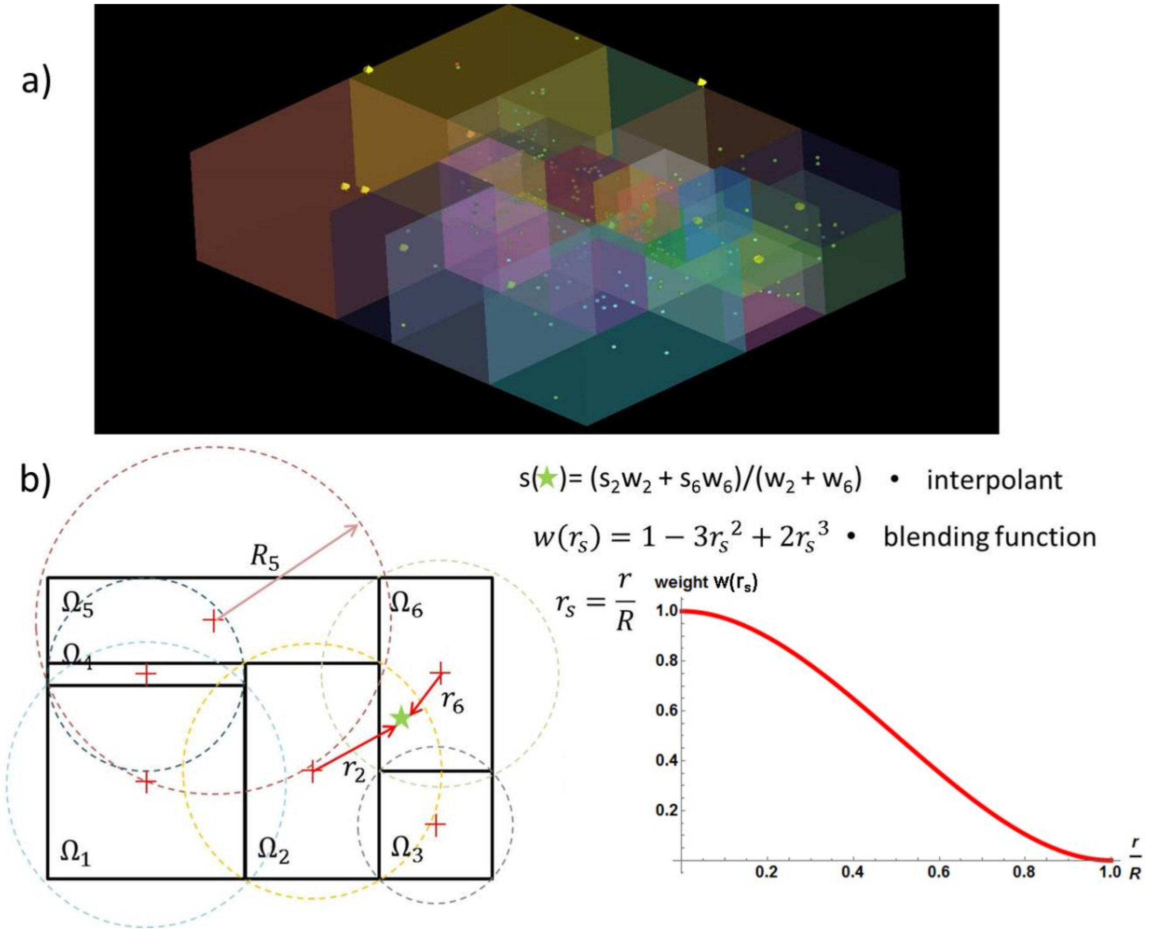

Figure 5. Domain decomposition method applied to GRBF (generalized radial basis function) interpolants. a) Visualization of 3D sub-domains generated from kd-tree algorithm. b) Partition of unity method.

Global Plunge Modelling

The global plunge modelling option can be used to incorporate data-mined or user-specified global anisotropy. Modelling of geological surfaces with incorporated anisotropy significantly enhances smoothness of surfaces oriented in the direction of anisotropy. In effect, this maintains fold hinges up and down fold axes away from data to model more geologically realistic surfaces. That can be demonstrated in the LMC (Lower-Middle Aldridge contact) horizon in to Purcell Basin as shown in Figure 6.

Smoothing

The “smoothing” option changes modelled results from being an interpolation (fits input data exactly) to an approximation. Larger smoothing values introduce larger residuals in order to obtain smoother modelled results. Smoothing is particularly useful when using noisy data or data characterized by large uncertainties.

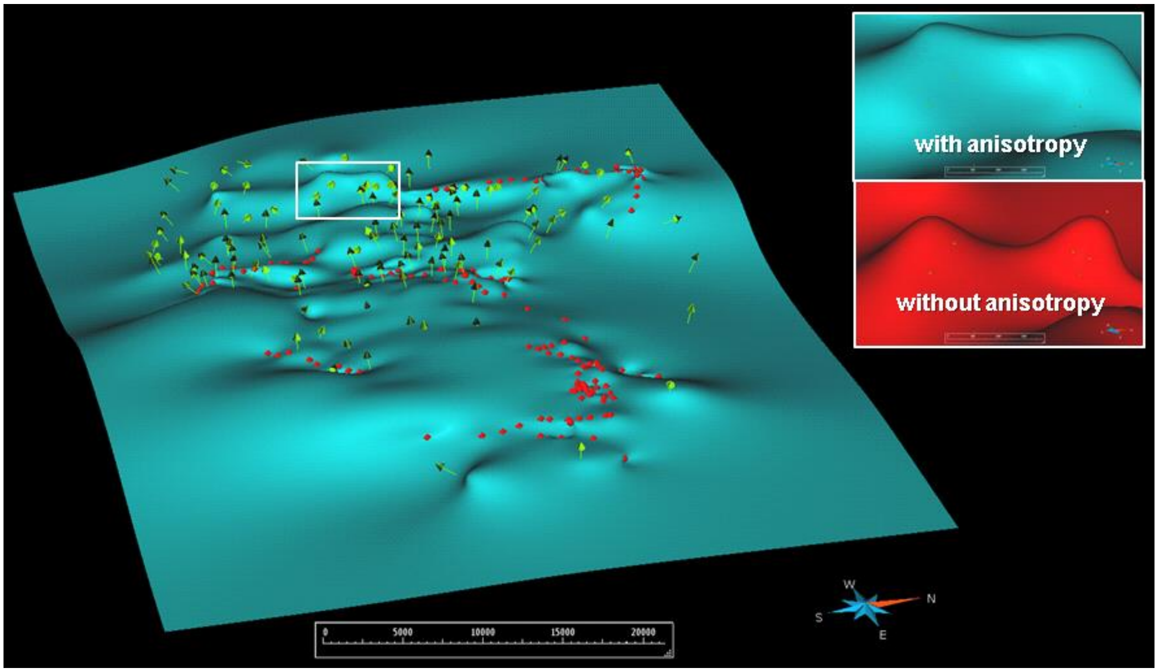

Figure 6. The effect of including global anisotropy on modelled results of LMC (Lower-Middle Aldridge contact) in Purcell Basin.

Matrix Solver

The purpose of the "matrix solver" option is to give the user access to a faster, although less precise, matrix solver known as GMRES (generalized minimal residual method) (Saad and Schultz, 1986) over the default solver which uses the traditional lower upper (LU) decomposition method. When the GMRES method is selected the user will have to provide the total percentage error permitted into the final solution. Since the solver is not required to solve the system of equations exactly, the computational time needed to find a solution with some error is significantly reduced. Coincidently, this option also acts as a smoothing mechanism.

Sample GRBF results

To demonstrate the applicability and flexibility of the GRBF algorithm in various geological settings with varying degrees of structural complexity a number of examples are given. In the first example, illustrated in Figure 7, a complex synthetic fold is modelled using the algorithm. Demonstrated in the results is the improvement of the modelled surface's geometry when inequality constraints are included in the solution. In general, adding lithostratigraphic observations above or below targeted geological contacts in the form of inequality constraints enhances structural variability in modelled results. These enhancements provide more accurate representations of the geology. Another example of these enhancements is shown in Figure 8, a small region from the Purcell Basin, also illustrates improvements of modelled geometry where there are many inequality constraints available. In the final example, shown in Figure 9, an intrusion is modelled from point data sampling inside, outside, and boundary locations.

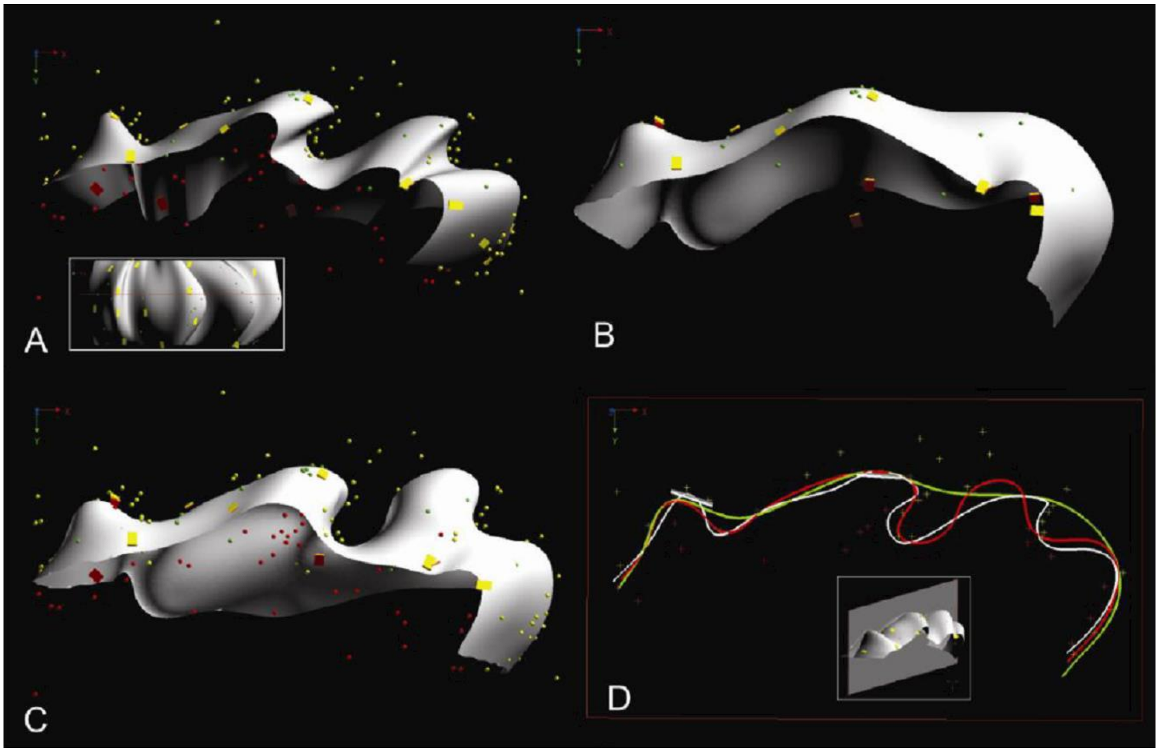

Figure 7. (A) Synthetic complex folded geological surface. (B) Modelled surface using sparsely distributed on-contact and gradient constraints. (C) GRBF modelled surface when inequality constraints, on-contact, and gradient constraints are included into the solution. (D) Cross-section comparison of the modelled (green (B) and red (C)) results with synthetic structure (white). (Taken from Hillier et al., 2014).

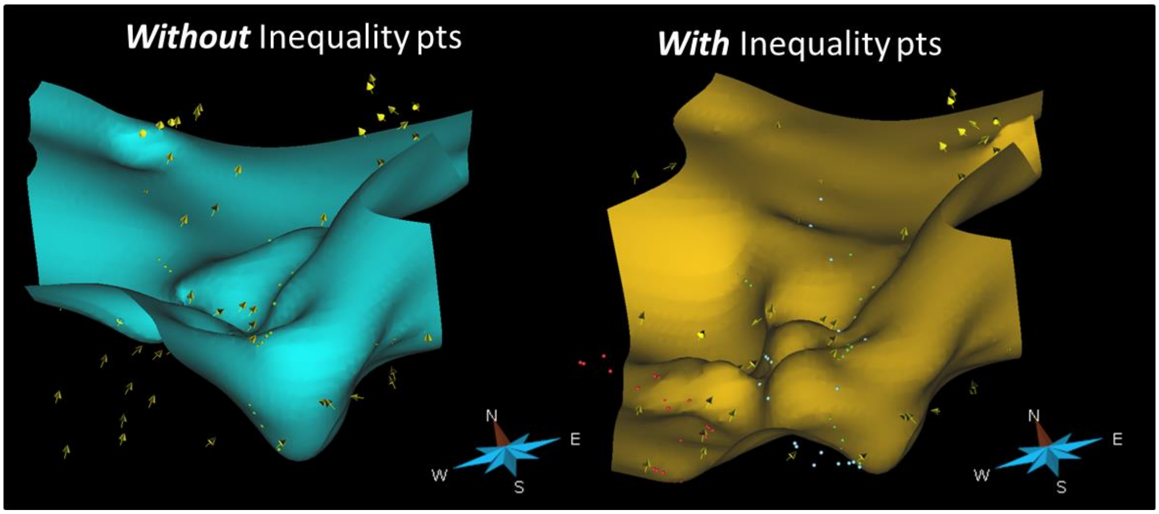

Figure 8. The effect of including inequality constraints into the generalized radial basis function (GRBF) algorithm on modelled geological surfaces.

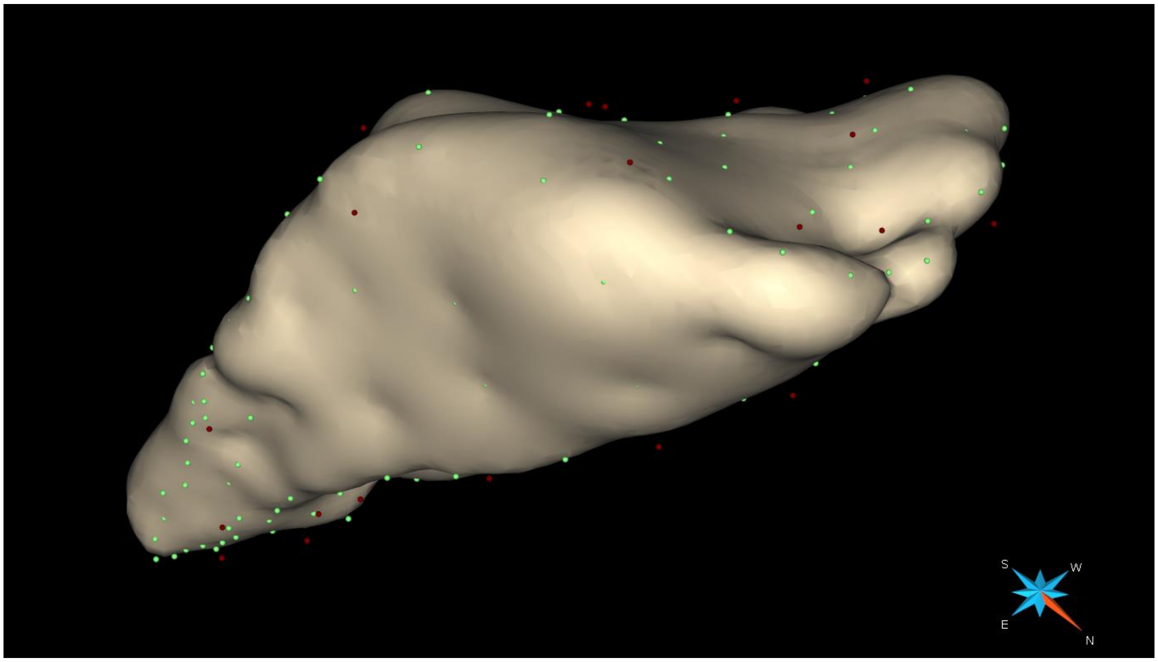

Figure 9. Modelled intrusion from point data sampling inside (blue – not visible), outside (red), and boundary (green) locations.

3D Structural Modelling of the Purcell Basin

The GRBF algorithm presented in this paper was used to visualize and predict the upper and Lower Aldridge Formation contact, a key stratigraphic target horizon and host of the Sullivan Zn-Pb-Ag deposit within the Purcell Anticlinorium, Southern British Columbia, Canada. This work was a project under the Targeted Geoscience Initiative (TGI) 4 program. One of the outputs for the project was a regional 3D structural model constructed from map-based structural and stratigraphic information, regional geophysics, and limited borehole data. The dimensions of the model were roughly equal to 98 km wide by 112 km long by 15 km depth. The GRBF algorithm was a key component in constructing the fault network and stratigraphic horizons in the regional structural model.

Individual fault surfaces in the Purcell Basin were modelled separately. Typically, each fault was modelled using interpretative map traces of the fault in addition to very limited structural observation data at surface. In a few instances, locations of faults at depth were derived from seismic profiles clearly indicating the presence of faults. Using SKUA the set of fault surfaces were properly cut using user specified topological relationships. Figure 10a shows the final modelled fault network.

Key stratigraphic horizons were modelled separately within each modelled fault domain using the appropriate structural and stratigraphic data from its domain. Portions of modelled surfaces far away from data were removed, as can be seen in Figure 10b, resulting in an incomplete covering over the model space. These

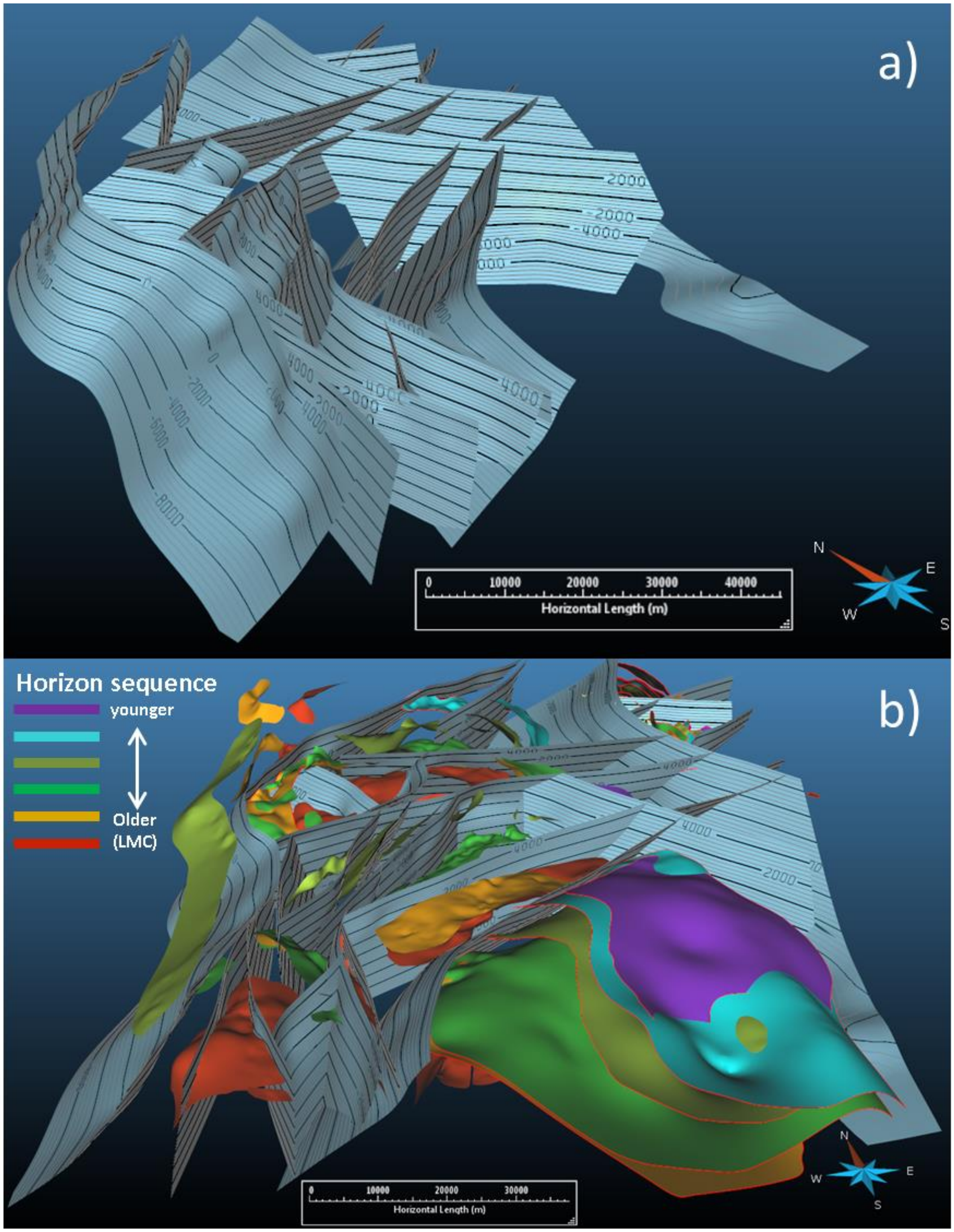

Figure 10. Generalized radial basis function (GRBF) modelling of the a) fault architecture and b) key stratigraphic horizons in the Purcell Basin. Elevation contours in metres, marked as black curves, are indicated on blue fault surfaces in (a). Lower-Middle Aldridge contact (LMC) indicated in stratigraphic horizon sequence legend.

portions were removed because the remaining stratigraphic horizon patches, possessing higher levels of confidence, will act as data constraints in the final stage of the modelling process. The complete set of modelled stratigraphic horizon patches and fault network are then used in a SKUA workflow that employs a UVT transformation (Mallet, 2004) to generate a complete 3D structural model topologically consistent throughout the model space (even across faults). The final model is shown in Figure 11.

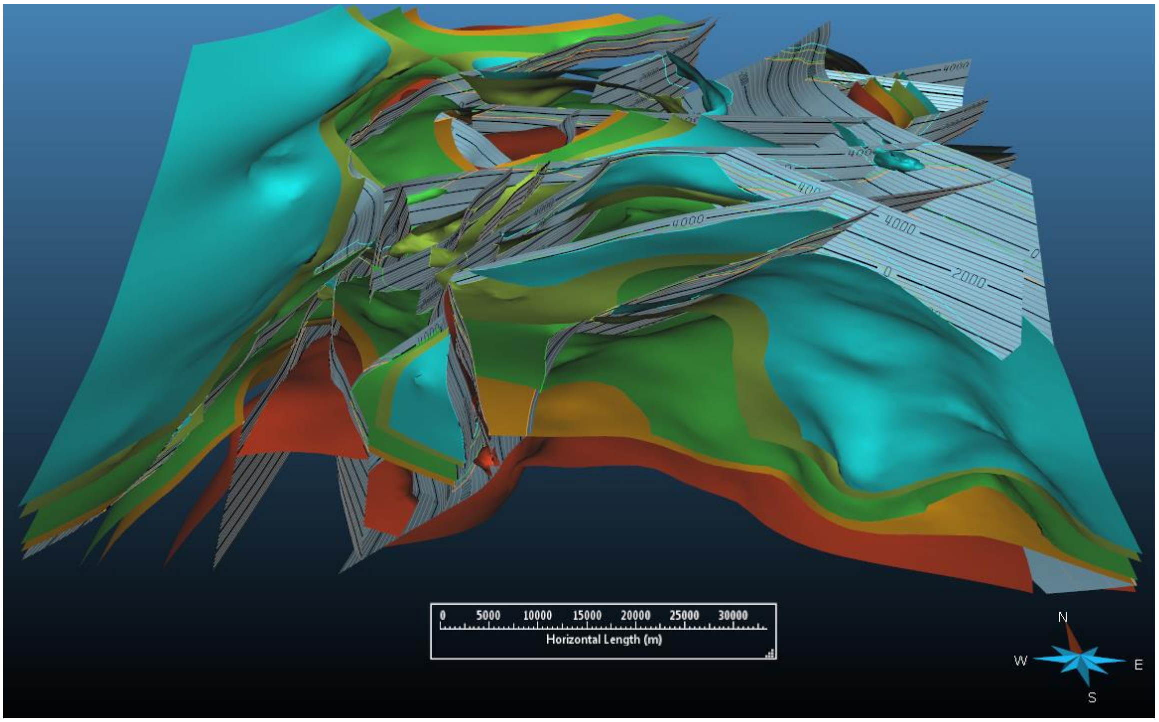

Figure 11. Final 3D structural model of key stratigraphic horizons in the Purcell Basin.

Discussion/Models

The GRBF algorithm was a tool developed with the goal to implicitly model 3D structural geologic surfaces on regional scales using sparsely scattered structural observations. Currently there are no tools or software implementing implicit approaches specifically developed for 3D geological modelling on regional scales using sparse data. The future of mineral exploration will increasingly need such tools to reduce risk (both from economical and geotechnical perspectives) and to find deeper ore deposits.

Further research and development is needed to make increasingly more sophisticated tools which incorporate all available geological data and expert knowledge to obtain more quantitative representations of the regional geology. The algorithm presented in this paper is capable of modelling 3D geological surfaces reasonably well in most circumstances, as can be shown from the 3D structural models of the Purcell Basin (Figure 11). There are, however, many more modelling capabilities that are needed to produce more geological realistic and accurate models. Future work involves enhancing the algorithm to model multiple surfaces simultaneously and to incorporate geological rules such as stratigraphic relationships.

Implications for Exploration

The GRBF algorithm provides geoscientists with a set of tools that can enhance their current understanding of the regional geometry of key stratigraphic horizons, especially in regions with sparse or no data. In areas where key stratigraphic horizons host ore deposits, such as the Zn-Pb-Ag deposit within the Purcell Anticlinorium, modelled horizons have the potential to guide drilling campaigns and yield new ore deposit discoveries.

References

Babuska, I., and Melenk, J.M., 1997, The partition of unity method: International Journal for Numerical Methods in Engineering, v. 40, p. 727-758.

Beatson, R.K., Light, W.A., and Billings, S., 2000, Fast solution of the radial basis function interpolation equations: domain decomposition methods: Society for Industrial and Applied Mathematics, Journal on Scientific Computing, v. 22, p. 1717–1740.

Bentley, J.L., 1975, Multidimensional binary search trees used for associative searching: Communications of the Association for Computing Machinery, v. 18(9), p. 509-517.

Carr, J.C., Beatson, R.K., Cherrie, J.B., Mitchell, T.J., Fright, W.R., McCallum, B.C., and Evans, T.R., 2001, Reconstruction and representation of 3D objects with radial basis functions, *in* ACM SIGGRAPH 2001, Computer graphics proceedings: ACM Press, New York, p. 67–76.

Caumon, G., Antoine, C., and Tertois, A.L., 2007, Building 3D geological surfaces from field data using implicit surfaces, *in* Proceedings of the 27th GoCad Meeting, Nancy, France.

Cuomo, S., Galletti, A., Giunta, G., and Starace, A., 2013, Surface reconstruction from scattered point via RBF interpolation on GPU, *in* 2013 Federated Conference on Computer Science and Information Systems, p. 433-440

Hillier, M., Schetselaar, E., de Kemp, E., and Perron, G., 2014, Three-dimensional modelling of geological surfaces using generalized interpolation with radial basis functions: Mathematical Geology, v. 46, p. 931-953.

Lorensen, W.E., and Cline, H.E., 1987, Marching cubes: a high resolution 3D surface construction algorithm, *in* Association for Computing Machinery, SIGGRAPH: Computer Graphics, v. 21, p.163–169.

Mallet, J.L., 2004, Space-time mathematical framework for sedimentary geology: Mathematical Geology, v. 36, p. 1-32.

Moore, G.E., 1965, Cramming more components onto integrated circuits: Electronics, v. 38, p. 114-117.

Saad, Y., and Schultz, M.H., 1986, GMRES: a generalized minimal residual algorithm for solving nonsymmetric linear systems: Society for Industrial and Applied Mathematics, Journal on Scientific Computing, v. 7, p. 856–869.

Treece, G.M., Prager, R.W., and Gee, A.H., 1999, Regularized marching tetrahedral: improved iso-surface extraction: Computers and Graphics, v. 23, p. 583–598.

Turk, G., and O'Brien, J., 1999, Shape transformation using variational implicit functions, *in* ACM (Association for Computing Machinery) SIGGRAPH'99: Computer Graphics Proceedings, ACM Press, New York, p. 335–342.

Magnetic Modelling Insights into the Third Dimension of the Purcell Anticlinorium

M.D. Thomas
Geological Survey of Canada, 615 Booth Street, Ottawa, ON, K1A 0E9
Mike.Thomas@NRCan.gc.ca

Abstract

Distinct magnetic anomalies, widely distributed throughout the Purcell Anticlinorium, are modelled to define deeper portions of structures observed at surface, providing insights not always attainable through conventional structural modelling. The nature of such insights is illustrated by the examination, in some detail, of four magnetic models crossing major structures. Models crossing the northwestern flank of the Moyie anticline outline a wedge-shaped package of mainly magnetic Creston Formation rocks. These persist along the length of the flank and are truncated by a steeply northwest-dipping Moyie Fault. They provide information on the dip of the fault and estimates of minimum dip-slip displacement. The eastern flank displays a relatively undisturbed monoclinal sequence of Lower Aldridge Formation up to Kitchener Formation, and in some cases up to Van Creek Formation or Nicol Creek Formation. One eastern flank model, supported by a seismic image, indicates local disruption of the sequence by gently dipping thrust faults. Moyie sills mapped at surface have been extended by modelling to depths of many kilometres, with some of them defining the antiformal nature of the Moyie and Goat River anticlines. Their distribution to depths of at least 11.5 km, on the evidence of seismic data, is supported by magnetic modelling.

The Iron Range Fault is modelled as a near-vertical zone comprising several narrow, steep and relatively strongly magnetic units; magnetite and hematite have previously been recognized as the principal sources of an associated positive magnetic anomaly. The modelled zone is significantly wider than geological estimates and considering possible ties of the iron oxide mineralization to Olympic Dam- and porphyry-type mineralization a larger footprint for exploration is possible. The St. Mary Fault is geologically mapped as a north-side-up thrust fault, but information on its dip is apparently lacking. Magnetic models indicate that it is near-vertical in two localities and dips 20^{O} north in a third.

Introduction

A major objective of the TGI4 SEDEX ore systems initiative is creation of a regional three-dimensional model of a greater part of the Purcell Anticlinorium (de Kemp et al., 2015) (Figure 1). Unlike typical 3D models at the scale of a mining property, regional models suffer from a lack of closely spaced drillholes that generally descend close to the maximum depth of interest. The drillholes and logs derived therefrom are the main source of critical geological and structural information used to outline the geometries of

Recommended citation
Thomas, M.D., 2015. Magnetic modelling insights into the third dimension of the Purcell Anticlinorium, *in* Paradis, S., ed., Targeted Geoscience Initiative 4: sediment-hosted Zn-Pb deposits: processes and implications for exploration; Geological Survey of Canada, Open File 7838, p. 267-286. doi:10.4095/296328

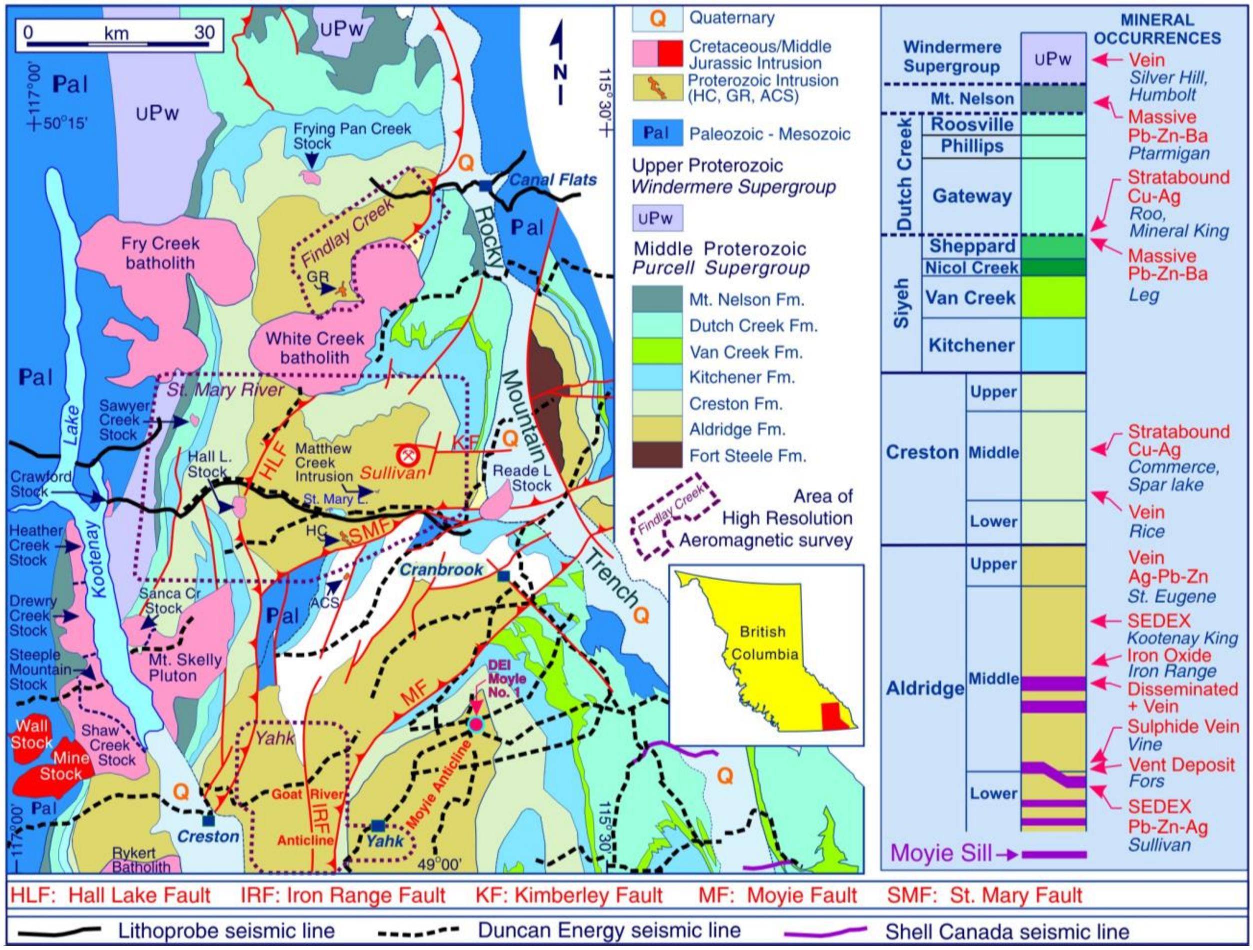

Figure 1. Simplified geological map of the Purcell Anticlinorium modified from Lowe et al. (2000) after Höy et al. (1995). The stratigraphic column is modified from T. Höy (written communication, 1996 according to Lowe et al. (2000)). Proterozoic intrusions: HC, Hellroaring Creek stock; GR, Greenland Creek intrusions; ACS, Angus Creek stock. The Dutch Creek Formation along the eastern flank of the anticlinorium includes the Nicol Creek, Sheppard, Gateway, Phillips and Roosville formations described as correlative with the Dutch Creek Formation (Höy et al., 1995), though the Nicol Creek and Sheppard formations are included in the Siyeh Formation in the stratigraphic column. Locations of seismic reflection lines (Cook and Van der Velden, 1995; Van der Velden and Cook, 1996) are indicated. DEI Moyie No. 1 is the Duncan Energy Inc. Moyie No. 1 drillhole.

geological units. At a regional scale, however, drillholes are inevitably irregularly and thinly distributed and depths are relatively shallow in the context of the scale of investigation. Nevertheless they can yield important glimpses of 3D structure, which may be enhanced when drillhole data are combined with structural, contact and lithological information on geological maps. In this respect the 3D study benefits from the relatively recent release of 1:50 000 scale geological maps (Brown and MacLeod, 2011a, b, c, d; Brown et al., 2011a, b, c, d, e, f; Glombick et al., 2011a, b) collectively covering much of the Purcell Anticlinorium. Other benefits are the significant vertical relief of well over 2000 m in the area, and several reflection seismic traverses (Figure 1) crossing various parts of the anticlinorium (Cook and Van der Velden, 1995; Van der Velden and Cook, 1996).

Another means of investigating the 3D structure of the Purcell Anticlinorium is by modelling magnetic anomalies, many of which are distributed throughout the anticlinorium, with some associated with critical structures (Figure 2). These have been defined by surveys flown at 805 m line-spacing and 305 m mean terrain clearance (MTC) across the entire anticlinorium, and higher resolution surveys flown at 400 m line-spacing (60 m MTC) covering areas near St. Mary River, Yahk and Findlay Creek (Figure 1). Data from these surveys may be downloaded at no cost from Natural Resources Canada's Geoscience Data Repository website http://gdr.agg.nrcan.gc.ca/gdrdap/dap/search-eng.php (March 2015). Distinct magnetic anomalies are modelled to extrapolate surface structures and units to depth, to provide details of geology within near-surface blanks in the seismic sections, and to link surface and deeper seismic features. These objectives are here exemplified with the results of modelling prominent anomalies in the areas of the Moyie anticline, Iron Range Fault and St. Mary Fault.

Geology of the Area

The north-trending Purcell Anticlinorium (Figure 1) represents an inverted version of the preceding Middle Proterozoic Purcell Basin, part of an intra-continental rift system (Lydon, 2000). It developed during Late Cretaceous to early Paleocene collision of a collage of Cordilleran accreted terranes with the North American Craton (Price, 1981; Sears, 1994; Price and Sears, 2000). The core of the essentially metasedimentary anticlinorium is dominated by the Middle Proterozoic Aldridge and Creston formations, which are flanked by the succeeding Middle Proterozoic Kitchener, Van Creek, Dutch Creek, and Mount Nelson formations. The Upper Proterozoic metasedimentary Windermere Formation has a significant presence along the western flank of the anticlinorium. The core and western flank of the anticlinorium, in particular, are invaded by Cretaceous "granitic" intrusions of various sizes, and some very small Proterozoic intrusions.

The Aldridge Formation is composed largely of turbidites commonly having a dominantly arenite base and siltite or argillite top (Lydon et al., 2000). The succeeding Creston Formation, a rift-sag sequence (Lydon, 2000), includes siltstone, argillite, quartz arenite and quartz wacke. Both formations are divided into three main subdivisions (Lower, Middle, Upper). The Kitchener Formation is a dominantly carbonate unit, and the succeeding Van Creek Formation is dominated by siltstone and argillite. The overlying Nicol Creek Formation is distinct in being a predominantly volcanic sequence (Höy, 1993). All succeeding formations in Figure 1 are metasedimentary.

The Purcell Anticlinorium is invaded by mafic Proterozoic Moyie sills intruding the Aldridge Formation. Höy (1993) claims they "… are restricted to the lower Aldridge, the lower part of middle Aldridge, and to correlative rocks in the northern Hughes Range east of the Rocky Mountain Trench." This view is generally supported by Gorton et al.

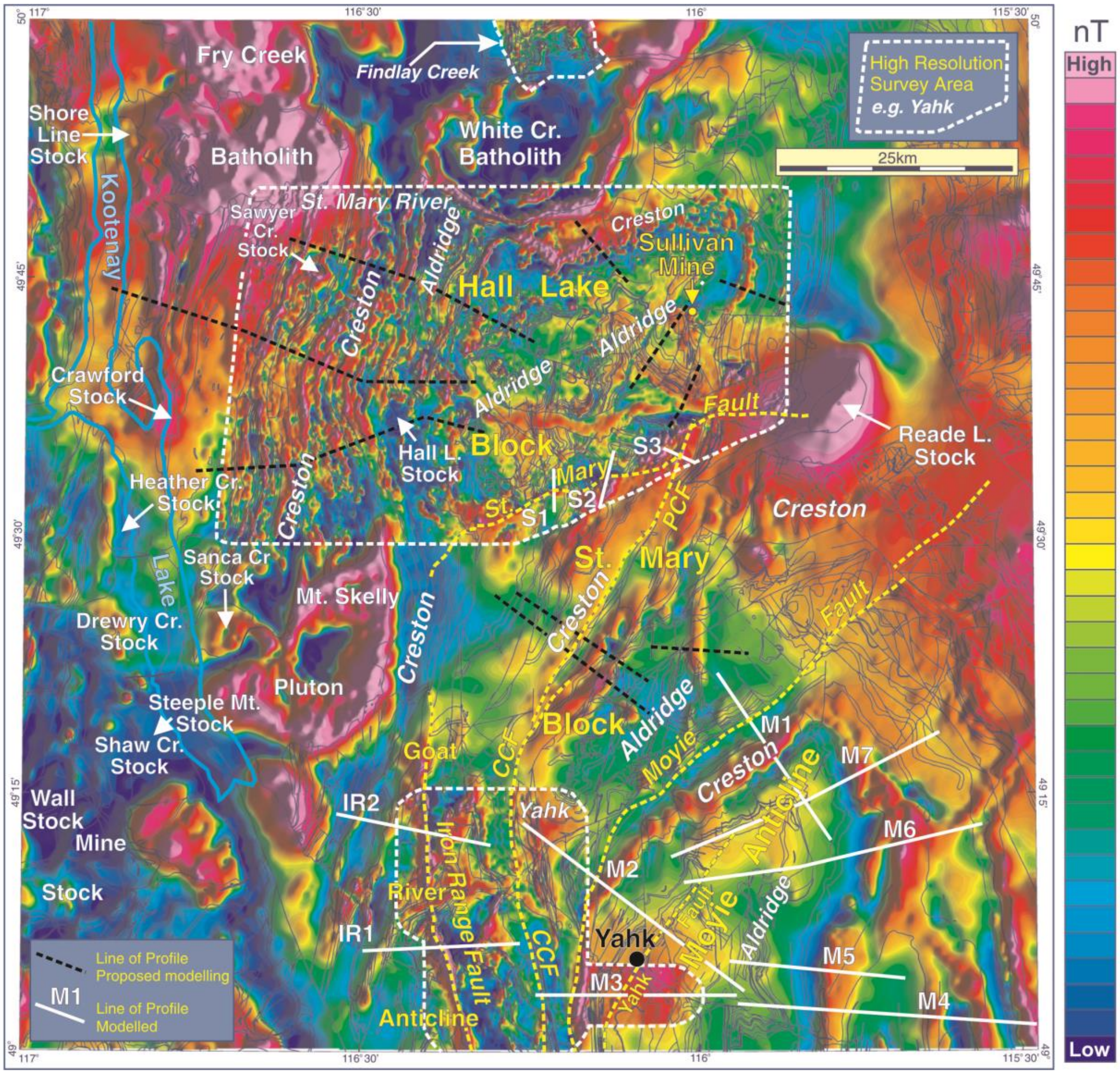

Figure 2. Residual total magnetic field map covering area of interest within the Purcell Anticlinorium. Most of the map is defined by surveys flown along lines 805 m apart and at a nominal mean terrain clearance of 305 m, but three areas outlined by white dashed lines (Findlay Creek, St. Mary River, Yahk) were flown at 400 m line-spacing and 60 m mean terrain clearance. Geological contacts are superposed as a frame of reference. CCF is the Carroll Creek Fault; PCF is the Perry Creek Fault. Lines along which magnetic profiles have been or will be modelled are indicated.

(2000), though they suggest that they intrude the central part of the Middle Aldridge Formation, rather than the lower part, and also the Fort Steele Formation east of the trench. Höy (1993) reported that the aggregate thickness of the sills in the Purcell Mountains is > 2000 m, and that they commonly form up to 30 per cent of "lower and lower-middle Aldridge successions"; they are generally a few tens to several hundred metres thick and commonly persist laterally for tens of kilometres. Sills are formed predominantly of gabbro and diorite (Höy, 1993). In most Moyie sills ferro- and magnesio-hornblendes are the principal mafic minerals (Anderson and Goodfellow, 2000). Rare unaltered portions of one sill consisting of two-pyroxene gabbro with a subophitic texture reveal the primary magmatic mineralogy of sills that includes early augitic pyroxene and later inverted pigeonite intergrown with plagioclase. The latest primary minerals are amphibole, biotite, ilmenite, magnetite and quartz intergrown in the interstices of the three main minerals.

Results/Data Analysis

Magnetic Rock Properties

Magnetic modelling is enhanced by a variety of constraints. Commonly geological contact and structural information help initiate definition of the shallow geometry of a potential magnetic unit, and drillhole intersections provide tie-points for unit boundaries. Seismic imagery is another important constraint. These constraints are spatial, but in terms of constraining the size of a magnetic unit, the rock properties of magnetic susceptibility and remanent magnetization are key factors. Susceptibility data are typically available in modelling studies, because of the ease with which measurements can be made using a hand-held susceptibility meter on outcrop, core or hand samples. Measurements of remanent magnetizations, however, require a laboratory, which may not always be available. It is common practice, therefore, to assume that all magnetizations in investigated rock units are induced, and such is the case in the present study. If the ratio of remanent magnetization to induced magnetization (Q ratio or Koenigsberger ratio) is very small (<<1) then errors in modelling related to non-inclusion of the remanent component are relatively insignificant. Apparently, the only information on remanent magnetizations for the study area was reported by Lowe et al. (1998), who made measurements on 55 rock samples from the three high resolution airborne survey areas (Figure 1) and determined Q ratios significantly less than 1 in 43 samples. The remaining 12 samples from the Middle Aldridge Formation yielded a mean value of 4.11. Magnetic susceptibilities for the area have been reported by Lowe et al. (1998, 2000) and more recently by Thomas (2013), who included discussion of the earlier studies. A summary of the magnetic susceptibilities reported by Thomas (2013) is shown in Table 1.

Principal targets for magnetic modelling include strong magnetic anomalies within the Creston Formation, many being linear and extensive. The most prominent example is that following the flanks of the Moyie anticline (southeast corner of Figure 2). Lowe et al. (2000) noted that moderate to intense magnetic anomalies were associated with portions of the Middle Creston Formation characterized by quartz arenite and arenaceous siltstone metamorphosed at upper greenschist facies (Reesor, 1996); samples of arenite contain > 2% porphyroblastic magnetite. The Lower Creston Formation is atypically magnetic in a north-south belt west and southwest of Yahk (Figure 2) producing anomalies as large as those over the Middle Creston Formation (Lowe et al., 1998). The belt coincides with the Kingsgate graben and here magnetism is attributed to disseminated and stringer magnetite in fine-grained argillites (Lowe et al., 1998). Thomas (2013) estimated a mean susceptibility value of 10.16 ± 25.28 x 10^{-3} SI

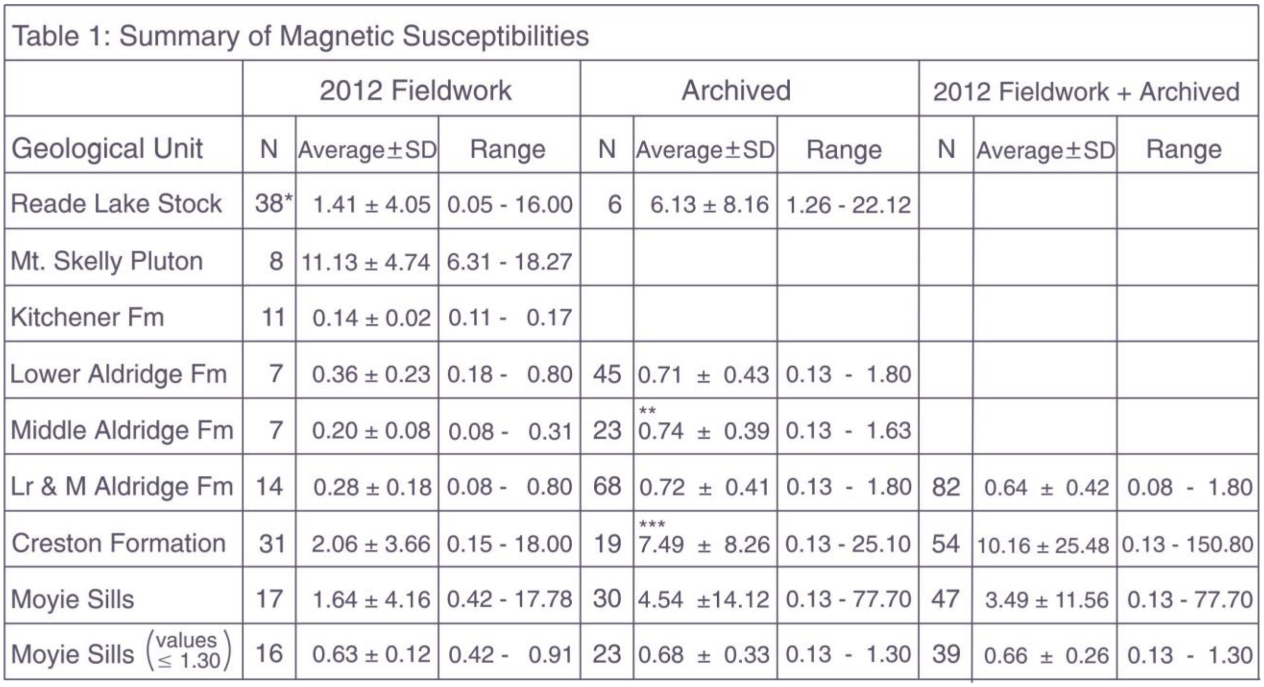

Table 1: Summary of Magnetic Susceptibilities

	2012 Fieldwork			Archived			2012 Fieldwork + Archived		
Geological Unit	N	Average±SD	Range	N	Average±SD	Range	N	Average±SD	Range
Reade Lake Stock	38*	1.41 ± 4.05	0.05 - 16.00	6	6.13 ± 8.16	1.26 - 22.12			
Mt. Skelly Pluton	8	11.13 ± 4.74	6.31 - 18.27						
Kitchener Fm	11	0.14 ± 0.02	0.11 - 0.17						
Lower Aldridge Fm	7	0.36 ± 0.23	0.18 - 0.80	45	0.71 ± 0.43	0.13 - 1.80			
Middle Aldridge Fm	7	0.20 ± 0.08	0.08 - 0.31	23	** 0.74 ± 0.39	0.13 - 1.63			
Lr & M Aldridge Fm	14	0.28 ± 0.18	0.08 - 0.80	68	0.72 ± 0.41	0.13 - 1.80	82	0.64 ± 0.42	0.08 - 1.80
Creston Formation	31	2.06 ± 3.66	0.15 - 18.00	19	*** 7.49 ± 8.26	0.13 - 25.10	54	10.16 ± 25.48	0.13 - 150.80
Moyie Sills	17	1.64 ± 4.16	0.42 - 17.78	30	4.54 ±14.12	0.13 - 77.70	47	3.49 ± 11.56	0.13 - 77.70
Moyie Sills (values ≤ 1.30)	16	0.63 ± 0.12	0.42 - 0.91	23	0.68 ± 0.33	0.13 - 1.30	39	0.66 ± 0.26	0.13 - 1.30

N = number of outcrops and/or rock samples upon which susceptibility measurements were made.

Averages and standard deviations (SD) are based on the average of the N average values obtained at a particular outcrop and/or on a rock sample from a particular outcrop. They do not represent the average value of all individual measurements made on that particular rock unit, except in the case of 2012 fieldwork measurements on the Reade Lake stock. Susceptibility values are in the unit of (x 10^{-3}) SI.

* In this case N = number of individual measurements made on 1 outcrop.

** 2 anomalously high values of 3.90 and 27.6 x 10^{-3} SI are not included in the derivation of these values.

*** 4 anomalously high values ranging from 31.4 to 150.8 x 10^{-3} SI are not included in the derivation of these values.

Moyie Sills statistics for values ≤ 1.30 x 10^{-3} SI are for strong modal groups of low values.

for the Creston Formation, with the largest value for 50 samples out of a total of 54 being 25.10 x 10^{-3} SI. It is noted that most of the measurements were concentrated near the northern apex of the Moyie anticline; the range of values for the other 4 samples is 31.54 to 150.8 x 10^{-3} SI. Lowe et al. (2000) reported a mean value of 15. 2 x 10^{-3} SI (maximum 125.7 x 10^{-3} SI) based on 330 measurements. These relatively strong mean susceptibilities (10.16 and 15.2 x 10^{-3} SI) compare with weak mean susceptibilities for the areally dominant Aldridge Formation or its constituent members, which are < 0.74 x 10^{-3} SI.

According to Lowe et al. (2000) Moyie sills are also more magnetic than the Aldridge Formation. They determined a mean value of 6.67 x 10^{-3} SI for 200 measurements, implying that sills would be associated with a fairly strong magnetic signature. These authors noted, however, that magnetic responses were variable, most sills being poorly magnetized, and that the response could vary within a single sill. Noteworthy, also, was the observation that magnetic sills are associated with faults or marginal areas of large intrusions in the area. Associated high magnetic susceptibilities, typifying only a relatively small percentage of the total population, can bias the average susceptibility. It is assumed that the mean value of 6.67 x 10^{-3} SI for Moyie sills reported by Lowe et al. (2000) reflects such a bias.

Thomas' (2013) study indicated that susceptibility of Moyie sills is generally very consistent throughout the Purcell Anticlinorium, a mean value of 0.66 ± 0.26 x 10^{-3} SI being obtained if 8 values > 1.30 x 10^{-3} SI out of a population of 47 are ignored; the highest value is 77.7 x 10^{-3} SI. Effectively, based on this mean value, which is slightly smaller than the mean value for the Aldridge Formation, significant positive magnetic responses would not be expected for Moyie sills. This expectation is contradicted by the presence of relatively low amplitude, but distinct, broad magnetic highs in the core of the Moyie anticline, one centred east of Yahk (Figure 2) and partially covering an area where Thomas (2015) obtained a mean susceptibility of 0.61 ± 0.14 x 10^{-3} SI from measurements at 9 sites on sills. It was concluded that the main magnetization resides in buried sills. Lowe et al. (1998) reported that susceptibilities of sills in this same area are unusual in their lack of variation along strike, and that nowhere were they more than 7.5 x 10^{-3} SI. They too concluded that the low susceptibilities of outcropping rocks required the source of the magnetic anomaly to be at some depth in the crust.

Discussion/Models

Magnetic Models

As a consequence of a lack of information on remanent magnetizations in the area, magnetizations within all modelled units are assumed to be induced. Constraints for modelling were: (1) geological contacts and structural data from 1:50 000 scale geological maps (Brown and MacLeod, 2011d; Brown et al., 2011c; Glombick et al., 2011a, b) and a 1:100 000 scale map (Höy, 1993), (2) magnetic susceptibility data (Lowe et al., 1998, 2000; Thomas, 2013), (3) drillhole logs (Schetselaar et al., 2015) and (4) seismic reflection images. Dips of bedding shown in models are apparent dips derived by transforming measured dips into the direction of each modelled profile. The approach to modelling was to model shallow portions using surface geology and drillhole constraints, and then to integrate deeper parts using seismic images.

Data obtained from seismic reflection traverses crossing the Purcell Anticlinorium (Figure 1) relating to exploration programs by Duncan Energy Inc. (Cook and Van der Velden, 1995; Van der Velden and Cook, 1996) were used to constrain modelling of both upper and lower crustal geology. The main contribution of seismic sections is a perspective on the distribution and concentration of Moyie sills, as typically large portions of seismic sections are characterized by strong reflections attributed to the sills (Cook and Van der Velden, 1995; Van der Velden and Cook, 1996). This conclusion was based on a comparison of the lithologic log from the Duncan Energy Inc. Moyie No.1 drillhole (DEI No. 1 drillhole), collared in the Middle Aldridge Formation and 3477 m deep, with nearby seismic sections. The log shows Middle Aldridge Formation extending to a depth of about 1650 m and overlying Lower Aldridge Formation, both of which are intruded by Moyie sills (Cook and Van der Velden, 1995). A synthetic seismic trace, computed for the drillhole using measured densities and seismic velocities, displayed strong reflections near contacts of logged sills, which also correlated with reflections in a seismic section. An up-dip projection of the so called "MAMA" reflection coincides with the Middle Aldridge marker sill at surface. Thomas (2015) compared the DEI No. 1 drillhole log with reprocessed sections of nearby seismic lines noting that while reflections occur in the vicinity of logged sills, they would not necessarily define the sills. The main contribution of the reflections is in delineating portions of crust occupied by sills. Where magnetic models obliquely intersect a seismic section, a roughly 1.1 to 1.8 km width of the section is displayed to show the probable positions and concentrations of sills.

Models across the Moyie Anticline

Descriptions of seven magnetic models derived along profiles crossing the flanks of the Moyie anticline are presented by Thomas (2015); some earlier preliminary models were presented by Thomas et al. (2013). The anticline is an open, upright fold with a steep west-dipping axial surface and shallow northerly plunge (Höy, 1993) cored by metasedimentary Aldridge Formation heavily intruded by gabbroic Moyie sills. The flanks comprise the younger metasedimentary Creston Formation and succeeding mainly metasedimentary formations. The Aldridge Formation is formed mainly of turbidites that include arenites, siltites and argillites (Lydon et al., 2000) deposited in an intracontinental rift, and the succeeding rift-sag sequence of the Creston Formation consists of argillites and siltites (Lydon, 2000). The Moyie Fault marks the western limit of the Moyie anticline, separating Creston Formation and younger formations to the east from the Aldridge Formation to the west. It is a right-lateral reverse fault dipping 60^{O} to 70^{O} northwest, and zone of intense shearing up to several hundred metres wide (Höy, 1993). Two magnetic models, one crossing the northwest flank (M2) and the other crossing the eastern flank (M6) are briefly described.

Magnetic profile M2 extends southeast from near the Carroll Creek Fault, passes north of Yahk and ends on the eastern limb of the anticline (Figure 2). A central prominent magnetic high over the Creston Formation is flanked either side by broader lower amplitude highs doubtlessly related to Moyie sills (Figure 3). A southeast-dipping sequence of alternating Middle Aldridge Formation and Moyie sills is modelled northwest of the central high and a similar broad antiformal sequence to the southeast. Several relatively high magnetic susceptibility ($10 - 17 \times 10^{-3}$ SI) units within the Lower and Middle Creston Formation explain the central high. They dip steeply near surface, from about 50^{O} to 65^{O}, decreasing to roughly 35^{O} at depth. Mapped dips at surface are slightly less steep, ranging from 45^{O} to 51^{O}. The modelled Creston and Upper Aldridge formations form a northwestward-thickening wedge bounded to the northwest by the Moyie Fault, which truncates a southeast-dipping sequence of alternating sills and Aldridge Formation to the northwest. The wedge attains a depth of roughly 6.3 km at the fault. The modelled Moyie Fault dips 55^{O} northwest near the surface, steepening to about 62^{O} at the deepest point of the wedge. Similar wedges and steeply dipping Moyie fault have been modelled along strike to the northeast and south.

Modelling deeper parts of the crust lacking an apparent link with surface geology was guided by seismic images at their intersection points with the magnetic profile (Figure

3). They are the basis for defining a large unit of Aldridge Formation heavily intruded by Moyie sills, whose upper surface is antiformal southeast of the Moyie Fault, as expected in the core area of the Moyie anticline. A modelled overlying separate sill-rich unit likewise is antiformal, and also highlights the gradual steepening of dips towards the steeply inclined Creston Formation.

The seismic image for line L16 displays prominent reflections only in approximately the uppermost 4 km of crust. The rationale for extending the unit of Aldridge Formation impregnated with Moyie sills to greater depth is based on the seismic image at the point where L16 intersects another magnetic model, M5, just north of its intersection with M2, in which reflectivity is more widely distributed. Extending the unit down to about 8.5 km depth ensures compatibility with the unit modelled at the west end of M5 (Figure 2).

Magnetic profile M6 runs east-northeast across the northern half of the Moyie anticline from near the Yahk Fault to the northeast flank (Figure 2), a large portion of it coinciding with seismic line L12p. The seismic section clearly shows the distribution of Moyie sills, indicating moderate to strong concentrations invading presumably Middle Aldridge Formation between depths of about 1 to 4 km to at least 11 km depth (Figure 4). Seismic reflections are generally horizontal to gently dipping and display a persistent gentle eastward dip in the eastern portion of the section, as do two near-surface sills (or tabular concentrations of sills) partially constrained by distinct reflections and intersecting surface in the centre of the model. The uppermost sill apparently continues to the eastern end of the model, but is offset by gently west-dipping faults possibly indicating west over east thrusting.

Two narrow, distinct magnetic highs correlate with the Middle Creston Formation. The larger eastern high has a broad eastern flank disturbed by three small positive perturbations possibly representing interfering highs. An absence of reflections in the upper crust between the Upper Aldridge and Van Creek formations helps define the area occupied by this portion of the stratigraphic succession, indicating a probable absence of Moyie sills, and by association Middle Aldridge Formation. Relatively strong magnetic units (susceptibilities range from 6.6×10^{-3} SI to 22×10^{-3} SI) separated by steep boundaries (80^{O} to 90^{O}) in the Middle Creston Formation explain the main magnetic highs. The steep boundary dips are puzzling given the gentle bedding dips (3^{O} to 17^{O}) mapped at surface. These boundaries may be faults cutting bedding that link in listric fashion with shallow-dipping faults interpreted deeper in the section. Three other magnetic models of the eastern flank indicate a more conformable stratigraphy undisturbed by such faulting.

Models across the Iron Range Fault

The north-south Iron Range Fault (bottom centre, Figure 2) trends along the axial area of the Goat River anticline in the southwestern part of the Purcell Anticlinorium. It is steeply dipping and cuts mainly metasedimentary rocks of the Middle Aldridge Formation and also of the Lower Aldridge Formation Rampart Facies and Moyie sills. It is associated with iron oxide mineralization having characteristics similar to those of iron

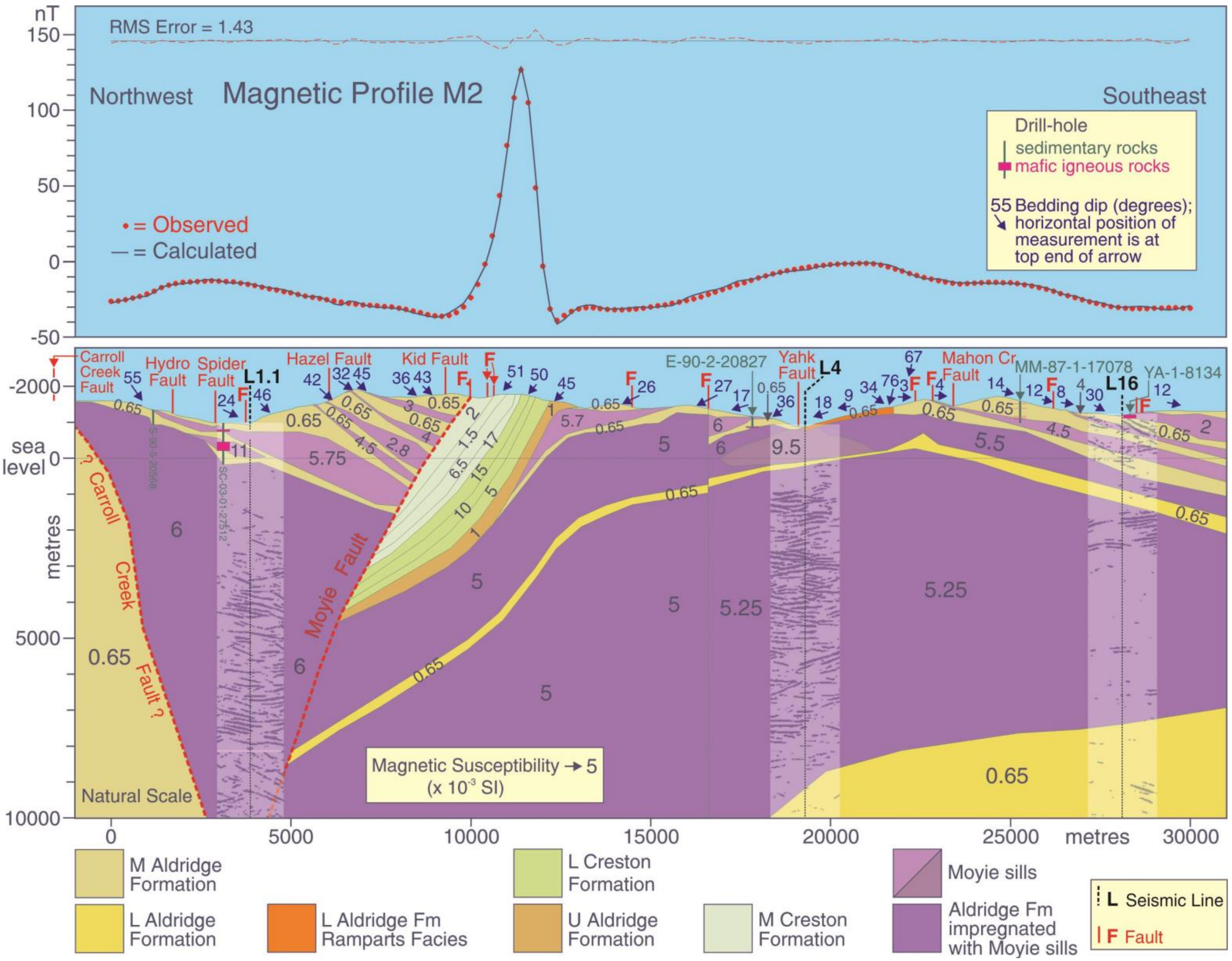

Figure 3. Magnetic model M2 crossing the northwest flank and core of the Moyie anticline.

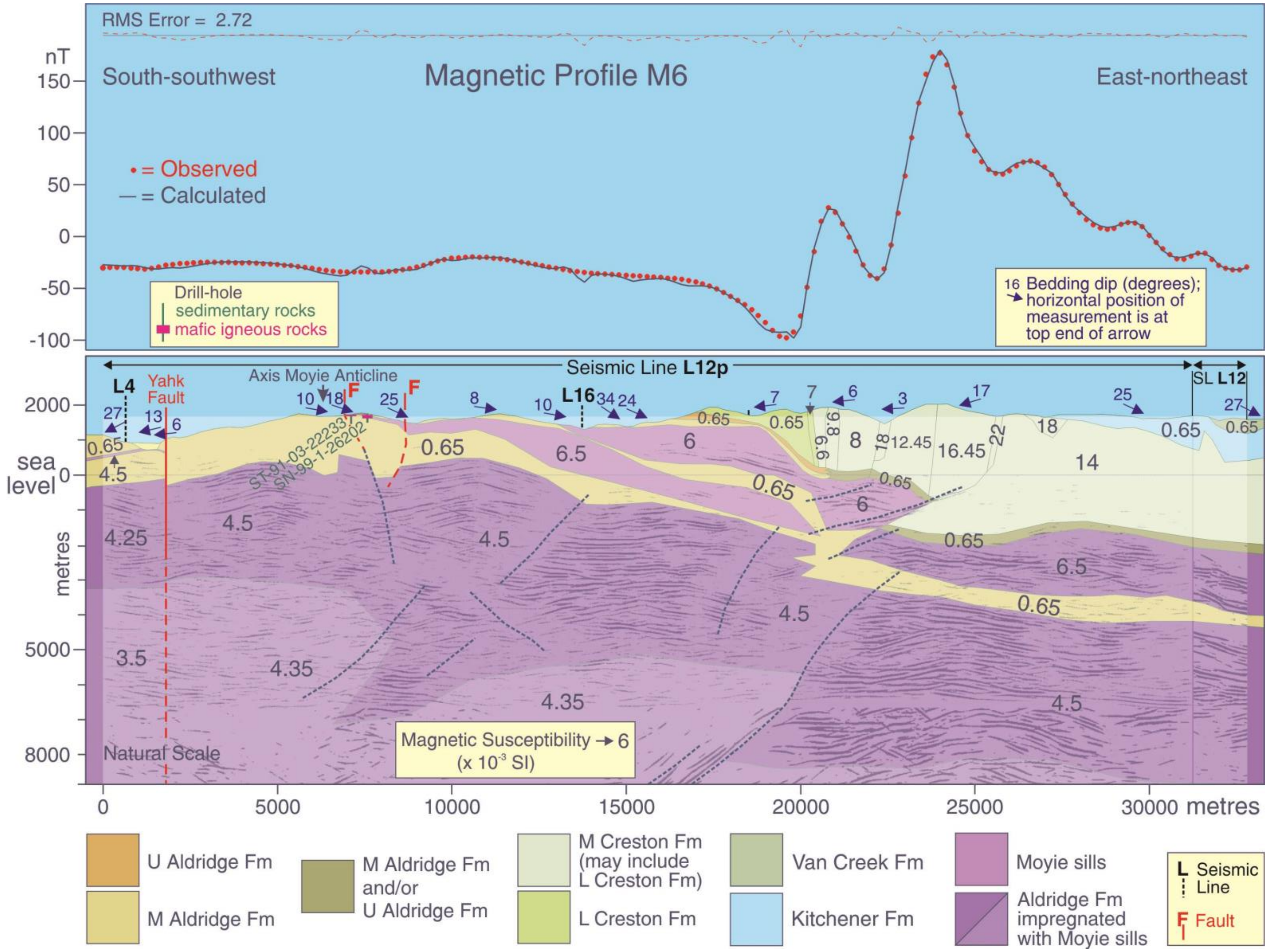

Figure 4. Magnetic model M6 crossing the eastern flank of the Moyie anticline.

oxide-Cu-Au deposits (IOCG) (Galicki, 2011; Staples et al., 2008; Stinson and Brown, 1995). Galicki (2011) also noted similarities to porphyry-related deposits. A single occurrence of SEDEX mineralization (Lowe et al., 1998) is located within about 1 km of the Iron Range Fault. A conspicuous linear magnetic high runs along the fault, and though distinct, the largest amplitude peak defined by the lower resolution data is only about 320 nT above general background. On the map of higher resolution data for the Yahk survey area (Figure 2), collected at a much lower altitude (60 m compared to 305 m for lower resolution data), the peak amplitude is a much larger 1130 nT (Lowe et al., 2000). These authors indicate the primary sources of the high to be 0.3 m to 5 m wide lenses of magnetite and hematite grading outward to wider and less brecciated, magnetite-rich zones.

The strong magnetic anomaly affords a means to investigate the deeper structure of the fault and models have been derived along two profiles, IR1 and IR2. Magnetic profile IR2 (Figure 5) runs east-southeastward across the northern part of the Iron Range Fault traversing most of the Goat River anticline (Figure 2). A portion of seismic line L1.1, lying between roughly 4.5 to 10 km to the south, is used constrain the deeper part of the model. It follows a somewhat tortuous path running essentially eastward from just north of Creston (Figure 1). Although at some distance from the magnetic profile IR2, it is believed that the projected associated seismic image presents a reasonable picture of reflectivity at depth below the profile, which helps define a large body of Aldridge Formation intruded by Moyie sills. The magnetic high is explained by several narrow contiguous vertical magnetic sheets on both sides of the fault, collectively ranging in width from about 500 m at surface to 700 m at depth, and having magnetic susceptibilities ranging from 12 x 10^{-3} to 42.2 x 10^{-3} SI. The bottoms of the sheets are arbitrarily terminated at ~5700 m below surface. Large, buried and moderately magnetic (susceptibilities range from 3.5 to 11 x 10^{-3} SI) Moyie sills have been modelled both sides of the central magnetic peak within the uppermost 2.5 km of crust to explain smaller amplitude magnetic highs. They present an antiformal pattern in keeping with the structure of the Goat River anticline. The model for IR1 crossing the southern part of the Iron Range Fault (Figure 2) similarly indicates that the Iron Range Fault zone is vertical and descends to several kilometres depth. It is much wider at surface and depth, about 870 m and 1760 m, respectively, than the zone for model IR2.

Models across the St. Mary Fault

The St. Mary Fault is probably a pre-mid Cretaceous imbricate thrust fault (Cook and Van der Velden, 1995). Geological maps present it as a thrust fault with its upthrust side to the north, e.g., Brown and MacLeod (2011b, c). The fault is portrayed as a thrust fault dipping roughly 30^{O} northward along the line of section of a southwest-northeast reflection seismic line (Van der Velden and Cook, 1996), though no reflections are present in approximately the uppermost 3 km of the seismic image.

The high resolution coverage for the St. Mary River area (Figure 2) displays a belt of prominent magnetic anomalies along the fault, mainly to the south, but also straddling it. No singular magnetic anomaly follows the length of the fault, but certain anomalies have

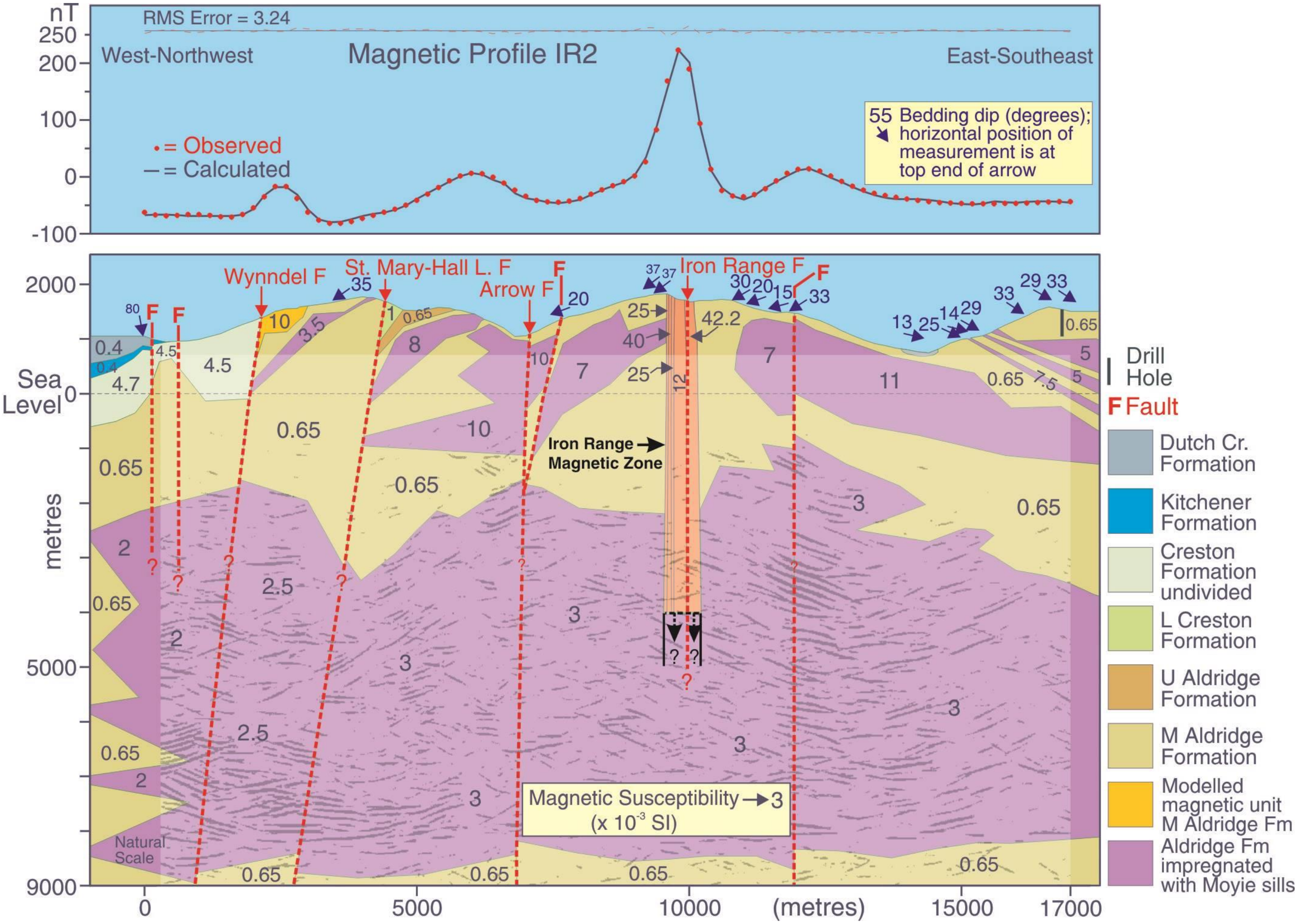

Figure 5. Magnetic model IR2 crossing the Iron Range Fault.

steep gradients that coincide with the fault. Three were selected for modelling with a view to obtaining information on the dip of the fault in the uppermost few kilometres of crust. The profile lines crossing them (S1, S2, S3) are shown in Figure 2, derived models for which were described by Thomas et al. (2013); a model for S3 is shown in Figure 6.

A strong magnetic high straddles the St. Mary Fault very close to its intersection with the Perry Creek Fault (Figure 6). It coincides with sedimentary rocks of the Middle Aldridge Formation to the northwest and Middle Creston Formation to the southeast. The source of the high is most probably a magnetite-rich horizon(s) in the latter formation. Presumed magnetite-rich rocks of the Middle Creston Formation are modelled to extend roughly 700 m northwest from the St. Mary Fault beneath a thin wedge (maximum thickness ~150 m) of Middle Aldridge Formation overlying the St. Mary Fault. By this interpretation the St. Mary Fault dips ~20^{O} northwest (measured at natural scale; vertical exaggeration in Figure 6 is 0.3). Steeply dipping magnetic horizons in the Middle Creston Formation beneath and south of the St. Mary Fault are truncated by a southeast-dipping contact with underlying Middle Aldridge Formation. This dips very steeply at 80^{O} in the uppermost 1 km, but at greater depth has an overall dip of about 55^{O}. It may represent a southeast-dipping fault. The steep dips modelled within the Middle Creston Formation (~75^{O}) seem reasonable, given steep dips ranging from 89^{O} to 60^{O} in the Middle Aldridge Formation to the northwest, and from 64^{O} to 75^{O} approximately 2 km along strike from the profile in the Middle Creston Formation.

If the interpretation of the St. Mary Fault in model S3 as a gently northward-dipping thrust is correct, it differs significantly from the models for S1 and S2 where boundaries of magnetic units at or very close to the St. Mary Fault dip southward at 85^{O} and 88^{O}, respectively. The difference in S3 is perhaps influenced by the proximity of the profile to the point of dextral displacement of the St. Mary Fault along the Perry Creek Fault (Figure 2).

Conclusions

The widespread distribution of prominent magnetic anomalies throughout the Purcell Anticlinorium, some associated with major structures, provides an independent perspective on 3D crustal structure. Modelling of the Moyie anticline has defined a magnetic “wedge” of mainly Creston Formation rocks along the Moyie Fault which provides information on the dip of the fault and estimates of minimum dip-slip displacement. The eastern flank of the anticline displays a generally monoclinal, conformable stratigraphy along its length, though apparently it is disrupted by faulting in at least one location. Magnetic modelling reinforces the case for distribution of Moyie sills in the upper crust over vertical distances ranging from about 8 to 11.5 km, which supports Ainsworth’s (2009) proposal that a large gravity high associated with the Moyie anticline is related to high density Moyie sills at relatively shallow depths, rather than to a deeper high density basement core of the anticline. A strong magnetic high associated with the Iron Range Fault suggests that relatively magnetic rocks are

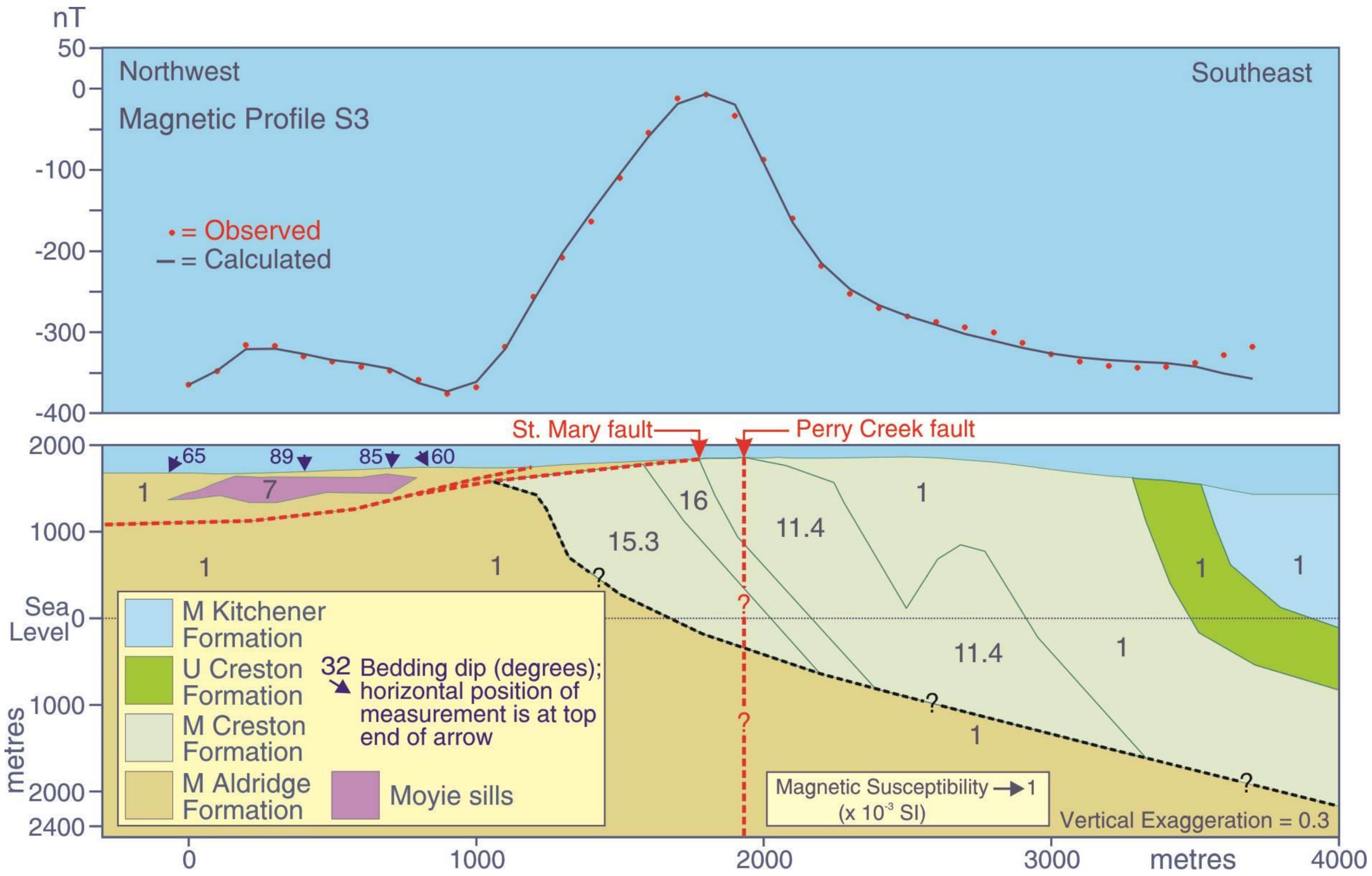

Figure 6. Magnetic model S3 crossing the St. Mary Fault.

distributed in a vertical zone much wider (500 m to 1760 m based on two models) than the 10 to 150 m width of deformation and mineralization reported by Stinson and Brown (1995), though Brown et al. (1994) describe the Iron Range Fault zone as “a series of faults across about a 1-kilometre width”. Modelling along the St. Mary Fault provided different scenarios with the possibility of a near-vertical attitude in some locations and a gently-dipping thrust in another.

Magnetic models have provided a different perspective on some structural features, and while not necessarily definitive they provide insights for consideration and possibly will raise questions that may prompt further research.

Implications for Exploration

On a relatively local scale the magnetic models provide new and deep perspectives on the individual investigated structures. On a regional scale they contribute to a three-dimensional model of a large portion of the Purcell Anticlinorium (de Kemp et al., 2015). The anticlinorium hosted one of the world’s largest SEDEX deposits, the now depleted Sullivan orebody. It also hosts many polymetallic mineralized showings and several polymetallic past producers (MapPlace, 2015). In general terms, the presented deep magnetic models may outline certain facets of deeper geology that combined with other information and geological and/or geochemical models, could influence exploration strategies.

More specifically, the distribution of Moyie sills between the surface and depths up to 12 km has been modelled in the Moyie anticline using robust seismic constraints. There has been significant discussion of the role of Moyie sills as a heat source for hydrothermal activity associated with development of the Sullivan deposit. Anderson and Goodfellow (2000) concluded that heat from the intrusion of one group of sills may have triggered such activity. A clearer picture of the distribution of these sills may thus have a bearing on exploration models investigating centres of potentially enhanced hydrothermal activity.

Models along the Iron Range Fault indicate that strongly magnetic rocks that include magnetite- and hematite-rich lenses and zones form a vertical unit that is significantly wider (500 to 1760 m) than a 10 to 150 m wide zone of deformation and mineralization reported by Stinson and Brown (1995). Depending on other geological factors, this result suggests a considerably larger target for exploration of the potential types of mineralization associated with the structure (e.g., Galicki, 2011).

Along the St. Mary Fault selection of magnetic profiles was governed by the presence of an associated magnetic anomaly. Three anomalies having potential to shed light on the nature of the fault were selected for modelling, but the associated geology differs. The model displayed for profile S3 (Figures 2, 6) indicates that at this location the fault is a gently northwest-dipping (~20^{O}) thrust fault. In models derived for two other profiles, boundaries of magnetic units at or very close to the St. Mary Fault dip southward at 85^{O} and 88^{O}. There are only a few metallic mineral showings close to the fault in the area of the profiles, and only one past producer and one developed prospect (Brown et al., 2011c). Although perhaps not a high priority area for exploration, the various magnetic models show that an understanding of local structure is mandatory given the possible range of fault attitudes indicated by the magnetic models.

Future Work

Proposed Modelling

Preliminary models have been created of the west flank of the Purcell Anticlinorium, west side of the Hall Lake Block, where high resolution magnetic data from the St. Mary River survey define many prominent linear anomalies (Figure 2). Many narrow near-vertical magnetic units extending within the uppermost 2 km of crust are modelled. Many lie within the Creston Formation providing insight into the internal structure and possible compositional variation of this formation. More modelling will be conducted on this western flank. Prominent linear anomalies near the Sullivan mine and within the St. Mary block will also be targeted. In addition to the focus on magnetic anomalies, modelling of airborne gravity gradiometer data along the Iron Range Fault in collaboration with Eagle Plains Resources Ltd., which kindly made the gravity data available, is in progress.

Acknowledgements

Over the course of several years many people have afforded various kinds of advice, assistance and data. I thank Suzanne Paradis, Geological Survey of Canada, leader of the SEDEX component of TGI4 for continuing support. Thanks also to Geological Survey of Canada associates Eric de Kemp, Carmel Lowe, John Lydon and Ernst Schetselaar, and to Jim Logan, British Columbia Geological Survey and Paul Ransom, Consulting Geologist, Cranbrook for consultations and data.

I thank my colleague Warner Miles, Geological Survey of Canada for a constructive review of this manuscript.

References

Ainsworth, H.L., 2009, Structure of the Moyie Anticline delineated on a grid of reflection seismic profiles in southeastern British Columbia: M.Sc. thesis, University of Calgary, Calgary, Alberta, 71 p.

Anderson, H.E., and Goodfellow, W.D., 2000, Geochemistry and isotope chemistry of the Moyie sills: Implications for the early tectonic setting of the Mesoproterozoic Purcell basin. Chapter 17 *in* Lydon, J.W., Höy, T., Slack, J.F., and Knapp, M.E., ed., The geological environment of the Sullivan deposit, British Columbia: Geological Association of Canada, Mineral Deposits Division, Special Publication no. 1, p. 302-321.

Brown, D.A., Bradford, J.A., Melville, D.M., Legun, A.S., and Anderson, D., 1994, Geology and mineral deposits of Purcell Supergroup in Yahk map area, southeastern British Columbia (82F/1), *in* Grant, B., and Newell, J.M., ed., Geological Fieldwork 1993, A Summary of Field Activities and Current Research: British Columbia Ministry of Energy, Mines and Petroleum Resources, Geological Survey Branch Paper 1994-1, p. 129-151.

Brown, D.A., and MacLeod, R.F. (Compilers), 2011a, Geology, Boswell, British Columbia: Geological Survey of Canada, Open File 6310, Map at scale of 1: 50,000, doi: 10.4095/288546

Brown, D.A., and MacLeod, R.F. (Compilers), 2011b, Geology, Cranbrook, British Columbia: Geological Survey of Canada, Open File 6302, Map at scale of 1: 50,000, doi: 10.4095/288544

Brown, D.A., and MacLeod, R.F. (Compilers), 2011c, Geology, Skookumchuck, British Columbia: Geological Survey of Canada, Open File 6301, Map at scale of 1: 50,000, doi: 10.4095/288543

Brown, D.A., and MacLeod, R.F. (Compilers), 2011d, Geology, Yahk River, British Columbia: Geological Survey of Canada, Open File 6304, Map at scale of 1: 50,000, doi: 10.4095/288564

Brown, D.A., MacLeod, R.F., and Wagner, C.L. (Compilers), 2011a, Geology, Dewar Creek, British Columbia: Geological Survey of Canada, Open File 6305, Map at scale of 1: 50,000, doi: 10.4095/288563

Brown, D.A., MacLeod, R.F., and Wagner, C.L. (Compilers), 2011b, Geology, Kaslo, British Columbia: Geological Survey of Canada, Open File 6306, Map at scale of 1: 50,000, doi: 10.4095/288565

Brown, D.A., MacLeod, R.F., and Wagner, C.L. (Compilers), 2011c, Geology, St. Mary Lake, British Columbia: Geological Survey of Canada, Open File 6308, Map at scale of 1: 50,000, doi: 10.4095/288567

Brown, D.A., MacLeod, R.F., Wagner, C.L., and Chow, W. (Compilers), 2011d, Geology, Crawford Bay, British Columbia: Geological Survey of Canada, Open File 6307, Map at scale of 1: 50,000, doi: 10.4095/288566

Brown, D.A., MacLeod, R.F., Wagner, C.L., and Chow, W. (Compilers), 2011e, Geology, Grassy Mountain, British Columbia: Geological Survey of Canada, Open File 6309, Map at scale of 1: 50,000, doi: 10.4095/288568

Brown, D.A., MacLeod, R.F., Wagner, C.L., and Chow, W. (Compilers), 2011f, Geology, Moyie Lake, British Columbia: Geological Survey of Canada, Open File 6303, Map at scale of 1: 50,000, doi: 10.4095/288545

Cook, F. A., and Van der Velden, A.J., 1995, Three-dimensional crustal structure of the Purcell Anticlinorium in the Cordillera of southwestern Canada: Geological Society of America Bulletin, v. 107, p. 642-664.

de Kemp, E.A., Schetselaar, E., Hillier, M., Lydon, J., Montsion, R., and Joseph, J., 2015, 3D modelling and data exploration of the Purcell-Sullivan SEDEX mineral system (Poster). AME BC Mineral Exploration Roundup 2015, January 26th-29th, Vancouver, British Columbia.

Galicki, M., 2011, Investigation of the iron-oxide mineralization at the Iron Range, southeastern British Columbia: M.Sc. Thesis, Simon Fraser University, Burnaby, British Columbia, 105 p.

Glombick, P., Brown, D.A., and MacLeod, R.F. (Compilers), 2011a, Geology, Creston, British Columbia: Geological Survey of Canada, Open File 6152 (revised), Map at scale of 1: 50,000, doi: 10.4095/288925

Glombick, P., Brown, D.A., and MacLeod, R.F. (Compilers), 2011b, Geology, Yahk, British Columbia: Geological Survey of Canada, Open File 6153 (revised), Map at scale of 1: 50,000, doi: 10.4095/288927

Gorton, M.P., Schandl, E.S., and Höy, T., 2000, Mineralogy and geochemistry of the Middle Proterozoic Moyie sills in southeastern British Columbia. Chapter 18 *in* Lydon, J.W., Höy, T., Slack, J.F., and Knapp, M.E., ed., The geological environment of the Sullivan deposit, British Columbia: Geological Association of Canada, Mineral Deposits Division, Special Publication no. 1, p. 322-335.

Höy, T., 1993, Geology of the Purcell Supergroup in the Fernie west-half map area, southeastern British Columbia: British Columbia Ministry of Energy, Mines and Petroleum Resources, Geological Survey Branch, Bulletin 84, 157 p. (includes map at 1:100,000 scale and geological cross sections).

Höy, T., Price, R.A., Legun, A., Grant, B., and Brown, D., 1995, Geoscience Map 1995-1, Purcell Supergroup, Southeastern British Columbia. Geological Compilation Map NTS 82G; 82F/E; 82J/SW; 82K/SE, Scale: 1:250,000: British Columbia Ministry of Energy, Mines and Petroleum Resources, Geological Survey Branch.

Lowe, C., Brown, D.A., Best, M.E., Woodfill, R., and Kennedy, C., 1998, New geophysical data from the Yahk map area, southeastern British Columbia - part of the East Kootenay multiparameter geophysical survey: Geological Survey of Canada, Current Research 1998-A, p. 207-216.

Lowe, C., Brown, D.A., Best, M.E., and Shives, R.B.K., 2000, High resolution geophysical survey of the Purcell Basin and Sullivan deposit: implications for bedrock geology and mineral exploration. Chapter 20 *in* Lydon, J.W., Höy, T., Slack, J.F., and Knapp, M.E., ed., The Geological Environment of the Sullivan deposit, British Columbia: Geological Association of Canada, Mineral Deposits Division, Special Publication no. 1, p. 355-369.

Lydon, J., 2000, A synopsis of the current understanding of the geological environment of the Sullivan deposit. Chapter 3 *in* Lydon, J.W., Höy, T., Slack, J.F., and Knapp, M.E., ed., The geological environment of the Sullivan deposit, British Columbia: Geological Association of Canada, Mineral Deposits Division, Special Publication no. 1, p. 12-31.

Lydon, J.W., Walker, R., and Anderson, E.H., 2000, Lithogeochemistry of the Aldridge Formation and the chemical effects of burial diagenesis. Chapter 9 *in* Lydon, J.W., Höy, T., Slack, J.F., and Knapp, M.E., ed., The Geological Environment of the Sullivan deposit, British Columbia: Geological Association of Canada, Mineral Deposits Division, Special Publication no. 1, p. 136-179.

Price, R.A., 1981, The Cordilleran foreland thrust and fold belt in the southern Canadian Rocky Mountains, *in* McClay, K.R., and Price, N.J., ed., Thrust and Nappe Tectonics: Geological Society of London, Special Publication no. 9, p. 427-448.

Price, R.A., and Sears, J.W., 2000, A preliminary palinspastic map of the Mesoproterozoic Belt-Purcell Supergroup, Canada and USA: Implications for the tectonic setting and structural evolution of the Purcell Anticlinorium and the Sullivan deposit. Chapter 5 *in* Lydon, J.W., Höy, T., Slack, J.F., and Knapp, M.E., ed., The Geological Environment of the Sullivan deposit, British Columbia: Geological Association of Canada, Mineral Deposits Division, Special Publication no. 1, p. 61-81.

Reesor, J.E., 1996, Geology of Kootenay Lake, British Columbia: Geological Survey of Canada, Map 1864A, Map at Scale of 1:100,000 (2 sheets), doi: 10.4095/207805

Schetselaar, E., de Kemp, E., Ransom, P., Buenviaje, R., Nguyen, K., Montsion, R., and Joseph, J., 2015, 3D drill hole database of the Purcell Anticlinorium. Geological Survey of Canada, Open File 7817, 14 p.

Sears, J.W., 1994, Thrust rotation of the Belt Basin, Canada and United States: Northwest Geology, v. 23, p. 81-91.

Staples, R.D., Marshall, D., Fecova, K., Downie, C.C., Thorkelson, D.J., and Loughrey, L., 2008, Structurally controlled iron oxide mineralization in the Iron Range Mountain and Mount Thompson region, British Columbia: Geological Survey of Canada, Current Research 2008-15, 10p.

Stinson, P., and Brown, D.A., 1995, Iron Range deposits, southeastern British Columbia (82F/1), *in* Grant, B., and Newell, J.M., ed., Geological Fieldwork 1994: British Columbia Ministry of Energy, Mines and Petroleum Resources, Geological Survey Branch, Paper 1995-1, p. 127-134.

Thomas, M.D., 2013, Magnetic susceptibilities in the Purcell Anticlinorium, southeastern British Columbia: Geological Survey of Canada, Current Research (Online) 2013-22, 2013; 22 p., doi: 10.4095/292912

Thomas, M.D., 2015 (in press), Magnetic models of the Moyie anticline, Purcell Anticlinorium, southeastern Canadian Cordillera: Canadian Journal of Earth Sciences.

Thomas, M.D., Schetselaar, E., and de Kemp, E., 2013, Magnetic contribution to 3D crustal modelling in the Purcell Anticlinorium, southeastern Cordillera (Poster): Geological Survey of Canada, Open File 7321, 2013; 1 sheet, doi:10.4095/292187

Van der Velden, A.J., and Cook, F.A., 1996, Structure and tectonic development of the southern Rocky Mountain trench: Tectonics, v. 15, p. 517-544.

Websites

MapPlace (2015). http://webmap.em.gov.bc.ca/mapplace/minpot/bcgs.cfm

Natural Resources Canada's Geoscience Data Repository, March 2015, http://gdr.agg.nrcan.gc.ca/gdrdap/dap/search-eng.php

TGI-4 Sediment-hosted Zn-Pb Deposits: Research Highlights

S. Paradis
Geological Survey of Canada, 9860 West Saanich Road, Sidney, BC, V8L 4B2
Suzanne.paradis@NRcan-RNcan.gc.ca

Introduction

The genetic model for SEDimentary EXhalative (SEDEX) deposits, on which most modern exploration strategies for this deposit type, was formulated more than 30 years ago. New data collected during the Targeted Geoscience Initiative 4 (TGI-4) program, a five-year (2010-2015) collaborative federal geoscience program, indicates that significant changes to several concepts behind the genetic model need to be made. This should lead to more realistic and efficient exploration strategies and exploration techniques. In doing so, we achieves the goal of the TGI-4 program, which was to provide the mining and exploration industry with new geoscience knowledge and innovative techniques to target buried deposits more effectively.

The term "SEDEX" has a genetic connotation, implying that the sulphide deposit formed on the sea floor from exhaled ore fluids. For lack of better terminology, the term is used in this open file despite the evidence generated by the project (e.g. Magnall et al., 2015; Gadd et al., 2015) that subsurface deposition and replacement is a major process in the formation of SEDEX deposits, at least those of the MacMillan Pass and Howard's Pass districts.

Objectives

The main objectives of the "TGI-4 SEDEX" project" were to:

- characterize the physico-geochemical processes of the hydrothermal system related to sediment-hosted Zn-Pb deposits,
- identify new mineralogical, geochemical, and isotopic tools to vector to ore deposits,
- understand the processes that control surficial geochemical dispersion of metals around sediment-hosted Zn-Pb deposits, and
- develop new methods for regional-scale 3D geological extrapolation in sedimentary basins.

Research Activities

Most field work for research activities was carried out on three major sedimentary basins of western Canada, listed below (Figure 1 and Table 1).

- Mesoproterozoic Purcell Basin in southeastern British Columbia, which hosts the world-class Sullivan Pb-Zn-Ag deposit and other smaller deposits such as North Star and Kootenay King.
- Phanerozoic Selwyn Basin, containing the Howard's Pass and MacMillan Pass districts in Yukon, and the Prairie Creek district and Misty Creek Embayment in the Northwest Territories.

Recommended citation
Paradis, S., 2015. TGI-4 Sediment-hosted Zn-Pb deposits: Research highlights, *in* Paradis, S., ed., Targeted Geoscience Initiative 4: sediment-hosted Zn-Pb deposits: processes and implications for exploration; Geological Survey of Canada, Open File 7838, p. 287-297. doi:10.4095/296328

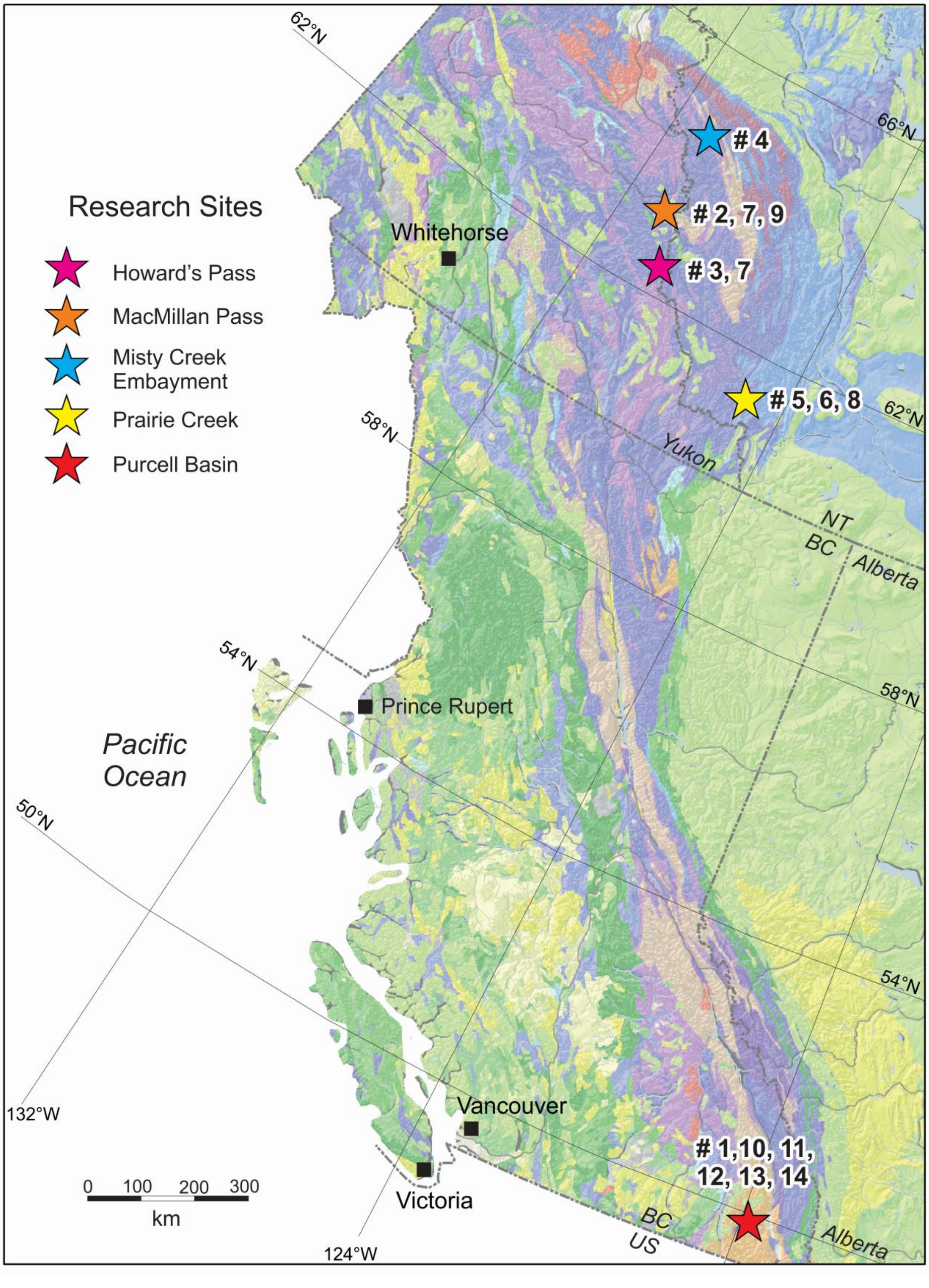

Figure 1. Location of research activities (corresponding to paper # in the open file) within the Purcell Basin and the Howard's Pass, MacMillan Pass, Misty Creek Embayment, and Prairie Creek districts of the Selwyn Basin. Refer to Table 1 for the list of papers (activities).

Table 1. List of papers presented in the open file. The papers are organized according to the four themes that follow the objectives of the "TGI-4 SEDEX" project. Location of research activities is shown in Fig. 1.

Physico-geochemical characteristics of the hydrothermal system of sediment-hosted Zn-Pb deposits

Paper # 1: Lydon, J.W. The leachability of metals from sedimentary rocks.

Paper # 2: Magnall, J.M., Stern, R.A., Gleeson, S.A, and Paradis, S. Widespread euxinic conditions are not a prerequisite for sediment-hosted base metal (Pb-Zn-Ba) mineralization at Macmillan Pass, Yukon.

Paper # 3: Gadd M.G., Layton-Matthews, D., Peter, J.M., and Paradis, S. In situ trace element and sulphur isotope analyses of pyrite constrain timing of mineralization and sources of sulphur in the Howard's Pass SEDEX Zn-Pb District, Yukon.

Mineralogical, geochemical, and isotopic tools to vector to sediment-hosted Zn-Pb deposits

Paper #4: Turner, E.C. Base-metal enrichment in Stage-5 (mid-Cambrian) black shale of the Hess River Formation, Misty Creek Embayment, Selwyn Basin.

Paper #5: Taylor, B.E., Paradis, S., Falck, H., and Wing, B. In situ sulphur isotope study of the Prairie. Creek deposit, Southern Mackenzie Mountains, Northwest Territories: Deciphering the conundrum of three deposit styles in one.

Paper #6: Paradis, S. Sulphides and nonsulphides of the Prairie Creek district; update on the isotope geochemistry.

Paper #7: Peter J.M., Layton-Matthews, D., Gadd, M.G., Gill, S., Baker, S., Plett, S., and Paradis, S. Application of visible-near infrared and short wave infrared spectroscopy to sediment-hosted Zn-Pb deposit exploration in the Selwyn Basin, Yukon.

Processes controlling the surficial geochemical dispersion of metals around sediment-hosted Zn-Pb deposits

Paper #8: Stavinga, D.B, Jamieson, H., Paradis, S., and Falck, H. Geochemical and mineralogical controls on metal(loid) mobility in the Oxide Zone at Prairie Creek, Northwest Territories.

Paper #9: Bryson, S.E., Fortin, D., McCurdy, M.W., and Nyheim-Rivet, A. Geochemical signatures of the South MacMillan River in the MacMillan Pass, Yukon, including drainages from the Tom and Jason Pb-Zn deposits.

Regional-scale 3D geological modelling of the Purcell Basin, southern British Columbia

Paper #10: de Kemp, E.A., Schetselaar, E.M., Hillier, M.J., Lydon, J.W., Ransom, P.W., Montsion, R. and Joseph, J. 3D geological modelling of the Sullivan time horizon, Purcell Anticlinorium and Sullivan Mine, East Kootenay region, southeastern British Columbia.

Paper #11: Schetselaar, E.M., de Kemp, E.A., Ransom, P.W., Buenviaje, R., Nguyen, K., Montsion R. and Joseph, J. Drillhole database compilation from legacy archives in support of 3D geological modelling and mineral exploration in the Purcell Anticlinorium, British Columbia.

Paper #12: Montsion, R., de Kemp, E.A., Lydon, J.W., Ransom, P.W., and Joseph, J. 3D stratigraphic, structural and metal zonation modelling of the Sullivan Mine, Kimberley, British Columbia.

Paper # 13: Hillier, M.J., de Kemp, E.A., and Schetselaar, E.M. Implicit 3D modelling of geological surfaces with the generalized radial basis functions (GRBF) algorithm.

Paper #14: Thomas, M.D. Magnetic modelling insights into the third dimension of the Purcell Anticlinorium.

- Western Canada Sedimentary Basin of Saskatchewan, Alberta and British Columbia, which hosts metalliferous brines.

Other research activities were not area specific, and included a spectrum of activities ranging from innovative laboratory techniques to devising new mathematical algorithms for 3-D geological modelling.

Physico-geochemical processes of the hydrothermal system related to sediment-hosted Zn-Pb deposits

Most models explaining the origin of SEDEX deposits envisage that metals were derived from the basinal sediments hosting the deposits (Lydon et al., 2000; Goodfellow and Lydon, 2007; Emsbo, 2009; Wilkinson, 2014). As part of this project, Lydon (2015) tested the leachability of metals and other elements on outcrop and core samples of marine sedimentary rocks at different stages of burial metamorphism. The samples were collected along a transect across western Canada, stretching from Mesozoic rocks of the Western Canada Sedimentary Basin in Saskatchewan, via Paleozoic and Mesoproterozoic rocks of eastern British Columbia, to modern ocean sediments west of Vancouver Island. His findings indicate that nearly all the Zn, Pb, and Cu in fine-grained sedimentary rocks are contained within the structure of the rock-forming minerals, and not loosely adsorbed on to the surfaces of clays, iron or manganese oxides, or organic matter, as has been widely assumed in the scientific literature on the generation of ore fluids. Considering the low reactive capacity of pore fluids at the natural low water/rock ratios of sedimentary rocks, his results indicate that ore fluids containing >1 ppm metal can only be produced during leaching windows provided by metamorphic mineralogical transformations that are driven by increasing temperature and pressure during burial.

Historically, global euxinic conditions have been considered a pre-requisite for the formation of the SEDEX deposits of the Howard’s Pass and Macmillan Pass districts in the Selwyn Basin (Goodfellow and Jonasson, 1984; Goodfellow, 1987, 2004, 2007). This view considered the metal trap to be reduced sulphur in the marine water column produced by near-quantitative bacterial reduction of seawater sulphate. Research of Magnall et al. (2015) indicates that at MacMillan Pass, precipitation of base metal sulphides was mostly below the sediment water interface rather than from a stratified euxinic water column. The mineral paragenesis of the MacMillan Pass deposits shows that barite and two generations of pyrite formed during early diagenesis, pre-dating the hydrothermal sulphides (pyrite, sphalerite and galena), which replace the diagenetic barite-pyrite assemblage. This suggests that one potential sulphur source would be the recycling of barite-sulphur by the hydrothermal fluid. At Howard’s Pass, the research of Gadd et al. (2015) is based on detailed field and petrographic observations and LA-ICP-MS (laser ablation-inductively coupled plasma-mass spectrometry) and SIMS (secondary ion mass spectrometry) geochemical analyses. Their data shows that mineral paragenesis is complex and involves several generations of pyrite (synsedimentary to early diagenetic, diagenetic and metamorphic). The variation of minor and trace elements of pyrite mimics the textural characteristics of the grains. The base metal sulphides post-date the formation of the synsedimentary-early diagenetic pyrite and therefore interpreted to be of diagenetic origin, similar to the MacMillan Pass deposits (Magnall et al., 2015). In situ sulphur isotope microanalyses done on galena, and several generations of pyrite revealed distinct negative and positive values that reflect the contribution of bacterially reduced (negative) and thermochemically reduced (positive) seawater sulphate. Importantly, the earliest pyrite generation yields negative sulphur isotope values, whereas the later diagenetic pyrite and galena yields positive ones in mineralized strata. The model for the Howard's Pass deposits invoked by Gadd et al. (2015) calls for dense, bottom-hugging metalliferous brines that were exhaled in pulses from a submarine vent distal to the present location of the deposit. The hydrothermal pulses were related to the reactivation of growth faults. The brines migrated to, and eventually settled into, a bathymetric low (i.e. the Howard's Pass sub-basin), and percolated downwards through, unconsolidated sulphidic carbonaceous muds and precipitated metals.

Mineralogical, geochemical, and isotopic tools to vector to ore deposits

Deep-water turbiditic limestone of the Cambrian Hess River Formation in the Misty Creek Embayment (MCE) of the Selwyn Basin contains a >20 m-thick black shale interval with elevated base metal and barium content which constitute geochemical evidence of hydrothermal venting (Turner, 2015). Carbon isotope stratigraphy of the formation indicates that the black shale interval was deposited in mid-Cambrian. This depositional age may be identical to that of strata hosting SEDEX mineralization in the Anvil District, Yukon Territory (YT). The MCE is remote and has received very little exploration attention, but its litho- and chemostratigraphic characteristics suggest potential for SEDEX mineralization.

The Prairie Creek district, located in another embayment of the Selwyn Basin, hosts three styles of sediment-hosted Zn-Pb-Ag mineralization: classic (open-space filling) Mississippi Valley-type (MVT), stratabound replacement sulphides, and quartz-carbonate-sulphide veins (Taylor et al., 2015; Paradis, 2015). Preliminary in situ sulphur isotope analyses reveal similarity in $\delta^{34}S$ between the stratabound [18.4 to 26.8‰ (avg. 22‰)] and vein [19.6 to 21.7‰ (avg. 20.3‰)] sulphides, suggesting a connection between the two (Taylor et al., 2015). However, the MVT sulphides have lower $\delta^{34}S$ values [12.9 to 17.1‰ (avg. 15.2‰)], and are therefore not connected (in terms of sulphur source) to the stratabound replacement sulphides. The principal stratabound sulphide lens (SD1) records a variation in calculated isotopic temperatures, from ~250°C near the centre of the lens and close to the vein system, and cooler values of ~150°C towards the margins of the sulphide lens. This suggests that thermal gradients can be potentially used to vector towards centers of mineralizing systems, which would increase the efficiency of deposit scale mineral exploration.

Another way to vector towards base metal mineralization was demonstrated by Peter et al. (2015) using the visible-near infrared and short wave infrared spectroscopy (VNIR-SWIR) on sediments of the Howard's Pass and MacMillan Pass districts. In the Howard's Pass District, the Active member of the Duo Lake Formation, hosting the Zn-Pb mineralization, is spectrally weak to unresponsive, except in and adjacent to significant mineralization. The spectra of sediments spatially associated with the base metal sulphide mineralization include siderite, montmorillonite, and phengite, and are also characterized by high mean spectral reflectances. A similar pattern occurs in the MacMillan Pass District, where siderite, muscovite, phengite and montmorillonite are spectrally identified within the feeder zone of the Tom Pb-Zn-Ba deposit. At the base of the stratiform mineralization overlying the feeder zone, there is a 5m-wide interval of siderite-montmorillonite that has high reflectance values, but the immediate hangingwall and footwall rocks to mineralization do not have a spectral expression.

Processes controlling the surficial geochemical dispersion of metals around sediment-hosted Zn-Pb deposits

The third part of this open file documents the surficial geochemical dispersion of Zn, Pb, and Ag (±Cu, ±As, ±Sb, ±Cd, ±Se, ±Hg) around sediment-hosted Zn-Pb deposits of the Prairie Creek (Stavinga et al., 2015) and Macmillan Pass (Bryson et al., 2015) districts. Mobility of these elements in near surface environments is important from an economic and environmental point of view. At Prairie Creek, the oxidized upper portion of the quartz-carbonate-sulphide veins forms high grade zones rich in smithsonite ($ZnCO_3$), cerussite ($PbCO_3$), and other secondary metal carbonates, arsenates, and sulphides (Paradis, 2015; Stavinga et al., 2015). These secondary minerals represent a significant resource and also a potential component of future mine waste material. In the short term, the near-neutral pH conditions of the mine waste dumps, trace metal(loid)s will be retained in solids. In the long term, oxidation and dissolution of the secondary metal carbonates, arsenates, and sulphides will affect the eH and pH in the mine waste setting, which could significantly increase metal release in the environment.

At Macmillan Pass, the geochemical signatures of stream waters of a system draining the Tom and Jason Zn-Pb deposits and the surrounding barren shales of the Devonian Earn Group vary widely in dissolved metal concentrations and pH values (2.9 to 8.2) (Bryson et al., 2015). Streams draining the Tom and Jason deposits are acidic (pH = 3.0) and neutral, respectively. The Tom deposit drainage contains 14,575 ppb dissolved Zn, and 33.6 ppb dissolved Pb. The fine sediment fraction of the drainage system contains 549.4 ppm Zn and 483.1 ppm Pb, which means that the presence of the mineral deposits would be easily recognized during an exploration geochemical program. Neutral streams (pH = 7.7) draining the Jason deposit have overall lower metal concentrations, but do show elevated zinc (470 ppm) and lead (53 ppm) in the fine sediment fraction downstream from the deposit.

Regional-scale 3D geological modelling of the Purcell Basin

Regional-scale 3D modelling enhances our geological understanding of the subsurface to explore for mineral deposits occurring at depth. The challenge is to extrapolate information available in densely drilled mine sites to regional 3D models where subsurface data is sparse. A series of papers (de Kemp et al., 2015; Hillier et al., 2015; Montsion et al., 2015; Schetselaar et al., 2015) present innovative methods used for regional-scale 3D geological modelling of the Purcell Anticlinorium in BC, which host the world-class Sullivan Pb-Zn-Ag deposit. To achieve a regional-scale 3D model, integration of geological map, drillhole and geophysical data (Thomas, 2015) was leveraged in a 3D environment to support interpretation of the entire ore system, thereby increasing the potential for deep discovery.

Implications for Exploration

Mineral exploration is guided by deposit models, and therefore providing the industry with accurate and up-to-date genetic models is essential for the industry to formulate the most efficient exploration programs targeting these deposits across Canada. Key factors identified during the course of the project and described in this open file which have potential application to improve the success rate of the search for new deposits include:

Genetic implications - Physico-geochemical processes of the hydrothermal system:

- Maximum leaching of metals, notably Zn and Pb by chloride brines in SEDEX/MVT systems is restricted to the 90-130ºC smectite-illite thermal transition window of burial diagenesis (Lydon, 2015).
- SEDEX/MVT ore systems can develop only in sedimentary basins with a prior history of evaporitic conditions that existed within the basin or adjacent carbonate platform (Lydon, 2015).
- Regional euxinic condition in the Selwyn Basin is not a prerequisite for the formation of SEDEX deposits (Magnall et al., 2015).
- Howard's Pass and MacMillan Pass sulphide deposits are diagenetic, and not syngenetic as previously suggested, and the bulk of sulphides (± barite) formed subseafloor (Gadd et al., 2015; Magnall et al., 2015). Therefore exploration for SEDEX deposits in Howard's Pass and MacMillan Pass districts should not be limited to specific stratigraphic units.

Mineralogical, geochemical, and isotopic tools to vector to ore:

- Detailed petrographic and geochemical examinations of sulphide minerals can yield valuable information about the hydrothermal processes involved in sediment-hosted Zn-Pb formation (Gadd et al., 2015; Magnall et al., 2015). For example, several generations of pyrite can be recognized; and sulphur isotopes and minor and trace elements mimic the zonation within pyrite grains. Ore-stage diagenetic pyrite that are texturally sooty (i.e. inclusion-rich) and composed of fine-grained aggregates, and bedded (laminated) and nodular pyrite sequestered several trace elements (e.g. Tl, As, Sb and possibly Mn) that can be indicative of hydrothermal input. Recrystallized metamorphic pyrite is usually poor in these trace elements.
- Carbon isotope stratigraphy can be a powerful tool to decipher the tectonic, stratigraphic, and metallogenic history of sedimentary basins, especially in correlating monotonous deep-water successions with sparse biostratigraphic control, or recognizing subtle differences between formations, and diachronous changes in sedimentation regimes. Using this tool within the deep-water lower Paleozoic strata of the Misty Creek Embayment in the northern Mackenzie Mountains (NT) allows establishment of a stratigraphic framework for the basin's evolution, including sediment accumulation rates and the recognition of periods

of sediment starvation and black shale deposition intervals (Turner, 2015). A black shale interval identified is possibly of the same age as the host rocks of the SEDEX Anvil District.

- In situ sulphur isotope analyses on the micrometer-scale can be used to document isotopic variation of minerals within their textural context. At Prairie Creek, Taylor et al. (2015) observed that isotopic disequilibrium is common within the three ore styles of the district: Mississippi Valley-type (MVT), stratabound replacement sulphides (SRS), and quartz-carbonate-sulphide veins. The preliminary in situ sulphur isotope analyses indicate both connections and disconnections between the three styles of mineralization (e.g. SRS and vein sulphides are related but SRS and MVT sulphides are not related in terms of sulphur sources). The in situ sulphur isotope analyses also suggest temperatures of formation (~170-250ºC for SRS) and recognize isotopic gradients within the main SRS lens that could indicate paleo-hydrothermal flow.
- Zinc or lead oxides, silicates and carbonates are direct indicators for nonsulphide base metal deposits and indirect indicator minerals of MVT, SEDEX, Irish-type, and vein-type Zn-Pb deposits (Paradis, 2015).
- Portable analytical tools, such as the VNIR-SWIR (short wavelength infrared spectrometer) can be of some use in the exploration for sediment-hosted Zn-Pb deposits in the Howard's Pass and MacMillan Pass districts of the Selwyn Basin (Peter et al., 2015). Siderite, muscovite, phengite, and montmorillonite are spatially associated with sulphide (± barite) mineralization and can be spectrally recognized, though the response may be quite muted.

Surficial geochemical dispersion of metals:

- Detailed microanalytical techniques [e.g. ICP-OES, SEM, EMP, LA-ICP-MS, XRD, synchrotron based trace element mapping, synchrotron-based grain-scale micro-X-ray Diffraction (µXRD), micro-X-ray Fluorescence (µXRF), and SEM-based MLA] can reveal the presence of valuable (e.g. Ag) or deleterious (e.g. Hg) elements in carbonate-hosted sulphide and nonsulphide minerals (Stavinga et al., 2015).
- Sediment and water samples from the South MacMillan River and streams from the Tom and Jason Pb-Zn-Ba deposits in the MacMillan Pass District, Yukon, are anomalous in ore-forming and ore-associated elements (Bryson et al., 2015). The Tom deposit stream waters are acidic and high in dissolved Pb and Zn, and the fine fraction of the stream silt sediments are high in Pb, signatures that can be readily detected by routine geochemical techniques. On the other hand, neutral pH streams draining the Jason deposit have low to moderate dissolved Pb and Zn; and high Pb concentrations in fine sediments. The water pH values should be taken into consideration in studies of metal dispersion, this would assure that careful analysis of drainage systems with low to moderate Pb and Zn values are investigated.

Regional-scale 3D geological modelling:

- Methods developed for 3D regional- and local-scale geological modelling of the Purcell Basin (de Kemp et al., 2015; Schetselaar et al., 2015; Hillier et al., 2015) and Sullivan Mine (Montsion et al., 2015) allow an objective assessment of basin architecture for distal indications of SEDEX deposits (e.g. synsedimentary faults, sub-basins, cryptic geophysical response, geochemical dispersal patterns, etc.).

- Magnetic anomalies are modelled to provide new and deep perspectives on individual structures (e.g. northwestern flank of the Moyie anticline, Moyie Fault, Moyie sills, St. Mary Fault, Iron Range Fault) within the Purcell Basin (Thomas, 2015). They also provided insights into the 3D modelling of the basin.

Future Work

The papers in this open file represent preliminary results, and will be superseded by more detailed documents in the form of refereed journal publications and student theses. Even at this early stage, it is apparent that significant research milestones were reached as to the knowledge of sediment-hosted Zn-Pb deposits, and the identification of new vectoring tools to point to mineralized domains within sedimentary basins. Although early results are impressive, many knowledge gaps remain in our understanding of these deposits. Thus, there is a need for new “SEDEX” geoscience studies in Canada as existing and future exploration, mining, and land-use challenges arise.

References

Bryson, S.E., Fortin, D., McCurdy, M.W., and Nyheim-Rivet, A., 2015, Geochemical signatures of the South MacMillan River in the MacMillan Pass, Yukon, including drainages from the Tom and Jason Pb-Zn deposits, *in* Paradis, S., ed., Targeted Geoscience Initiative 4: sediment-hosted Zn-Pb deposits: processes and implications for exploration: Geological Survey of Canada, Open File 7838, p. 188-203.

de Kemp, E.A., Schetselaar, E.M., Hillier, M.J., Lydon, J.W., Ransom, P.W., Montsion, R., and Joseph, J., 2015, 3D geological modelling of the Sullivan time horizon, Purcell Anticlinorium and Sullivan Mine, East Kootenay region, *in* Paradis, S., ed., Targeted Geoscience Initiative 4: sediment-hosted Zn-Pb deposits: processes and implications for exploration: Geological Survey of Canada, Open File 7838, p. 204-225.

Emsbo, P., 2009, Geologic criteria for the assessment of sedimentary exhalative (SEDEX) Zn-Pb-Ag deposits: U.S. Geological Survey, Open-File Report 2009-1209, 21p.

Gadd M.G., Layton-Matthews, D., Peter, J.M., and Paradis, S., 2015, In situ trace element and sulphur isotope analyses of pyrite constrain timing of mineralization and sources of sulphur in the Howard’s Pass SEDEX Zn-Pb District, Yukon, *in* Paradis, S., ed., Targeted Geoscience Initiative 4: sediment-hosted Zn-Pb deposits: processes and implications for exploration: Geological Survey of Canada, Open File 7838, p. 58-74.

Goodfellow, W.D., 1987, Anoxic stratified oceans as a source of sulphur in sediment-hosted stratiform Zn-Pb deposits (Selwyn Basin, Yukon, Canada): Chemical Geology, Isotope Geoscience Section, v. 65, p. 359-382.

Goodfellow, W.D., 2004, Geology, genesis, and exploration of SEDEX deposits, with emphasis on the Selwyn Basin, Canada, *in* Deb, M., and Goodfellow, W.D., ed., sediment-hosted lead-zinc sulphide deposits: attributes and models of some major deposits of India, Australia, and Canada: Delhi, India, Narosa Publishing House, p. 24-99.

Goodfellow, W.D., 2007, Base Metallogeny in the Selwyn Basin, Canada, *in* Goodfellow, W.D., ed., Mineral deposits of Canada: A synthesis of major deposit types, district metallogeny, the evolution of geological provinces, and exploration methods: Geological Association of Canada, Mineral Deposits Division, Special Publication no. 5, p. 553-579.

Goodfellow, W.D., and Jonasson, I.R., 1984, Ocean stagnation and ventilation defined by secular trends in pyrite and barite, Selwyn Basin, Yukon: Geology, v. 12, p. 583-586.

Goodfellow, W.D., and Lydon, J.W., 2007, Sedimentary exhalative (SEDEX) deposits, *in* Goodfellow, W.D., ed., Mineral deposits of Canada: A synthesis of major deposit types, district metallogeny, the evolution of geological provinces, and exploration methods: Geological Association of Canada, Mineral Deposits Division, Special Publication no. 5, p. 163-183.

Hillier, M.J., de Kemp, E.A., and Schetselaar, E.M., 2015, Implicit 3D modelling of geological surfaces with the generalized radial basis functions (GRBF) algorithm, *in* Paradis, S., ed., Targeted Geoscience Initiative 4: sediment-hosted Zn-Pb deposits: processes and implications for exploration: Geological Survey of Canada, Open File 7838, p. 253-266.

Lydon, J.W., 2015, The leachability of metals from sedimentary rocks, *in* Paradis, S., ed., Targeted Geoscience Initiative 4: sediment-hosted Zn-Pb deposits: processes and implications for exploration: Geological Survey of Canada, Open File 7838, p. 11-42.

Lydon, J.W., Walker, R., and Anderson, E.H., 2000, Lithogeochemistry of the Aldridge formation and the chemical effects of burial diagenesis, *in* Lydon, J.W., Höy, T., Knapp, M., and Slack, J., ed., The geological environment of the Sullivan deposit, British Columbia: Geological Association of Canada, Mineral Deposits Division, Special Publication no. 1, p. 137–179.

Magnall, J.M., Stern, R.A., Gleeson, S.A., and Paradis, S., 2015, Widespread euxinic conditions are not a prerequisite for sediment-hosted base metal (Pb-Zn-Ba) mineralization at Macmillan Pass, Yukon, *in* Paradis, S., ed., Targeted Geoscience Initiative 4: sediment-hosted Zn-Pb deposits: processes and implications for exploration: Geological Survey of Canada, Open File 7838, p. 43-57.

Montsion, R., de Kemp, E.A, Lydon, J.W, Ransom, P.W., and Joseph, J., 2015, 3D stratigraphic, structural and metal zonation modelling of the Sullivan Mine, Kimberley, British Columbia, *in* Paradis, S., ed., Targeted Geoscience Initiative 4: sediment-hosted Zn-Pb deposits: processes and implications for exploration: Geological Survey of Canada, Open File 7838, p. 236-252.

Paradis, S., 2015, Sulphides and nonsulphides of the Prairie Creek district; update on the isotope geochemistry, *in* Paradis, S., ed., Targeted Geoscience Initiative 4: sediment-hosted Zn-Pb deposits: processes and implications for exploration: Geological Survey of Canada, Open File 7838, p. 152-172.

Peter J.M., Layton-Matthews, D., Gadd, M.G., Gill, S., Baker, S., Plett, S., and Paradis, S., 2015, Application of visible-near infrared and short wave infrared spectroscopy to sediment-hosted Zn-Pb deposit exploration in the Selwyn Basin, Yukon, *in* Paradis, S., ed., Targeted Geoscience Initiative 4: sediment-hosted Zn-Pb deposits: processes and implications for exploration: Geological Survey of Canada, Open File 7838, p. 152-172.

Schetselaar, E.M., de Kemp, E.A., Ransom, P.W., Buenviaje, R., Nguyen, K., Montsion, R., and Joseph, J., 2015, Drillhole database compilation from legacy archives in support of 3D geological modelling and mineral exploration in the Purcell Anticlinorium, British Columbia, *in* Paradis, S., ed., Targeted Geoscience Initiative 4: sediment-hosted Zn-Pb deposits: processes and implications for exploration: Geological Survey of Canada, Open File 7838, p. 226-235.

Stavinga, D.B, Jamieson, H., Paradis, S., and Falck, H., 2015, Geochemical and mineralogical controls on metal(loid) mobility in the Oxide Zone at Prairie Creek, Northwest Territories, *in* Paradis, S., ed., Targeted Geoscience Initiative 4: sediment-hosted Zn-Pb deposits: processes and implications for exploration: Geological Survey of Canada, Open File 7838, p. 173-187.

Taylor, B.E., Paradis, S., Falck, H., and Wing, B., 2015, In situ sulphur isotope study of the Prairie Creek deposit, Southern Mackenzie Mountains, Northwest Territories: Deciphering the conundrum of three deposit styles in one, *in* Paradis, S., ed., Targeted Geoscience Initiative 4: sediment-hosted Zn-Pb deposits: processes and implications for exploration: Geological Survey of Canada, Open File 7838, p. 96-133.

Thomas, M.D., 2015, Magnetic modelling insights into the third dimension of the Purcell Anticlinorium, *in* Paradis, S., ed., Targeted Geoscience Initiative 4: sediment-hosted Zn-Pb deposits: processes and implications for exploration: Geological Survey of Canada, Open File 7838, p. 267-286.

Turner, E.C., 2015, Base-metal enrichment in Stage-5 (mid-Cambrian) black shale of the Hess River Formation, Misty Creek Embayment, Selwyn Basin, *in* Paradis, S., ed., Targeted Geoscience Initiative 4: sediment-hosted Zn-Pb deposits: processes and implications for exploration: Geological Survey of Canada, Open File 7838, p. 75-95.

Wilkinson, J.J., 2014, Sediment-hosted zinc-lead mineralization: Processes and perspectives, *in* Scott, S.D., ed., Geochemistry of mineral deposits: Treatise on geochemistry v. 13 (second edition), p. 219–249.